marine drugs

Special Issue Reprint

# Collagen and Chitin from Marine Resources and Their Interdisciplinary Applications

Edited by
Azizur Rahman

mdpi.com/journal/marinedrugs

MDPI

# Collagen and Chitin from Marine Resources and Their Interdisciplinary Applications

# Collagen and Chitin from Marine Resources and Their Interdisciplinary Applications

Editor

**Azizur Rahman**

MDPI

Basel • Beijing • Wuhan • Barcelona • Belgrade • Novi Sad • Cluj • Manchester

*Editor*
Azizur Rahman
University of Toronto
(ONRamp at UTE)
Toronto, ON
Canada

*Editorial Office*
MDPI AG
Grosspeteranlage 5
4052 Basel, Switzerland

This is a reprint of articles from the Special Issue published online in the open access journal *Marine Drugs* (ISSN 1660-3397) (available at: https://www.mdpi.com/journal/marinedrugs/special_issues/Z7JTMCG4F5).

For citation purposes, cite each article independently as indicated on the article page online and as indicated below:

Lastname, A.A.; Lastname, B.B. Article Title. *Journal Name* **Year**, *Volume Number*, Page Range.

**ISBN 978-3-7258-2553-0 (Hbk)**
**ISBN 978-3-7258-2554-7 (PDF)**
**doi.org/10.3390/books978-3-7258-2554-7**

Cover image courtesy of Azizur Rahman

# Contents

**About the Editor** . . . . . **vii**

**Preface** . . . . . **ix**

**Azizur Rahman**
Marine Collagen and Chitin: Promising Applications in Interdisciplinary Fields
Reprinted from: *Mar. Drugs* **2024**, *22*, 379, doi:10.3390/md22090379 . . . . . **1**

**Fang Luan, Zhenhua Xu, Kai Wang, Xin Qi and Zhanyong Guo**
Synthesis of Water-Soluble Sulfonated Chitin Derivatives for Potential Antioxidant and Antifungal Activity
Reprinted from: *Mar. Drugs* **2022**, *20*, 668, doi:10.3390/10.3390/md20110668 . . . . . **8**

**Kavitha Ganesan Nathan, Krishnamurithy Genasan and Tunku Kamarul**
Polyvinyl Alcohol-Chitosan Scaffold for Tissue Engineering and Regenerative Medicine Application: A Review
Reprinted from: *Mar. Drugs* **2023**, *21*, 304, doi:10.3390/md21050304 . . . . . **22**

**Azizur Rahman, Rameesha Rehmani, Diana Gabby Pirvu, Siqi Maggie Huang, Simron Puri and Mateo Arcos**
Unlocking the Therapeutic Potential of Marine Collagen: A Scientific Exploration for Delaying Skin Aging
Reprinted from: *Mar. Drugs* **2024**, *22*, 159, doi:10.3390/md22040159 . . . . . **40**

**Honghui Jiang, Yuanyuan Kong, Lili Song, Jing Liu and Zhihong Wang**
A Thermostable Type I Collagen from Swim Bladder of Silver Carp (*Hypophthalmichthys molitrix*)
Reprinted from: *Mar. Drugs* **2023**, *21*, 280, doi:10.3390/md21050280 . . . . . **56**

**Izabela Dziedzic, Alona Voronkina, Martyna Pajewska-Szmyt, Martyna Kotula, Anita Kubiak, Heike Meissner, et al.**
The Loss of Structural Integrity of 3D Chitin Scaffolds from *Aplysina aerophoba* Marine Demosponge after Treatment with LiOH
Reprinted from: *Mar. Drugs* **2023**, *21*, 334, doi:10.3390/md21060334 . . . . . **71**

**Nathanael D. Arnold, Daniel Garbe and Thomas B. Brück**
Proteomic and Transcriptomic Analyses to Decipher the Chitinolytic Response of *Jeongeupia* spp.
Reprinted from: *Mar. Drugs* **2023**, *21*, 448, doi:10.3390/md21080448 . . . . . **91**

**Anita Kubiak, Martyna Pajewska-Szmyt, Martyna Kotula, Bartosz Leśniewski, Alona Voronkina, Parvaneh Rahimi, et al.**
Spongin as a Unique 3D Template for the Development of Functional Iron-Based Composites Using Biomimetic Approach In Vitro
Reprinted from: *Mar. Drugs* **2023**, *21*, 460, doi:10.3390/md21090460 . . . . . **116**

**Tomas Duminis, Marcin Heljak, Wojciech Święszkowski, Alexander Ereskovsky, Izabela Dziedzic, Marek Nowicki, et al.**
On the Mechanical Properties of Microfibre-Based 3D Chitinous Scaffolds from Selected Verongiida Sponges
Reprinted from: *Mar. Drugs* **2023**, *21*, 463, doi:10.3390/md21090463 . . . . . **141**

**Marc Roig-Puche, Federico Lopez-Moya, Miguel Valverde-Urrea, Pablo Sanchez-Jerez, Luis Vicente Lopez-Llorca and Victoria Fernandez-Gonzalez**
Chitosan from Marine Amphipods Inhibits the Wilt Banana Pathogen *Fusarium oxysporum* f. sp. Cubense Tropical Race 4
Reprinted from: *Mar. Drugs* **2023**, *21*, 601, doi:10.3390/md21120601 . . . . . **158**

**Linqing Wang, Rui Guo, Xiaorui Liang, Yuting Ji, Jingjing Zhang, Guowei Gai and Zhanyong Guo**
Preparation and Antioxidant Activity of New Carboxymethyl Chitosan Derivatives Bearing Quinoline Groups
Reprinted from: *Mar. Drugs* **2023**, *21*, 606, doi:10.3390/md21120606 . . . . . **169**

**Wonhee Cho, Jeongjin Park, Jinhee Kim, Minhee Lee, So Jung Park, Kyung Seok Kim, et al.**
Low-Molecular-Weight Fish Collagen Peptide (Valine-Glycine-Proline-Hydroxyproline-Glycine-Proline-Alanine-Glycine) Prevents Osteoarthritis Symptoms in Chondrocytes and Monoiodoacetate-Injected Rats
Reprinted from: *Mar. Drugs* **2023**, *21*, 608, doi:10.3390/md21120608 . . . . . **190**

**Anna Paradowska-Stolarz, Marcin Mikulewicz, Joanna Laskowska, Bożena Karolewicz and Artur Owczarek**
The Importance of Chitosan Coatings in Dentistry
Reprinted from: *Mar. Drugs* **2023**, *21*, 613, doi:10.3390/md21120613 . . . . . **203**

**Miguel S. Rocha, Catarina F. Marques, Ana C. Carvalho, Eva Martins, Alexander Ereskovsky, Rui L. Reis and Tiago H. Silva**
The Characterization and Cytotoxic Evaluation of *Chondrosia reniformis* Collagen Isolated from Different Body Parts (Ectosome and Choanosome) Envisaging the Development of Biomaterials
Reprinted from: *Mar. Drugs* **2024**, *22*, 55, doi:10.3390/md22020055 . . . . . **217**

# About the Editor

**Azizur Rahman**

Dr. Azizur Rahman is a distinguished scientist and leader, currently serving as the Research Lead, President, and CEO of the Centre for Climate Change Research at the University of Toronto. He is also the founder and President of two innovative companies, AR Environmental Solutions and AR Biotech Canada, launched through the University of Toronto Entrepreneurship program.

Dr. Rahman is highly regarded for his pioneering contributions to science and research innovation, recognized through numerous prestigious awards. Among these honors is the Presidential Honorary Award for Scientists from the University of Ryukyus in Japan, the institution's highest accolade for groundbreaking research. He also received the Global Peer Review Award from the Web of Science Group in both 2018 and 2019, a testament to his international influence in research. Over his career, Dr. Rahman has been awarded more than 20 major national and international distinctions, including best paper awards and a gold medal. Most recently, in 2024, he was recognized as the most cited and viewed author in MDPI's scientific journals.

In addition to his scientific endeavors, Dr. Rahman is passionate about leveraging science to foster community development through innovation and entrepreneurship. His expertise drives impactful initiatives at the intersection of scientific research and social innovation. As a serial entrepreneur, Dr. Rahman has founded multiple companies and non-profit organizations dedicated to advancing scientific and social progress.

Dr. Azizur Rahman's career is marked by his unwavering commitment to research excellence and his dedication to using science as a tool for societal betterment. His work continues to inspire and catalyze significant advancements across various disciplines.

# Preface

Chitin and collagen stand as two of the most crucial biopolymers in nature, each playing a vital role in various biological processes and applications. Despite their different sources, these biopolymers share a remarkable similarity in their hierarchical structural organization, providing them with a wide range of uses across diverse fields such as medicine, environmental science, and agriculture.

Chitin, abundant in the exoskeletons of crustaceans and other organisms, represents an easily accessible biopolymer with significant potential. Collagen, on the other hand, is the primary fibrous structural protein found in the extracellular matrix and connective tissues of animals. Particularly abundant in marine organisms, collagen is highly valued for its contributions to biotechnology and medical applications.

This reprint highlights recent innovations involving both chitin and collagen, with a focus on their potential application across multiple interdisciplinary sectors. Furthermore, it compiles the latest scientific research and emerging trends, particularly in the realm of marine drugs, and showcases the advances made in the utilization of these two biopolymers.

I hope this reprint will provide valuable insights into the current state of applied research and inspire further innovation in the application of chitin and collagen.

**Azizur Rahman**
*Editor*

marine drugs

MDPI

*Editorial*

# Marine Collagen and Chitin: Promising Applications in Interdisciplinary Fields

**Azizur Rahman** [1,2,3]

[1] Centre for Climate Change Research, University of Toronto, ONRamp at UTE, Toronto, ON M5G 0C6, Canada; aziz@climatechangeresearch.ca or mazizur.rahman@utoronto.ca
[2] A.R. Environmental Solutions, ICUBE-University of Toronto, Mississauga, ON L5L 1C6, Canada
[3] AR Biotech Canada, Toronto, ON M2H 3P8, Canada

Marine collagen and chitin derived from marine organisms are gaining significant attention for their diverse applications across various fields. This Editorial explores the potential of these biopolymers in different interdisciplinary applications. Chitin and that enzymatically deacetylated to chitosan have many applications, including in the medical, environmental, and agricultural sectors [1–6]. Likewise, nature is a source of significant quantities of collagen, especially in marine organisms. Marine-based collagen contributes greatly to biotechnology products and medical applications [7–11]. Considering the importance of these two biopolymers and their multidisciplinary applications, I was interested in editing this Special Issue.

Highlighted below are the interdisciplinary applications of collagen and chitin:

## 1. Biomedical Applications

### *1.1. Wound Healing*

Collagen: Promotes cellular regeneration and provides a scaffold for new tissue formation [9,10].

Chitin: Exhibits antibacterial properties, reducing infection risks and enhancing healing.

### *1.2. Drug Delivery Systems*

Collagen: Used for targeted drug delivery due to its biocompatibility and ability to be engineered into nanoparticles.

Chitin: Chitosan, a derivative of chitin, forms hydrogels and nanoparticles, improving the controlled release of drugs.

### *1.3. Tissue Engineering*

Collagen: Supports the growth of various cell types and can be used to engineer tissues such as skin, bone, and cartilage.

Chitin: Provides structural integrity and can be combined with other materials for scaffolding in tissue engineering.

## 2. Cosmetic Industry

### *2.1. Anti-Aging Products*

Collagen: Hydrates the skin, improves elasticity, and reduces wrinkles.

Chitin: Enhances moisture retention and provides a protective barrier.

### *2.2. Hair and Nail Care*

Collagen: Strengthens hair and nails, promoting growth and resilience.

Chitin: Adds volume and shine to hair and protects nails from damage.

**Citation:** Rahman, A. Marine Collagen and Chitin: Promising Applications in Interdisciplinary Fields. *Mar. Drugs* **2024**, *22*, 379. https://doi.org/10.3390/md22090379

Received: 16 August 2024
Accepted: 21 August 2024
Published: 23 August 2024

**3. Environmental Applications**

*3.1. Biodegradable Materials*

Collagen: Used to produce biodegradable films and packaging materials.

Chitin: Forms biodegradable plastics and can be used in the production of eco-friendly materials.

*3.2. Waste Water Treatment*

Collagen: Acts as a flocculant, helping to aggregate and remove contaminants.

Chitin: Chitosan efficiently absorbs heavy metals and organic pollutants from water.

**4. Agricultural Sector**

*4.1. Soil Health*

Collagen: Improves soil structure and fertility when used as an amendment.

Chitin: Acts as a biopesticide and enhances the growth of beneficial microorganisms in the soil.

*4.2. Animal Feed*

Collagen: Enhances the nutritional quality of animal feed, promoting better growth and health.

Chitin: Improves gut health and immunity in livestock.

**5. Food Industry**

*5.1. Functional Foods*

Collagen: Used in supplements and health drinks for its joint and skin benefits.

Chitin: Acts as a dietary fiber, aiding in digestion and weight management.

*5.2. Food Packaging*

Collagen: Creates edible films that preserve food quality and extend shelf life.

Chitin: Chitosan coatings prevent microbial growth and spoilage.

This Special Issue, "**Collagen and Chitin from Marine Resources and Their Interdisciplinary Applications**", contains 10 original and 3 review articles. An overview of the research results and reviews of the existing public literature by the authors is provided, which can help readers find appropriate articles in their field of interest. The contributions are listed in the List of Contributions.

Contribution 1 provides valuable information for the establishment of *Chondrosia reniformis* as an ecological and biomedically relevant source of collagen and is paramount for the future development of marine collagen-based biomaterials.

Contribution 2 investigates the effect of low-molecular-weight fish collagen (valine-glycine-proline-hydroxyproline-glycine-proline-alanine-glycine; LMWCP) on $H_2O_2$- or LPS-treated primary chondrocytes and monoiodoacetate (MIA)-induced osteoarthritis rat models.

In contribution 3, the authors report the carboxymethyl chitosan derivatives in bearing quinoline groups that showed remarkable antioxidant ability and weak cytotoxicity, highlighting their potential use in food and medical applications. The results indicate that most of the derivatives exhibited strong free radical scavenging ability while also showing low cytotoxicity.

In contribution 4, the authors extract chitosan from marine amphipods associated with aquaculture facilities and test its use in crop protection. This new chitosan valorizes aquaculture residues and has the potential to manage diseases in food security crops such as bananas. This is the first time that chitosan has been obtained from biofouling amphipods.

In contribution 5, Ehrlich, H. and his team [12] report the mechanical properties of microfiber-based 3D chitinous scaffolds from selected Verongiida sponges. In this manuscript, the authors show that the scaffolds isolated from diverse representatives of

cultivated marine demosponges, which belong to the Verongiida order (Figure 1), remain candidates with high potential in biomedicine and bioinspired materials science.

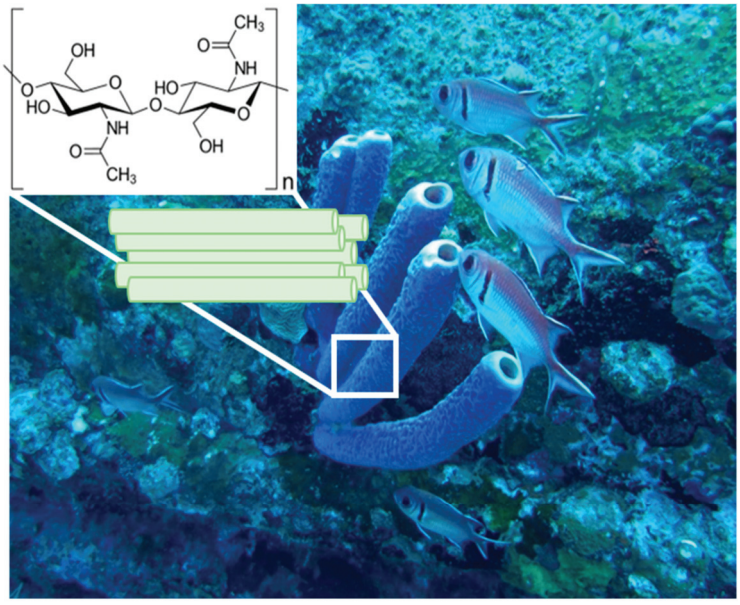


**Figure 1.** An underwater image of 30 cm long marine demosponges belonging to the Verongiida order in their original environment (photograph courtesy of Dr. V. Ivanenko).

In contribution 6, the authors highlight the interaction between biomaterial spongin and iron ions in marine environments due to biocorrosion, which leads to the occurrence of the biomineral lepidocrocite. For this purpose, a biomimetic approach for the creation of a new lepidocrocite-containing 3D spongin scaffold using artificial seawater and iron powder under laboratory conditions at 24 °C is described for the first time.

In contribution 7, the authors demonstrate a holistic model for the chitinolytic machinery of *Jeongeupia* spp. based on cumulative data found by conducting proteomic and transcriptomic analyses. In this study, the authors identified the involvement of over 350 unique enzymes and 570 unique genes in the catabolic chitin response of a Gram-negative bacterium through three-way systems biology.

Contribution 8 [13] shows a loss of structural integrity in 3D chitin scaffolds from a marine demosponge, *Aplysina aerophoba*, after treatment with LiOH. Figure 2 shows SEM images of the sponge chitin fibers isolated after NaOH treatment (a,c) and those after dissolution in LiOH solution (b,d). The difference in the structural integrity is clear. The surface of the NaOH-treated chitin scaffold is rough and monolithic (Figure 2a,c). The micrograph of the dissolved sponge chitin after freeze-drying presents a structure consisting of smooth layers (Figure 2b). A closer look at the disintegrated smooth surface reveals the presence of chitin nanofibers (Figure 2d).

Contribution 9 reports a thermostable type I collagen from a swim bladder of silver carp, *Hypophthalmichthys molitrix*. In this report, collagen from the swim bladder of silver carp and collagens from the swim bladders of grass carp, bovine pericardium, and mouse tail were extracted for comparison using the pepsin extraction method. SDS-PAGE, peptide maps, and amino acid composition identified the compositional differences in the isolated collagens. Their physicochemical properties were determined using ultraviolet–visible spectroscopic (UV) analysis, Fourier transform infrared spectroscopy (FTIR) analysis, and circular dichroism (CD) measurement. In addition, the thermal stability of the isolated collagens was confirmed by CD. Also, the fibril-forming and antioxidant capacities of the

isolated collagens were investigated. These results indicate that the swim bladder of silver carp, *Hypophthalmichthys molitrix*, is a promising alternative source of mammalian collagen for pharmaceutical and biomedical applications.

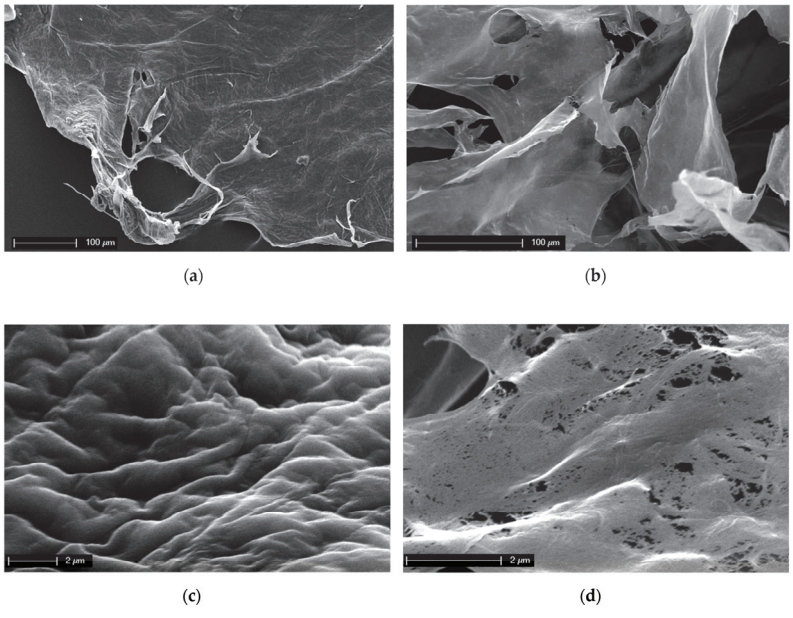


(**a**) (**b**)

(**c**) (**d**)

**Figure 2.** SEM images of the *A. aerophoba* chitin scaffold after NaOH treatment (**a**,**c**) and after dissolution in LiOH (**b**,**d**). The destruction of the structural integrity after insertion into LiOH solution at the micro-level is clearly visible.

Contribution 10 synthesizes chitin derivatives with propane sulfonated groups and demonstrates potential antioxidant and antifungal activity. The chitin and sulfonated chitin derivatives were tested in vitro for antioxidant and antifungal activity.

In contribution 11, Rahman et al. [14] report a scientific exploration for delaying skin aging by applying the therapeutic potential of marine collagen. Figure 3a shows how marine collagen proteins can delay skin aging. The authors also explore how CRISPR technology could be used to target and modify specific genes associated with aging and skin degeneration. An overview of this technology can be seen in Figure 3b.

In contribution 12, the authors review the function of chitosan in dental implantology. This review discusses chitosan as a biocompatible and bioactive material with many benefits in surgery, restorative dentistry, endodontics, prosthetics, orthodontics, and disinfection.

Contribution 13, a review, focuses on the scaffold polyvinyl alcohol (PVA)–chitosan (CS) and its multiple functions in tissue engineering and regenerative medicine applications. The authors also discuss the challenges and limitations associated with its use.

This Editorial's concluding remarks are as follows:

The diverse applications of marine collagen and chitin across various fields highlight their interdisciplinary potential. The continued research and development of these biopolymers can lead to innovative solutions addressing current challenges in medicine, cosmetics, the environment, agriculture, and the food industry.

I want to thank the Editorial Board, Managing Editors and Editorial Assistant. I greatly appreciate the efforts provided by the authors who contributed their results to this Special Issue. I thank the reviewers who carefully evaluated the submitted manuscripts for their support.

[a]

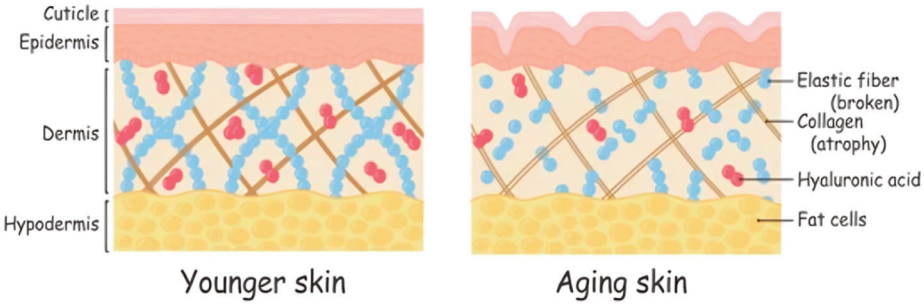


[b]

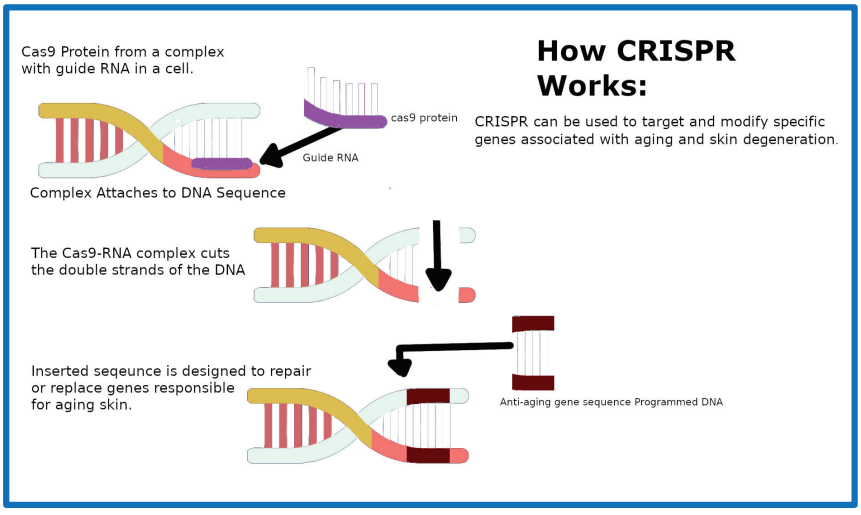


**Figure 3.** (**a**). Illustration of the structural differences between younger and aging skin. In the dermis of young human skin, collagen fibrils are intact and normal in size (**left**), in contrast with reduced collagen fibrils in the dermis of aged human skin, which leads to a reduction in cell size (**right**). The aging skin on the right shows a reduction and fragmentation of collagen fibers, broken elastic fibers, and diminished Hyaluronic Acid (red dots), leading to thinner fat layers and an overall loss of structural integrity and elasticity. (**b**). Illustration of the CRISPR-Cas9 mechanism for skin regeneration. This graphic outlines the use of CRISPR-Cas9 technology for targeted gene editing in eukaryotic cells, specifically for skin regeneration. The process begins with the Cas9 protein forming a complex with a guide RNA that is complementary to a specific gene sequence associated with skin aging. This complex then locates and binds to the target DNA sequence, where Cas9 makes a precise cut. A new DNA sequence with the desired genetic information can then be inserted at the cut site for potential therapeutic purposes, such as reversing aging effects or repairing skin damage.

**Conflicts of Interest:** The author declares no conflict of interest.

## List of Contributions

1. Rocha, M.S.; Marques, C.F.; Carvalho, A.C.; Martins, E.; Ereskovsky, A.; Reis, R.L.; Silva, T.H. The Characterization and Cytotoxic Evaluation of *Chondrosia reniformis* Collagen Isolated from Different Body Parts (Ectosome and Choanosome) Envisaging the Development of Biomaterials. *Mar. Drugs* **2024**, *22*, 55. https://doi.org/10.3390/md22020055.

2. Cho, W.; Park, J.; Kim, J.; Lee, M.; Park, S.J.; Kim, K.S.; Jun, W.; Kim, O.-K.; Lee, J. Low-Molecular-Weight Fish Collagen Peptide (Valine-Glycine-Proline-Hydroxyproline-Glycine-Proline-Alanine-Glycine) Prevents Osteoarthritis Symptoms in Chondrocytes and Monoiodoacetate-Injected Rats. *Mar. Drugs* **2023**, *21*, 608. https://doi.org/10.3390/md21120608.
3. Wang, L.; Guo, R.; Liang, X.; Ji, Y.; Zhang, J.; Gai, G.; Guo, Z. Preparation and Antioxidant Activity of New Carboxymethyl Chitosan Derivatives Bearing Quinoline Groups. *Mar. Drugs* **2023**, *21*, 606. https://doi.org/10.3390/md21120606.
4. Roig-Puche, M.; Lopez-Moya, F.; Valverde-Urrea, M.; Sanchez-Jerez, P.; Lopez-Llorca, L.V.; Fernandez-Gonzalez, V. Chitosan from Marine Amphipods Inhibits the Wilt Banana Pathogen *Fusarium oxysporum* f. sp. Cubense Tropical Race 4. *Mar. Drugs* **2023**, *21*, 601. https://doi.org/10.3390/md21120601.
5. Duminis, T.; Heljak, M.; Święszkowski, W.; Ereskovsky, A.; Dziedzic, I.; Nowicki, M.; Pajewska-Szmyt, M.; Voronkina, A.; Bornstein, S.R.; Ehrlich, H. On the Mechanical Properties of Microfibre-Based 3D Chitinous Scaffolds from Selected Verongiida Sponges. *Mar. Drugs* **2023**, *21*, 463. https://doi.org/10.3390/md21090463.
6. Kubiak, A.; Pajewska-Szmyt, M.; Kotula, M.; Leśniewski, B.; Voronkina, A.; Rahimi, P.; Falahi, S.; Heimler, K.; Rogoll, A.; Vogt, C.; et al. Spongin as a Unique 3D Template for the Development of Functional Iron-Based Composites Using Biomimetic Approach In Vitro. *Mar. Drugs* **2023**, *21*, 460. https://doi.org/10.3390/md21090460.
7. Arnold, N.D.; Garbe, D.; Brück, T.B. Proteomic and Transcriptomic Analyses to Decipher the Chitinolytic Response of *Jeongeupia* spp. *Mar. Drugs* **2023**, *21*, 448. https://doi.org/10.3390/md21080448.
8. Dziedzic, I.; Voronkina, A.; Pajewska-Szmyt, M.; Kotula, M.; Kubiak, A.; Meissner, H.; Duminis, T.; Ehrlich, H. The Loss of Structural Integrity of 3D Chitin Scaffolds from *Aplysina aerophoba* Marine Demosponge after Treatment with LiOH. *Mar. Drugs* **2023**, *21*, 334. https://doi.org/10.3390/md21060334.
9. Jiang, H.; Kong, Y.; Song, L.; Liu, J.; Wang, Z. A Thermostable Type I Collagen from Swim Bladder of Silver Carp (*Hypophthalmichthys molitrix*). *Mar. Drugs* **2023**, *21*, 280. https://doi.org/10.3390/md21050280.
10. Luan, F.; Xu, Z.; Wang, K.; Qi, X.; Guo, Z. Synthesis of Water-Soluble Sulfonated Chitin Derivatives for Potential *Antioxidant* and Antifungal Activity. *Mar. Drugs* **2022**, *20*, 668. https://doi.org/10.3390/md20110668.
11. Rahman, A.; Rehmani, R.; Pirvu, D.G.; Huang, S.M.; Puri, S.; Arcos, M. Unlocking the Therapeutic Potential of *Marine* Collagen: A Scientific Exploration for Delaying Skin Aging. *Mar. Drugs* **2024**, *22*, 159. https://doi.org/10.3390/md22040159.
12. Paradowska-Stolarz, A.; Mikulewicz, M.; Laskowska, J.; Karolewicz, B.; Owczarek, A. The Importance of Chitosan Coatings in Dentistry. *Mar. Drugs* **2023**, *21*, 613. https://doi.org/10.3390/md21120613.
13. Nathan, K.G.; Genasan, K.; Kamarul, T. Polyvinyl Alcohol-Chitosan Scaffold for Tissue Engineering and Regenerative Medicine Application: A Review. *Mar. Drugs* **2023**, *21*, 304. https://doi.org/10.3390/md21050304.

## References

1. Baharlouei, P.; Rahman, A. Chitin and Chitosan: Prospective Biomedical Applications in Drug Delivery, Cancer Treatment, and Wound Healing. *Mar. Drugs* **2022**, *20*, 460. [CrossRef] [PubMed]
2. Kurita, K. Chitin and Chitosan: Functional Biopolymers from Marine Crustaceans. *Mar. Biotechnol.* **2006**, *8*, 203. [CrossRef] [PubMed]
3. Ehrlich, H. Chitin and collagen as universal and alternative templates in biomineralization. *Int. Geol. Rev.* **2010**, *52*, 661. [CrossRef]
4. Rahman, M.A.; Halfar, J. First evidence of chitin in calcified coralline algae: New insights into the calcification process of Clathromorphum compactum. *Sci. Rep.* **2014**, *4*, 6162. [CrossRef] [PubMed]
5. Da Sacco, L.; Masotti, A. Chitin and Chitosan as Multipurpose Natural Polymers for Groundwater Arsenic Removal and As2O3 Delivery in Tumor Therapy. *Mar. Drugs* **2010**, *8*, 1518–1525. [CrossRef] [PubMed]
6. El Hadrami, A.; Adam, L.R.; El Hadrami, I.; Daayf, F. Chitosan in Plant Protection. *Mar. Drugs* **2010**, *8*, 968–987. [CrossRef] [PubMed]

7. Ehrlich, H.; Wysokowski, M.; Żółtowska-Aksamitowska, S.; Petrenko, I.; Jesionowski, T. Collagens of Poriferan Origin. *Mar. Drugs* **2018**, *16*, 79. [CrossRef] [PubMed]
8. Benayahu, D.; Sharabi, M.; Pomeraniec, L.; Awad, L.; Haj-Ali, R.; Benayahu, Y. Unique Collagen Fibers for Biomedical Applications. *Mar. Drugs* **2018**, *16*, 102. [CrossRef]
9. Geahchan, S.; Baharlouei, P.; Rahman, A. Marine Collagen: A Promising Biomaterial for Wound Healing, Skin Anti-Aging, and Bone Regeneration. *Mar. Drugs* **2022**, *20*, 61. [CrossRef] [PubMed]
10. Chen, J.; Gao, K.; Liu, S.; Wang, S.; Elango, J.; Bao, B.; Dong, J.; Liu, N.; Wu, W. Fish Collagen Surgical Compress Repairing Characteristics on Wound Healing Process In Vivo. *Mar. Drugs* **2019**, *17*, 33. [CrossRef] [PubMed]
11. Carvalho, A.M.; Marques, A.P.; Silva, T.H.; Reis, R.L. Evaluation of the Potential of Collagen from Codfish Skin as a Biomaterial for Biomedical Applications. *Mar. Drugs* **2018**, *16*, 495. [CrossRef]
12. Duminis, T.; Heljak, M.; Święszkowski, W.; Ereskovsky, A.; Dziedzic, I.; Nowicki, M.; Pajewska-Szmyt, M.; Voronkina, A.; Bornstein, S.R.; Ehrlich, H. On the Mechanical Properties of Microfibre-Based 3D Chitinous Scaffolds from Selected Verongiida Sponges. *Mar. Drugs* **2023**, *21*, 463. [CrossRef] [PubMed]
13. Dziedzic, I.; Voronkina, A.; Pajewska-Szmyt, M.; Kotula, M.; Kubiak, A.; Meissner, H.; Duminis, T.; Ehrlich, H. The Loss of Structural Integrity of 3D Chitin Scaffolds from *Aplysina aerophoba* Marine Demosponge after Treatment with LiOH. *Mar. Drugs* **2023**, *21*, 334. [CrossRef]
14. Rahman, A.; Rehmani, R.; Pirvu, D.G.; Huang, S.M.; Puri, S.; Arcos, M. Unlocking the Therapeutic Potential of Marine Collagen: A Scientific Exploration for Delaying Skin Aging. *Mar. Drugs* **2024**, *22*, 159. [CrossRef]

*marine drugs*

MDPI

*Article*

# Synthesis of Water-Soluble Sulfonated Chitin Derivatives for Potential Antioxidant and Antifungal Activity

**Fang Luan [1,*], Zhenhua Xu [1], Kai Wang [1], Xin Qi [1] and Zhanyong Guo [2,3,*]**

[1] Naval Architecture and Port Engineering College, Shandong Jiaotong University, Weihai 264200, China
[2] Key Laboratory of Coastal Biology and Bioresource Utilization, Yantai Institute of Coastal Zone Research, Chinese Academy of Sciences, Yantai 264003, China
[3] University of Chinese Academy of Sciences, Beijing 100049, China
* Correspondence: 221010@sdjtu.edu.cn (F.L.); zyguo@yic.ac.cn (Z.G.); Tel.: +86-535-2109171 (F.L.); +86-6313998919 (Z.G.)

**Abstract:** Chitin is a natural renewable and useful biopolymer limited by its insolubility; chemical derivatization can enhance the solubility and bioactivity of chitin. The purpose of this study was to synthesize novel water-soluble chitin derivatives, sulfo-chitin (SCT) and sulfopropyl-chitin (SPCT), as antioxidant and antifungal agents. The target derivatives were characterized by means of elemental analysis, FTIR, $^{13}C$ NMR, TGA and XRD. Furthermore, the antioxidant activity of the chitin derivatives was estimated by free radical scavenging ability (against DPPH-radical, hydroxyl-radical and superoxide-radical) and ferric reducing power. In addition, inhibitory effects against four fungi were also tested. The findings show that antioxidant abilities and antifungal properties were in order of SPCT > SCT > CT. On the basis of the results obtained, we confirmed that the introduction of sulfonated groups on the CT backbone would help improve the antioxidant and antifungal activity of CT. Moreover, its efficacy as an antioxidant and antifungal agent increased as the chain length of the substituents increased. This derivatization strategy might provide a feasible way to broaden the utilization of chitin. It is of great significance to minimize waste and realize the high-value utilization of aquatic product wastes.

**Keywords:** water-soluble chitin derivative; sulfonated chitin; antioxidant ability; antifungal activity

**Citation:** Luan, F.; Xu, Z.; Wang, K.; Qi, X.; Guo, Z. Synthesis of Water-Soluble Sulfonated Chitin Derivatives for Potential Antioxidant and Antifungal Activity. *Mar. Drugs* **2022**, *20*, 668. https://doi.org/10.3390/md20110668

Academic Editor: Azizur Rahman

Received: 12 September 2022
Accepted: 21 October 2022
Published: 26 October 2022



## 1. Introduction

Chitin, comprising β-(1-4)-linked N-acetyglucopyranose units, was first characterized and described in 1884 [1]. It is a linear polysaccharide widely distributed in crustacean shells (such as shrimp, crab and lobster) and the cell walls of fungi, and it is the second most abundant biopolymer on earth. Unlike other forms of biopolymer such as cellulose, chitin has an acetamido group ($NHCOCH_3$). Nitrogen-containing compounds have a huge market, with applications such as drug delivery, cell nano patch and biological membranes, etc. [2–5]. Annually, it has been estimated that chitin is produced in nature on the order of 100 billion tons, and its main source is by-product generated in the crustacean processing industries. It is estimated that 6–8 million tons of crustacean shell waste are discarded annually in the world, resulting in a huge amount of waste and vast disposal cost [6]. One of the economically as well as ecologically sustainable solutions is the extraction of chitin from crustaceans' shells, which may be a way of minimizing the waste and producing value-added compounds with noteworthy biological properties that can be applied in multifarious fields.

As a natural renewable resource, chitin has been widely applied due to its complete biodegradability and excellent biocompatibility in combination with non-toxic properties [7–9]. Although it is widely available, the insolubility of chitin in water and even most organic solvents becomes the biggest limitation in its practical application. To increase the solubility of chitin, its chemical modification is required. Yet, water-soluble chitin derivatives are

mostly obtained by different methods: deacetylation, alkylation, carboxylation and so on [10–12]. Among them, sulfonation is an efficient method to improve the water-solubility of derivatives, and polysaccharides exhibit biological activities after sulfation [13,14].

Oxygen in cells can generate reactive oxygen species (ROS) during metabolism, such as hydroxyl radical (•OH), superoxide anion ($O_2^-$), ozone ($O_3$), hydrogen peroxide ($H_2O_2$), etc. [15]. Cellular damage by free radicals gives rise to various disorders, for instance chronic renal failure, arthritis, diabetes, sepsis, respiratory distress syndrome, Alzheimer's disease and cancer [16,17]. Antioxidants have been found to be effective in scavenging these free radicals to protecting cells from various diseases. However, the use of synthetic small-molecule antioxidants has been correlated with detrimental effects to human health and food safety, resulting in rigorous supervision by many governmental agencies [18,19]. With the changes in consumer preferences for safe food, investigations on natural polysaccharides and their unique antioxidant properties have sparked people's interest. The biocompatibility and biodegradability of chitin and its derivatives, coupled with their capacity to eliminate free radicals, makes them potential functional constituents used in different fields, ranging from food formulations to functional materials and medicine to agriculture [20,21].

Chemical pesticides are usually used to prevent plant pathogens; with the development of the environmentally friendly society, the problems associated with farm chemicals have aroused widespread concern. In recent years, many effective antibacterials have been prohibited due to dangers towards the environment and the health of humans. In this view, it is urgently critical to find new chemical fungistats that not only can hold back the growth of the microorganism effectively, but also are biocompatible, biodegradable and low toxicity. Therefore, novel polysaccharide derivatives emerge as a new class of environmentally friendly biomaterials.

To the best of our knowledge, there are few papers about chitin derivatives with sulfonated side chains. In the current study, sulfonated chitin could be prepared by modifying chitin using sulfur trioxide pyridine and 1,3-propane sultone, thus obtaining water-soluble derivatives with biological activities. The chitin derivatives designed in this way were expected to have advantageous characteristics such as good antioxidant and antifungal activity. Then, we estimated their antioxidant ability and antifungal activity in vitro, and the relationship between the structure and the antioxidant and antifungal activities of chitin was discussed.

## 2. Results and Discussion

### *2.1. Synthesis and Characterization of Chitin Derivatives*

#### 2.1.1. Synthesis of Chitin Derivatives

Sulfo-chitin (SCT) and sulfopropyl-chitin (SPCT) were prepared in four steps (Scheme 1), namely tosylation, azidation, reduction, and sulfonation. The first step was to obtain 6-tosyl-chitin through processing chitin (treated with 40% concentrated sodium hydroxide solution) with 4-toluene sulfonyl chloride and chloroform. Afterwards, the azide treatment was used to remove the tosyl group for producing azido-chitin (ACT). Then, amino-chitin (NCT) was successfully synthesized through the reduction reaction of $PPh_3$. Raw chitin and all intermediate products (TCT, ACT, NCT) were water insoluble. Lastly, the water-soluble chitin derivatives SCT and SPCT were synthesized by sulfonation. Their solubilities in water were up to 2.0 mg/mL and 6.0 mg/mL, and good water solubility leads to wider use. The enhanced water solubility of derivatives due to the introduction of the (propane) sulfonated group led to an increase in the intermolecular spaces between the chains and partially broke the initial hydrogen bonds.

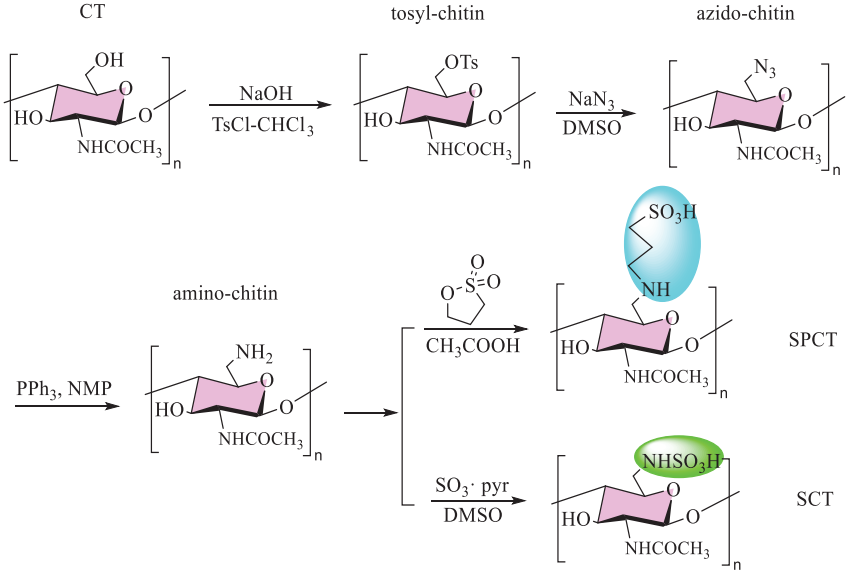


**Scheme 1.** Synthetic route for sulfo-chitin (SCT) and sulfopropyl-chitin (SPCT).

The elemental analyses of chitin derivatives and the degree of substitution (DS) are reported in Table 1, as calculated by the S/N (TCT, SCT and SPCT) or C/N (other derivatives) ratio obtained from the elemental analysis.

**Table 1.** The elemental analyses and the degrees of substitution of chitin derivatives.

| Full Name | Sample (Abbreviations) | Found (%) | | | | DS | Formula |
|---|---|---|---|---|---|---|---|
| | | C | H | N | S | | |
| chitin | CT | 45.23 | 7.19 | 6.59 | | 1.0 | $C_8H_{13}NO_5$ |
| tosyl-chitin | TCT | 50.02 | 6.56 | 4.53 | 7.86 | 0.93 | $(C_{15}H_{19}NO_7S)_{0.89}(CT)_{0.11}$ |
| azido-chitin | ACT | 44.25 | 5.22 | 20.87 | | 0.90 | $(TCT)_{0.1}$ $(C_8H_{12}N_4O_4)_{0.9}$ |
| amino-chitin | NCT | 46.95 | 6.80 | 14.97 | | 0.87 | $(ACT)_{0.04}$ $(C_8H_{14}N_2O_4)_{0.87}$ |
| sulfo-chitin | SCT | 36.90 | 5.85 | 9.84 | 8.74 | 0.40 | $(NCT)_{0.6}(C_8H_{14}N_2O_7S)_{0.4}$ |
| sulfopropyl-chitin | SPCT | 39.62 | 6.11 | 9.88 | 8.14 | 0.41 | $(NCT)_{0.59}(C_{11}H_{19}N_2O_7S)_{0.41}$ |

2.1.2. FTIR Analysis

The formation of chitin and its derivatives were also confirmed via FTIR spectroscopy (Figure 1).

The spectrum of unmodified chitin (CT) indicates that the polysaccharide mainly contains the following characteristic bands: 3444 and 3104 $cm^{-1}$ (–OH and –NH), 2922 $cm^{-1}$ (aliphatic –CH), 1662, 1562 and 1315 $cm^{-1}$ (amide I, II and III), 1427 $cm^{-1}$ (pyranose ring), 1377 $cm^{-1}$ (acetamide groups) and 1072 and 1030 $cm^{-1}$ (C–O) [22].

In the NCT spectra, the bending vibration bands of $–NH_2$ groups at around 1600 $cm^{-1}$ was not observed, which may be attributable to the influence of amide. Moreover, the absorption intensities at 1030 $cm^{-1}$ decrease, indicating successful incorporation of the amine group.

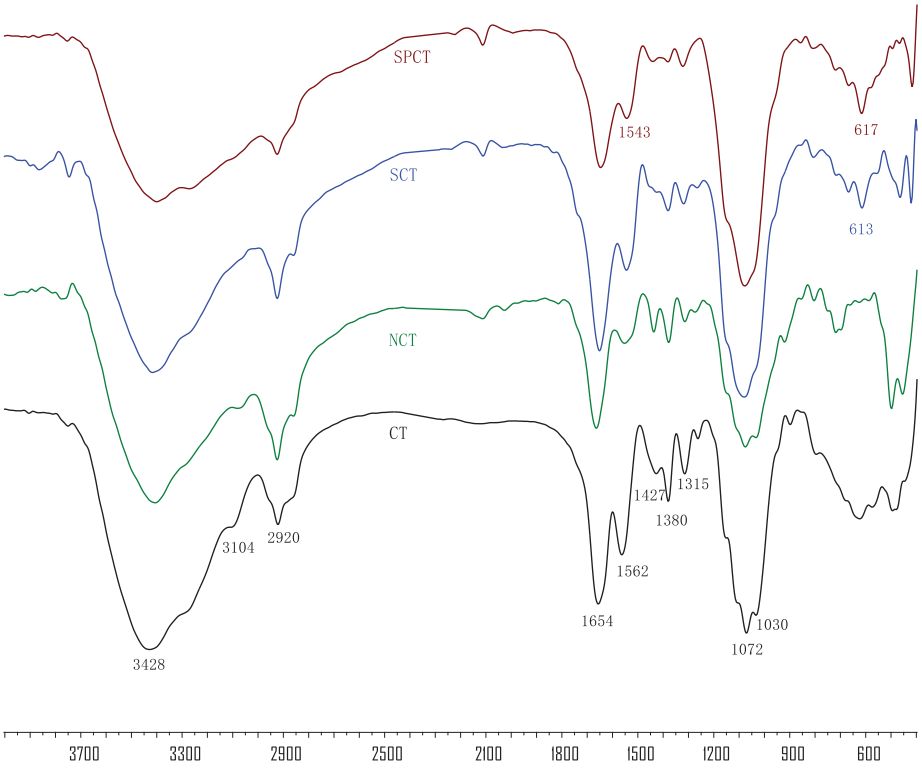


**Figure 1.** IR spectra of chitin and its derivatives.

For SCT, the new peak at 613 $cm^{-1}$, attributed to the S=O stretching vibration of the sulfonic acid group [23,24], suggests that a sulfonation reaction took place on the amine group and the synthesis of the desired compound was achieved.

Finally, for SPCT, the new peaks at 617 $cm^{-1}$, corresponding to the stretching vibration of the $SO_2$ group in sulfonic acid, suggest the presence of the $SO_3H$ group in SPCT; the peak at 1543 $cm^{-1}$ was assigned to the C–N–C bending vibration of the SPCT branch, suggesting that reaction occurred at the amine group to produce sulfopropyl-chitin [13].

### 2.1.3. NMR Analysis

Solid-state $^{13}C$ NMR spectroscopy was applied to further elucidate the chemical structures of chitin and its derivatives (Figure 2).

In the $^{13}C$ NMR spectrum of chitin (CT) shows eight peaks: one at 104 ppm for C1, the second at 83 ppm for C4, the third at 76 ppm for C5, the fourth at 74 ppm for C3, the fifth at 61 ppm for C6 and the sixth at 55 ppm for C2. The other signals at 173 and 23 ppm are assigned to C=O and CH3.

In the spectra of NCT, peaks ranging from 85 ppm to 64 ppm were assigned to C3, C4 and C5. At the same time, the peak at 61 ppm shifted to a higher field (43 ppm) compared with the signals of C-6 of CT. This indicates that the amino groups were introduced into chitin successfully.

In the SCT spectrum, the C6-$NH_2$ participation in the reaction was marked as C6′ and that which was not involved was marked as C6. The C6′ signal shifted from 42 to 57 ppm. In addition, the signal at 42 ppm was still observed, which adequately indicates that the C6-$NH_2$ moiety was only partially replaced in SCT.

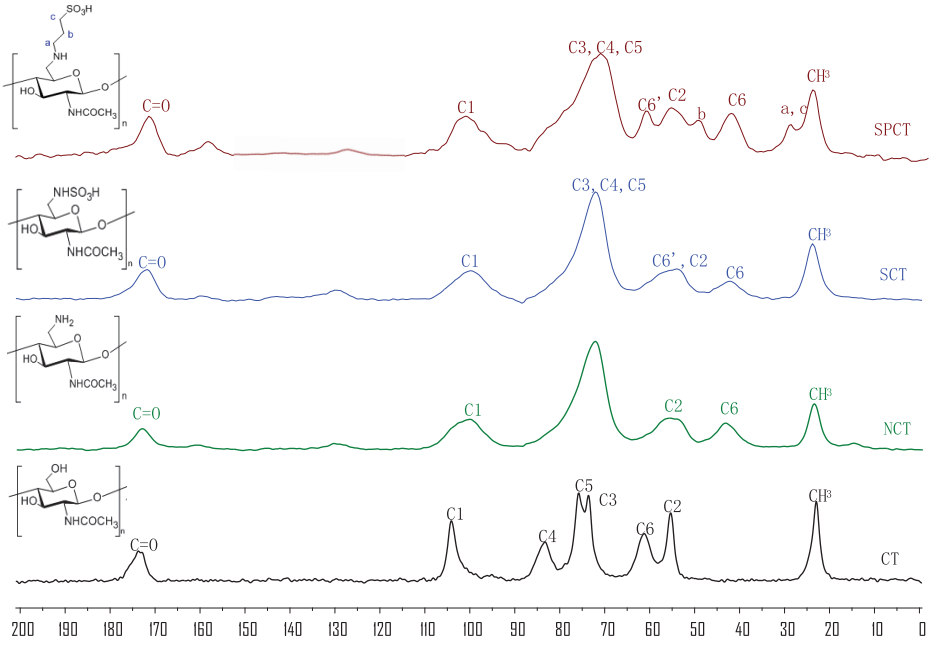


**Figure 2.** Solid-state $^{13}C$ NMR spectra of chitin and its derivatives.

Similarly, in the SPCT spectra, the C6-$NH_2$ participation in the reaction was marked as C6′ and C6-$NH_2$, and that which was not involved was marked as C6. The signal at 61 ppm was attributed to the substituted C6′; furthermore, the signal at 42 ppm was assigned to partial replacement at C6. This implies that free amino groups at C6 were incompletely replaced. Two new signals at 27 ppm and 48 ppm appeared, which were assigned to the carbons in 1,3-propane sultone [25]. According to the results, we speculate that the amino groups reacted with the 1,3-propane sultone and the successful synthesis of the desired chitin derivatives was achieved.

2.1.4. Thermogravimetric and Derivative Thermogravimetric Analysis (TGA/DTG)

The thermogravimetric analyses (TGA) and the corresponding derivative thermogravimetric (DTG) curves of CT, SCT and SPCT are represented in Figure 3. All the TGA curves of samples exhibit two stages of weight loss. CT underwent a 4.4% loss of mass from 45 °C to 140 °C, which was attributed to evaporation of water already within the polymer structure [26]. In the following step, a sudden decrease in weight was observed at about 260–396 °C (DTGmax at 357 °C); 72.2% mass loss was observed. This mass loss could be ascribed to the decomposition of the saccharide structure of the chitin molecule, which contains the dehydration of saccharide rings and the disintegration of both the N-acetylated units as well as the degradation of other proteins associated with the chitin structure [27,28].

Similar TGA behavior was seen for SCT and SPCT. Firstly, the TGA curve of SCT exhibited a 7.4% loss of mass from 45 °C to 160 °C. Then, the major weight loss of SCT (59.8%) occurred at about 200–600 °C (DTGmax at 233 °C). The following loss was likely caused by the declined hydrogen bonding and disruption of glycoside linkages. In the case of SPCT, a comparatively similar behavior was observed as seen in SCT. The TGA curve of SPCT exhibited a 7.9% loss of mass from 40 °C to 152 °C, followed by a 61.2% loss of mass at about 160–600 °C (DTGmax at 240 °C). In addition, the initial decomposition temperatures of CT, SCT and SPCT were found to be 260, 200 and 160 °C, respectively. Compared to CT, SCT and SPCT have lower initial decomposition temperatures, and SCT and SPCT are thermally instable due to

the introduction of the (propane) sulfonated group, which disrupted the H-bond formation between the chains, as discussed in the solubility test.

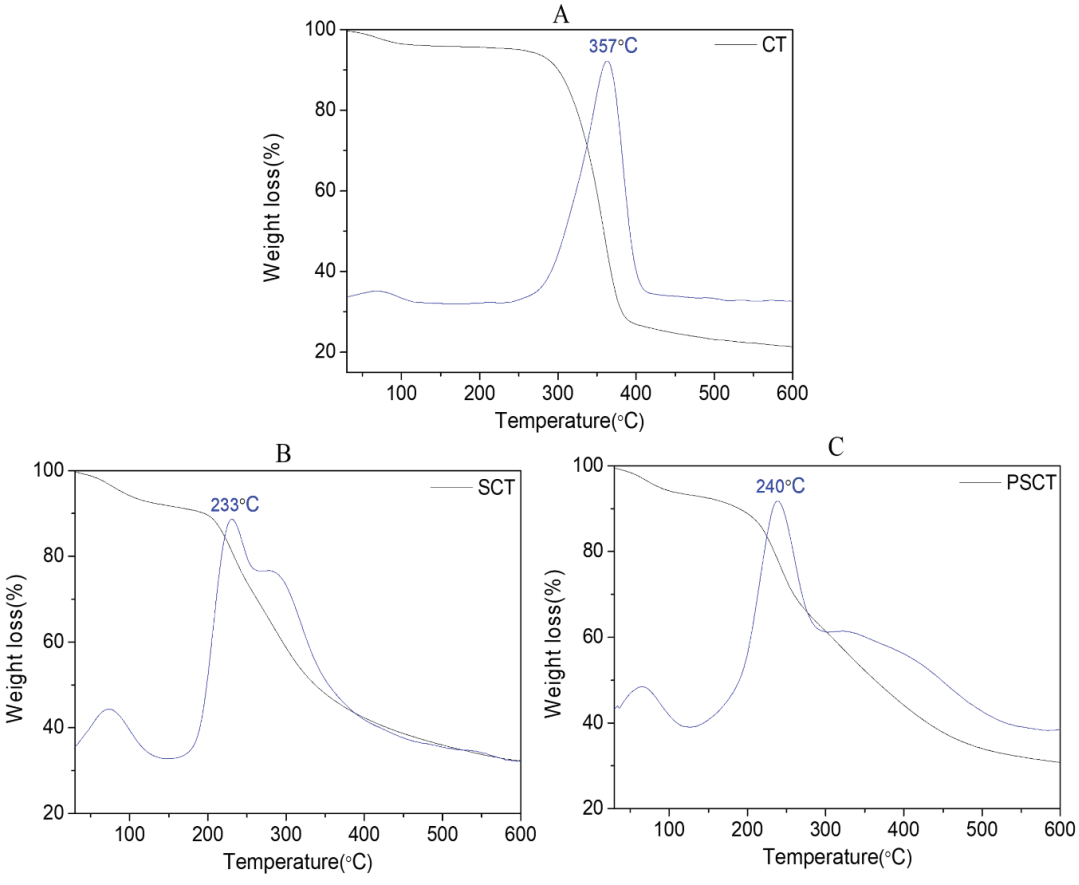


**Figure 3.** TGA thermogram and DTG curves. (**A**) CT, (**B**) SCT, (**C**) SPCT.

Comprehensively, it is reasonable to presume that chitin derivatives were more susceptible to the thermal decomposition temperature than raw chitin. A possible reason is that chemical reactions lowered the regularity of chitin molecular chain and resulted in the breakage of hydrogen bonds, thereby reducing its resistance to thermal degradation. Our results were in accordance with previous studies [29,30].

2.1.5. X-ray Diffraction (XRD) Analysis

The crystalline structure of chitin and its derivatives were analyzed via X-ray diffraction (Figure 4). CT exhibited four peaks at 9.4°, 12.8°, 19.5° and 25.2°. Two of them are faint (12.8° and 25.2°) and the other two are sharp (9.4° and 19.5°). Compared to CT, the XRD patterns of SCT and SPCT exhibited some changes in their peak width, peak intensity and angles. The sharp peak of CT at 9.4° moved to 10.5° and 10.8° in the patterns of SCT and SPCT, owing to the introduction of sulfonated groups and propane sulfonated groups to the structure of chitin. In addition, for SCT, the peak at 19.5° shifted to 19.9°, its intensity decreased and its width increased. Similarly, for SPCT, the peak at 19.5° shifted to 20.6°, and the intensity and width of the peak had the same changes as well. Meanwhile, the diffraction peak at 2θ = 12.8° and 25.2° disappeared, which may be due to the damaging of

inter- and intra-molecular hydrogen bonds [31]. The results demonstrate that the (propane) sulfonated group grafted on chitin resulted in a decrease in crystallinity, which can be observed in the form of relatively weaker reflection in the spectra of SCT, and SPCT. A lower crystallinity index leads to better water solubility [32]; as a result, SCT, and SPCT should have a much better aqueous solubility than chitin, which is consistent with the solubility test.

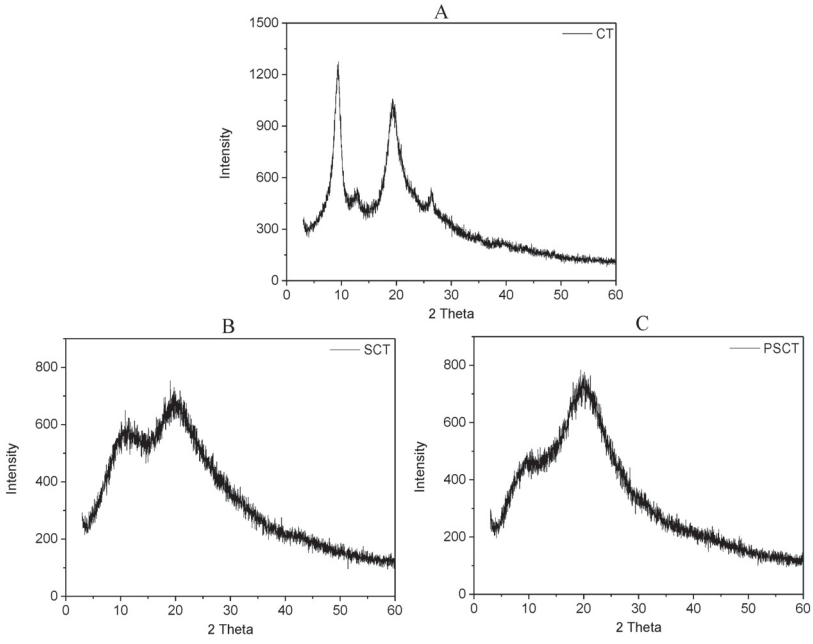


**Figure 4.** XRD spectra of CT (**A**), SCT (**B**) and SPCT (**C**).

*2.2. Antioxidant Activities*

The antioxidant assay of chitin could not be performed owing to its insolubility. Therefore, the default is 0 (red line in Figure 5).

2.2.1. DPPH-Radical Scavenging Ability Assay

The DPPH-radical scavenging activity of SCT and SPCT is illustrated in Figure 5A. In this experiment, we can clearly see that the scavenging effect increased with the increasing concentration. Meanwhile, the scavenging capability against DPPH-radical was in order of SPCT > SCT > CT at the concentrations studied. Moreover, SPCT and SCT show antioxidant activities at 1.6 mg/mL of 79.7% and 47.3%, respectively.

The scavenging activity may be correlated with DPPH-radicals reacting with active hydrogen in chitin derivatives to form a stable macromolecule. The more active the hydrogen, the higher the scavenging capability. Therefore, the scavenging effect of all samples increased with increasing concentration. The sulfonated groups grafted on CT are able to act as hydrogen donors. Furthermore, SPCT is more reactive than SCT as it is sterically less hindered; as a result, the hydrogens of the derivative are more exposed to the outside.

Meanwhile, the 50% inhibition concentration ($IC_{50}$) is a good parameter to evaluate scavenging capability. A lower $IC_{50}$ value indicates a greater antioxidant activity. According to the results, SPCT had the highest activity compared to CT and SCT. The $IC_{50}$ of SPCT was 0.10 mg/mL. In other words, the SPCT can act as a reducing agent, and propane sulfonated groups play an important role in scavenging activity against DPPH-radicals.

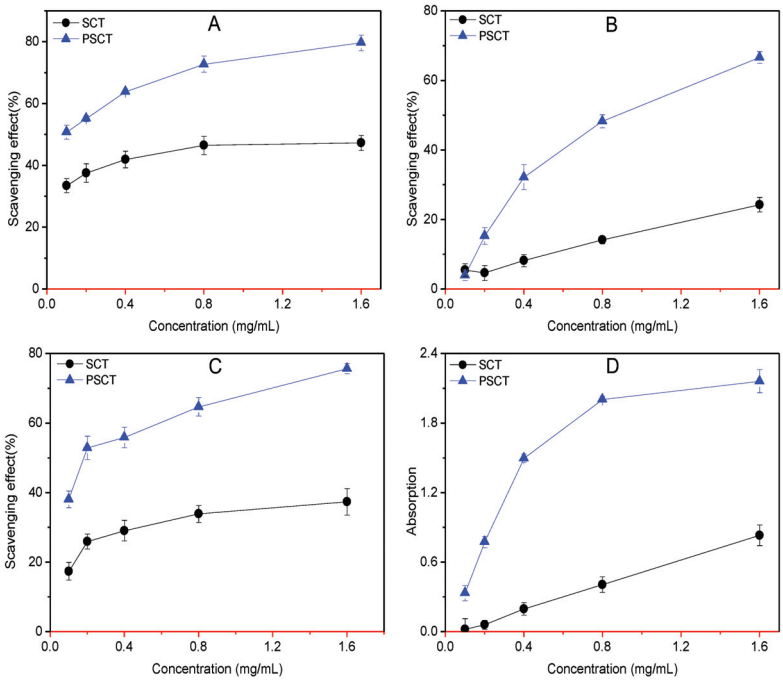


**Figure 5.** Antioxidant effect of samples: (**A**) DPPH-radical scavenging ability; (**B**) hydroxyl-radical scavenging ability; (**C**) superoxide-radical scavenging ability; (**D**) reducing power.

### 2.2.2. Hydroxyl-Radical Scavenging Ability Assay

There is no doubt that timely removal of excess hydroxyl radicals is crucial to create a healthier body. From Figure 5B, we can clearly see that the scavenging capability against hydroxyl-radicals was in the order of SPCT > SCT > CT at the concentrations studied. Results indicate that SPCT and SCT exhibited enhancement on hydroxyl-radical scavenging capability; the scavenging effects at 1.6 mg/mL were 66.6% and 24.3%, respectively. In additional, $IC_{50}$ of SPCT was 0.86 mg/mL.

The scavenging activity may be correlated with active hydrogen in chitin derivatives. Active hydrogen in the polysaccharide unit can react with ·OH by the typical H abstraction reaction. The grafting of propane sulfonated groups onto CT can donate more protons to free radicals; this principle was discussed in the DPPH-radical assay. These results suggest that sulfonated groups could be an important factor in affecting hydroxyl-radical scavenging activity.

### 2.2.3. Superoxide-Radical Scavenging Ability Assay

Superoxide scavenging activity was determined in the NBT assay. According to Figure 5C, the result concurred with the scavenging properties against DPPH-radicals. Moreover, the scavenging capability of the samples increased with the increase in concentration at 0.1–1.6 mg/mL. The maximum of 37.4% inhibition was observed at the concentration of 1.6 mg/mL of SCT. SPCT also had the strongest scavenging activity, reaching 75.7% at 1.6 mg/mL. Moreover, the $IC_{50}$ of SPCT was 0.17 mg/mL.

As reported, the scavenging effect is correlated with the number of active hydrogens in the molecule. As mentioned in the DPPH-radical and hydroxyl-radical assay, SCT and SPCT can be proton donors that react with superoxide anions. The results clearly indicate that SPCT can be regarded as an efficient antioxidant polymer and propane sulfonated groups undoubtedly play crucial roles in its free radical scavenging capability.

2.2.4. Reducing Power Assay

The reducing powers of chitin and its derivatives are shown in Figure 5D. The results clearly indicate that the reducing power of samples exhibited an upward trend with the increase in sample concentration. SPCT exhibited stronger reducing power than SCT, and they were found to have reducing powers at 1.6 mg/mL of 2.2 and 0.8, respectively.

Accordingly, the reducing capacity of a compound may serve as a significant indicator of its potential antioxidant activity [33]. Based on the results, it is concluded that propane sulfonated groups can enhance the ability of the reducing power.

These data demonstrate that the scavenging effect of all samples increased with increasing concentration. Additionally, the scavenging abilities were in order of SPCT > SCT > CT in the tested concentration. It is valid to find that the antioxidant ability increases with the increasing chain length of alkyl substituent. This observation is in agreement with previous reports [34]. According to the results, we could conclude SPCT with presumed antioxidant properties may be developed into new antioxidants as a possible food ingredient or supplement in the pharmaceutical industry.

*2.3. Antifungal Activity*

The action of phytopathogenic fungi causes severe damage to plants; thus, control of these plant-threatening fungi is of great interest. Here, we tested CT, SCT and SPCT against destructive plant-threatening fungi (*P. asparagi*, *F. oxyspirum* f. *niveum*, *B. cinerea* and *F. oxysporum* f. sp. *Cucumerium*). The results are shown in Figure 6. It is clear from the plots that the antifungal activities of the derivatives correlated well with the increase in concentration. Additionally, chitin derivatives exhibited the best antifungal activity at 1.0 mg/mL. Simultaneously, the inhibitory index was in the order of SPCT > SCT > CT. Details are as follows.

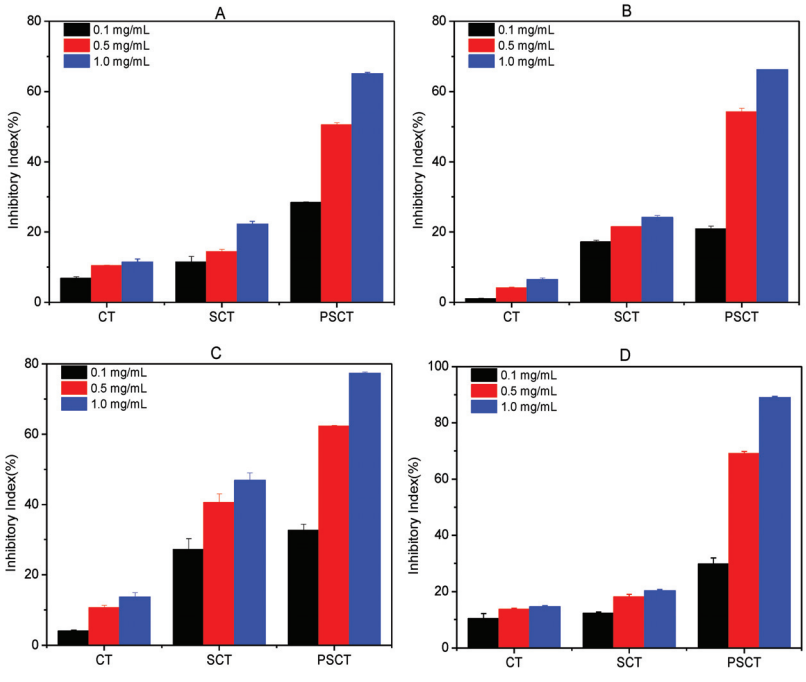


**Figure 6.** Antifungal activity against *P. asparagi* (**A**), *F. oxyspirum* f. *niveum* (**B**), *B. cinerea* (**C**), and *F. oxysporum* f. sp. *Cucumerium* (**D**) at 0.1, 0.5 and 1.0 mg/mL.

As depicted in Figure 6A, CT and SCT slightly inhibited the growth of *P. asparagi* and the inhibitory rates were 11.5% and 22.3% at 1.0 mg/mL, respectively. Compared to both, SPCT had better antifungal activity, and the inhibitory index was up to 65.1% at 1.0 mg/mL. In other words, SPCT possesses powerful antifungal activity against *P. asparagi*, and propane sulfonated groups are an important factor that affects antifungal activity.

As depicted in Figure 6B, CT also slightly inhibited the growth of *F. oxyspirum* f. *niveum* and the inhibitory rate was 6.5% at 1.0 mg/mL. Compared with CT, the inhibitory indices of SCT and SPCT at 1.0 mg/mL were 24.2% and 66.2%, respectively. Namely, both SCT and SPCT have a better ability to inhibit *F. oxysporum*, and propane sulfonated groups might help to improve the antifungal activity of chitin derivatives.

The antifungal assays against *B. cinerea* suggest that the antifungal activities of the chitin derivatives exhibited a dose-dependent manner (Figure 6C). It is evident that the antifungal activity of the chitin derivatives was much better than that of chitin at the same concentration. The inhibitory rates of CT, SCT and SPCT against *B. cinerea* at 1.0 mg/mL were 13.6%, 46.9% and 77.3%, respectively.

The inhibitory rates of CT, SCT and SPCT against *F. oxysporum* f. sp. *Cucumerium* are shown in Figure 6D. The results are similar to the antifungal activity against *P. asparagi*. The inhibitory rate of CT was 14.6% at 1.0 mg/mL, while those of SCT and SPCT at 1.0 mg/mL were 20.3% and 89.0%, respectively.

Based on the results mentioned above, sulfonated chitin can serve to repress the growth of fungus, and SPCT with propane sulfonated groups exhibits higher antifungal activity than SCT with sulfonated groups and CT. The result also concurs with the previous studies reported by Sajomsang and Li, in which they also discovered that the antifungal activity of chitosan derivatives against the plant pathogenic fungi was enhanced by the increasing chain length of alkyl substituent [35,36]. According to the results mentioned above, propane sulfonated groups are considered efficacious antifungal groups. Therefore, SPCT that exhibits selective bactericidal activity could be used in agricultural industries.

## 3. Materials and Methods

### *3.1. Materials*

Chitin was purchased from Sinopharm Chemical Reagent Co., and its degree of deacetylation was 10%. The other reagents, such as chloroform, sodium azide, triphenylphosphine ($Ph_3P$), 4-toluene sulfonyl chloride, 1,3-propanesulfonate, sulfur trioxide pyridine, N-Methyl pyrrolidone (NMP) and dimethyl sulfoxide (DMSO), etc., were provided by Sinopharm Chemical Reagent Co., Ltd., Shanghai, China.

### *3.2. Analytical Methods*

FT-IR spectra of the samples diluted in KBr pellets were performed on a Fourier transform infrared spectrometer (JASCO Co., Ltd. Shanghai, China). The elemental analyses (C, H, and N) were carried out using a Vario Micro Elemental Analyzer (Elementar, Germany). The UV–Vis absorbance was measured using a T6 New Century UV spectrometer (P General Co., Ltd., Beijing, China). $^{13}C$ nuclear magnetic resonance ($^{13}C$ NMR) spectra were carried out on a Bruker AVANCE III spectrometer (Bruker Tech. and Serv. Co., Ltd. Beijing, China.) The thermogravimetric analysis (TGA) was recorded on the TGA/DSC1/1100 (Mettler-Toledo). The X-ray patterns of samples were measured using an X-ray diffractometer (D8 advance, Bruker, Germany).

### *3.3. Synthesis*

As shown in Scheme 1, amino-chitin was synthesized according to the earlier literature [37]. The synthesis and characterization of amino-chitin are provided in the Supplementary Materials. SCT and SPCT were prepared as follows.

3.3.1. Preparation of Sulfo-Chitin (SCT)

A mixture of 0.3 g amino-chitin and 80 mL DMSO was treated with sulfur trioxide pyridine complex (1.2 g) at 80 °C for 24 h. The crude product was dialyzed for 2 days and lyophilized. Yield: 64%.

3.3.2. Preparation of Sulfopropyl-Chitin (SPCT)

We dispersed 0.3 g of amino-chitin into 50 mL of 2% acetic acid solution via magnetic stirring. Then, 1.0 mL of 1,3-propanesulfonate was added into solution, and the solution was raised to 80 °C and maintained for 24 h. The crude product was dialyzed for 2 days and lyophilized. Yield: 40%.

*3.4. Investigation of the Antioxidant Activity*

Antioxidant activity models can be classified into two basic mechanisms: single electron transfer (SET) and hydrogen atom transfer (HAT). The SET mechanism studies one electron's transferring ability to reduce metals and radicals with changes in color as a result, such as 2,2-diphenyl-1-picrylhydrazyl radical (DPPH) scavenging, hydrogen peroxide scavenging and ferric ion reducing antioxidant power. On the contrary, the HAT mechanism is the ability to quench free radicals by hydrogen donation, which can be measured by various assays such as oxygen radical absorbance and total oxyradical scavenging capacity assay.

3.4.1. DPPH-Radical Scavenging Activity

The DPPH scavenging activities of the samples were determined using the method described by Luan [38]. Testing samples (SCT and SPCT) and 180 μM DPPH ethanol solution were incubated for 0.5 h at 25 °C. Afterwards, the reaction system was shaken evenly and incubated in dark for 20 min. Finally, the absorbance of the mixture was recorded at 517 nm spectrophotometrically. The assay was performed in triplicate and the DPPH-radical scavenging activity was computed using the following Equation (1):

$$\text{Scavenging effect } (\%) = \left[1 - \frac{A_{\text{sample 517 nm}} - A_{\text{control 517 nm}}}{A_{\text{blank 517 nm}}}\right] \times 100 \quad (1)$$

where $A_{\text{sample 517 nm}}$ is the absorbance of the sample at 517 nm; $A_{\text{control 517 nm}}$ is the absorbance of the control at 517 nm; and $A_{\text{blank 517 nm}}$ is the absorbance of the blank at 517 nm.

3.4.2. Hydroxyl-Radical Scavenging Activity

The hydroxyl-radical scavenging power of the samples was performed in accordance with the approach of Sun [39]. The reaction mixture, with a total volume of 4.5 mL and involving testing samples (SCT and SPCT), was incubated with EDTA-$Fe^{2+}$ (220 μmol/L), $H_2O_2$ (60 μmol/L) and safranine T (0.23 μmol/L) in phosphate buffer (pH 7.4) for 0.5 h at 37 °C under shaken condition. The absorbance of the resulting solution was recorded at 520 nm against a blank. The assay was performed in triplicate and the hydroxyl-radical scavenging activity was computed using the following Equation (2):

$$\text{Scavenging effect } (\%) = \frac{A_{\text{sample 520 nm}} - A_{\text{blank 520 nm}}}{A_{\text{control 520 nm}} - A_{\text{blank 520 nm}}} \times 100 \quad (2)$$

where $A_{\text{sample 520 nm}}$ is the absorbance of the sample at 520 nm; $A_{\text{control 520 nm}}$ is the absorbance of the control at 520 nm; and $A_{\text{blank 520 nm}}$ is the absorbance of the blank at 520 nm.

3.4.3. Superoxide-Radical Scavenging Activity

The superoxide-radical scavenging capability was determined based on the procedure reported with slight modifications [40]. It involving testing samples (SCT and SPCT), reduced nicotinamide adenine dinucleotide (338 μmol), phenazine mothosulfate (30 μmol) and nitro blue tetrazolium (72 μmol) in Tris-HCl buffer (16 mM, pH 8.0). After the resulting

solution was incubated for 5 min at room temperature, the absorbance was read quickly at 560 nm. The assay was performed in triplicate and the superoxide-radical scavenging effect was computed according to the following Equation (3):

$$\text{Scavenging effect } (\%) = \left[1 - \frac{A_{\text{sample 560 nm}} - A_{\text{control 560 nm}}}{A_{\text{blank 560 nm}}}\right] \times 100 \quad (3)$$

where $A_{\text{sample 560 nm}}$ is the absorbance of the sample at 560 nm; $A_{\text{control 560 nm}}$ is the absorbance of the control at 560 nm; and $A_{\text{blank 560 nm}}$ is the absorbance of the blank at 560 nm.

#### 3.4.4. Reducing Power Activity

The reducing power was measured following the earlier methods [41]. In summary, 1.5 mL of 1% potassium ferricyanide was mixed with 1.5 mL of testing sample (CT, SCT and SPCT), and the resulting solution was incubated at 50 °C for 20 min. Then, 10% trichloroacetic acid (1.5 mL) was added. Subsequently, the upper layer (2.0 mL) was blended with distilled water (2.0 mL) and 0.1% ferric chloride (0.2 mL). After standing undisturbed for 10 min, the absorbance of the mixture was recorded at 700 nm. The reducing power of the samples increased with the absorbance.

### *3.5. Evaluation of Antifungal Activity In Vitro*

Antifungal assays were determined according to the method reported by Zhang [42]. In brief, each sample solution (CT, SCT and SPCT) was added to fungal medium to give a final concentrations of 0.1, 0.5 and 1.0 mg/mL and sterilized by autoclaving at 120 °C for 40 min. After the PDA medium was cooled, the fungal mycelia disk (5 mm) was transferred to the nutrient agar plate and incubated at 27 °C. All the samples were plated in triplicate on agar plates, and the inhibition rate was calculated as follows with Equation (4):

$$\text{Antifungal index } (\%) = \left[1 - \frac{D_a}{D_b}\right] \times 100 \quad (4)$$

where $D_a$ is the diameter of growth zone in the test plate and $D_b$ is the diameter of growth zone in the control plate.

### *3.6. Statistical Analysis*

All data were reported as means ± standard deviation. The differences in the assays were determined via Scheffe's method. Data were analyzed by the analysis of variance to guarantee statistical significance.

## 4. Conclusions

In summary, chitin derivatives with propane sulfonated groups were successfully synthesized. In addition, the antioxidant and antifungal activities of chitin and sulfonated chitin derivatives were tested in vitro. Chemical derivatization and the incorporation of (propane) sulfonated groups were done on chitin to yield better solubility, antioxidant and antifungal activities. We found that antioxidant abilities and antifungal properties were in the order of SPCT > SCT > CT. From the results, it can be inferred that the antioxidant ability and antifungal activity increased with an increase in the chain length of alkyl substituents. At the same time, propane sulfonated groups led to an enhancement of the antioxidant and antifungal activity. Furthermore, chitin derivatives with enhanced biological activities could be utilized as potential biomaterial for antioxidant and antifungal applications. Therefore, this work can offer a feasible way to overcome chitin's limitation by generating soluble derivatives. Undoubtedly, the further modification and utilization of chitin can minimize the waste of shell-waste and create new industrial opportunities.

**Supplementary Materials:** The following supporting information can be downloaded at: https://www.mdpi.com/article/10.3390/10.3390/md20110668/s1, Figure S1: FTIR spectra of TCT and ACT; Figure S2: Solid-state $^{13}C$ NMR spectra of TCT and ACT.

**Author Contributions:** F.L. participated in designing the experiments, wrote the paper and was the chief experimenter. Z.X. also performed the experiments and participated in analyzing the data. K.W. and X.Q. participated in analyzing the data and were responsible for language modification. Z.G. was the chief designer and the instructor of the experiment and analyzed the experimental data. All authors have read and agreed to the published version of the manuscript.

**Funding:** This research was funded by the Natural Science Foundation of Shandong Province of China (ZR2020QD080) for financial support of this work.

**Acknowledgments:** We would like to thank the Institutional Center for the shared technologies and facilities of the Yantai Institute of Coastal Zone Research.

**Conflicts of Interest:** The authors declare that there is no conflict of interest.

## References

1. Younes, I.; Rinaudo, M. Chitin and chitosan preparation from marine sources. Structure, properties and applications. *Mar. Drugs* **2015**, *13*, 1133–1174. [CrossRef] [PubMed]
2. Zhang, X.; Zhang, H.; Yin, L.; Hu, R.; Qiu, T.; Yin, Y.; Xiong, X.; Zheng, H.; Wang, Q. A pH-Sensitive Nanosystem Based on Carboxymethyl Chitosan for Tumor-Targeted Delivery of Daunorubicin. *J. Biomed. Nanotechnol.* **2016**, *12*, 1688–1698. [CrossRef] [PubMed]
3. Hu, R.; Zheng, H.; Cao, J.; Davoudi, Z.; Wang, Q. Synthesis and In Vitro Characterization of Carboxymethyl Chitosan-CBA-Doxorubicin Conjugate Nanoparticles as pH-Sensitive Drug Delivery Systems. *J. Biomed. Nanotechnol.* **2017**, *13*, 1097–1105. [CrossRef]
4. Chen, J.; Zhan, Y.; Wang, Y.; Han, D.; Tao, B.; Luo, Z.; Ma, S.; Wang, Q.; Li, X.; Fan, L.; et al. Chitosan/silk fibroin modified nanofibrous patches with mesenchymal stem cells prevent heart remodeling post-myocardial infarction in rats. *Acta Biomater.* **2018**, *80*, 154–168. [CrossRef]
5. Wei, X.; Liao, J.; Davoudi, Z.; Zheng, H.; Chen, J.; Li, D.; Xiong, X.; Yin, Y.; Yu, X.; Xiong, J.; et al. Folate Receptor-Targeted and GSH-Responsive Carboxymethyl Chitosan Nanoparticles Containing Covalently Entrapped 6-Mercaptopurine for Enhanced Intracellular Drug Delivery in Leukemia. *Mar. Drugs* **2018**, *16*, 439. [CrossRef]
6. Yan, N.; Chen, X. Don't waste seafood waste. *Nature* **2015**, *524*, 155–157. [CrossRef]
7. Mohan, K.; Ganesan, A.R.; Muralisankar, T.; Jayakumar, R.; Sathishkumar, P.; Uthayakumar, V.; Chandirasekar, R.; Revathi, N. Recent insights into the extraction, characterization, and bioactivities of chitin and chitosan from insects. *Trends Food Sci. Technol.* **2020**, *105*, 17–42. [CrossRef]
8. Uranga, J.; Etxabide, A.; Cabezudo, S.; de la Caba, K.; Guerrero, P. Valorization of marine-derived biowaste to develop chitin/fish gelatin products as bioactive carriers and moisture scavengers. *Sci. Total Environ.* **2020**, *706*, 135747. [CrossRef]
9. Kertmen, A.; Ehrlich, H. Patentology of chitinous biomaterials. Part I: Chitin. *Carbohydr. Polym.* **2022**, *282*, 119102. [CrossRef]
10. Li, F.; You, X.; Li, Q.; Qin, D.; Wang, M.; Yuan, S.; Chen, X.; Bi, S. Homogeneous deacetylation and degradation of chitin in NaOH/urea dissolution system. *Int. J. Biol. Macromol.* **2021**, *189*, 391–397. [CrossRef]
11. Mohan, K.; Ganesan, A.R.; Ezhilarasi, P.N.; Kondamareddy, K.K.; Rajan, D.K.; Sathishkumar, P.; Rajarajeswaran, J.; Conterno, L. Green and eco-friendly approaches for the extraction of chitin and chitosan: A review. *Carbohydr. Polym.* **2022**, *287*, 119349. [CrossRef] [PubMed]
12. Yang, Y.; Zhang, H.; Zeng, F.; Jia, Q.; Zhang, L.; Yu, A.; Duan, B. A quaternized chitin derivatives, egg white protein and montmorillonite composite sponge with antibacterial and hemostatic effect for promoting wound healing. *Compos. Part B Eng.* **2022**, *234*, 109661. [CrossRef]
13. Luan, F.; Wei, L.; Zhang, J.; Mi, Y.; Dong, F.; Li, Q.; Guo, Z. Antioxidant Activity and Antifungal Activity of Chitosan Derivatives with Propane Sulfonate Groups. *Polymers* **2018**, *10*, 395. [CrossRef] [PubMed]
14. Seedevi, P.; Moovendhan, M.; Vairamani, S.; Shanmugam, A. Evaluation of antioxidant activities and chemical analysis of sulfated chitosan from Sepia prashadi. *Int. J. Biol. Macromol.* **2017**, *99*, 519–529. [CrossRef] [PubMed]
15. Ouerghemmi, S.; Dimassi, S.; Tabary, N.; Leclercq, L.; Degoutin, S.; Chai, F.; Pierlot, C.; Cazaux, F.; Ung, A.; Staelens, J.N.; et al. Synthesis and characterization of polyampholytic aryl-sulfonated chitosans and their in vitro anticoagulant activity. *Carbohydr. Polym.* **2018**, *196*, 8–17. [CrossRef]
16. Baldisserotto, A.; Demurtas, M.; Lampronti, I.; Tacchini, M.; Moi, D.; Balboni, G.; Pacifico, S.; Vertuani, S.; Manfredini, S.; Onnis, V. Synthesis and evaluation of antioxidant and antiproliferative activity of 2-arylbenzimidazoles. *Bioorg. Chem.* **2020**, *94*, 103396.
17. Khan, A.Q.; Rashid, K.; AlAmodi, A.A.; Agha, M.V.; Akhtar, S.; Hakeem, I.; Raza, S.S.; Uddin, S. Reactive oxygen species (ROS) in cancer pathogenesis and therapy: An update on the role of ROS in anticancer action of benzophenanthridine alkaloids. *Biomed. Pharmacother.* **2021**, *143*, 112142. [CrossRef]

18. Ma, Y.; Fu, L.; Hussain, Z.; Huang, D.; Zhu, S. Enhancement of storability and antioxidant systems of sweet cherry fruit by nitric oxide-releasing chitosan nanoparticles (GSNO-CS NPs). *Food Chem.* **2019**, *285*, 10–21. [CrossRef] [PubMed]
19. Min, T.; Zhu, Z.; Sun, X.; Yuan, Z.; Zha, J.; Wen, Y. Highly efficient antifogging and antibacterial food packaging film fabricated by novel quaternary ammonium chitosan composite. *Food Chem.* **2020**, *308*, 125682. [CrossRef] [PubMed]
20. Hamed, I.; Özogul, F.; Regenstein, J.M. Industrial applications of crustacean by-products (chitin, chitosan, and chitooligosaccharides): A review. *Trends Food Sci. Technol.* **2016**, *48*, 40–50. [CrossRef]
21. Bahrami, B.; Behzad, T.; Salehinik, F.; Zamani, A.; Heidarian, P. Incorporation of Extracted Mucor indicus Fungus Chitin Nanofibers into Starch Biopolymer: Morphological, Physical, and Mechanical Evaluation. *Starch-Stärke* **2021**, *73*, 2000218. [CrossRef]
22. Barkhordari, M.R.; Fathi, M. Production and characterization of chitin nanocrystals from prawn shell and their application for stabilization of Pickering emulsions. *Food Hydrocoll.* **2018**, *82*, 338–345. [CrossRef]
23. Vikhoreva, G.; Bannikova, G.; Stolbushkina, P.; Panov, A.; Drozd, N.; Makarov, V.; Varlamov, V.; Galbraikh, L. Preparation and anticoagulant activity of a low-molecular-weight sulfated chitosan. *Carbohydr. Polym.* **2005**, *62*, 327–332. [CrossRef]
24. Jeon, J.H.; Cheedarala, R.K.; Kee, C.D.; Oh, I.K. Dry-Type Artificial Muscles Based on Pendent Sulfonated Chitosan and Functionalized Graphene Oxide for Greatly Enhanced Ionic Interactions and Mechanical Stiffness. *Adv. Funct. Mater.* **2013**, *23*, 6007–6018. [CrossRef]
25. Tsai, H.S.; Wang, Y.Z.; Lin, J.J.; Lien, W.F. Preparation and properties of sulfopropyl chitosan derivatives with various sulfonation degree. *J. Appl. Polym. Sci.* **2009**, *116*, 1686–1693. [CrossRef]
26. Kaya, M.; Cakmak, Y.S.; Baran, T.; Asan-Ozusaglam, M.; Mentes, A.; Tozak, K.O. New chitin, chitosan, and O-carboxymethyl chitosan sources from resting eggs of Daphnia longispina (Crustacea); with physicochemical characterization, and antimicrobial and antioxidant activities. *Biotechnol. Bioprocess Eng.* **2014**, *19*, 58–69. [CrossRef]
27. Kaya, M.; Baran, T.; Asan-Ozusaglam, M.; Cakmak, Y.S.; Tozak, K.O.; Mol, A.; Mentes, A.; Sezen, G. Extraction and characterization of chitin and chitosan with antimicrobial and antioxidant activities from cosmopolitan *Orthoptera* species (Insecta). *Biotechnol. Bioprocess Eng.* **2015**, *20*, 168–179. [CrossRef]
28. Abdel-Rahman, R.M.; Hrdina, R.; Abdel-Mohsen, A.M.; Fouda, M.M.; Soliman, A.Y.; Mohamed, F.K.; Mohsin, K.; Pinto, T.D. Chitin and chitosan from Brazilian Atlantic Coast: Isolation, characterization and antibacterial activity. *Int. J. Biol. Macromol.* **2015**, *80*, 107–120. [CrossRef] [PubMed]
29. Luan, F.; Wei, L.; Zhang, J.; Tan, W.; Chen, Y.; Wang, P.; Dong, F.; Li, Q.; Guo, Z. Synthesis, Characterization, and Antifungal Activity of N-Quaternized and N-Diquaternized Chitin Derivatives. *Starch-Stärke* **2018**, *70*, 1800026. [CrossRef]
30. Cai, J.; Dang, Q.; Liu, C.; Wang, T.; Fan, B.; Yan, J.; Xua, Y. Preparation, characterization and antibacterial activity of O-acetyl-chitosan-N-2-hydroxypropyl trimethyl ammonium chloride. *Int. J. Biol. Macromol.* **2015**, *80*, 8–15. [CrossRef]
31. Shahzad, S.; Shahzadi, L.; Mahmood, N.; Siddiqi, S.A.; Rauf, A.; Manzoor, F.; Chaudhry, A.A.; Rehman, I.U.; Yar, M. A new synthetic methodology for the preparation of biocompatible and organo-soluble barbituric- and thiobarbituric acid based chitosan derivatives for biomedical applications. *Mater. Sci. Eng. C* **2016**, *66*, 156–163. [CrossRef] [PubMed]
32. Ioelovich, M. Crystallinity and hydrophility of chitin and chitosan. *J. Chem.* **2014**, *3*, 7–14.
33. Duh, P.D.; Du, P.C.; Yen, G.C. Action of Methanolic Extract of Mung Bean Hulls as Inhibitors of Lipid Peroxidation and Non-lipid Oxidative Damage. *Food Chem. Toxicol.* **1999**, *37*, 1055–1061. [CrossRef]
34. Chen, Y.; Liu, X.; Sun, X.; Zhang, J.; Mi, Y.; Li, Q.; Guo, Z. Synthesis and Antioxidant Activity of Cationic 1,2,3-Triazole Functionalized Starch Derivatives, Polymers. *Polymers* **2020**, *12*, 112. [CrossRef]
35. Li, Q.; Ren, J.; Dong, F.; Feng, Y.; Gu, G.; Guo, Z. Synthesis and antifungal activity of thiadiazole-functionalized chitosan derivatives. *Carbohydr. Res.* **2013**, *373*, 103–107. [CrossRef]
36. Sajomsang, W.; Gonil, P.; Saesoo, S.; Ovatlarnporn, C. Antifungal property of quaternized chitosan and its derivatives. *Int. J. Biol. Macromol.* **2012**, *50*, 263–269. [CrossRef] [PubMed]
37. Zhang, J.; Luan, F.; Li, Q.; Gu, G.; Dong, F.; Guo, Z. Synthesis of Novel Chitin Derivatives Bearing Amino Groups and Evaluation of Their Antifungal Activity. *Mar. Drugs* **2018**, *16*, 380. [CrossRef]
38. Mi, Y.; Tan, W.; Zhang, J.; Guo, Z. Modification of Hydroxypropyltrimethyl Ammonium Chitosan with Organic Acid: Synthesis, Characterization, and Antioxidant Activity. *Polymers* **2020**, *12*, 2460. [CrossRef]
39. Sun, X.; Zhang, J.; Chen, Y.; Mi, Y.; Tan, W.; Li, Q.; Dong, F.; Guo, Z. Synthesis, Characterization, and the Antioxidant Activity of Carboxymethyl Chitosan Derivatives Containing Thiourea Salts. *Polymers* **2019**, *11*, 1810. [CrossRef]
40. Zhu, X.; Zhang, X.; Gao, X.; Meng, X.; Yi, Y. Synthesis and Characterization of Inulin Butyrate Ester, and Evaluation of Its Antioxidant Activity and In Vitro Effect on SCFA Production. *Starch-Stärke* **2020**, *72*, 1900323. [CrossRef]
41. Luan, F.; Li, Q.; Tan, W.; Wei, L.; Zhang, J.; Dong, F.; Gu, G.; Guo, Z. The evaluation of antioxidant and antifungal properties of 6-amino-6-deoxychitosan in vitro. *Int. J. Biol. Macromol.* **2018**, *107*, 595–603. [CrossRef]
42. Zhang, J.; Tan, W.; Mi, Y.; Luan, F.; Wei, L.; Li, Q.; Dong, F.; Guo, Z. Synthesis and Characterization of Inulin Derivatives Bearing Urea Groups with Promising Antifungal Activity. *Starch-Stärke* **2019**, *71*, 1800058. [CrossRef]

marine drugs

MDPI

*Review*

# Polyvinyl Alcohol-Chitosan Scaffold for Tissue Engineering and Regenerative Medicine Application: A Review

**Kavitha Ganesan Nathan [1], Krishnamurithy Genasan [2,*] and Tunku Kamarul [1,3,*]**

[1] Department of Orthopedic Surgery, Faculty of Medicine, University Malaya, Kuala Lumpur 50603, Malaysia; kavitha.gnathan@um.edu.my
[2] Department of Physiology, Faculty of Medicine, University Malaya, Kuala Lumpur 50603, Malaysia
[3] Advanced Medical and Dental Institute (AMDI), University Sains Malaysia, Bertam, Kepala Batas 13200, Malaysia
* Correspondence: krishna_82@um.edu.my (K.G.); tkzrea@um.edu.my (T.K.)

**Abstract:** Tissue engineering and regenerative medicine (TERM) holds great promise for addressing the growing need for innovative therapies to treat disease conditions. To achieve this, TERM relies on various strategies and techniques. The most prominent strategy is the development of a scaffold. Polyvinyl alcohol-chitosan (PVA-CS) scaffold emerged as a promising material in this field due to its biocompatibility, versatility, and ability to support cell growth and tissue regeneration. Preclinical studies showed that the PVA-CS scaffold can be fabricated and tailored to fit the specific needs of different tissues and organs. Additionally, PVA-CS can be combined with other materials and technologies to enhance its regenerative capabilities. Furthermore, PVA-CS represents a promising therapeutic solution for developing new and innovative TERM therapies. Therefore, in this review, we summarized the potential role and functions of PVA-CS in TERM applications.

**Keywords:** polyvinyl alcohol; chitosan; scaffold; tissue engineering; regenerative medicine

**Citation:** Nathan, K.G.; Genasan, K.; Kamarul, T. Polyvinyl Alcohol-Chitosan Scaffold for Tissue Engineering and Regenerative Medicine Application: A Review. *Mar. Drugs* **2023**, *21*, 304. https://doi.org/10.3390/md21050304

Academic Editor: Azizur Rahman

Received: 31 March 2023
Revised: 23 April 2023
Accepted: 24 April 2023
Published: 17 May 2023



## 1. Introduction

Tissue engineering (TE) is an interdisciplinary field that uses the principles of engineering and biological sciences to create biological substitutes that can reinstate, sustain, or improve tissues or organs functionality in the body [1]. It provides a combination of scientific disciplines, including cell biology, medicine, and engineering, to design systems that can contribute to the development of novel cells and tissues [2]. On the other hand, regenerative medicine (RM) is a field that integrates knowledge from multidisciplinary basic research to develop clinical interventions that can substitute or rejuvenate human cells and regrow damaged tissue to restore its normal function [3]. It uses various approaches, including cell-based treatment, gene therapy, immunomodulation, nanomedicine, and TE itself, to stimulate the repair or regeneration of organ(s) [4].

Tissue engineering and regenerative medicine (TERM) were explored for over 30 years. Due to their similar goals, these two fields converged in recent years and became a potential strategy to satisfy the future requirements of patients [5]. Tissues in the human body have a limited capacity to repair or regenerate. This presents a challenge that is often difficult for clinicians to overcome. Therefore, TERM relies on various strategies and techniques to achieve its goals. The most prominent strategies are the use of scaffolds [6–8], cells [9–11], and growth factors [12–14]. This review focuses on the scaffold polyvinyl alcohol (PVA)-chitosan (CS) and its multiple functions in TERM applications. We also discuss the challenges and limitations associated with its use.

### *1.1. An Overview of PVA and Chitosan*

Hydrogels are three-dimensional (3D) systems composed of hydrophilic polymeric materials, which exhibit a structure conducive to water absorption. This feature enables

one to retain significant amounts of water. Their high-water content, softness, and porosity make them resemble living tissue and exhibit excellent biocompatibility [15,16]. They are also sensitive and intelligent enough to respond to environmental stimuli such as ionic strength, temperature, pH, electric fields, enzymes, etc. [15]. Hydrogels can be prepared from natural or synthetic polymers or their blends to produce enhanced characteristics of materials than starting polymers [17].

Polyvinyl alcohol (PVA) is a synthetic, biocompatible polymer extensively studied for developing scaffolds owing to its high strength, resistance to deformation under load, capacity for water retention, and porous architecture [18]. At the same time, chitosan (CS) is a biocompatible polysaccharide that is semi-crystalline and has a linear structure. CS is derived from the exoskeletons of crustaceans [19]. The most intriguing property of CS is its ability to be processed into porous structure that is well-suited for cell transplantation and tissue regeneration applications [20]. Although CS-based hydrogels are promising for biomedical applications, their mechanical characteristic was often a drawback [21]. Therefore, a combined material such as nanoparticles, biopolymers, and synthetic polymers could solve this challenge by offsetting the limitations of one another and creating an ideal biomaterial.

Incorporating PVA into the CS-based hydrogel matrix can enhance its mechanical properties. Several recent studies focused on the combination of PVA and CS, and the combination was shown to have good mechanical and chemical properties due to their unique intermolecular interactions based on their chemical structure and physical properties [22–24]. PVA is a water-soluble synthetic polymer with a high degree of hydrogen bonding between its hydroxyl groups (-OH), while CS has amino groups (-$NH_2$) in its chemical structure, which can form hydrogen bonds with the hydroxyl groups of PVA (Figure 1). Due to hydrogen bonding and electrostatic interactions, the PVA-CS mixture can also form physical crosslinks that can contribute to the unique properties of the material, such as increased tensile strength, toughness, and stability in aqueous environments [25].

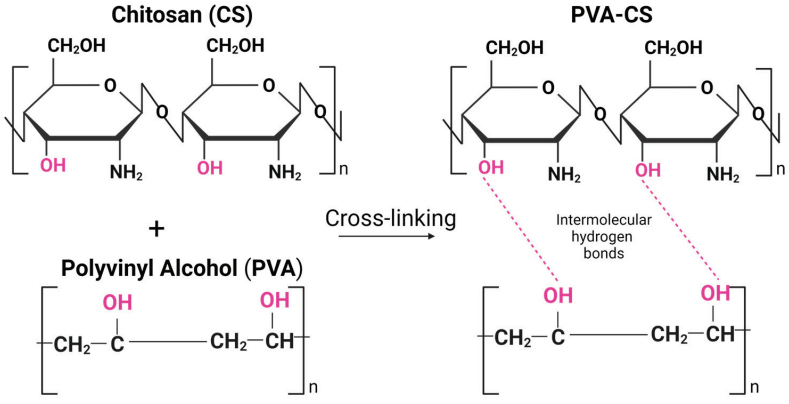


**Figure 1.** Intermolecular hydrogen bonds between chitosan (CS) and polyvinyl alcohol (PVA) polymeric chains. Created by BioRender.com (accessed on 23 April 2023).

In addition, PVA-CS blends exhibit high blood compatibility [26] and have the potential to serve as effective drug delivery platforms [27]. Therefore, PVA–CS combinations are extensively investigated in membrane filtration, dye adsorption, packaging, and biomedical applications [28,29].

### *1.2. Physical and Biological Properties of PVA-CS Hydrogel*

A biomaterial for TE should be biocompatible because the interplay between the implanted growing cells and the biomaterial significantly influences the development of new tissue. Biomedical material should not cause harm, including toxic, injurious,

or immunological responses in living human tissue, blood, or the immune system [30]. PVA blends hydrogels were used in various combinations and compositions with either chemical or thermal cross-linking agents such as glutaraldehyde [31,32], sulfosuccinic acid [33,34], succinic acid [33], glyoxal [35], dianhydrides [36], maleic acid [37], sodium hexametaphosphate [38], citric acid [39], trimetaphosphate [38], and formaldehyde [26]. The existence of residual cross-linking agents may result in detrimental adverse reactions. Moreover, the drug-cross-linker interactions can give rise to the creation of noxious or ineffectual derivatives [40]. Therefore, biocompatibility and toxicity tests are necessary before biomaterials can be used for clinical applications.

Freeze/thaw processing is another method to produce hydrogel without using chemical cross-linkers [41]. PVA hydrogels prepared by freeze/dry cycles are excellent biomaterials owing to their water swelling capacity, rubbery elasticity, non-toxic, non-carcinogenic and are well tolerated by the body [41]. Several studies focused on combining PVA with CS to produce soft, swellable, and flexible PVA-CS hydrogels using this method [23,42,43].

PVA-CS hydrogel has unique physical and biological properties, making it a popular choice for biomedical applications. This combination of soft, elastic, and flexible nature makes it suitable for TE and wound-healing applications [44–46]. In addition, its high-water absorption capacity makes it an excellent choice for wound dressings [44] and drug delivery applications [47]. The water content of the hydrogel can be adjusted by varying the ratio of PVA and CS, which affects the mechanical strength and swelling properties [48]. In addition, CS has antibacterial properties that can help preventing infections during wound healing. Therefore, due to its unique physical and biological properties, PVA-CS was introduced as a promising material for various biomedical applications.

### *1.3. Characterization Techniques for PVA-CS*

PVA-CS hydrogels with different ratios underwent evaluations for their physiochemical and mechanical traits, cytotoxicity, and biocompatibility [24,49]. Various approaches can be used to study the properties of PVA-CS hydrogels. The most common techniques include; (i) the swelling behavior can be studied by measuring its weight before and after swelling, (ii) the water content can be determined by weighing before and after drying, (iii) the mechanical properties such as elasticity, tensile strength, and modulus can be determined by various methods including shear, tensile, and compression tests, (iv) the transparency and optical properties can be analyzed using UV spectroscopy and transmission electron microscopy (TEM), (v) the morphology can be analyzed using TEM or scanning electron microscopy (SEM), (vi) the biocompatibility can be tested by performing cell culture assays for cell viability, proliferation, and differentiation, (vii) the antibacterial properties can be evaluated using disc diffusion assays, colony forming units (CFU), or minimum inhibitory concentrations (MIC) assays, and (viii) the biodegradability can be evaluated by measuring the weight loss or degradation of the hydrogel over time [24,50–52].

## 2. Applications of PVA-CS Hydrogel

The biocompatible and biodegradable properties of PVA and CS make them attractive biomaterials for the application in the field of TERM [44]. Many studies showed that the combination of PVA and CS has several desirable properties that make them suitable for various medical applications [53,54]. Therefore, this review is a brief overview of the recent application of the PVA-CS scaffold in TERM Table 1.

**Table 1.** Summary of the PVA-CS applications in TERM.

| Composites | Methods | Applications | Advantages | Ref |
|---|---|---|---|---|
| PVA-CS-BMSCs hydrogel | Freeze–thaw cycles | Osteochondral tissue repair in a rabbit model | • Exhibit stable physical and chemical properties.<br>• No cytotoxicity.<br>• Promote cell proliferation. | [24] |
| CS/PVA/ZnO beads | Hydrothermal | Antibacterial agent and wound healing | • Exhibit high antibacterial activities against *Escherichia coli* and *Staphylococcus aureus* bacteria.<br>• Fast wound healing in mice skin. | [45] |
| PVA-CS-Curcumin patch | Glutaraldehyde reagent crosslinker | Antibacterial agent and wound healing | • Increase cell proliferation.<br>• Antibacterial activities against *Escherichia coli*, *Pseudomonas aeruginosa*, *Staphylococcus aureus*, and *Bacillus subtilis*.<br>• Wound healing ability. | [46] |
| PVA-CS-BMSCs scaffold | Freeze–thaw | Focal cartilage repair in a rabbit model | • Cartilage repair. | [49] |
| PVA-CS Lactate hydrogel | Glutaraldehyde reagent crosslinker | Drug delivery | • Facilitate cell adhesion.<br>• Facilitate antimicrobial activity. | [54] |
| PVA-CS-ADSCs nanofibrous scaffold | Electrospun | Cartilage TE | • Exhibit uniform cell distribution and high biocompatibility.<br>• ADSCs were able to proliferate and differentiate into chondrogenic cells. | [55] |
| PVA-CS-HA(PRP) scaffold with or without MSCs | Electrospun | Osteogenic differentiation and bone reconstruction | • Have a positive effect on MSCs.<br>• MSCs seeded scaffold has a huge osteoconductivity. | [56] |
| PVA-CS-poly(ε-caprolactone) scaffold | Multi-jet electrospun | Bone TE | • Support cell attachment and osteogenic differentiation of rat MSCs. | [57] |
| PVA-CS-carbonated HA scaffold | Electrospun | Bone TE | • Facilitate osteoblast cells to attach and proliferate.<br>• Increase cell viability. | [58] |
| PVA-CS-gelatinnanoHA | Paraformaldehyde reagent crosslinker | Bone TE | • Promote cell proliferation and adhesion.<br>• Scaffolds containing 12.5% of nanHA were demonstrated to have high osteogenic differentiation ability. | [59] |
| PVA-CS-Lidocaine hydrochloride | Electrospun and glutaraldehyde reagent crosslinker | Drug delivery | • Form a dual drug release delivery system.<br>• Exhibit excellent antibacterial activity against *Staphylococcus aureus and Pseudomonas aeruginosa* strains. | [60] |
| PVA-CS-Cloisite 30B | Glutaraldehyde reagent crosslinker | Drug delivery | • Drug release was reported based on time, drug loading percentage, and pH of the medium.<br>• Drug release is more pronounced in the basic medium compared to the acidic medium.<br>• Kinetics of the drug release reported based on the non-Fickian type of mechanism. | [61] |

**Table 1.** *Cont.*

| Composites | Methods | Applications | Advantages | Ref |
|---|---|---|---|---|
| PVA-CS nanofiber | Electrospun and glutaraldehyde reagent crosslinker | Transdermal drug delivery | • Crosslinked PVA/CS composite had a lower drug release rate and smaller drug burst release.<br>• Release of ampicillin sodium fit to the Fickian diffusion mechanism. | [62] |
| PVA-CS-Dextran | Glutaraldehyde reagent crosslinker | Wound dressing | • Present high cell proliferation.<br>• Promote thermostability and mechanical properties.<br>• Promote moisture and water retention.<br>• Exhibit high antimicrobial properties. | [63] |
| PVA-CS nanofiber mats | Electrospun | Wound healing | • Non-toxic to normal human fibroblast cells.<br>• Satisfactory antibacterial activity against *Staphylococcus aureus* and *Escherichia coli*.<br>• Showed greatest wound-healing activity during the first four days after wounds. | [64] |

### *2.1. Tissue Engineering*

TE is a vital area of biomaterials application as the various approaches can be used to treat abnormalities in tissues and organs [65,66]. TE aims to create a 3D cell-containing scaffold implanted into the body to treat a disease or repair damage [67]. The standard in vitro culture system cannot mimic the intricacies of the cellular microenvironment and seldom facilitates the integration of cells into fully functional tissue. Therefore, providing an appropriate scaffold of a diverse range of natural and synthetic materials will lead to the development of functional tissue.

In recent years, PVA-CS was widely used as a TE scaffold. PVA-CS scaffold could be a good platform for tissue regeneration alone or in combination with other polymers and cellular components [53]. The scaffold provides a 3D architecture that imitates the original tissue's extracellular matrix (ECM), providing a favorable environment for stem cell growth and differentiation [68]. Stem cells are undifferentiated cells that can develop into distinct types of specialized cells. Depending on the application and regenerated tissue, different types of stem cells can be integrated with biomaterial scaffolds. The combination of stem cells and biomaterial scaffolds presents a promising approach for both in vitro and in vivo TE applications [68].

PVA-CS scaffold is a promising biomaterial for cartilage repair, while mesenchymal stem cells (MSCs) are emerging as a better option due to their unique properties and potential to promote tissue regeneration and repair [69]. MSCs are a type of adult stem cell that can differentiate into multiple cell types, including chondrocytes, adipocytes, osteocytes, etc. When MSCs are introduced into damaged cartilage tissue, they can help stimulating the repair process and promote the growth of new cartilage cells. One of the advantages of using MSCs for cartilage repair is that they can be obtained from a variety of tissues, including bone marrow (BM), adipose tissue (AT), and umbilical cord tissue (UCT). This means that MSCs can be easily isolated and propagated in vitro, making them a readily available option for cartilage repair and cell-based therapy [70]. In addition, MSCs were shown to secrete various growth factors and cytokines that can promote tissue regeneration and repair. These factors can help stimulate new blood vessel growth, reduce inflammation, and promote the growth of new cartilage cells [69]. This could be the reason why MSCs are often combined with natural or synthetic hydrogels to enhance biocompatibility, biodegradability, and cellular response.

In 2015, Dashtdar et al. investigated whether MSCs seeded in PVA-CS hydrogel could result in comparable or even better cartilage healing than that of previously established alginate-transplanted model. This study confirmed that the PVA-CS-MSCs construct leads to comparable treatment outcomes in the rabbit cartilage defect model, thus suggested for for clinical applications in cartilage regeneration [49]. In extension to this study, our group implanted the PVA-CS in a cadaveric knee cartilage defect using a minimally invasive arthroscopic technique as part of the technical validity prior to our clinical trial study (Figure 2). In 2019, Peng et al. demonstrated that the hydrogel PVA-CS provided an excellent surface for rabbit bone marrow mesenchymal stem cells (rBM-MSCs) adhesion and proliferation. In addition, this group demonstrated that PVA-CS caused no cytotoxicity and achieved the best cartilage repair compared to scaffold alone in an in vivo rabbit model [24].

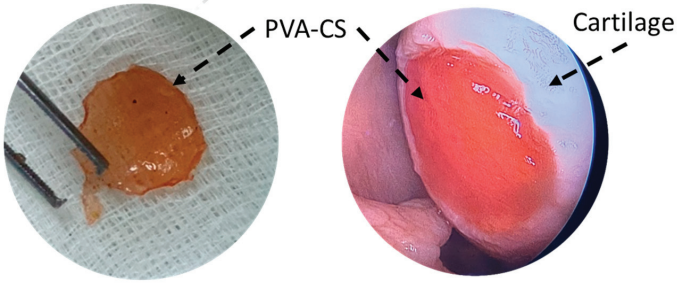


**Figure 2.** PVA-CS was implanted at the cadaveric knee cartilage defect using a minimally invasive arthroscopic technique.

Nour-Eldeen et al. established a scaffold that allowed adipose-derived mesenchymal stem cells (ADSCs) to proliferate and differentiate into chondrocyte-like cells using PVA-CS nanofiber scaffolds [55]. Characterization of seeded cells, including cell morphology, analysis of surface markers, and chondrogenic differentiation, were studied in vitro. This study suggests that using PVA-CS nanofiber scaffolds had a promoting effect on chondrogenic differentiation of ADSCs, as demonstrated by significant upregulation of aggrecan and collagen type II alpha 1 Chain (COL2A1), suggesting PVA-CS-ADSCs nanofiber scaffolds can potentially be used to improve the pathophysiology of osteoarthritis (OA). Various types of PVA-CS nanofibers were investigated for biomedical applications. PVA-CS nanofibers can be synthesized through different electrospinning techniques, resulting in different fiber morphologies and properties [71]. Many studies incorporated various biological and polymeric materials into PVA-CS nanofibers to improve their properties.

Moreover, the osteoconductive and tissue regeneration performance of the fabricated scaffold was demonstrated with and without AT-MSCs in vivo rat model [56]. Abazari et al. incorporated hydroxyapatite (HA) and platelet-rich plasma (PRP) into PVA-CS to study MSCs survival and osteogenic differentiation potential in vitro. The in vivo study showed that PVA-chitosan-HA(PRP) successfully repaired bone defects to a considerable extent. However, when MSCs were seeded onto PVA-chitosan-HA(PRP), the defects were almost filled. Therefore, it can be inferred that PVA-chitosan-HA(PRP) alone or with cultured stem cells has a promising option as an efficient bone implant.

Recently, Wee et al. investigated the impact of transforming growth factor-beta 1 (TGF-β1) and -β3 on the chondrogenic differentiation of rBM-MSCs, grown on the PVA-CS-PEG (polyethylene glycol) scaffold in comparison to pellet cultures [72]. The study reported that utilization of the PVA-CS-PEG scaffold improved both the proliferation and chondrogenic differentiation of rBM-MSCs. However, no significant differences were observed between the cultures supplemented with or without TGF-β, suggesting no effect of TGF-β1 and TGF-β3 in chondrogenic differentiation. Enhanced cell proliferation observed in PVA-CS-PEG scaffolds may be attributed to the positive charge of chitosan, which facilitates the

adhesion and proliferation of BM-MSCs on the scaffold [73]. Moreover, the PVA-CS-PEG scaffold offers a beneficial 3D porous structure that enables high-density cell proliferation of BM-MSCs within the scaffold due to its large surface area-to-volume ratio [72].

Mohammadi et al. developed a novel 3D nanofiber hybrid scaffold of poly(ε-caprolactone), PVA, and CS for bone tissue engineering using MSCs via a multi-jet electrospinning method [57]. The scaffolds' chemical, physical, and structural properties were investigated to determine their impact on the differentiation of MSCs into osteoblasts and the proliferation of the differentiated cells. SEM microscopic images of MSCs seeded and differentiated on the scaffold showed that the cells attached, permeated, and uniformly distributed within the construct. Additionally, the expression of osteoblastic differentiation markers, including osteocalcin (OCN), osteopontin (OPN), alkaline phosphatase (ALP), and bone sialoprotein (BSP) exhibited an upregulation in constructs cultured in osteogenic media suggested that nanofibrous scaffolds may be favorable for TE [57]. The mechanisms by which PVA-CS nanofibers scaffold promotes osteoblasts differentiation and proliferation of MSCs are multifactorial and involve both physical and chemical cues. The 3D structure of the nanofibers scaffolds that mimic the natural ECM of bone tissue allows for the adhesion and proliferation of MSCs, providing a suitable microenvironment for osteoblast differentiation. Additionally, the high surface area-to-volume ratio allows for the efficient exchange of nutrients and waste products between the cells and the culture medium [58,59].

Interestingly, CS was shown to stimulate osteoblast differentiation and mineralization. Mathews et al. demonstrated the osteogenic potential of CS in a 2D culture system. This study presented novel findings indicating that CS enhanced mineralization by upregulating the genes involved in mineralization as well as calcium-binding proteins such as OPN, Integrin binding sialoprotein (IBSP), Collagen type I alpha 1 chain (COL1A1), ALP, and OCN [74]. Chen et al. developed chitosan nanofibers to investigate their impact on osteoblast maturation and the underlying mechanisms of action in vitro [75]. This study reported that chitosan nanofibers could promote the growth and development of osteoblasts by regulating the expression of genes associated with osteoblasts function, including OPN, OCN, and ALP through the Runt-related transcription factor 2 (RUNX2) pathway [75].

For cardiovascular TE, PVA/CS or PVA-CS was used as a coating material for cardiovascular stents to improve their biocompatibility and reduce the risk of restenosis [76]. In addition, PVA/CS was studied as a potential material for artificial blood vessels and heart valves TE [77]. Research showed that the combination of PVA and CS can yield a composite material with enhanced properties and biocompatibility compared to any single polymer. For example, a study published in the Journal of Biomaterials Science, Polymer Edition, found that a PVA-CS composite coating on a cardiovascular stent reduced the risk of restenosis and improved endothelial cell proliferation compared with a stent coated with PVA or CS alone. Karami et al. reported that PVA-CS composite coating on a cardiovascular stent reduced the risk of restenosis and improved endothelial cell proliferation compared to a stent coated with only PVA or CS [78].

### *2.2. Drug Delivery System*

Hydrogel delivery systems are used clinically and can provide therapeutically beneficial effects. The use of hydrogels allows for the precise control of the time and location of therapeutic agent delivery, including small-molecule drugs, macromolecular drugs, and cells [47].

PVA-CS was used as a drug delivery system for various therapeutic agents in TE. This combination was shown to enhance drug solubility and stability, increase drug uptake by cells, and improve drug release kinetics. The hydrophilic nature of PVA and the cationic characteristic of CS provides an ideal environment for drug loading and delivery.

In drug delivery, PVA-CS can be used in multiple forms, such as nanoparticles, microparticles, and hydrogels. The different forms have different advantages and can be tailored to meet specific drug delivery requirements. Mahato et al. developed PVA-CS

lactate hydrogel and investigated it as a matrix for the continuous and gradual release of hydrophilic drugs [54]. The developed PVA-CS lactate was cross-linked, and freeze-bound water was measured to analyze the cold crystallization properties. Cell adhesion, cytotoxicity, hemolysis, and drug release properties were also investigated. In vitro cell viability of L929 cells showed that PVA-CS lactate hydrogels were compatible with cells and improved cell adhesion. Moreover, the release of ciprofloxacin from the drug-loaded PVA-CS lactate hydrogels inhibited the growth of E. coli, which provided antibacterial activity under physiological conditions [54]. Fathollahipour et al. synthesized a series of hydrogel by blending PVA-CS and adding different amounts of graphene oxide (GO) to develop composite hydrogels [60]. In this study, the drug release profile and kinetics of the drug were studied to predict the mechanism of drug release.

In recent years, PVA-CS nanoparticles were used to encapsulate various drugs, including anticancer drugs, antibiotics, and anti-inflammatory agents. They were shown to increase drug bioavailability and potentially target specific cells or regions. In 2011, Parida et al. included Cloisite 30B in the formulation of PVA-CS as a matrix material component, and curcumin was prepared at various concentrations and loaded with PVA-CS/C 30B nanocomposites to investigate the in vitro drug delivery system for anticancer drugs [61]. They studied the kinetics of the drug release in order to ascertain the type of release mechanism. The kinetics results showed that the drug release was much more significant in the basic medium than in the acidic medium [61].

Shagholani et al. has improved the interaction between PVA and CS hydrogel by magnetite nanoparticles, making them a favorable option for drug delivery and clinical applications [79]. They synthesized magnetite nanoparticles by co-precipitation with ultrasound and then coated them with CS. The CS-coated magnetite nanoparticles were then coated with PVA. These modified nanoparticles present minimal protein adsorption, making them feasible for evading opsonization during clinical applications and drug administration [79]. Cui et al. fabricated PVA-CS nanofibers containing ampicillin sodium using the electrospinning technique. This study reported that the drug release studies, and kinetic analysis of the drug delivery system fitted to the Korsmeyer–Peppas model [62].

Microparticles, microcapsules, and microspheres are common constituents of multiparticulate drug delivery systems. Microparticles are spherical particles ranging in size from 1 to 1000 μm and are used as multiparticulate drug delivery systems to improve efficacy, tolerability, and patient compliance [80]. Microparticles from PVA-CS were used to sustain drug release over an extended period. These particles were loaded with drugs and implanted into the patient's body for controlled drug delivery [81]. Morelli et al. fabricated PVA-CS microparticles by emulsification for the purpose of encapsulation and controlled release under pH conditions. This study developed a novel technique combining cross-linking with emulsion formation to produce particles with different release profiles based on polymer composition and cross-linking. The study reported that when negatively charged drugs like sodium salicylate are encapsulated, the release of the drug is delayed, and it impacts the selective release under acidic pH conditions [82].

In 2010, the hydrogel PVA-CS was developed to deliver insulin through the nasal cavity [83]. The PVA-CS hydrogels were prepared with different formulations, and the pH was adjusted to a near-neutral value of 1.0 M $NaHCO_3$. Insulin was incorporated into the formulated delivery system, resulting in a final solution with a concentration of 1 IU of insulin per 200 μL. The in vitro insulin release assay showed that glucose levels were maintained for 6 h, while in the in vivo experiment, the greatest reduction was observed 4 h after administration [83]. This suggests that slow release was achieved via the PVA-CS network. In 2017, a similar study was conducted to evaluate the potential of PVA-CS microspheres as a vehicle for insulin drug delivery via intranasal administration [84]. The authors developed different formulations, and morphological analysis of the optimized formulas showed that the size range was between 200 nm to 2 μm. The in vitro study showed that microspheres from PVA-CS exhibited immediate, sharp, and erratic drug release, while the in vivo investigation in rats demonstrated a reduced drug release rate

and better mucoadhesive properties [84]. Thus, using PVA-CS in drug delivery systems produced favorable outcomes.

### *2.3. Wound Healing*

PVA-CS was extensively studied for its potential use in wound healing, as its water retention capacity and antibacterial activity indicate that it is a perfect material for wound treatment [44,45]. CS was shown to have antimicrobial properties due to its ability to interact with bacterial cell membranes and disrupt their structure [84]. The antimicrobial activity of CS may be due to several factors, including its positive charge, which allows it to bind to negatively charged bacterial cell membranes, and its ability to form a gel-like that can physically block the growth and spread of bacteria [84–86]. For this reason, it was used in various forms, including hydrogel patches, films, nanofibers, and scaffolds.

PVA-CS hydrogels and films are most used as wound dressings because they can retain water, which is critical for healing. This hydrogel absorbs exudate and creates a protective barrier that shields the wound from external contaminants. Several studies reported the antibacterial activity and healing properties of PVA-CS loaded with other active ingredients [45,46,63,87,88]. Niranjan R. et al. combined PVA-CS with curcumin (CUR) and obtained as PVA-CS-CUR patches by gel casting showed antibacterial activity against the most prevalent strains found (*Escherichia coli*, *Pseudomonas aeruginosa*, *Staphylococcus aureus*, *Bacillus subtilis*) in wound sites [46]. Furthermore, in vivo studies in albino Wistar rats on wound healing ability showed that this patch has an excellent wound healing ability and can treat all kinds of epidermal damage. Similarly, Gutha et al. developed PVA-CS-zinc oxide (ZnO) beads as a novel wound-healing agent that exhibits antibacterial properties. The antibacterial activity against *Escherichia coli* and *Staphylococcus aureus* was evaluated by the inhibition method, and the wound healing properties were tested in mice skin. The PVA-CS -ZnO showed excellent antibacterial and wound-healing activity, suggesting its potential use for wound-healing applications [45].

High cell proliferation capacity is critical for wound healing. Lin et al. reported that the combination of PVA, CS, and dextran exhibited high cell proliferation ability, making them ideal for wound dressing [63]. Recently, Feng et al. reviewed that CS plays a vital role in wound healing [89]. Wound healing processes generally involve four crucial phases: hemostasis, inflammation, proliferation, and skin remodeling. The initial three stages rely significantly on the involvement of CS during the hemostasis stage. CS helps prevent bleeding by promoting platelet and red cell aggregation and preventing fibrin disintegration. In the inflammation stage, CS helps eliminate microorganisms from the wound and finally increases skin proliferation by promoting the growth of granulation tissue in the proliferation stage [89].

Due to their high surface area and ability to mimic natural tissue structure, PVA-CS nanofibers can be used as wound dressings. Nanofibers can increase cell adhesion and migration, critical for wound healing. PVA-CS nanofibers can also be loaded with active ingredients to improve wound healing. Electrospun nanofibers are well suited as wound dressing materials because they have a high surface area ratio, variable pore size distribution, and oxygen permeability [64]. Moreover, the morphology of electrospun nanofibers is comparable to skin ECM, which stimulates cell adhesion, migration, and proliferation [64,90,91] Campa-Siqueiros et al. prepared electrospun gelatin (G) and PVA-CS nanofibers and studied their physicochemical properties and antimicrobial activity [91]. They reported that PVA-CS-G could be used as a wound dressing and combined with common bioactive chemicals or growth factors for its sustained release in treating chronic diabetic patients [91]. In contrast, Liu et al. used the solution-blowing method to prepare hydrogel nanofiber mats from PVA-CS with various ethylene glycol diglycidyl ether (EDGE) content as cross-linker [92]. SEM, FTIR, and X-ray photoelectron spectroscopy (XPS) results suggested that the PVA-CS hydrogel nanofiber mats had both the advantages of a hydrogel and a fiber mat, including excess exudate absorption, facilitation of a moist wound healing environment, permitting gas exchange, and displaying strong antibacterial properties [92].

Fatahian et al. developed a hybrid fiber mat through a co-electrospun hybrid of PVA, CS, and silk fiber mats. The hybrid fiber mat characteristics, including porosity, degradability, pore size, tensile strength, and hydrophilic properties for wound healing, were investigated in vitro and in vivo by localizing BMMSC keratinocytes on the mat [87]. Compared to PVA alone and the fiber PVA-CS, incorporating mixed CS and co-electrospun silk into the PVA-based fiber mat showed excellent cell attachment and growth. In vivo tests also showed that the composite PVA-CS + silk fiber mat incorporating keratinocytes MSCs may promote wound healing and facilitate skin tissue generation [87].

## 3. Other Biomedical Applications

PVA-CS composite is also commonly used in other applications, including periodontal treatment [93], ophthalmic, orthopedic, cancer therapy, immunotherapy, gene therapy, and cosmetics Table 2.

**Table 2.** Summary of the PVA-CS applications in other biomedical applications.

| Composites | Methods | Applications | Advantages | Ref |
|---|---|---|---|---|
| PVA-oxidized CS-silver Nanoparticles/Ibuprofen film | Cross-linked | Periodontal pockets | • The film has good antimicrobial properties against *Staphylococcus aureus*, *Klebsiella pneumoniae*, *Pseudomonas aeruginosa*, and *Porphyromonas gingivalis gingivalis*.<br>• Biocompatible as demonstrated by in vitro on HDFa cell lines. | [94] |
| PVA-CS-graphene oxide-astaxanthin nanofiber | Electrospun | Anti-inflammation and bone regeneration of periodontal therapy | • Anti-inflammatory and osteogenic activity evaluated in vitro.<br>• Promote high expression of osteogenic genes OCN and Runx2 in BMSCs.<br>• Induce M2 polarization.<br>• Promote high expression of GPNMB in RAW264.7 cells. Glycoprotein nonmetastatic melanoma protein. | [95] |
| PVA-CS-Ofloxavin | Electrospun | Ocular drug delivery | • Antimicrobial efficiency against *Staphylococcus aureus* and *Escherichia coli*.<br>• The use of Ofloxavin nanofibrous inserts on a rabbit eye demonstrated a sustained release pattern for up to 96 h.<br>• Demonstrates the potential of the nanofiber technology to sustain drug release in ocular drug delivery systems. | [96] |
| PVA-CS corneal shield | Electrospun | Ocular surface disorder | • In vivo study demonstrated that the corneal shield applied to the rabbit eyes has good biocompatibility and drug delivery effect.<br>• No inflammatory reaction.<br>• No corneal edema. | [97] |
| PVA-CS-Silver/PVA-CS-Gold | Gamma-irradiated | Prostatic cancer | • Significant effectiveness against prostatic cancer. | [98] |
| PVA-CS-Tea tree oil film | Emulsion | Biomedical application | • Better resorption and biocompatibility.<br>• The incorporation of oil stimulates significant interaction with phagocytic cells. | [99] |

### *3.1. Periodontal*

Several studies showed that PVA-CS has properties that can be useful in periodontal treatment. Its biocompatibility, drug delivery, antibacterial, and wound healing properties showed promising treatment options for periodontal diseases. Dong et al. synthesized CS-

decorated metronidazole (MTZ) microcapsules (CS@MTZ) and used them as cross-linkers for injectable PVA hydrogel preparation for periodontal drug delivery [100]. The study showed that PVA-CS-MTZ hydrogel is a suitable formulation for periodontal therapy due to its injectability, antibacterial efficacy, and underwater adhesion [100].

In periodontitis treatment, local administration of drugs or antimicrobial agents is an appropriate strategy when an infection is intensely localized in the pockets and does not respond well to mechanical debridement and systemic antibiotic treatment. Constantin et al. synthesized a PVA-CS film containing silver nanoparticles and ibuprofen to treat periodontal disease [94]. The film was evaluated for its biological activity, morphology, loading amount, mechanical properties, and ibuprofen release. The authors reported that the films had suitable antimicrobial properties against oral cavity pathogens and were biocompatible, as demonstrated by an in vitro study on human dermal fibroblasts, adult (HDFa) skin cell lines [94].

In recent years, TE scaffolds emerged as a potential treatment strategy for the repair and regeneration of tissue defects in periodontal disease [101,102]. A recent study published in the Journal of Dental Sciences found that PVA-CS could be an excellent flexible film for membranes used in periodontal regeneration, which can prevent fibroblasts from entering the wound and be used in periodontal regeneration surgery [93]. Dang et al. demonstrated the anti-inflammatory and osteogenic activity of PVA-CS-graphene oxide-astaxanthin nanofiber membranes in vitro. The electrospun membranes were found to stimulate a significant upregulation of osteogenic genes, osteocalcin (OCN), and RUNX2 in BMMSCs, and high expression of GPNMB in RAW26407 cells, leading to M2 polarization. These findings suggest that the nanofiber membranes can potentially enhance inflammatory dissipation and osteoblast differentiation [95].

### *3.2. Ophthalmic*

PVA-CS blend was evaluated for its potential for ophthalmic applications as an ocular drug delivery system. It is used to improve drug bioavailability and residence time in the eye [96,103,104]. Under physiological conditions, the mixture can form a gel-like substance that can prolong drug release and minimize the frequency of administration. In addition, PVA-CS was investigated for its potential use in the treatment of ocular surface disorders such as dry eye syndrome. It was shown to improve tear film integrity and minimize ocular surface damage [97,105]. Therefore, PVA-CS seems to be a good system for drug delivery in ophthalmology and for treating ocular surface diseases. Further research and clinical trials are needed to evaluate its safety and efficacy in humans.

### *3.3. Gene Therapy*

Gene therapy is a procedure that involves delivering genetic material to cells to treat or prevent diseases. Viral and non-viral vectors are commonly utilized to transport therapeutic genes into specific cells for effective treatment [106]. Non-viral vectors in gene delivery systems always refer to methods that do not involve viruses for gene transfer. In recent years, several studies reported the use of lipid-based nanoparticles [107], polymeric nanoparticles [108], and naked DNA [109] as a non-viral vector for gene transfer.

CS-based polymeric nanoparticles can be used as a non-viral vector for gene delivery. It has numerous advantages over viral vectors, such as safety and low immunogenicity [110]. In cancer research, several studies showed that siRNA-loaded CS-based nanoparticles are a promising therapeutic strategic [98,111–113]. Furthermore, CS was used as a carrier for in vivo delivery of interference agents such as siRNA [114]. Mulholland et al. used PVA-CS nanoparticles as a carrier to deliver a siRNA targeting FKBPL in both in vivo and in vitro models for angiogenesis in wound healing [115]. The in vitro results showed enhanced cell migration and increased endothelial tubule formation, while the in vivo study in mice demonstrated increased angiogenesis and blood vessel density [115].

### *3.4. Cosmetics*

PVA-CS was widely used in the cosmetics industry. A combination of PVA-CS can offer several benefits to cosmetic products, especially skin and hair care products [116,117]. Since PVA-CS is a water-soluble polymer blend, it can improve the hydration properties of cosmetic formulations. Thin film formation on the skin can help lock in moisture and prevent dryness [116,117].

Castor et al. synthesized four distinct composite films composed of PVA-CS and tea tree (*Melaleuca alternifolia*) essential oil and tested them on Wistar rats through subdermal implantations [99]. This study indicated that the composite films exhibit excellent thermal and mechanical stability and simulated body fluid stability. These were confirmed by mechanical and thermal analyses when there was a rise in Young's modulus and decomposition temperatures. Furthermore, the biocompatibility of the films was found to be like that of porcine collagen and with higher tea tree essential oil showing more significant signs of resorption [99].

## 4. Challenges and Limitations

PVA-CS showed potential material for TERM (Figure 3), but there are also some challenges and limitations associated with its use. Although the mechanical properties of PVA-CS can be modified, they may not be sufficient for all TERM applications, as the material can also degrade over time, which can affect its mechanical properties and lead to loss of structural integrity [118]. Although PVA-CS was shown to be biocompatible [18], further studies are needed to evaluate its long-term safety and efficacy in vivo.

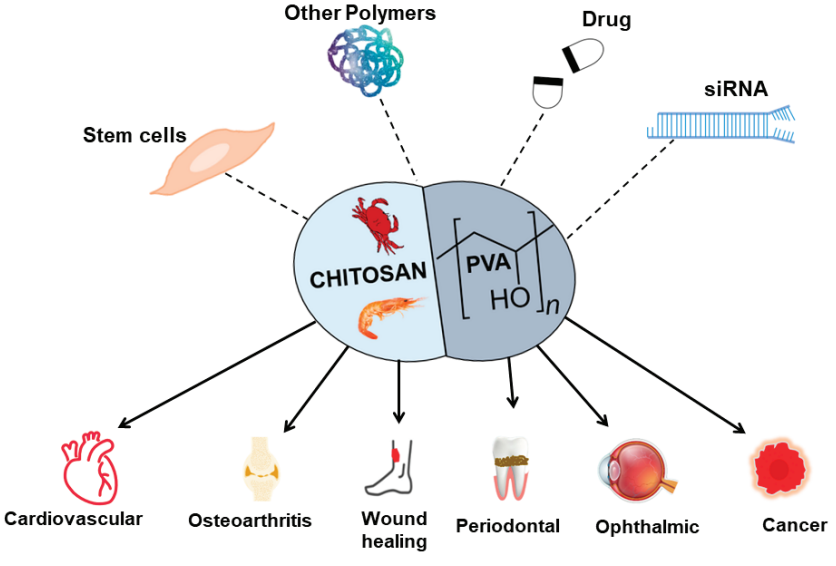


**Figure 3.** An overview of the PVA-CS combined with other materials and their application in TERM.

Fabrication of the PVA-CS scaffold itself may be challenging due to difficulties in optimizing the pore size and porosity of the scaffold. Poor pore size and porosity of a scaffold can impair cell adhesion, proliferation, and differentiation. The shape of the scaffold can influence its porosity and pore size in several ways. For example, a flat, planar scaffold may have lower porosity than a 3D scaffold with more complex geometry, such as a cylindrical or spherical shape. This is because a planar scaffold has a lower surface area-to-volume ratio, which limits the number of pores created in the material.

On the other hand, a more complex-shaped scaffold may provide a greater surface area-to-volume ratio, allowing a larger number of pores to form [119,120]. In addition,

these scaffolds must be sterilized before being used in medical and clinical applications. Some sterilization methods may affect the mechanical and chemical properties of the scaffold [121].

PVA-CS nanoparticles are pH-dependent [98], which means that their physicochemical properties change with the change in pH. Therefore, their stability and functionality can be affected by changes in the pH of the surrounding environment.

The limited availability of CS, which is derived from crustacean shells, can increase the cost of production. Additionally, PVA-CS must undergo rigorous testing and regulatory approval when combined with other biologically active components and polymer materials before it can be widely used in TERM applications.

PVA-CS showed promising results in the laboratory, but producing large quantities of PVA-CS products for commercial use can be challenging. The process of synthesizing PVA-CS products can be complex and time-consuming, and scaling up the production process while maintaining desired quality and consistency can be difficult.

## 5. Conclusions

The PVA-CS blend is a promising material for TERM applications due to its biocompatibility, antimicrobial properties, and ability to support cell growth and tissue regeneration. The best is that it can be fabricated and customized to fit the specific requirements of different cells, tissues, and organs, making it a versatile tool in RM. PVA-CS nanoparticles were investigated for their potential use as drug delivery vehicles, as they can protect the encapsulated drug from degradation and improve its bioavailability. Films prepared from PVA and CS were shown to have good mechanical strength, biocompatibility, and controlled drug release. On the other hand, hydrogels based on PVA-CS can be used for TE and drug delivery due to their large water absorption capacity and 3D network for cell growth. PVA-CS can also be used in the form of scaffolds for TE and wound healing applications as they provide mechanical support and promote cell growth.

**Author Contributions:** K.G.N., conceptualization, writing—original manuscript and editing; K.G., review and checking final version of the manuscript; T.K., supervision. All authors have read and agreed to the published version of the manuscript.

**Funding:** This research was funded by Ministry of Science, Technology and Innovation (MOSTI), through MOSTI Ted 2 grant number "TEF07211061".

**Institutional Review Board Statement:** Not applicable.

**Data Availability Statement:** Not applicable.

**Conflicts of Interest:** The authors declare no conflict of interest.

## References

1. Langer, R.; Vacanti, J. Tissue Engineering. *Science* **1993**, *260*, 920–926. [CrossRef] [PubMed]
2. Jafari, M.; Paknejad, Z.; Rad, M.R.; Motamedian, S.R.; Eghbal, M.J.; Nadjmi, N.; Khojasteh, A. Polymeric scaffolds in tissue engineering: A literature review. *J. Biomed. Mater. Res. Part B Appl. Biomater.* **2015**, *105*, 431–459. [CrossRef] [PubMed]
3. Mason, C.; Dunnill, P. A brief definition of regenerative medicine. *Regen. Med.* **2008**, *3*, 1–5. [CrossRef] [PubMed]
4. Salgado, A.J.; Oliveira, J.M.; Martins, A.; Teixeira, F.G.; Silva, N.A.; Neves, N.M.; Sousa, N.; Reis, R.L. Tissue Engineering and Regenerative Medicine. *Int. Rev. Neurobiol.* **2013**, *108*, 1–33. [CrossRef] [PubMed]
5. Han, F.; Wang, J.; Ding, L.; Hu, Y.; Li, W.; Yuan, Z.; Guo, Q.; Zhu, C.; Yu, L.; Wang, H.; et al. Tissue Engineering and Regenerative Medicine: Achievements, Future, and Sustainability in Asia. *Front. Bioeng. Biotechnol.* **2020**, *8*, 83. [CrossRef]
6. Zheng, D.; Dan, Y.; Yang, S.; Liu, G.; Shao, Z.; Yang, C.; Xiao, B.; Liu, X.; Wu, S.; Zhang, T.; et al. Controlled chondrogenesis from adipose-derived stem cells by recombinant transforming growth factor-β3 fusion protein in peptide scaffolds. *Acta Biomater.* **2015**, *11*, 191–203. [CrossRef]
7. Xue, C.; Ren, H.; Zhu, H.; Gu, X.; Guo, Q.; Zhou, Y.; Huang, J.; Wang, S.; Zha, G.; Gu, J.; et al. Bone marrow mesenchymal stem cell-derived acellular matrix-coated chitosan/silk scaffolds for neural tissue regeneration. *J. Mater. Chem. B* **2017**, *5*, 1246–1257. [CrossRef]

8. Xiao, B.; Yang, W.; Lei, D.; Huang, J.; Yin, Y.; Zhu, Y.; You, Z.; Wang, F.; Sun, S. PGS Scaffolds Promote the In Vivo Survival and Directional Differentiation of Bone Marrow Mesenchymal Stem Cells Restoring the Morphology and Function of Wounded Rat Uterus. *Adv. Healthc. Mater.* **2019**, *8*, 1801455. [CrossRef]
9. Fontaine, M.J.; Shih, H.; Schäfer, R.; Pittenger, M.F. Unraveling the Mesenchymal Stromal Cells' Paracrine Immunomodulatory Effects. *Transfus. Med. Rev.* **2016**, *30*, 37–43. [CrossRef]
10. Schäfer, R.; Spohn, G.; Baer, P.C. Mesenchymal Stem/Stromal Cells in Regenerative Medicine: Can Preconditioning Strategies Improve Therapeutic Efficacy? *Transfus. Med. Hemotherapy* **2016**, *43*, 256–267. [CrossRef]
11. Bertheuil, N.; Chaput, B.; Ménard, C.; Varin, A.; Laloze, J.; Watier, E.; Tarte, K. Adipose mesenchymal stromal cells: Definition, immunomodulatory properties, mechanical isolation and interest for plastic surgery. *Ann. Chir. Plast. Esthétique* **2019**, *64*, 1–10. [CrossRef] [PubMed]
12. James, A.W.; LaChaud, G.; Shen, J.; Asatrian, G.; Nguyen, V.; Zhang, X.; Ting, K.; Soo, C. A Review of the Clinical Side Effects of Bone Morphogenetic Protein-2. *Tissue Eng. Part B Rev.* **2016**, *22*, 284–297. [CrossRef] [PubMed]
13. Aldag, C.; Nogueira Teixeira, D.; Leventhal, P.S. Skin rejuvenation using cosmetic products containing growth factors, cytokines, and matrikines: A review of the literature. *Clin. Cosmet. Investig. Dermatol.* **2016**, *9*, 411–419. [CrossRef]
14. Kakudo, N.; Morimoto, N.; Ogawa, T.; Taketani, S.; Kusumoto, K. FGF-2 combined with bilayer artificial dermis composed of collagen matrix prompts generation of fat pad in subcutis of mice. *Med. Mol. Morphol.* **2018**, *52*, 73–81. [CrossRef]
15. Sigh, S.K.; Dhyani, A.; Juyal, D. Hydrogel: Preparation, characterization and applications. *Pharma Innov.* **2017**, *6*, 25–32.
16. Mohite, P.; Adhav, S. A hydrogels: Methods of preparation and applications. *Int. J. Adv. Pharm.* **2017**, *6*, 79–85. [CrossRef]
17. Ahmed, E.M. Hydrogel: Preparation, characterization, and applications: A review. *J. Adv. Res.* **2015**, *6*, 105–121. [CrossRef]
18. Harpaz, D.; Axelrod, T.; Yitian, A.L.; Eltzov, E.; Marks, R.S.; Tok, A.I.Y. Dissolvable Polyvinyl-Alcohol Film, a Time-Barrier to Modulate Sample Flow in a 3D-Printed Holder for Capillary Flow Paper Diagnostics. *Materials* **2019**, *12*, 343. [CrossRef]
19. Mulchandani, N.; Shah, N.; Mehta, T. Synthesis of Chitosan-Polyvinyl Alcohol Copolymers for Smart Drug Delivery Application. *Polym. Polym. Compos.* **2017**, *25*, 241–246. [CrossRef]
20. Francis Suh, J.-K.; Matthew, H.W.T. Application of chitosan-based polysaccharide biomaterials in cartilage tissue engineering: A review. *Biomaterials* **2000**, *21*, 2589–2598. [CrossRef]
21. Kamoun, E.A.; Chen, X.; Mohy Eldin, M.S.; Kenawy, E.-R.S. Crosslinked poly(vinyl alcohol) hydrogels for wound dressing applications: A review of remarkably blended polymers. *Arab. J. Chem.* **2015**, *8*, 1–14. [CrossRef]
22. Abraham, A.; Soloman, P.A.; Rejini, V.O. Preparation of Chitosan-Polyvinyl Alcohol Blends and Studies on Thermal and Mechanical Properties. *Procedia Technol.* **2016**, *24*, 741–748. [CrossRef]
23. Kamoun, E.A.; Kenawy, E.-R.S.; Chen, X. A review on polymeric hydrogel membranes for wound dressing applications: PVA-based hydrogel dressings. *J. Adv. Res.* **2017**, *8*, 217–233. [CrossRef] [PubMed]
24. Peng, L.; Zhou, Y.; Lu, W.; Zhu, W.; Li, Y.; Chen, K.; Zhang, G.; Xu, J.; Deng, Z.; Wang, D. Characterization of a novel polyvinyl alcohol/chitosan porous hydrogel combined with bone marrow mesenchymal stem cells and its application in articular cartilage repair. *BMC Musculoskelet. Disord.* **2019**, *20*, 257. [CrossRef]
25. Chetouani, A.; Elkolli, M.; Bounekhel, M.; Benachour, D. Chitosan/oxidized pectin/PVA blend film: Mechanical and biological properties. *Polym. Bull.* **2017**, *74*, 4297–4310. [CrossRef]
26. Lee, K.Y.; Ha, W.S.; Park, W.H. Blood compatibility and biodegradability of partially N-acylated chitosan derivatives. *Biomaterials* **1995**, *16*, 1211–1216. [CrossRef]
27. Kim, J.H.; Kim, J.Y.; Lee, Y.M.; Kim, K.Y. Controlled release of riboflavin and insulin through crosslinked poly(vinyl alcohol)/chitosan blend membrane. *J. Appl. Polym. Sci.* **1992**, *44*, 1823–1828. [CrossRef]
28. Nakano, Y.; Bin, Y.; Bando, M.; Nakashima, T.; Okuno, T.; Kurosu, H.; Matsuo, M. Structure and Mechanical Properties of Chitosan/Poly(Vinyl Alcohol) Blend Films. *Macromol. Symp.* **2007**, *258*, 63–81. [CrossRef]
29. Liang, S.; Liu, L.; Huang, Q.; Yam, K.L. Preparation of single or double-network chitosan/poly(vinyl alcohol) gel films through selectively cross-linking method. *Carbohydr. Polym.* **2009**, *77*, 718–724. [CrossRef]
30. He, Z.; Xiong, L. Drug Controlled Release and Biological Behavior of Poly(D,L-Lactide-Co-Glycolide) Microspheres. *J. Macromol. Sci. Part B* **2011**, *50*, 1154–1161. [CrossRef]
31. Liu, L.; Kentish, S.E. Pervaporation performance of crosslinked PVA membranes in the vicinity of the glass transition temperature. *J. Membr. Sci.* **2018**, *553*, 63–69. [CrossRef]
32. Ji, W.; Afsar, N.U.; Wu, B.; Sheng, F.; Shehzad, M.A.; Ge, L.; Xu, T. In-situ crosslinked SPPO/PVA composite membranes for alkali recovery via diffusion dialysis. *J. Membr. Sci.* **2019**, *590*, 117267. [CrossRef]
33. Kudoh, Y.; Kojima, T.; Abe, M.; Oota, M.; Yamamoto, T. Proton conducting membranes consisting of poly(vinyl alcohol) and poly(styrene sulfonic acid): Crosslinking of poly(vinyl alcohol) with and without succinic acid. *Solid State Ion.* **2013**, *253*, 189–194. [CrossRef]
34. Ajith, C.; Deshpande, A.P.; Varughese, S. Proton conductivity in crosslinked hydrophilic ionic polymer system: Competitive hydration, crosslink heterogeneity, and ineffective domains. *J. Polym. Sci. Part B Polym. Phys.* **2016**, *54*, 1087–1101. [CrossRef]
35. Zhang, Y.; Zhu, P.C.; Edgren, D. Crosslinking reaction of poly(vinyl alcohol) with glyoxal. *J. Polym. Res.* **2009**, *17*, 725–730. [CrossRef]
36. Xu, S.; Shen, L.; Li, C.; Wang, Y. Properties and pervaporation performance of poly(vinyl alcohol) membranes crosslinked with various dianhydrides. *J. Appl. Polym. Sci.* **2018**, *135*, 46159. [CrossRef]

37. Bolto, B.; Tran, T.; Hoang, M.; Xie, Z. Crosslinked poly(vinyl alcohol) membranes. *Prog. Polym. Sci.* **2009**, *34*, 969–981. [CrossRef]
38. Leone, G.; Consumi, M.; Pepi, S.; Pardini, A.; Bonechi, C.; Tamasi, G.; Donati, A.; Rossi, C.; Magnani, A. Poly-vinyl alcohol (PVA) crosslinked by trisodium trimetaphosphate (STMP) and sodium hexametaphosphate (SHMP): Effect of molecular weight, pH and phosphorylating agent on length of spacing arms, crosslinking density and water interaction. *J. Mol. Struct.* **2020**, *1202*, 127264. [CrossRef]
39. Birck, C.; Degoutin, S.; Tabary, N.; Miri, V.; Bacquet, M. New crosslinked cast films based on poly(vinyl alcohol): Preparation and physico-chemical properties. *Express Polym. Lett.* **2014**, *8*, 941–952. [CrossRef]
40. Liu, X.; Sun, Q.; Wang, H.; Zhang, L.; Wang, J.-Y. Microspheres of corn protein, zein, for an ivermectin drug delivery system. *Biomaterials* **2005**, *26*, 109–115. [CrossRef]
41. Hassan, C.M.; Peppas, N.A. Structure and Applications of Poly(vinyl alcohol) Hydrogels Produced by Conventional Crosslinking or by Freezing/Thawing Methods. In *Biopolymers·PVA Hydrogels, Anionic Polymerisation Nanocomposites*; Springer: Berlin/Heidelberg, Germany, 2000; pp. 37–65. [CrossRef]
42. Rafique, A.; Mahmood Zia, K.; Zuber, M.; Tabasum, S.; Rehman, S. Chitosan functionalized poly(vinyl alcohol) for prospects biomedical and industrial applications: A review. *Int. J. Biol. Macromol.* **2016**, *87*, 141–154. [CrossRef]
43. Figueroa-Pizano, M.D.; Vélaz, I.; Martínez-Barbosa, M.E. A Freeze-Thawing Method to Prepare Chitosan-Poly(vinyl alcohol) Hydrogels Without Crosslinking Agents and Diflunisal Release Studies. *J. Vis. Exp.* **2020**, *155*, e59636. [CrossRef]
44. Fan, L.; Yang, H.; Yang, J.; Peng, M.; Hu, J. Preparation and characterization of chitosan/gelatin/PVA hydrogel for wound dressings. *Carbohydr. Polym.* **2016**, *146*, 427–434. [CrossRef]
45. Gutha, Y.; Pathak, J.L.; Zhang, W.; Zhang, Y.; Jiao, X. Antibacterial and wound healing properties of chitosan/poly(vinyl alcohol)/zinc oxide beads (CS/PVA/ZnO). *Int. J. Biol. Macromol.* **2017**, *103*, 234–241. [CrossRef] [PubMed]
46. Niranjan, R.; Kaushik, M.; Prakash, J.; Venkataprasanna, K.S.; Christy, A.; Pannerselvam, B.; Venkatasubbu, G.D. Enhanced wound healing by PVA/Chitosan/Curcumin patches: In vitro and in vivo study. *Colloids Surf. B Biointerfaces* **2019**, *182*, 110339. [CrossRef]
47. Li, J.; Mooney, D.J. Designing hydrogels for controlled drug delivery. *Nat. Rev. Mater.* **2016**, *1*, 16071. [CrossRef] [PubMed]
48. Asy-Syifa, N.; Kusjuriansah; Waresindo, W.X.; Edikresnha, D.; Suciati, T.; Khairurrijal, K. The Study of the Swelling Degree of the PVA Hydrogel with varying concentrations of PVA. *J. Phys. Conf. Ser.* **2022**, *2243*, 012053. [CrossRef]
49. Dashtdar, H.; Murali, M.R.; Abbas, A.A.; Suhaeb, A.M.; Selvaratnam, L.; Tay, L.X.; Kamarul, T. PVA-chitosan composite hydrogel versus alginate beads as a potential mesenchymal stem cell carrier for the treatment of focal cartilage defects. *Knee Surg. Sport. Traumatol. Arthrosc.* **2013**, *23*, 1368–1377. [CrossRef] [PubMed]
50. Abdel-Mohsen, A.M.; Aly, A.S.; Hrdina, R.; Montaser, A.S.; Hebeish, A. Eco-Synthesis of PVA/Chitosan Hydrogels for Biomedical Application. *J. Polym. Environ.* **2011**, *19*, 1005–1012. [CrossRef]
51. Kamarul, T.; Krishnamurithy, G.; Salih, N.D.; Ibrahim, N.S.; Raghavendran, H.R.B.; Suhaeb, A.R.; Choon, D.S.K. Biocompatibility and Toxicity of Poly(vinyl alcohol)/N,O-Carboxymethyl Chitosan Scaffold. *Sci. World J.* **2014**, *2014*, 905103. [CrossRef]
52. Gonzalez, J.S.; Alvarez, V.A. Mechanical properties of polyvinylalcohol/hydroxyapatite cryogel as potential artificial cartilage. *J. Mech. Behav. Biomed. Mater.* **2014**, *34*, 47–56. [CrossRef]
53. Wagenbrenner, M.; Mayer-Wagner, S.; Rudert, M.; Holzapfel, B.M.; Weissenberger, M. Combinations of Hydrogels and Mesenchymal Stromal Cells (MSCs) for Cartilage Tissue Engineering—A Review of the Literature. *Gels* **2021**, *7*, 217. [CrossRef]
54. Mahato, K.K.; Yadav, I.; Singh, R.; Monika; Singh, B.N.; Singh, S.K.; Ray, B.; Kumar, M.; Misra, N. Polyvinyl alcohol/chitosan lactate composite hydrogel for controlled drug delivery. *Mater. Res. Express* **2019**, *6*, 115408. [CrossRef]
55. Nour-Eldeen, G.; Abdel-Rasheed, M.; EL-Rafei, A.M.; Azmy, O.; El-Bassyouni, G.T. Adipose tissue-derived mesenchymal stem cells and chitosan/poly (vinyl alcohol) nanofibrous scaffolds for cartilage tissue engineering. *Cell Regen.* **2020**, *9*, 7. [CrossRef]
56. Abazari, M.F.; Nejati, F.; Nasiri, N.; Khazeni, Z.A.S.; Nazari, B.; Enderami, S.E.; Mohajerani, H. Platelet-rich plasma incorporated electrospun PVA-chitosan-HA nanofibers accelerates osteogenic differentiation and bone reconstruction. *Gene* **2019**, *720*, 144096. [CrossRef]
57. Mohammadi, Y.; Soleimani, M.; Fallahi-Sichani, M.; Gazme, A.; Haddadi-Asl, V.; Arefian, E.; Kiani, J.; Moradi, R.; Atashi, A.; Ahmadbeigi, N. Nanofibrous Poly(ε-Caprolactone)/Poly(Vinyl Alcohol)/Chitosan Hybrid Scaffolds for Bone Tissue Engineering using Mesenchymal Stem Cells. *Int. J. Artif. Organs* **2007**, *30*, 204–211. [CrossRef] [PubMed]
58. Januariyasa, I.K.; Ana, I.D.; Yusuf, Y. Nanofibrous poly(vinyl alcohol)/chitosan contained carbonated hydroxyapatite nanoparticles scaffold for bone tissue engineering. *Mater. Sci. Eng. C* **2020**, *107*, 110347. [CrossRef] [PubMed]
59. Ma, P.; Wu, W.; Wei, Y.; Ren, L.; Lin, S.; Wu, J. Biomimetic gelatin/chitosan/polyvinyl alcohol/nano-hydroxyapatite scaffolds for bone tissue engineering. *Mater. Des.* **2021**, *207*, 109865. [CrossRef]
60. Fathollahipour, S.; Abouei Mehrizi, A.; Ghaee, A.; Koosha, M. Electrospinning of PVA/chitosan nanocomposite nanofibers containing gelatin nanoparticles as a dual drug delivery system. *J. Biomed. Mater. Res. Part A* **2015**, *103*, 3852–3862. [CrossRef]
61. Parida, U.K.; Nayak, A.K.; Binhani, B.K.; Nayak, P.L. Synthesis and Characterization of Chitosan-Polyvinyl Alcohol Blended with Cloisite 30B for Controlled Release of the Anticancer Drug Curcumin. *J. Biomater. Nanobiotechnol.* **2011**, *2*, 414–425. [CrossRef]
62. Cui, Z.; Zheng, Z.; Lin, L.; Si, J.; Wang, Q.; Peng, X.; Chen, W. Electrospinning and crosslinking of polyvinyl alcohol/chitosan composite nanofiber for transdermal drug delivery. *Adv. Polym. Technol.* **2017**, *37*, 1917–1928. [CrossRef]
63. Lin, S.-P.; Lo, K.-Y.; Tseng, T.-N.; Liu, J.-M.; Shih, T.-Y.; Cheng, K.-C. Evaluation of PVA/dextran/chitosan hydrogel for wound dressing. *Cell. Polym.* **2019**, *38*, 15–30. [CrossRef]

64. Charernsriwilaiwat, N.; Rojanarata, T.; Ngawhirunpat, T.; Opanasopit, P. Electrospun chitosan/polyvinyl alcohol nanofibre mats for wound healing. *Int. Wound J.* **2012**, *11*, 215–222. [CrossRef]
65. Dzobo, K.; Thomford, N.E.; Senthebane, D.A.; Shipanga, H.; Rowe, A.; Dandara, C.; Pillay, M.; Motaung, K.S.C.M. Advances in Regenerative Medicine and Tissue Engineering: Innovation and Transformation of Medicine. *Stem Cells Int.* **2018**, *2018*, 2495848. [CrossRef] [PubMed]
66. Ebhodaghe, S.O. Hydrogel—Based biopolymers for regenerative medicine applications: A critical review. *Int. J. Polym. Mater. Polym. Biomater.* **2022**, *71*, 155–172. [CrossRef]
67. Heng, B.C.; Cao, T.; Stanton, L.W.; Robson, P.; Olsen, B. Strategies for Directing the Differentiation of Stem Cells Into the Osteogenic Lineage In Vitro. *J. Bone Miner. Res.* **2004**, *19*, 1379–1394. [CrossRef]
68. Willerth, S.M.; Sakiyama-Elbert, S.E. Combining Stem Cells and Biomaterial Scaffolds for Constructing Tissues and Cell Delivery. *StemJournal* **2019**, *1*, 1–25. [CrossRef]
69. Le, H.; Xu, W.; Zhuang, X.; Chang, F.; Wang, Y.; Ding, J. Mesenchymal stem cells for cartilage regeneration. *J. Tissue Eng.* **2020**, *11*, 204173142094383. [CrossRef]
70. Somoza, R.A.; Welter, J.F.; Correa, D.; Caplan, A.I. Chondrogenic Differentiation of Mesenchymal Stem Cells: Challenges and Unfulfilled Expectations. *Tissue Eng. Part B Rev.* **2014**, *20*, 596–608. [CrossRef]
71. Teixeira, M.A.; Amorim, M.T.P.; Felgueiras, H.P. Poly(Vinyl Alcohol)-Based Nanofibrous Electrospun Scaffolds for Tissue Engineering Applications. *Polymers* **2019**, *12*, 7. [CrossRef]
72. Wee, A.-S.; Lim, C.-K.; Tan, S.-L.; Ahmad, T.S.; Kamarul, T. TGF-β1 and -β3 for Mesenchymal Stem Cells Chondrogenic Differentiation on Poly (Vinyl Alcohol)-Chitosan-Poly (Ethylene Glycol) Scaffold. *Tissue Eng. Part C Methods* **2022**, *28*, 501–510. [CrossRef] [PubMed]
73. Nettles, D.L.; Elder, S.H.; Gilbert, J.A. Potential Use of Chitosan as a Cell Scaffold Material for Cartilage Tissue Engineering. *Tissue Eng.* **2002**, *8*, 1009–1016. [CrossRef] [PubMed]
74. Mathews, S.; Gupta, P.K.; Bhonde, R.; Totey, S. Chitosan enhances mineralization during osteoblast differentiation of human bone marrow-derived mesenchymal stem cells, by upregulating the associated genes. *Cell Prolif.* **2011**, *44*, 537–549. [CrossRef] [PubMed]
75. Chen, R.-M.; Ho, M.-H.; Liao, M.-H.; Lin, Y.-L.; Lai, C.-H.; Lin, P.-I. Improving effects of chitosan nanofiber scaffolds on osteoblast proliferation and maturation. *Int. J. Nanomed.* **2014**, *9*, 4293–4304. [CrossRef] [PubMed]
76. Lin, M.-C.; Lou, C.-W.; Lin, J.-Y.; Lin, T.A.; Chou, S.-Y.; Chen, Y.-S.; Lin, J.-H. Using spray-coating method to form PVA coronary artery stents: Structure and property evaluations. *J. Polym. Res.* **2018**, *25*, 101. [CrossRef]
77. Wan, W.K.; Campbell, G.; Zhang, Z.F.; Hui, A.J.; Boughner, D.R. Optimizing the tensile properties of polyvinyl alcohol hydrogel for the construction of a bioprosthetic heart valve stent. *J. Biomed. Mater. Res.* **2002**, *63*, 854–861. [CrossRef]
78. Karami, A.; Rezvani Zadeh, S.; Jafari, A.; Jahanbani, A. Preparation and characterization of a polyvinyl alcohol/chitosan composite coating for cardiovascular stents. *J. Biomater. Sci. Polym. Ed.* **2017**, *28*, 1846–1861.
79. Shagholani, H.; Ghoreishi, S.M.; Mousazadeh, M. Improvement of interaction between PVA and chitosan via magnetite nanoparticles for drug delivery application. *Int. J. Biol. Macromol.* **2015**, *78*, 130–136. [CrossRef]
80. Lengyel, M.; Kállai-Szabó, N.; Antal, V.; Laki, A.J.; Antal, I. Microparticles, Microspheres, and Microcapsules for Advanced Drug Delivery. *Sci. Pharm.* **2019**, *87*, 20. [CrossRef]
81. Xu, J.; Song, W.; Wu, N.; Tong, J.; Ren, L. Preparation and characterization of chitosan/polyvinyl porous alcohol aerogel microspheres with stable physicochemical properties. *Int. J. Biol. Macromol.* **2021**, *187*, 614–623. [CrossRef]
82. Morelli, S.; Holdich, R.G.; Dragosavac, M.M. Chitosan and Poly (Vinyl Alcohol) microparticles produced by membrane emulsification for encapsulation and pH controlled release. *Chem. Eng. J.* **2016**, *288*, 451–460. [CrossRef]
83. Agrawal, A.K.; Gupta, P.N.; Khanna, A.; Sharma, R.K.; Chandrawanshi, H.K.; Gupta, N.; Patil, U.K.; Yadav, S.K. Development and characterization of in situ gel system for nasal insulin delivery. *Die Pharm.* **2010**, *65*, 188–193.
84. Ali Darbandi, M. Mucoadhesive Microspheres of Chitosan and Polyvinyl Alcohol as A Carrier for Intranasal Delivery of Insulin: In Vitro and In Vivo Studies. *MOJ Bioequivalence Bioavailab.* **2017**, *3*, 39–45. [CrossRef]
85. Yilmaz Atay, H. Antibacterial Activity of Chitosan-Based Systems. *Funct. Chitosan* **2020**, 457–489. [CrossRef]
86. Guarnieri, A.; Triunfo, M.; Scieuzo, C.; Ianniciello, D.; Tafi, E.; Hahn, T.; Zibek, S.; Salvia, R.; De Bonis, A.; Falabella, P. Antimicrobial properties of chitosan from different developmental stages of the bioconverter insect Hermetia illucens. *Sci. Rep.* **2022**, *12*, 8084. [CrossRef] [PubMed]
87. Nokhasteh, S.; Molavi, A.M.; Khorsand-Ghayeni, M.; Sadeghi-Avalshahr, A. Preparation of PVA/Chitosan samples by electrospinning and film casting methods and evaluating the effect of surface morphology on their antibacterial behavior. *Mater. Res. Express* **2019**, *7*, 015401. [CrossRef]
88. Fatahian, R.; Mirjalili, M.; Khajavi, R.; Rahimi, M.K.; Nasirizadeh, N. Fabrication of antibacterial and hemostatic electrospun PVA nanofibers for wound healing. *SN Appl. Sci.* **2020**, *2*, 1288. [CrossRef]
89. Feng, P.; Luo, Y.; Ke, C.; Qiu, H.; Wang, W.; Zhu, Y.; Hou, R.; Xu, L.; Wu, S. Chitosan-Based Functional Materials for Skin Wound Repair: Mechanisms and Applications. *Front. Bioeng. Biotechnol.* **2021**, *9*, 650598. [CrossRef]
90. Jayakumar, R.; Prabaharan, M.; Sudheesh Kumar, P.T.; Nair, S.V.; Tamura, H. Biomaterials based on chitin and chitosan in wound dressing applications. *Biotechnol. Adv.* **2011**, *29*, 322–337. [CrossRef]

91. Campa-Siqueiros, P.; Madera-Santana, T.J.; Ayala-Zavala, J.F.; López-Cervantes, J.; Castillo-Ortega, M.M.; Herrera-Franco, P.J. Nanofibers of gelatin and polivinyl-alcohol-chitosan for wound dressing application: Fabrication and characterization. *Polímeros* **2020**, *30*, e2020006. [CrossRef]
92. Liu, R.; Xu, X.; Zhuang, X.; Cheng, B. Solution blowing of chitosan/PVA hydrogel nanofiber mats. *Carbohydr. Polym.* **2014**, *101*, 1116–1121. [CrossRef] [PubMed]
93. Huang, C.-L.; Huang, H.-Y.; Lu, Y.-C.; Cheng, C.-J.; Lee, T.-M. Development of a flexible film made of polyvinyl alcohol with chitosan based thermosensitive hydrogel. *J. Dent. Sci.* **2023**, *18*, 822–832. [CrossRef] [PubMed]
94. Constantin, M.; Lupei, M.; Bucatariu, S.-M.; Pelin, I.M.; Doroftei, F.; Ichim, D.L.; Daraba, O.M.; Fundueanu, G. PVA/Chitosan Thin Films Containing Silver Nanoparticles and Ibuprofen for the Treatment of Periodontal Disease. *Polymers* **2022**, *15*, 4. [CrossRef] [PubMed]
95. Dang, X.; Zhang, H.; Lin, L.; Li, P.; Ren, L.; Zhang, W.; Song, R. The anti-inflammatory and osteogenic activity of chitosan/polyvinyl alcohol/graphene oxide/astaxanthin nanofibers membranes in vitro study. *J. Biomater. Appl.* **2022**, *36*, 1873–1881. [CrossRef]
96. Mirzaeei, S.; Taghe, S.; Asare-Addo, K.; Nokhodchi, A. Polyvinyl Alcohol/Chitosan Single-Layered and Polyvinyl Alcohol/Chitosan/Eudragit RL100 Multi-layered Electrospun Nanofibers as an Ocular Matrix for the Controlled Release of Ofloxacin: An In Vitro and In Vivo Evaluation. *AAPS PharmSciTech* **2021**, *22*, 170. [CrossRef]
97. Li, G.-X.; Gu, X.; Song, H.-Y.; Nan, K.-H.; Chen, H. Biocompatibility and drug release behavior of chitosan/poly (vinyl alcohol) corneal shield in vivo. *Int. J. Clin. Exp. Med.* **2015**, *8*, 12949–12955.
98. Abaza, A.; Hegazy, E.A.; Mahmoud, G.A.; Elsheikh, B. Characterization and Antitumor Activity of Chitosan/Poly (Vinyl Alcohol) Blend Doped with Gold and Silver Nanoparticles in Treatment of Prostatic Cancer Model. *J. Pharm. Pharmacol.* **2018**, *6*, 659–673. [CrossRef]
99. Castro, J.I.; Valencia-Llano, C.H.; Valencia Zapata, M.E.; Restrepo, Y.J.; Mina Hernandez, J.H.; Navia-Porras, D.P.; Valencia, Y.; Valencia, C.; Grande-Tovar, C.D. Chitosan/Polyvinyl Alcohol/Tea Tree Essential Oil Composite Films for Biomedical Applications. *Polymers* **2021**, *13*, 3753. [CrossRef]
100. Dong, Z.; Sun, Y.; Chen, Y.; Liu, Y.; Tang, C.; Qu, X. Injectable Adhesive Hydrogel through a Microcapsule Cross-Link for Periodontitis Treatment. *ACS Appl. Biomater.* **2019**, *2*, 5985–5994. [CrossRef]
101. Liu, J.; Ruan, J.; Weir, M.D.; Ren, K.; Schneider, A.; Wang, P.; Oates, T.W.; Chang, X.; Xu, H.H.K. Periodontal Bone-Ligament-Cementum Regeneration via Scaffolds and Stem Cells. *Cells* **2019**, *8*, 537. [CrossRef]
102. Sharma, P.; Kumar, P.; Sharma, R.; Bhatt, V.D.; Dhot, P. Tissue Engineering; Current Status & Futuristic Scope. *J. Med. Life* **2019**, *12*, 225–229. [CrossRef] [PubMed]
103. Zamboulis, A.; Nanaki, S.; Michailidou, G.; Koumentakou, I.; Lazaridou, M.; Ainali, N.M.; Xanthopoulou, E.; Bikiaris, D.N. Chitosan and its Derivatives for Ocular Delivery Formulations: Recent Advances and Developments. *Polymers* **2020**, *12*, 1519. [CrossRef] [PubMed]
104. Allyn, M.M.; Luo, R.H.; Hellwarth, E.B.; Swindle-Reilly, K.E. Considerations for Polymers Used in Ocular Drug Delivery. *Front. Med.* **2022**, *8*, 787644. [CrossRef] [PubMed]
105. Arribada, R.G.; Behar-Cohen, F.; de Barros, A.L.B.; Silva-Cunha, A. The Use of Polymer Blends in the Treatment of Ocular Diseases. *Pharmaceutics* **2022**, *14*, 1431. [CrossRef]
106. Xu, X.; Qiu, S.; Zhang, Y.; Yin, J.; Min, S. PELA microspheres with encapsulated arginine–chitosan/pBMP-2 nanoparticles induce pBMP-2 controlled-release, transfected osteoblastic progenitor cells, and promoted osteogenic differentiation. *Artif. Cells Nanomed. Biotechnol.* **2016**, *45*, 330–339. [CrossRef]
107. Hou, X.; Zaks, T.; Langer, R.; Dong, Y. Lipid nanoparticles for mRNA delivery. *Nat. Rev. Mater.* **2021**, *6*, 1078–1094. [CrossRef]
108. Werfel, T.; Duvall, C. Polymeric nanoparticles for gene delivery. *Polym. Nanomater. Gene Ther.* **2016**, 147–188. [CrossRef]
109. Herweijer, H.; Wolff, J.A. Progress and prospects: Naked DNA gene transfer and therapy. *Gene Ther.* **2003**, *10*, 453–458. [CrossRef]
110. Mansouri, S.; Lavigne, P.; Corsi, K.; Benderdour, M.; Beaumont, E.; Fernandes, J.C. Chitosan-DNA nanoparticles as non-viral vectors in gene therapy: Strategies to improve transfection efficacy. *Eur. J. Pharm. Biopharm.* **2004**, *57*, 1–8. [CrossRef]
111. Sun, P.; Huang, W.; Jin, M.; Wang, Q.; Fan, B.; Kang, L.; Gao, Z. Chitosan-based nanoparticles for survivin targeted siRNA delivery in breast tumor therapy and preventing its metastasis. *Int. J. Nanomed.* **2016**, *11*, 4931–4945. [CrossRef]
112. Dowaidar, M.; Nasser Abdelhamid, H.; Hällbrink, M.; Langel, Ü.; Zou, X. Chitosan enhances gene delivery of oligonucleotide complexes with magnetic nanoparticles–cell-penetrating peptide. *J. Biomater. Appl.* **2018**, *33*, 392–401. [CrossRef]
113. Ramnandan, D.; Mokhosi, S.; Daniels, A.; Singh, M. Chitosan, Polyethylene Glycol and Polyvinyl Alcohol Modified MgFe2O4 Ferrite Magnetic Nanoparticles in Doxorubicin Delivery: A Comparative Study In Vitro. *Molecules* **2021**, *26*, 3893. [CrossRef] [PubMed]
114. Vauthier, C.; Zandanel, C.; Ramon, A.L. Chitosan-based nanoparticles for in vivo delivery of interfering agents including siRNA. *Curr. Opin. Colloid Interface Sci.* **2013**, *18*, 406–418. [CrossRef]
115. Mulholland, E.J.; Ali, A.; Robson, T.; Dunne, N.J.; McCarthy, H.O. Delivery of RALA/siFKBPL nanoparticles via electrospun bilayer nanofibres: An innovative angiogenic therapy for wound repair. *J. Control. Release* **2019**, *316*, 53–65. [CrossRef] [PubMed]
116. Guzmán, E.; Ortega, F.; Rubio, R.G. Chitosan: A Promising Multifunctional Cosmetic Ingredient for Skin and Hair Care. *Cosmetics* **2022**, *9*, 99. [CrossRef]
117. Kulka, K.; Sionkowska, A. Chitosan Based Materials in Cosmetic Applications: A Review. *Molecules* **2023**, *28*, 1817. [CrossRef]

118. Jain, N.; Singh, V.K.; Chauhan, S. A review on mechanical and water absorption properties of polyvinyl alcohol based composites/films. *J. Mech. Behav. Mater.* **2017**, *26*, 213–222. [CrossRef]
119. Abbasi, N.; Hamlet, S.; Love, R.M.; Nguyen, N.T. Porous scaffolds for bone regeneration. *J. Sci. Adv. Mater. Devices* **2020**, *5*, 1–9. [CrossRef]
120. Prochor, P.; Gryko, A. Numerical Analysis of the Influence of Porosity and Pore Geometry on Functionality of Scaffolds Designated for Orthopedic Regenerative Medicine. *Materials* **2020**, *14*, 109. [CrossRef]
121. Rojas-Rojas, L.; Ulloa-Fernández, A.; Castro-Piedra, S.; Vargas-Segura, W.; Guillén-Girón, T. Evaluation of Biomechanical and Chemical Properties of Gamma-Irradiated Polycaprolactone Microfilaments for Musculoskeletal Tissue Engineering Applications. *Int. J. Biomater.* **2022**, *2022*, 5266349. [CrossRef]

marine drugs

MDPI

*Review*

# Unlocking the Therapeutic Potential of Marine Collagen: A Scientific Exploration for Delaying Skin Aging

**Azizur Rahman [1,2,3,*], Rameesha Rehmani [1,2,4], Diana Gabby Pirvu [1,2], Siqi Maggie Huang [1,2,5], Simron Puri [1,2] and Mateo Arcos [1,2,6]**

[1] Centre for Climate Change Research (CCCR), University of Toronto, ONRamp at UTE, Toronto, ON M5G 1L5, Canada; rameesha.rehmani@mail.utoronto.ca (R.R.); gabrielapirvu@hotmail.com (D.G.P.); sqmaggie.huang@mail.utoronto.ca (S.M.H.); simron@climatechangeresearch.ca (S.P.); mateo.arcos@mail.utoronto.ca (M.A.)
[2] A.R. Environmental Solutions, ICUBE-University of Toronto, Mississauga, ON L5L 1C6, Canada
[3] AR Biotech Canada, Toronto, ON M2H 3P8, Canada
[4] Department of Biological Anthropology, University of Toronto, Mississauga, ON L5L 1C6, Canada
[5] Department of Ecology and Evolutionary Biology, University of Toronto, St. George, Toronto, ON M5S 3B2, Canada
[6] Computer Science, Mathematics and Statistics, University of Toronto, Mississauga, ON L5L 1C6, Canada
* Correspondence: mazizur.rahman@utoronto.ca or aziz@climatechangeresearch.ca

**Abstract:** Aging is closely associated with collagen degradation, impacting the structure and strength of the muscles, joints, bones, and skin. The continuous aging of the skin is a natural process that is influenced by extrinsic factors such as UV exposure, dietary patterns, smoking habits, and cosmetic supplements. Supplements that contain collagen can act as remedies that help restore vitality and youth to the skin, helping combat aging. Notably, collagen supplements enriched with essential amino acids such as proline and glycine, along with marine fish collagen, have become popular for their safety and effectiveness in mitigating the aging process. To compile the relevant literature on the anti-aging applications of marine collagen, a search and analysis of peer-reviewed papers was conducted using PubMed, Cochrane Library, Web of Science, and Embase, covering publications from 1991 to 2024. From in vitro to in vivo experiments, the reviewed studies elucidate the anti-aging benefits of marine collagen, emphasizing its role in combating skin aging by minimizing oxidative stress, photodamage, and the appearance of wrinkles. Various bioactive marine peptides exhibit diverse anti-aging properties, including free radical scavenging, apoptosis inhibition, lifespan extension in various organisms, and protective effects in aging humans. Furthermore, the topical application of hyaluronic acid is discussed as a mechanism to increase collagen production and skin moisture, contributing to the anti-aging effects of collagen supplementation. The integration of bio-tissue engineering in marine collagen applications is also explored, highlighting its proven utility in skin healing and bone regeneration applications. However, limitations to the scope of its application exist. Thus, by delving into these nuanced considerations, this review contributes to a comprehensive understanding of the potential and challenges associated with marine collagen in the realm of anti-aging applications.

**Keywords:** marine collagen; biopeptide; antioxidant; skin; anti-aging; prevention; bone regeneration; extracellular matrix (ECM); fish collagen

**Citation:** Rahman, A.; Rehmani, R.; Pirvu, D.G.; Huang, S.M.; Puri, S.; Arcos, M. Unlocking the Therapeutic Potential of Marine Collagen: A Scientific Exploration for Delaying Skin Aging. *Mar. Drugs* **2024**, *22*, 159. https://doi.org/10.3390/md22040159

Academic Editor: Hermann Ehrlich

Received: 25 January 2024
Revised: 26 March 2024
Accepted: 26 March 2024
Published: 30 March 2024



## 1. Introduction

Collagen is a fibrous protein that provides support to various structures of the body, such as the skin, cartilage, and bones [1–3]. Functioning as a crucial structural and connective component of the extracellular matrix (ECM), collagen helps regulate cell growth, adhesion, and migration [4,5]. As a naturally abundant protein found in all animals, there are 28 different types of collagens, which account for approximately 30% of the total protein

found in the body [2]. Type 1 collagen is the most abundant type and provides support to most tissues of the body, such as the skin and muscles. Type II is responsible for the maintenance and repair of cartilage [2]. Type III is the main element of tissue sealants and reticular fibers commonly found in blood vessels and muscles [2]. Type IV is a key element in the basement membrane, functioning as a barrier between tissues, and can act as a diabetic neuropathy indicator [2]. Finally, Type V is the main collagen in corneal solutions and is found in the placenta and hair [2].

Collagen is often used as a regenerative biomaterial due to its high biodegradability, solubility, and tensile strength [4–9]. Its low immunogenicity and excellent biocompatibility have prompted extensive research into its application as a polymer across various biomedical products, including cosmetics and pharmaceuticals [5]. Moreover, collagen serves as a safe and efficient biomaterial in tissue engineering and clinical settings [9,10]. The food industry also exhibits a substantial demand for collagen due to its elevated protein content and beneficial functional attributes, including water absorption capacity and emulsion-forming ability [5]. However, the natural degradation of collagen accelerates with age, which can impact skin elasticity, wound healing, bone density, and even immune and neural function [4,11–13]. Skin aging results from diminished collagen density and dermal thickness, alongside reduced synthesis and replacement of crucial structural proteins [5]. The effects of reduced collagen density especially impact the dermis layer of the skin, resulting in notable signs of aging such as increased wrinkling, sagging, laxity, and a textured appearance [14,15].

While the aging process of the skin is considered complex, the incorporation of marine collagen in anti-aging supplements has been used to treat select skin concerns, including visible signs of aging [1]. In particular, the application of marine collagen peptides (MCPs) emerges as a promising therapeutic according to multiple animal and in vitro studies [7,11,16–18]. MCPs are obtained by hydrolyzing collagen into small peptides of low molecular weight to improve bioavailability and absorption [19]. MCPs can exert bioactive properties, including anti-microbial and antioxidant functions [19]. Thus, MCPs are commonly utilized in cosmeceutical skin products for their anti-aging properties [19–22]. Over the past decade, there has been a remarkable surge in market demand for marine-based cosmetics [21].

While the previous literature has demonstrated the effectiveness of bioactive natural peptides in mitigating the effects of aging across diverse models, including cell studies, animal studies, and clinical trials [1,5,23–25], there is limited information regarding the diversity of anti-aging collagen peptides found in marine organisms. Various bioactive compounds can be sustainably extracted from marine waste and harnessed as potent ingredients for the formulation of cosmetic products, reducing environmental pollution and lowering production costs [25–29]. Examples include collagen derived from fish waste and chitin obtained from crustacean waste, which can be incorporated into cosmetic formulations targeting anti-wrinkle and skin barrier enhancements [28]. While fish are widely used as food resources, there is limited utilization of marine proteins from other species such as sea cucumbers, sea urchins, mussels, and various kinds of algae. Thus, this review addresses this gap by presenting recent insights into the anti-aging potential of bioactive collagen peptides sourced from under-utilized marine resources, examining examples that can scavenge free radicals in vitro and showcase clinical benefits for the skin and body [15,28]. Interestingly, the potential combination of CRISPR technology with marine collagen offers a novel perspective for groundbreaking anti-aging treatments. This synergy harnesses CRISPR's precision in gene editing to specifically target aging-related genes, complemented by the supportive properties of marine collagen. The result is an innovative approach with enhanced therapeutic effects, particularly in skin elasticity and hydration [30]. The findings lay the groundwork for the development of revolutionary anti-aging collagen treatments derived from underexplored marine organisms.

Table 1 displays the five common types of collagens along with their functions. Marine collagen is predominantly Type I collagen, which is the primary component of the calcium-

depleted tissue of the teeth and bone [2]. It is found in the skin, in tendons, in the vasculature of the lungs, and in the heart [2]. Table 1 significantly highlights the use of porcine collagen (Type I and Type III collagen), which is essential in the prevention and treatment of osteoporosis [2].

**Table 1.** The function of the 5 most common types of collagens [2].

| Collagen | Function or Application | Tissue or Organ |
|---|---|---|
| Type I | the organic part of the bone, membranes for guided tissue regeneration | skin, bone, teeth, tendon, ligament, vascular ligature |
| Type II | the main constituent of cartilage, cartilage repair, and arthritis treatment | cartilage |
| Type III | the main constituent of reticular fibers, hemostats, and tissue sealants | muscle, blood vessels |
| Type IV | the major component of the basement membrane, attachment enhancer of cell culture, and diabetic nephropathy indicator | basal lamina, the epithelium-secreted layer of the basement membrane |
| Type V | feedstock for biomaterials in corneal treatments | hair, cell surfaces, and placenta. |

Our literature review explores the anti-aging activities of collagen peptides from marine organisms, focusing on their capacity to regulate oxidative stress in diverse models including cells, fruit flies, nematodes, mice, and humans [1]. By analyzing the findings of these papers, we aim to contribute valuable insights that help enhance the utilization of marine sources for anti-aging applications. However, limitations regarding the lack of long-term studies may hinder its potential use. Thus, this review highlights the applications and limitations of anti-aging marine collagen research while outlining future directions for this field.

## 2. Marine Collagen: Effects on Skin Aging

The anti-aging industry is growing rapidly with the release of new supplements and nutraceuticals that promise youthful skin, better joint and bone health, and even stronger immune systems [29,31,32]. Among the most popular products is marine-derived collagen used for skin health and restoration. Several papers have cited the effects of collagen supplementation on skin appearance [7,8,20–22,32].

A recent study by Lee et al. (2022) investigated the importance of collagen formulation on anti-aging efficacy [32]. Only compounds with low molecular weights may penetrate the skin barrier, limiting the efficacy of intact collagen application, and oral administration of collagen peptides is limited by their poor stability and absorption in the gastrointestinal tract [32]. Thus, to increase absorptive ability, the fish collagen was hydrolyzed into small, bioactive collagen peptides and administered as an orally disintegrating film, allowing the collagen to be directly absorbed into the bloodstream [32].

After applying the film for 12 weeks, the authors concluded that fish-derived collagen administered as an orally disintegrating film was effective at significantly reducing skin wrinkle depth and number, as well as increasing skin elasticity and density in women aged 20 to 60 years old [32]. As evident in Figure 1, at individual ages, a number of changes occur in the density and structure of collagen fibers [33]. Figure 1 displays a decline in the number of collagen fibrils and the size of the fibroblast cells as the skin ages, emphasizing the importance of collagen fibrils in the maintenance of cell size and skin elasticity for healthy skin [33].

Further on, the results of a 2018 randomized placebo-controlled trial revealed the hydrating, anti-aging effects of a low molecular weight collagen hydrolysate obtained from sutchi catfish skin [7]. After 6 weeks, skin hydration was 7.23-fold higher in the treatment group compared to the placebo ($p < 0.001$). This hydrating benefit was observed

after 12 weeks as well, although at only 2.9-fold higher than the placebo ($p < 0.01$) [7]. Moreover, wrinkle formation was also reduced, considering parameters such as skin roughness, smoothness depth, and visual grading, demonstrating the anti-aging potential of hydrolyzed marine collagen on the skin of older adults [14]. Longer-term studies should be conducted to determine whether this beneficial effect holds true over time.

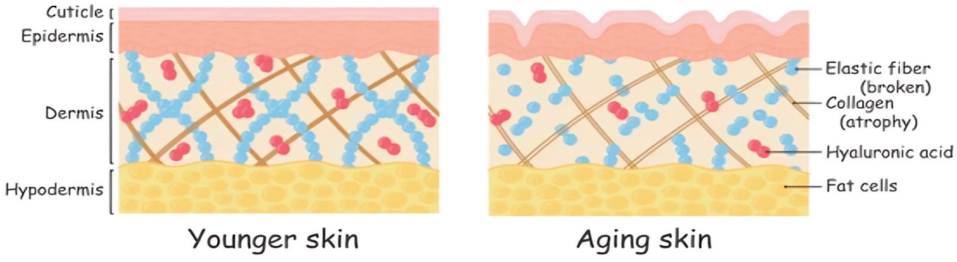


**Figure 1.** Illustrates the structural differences between younger and aging skin. In young human skin dermis, collagen fibrils are intact and normal in size (**left**) in contrast with reduced collagen fibrils in aged human skin dermis which leads to a reduction in cell size (**right**). The aging skin on the right shows a reduction and fragmentation of collagen fibers, broken elastic fibers, and diminished Hyaluronic Acid (red dots), leading to thinner fat layers and an overall loss of structural integrity and elasticity.

Another study used a mouse model of aging to demonstrate that marine collagen may restore a youthful skin appearance [16]. In this study, mice were fed a collagen hydrolysate-containing diet derived from fish scales for 12 weeks. Notably, the epidermal barrier and dermal elasticity dysfunctions observed in the aging group were significantly attenuated in the collagen hydrolysate treatment group after 2 weeks [16]. Further on, these positive effects were maintained for the entirety of the study duration, demonstrating a prolonged restoration of skin elasticity and water content following collagen supplementation [16].

### 3. Marine Bioactive Peptides: Antioxidant and Anti-Carcinogenic Roles

On top of providing valuable sources of nitrogen and amino acids, many bioactive MCPs have demonstrated powerful antioxidant, anti-microbial, and immunomodulatory effects. The active peptide products isolated from fish, sea cucumbers, sponges, urchins, mussels, and other marine life have shown the potential to lower oxidative stress, inhibit cellular senescence, and extend lifespans in multiple animal studies of aging [17,34,35]. For example, one study found that jellyfish collagen hydrolysate (JCH) improved the exercise tolerance of mice in a dose-dependent manner after 6 weeks [17]. In the same study, the authors used d-galactose to induce the aging process in mice, then investigated the effect of JCH on oxidative stress by measuring malondialdehyde (MDA), superoxide dismutase (SOD), and glutathione peroxidase (GSH-Px) activity [17]. MDA is a product of lipid peroxidation, which increases with age, whereas SOD and GSH-Px are enzymatic antioxidant systems that neutralize free radicals implicated in the aging process, wherein activity declines with age [18]. Significantly, the 6-week administration of JHC inhibited the decrease in GSH-Px/SOD activity and the increase in MDA seen in the ageing model [17]. These results are displayed in Figure 2 [17], showcasing the powerful in vivo antioxidant capacity of marine peptides and demonstrating their benefit in anti-aging products.

Similarly, Liang et al (2010) discovered that rats fed chum salmon MCPs over the course of their lifespan showed increased GSH-Px and SOD enzymatic activity compared to control rats; however, this change was only significant in rats older than 12 months [18]. Further on, the observed age-related MDA increase was attenuated in MCP-treated rats, suggesting that MCPs can interfere with the cellular and physiological effects of aging by exerting antioxidant effects [18]. Significantly, this study also demonstrated that MCP-treated rats on average had longer life spans and better survival outcomes after 28 months [18].

MCP treatment also delayed tumor growth, decreased tumor size and number, and lowered the incidence of deaths from tumors after 16 months when compared to the control [18]. Genetic mutations increase in frequency with age, predisposing the cells to various oncogenic processes; thus, MCP may act in a protective, anti-carcinogenic capacity to slow the progression of aging-related diseases such as cancer [18]. Taken together, these findings suggest that marine collagen may exert antioxidant capabilities that interfere with the aging process, leading to longer, healthier lives.

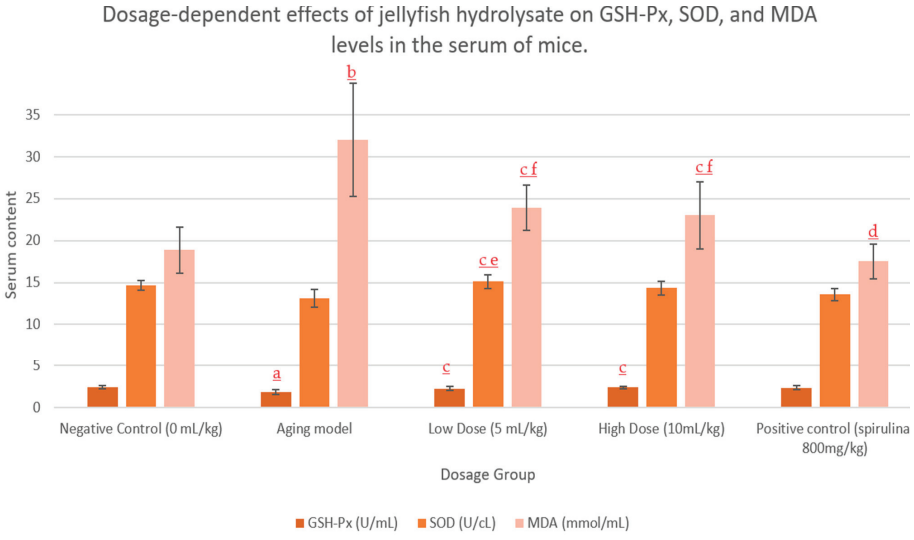


**Figure 2.** Serum levels of GSH-Px, SOD, and MDA in mice. Data from J.F. Ding et al. (2011). a = $p < 0.05$, b = $p < 0.01$ compared to control. c = $p < 0.05$, d = $p < 0.01$ compared to aging model. e = $p < 0.05$, f = $p < 0.01$ compared to positive.

## 4. Marine Collagen in Tissue Engineering for Anti-Aging

Marine collagen is recognized for its bioactive properties and is used in skin tissue engineering due to its water solubility, metabolic compatibility, and accessibility. It has shown effectiveness in healing skin injuries of varying severity and in delaying aging processes, promoting keratinocyte and fibroblast migration, and vascularization of the skin [36]. In animal model studies, marine collagen from different species has shown promising results in skin tissue healing [37,38]. Treatments using marine collagen have led to increased deposition of granulation tissue, enhanced re-epithelialization, stimulated neoangiogenesis, and improved the morphological aspect of wounds [38]. These findings underscore its potential in tissue engineering and wound healing applications [37,38]. The marine environment has been a significant source of biological macromolecules for developing tissue-engineered substitutes with wound-healing properties. These molecules play a key role in enhancing the wound-healing process and are crucial in advancing wound-care management [34]. Moreover, studies on collagen-derived peptides from the marine sponge *Chondrosia reniformis* reveal their antioxidant activity, ability to stimulate cell growth, and protection against UV-induced cell death [34]. These peptides have shown no toxicity in cell lines, and their significant ROS scavenging activity indicates their potential in drug and cosmetic formulations, especially for damaged or photoaged skin repair [34].

Marine collagen's role in bioprinting and scaffold development is pivotal for tissue regeneration. Marine collagen, particularly Type I, is ideal for creating 3D bioprinted structures due to its biocompatibility, biodegradability, and low immunogenicity [39,40]. These structures mimic the natural ECM of human tissues, which is essential for effective tissue regeneration. In tissue engineering scaffolds, marine collagen offers a structure that

supports cell attachment, proliferation, and differentiation, key factors for tissue repair and regeneration [40]. These properties of marine collagen are particularly significant in anti-aging applications, as they support the growth and repair of various tissues, including skin, bone, and cartilage. As aging is associated with the degradation of these tissues, marine collagen scaffolds can be used to replace or support damaged tissues, thereby counteracting some of the effects of aging. Ongoing research is optimizing marine collagen properties for bioprinting and scaffold design, enhancing its mechanical strength, stability, and compatibility with human tissues. The development of hybrid scaffolds, combining marine collagen with other biomaterials, is also an area of interest to improve functionality and efficacy in tissue regeneration [4,40–42].

## 5. The Integration of CRISPR Technology with Marine Collagen

The integration of CRISPR technology with marine collagen is an innovative area of research, combining the genetic editing capabilities of CRISPR with the beneficial properties of marine-derived collagen. Marine collagen has shown promise as a biomaterial in various applications, including wound healing, skin anti-aging, and bone regeneration. Its biocompatibility makes it an excellent candidate for tissue engineering and regenerative medicine. On the other hand, CRISPR technology offers a groundbreaking approach to gene editing, allowing for precise modifications at the DNA level. An overview of this technology can be seen in Figure 3. CRISPR technology has been making strides in various medical applications, including the development of more refined editing techniques such as base and prime editing. These newer methods aim for uniform and predictable gene-editing results while minimizing potential risks associated with traditional CRISPR-Cas9 techniques, such as the creation of double-strand DNA breaks [43–45].

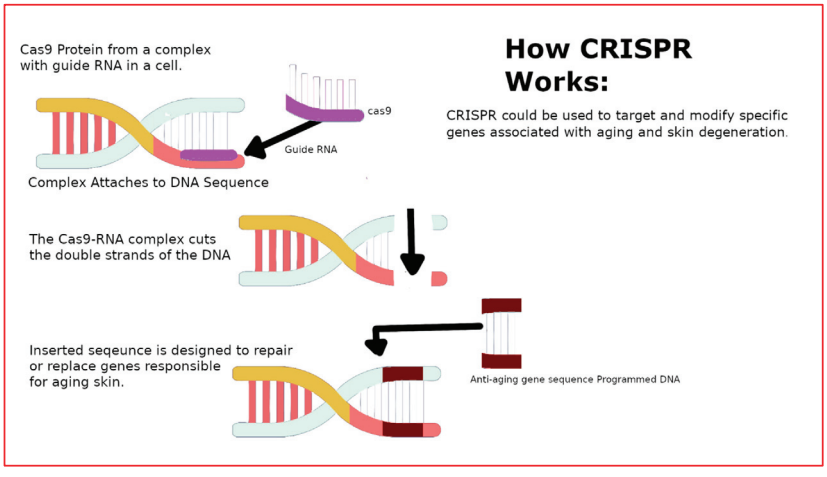


**Figure 3.** Illustration of the CRISPR-Cas9 Mechanism for Skin Regeneration. This graphic outlines the use of CRISPR-Cas9 technology for targeted gene editing in eukaryotic cells, specifically for skin regeneration. The process begins with the Cas9 protein forming a complex with a guide RNA that is complementary to a specific gene sequence associated with skin aging. This complex then locates and binds to the target DNA sequence, where Cas9 makes a precise cut. A new DNA sequence with the desired genetic information can then be inserted at the cut site for potential therapeutic purposes, such as reversing aging effects or repairing skin damage. This advanced molecular technique is also being applied to edit the genetic code of various organisms, encompassing eukaryotic cells similar to those in humans. Specifically, in the context of combating skin aging, this method allows for precise alterations to DNA sequences, facilitating the repair or reversal of age-related genetic changes in the skin. It might also offer a tool for curing genetically based diseases [46].

Dermatological applications of CRISPR technology have been highly promising [30,47,48]. Despite there being no direct research on using CRISPR technology on marine collagen, the integration of these two fields could potentially lead to effective anti-aging treatments. For instance, CRISPR technology could be employed to target and modify specific genes associated with aging and skin degeneration. The progressive alterations observed in aging skin are now being comprehensively observed at both the molecular and cellular levels, leading to enhanced insights into the structural and functional decline resulting from these changes [33]. By precisely editing these genes, it might be possible to slow down or reverse certain aging processes at a molecular level. Meanwhile, marine collagen could play a supportive role in this integration. Its ability to enhance cell viability and support tissue regeneration could be crucial in facilitating the effectiveness of CRISPR-mediated gene edits. For example, in a scenario where CRISPR is used to edit genes related to skin elasticity, marine collagen could provide the necessary ECM support, enhancing the overall therapeutic effect.

Another potential approach to integrating CRISPR with marine collagen could focus on enhancing skin hydration and barrier function. This would involve using CRISPR to edit genes crucial for maintaining skin moisture, such as those involved in hyaluronic acid synthesis. Concurrently, marine collagen could be developed as a topical delivery system for CRISPR components, leveraging its skin absorption properties and biocompatibility. This could involve encapsulating CRISPR components (such as Cas9 and guide RNA) within marine collagen-based nano-carriers that can penetrate the skin layers.

While direct research on the integration of CRISPR technology with marine collagen in anti-aging has yet to be performed, the combination of CRISPR's precision in genetic editing and marine collagen's supportive properties presents a possibility. Future research in this area could lead to innovative and effective anti-aging therapies, potentially revolutionizing the way we approach aging and skin health.

## 6. Marine Collagen Use: The Pros and Cons

The ECM plays a fundamental role in ensuring cell integrity and aiding in various cell functions, such as proliferation, differentiation, migration, and adhesion [41]. Marine organisms, including fish, jellyfish, sponges, and other invertebrates, provide a valuable source of collagen that is free from religious restrictions and animal pathogens (Figure 4). This type of collagen is metabolically compatible and has advantages over other sources [41]. Fish skin is often used to extract Type I collagen because it is abundant and not suitable for industrial use. Overall, marine sources of collagen are a safe, convenient, and promising option. The combination of biomaterials and single gene delivery has shown promising potential for tissue engineering. Studies have found that marine collagen from organisms such as fish, jellyfish, and sponges can promote wound healing, enhance blood circulation, and prevent infection [41]. Additionally, marine collagen has anti-aging properties that have been demonstrated in mice with osteoporosis [41]. It can increase bone mineral density, protect against bone loss and osteoarthritis, induce plastic differentiation, and even improve skin elasticity while slowing the aging process [41,49]. Finally, drug delivery and immobilization are two ways marine collagen is used within the human body [41]. Marine collagen offers several advantages compared to other popular sources of collagen, notably bovine or porcine collagen. One significant benefit is its resource abundance, as marine collagen is derived from the massive amounts of marine waste produced by the fishing industry, helping reduce environmental contamination while providing high yields at lower costs [50]. Marine collagen also presents with a higher biocompatibility and no disease transmission risk; thus, considering mammalian collagen has been associated with incidents of prion transmission leading to conditions such as bovine spongiform encephalopathy (BSE), marine collagen is considered a safer alternative [51]. However, marine collagen sources, such as fish and marine sponges, still carry the threat of allergens [52,53]. Allergenicity refers to the likelihood of a product causing an adverse immune response in the body. Depending on the type of fish or fish product that the collagen is sourced

from, the level of allergenicity will vary. For example, collagen from bony fish has been shown to have higher allergenicity than collagen from cartilaginous fish [53]. To reduce the likelihood of adverse effects, standardized methods for extraction and purification of marine collagen need to be further investigated. Ultimately, the anti-aging effect of marine collagen can be evident throughout the body both externally and internally. Externally, through reversing the aging effects of the skin, and internally, through regulating bone health, tissue regeneration, and dietary and metabolic processes [54,55]. Together, these effects improve overall health, skin appearance, and well-being.

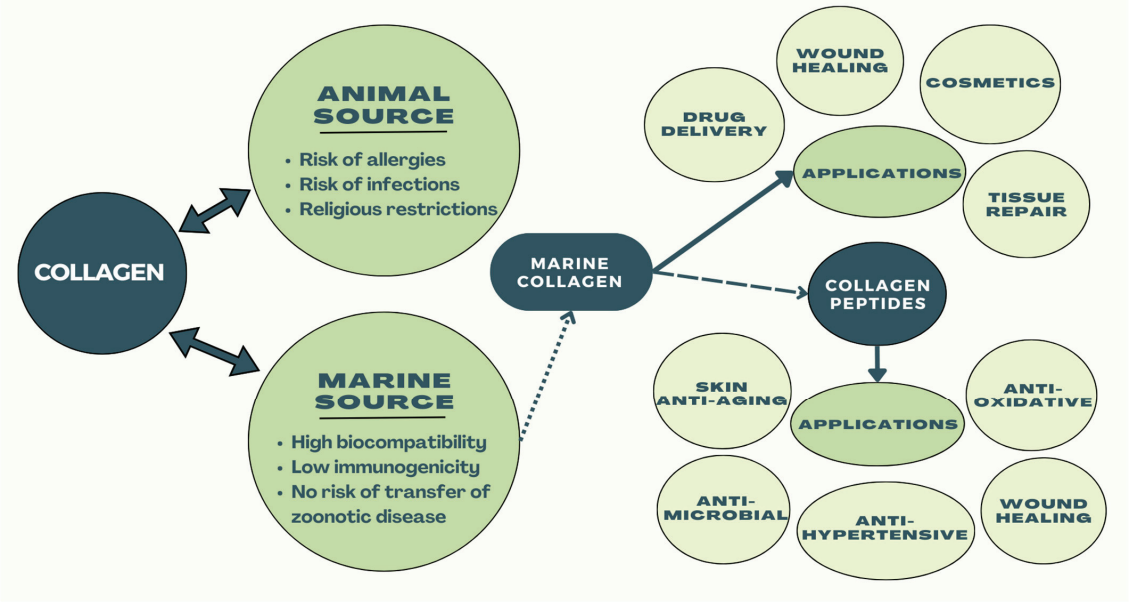


**Figure 4.** Illustrates biomedical applications and advantages of marine collagen compared to land animal-derived collagen.

*6.1. Hydration*

Hyaluronic acid plays an important role in skin moisture retention [56]. Previous literature on oral collagen supplements has shown evidence of targeting age-related concerns and improving skin integrity [57,58]. Marine collagen and collagen peptides, especially from fish, have demonstrated significant effects on skin hydration. When administered orally, collagen hydrolysates can restore the production of hyaluronic acid to improve skin hydration [57,58]. Other studies have reported that canary seed peptides (CSPs) show promising results for skin aging treatments [59]. However, fish collagen is considered an optimal source due to its diverse amino acid compositions and high bioavailability [60]. Limited research on chicken-derived collagen suggests potential benefits, but more studies are needed for conclusive results [57].

*6.2. Elasticity*

Elastin and microfibrils in the elastic fabric network relay elasticity and resilience to the skin. Consuming oral collagen has been expressed to improve skin elasticity, resulting in increased levels of Type I collagen [56]. Numerous studies exhibit positive effects on skin elasticity, including improvements in surface elasticity [56]. Collagen peptides have been found to increase collagen content and improve skin laxity in a variety of animal and human studies. However, there are limitations to this research, such as differences in

the duration and dosage quantities, small sample sizes, and self-reported skin elasticity measurements [61].

## 7. Collagen as a Biomaterial for Tissue Engineering

One of the most common and prominent biomaterials in tissue engineering and regenerative medicine is collagen, such as collagen proteins in the ECM of marine invertebrates [4] (Figure 5). Although fish collagen peptides (FCPs) have been used as a dietary supplement, little is known about how they affect cellular function in the human body [62]. ECM replacements can significantly affect cell proliferation and function based on recent research [36,63]. These extracellular matrixes, however, are mainly used in a general sense and are not yet tailored to certain cell types [63]. This paper focuses on ECM-based coating substrates tailored to the individual needs of skin, skeletal muscle, and liver cell cultures [63]. With ongoing advancements, neural tissue engineering (NTE) indicates significant potential to treat a number of debilitating neurological illnesses [5]. For NET design strategies that facilitate axonal growth and neural and non-neural cell differentiation, choosing the best scaffolding material is essential. As the nervous system is naturally resistant to regeneration, collagen is often used in NTE applications [5]. It can function with neurotrophic factors, neural growth inhibitors, and other compounds that promote neural growth [5]. It can also be used for neural repair and thus mitigate neurodegenerative diseases that come with age [5]. The ECM is a powerful structure that influences the cells in contact with it [64]. A poor prognosis has been linked to the composition and collagen density of the tumor-specific ECM in a number of cancer forms [64]. The cause of this correlation is still mainly a mystery [64]. Collagen can stimulate the development and migration of cancer cells, although collagen has been found in recent research to influence the activity and phenotype of T cells and tumor-associated macrophages (TAMs), two types of immune cells that infiltrate tumors [64].

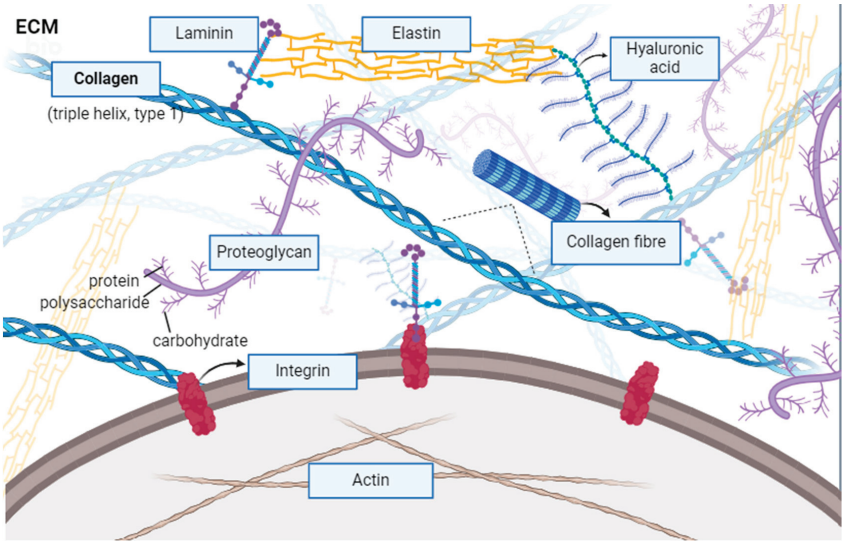


**Figure 5.** Collagen found in the ECM. The ECM is a dynamic network of proteins and molecules that play a fundamental role in organizing and maintaining tissue structure and function. Components of the ECM include fibrillar proteins (i.e., collagen, elastin) which confer tensile strength and elasticity, adhesive glycoproteins (i.e., fibronectins, laminins) which mediate cell–ECM interactions critical for tissue organization and homeostasis, and proteoglycans (i.e., fibromodulin), which can have biologically active properties (i.e., growth factors) and mediate ECM assembly and organization [65]. Created in Biorender.com.

## 8. Applications of Marine Collagen in the Cosmetic Market

The cosmeceutical industry is flooded with a variety of anti-aging products that claim to address wrinkles, fine lines, and other signs of aging through various mechanisms of action. Some of the most popular products on the market include retinoids such as retinol, retinyl esters, and retinaldehyde--vitamin A derivatives known for their ability to stimulate collagen production and promote cell turnover, thereby increasing skin elasticity and reducing the appearance of fine lines and wrinkles [52]. Alternatively, vitamin C- and vitamin E-based serums provide anti-aging benefits through their powerful antioxidant effects that protect the skin against UV-induced photodamage and oxidative stress [52]. Vitamin C stimulates collagen synthesis, and both vitamins have anti-inflammatory functions that aid in wound healing. Another widely used anti-aging ingredient is hyaluronic acid, a hydrating glycosaminoglycan (GAG) that can act as a barrier against trans-epidermal water loss to retain skin moisture and reduce the appearance of fine lines [52]. Other popular products include alpha hydroxy acids (i.e., lactic acid, glycolic acid, citric acid) and beta hydroxy acids (i.e., salicylic acid) that exfoliate the skin, promote cell turnover, and facilitate GAG and collagen synthesis to improve skin texture and tone [50,52]. Finally, numerous bioactive peptide formulations can help stimulate collagen production and improve skin elasticity [52,54]. For example, extracts from brown algae have proven a plentiful resource for anti-inflammatory and antioxidant compounds (Figure 6) [66]. Because of their photoprotective properties, these bioactive peptides can be used in cosmetic preparations for anti-aging skincare and sunscreen [66]. In one study, the brown algae, *Ericaria amentacea*, showed dose-dependent in vitro activity for reducing various markers of oxidative stress, inflammation, and collagen and hyaluronic degradation. The results of various antioxidant assays are displayed in Figure 7 [66], demonstrating the remarkable potential of anti-aging cosmetics.

While these products demonstrate numerous anti-aging benefits, there are associated drawbacks that may limit their efficacy and applicability. For one, prescription-strength retinoid formulations and AHAs may induce adverse reactions such as skin irritation, burning, and dermatitis [52]. In addition, the oxidation of retinol, vitamin C, and vitamin E over time poses a problem for the stability of the product, which can affect the overall quality and efficacy of the cosmetic preparation [41]. Further on, in rare cases, topical application of vitamin E has been linked to cases of contact dermatitis, erythema multiforme, and xanthomatous reaction [52]. As a result, recent trends in the anti-aging industry have demonstrated rising consumer interest in the natural bioactive compounds found in marine collagen rather than synthetic ingredients [66–68]. A recent study of the Portuguese anti-aging cosmetic market revealed a 27% increase in marine collagen cosmetics from 2011 to 2018, with red algae being the most widely used marine ingredient [66].

A potential explanation for the increasing popularity of marine collagen products may lie in the manufacturing, safety, and efficacy advantages that they provide. For one, marine sources are biodiverse, abundant, and easy to cultivate and modulate during their life cycles. Furthermore, marine collagen is easily absorbed by the body and efficiently utilized for collagen synthesis. These characteristics make it possible to harness the production of specific bioactive compounds involved in collagen synthesis and wound healing [50,67]. Further on, collagen-based cosmetics predominantly utilize Type I collagen, valued for its moisturizing, anti-wrinkle, anti-aging, wound-healing, and UV radiation protection properties [20]. Figure 8 further illustrates the various utilizations and applications of marine collagen in the cosmetic market.

Although marine collagen has a wide range of benefits, the effectiveness of any anti-aging product can vary depending on individual genetic and environmental factors, including chronic autoimmune conditions, exposure to sun and air pollution, and lifestyle choices [20].

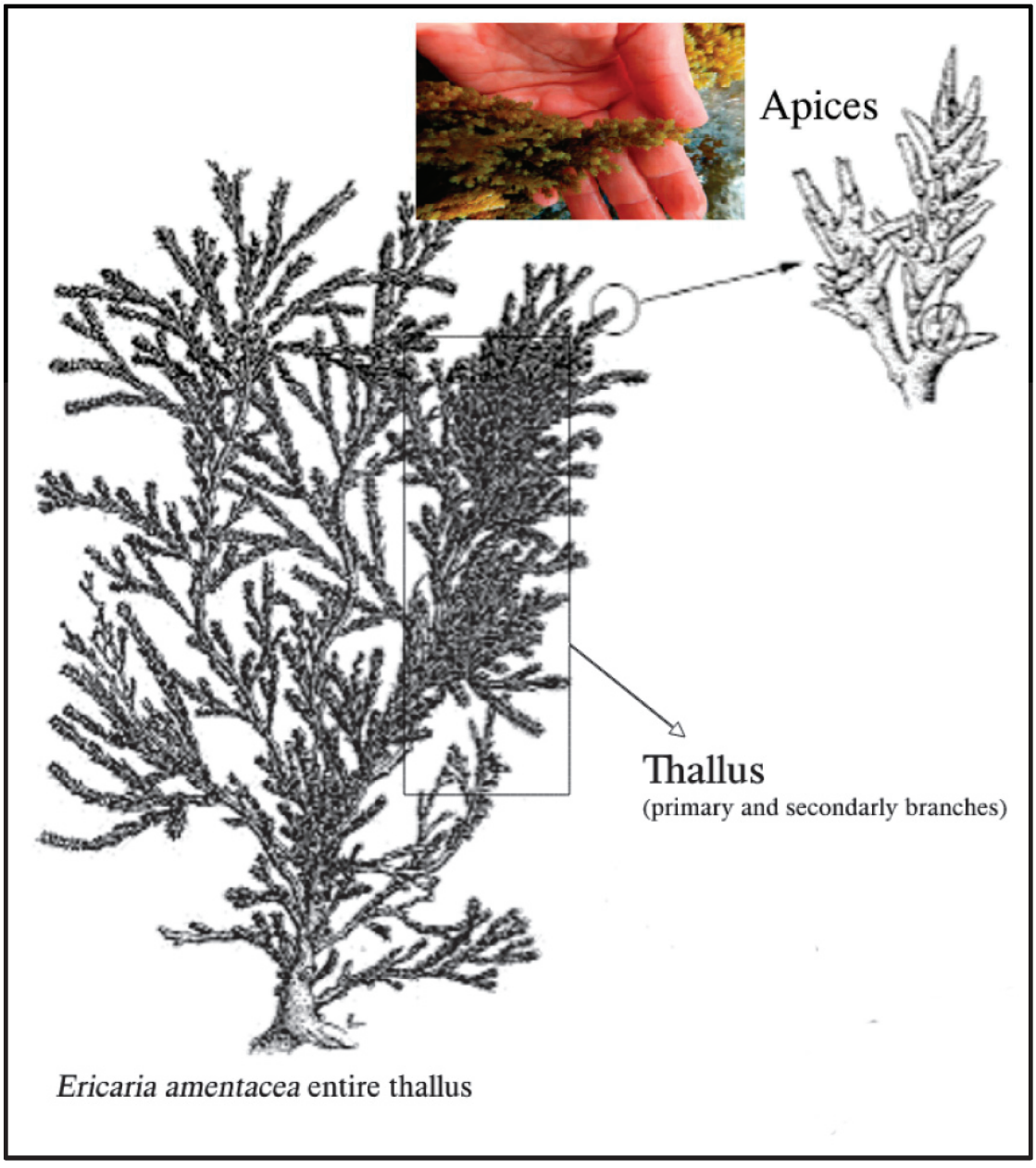


**Figure 6.** Schematic representation of *E. amentacea* seaweed body parts, and antioxidant activity of *E. amentacea* extracts in spectrophotometric tests.

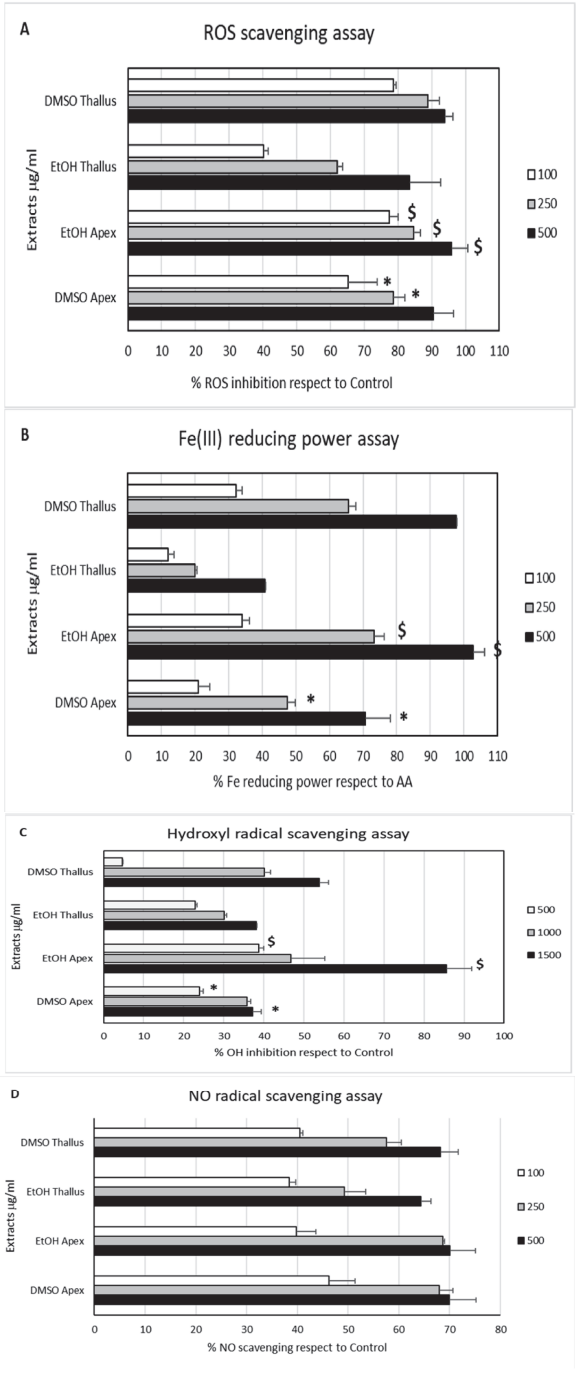


**Figure 7.** Marine seaweed displays anti-aging properties. In (**A**,**C**), * $p < 0.05$; Tukey of EtOH apex vs. EtOH thallus' respective concentrations, \$ $p < 0.05$. In (**B**), * $p < 0.05$; Tukey of EtOH apex vs. EtOH thallus' respective concentrations, \$ $p < 0.005$. (**A**) ROS scavenging activity. (**B**) Fe (III)-reducing power assay compared to ascorbic acid (AA). (**C**) OH radical scavenging activity. (**D**) NO radical scavenging activity. Taken from Mirata et al. (2023) [66].

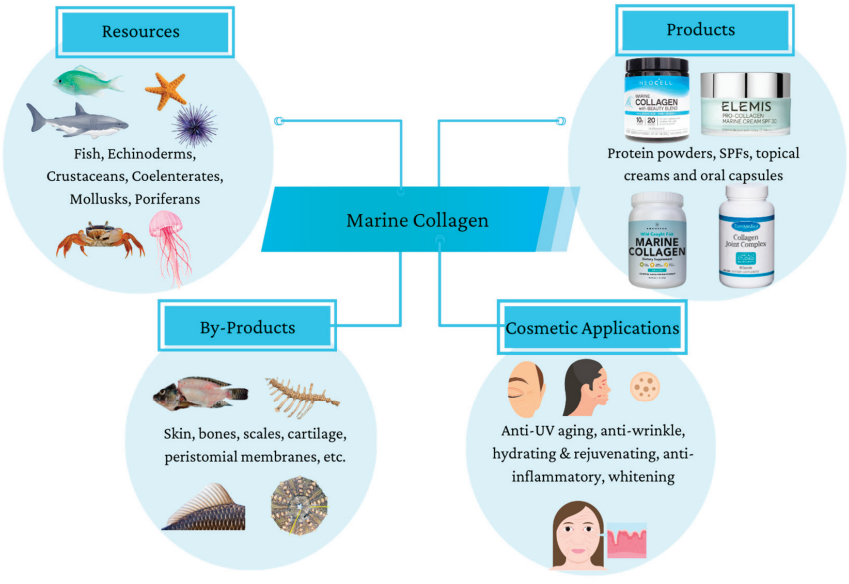


**Figure 8.** Potential utilization of marine by-products in anti-aging cosmetic preparations.

## 9. Concluding Remarks

This literature review highlights the diverse biomedical anti-aging applications of marine collagen, establishing it as a versatile biomaterial in tissue engineering and regenerative medicine. Marine collagen's unique properties, such as promoting osteogenesis, collagen synthesis, and anti-inflammation, highlight its pivotal roles in accelerating the healing process, promoting skin health, and maintaining free radical homeostasis. Compared to land animal sources, advantages such as metabolic compatibility, safety, and environmental sustainability further position marine collagen as a compelling choice for anti-aging applications. Utilizing readily available marine waste from the fishing industry ensures cost-effective production and addresses environmental concerns. Marine collagen also proves valuable in vascular tissue engineering, demonstrating promise in crafting advanced scaffolds for vascular grafts, enhancing mechanical strength, and fostering vascular endothelial cell development. Ongoing research and innovation efforts focused on marine collagen extraction, processing, and application, as well as synergy with anti-aging CRISPR technology, underscore its continued importance in advancing the fields of tissue engineering and biomedicine. To discover further anti-aging applications of various marine collagen sources, further research efforts should continue exploring this protein's remarkable therapeutic efficacy and versatility.

**Author Contributions:** Conceptualization, A.R.; validation, A.R.; writing—original draft preparation, R.R., D.G.P., S.M.H., S.P., M.A. and A.R.; writing—review and editing, A.R., D.G.P. and R.R.; visualization, D.G.P., R.R, S.P., M.A. and A.R.; supervision, A.R.; project administration, A.R.; funding acquisition, A.R. All authors have read and agreed to the published version of the manuscript.

**Funding:** This research received no external funding.

**Conflicts of Interest:** The authors declare no conflicts of interest.

## References

1. Xia, E.; Zhu, X.; Gao, X.; Ni, J.; Guo, H. Antiaging Potential of Peptides from Underused Marine Bioresources. *Mar. Drugs* **2021**, *19*, 513. [CrossRef] [PubMed]
2. Ricard-Blum, S. The Collagen Family. *Cold Spring Harb. Perspect. Biol.* **2011**, *3*, a004978. [CrossRef] [PubMed]

3. Gelse, K.; Pöschl, E.; Aigner, T. Collagens—structure, function, and biosynthesis. *Adv. Drug Deliv. Rev.* **2003**, *55*, 1531–1546. [CrossRef] [PubMed]
4. Xu, N.; Peng, X.-L.; Li, H.-R.; Liu, J.-X.; Cheng, J.-S.; Qi, X.-Y.; Ye, S.-J.; Gong, H.-L.; Zhao, X.-H.; Yu, J.; et al. Marine-Derived Collagen as Biomaterials for Human Health. *Front. Nutr.* **2021**, *8*, 702108. [CrossRef] [PubMed]
5. Wang, H. A Review of the Effects of Collagen Treatment in Clinical Studies. *Polymers* **2021**, *13*, 3868. [CrossRef] [PubMed]
6. Li, P.; Wu, G. Roles of dietary glycine, proline, and hydroxyproline in collagen synthesis and animal growth. *Amino Acids* **2018**, *50*, 29–38. [CrossRef] [PubMed]
7. Kim, D.-U.; Chung, H.-C.; Choi, J.; Sakai, Y.; Lee, B.-Y. Oral intake of low-molecular-weight collagen peptide improves hydration, elasticity, and wrinkling in human skin: A randomized, double-blind, placebo-controlled study. *Nutrients* **2018**, *10*, 826. [CrossRef] [PubMed]
8. Bolke, L.; Schlippe, G.; Gerß, J.; Voss, W. A collagen supplement improves skin hydration, elasticity, roughness, and density: Results of a randomized, placebo-controlled, blind study. *Nutrients* **2019**, *11*, 2494. [CrossRef] [PubMed]
9. Agustina, L.; Miatmoko, A.; Hariyadi, D.M. Challenges and strategies for collagen delivery for tissue regeneration. *J. Public Health Afr.* **2023**, *14*. [CrossRef]
10. Ghomi, E.R.; Nourbakhsh, N.; Kenari, M.A.; Zare, M.; Ramakrishna, S. Collagen-based biomaterials for biomedical applications. *J. Biomed. Mater. Res. B Appl. Biomater.* **2021**, *109*, 1986–1999. [CrossRef]
11. Mays, P.K.; McAnulty, R.J.; Campa, J.S.; Laurent, G.J. Age-related changes in collagen synthesis and degradation in rat tissues. Importance of degradation of newly synthesized collagen in regulating collagen production. *Biochem. J.* **1991**, *276*, 307–313. [CrossRef] [PubMed]
12. Geahchan, S.; Baharlouei, P.; Rahman, A. Marine Collagen: A Promising Biomaterial for Wound Healing, Skin Anti-Aging, and Bone Regeneration. *Mar. Drugs* **2022**, *20*, 61. [CrossRef] [PubMed]
13. Prasad, K.N. A micronutrient mixture with collagen peptides, probiotics, cannabidiol, and diet may reduce aging, and development and progression of age-related alzheimer's disease, and improve its treatment. *Mech. Ageing Dev.* **2023**, *210*, 111757. [CrossRef] [PubMed]
14. Žmitek, K.; Žmitek, J.; Butina, M.R.; Pogačnik, T. Effects of a Combination of Water-Soluble Coenzyme Q10 and Collagen on Skin Parameters and Condition: Results of a Randomised, Placebo-Controlled, Double-Blind Study. *Nutrients* **2020**, *12*, 618. [CrossRef] [PubMed]
15. Aziz, J.; Shezali, H.; Radzi, Z.; Yahya, N.A.; Abu Kassim, N.H.; Czernuszka, J.; Rahman, M.T. Molecular Mechanisms of Stress-Responsive Changes in Collagen and Elastin Networks in Skin. *Ski. Pharmacol. Physiol.* **2016**, *29*, 190–203. [CrossRef] [PubMed]
16. Oba, C.; Ito, K.; Ichikawa, S.; Morifuji, M.; Nakai, Y.; Ishijima, T.; Abe, K.; Kawahata, K. Effect of orally administered collagen hydrolysate on gene expression profiles in mouse skin: A DNA microarray analysis. *Physiol. Genom.* **2015**, *47*, 355–363. [CrossRef] [PubMed]
17. Ding, J.-F.; Li, Y.-Y.; Xu, J.-J.; Su, X.-R.; Gao, X.; Yue, F.-P. Study on effect of jellyfish collagen hydrolysate on anti-fatigue and anti-oxidation. *Food Hydrocoll.* **2011**, *25*, 1350–1353. [CrossRef]
18. Liang, J.; Pei, X.-R.; Wang, N.; Zhang, Z.-F.; Wang, J.-B.; Li, Y. Marine collagen peptides prepared from chum salmon (*Oncorhynchus keta*) skin extend the life span and inhibit spontaneous tumor incidence in sprague-dawley rats. *J. Med. Food* **2010**, *13*, 757–770. [CrossRef] [PubMed]
19. León-López, A.; Morales-Peñaloza, A.; Martínez-Juárez, V.M.; Vargas-Torres, A.; Zeugolis, D.I.; Aguirre-Álvarez, G. Hydrolyzed Collagen—Sources and Applications. *Molecules* **2019**, *24*, 4031. [CrossRef]
20. Prajaputra, V.; Isnaini, N.; Maryam, S.; Ernawati, E.; Deliana, F.; Haridhi, H.A.; Fadli, N.; Karina, S.; Agustina, S.; Nurfadillah, N.; et al. Exploring marine collagen: Sustainable sourcing, extraction methods, and cosmetic applications. *S. Afr. J. Chem. Eng.* **2024**, *47*, 197–211. [CrossRef]
21. Al-Atif, H. Collagen Supplements for Aging and Wrinkles: A Paradigm Shift in the Field of Dermatology and Cosmetics. *Dermatol. Pract. Concept.* **2022**, *12*, e2022018. [CrossRef]
22. Li, C.; Fu, Y.; Dai, H.; Wang, Q.; Gao, R.; Zhang, Y. Recent progress in preventive effect of collagen peptides on photoaging skin and action mechanism. *Food Sci. Hum. Wellness* **2022**, *11*, 218–229. [CrossRef]
23. Coppola, D.; Oliviero, M.; Vitale, G.A.; Lauritano, C.; D'ambra, I.; Iannace, S.; de Pascale, D. Marine collagen from alternative and sustainable sources: Extraction, processing and applications. *Mar. Drugs* **2020**, *18*, 214. [CrossRef]
24. Ao, H.; Yang, S.; Nie, B.; Fan, Q.; Zhang, Q.; Zong, J.; Gus, S.; Zheng, X.; Tang, T. Improved antibacterial properties of collagen I/hyaluronic acid/quaternized chitosan multilayer modified titanium coatings with both contact-killing and release-killing functions. *J. Mater. Chem. B* **2019**, *7*, 1951–1961. [CrossRef]
25. Aguilar-Toalá, J.E.; Vidal-Limon, A.; Liceaga, A.M. Nutricosmetics: A new frontier in bioactive peptides' research toward skin aging. In *Advances in Food and Nutrition Research*; Academic Press: Cambridge, MA, USA, 2023; Volume 104, pp. 205–228. [CrossRef]
26. Zhang, X.; Zhuang, H.; Wu, S.; Mao, C.; Dai, Y.; Yan, H. Marine Bioactive Peptides: Anti-Photoaging Mechanisms and Potential Skin Protective Effects. *Curr. Issues Mol. Biol.* **2024**, *46*, 990–1009. [CrossRef] [PubMed]
27. Ahmed, M.F.; Unnikrishnan, S.; Ramalingam, K. Anti-Aging Activity of Natural Products. In *Pharmacological Benefits of Natural Agents*; IGI Global: Harrisburg, United States, 2023; pp. 104–130. [CrossRef]

28. Siahaan, E.A.; Agusman; Pangestuti, R.; Shin, K.-H.; Kim, S.-K. Potential Cosmetic Active Ingredients Derived from Marine By-Products. *Mar. Drugs* **2022**, *20*, 734. [CrossRef] [PubMed]
29. Ahmed, M.; Verma, A.K.; Patel, R. Collagen extraction and recent biological activities of collagen peptides derived from sea-food waste: A review. *Sustain. Chem. Pharm.* **2020**, *18*, 100315. [CrossRef]
30. Bhat, P.; Garibyan, L. The Potential of CRISPR-Guided Therapies in the Dermatology Clinic. *JID Innov.* **2022**, *2*, 100103. [CrossRef]
31. Yang, H.; Zhang, Q.; Zhang, B.; Zhao, Y.; Wang, N. Potential Active Marine Peptides as Anti-Aging Drugs or Drug Candidates. *Mar. Drugs* **2023**, *21*, 144. [CrossRef]
32. Lee, Y.I.; Lee, S.G.; Kim, E.; Jung, I.; Suk, J.; Kim, J.; Lee, J.H. Anti-aging effect of an oral disintegrating collagen film: A prospective, single-arm study. *Int. J. Dermatol.* **2022**, *61*, 54–61. [CrossRef]
33. Farage, M.A.; Miller, K.W.; Elsner, P.; Maibach, H.I. Characteristics of the Aging Skin. *Adv. Wound Care* **2013**, *2*, 5–10. [CrossRef] [PubMed]
34. Pozzolini, M.; Millo, E.; Oliveri, C.; Mirata, S.; Salis, A.; Damonte, G.; Arkel, M.; Scarfì, S. Elicited ROS Scavenging Activity, Photoprotective, and Wound-Healing Properties of Collagen-Derived Peptides from the Marine Sponge *Chondrosia reniformis*. *Mar. Drugs* **2018**, *16*, 465. [CrossRef] [PubMed]
35. Chen, S.; Yang, Q.; Chen, X.; Tian, Y.; Liu, Z.; Wang, S. Bioactive peptides derived from crimson snapper and *in vivo* anti-aging effects on fat diet-induced high fat *Drosophila melanogaster*. *Food Funct.* **2020**, *11*, 524–533. [CrossRef] [PubMed]
36. Rahman, M.A. Collagen of Extracellular Matrix from Marine Invertebrates and Its Medical Applications. *Mar. Drugs* **2019**, *17*, 118. [CrossRef] [PubMed]
37. Cruz, M.A.; Araujo, T.A.; Avanzi, I.R.; Parisi, J.R.; de Andrade, A.L.M.; Rennó, A.C.M. Collagen from Marine Sources and Skin Wound Healing in Animal Experimental Studies: A Systematic Review. *Mar. Biotechnol.* **2021**, *23*, 1–11. [CrossRef] [PubMed]
38. Chandika, P.; Ko, S.-C.; Jung, W.-K. Marine-derived biological macromolecule-based biomaterials for wound healing and skin tissue regeneration. *Int. J. Biol. Macromol.* **2015**, *77*, 24–35. [CrossRef] [PubMed]
39. Liu, S.; Lau, C.-S.; Liang, K.; Wen, F.; Teoh, S.H. Marine collagen scaffolds in tissue engineering. *Curr. Opin. Biotechnol.* **2022**, *74*, 92–103. [CrossRef] [PubMed]
40. Lim, Y.-S.; Ok, Y.-J.; Hwang, S.-Y.; Kwak, J.-Y.; Yoon, S. Marine Collagen as A Promising Biomaterial for Biomedical Applications. *Mar. Drugs* **2019**, *17*, 467. [CrossRef] [PubMed]
41. Barzkar, N.; Sukhikh, S.; Babich, O.; Maran, B.A.V.; Jahromi, S.T. Marine Collagen: Purification, Properties and Application. *Front. Mar. Sci.* **2023**, *10*, 1245077. Available online: https://www.frontiersin.org/articles/10.3389/fmars.2023.1245077 (accessed on 30 December 2023). [CrossRef]
42. Lin, Z.; Tao, Y.; Huang, Y.; Xu, T.; Niu, W. Applications of marine collagens in bone tissue engineering. *Biomed. Mater.* **2021**, *16*, 042007. [CrossRef]
43. Pickar-Oliver, A.; Gersbach, C.A. The next generation of CRISPR–Cas technologies and applications. *Nat. Rev. Mol. Cell Biol.* **2019**, *20*, 490–507. [CrossRef] [PubMed]
44. Li, T.; Yang, Y.; Qi, H.; Cui, W.; Zhang, L.; Fu, X.; He, X.; Liu, M.; Li, P.-F.; Yu, T. CRISPR/Cas9 therapeutics: Progress and prospects. *Signal Transduct. Target. Ther.* **2023**, *8*, 36. [CrossRef]
45. He, S. The first human trial of CRISPR-based cell therapy clears safety concerns as new treatment for late-stage lung cancer. *Signal Transduct. Target. Ther.* **2020**, *5*, 168. [CrossRef]
46. Ball, P. (2016, November 17). CRISPR: Implications for Materials Science. MRS Bulletin. Cambridge University Press. Available online: https://www.cambridge.org/core/journals/mrs-bulletin/news/crispr-implications-for-materials-science (accessed on 20 February 2024).
47. Wan, T.; Pan, Q.; Ping, Y. Microneedle-assisted genome editing: A transdermal strategy of targeting *NLRP3* by CRISPR-Cas9 for synergistic therapy of inflammatory skin disorders. *Sci. Adv.* **2021**, *7*, eabe2888. [CrossRef] [PubMed]
48. Baker, C.; Hayden, M.S. Gene editing in dermatology: Harnessing CRISPR for the treatment of cutaneous disease. *F1000Research* **2020**, *9*, 281. [CrossRef]
49. Elango, J.; Robinson, J.; Zhang, J.; Bao, B.; Ma, N.; de Val, J.E.M.S.; Wu, W. Collagen Peptide Upregulates Osteoblastogenesis from Bone Marrow Mesenchymal Stem Cells through MAPK- Runx2. *Cells* **2019**, *8*, 446. [CrossRef]
50. Subhan, F.; Ikram, M.; Shehzad, A.; Ghafoor, A. Marine Collagen: An Emerging Player in Biomedical applications. *J. Food Sci. Technol.* **2014**, *52*, 4703–4707. [CrossRef] [PubMed]
51. Whelan, A.; Duffy, J.; Gaul, R.; O'reilly, D.; Nolan, D.; Gunning, P.; Lally, C.; Murphy, B. Collagen Fibre Orientation and Dispersion Govern Ultimate Tensile Strength, Stiffness and the Fatigue Performance of Bovine Pericardium. *J. Mech. Behav. Biomed. Mater.* **2019**, *90*, 54–60. [CrossRef]
52. Mohiuddin, A.K. Skin aging & Modern age Anti-Aging Strategies. *Int. J. Clin. Dermatol. Res.* **2019**, *7*, 22–70. [CrossRef]
53. Kourani, R.; Corazza, F.; Michel, O.; Virginie, D. What we know about fish allergy by the end of the decade. *J. Investig. Allergol. Clin. Immunol.* **2020**, *29*, 414–421. [CrossRef]
54. Venkatesan, J.; Anil, S.; Kim, S.-K.; Shim, M.S. Marine Fish Proteins and Peptides for Cosmeceuticals: A Review. *Mar. Drugs* **2017**, *15*, 143. [CrossRef] [PubMed]
55. Felician, F.F.; Xia, C.; Qi, W.; Xu, H. Collagen from Marine Biological Sources and Medical Applications. *Chem. Biodivers.* **2018**, *15*, e1700557. [CrossRef]

56. Bjørklund, G.; Shanaida, M.; Lysiuk, R.; Butnariu, M.; Peana, M.; Sarac, I.; Strus, O.; Smetanina, K.; Chirumbolo, S. Natural Compounds and Products from an Anti-Aging Perspective. *Molecules* **2022**, *27*, 7084. [CrossRef] [PubMed]
57. Pu, S.-Y.; Huang, Y.-L.; Pu, C.-M.; Kang, Y.-N.; Hoang, K.D.; Chen, K.-H.; Chen, C. Effects of Oral Collagen for Skin Anti-Aging: A Systematic Review and Meta-Analysis. *Nutrients* **2023**, *15*, 2080. [CrossRef] [PubMed]
58. Seong, S.H.; Lee, Y.I.; Lee, J.; Choi, S.; Kim, I.A.; Suk, J.; Jung, I.; Baeg, C.; Kim, J.; Oh, D.; et al. Low-molecular-weight collagen peptides supplement promotes a healthy skin: A randomized, double-blinded, placebo-controlled study. *J. Cosmet. Dermatol.* **2023**, *23*, 554–562. [CrossRef] [PubMed]
59. Aguilar-Toalá, J.E.; Vidal-Limon, A.; Liceaga, A.M.; Zambrano-Zaragoza, M.L.; Quintanar-Guerrero, D. Application of Molecular Dynamics Simulations to Determine Interactions between Canary Seed (*Phalaris canariensis* L.) Bioactive Peptides and Skin-Aging Enzymes. *Int. J. Mol. Sci.* **2023**, *24*, 13420. [CrossRef]
60. Pei, X.; Yang, R.; Zhang, Z.; Xu, Y.; Han, X.; Wang, J.; Li, Y. Effects of marine collagen peptide on delaying the skin aging. *Chin. J. Prev. Med.* **2008**, *42*, 235–238.
61. Gauza-Włodarczyk, M.; Kubisz, L.; Mielcarek, S.; Włodarczyk, D. Comparison of Thermal Properties of Fish Collagen and Bovine Collagen in the Temperature Range 298–670 K. *Mater. Sci. Eng. C* **2017**, *80*, 468–471. [CrossRef]
62. Yamada, S.; Nagaoka, H.; Terajima, M.; Tsuda, N.; Hayashi, Y.; Yamauchi, M. Effects of Fish Collagen Peptides on Collagen Post-Translational Modifications and Mineralization in an Osteoblastic Cell Culture System. *Dent. Mater. J.* **2013**, *32*, 88–95. [CrossRef]
63. Huang, W.-H.; Ding, S.-L.; Zhao, X.-Y.; Li, K.; Guo, H.-T.; Zhang, M.-Z.; Gu, Q. Collagen for neural tissue engineering: Materials, strategies, and challenges. *Mater. Today Bio* **2023**, *20*, 100639. [CrossRef] [PubMed]
64. Romero Askehoi, A.; Thorseth, M.; Madsen Hargbol, D. Immune Modulatory Properties of Collagen in Cancer. *Front. Immunol.* **2021**, *12*, 791453. [CrossRef] [PubMed]
65. Corrêa, M.E.A.B.; Haupenthal, D.P.d.S.; Mendes, C.; Zaccaron, R.P.; Casagrande, L.d.R.; Venturini, L.M.; Porto, G.D.; Bittencourt, J.V.S.; Silva, J.I.d.S.; Mariano, S.d.S.; et al. Effects of Percutaneous Collagen Induction Therapy Associated with Hyaluronic Acid on Inflammatory Response, Oxidative Stress, and Collagen Production. *Inflammation* **2020**, *43*, 2232–2244. [CrossRef] [PubMed]
66. Mirata, S.; Asnaghi, V.; Chiantore, M.; Salis, A.; Benvenuti, M.; Damonte, G.; Scarfì, S. Photoprotective and Anti-Aging Properties of the Apical Frond Extracts from the Mediterranean Seaweed *Ericaria amentacea*. *Mar. Drugs* **2023**, *21*, 306. [CrossRef] [PubMed]
67. Resende, D.I.; Ferreira, M.; Magalhães, C.; Lobo, J.M.; Sousa, E.; Almeida, I.F. Trends in the use of marine ingredients in anti-aging cosmetics. *Algal Res.* **2021**, *55*, 102273. [CrossRef]
68. Siahaan, E.A.; Pangestuti, R.; Munandar, H.; Kim, S.-K. Cosmeceuticals Properties of Sea Cucumbers: Prospects and Trends. *Cosmetics* **2017**, *4*, 26. [CrossRef]

marine drugs

MDPI

*Article*

# A Thermostable Type I Collagen from Swim Bladder of Silver Carp (*Hypophthalmichthys molitrix*)

**Honghui Jiang [1], Yuanyuan Kong [1], Lili Song [1], Jing Liu [1,2,*] and Zhihong Wang [1,*]**

[1] Tianjin Key Laboratory of Biomaterial Research, Institute of Biomedical Engineering, Chinese Academy of Medical Sciences and Peking Union Medical College, Tianjin 300192, China
[2] Tianjin Enterprise Key Laboratory for Application Research of Hyaluronic Acid, Tianjin 300385, China
* Correspondence: liujing@bme.pumc.edu.cn (J.L.); wangzhihong@bme.pumc.edu.cn (Z.W.)

**Abstract:** As a major component of the extracellular matrix, collagen has been used as a biomaterial for many purposes including tissue engineering. Commercial collagen derived from mammals is associated with a risk of prion diseases and religious restrictions, while fish-derived collagen can avoid such issues. In addition, fish-derived collagen is widely available and low-cost; however, it often suffers from poor thermal stability, which limits its biomedical application. In this study, collagen with a high thermal stability was successfully extracted from the swim bladder of silver carp (*Hypophthalmichthys molitrix*) (SCC). The results demonstrated that it was a type I collagen with high purity and well-preserved triple-helix structure. Amino acid composition assay showed that the amounts of threonine, methionine, isoleucine and phenylalanine in the collagen of swim bladder of silver carp were higher than those of bovine pericardium. After adding salt solution, swim-bladder-derived collagen could form fine and dense collagen fibers. In particular, SCC exhibited a higher thermal denaturation temperature (40.08 °C) compared with collagens from the swim bladder of grass carp (*Ctenopharyngodon idellus*) (GCC, 34.40 °C), bovine pericardium (BPC, 34.47 °C) and mouse tail (MTC, 37.11 °C). Furthermore, SCC also showed DPPH radical scavenging ability and reducing power. These results indicate that SCC presents a promising alternative source of mammalian collagen for pharmaceutical and biomedical applications.

**Keywords:** swim bladder; thermal stability; collagen; antioxidant activity; silver carp (*Hypophthalmichthys molitrix*)

**Citation:** Jiang, H.; Kong, Y.; Song, L.; Liu, J.; Wang, Z. A Thermostable Type I Collagen from Swim Bladder of Silver Carp (*Hypophthalmichthys molitrix*). *Mar. Drugs* **2023**, *21*, 280. https://doi.org/10.3390/md21050280

Academic Editor: Azizur Rahman

Received: 17 March 2023
Revised: 25 April 2023
Accepted: 26 April 2023
Published: 28 April 2023



## 1. Introduction

As the most abundant protein in human tissues, collagen is primarily distributed in the skin, tendons and cartilage, and is actively involved in biomechanical and biological processes. Owing to their weak antigenic activity, excellent biocompatibility and biodegradability, collagen-based biomaterials have been extensively used in biomedical research, including drug delivery, tissue engineering, and therapeutic drugs [1]. According to their sources, collagen can typically be divided into natural and recombinant collagen. The former collagen is typically made from mammalian tissues such as rat tails, porcine skin, or bovine tendon. However, mammalian-sourced collagens suffer from variable quality, low purity, risk of prion contamination and religious restrictions [2]. Recombinant collagens are produced using synthetic biology and recombinant technology under controlled laboratory conditions. However, it is still difficult to generalize the assembly of the supramolecular band pattern and biological function of native collagen [3].

In recent years, fish and their processing by-products have gained increasing attention due to their accessibility, low risk of disease transmission, lack of religious restrictions and high collagen yield [4,5]. For example, collagen fibrils from Bester Sturgeon were used to coat culture dishes for cell culture, and the results showed that ordered collagen fibers could guide 3T3-L1, MC3T3-E1, C2C12, and L929 cells to grow in the same direction and

further induced early osteogenic differentiation of MC3T3-E1 [6]. In addition, collagen from jellyfish (*Catostylus mosaicus*) outperformed rat tail collagen in promoting MC3T3 adhesion and proliferation [7]. Generally, fish collagen is extracted from fish scales, skin or bones [8]. However, fish scales contain more calcium impurities, and fish skin has a high pigment content and a low thermal denaturation temperature [9], which limits their biomedical application. The main components of the swim bladder are collagen, elastin and polysaccharides. A degraded sulfate glycosaminoglycan (D-SBSG) from the swim bladder of bighead carp has been found to have anticoagulant and anti-inflammatory properties, suggesting that it is a potential immunomodulatory drug component [10]. Besides, many studies have focused on the extraction of antioxidant and anti-aging active peptides from fish bladders and their application studies [11–14]. Compared with fish skin, scales, and other visceral organs, the imino acid content of collagen from swim bladders is typically higher, which corresponds to a higher thermal denaturation temperature [15]. In addition, fish habitat and body temperature are related to the thermal stability of collagen. Thus, collagen from warm-water fish species is more thermally stable than collagen from cold-water fish species [16]. Silver carp (*Hypophthalmichthys molitrix*) is the main fish species used for economic purposes in China, and its annual output value exceeds 3.8 million tons. During processing, approximately 80% of the byproducts from silver carp are not rationally utilized [17]. Taken together, we speculate that the collagen from swim bladder of silver carp is likely to have high thermal stability.

In this study, we prepared a collagen from the swim bladder of silver carp (SCC) using the pepsin extraction method, and collagens from swim bladder of grass carp (GCC), bovine pericardium (BPC) and mouse tail (MTC) were extracted for comparison. The compositional differences in the isolated collagens were identified by SDS-PAGE, peptide maps, and amino acid composition. Their physicochemical properties were identified by ultraviolet-visible spectroscopic (UV) analysis, Fourier transform infrared spectroscopy (FTIR) analysis as well as circular dichroism (CD) measurement. In addition, the thermal stability of the isolated collagens was confirmed by CD. Finally, the fibril-forming and antioxidant capacities of the isolated collagens were studied.

## 2. Results

### *2.1. Extraction Yields of Collagens*

The yields (%, *w*/*w*) of SCC, GCC and BPC were calculated based on the dry weight of the materials. The yields of SCC, GCC and BPC were 5.92%, 3.92% and 8.53%, respectively. The yield of collagens from two swim bladders were lower than that from bovine pericardium, indicating that the degree of cross-linking among collagen molecules might be stronger in swim bladders from silver carp and grass carp than in bovine pericardium. Similar results have been reported, including collagens from scales of silver carp (1.5%) [18], as well as swim bladder of Amur sturgeon (16.5%) [19] and catla (61.3%) [20]. Differences in collagen yields may be due to the species, structure and composition of tissue, and the extraction method [8].

### *2.2. SDS-PAGE*

All the extracted collagens were identified as type I collagen based on the electrophoretic pattern (Figure 1), which was primarily characterized by two chains (α1(I) and α2(I) with a ratio of roughly 2:1), and their crosslinked chains: β dimers and γ trimers [21]. The molecular weights of α1(I) and α2(I) were approximately 140 and 130 kDa, respectively. Moreover, no other small molecule peptide chains below the α2(I) chain were detected, indicating the high purity of the isolated collagens. Our result was in agreement with those of other type I collagens [22,23]. The electrophoretic patterns revealed that the high molecule crosslinks of collagens were more abundant in SCC than GCC, BPC and MTC, which may be because the cross-linked peptides of SCC are less susceptible to pepsin cleavage.

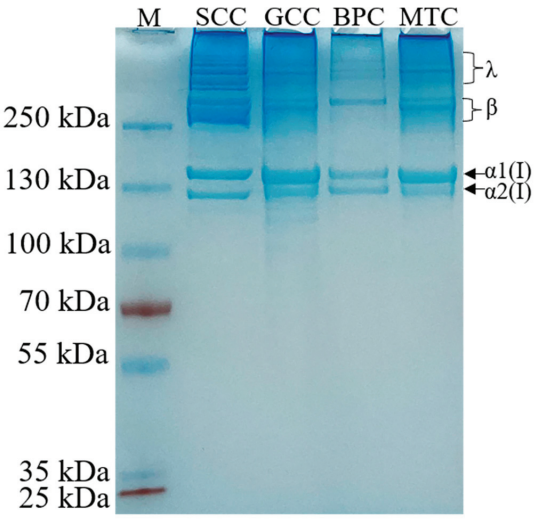


**Figure 1.** Electrophoretic pattern of collagens from swim bladders of silver carp (SCC) and grass carp (GCC), bovine pericardium (BPC) and mouse tail (MTC). M, marker for protein molecular weight.

*2.3. Peptide Maps*

The carboxy-terminal peptide chain of hydrophobic amino acids such as tryptophan, tyrosine, phenylalanine, and leucine can be hydrolyzed by chymotrypsin [24]. After chymotrypsin treatment, the densities of the α, β and γ chains decreased, and more bands with low molecular weight were observed (Figure 2). The difference in the band distribution of several collagen-hydrolyzed peptides was mainly distributed at an interval of 55~100 kDa. Thus, differences in peptide mapping suggested some variations in the primary structures of collagens, particularly in amino acid sequence and composition.

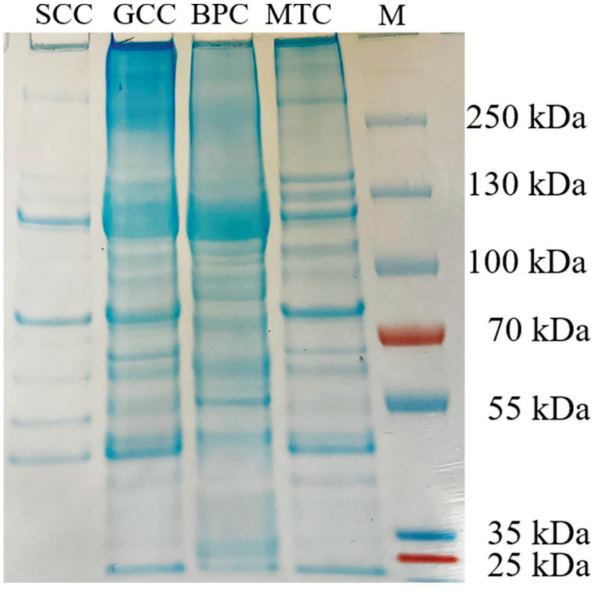


**Figure 2.** Peptide mapping pattern from collagens from swim bladders of silver carp (SCC) and grass carp (GCC), bovine pericardium (BPC) and mouse tail (MTC). M, marker for protein molecular weight.

### *2.4. Amino Acid Composition*

Decellularized extracellular matrix (dECM) is mainly composed of collagen, elastin and polysaccharide, and it has been widely used in tissue engineering and regenerative medicine because of its inherent structure, high bioactivity, low immunogenicity and good biodegradability. Table 1 shows the amino acid composition of the three dECMs and collagens. In three dECMs and collagens, glycine was the most prevalent amino acid, followed by proline, arginine, glutamic acid, and alanine. With the exception of the final 14 residues of the N-terminal amino acid residues and the first 10 residues of the C-terminal amino acid residues, glycine constitutes roughly one-third of all the residues in collagen [25]. Notably, bovine pericardium did not contain cystine, but swim-bladder-derived dECMs and collagens did. In addition, swim-bladder-derived dECMs and collagens had higher concentrations of threonine, methionine, isoleucine, and phenylalanine than bovine pericardium. The pyrrolidine rings found in proline help reinforce the triple helical structure of collagen [26]. The proline content of the collagens extracted in this study is similar to that of the reported collagens with good thermal stability, such as the collagen from swim bladder of rohu (*Labeo rohita*) (145.3 ± 6.28 μg/mg) [15], suggesting that the isolated collagens may have good thermostable abilities. Hydroxyproline can form interchain hydrogen bonds with other amino acids through hydroxyl groups, which are crucial for the thermal stability of collagen [27]. The differences in amino acid contents of collagens and dECMs of SC, GC and BP may be caused by different species. The difference in amino acid content between the dECM and collagen of the same species may be due to the elastin and other proteins contained in dECM.

**Table 1.** Amino acids composition from dECMs and isolated collagens (μg/mg). SC, swim bladder of silver carp; GC, swim bladder of grass carp; BP, bovine pericardium.

| Amino Acid | Collagens | | | dECMs | | |
|---|---|---|---|---|---|---|
| | SC | GC | BP | SC | GC | BP |
| Histidine | 4.06 | 4.22 | 4.10 | 5.93 | 5.53 | 3.89 |
| Hydroxyproline | 65.81 | 68.96 | 72.77 | 47.60 | 33.08 | 66.64 |
| Arginine | 89.23 | 95.38 | 94.62 | 83.80 | 75.22 | 85.29 |
| Serine | 33.35 | 37.03 | 32.23 | 34.92 | 36.43 | 29.80 |
| Glycine | 196.44 | 204.50 | 198.35 | 173.50 | 173.12 | 180.46 |
| Aspartic acid | 76.61 | 76.89 | 72.57 | 83.61 | 85.28 | 65.70 |
| Glutamic acid | 108.81 | 110.83 | 108.05 | 104.54 | 94.06 | 96.20 |
| Threonine | 28.86 | 29.60 | 18.61 | 34.05 | 40.48 | 16.58 |
| Alanine | 97.75 | 103.20 | 101.48 | 88.76 | 84.67 | 90.75 |
| Proline | 142.87 | 149.21 | 155.08 | 124.37 | 113.37 | 136.70 |
| Lysine | 16.92 | 18.39 | 17.04 | 14.62 | 13.33 | 12.72 |
| Cystine | 1.33 | 1.13 | 0.00 | 5.45 | 5.08 | 0.00 |
| Methionine | 15.24 | 11.37 | 5.01 | 17.00 | 12.97 | 4.90 |
| Tyrosine | 5.78 | 7.31 | 4.09 | 27.81 | 49.44 | 5.64 |
| Valine | 16.77 | 19.52 | 19.41 | 23.60 | 28.96 | 17.73 |
| Isoleucine | 14.06 | 15.93 | 13.16 | 18.92 | 21.90 | 11.76 |
| Leucine | 29.36 | 32.53 | 27.22 | 41.50 | 55.53 | 25.29 |
| Phenylalanine | 23.78 | 24.37 | 19.78 | 25.94 | 23.88 | 18.91 |
| Tryptophan | 0.45 | 0.07 | 0.04 | 0.02 | 0.02 | 0.07 |

### *2.5. UV Absorption Spectrum*

Figure 3 showed the UV absorption spectra of the isolated collagens at 200~400 nm. The findings revealed that the maximum absorption peaks of the extracted collagens were all situated between 230 and 240 nm, which was in line with the absorption properties of collagen, similar to that found in carp and barramundi [28,29]. This maximum absorption peak was caused by the $n \rightarrow \pi^*$ electron leap of C=O, -COOH and $CONH_2$. Additionally, SCC, GCC, and MTC all had specific absorption peaks at 260~280 nm, demonstrating the presence of a specific number of aromatic amino acids [17], which corresponds to the results

of amino acid composition analysis. It has been suggested that aromatic amino acids, such as tyrosine and phenylalanine, can enhance the antioxidant properties of proteins [30].

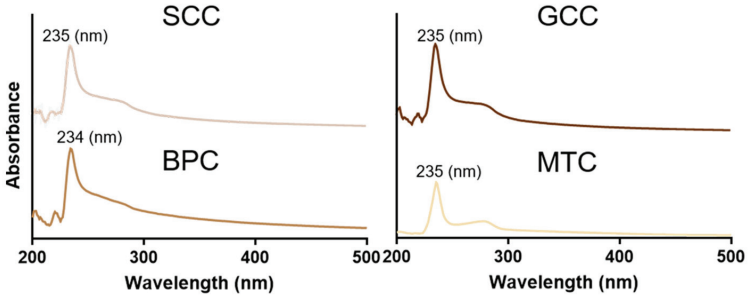


**Figure 3.** UV spectra of collagens from swim bladders of silver carp (SCC) and grass carp (GCC), bovine pericardium (BPC) and mouse tail (MTC).

*2.6. FTIR Spectroscopy*

The FTIR spectra of the isolated collagens demonstrated that they possessed distinctive infrared absorption bands of type I collagen (Figure 4), which are composed of amide A, B, I, II, and III bands [31]. These absorption peaks are caused by the vibration of peptide groups, and can reveal vital details regarding the secondary structure of the protein. In most cases, the amide A band oscillates between 3310 and 3270 $cm^{-1}$, which is correlated with the frequency of the stretching vibration of the O-H and N-H hydrogen bonds. In the present study, the amide A band appeared in the lower wavenumber range, suggesting that the collagen extracted in this study has a certain strength of hydrogen bonding structure [32]. The amide A bands of SCC, GCC, BPC and MTC were 3324.677, 3325.641, 3325.159 and 3338.658 $cm^{-1}$, respectively, indicating that SCC had a higher degree of hydrogen bonding than the other three collagens. Meanwhile, the peak near 2900 $cm^{-1}$ indicates the presence of the amide B band which is mainly produced by the stretching vibration of N–H [33]. An increase in $NH–NH_3^+$ free groups from both lysine residues and the N-terminus is related to the shift of amide B to a higher wavenumber [32]. As seen by the wavenumbers of the amide B bands of SCC, GCC, BPC, and MTC, which were 2936.573, 2930.305, 2935.126, and 2931.751 $cm^{-1}$, respectively, SCC possessed more $–NH_3^+$ free groups than the other three collagens. The amide I band is frequently used as a distinctive indicator of the secondary structure of a peptide. Because the amide I band primarily reflects the C=O stretching vibration and can successfully represent the triple-helix structure, its peak will shift to a lower wavenumber as the molecular order decreases [34]. All of the collagens extracted for this study have a well-preserved triple-helix structure, according to the wavenumbers of the amide I bands of SCC, GCC, BPC, and MTC, which were 1660.41, 1657.035, 1663.302, and 1654.142 $cm^{-1}$, respectively. The amide II band, which is related to the N–H bending vibration of collagen, is present in the wavelength range of 1580 to 1500 $cm^{-1}$ [35], and an amide II band with a lower wavenumber has more hydrogen bonds between N–H groups and a higher degree of structural order. The pyrrolidine ring vibrations of proline and hydroxyproline are related to the N–H bending vibration and C–N stretching vibration of collagen, which are primarily reflected by the amide III band [36]. Our research revealed that the triple helical structures were well-preserved, and that the secondary structures of the isolated collagen were slightly different.

*2.7. CD Spectrum*

Natural collagen has a triple-helix structure that results in a peak that is indicative of the helix at 196~198 nm and a peak that is characteristic of the negative peak at 221~222 nm [37]. Circular dichroism scanning spectra of the four collagens are shown in Figure 5. According to the findings, four collagens showed similar CD spectra line, strong positive absorption peaks close to 221 nm, crossover points on the x-axis at approximately

206 nm, and strong negative peaks at approximately 202 nm. The integrity of the collagen triple-helix structure can be determined by the intensity ratio of the positive and negative peaks ($R_{pn}$) [38]. CD data (Table 2) showed that SCC had the higher CD value at 221 nm (28.6594) and $R_{pn}$ (0.3566) than GCC, BPC and MTC, indicating that collagens had diverse secondary structures. Thus, the triple-helix structures of the extracted collagens were complete, which was in line with the distinctive absorption peaks of the triple-helix structure of collagen in FTIR.

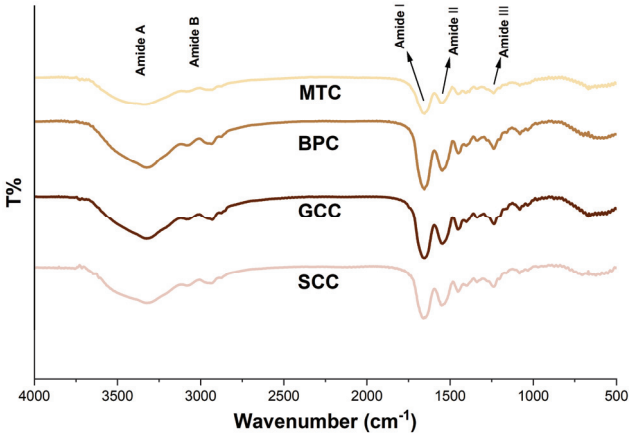


**Figure 4.** FTIR spectra of collagens from swim bladders of silver carp (SCC) and grass carp (GCC), bovine pericardium (BPC) and mouse tail (MTC).

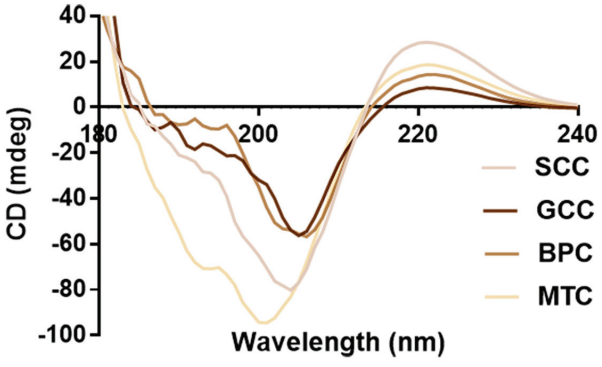


**Figure 5.** CD spectra of collagens from swim bladders of silver carp (SCC) and grass carp (GCC), bovine pericardium (BPC) and mouse tail (MTC).

**Table 2.** CD data of collagens from swim bladders of silver carp (SCC) and grass carp (GCC), bovine pericardium (BPC) and mouse tail (MTC).

| | CD [221 nm] (mdeg) | $R_{pn}$ |
|---|---|---|
| SCC | 28.6594 | 0.3566 |
| GCC | 8.75611 | 0.1530 |
| BPC | 14.4292 | 0.2533 |
| MTC | 18.7925 | 0.1958 |

$R_{pn}$ represents the intensity ratio of positive peak over negative peak (absolute values).

### *2.8. Thermal Stability*

The positive peak in the CD spectra may vanish completely as a result of complete collagen denaturation. In this study, the characteristics of the variation in CD value

with temperature for collagen in the wavelength range of 210~250 nm were investigated (Figure 6a). According to our findings, the decrease interval for the CD value of SCC was between 35 and 40 °C, whereas for GCC, BPC, and MTC, it was mainly between 30 and 35 °C. Thus, SCC had higher thermal stability than the other three groups. In order to exactly determine the thermal denaturation temperature of collagens, we examined how the CD value varied with temperature at 221 nm for collagens (Figure 6b,c). The conformational change process of the collagen triple-helix structure is reflected in the variation in the CD value with temperature, thus the characteristic absorbance of the collagen triple-helix structure can be represented by the absorbance (molar ellipticity) at 221 nm in the CD spectrum [39]. Figure 6b showed that as the temperature gradually increased, the CD value of collagen gradually would decrease from a horizontal curve until it stabilized. In our study, the absorbance differential curves of collagen (Figure 6c) were calculated, and the results showed that SCC had the highest denaturation temperature and its differential curve of CD value had two peaks, showing that its denaturation temperature was 40.08 and 40.99 °C, respectively, which may be due to the existence of two collagen molecules with different stability in SCC, or the existence of at least two regions with different stabilities in collagen molecules [40]. In contrast, the absorbance differential curves of GCC, BPC and MTC had single peaks, indicating denaturation temperatures of 34.40, 34.47 and 37.11 °C, respectively. Thus, our results showed that SCC exhibited good thermal stability.

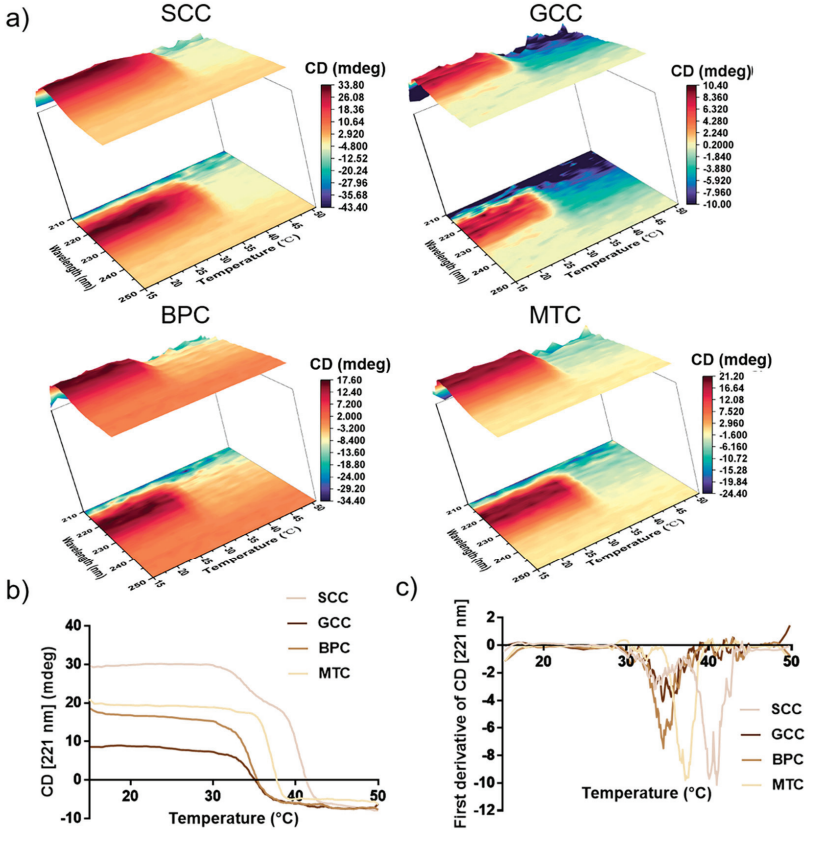


**Figure 6.** Thermal stability of collagens from swim bladders of silver carp (SCC) and grass carp (GCC), bovine pericardium (BPC) and mouse tail (MTC). (**a**) Thermal denaturation process of the isolated collagens in the wavelength range of 210~250 nm. (**b**) Thermal denaturation curves of four kinds of collagen species at 221 nm and (**c**) differential curve of absorbance of the isolated collagens at 221 nm.

### *2.9. Collagen Fibrillogenesis*

This study looked at the self-aggregation behavior of collagens from four different species sources and compared the effects of different ionic strengths. The findings showed that at a specific ionic strength, the collagen self-aggregation kinetic curves displayed an S-shaped curve (Figure 7a). At ionic strengths of 0 and 100 mM, collagens basically did not self-aggregate, while at ionic strengths higher than 500 mM, collagens could significantly self-aggregate, and the self-aggregation behavior basically reached the equilibrium phase after 1 h. Additionally, with increasing ionic strength (especially 1500 mM), collagen self-aggregation moved more quickly toward equilibrium. In contrast to the collagen fibrils of the bovine pericardium and mouse tail, which appeared as lamellar fibrous structures with larger pore sizes, the collagen fibrils of the two swim bladders were primarily slender fibrous meshwork with slimmer diameters and denser pores (Figure 7b). The degree of self-aggregation of the four collagens varied after 2 h of self-aggregation under the same conditions (Figure 7c), MTC and BPC could reach up to 100% (protein concentration in the supernatant was below the lower limit of detection), whereas SCC and GCC were 60.92% and 53.15%, respectively. The results showed that collagens of mammalian origin performed better in terms of self-aggregation. The different characteristics of collagen fibrils could be the result of varying species [41].

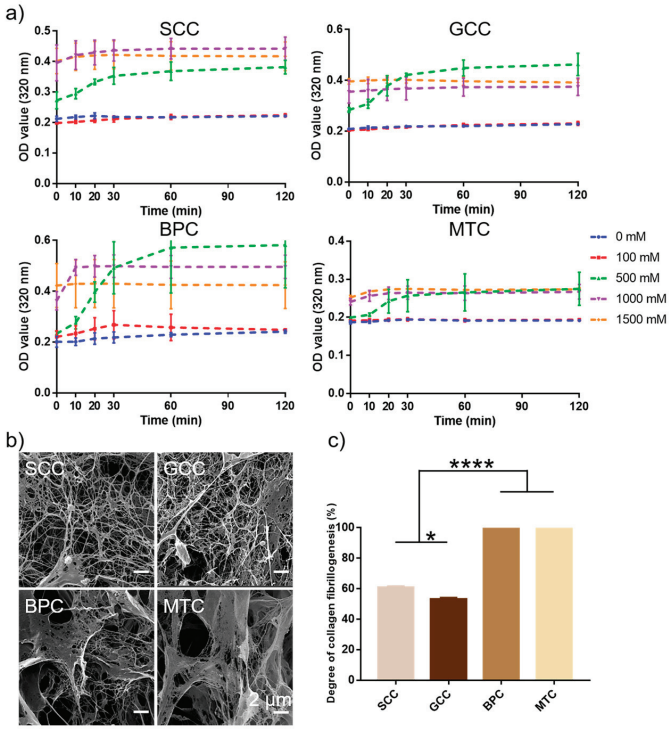


**Figure 7.** Collagen fibrillogenesis of collagens from swim bladders of silver carp (SCC) and grass carp (GCC), bovine pericardium (BPC) and mouse tail (MTC). (**a**) Self-aggregation kinetics curves of the isolated collagens under different ionic concentration. (**b**) Scanning electron micrographs of collagen fibrils and (**c**) the degree of collagen fibrillogenesis of the isolated collagens under the same conditions. * represents $p < 0.05$, **** represents $p < 0.0001$.

### *2.10. Antioxidant Activity*

Figure 8a showed that MTC had the highest DPPH radical scavenging rate (65.69%), followed by SCC (54.81%). According to Zhuang et al., collagen and collagen hydrolysate

from jellyfish could significantly shield skin lipids and collagen from UV radiation and promote the production of skin collagen [42]. The capacity of collagen to convert iron to ferrous ions determines its reducing power. In terms of reducing ability, SCC was the strongest with an absorbance of 0.145 at 700 nm, followed by that of vitamin E (0.144) (Figure 8b). According to Jeevithan et al., collagen from silvertip shark cartilage exhibited significant DPPH radical scavenging activity and reducing power [31].

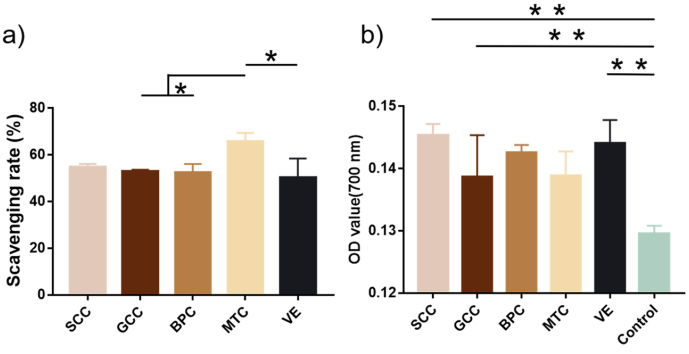


**Figure 8.** Antioxidant activities of collagens from swim bladders of silver carp (SCC) and grass carp (GCC), bovine pericardium (BPC) and mouse tail (MTC). (**a**) DPPH scavenging rate and (**b**) reducing power of collagens. * represents $p < 0.05$, ** represents $p < 0.01$.

## 3. Discussion

Owing to its unique properties, collagen is a highly versatile and high-performance biomaterial that is widely used in clinical medicine. The heat denaturation temperature of the protein material should be higher than 37 °C when it is applied to the human body in order to maintain its biological activity. The function of the extracted biomolecules is significantly affected by denaturation because it causes loss of the recognizable triple-helix conformation [43]. Rapid degradation of collagen *in vivo* reduces the effective duration of its biological activity, which is the main limitation of fish collagen. Existing methods usually enhance thermal stability by chemical cross-linking or compounding with other materials, but each method has its own drawbacks, such as the cytotoxicity of glutaraldehyde. Thermal stability of collagen is also directly impacted by the habitat temperatures and the body temperatures of various animal species [44], and SC and GC used in this study were from the same fishery, whose water temperature was approximately 20 °C. The thermal denaturation temperature of the protein can be verified by viscosity test, CD measurement and differential scanning calorimetry. The thermal denaturation temperature of the same collagen obtained using different test methods may vary owing to differences in the methods themselves. Direct detection of the triple-helix structure in collagens can be accomplished using CD measurement, including $R_{pn}$ measurement. In this study, a thermostable type I collagen from swim bladder of silver carp was extracted, and its physicochemical properties were studied. CD measurements showed that the thermal denaturation temperature ($T_d$) of SCC was up to 40.08 °C (Figure 5). Besides, SCC had the highest CD value at 221 nm and $R_{pn}$ (Table 2), suggesting a better triple-helix structural integrity. The conformation, amino acid sequence, and imino acid content of collagen play a role in the thermal stability [45]. The proline content of SCC, GCC and BPC were all above 140 μg/mg, similar to the reported thermostable collagens from scale (152.3 μg/mg) [28] and swim bladder (145.3 ± 6.28 μg/mg) [15] of rohu. However, the thermal denaturation temperatures of GCC and BPC were lower than that of SCC, indicating that there are other reasons why these collagen types have differences in thermal stability. We speculate that the following reasons exist for this: 1. Disulfide bonds have an important effect on the stability of tertiary structures, and SCC and GCC contain cystine with disulfide bonds, while BPC does not contain cystine [46], which could be confirmed by the FITR results

that the amide A band positions (Figure 4) indicated that the degree of hydrogen bonding interaction was higher for SCC than for the other three collagens. 2. Since serine residues can offer more freedom in the C-N and C-C bonds within the peptide bond than cyclic hydroxyproline residues, they could potentially replace hydroxyproline in collagen. The serine content of SCC, GCC and BPC were 33.35, 37.03 and 32.23 μg/mg, respectively, while the serine content was reported to be negatively correlated with the thermal denaturation temperature [47], which may be one of explanations why GCC has the lowest thermal stability.

Collagen is a typical amphiphilic molecule containing a large number of hydrophilic amino acids. The hydrated layer of collagen is destroyed by the addition of neutral salts, exposing the charged residues and hydrophobic groups, allowing the monomer collagen molecules to self-aggregate quickly through electrostatic and hydrophobic interactions. Type I collagen can form collagen fibrils by self-aggregation, that is, collagen molecules with a complete triple-helix structure are rearranged in an orderly intermolecular manner to form collagen fibrils with a staggered stripe structure (also known as the D-cycle structure), which can be divided into three processes: 1. Collagen molecules interact with each other to form collagen microfibrils; 2. Collagen microfibrils are assembled into collagen fibers; 3. Equilibrium stage [48]. Collagen fibers are more thermally-stable and resistant to degradation than collagen molecules alone, and can also exist as hydrogels, sponges, or thin films, which can be used in biomaterials and tissue engineering fields. The self-aggregation behavior of collagen is influenced by factors such as the solution pH, ionic strength, temperature, solvent and concentration. In this study, SCC can quickly form a dense fibril structure after adding PB solution containing a certain salt ion concentration, and it has good fibril-forming ability (Figure 7), so its application form and area can be further extended.

The ability of collagens to decrease hydroperoxides, inactivate ROS, chelate pro-oxidative transition metals, eliminate oxidants, and scavenge free radicals is thought to be part of their antioxidant mechanism [49]. The essential quality for cosmeceutical preparations meant to reduce photoaging and UV damage is their radical scavenging activity [50]. The antioxidant properties of proteins are significantly influenced by their size, structure, and amino acid composition [51], thus the high content of hydrophobic amino acids (methionine, isoleucine, and phenylalanine) in SCC may account for its antioxidant properties. In the present study, SCC showed a good ability to scavenge DPPH radicals and reducing power (Figure 8). Ischemic diseases and tumors can cause local tissues in the ROS environment, so further application studies of SCC are necessary in the treatment of these diseases.

There are some limitations in this study, that is, its biological activities, such as the influence on cell proliferation and differentiation and the ability to protect cells in an oxidative emergency environment, were not verified at the cellular level. In the future, SCC can be used to prepare into sheets and injectable materials for further applications.

## 4. Materials and Methods

### *4.1. Materials and Reagents*

Fresh swim bladders from silver carp and grass carp were purchased from a local farm, and fresh bovine pericardium was collected from Fuhua Meat Co., Ltd. (Hebei, China). All chemicals were of analytical grade. Acetic acid (AC) was purchased from DAMAO Chemical Reagent Factory (Tianjin, China). NaCl and NaOH were purchased from Sigma Aldrich (Milwaukee, WI, USA). Porcine pepsin was purchase from Shanghai Yuanye Bio-Tech Co., Ltd. (Shanghai, China).

### *4.2. Isolation and Purification of Collagen*

Swim bladders and bovine pericardium were rinsed twice with chilled distilled water immediately, cut into pieces, and stored at −80 °C. In order to eliminate pigments and non-collagenous proteins, the frozen materials were combined with 0.15 M NaOH and stirred for

6 h. The washed mixture was defatted with 10% isopropyl alcohol for 24 h and rinsed with chilled distilled water to remove any residual reagent. To extract the collagens, pretreated swim bladders and bovine pericardium were soaked for 48 h in 0.5 M AC with 0.2% (*w*/*v*) porcine pepsin (1:30,000). Then, 0.9 M NaCl was added to the AC solution containing the extracted collagen to salt-precipitate collagen. To ensure the unwanted protein was removed, the salt-precipitating extraction procedure was carried out three times. Collagen was reconstituted in 0.5 M AC, dialyzed for 24 h against 0.02 M AC, and then for 48 h against distilled water using dialysis bags (14 K MWCO, Solarbi, Beijing, China). Following that, the purified collagen was lyophilized for 48 h using a freeze dryer (SCIENTZ-10N, SCIENTZ, Ningbo, China), and then stored at −20 °C. The extraction method of collagen from C57 mouse tail is similar to the above steps, except that the extraction solution is 0.5 M AC without pepsin. dECMs were prepared as described in our previous paper [52]. Briefly, fresh swim bladders and bovine pericardium were firstly treated with sodium dodecyl sulfonate and Triton X-100 with gentle shaking, rinsed with PBS for several days, and then incubated with DNase and RNase overnight.

### *4.3. SDS–Polyacrylamide Gel Electrophoresis (SDS-PAGE)*

Lyophilized collagens were solubilized in 0.5 M AC at 2 mg/mL, combined with sample buffer solution, and boiled for 10 min to completely denature proteins. Then, 15 μL of samples was infused onto an 8% polyacrylamide gel for electrophoresis for 30 min at 120 V. The gel was then stained with Coomassie Brilliant Blue staining solution (Biosharp, Hefei, China) and excess stain was removed using deionized water with gentle stirring.

### *4.4. Peptide Maps*

Lyophilized collagens (1 mg) were mixed with 0.1 mL of 0.05 M Tris-HCl (pH 7.5, containing 10 mM $CaCl_2$) before incubation at 50 °C for 1 h. After that, the mixture received a 10 μL addition of chymotrypsin solution (0.1 mg/mL) for 5 min. The digestion was stopped by adding 130 μL of 5% (*w*/*v*) SDS and boiling at 85 °C for 10 min. The peptides produced by digestion were separated using SDS-PAGE.

### *4.5. Amino Acid Analysis*

A high-resolution mass spectrometer (Q Exactive, Thermo, Waltham, MA, USA) and ultra-high performance liquid chromatography (UPLC, Thermo, USA) were used for quantitative analysis to determine the amino acid composition of collagen. Complete hydrolysis of lyophilized collagens with 6 M HCl was performed at 110 °C for 24 h. After that, samples were centrifuged for 10 min at 15,000× *g*. The mixture was then given the AccQ·Tag Ultra Borate buffer after the supernatant had been neutralized with 2 M NaOH. The sample was then added in a UPLC vial along with Borate buffer and AccQ·Tag reagent. The mixture was boiled at 55 °C for 10 min after being kept at room temperature for 1 min. After cooling, 1 μL was then injected. In order to analyze the sample extracts, a UPLC-Orbitrap-MS system (UPLC, Vanquish, MS, QE) was used. Based on individual retention time of each amino acid, the peaks were determined. The amount was determined using the peak areas of the samples and the known concentrations of the standard amino acid mixtures. The μg/mg protein equivalent of each amino acid was then calculated.

### *4.6. Ultraviolet-Visible Spectroscopic Analysis*

Lyophilized collagens were solubilized in 0.5 M AC at 2 mg/mL. UV spectra were obtained using a spectrophotometer (Lambda35, PerkinElmer, Waltham, MA, USA) in the 190~400 nm range at 1 nm interval. A 0.5 M AC baseline was established.

### *4.7. Fourier Transform Infrared Spectroscopic Analysis*

Lyophilized collagens were combined with KBr at a ratio of 1:100 (*w*/*w*) before being squeezed into a tablet. All spectra were collected using an FTIR spectrophotome-

ter (NICOLET Is10, Thermo, Waltham, MA, USA) at 4000~400 $cm^{-1}$ wavenumber with 4 $cm^{-1}$ resolution.

*4.8. Circular Dichroism Measurement*

A spectrometer (J-750, JASCO, Tokyo, Japan) equipped with a temperature control system was used to perform CD spectroscopy of the collagen samples to determine their molecular conformation and denaturation temperature ($T_d$). Lyophilized collagens were solubilized in 0.5 M AC at 0.1 mg/mL and placed into a quartz cell with a 1 mm path length. Then, CD spectra were obtained at 190~250 nm with 0.1 mm interval and a scan rate of 50 nm/min.

To determine $T_d$, in the temperature range of 15 to 50 °C, the ellipticity at 221 nm was observed at a scan speed of 5 °C/min at 210~250 nm wavelength or 1 °C/min at 221 nm. The temperature at which the CD[221] value decreased at the fastest rate, $T_d$, was determined to be the temperature where the native-fold and fully unfolded structure met in the middle. A 0.5 M AC baseline was established.

*4.9. Collagen Fibrillogenesis In Vitro*

Lyophilized collagens ($n$ = 3 for each group) were solubilized in 0.5 M AC at 2 mg/mL. Samples were mixed with 0.1 M PB solution (pH = 7.0) with a certain concentration of NaCl at a ratio of 1:2 (*v:v*) and incubated for a period of time at 37 °C. The absorbance at 320 nm was obtained at various incubation time using a UV/Vis spectrophotometer (Varioskan Flash3001, Thermo, Waltham, MA, USA).

*4.10. Measurement of Degree of Collagen Fibrillogenesis*

Lyophilized collagens ($n$ = 3 for each group) were solubilized in 0.5 M AC at 2 mg/mL. Samples were mixed with 0.1 M PB solution (pH = 7.0) with 1 M NaCl at a ratio of 1:2 (*v:v*). The mixture was incubated for 3 h at 37 °C. During the collagen fibrillogenesis, the clear liquid would turn white. To precipitate collagen fibrils, the solution was centrifuged at 20,000× $g$ for 20 min. A BCA kit (Beyotime, Shanghai, China) was utilized to measure the protein content of the supernatant. The degree of collagen fibrillogenesis was defined as follows:

$$\text{Degree of collagen fibrillogenesis (\%)} = (C_o - C_s) \times 100\%/C_o \quad (1)$$

where $C_o$ denotes the protein content of the collagen sample before collagen fibrillogenesis, and $C_s$ denotes the protein content of the supernatant after collagen fibrillogenesis.

*4.11. Scanning Electron Microscopy (SEM) Observation*

Collagen fibrils were formed as described in Section 4.10, fixed with 2.5% (*v*/*v*) glutaraldehyde in 0.1 M PB solution (pH = 7.0) for 3 h, and then rinsed with PB. After gradient dehydration using ethanol solutions, collagen fibrils were dried using a freeze-drying device and coated with gold using a coater (Oxford Quorum SC7620, Laughton, UK). The microstructures of collagen fibrils were investigated using a SEM (TESCAN MIRA LMS, Brno, Czech Republic) at 3 kV.

*4.12. Antioxidant Activity*

4.12.1. DPPH(2,2-diphenyl-1-picrylhydrazyl) Radical Scavenging Activities

The DPPH radical scavenging activity of collagens was conducted according to a previous reported method [53]. Collagen solution (2 mg/mL, $n$ = 3 for each group) was mixed with an equal volume of DPPH-ethanol solution (0.1 mmol/L), incubated for 30 min at 25 °C and centrifugated for 10 min at 1500× $g$. A UV/Vis spectrophotometer was utilized to obtain the absorbance at 517 nm of each 100 μL of supernatant. DPPH radical scavenging activity was defined as follows:

$$\text{DPPH radical scavenging percentage (\%)} = (1 - (A_s - A_o)/A) \times 100\% \quad (2)$$

where $A_s$ is the sample absorbance, $A_o$ is the sample blank absorbance and A is the control absorbance. Vitamin E was utilized as the positive control.

#### 4.12.2. Reducing Power

The reducing power of collagens was determined according to a previous reported method [54]. 1 mL of collagen solutions (2 mg/mL, $n = 3$ for each group) were combined with 2.5 mL of 0.2 M PB solution (pH = 7.4) and 2.5 mL of 1% potassium ferricyanide. After that, the sample was incubated for 20 min at 50 °C. After adding 2.5 mL of 10% trichloro AC, the sample was centrifuged at 4500 rpm for 10 min. The supernatant (1 mL) was combined with deionized water (1 mL), and 0.1% ferric chloride (0.2 mL). After reacting for 5 min, the absorbance at 700 nm was measured using a UV/Vis spectrophotometer. Vitamin E was used as a positive control.

### *4.13. Statistical Analysis*

Quantitative experiments were conducted at least 3 times. Data were expressed as the mean ± standard deviation (SD). The one-way analysis of variance (ANOVA) from GraphPad Prism software (version 7, GraphPad Software, San Diego, CA, USA) was used to compare the differences. $p < 0.05$ was considered statistically significant, i.e., * represents $p < 0.05$, ** represents $p < 0.01$.

## 5. Conclusions

In this study, we successfully extracted a thermostable collagen from the swim bladder of silver carp. SCC is a type I collagen with high purity and well-preserved triple-helix structure. Compared with GCC, BPC and MTC, SCC exhibited difference on electrophoretic patterns, peptide maps, amino acid composition and biochemical properties. SCC can self-aggregate into fine and dense fibrils under certain conditions and shows well-defined protective ability against oxidation. Notably, $T_d$ of SCC could reach up to 40.08 °C, indicating that SCC will be well applied as a promising alternative of mammalian collagen for pharmaceutical and biomedical applications in human.

**Author Contributions:** H.J.: Data curation, Formal analysis, Investigation, Methodology, Resources, Writing—original draft; Y.K.: Data curation and Formal analysis; L.S.: Data curation and Formal analysis; J.L.: Conceptualization, Funding acquisition, Project administration, Resources, Supervision, Validation, Writing—review and editing; Z.W.: Conceptualization, Funding acquisition, Project administration, Supervision, Validation, Writing—review and editing. All authors have read and agreed to the published version of the manuscript.

**Funding:** This study was financially supported by CAMS Innovation Fund for Medical Sciences (no. 2022-I2M-1-023), Natural Science Fund for Distinguished Young Scholars of Tianjin (no. 22JCJQJC00110), Natural Science Foundation of China (no. 32071356, no. 82272158), Science & Technology Projects of Tianjin of China (no. 22JCYBJC00050), Fundamental Research Funds for the Central Universities (no. 3332022069) and the Open Fund of Tianjin Enterprise Key Laboratory of Hyaluronic Acid Application Research (no. KTRDHA-Z201902) provided by the Tianjin Kangting Bioengineering Group Corp. L.T.D.

**Institutional Review Board Statement:** Not applicable.

**Data Availability Statement:** The data presented in this study are available on request from the corresponding author.

**Conflicts of Interest:** The authors declare no conflict of interest.

## References

1. Fan, L.; Ren, Y.; Emmert, S.; Vučković, I.; Stojanovic, S.; Najman, S.; Schnettler, R.; Barbeck, M.; Schenke-Layland, K.; Xiong, X. The Use of Collagen-Based Materials in Bone Tissue Engineering. *Int. J. Mol. Sci.* **2023**, *24*, 3744. [CrossRef]
2. Nurilmala, M.; Suryamarevita, H.; Husein Hizbullah, H.; Jacoeb, A.M.; Ochiai, Y. Fish skin as a biomaterial for halal collagen and gelatin. *Saudi J. Biol. Sci.* **2022**, *29*, 1100–1110. [CrossRef] [PubMed]
3. Hu, J.; Li, J.; Jiang, J.; Wang, L.; Roth, J.; Mcguinness, K.N.; Baum, J.; Dai, W.; Sun, Y.; Nanda, V.; et al. Design of synthetic collagens that assemble into supramolecular banded fibers as a functional biomaterial testbed. *Nat. Commun.* **2022**, *13*, 6761. [CrossRef]

4. Jafari, H.; Lista, A.; Siekapen, M.M.; Ghaffari-Bohlouli, P.; Nie, L.; Alimoradi, H.; Shavandi, A. Fish Collagen: Extraction, Characterization, and Applications for Biomaterials Engineering. *Polymers* **2020**, *12*, 2230. [CrossRef]
5. Rajabimashhadi, Z.; Gallo, N.; Salvatore, L.; Lionetto, F. Collagen Derived from Fish Industry Waste: Progresses and Challenges. *Polymers* **2023**, *15*, 544. [CrossRef]
6. Moroi, S.; Miura, T.; Tamura, T.; Zhang, X.; Ura, K.; Takagi, Y. Self-assembled collagen fibrils from the swim bladder of Bester sturgeon enable alignment of MC3T3-E1 cells and enhance osteogenic differentiation. *Mater. Sci. Eng. C-Mater. Biol. Appl.* **2019**, *104*, 109925. [CrossRef] [PubMed]
7. Rastian, Z.; Putz, S.; Wang, Y.; Kumar, S.; Fleissner, F.; Weidner, T.; Parekh, S.H. Type I Collagen from Jellyfish Catostylus mosaicus for Biomaterial Applications. *ACS Biomater. Sci. Eng.* **2018**, *4*, 2115–2125. [CrossRef]
8. Ahmed, R.; Haq, M.; Chun, B.S. Characterization of marine derived collagen extracted from the by-products of bigeye tuna (*Thunnus obesus*). *Int. J. Biol. Macromol.* **2019**, *135*, 668–676. [CrossRef]
9. Guan, Y.; He, J.; Chen, J.; Li, Y.; Zhang, X.; Zheng, Y.; Jia, L. Valorization of Fish Processing By-Products: Microstructural, Rheological, Functional, and Properties of Silver Carp Skin Type I Collagen. *Foods* **2022**, *11*, 2985. [CrossRef]
10. Chen, J.; Zhou, S.; Wang, Z.; Liu, S.; Li, R.; Jia, X.; Chen, J.; Liu, X.; Song, B.; Zhong, S. Anticoagulant and anti-inflammatory effects of a degraded sulfate glycosaminoglycan from swimming bladder. *Food Res. Int.* **2022**, *157*, 111444. [CrossRef] [PubMed]
11. Sheng, Y.; Wang, W.Y.; Wu, M.F.; Wang, Y.M.; Zhu, W.Y.; Chi, C.F.; Wang, B. Eighteen Novel Bioactive Peptides from Monkfish (*Lophius litulon*) Swim Bladders: Production, Identification, Antioxidant Activity, and Stability. *Mar. Drugs* **2023**, *21*, 169. [CrossRef]
12. Cai, S.Y.; Wang, Y.M.; Zhao, Y.Q.; Chi, C.F.; Wang, B. Cytoprotective Effect of Antioxidant Pentapeptides from the Protein Hydrolysate of Swim Bladders of Miiuy Croaker (*Miichthys miiuy*) against H(2)O(2)-Mediated Human Umbilical Vein Endothelial Cell (HUVEC) Injury. *Int. J. Mol. Sci.* **2019**, *20*, 5425. [CrossRef]
13. Zheng, J.; Tian, X.; Xu, B.; Yuan, F.; Gong, J.; Yang, Z. Collagen Peptides from Swim Bladders of Giant Croaker (Nibea japonica) and Their Protective Effects against H(2)O(2)-Induced Oxidative Damage toward Human Umbilical Vein Endothelial Cells. *Mar. Drugs* **2020**, *18*, 430. [CrossRef] [PubMed]
14. Zhao, Y.Q.; Zeng, L.; Yang, Z.S.; Huang, F.F.; Ding, G.F.; Wang, B. Anti-Fatigue Effect by Peptide Fraction from Protein Hydrolysate of Croceine Croaker (*Pseudosciaena crocea*) Swim Bladder through Inhibiting the Oxidative Reactions including DNA Damage. *Mar. Drugs* **2016**, *14*, 221. [CrossRef] [PubMed]
15. Gaurav, K.P.; Nidheesh, T.; Govindaraju, K.; Jyoti; Suresh, P.V. Enzymatic extraction and characterisation of a thermostable collagen from swim bladder of rohu (*Labeo rohita*). *J. Sci. Food Agric.* **2017**, *97*, 1451–1458. [CrossRef]
16. Singh, P.; Benjakul, S.; Maqsood, S.; Kishimura, H. Isolation and characterisation of collagen extracted from the skin of striped catfish (*Pangasianodon hypophthalmus*). *Food Chem.* **2011**, *124*, 97–105. [CrossRef]
17. Abdollahi, M.; Rezaei, M.; Jafarpour, A.; Undeland, I. Sequential extraction of gel-forming proteins, collagen and collagen hydrolysate from gutted silver carp (*Hypophthalmichthys molitrix*), a biorefinery approach. *Food Chem.* **2018**, *242*, 568–578. [CrossRef]
18. Zhang, J.; Duan, R.; Ye, C.; Konno, K. Isolation and characterization of collagens from scale of silver carp (*Hypophthalmichthys molitrix*). *J. Food Biochem.* **2010**, *34*, 1343–1354. [CrossRef]
19. Zhang, X.; Adachi, S.; Ura, K.; Takagi, Y. Properties of collagen extracted from Amur sturgeon Acipenser schrenckii and assessment of collagen fibrils in vitro. *Int. J. Biol. Macromol.* **2019**, *137*, 809–820. [CrossRef]
20. Pal, G.K.; Suresh, P.V. Physico-chemical characteristics and fibril-forming capacity of carp swim bladder collagens and exploration of their potential bioactive peptides by in silico approaches. *Int. J. Biol. Macromol.* **2017**, *101*, 304–313. [CrossRef]
21. Gao, L.; Orth, P.; Cucchiarini, M.; Madry, H. Effects of solid acellular type-I/III collagen biomaterials on in vitro and in vivo chondrogenesis of mesenchymal stem cells. *Expert Rev. Med. Devices* **2017**, *14*, 717–732. [CrossRef]
22. Kaewdang, O.; Benjakul, S.; Kaewmanee, T.; Kishimura, H. Characteristics of collagens from the swim bladders of yellowfin tuna (*Thunnus albacares*). *Food Chem.* **2014**, *155*, 264–270. [CrossRef] [PubMed]
23. Liu, D.; Liang, L.; Regenstein, J.M.; Zhou, P. Extraction and characterisation of pepsin-solubilised collagen from fins, scales, skins, bones and swim bladders of bighead carp (*Hypophthalmichthys nobilis*). *Food Chem.* **2012**, *133*, 1441–1448. [CrossRef]
24. Appel, W. Chymotrypsin: Molecular and catalytic properties. *Clin. Biochem.* **1986**, *19*, 317–322. [CrossRef] [PubMed]
25. Kittiphattanabawon, P.; Benjakul, S.; Visessanguan, W.; Kishimura, H.; Shahidi, F. Isolation and Characterisation of collagen from the skin of brownbanded bamboo shark (*Chiloscyllium punctatum*). *Food Chem.* **2010**, *119*, 1519–1526. [CrossRef]
26. Burjanadze, T.V. New analysis of the phylogenetic change of collagen thermostability. *Biopolymers* **2000**, *53*, 523–528. [CrossRef]
27. Rigby, B.J. Amino-acid composition and thermal stability of the skin collagen of the Antarctic ice-fish. *Nature* **1968**, *219*, 166–167. [CrossRef]
28. Pal, G.K.; Suresh, P.V. Comparative assessment of physico-chemical characteristics and fibril formation capacity of thermostable carp scales collagen. *Mater. Sci. Eng. C-Mater. Biol. Appl.* **2017**, *70*, 32–40. [CrossRef]
29. Liao, W.; Guanghua, X.; Li, Y.; Shen, X.R.; Li, C. Comparison of characteristics and fibril-forming ability of skin collagen from barramundi (*Lates calcarifer*) and tilapia (*Oreochromis niloticus*). *Int. J. Biol. Macromol.* **2018**, *107*, 549–559. [CrossRef]
30. Zhao, W.H.; Chi, C.F.; Zhao, Y.Q.; Wang, B. Preparation, Physicochemical and Antioxidant Properties of Acid- and Pepsin-Soluble Collagens from the Swim Bladders of Miiuy Croaker (*Miichthys miiuy*). *Mar. Drugs* **2018**, *16*, 161. [CrossRef]

31. Jeevithan, E.; Jingyi, Z.; Wang, N.; He, L.; Bao, B.; Wu, W. Physico-chemical, antioxidant and intestinal absorption properties of whale shark type-II collagen based on its solubility with acid and pepsin. *Process Biochem.* **2015**, *50*, 463–472. [CrossRef]
32. Doyle, B.B.; Bendit, E.G.; Blout, E.R. Infrared spectroscopy of collagen and collagen-like polypeptides. *Biopolymers* **1975**, *14*, 937–957. [CrossRef] [PubMed]
33. Riaz, T.; Zeeshan, R.; Zarif, F.; Ilyas, K.; Muhammad, N.; Safi, S.Z.; Rahim, A.; Rizvi, S.A.A.; Rehman, I.U. FTIR analysis of natural and synthetic collagen. *Appl. Spectrosc. Rev.* **2018**, *53*, 703–746. [CrossRef]
34. Gauza-Włodarczyk, M.; Kubisz, L.; Mielcarek, S.; Włodarczyk, D. Comparison of thermal properties of fish collagen and bovine collagen in the temperature range 298-670K. *Mater. Sci. Eng. C-Mater. Biol. Appl.* **2017**, *80*, 468–471. [CrossRef]
35. Murphy, B.M.; D'Antonio, J.; Manning, M.C.; Al-Azzam, W. Use of the amide II infrared band of proteins for secondary structure determination and comparability of higher order structure. *Curr. Pharm. Biotechnol.* **2014**, *15*, 880–889. [CrossRef]
36. Cai, S.; Singh, B.R. A distinct utility of the amide III infrared band for secondary structure estimation of aqueous protein solutions using partial least squares methods. *Biochemistry* **2004**, *43*, 2541–2549. [CrossRef]
37. Oliveira, V.D.M.; Assis, C.R.D.; Costa, B.D.A.M.; Neri, R.C.D.A.; Monte, F.T.D.; Freitas, H.M.S.D.; França, R.C.P.; Santos, J.F.; Bezerra, R.D.S.; Porto, A.L.F. Physical, biochemical, densitometric and spectroscopic techniques for characterization collagen from alternative sources: A review based on the sustainable valorization of aquatic by-products. *J. Mol. Struct.* **2021**, *1224*, 129023. [CrossRef]
38. Sun, L.; Hou, H.; Li, B.; Zhang, Y. Characterization of acid- and pepsin-soluble collagen extracted from the skin of Nile tilapia (*Oreochromis niloticus*). *Int. J. Biol. Macromol.* **2017**, *99*, 8–14. [CrossRef]
39. Mu, C.; Li, D.; Lin, W.; Ding, Y.; Zhang, G. Temperature induced denaturation of collagen in acidic solution. *Biopolymers* **2007**, *86*, 282–287. [CrossRef] [PubMed]
40. Yuan, C.; Kaneniwa, M.; Wang, X.; Chen, S.; Cheng, Y.; Qu, Y.; Fukuda, Y.; Konno, K. Seasonal Expression of 2 Types of Myosin with Different Thermostability in Silver Carp Muscle (*Hypophthalmichthys molitrix*). *J. Food Sci.* **2006**, *71*, C39–C43. [CrossRef]
41. Pal, G.K.; Nidheesh, T.; Suresh, P.V. Comparative study on characteristics and in vitro fibril formation ability of acid and pepsin soluble collagen from the skin of catla (*Catla catla*) and rohu (*Labeo rohita*). *Food Res. Int.* **2015**, *76*, 804–812. [CrossRef] [PubMed]
42. Zhuang, Y.; Hou, H.; Zhao, X.; Zhang, Z.; Li, B. Effects of collagen and collagen hydrolysate from jellyfish (Rhopilema esculentum) on mice skin photoaging induced by UV irradiation. *J. Food Sci.* **2009**, *74*, H183–H188. [CrossRef]
43. Greenfield, N.J. Using circular dichroism spectra to estimate protein secondary structure. *Nat. Protoc.* **2006**, *1*, 2876–2890. [CrossRef]
44. Sinthusamran, S.; Benjakul, S.; Kishimura, H. Comparative study on molecular characteristics of acid soluble collagens from skin and swim bladder of seabass (*Lates calcarifer*). *Food Chem.* **2013**, *138*, 2435–2441. [CrossRef] [PubMed]
45. Matmaroh, K.; Benjakul, S.; Prodpran, T.; Encarnacion, A.B.; Kishimura, H. Characteristics of acid soluble collagen and pepsin soluble collagen from scale of spotted golden goatfish (*Parupeneus heptacanthus*). *Food Chem.* **2011**, *129*, 1179–1186. [CrossRef]
46. Wei, B.; Zenaidee, M.A.; Lantz, C.; Williams, B.J.; Totten, S.; Ogorzalek, L.R.; Loo, J.A. Top-down mass spectrometry and assigning internal fragments for determining disulfide bond positions in proteins. *Analyst* **2022**, *148*, 26–37. [CrossRef] [PubMed]
47. Akita, M.; Nishikawa, Y.; Shigenobu, Y.; Ambe, D.; Morita, T.; Morioka, K.; Adachi, K. Correlation of proline, hydroxyproline and serine content, denaturation temperature and circular dichroism analysis of type I collagen with the physiological temperature of marine teleosts. *Food Chem.* **2020**, *329*, 126775. [CrossRef]
48. Cisneros, D.A.; Hung, C.; Franz, C.M.; Muller, D.J. Observing growth steps of collagen self-assembly by time-lapse high-resolution atomic force microscopy. *J. Struct. Biol.* **2006**, *154*, 232–245. [CrossRef]
49. Venkatesan, J.; Anil, S.; Kim, S.K.; Shim, M.S. Marine Fish Proteins and Peptides for Cosmeceuticals: A Review. *Mar. Drugs* **2017**, *15*, 143. [CrossRef]
50. Gómez-Guillén, M.C.; Giménez, B.; López-Caballero, M.E.; Montero, M.P. Functional and bioactive properties of collagen and gelatin from alternative sources: A review. *Food Hydrocoll.* **2011**, *25*, 1813–1827. [CrossRef]
51. Jeevithan, E.; Bao, B.; Bu, Y.; Zhou, Y.; Zhao, Q.; Wu, W. Type II collagen and gelatin from silvertip shark (*Carcharhinus albimarginatus*) cartilage: Isolation, purification, physicochemical and antioxidant properties. *Mar. Drugs* **2014**, *12*, 3852–3873. [CrossRef] [PubMed]
52. Liu, J.; Li, B.; Jing, H.; Wu, Y.; Kong, D.; Leng, X.; Wang, Z. Swim Bladder as a Novel Biomaterial for Cardiovascular Materials with Anti-Calcification Properties. *Adv. Healthc. Mater.* **2020**, *9*, e1901154. [CrossRef]
53. Sheng, Y.; Qiu, Y.T.; Wang, Y.M.; Chi, C.F.; Wang, B. Novel Antioxidant Collagen Peptides of Siberian Sturgeon (Acipenserbaerii) Cartilages: The Preparation, Characterization, and Cytoprotection of H(2)O(2)-Damaged Human Umbilical Vein Endothelial Cells (HUVECs). *Mar. Drugs* **2022**, *20*, 325. [CrossRef] [PubMed]
54. Wang, Y.; Li, X.; Wang, J.; He, Y.; Chi, C.; Wang, B. Antioxidant peptides from protein hydrolysate of skipjack tuna milt: Purification, identification, and cytoprotection on $H_2O_2$ damaged human umbilical vein endothelial cells. *Process Biochem.* **2022**, *113*, 258–269. [CrossRef]

marine drugs

MDPI

Article

# The Loss of Structural Integrity of 3D Chitin Scaffolds from *Aplysina aerophoba* Marine Demosponge after Treatment with LiOH

**Izabela Dziedzic [1,2,*], Alona Voronkina [3,4], Martyna Pajewska-Szmyt [2], Martyna Kotula [1,2], Anita Kubiak [1,2], Heike Meissner [5], Tomas Duminis [2] and Hermann Ehrlich [2,*]**

1 Faculty of Chemistry, Adam Mickiewicz University, Uniwersytetu Poznańskiego 8, 61-614 Poznan, Poland; martyna.kotula97@gmail.com (M.K.); anitakubiak9@gmail.com (A.K.)
2 Center for Advanced Technologies, Adam Mickiewicz University, Uniwersytetu Poznańskiego 10, 61-614 Poznan, Poland; mpszmyt@amu.edu.pl (M.P.-S.); tomas.duminis@amu.edu.pl (T.D.)
3 Department of Pharmacy, National Pirogov Memorial Medical University, Pirogov Str. 56, 21018 Vinnytsia, Ukraine; algol2808@gmail.com
4 Institute of Electronics and Sensor Materials, TU Bergakademie Freiberg, Gustav Zeuner Str. 3, 09599 Freiberg, Germany
5 Department of Prosthetic Dentistry, Faculty of Medicine, University Hospital Carl Gustav Carus of Technische Universität Dresden, Fetscherstraße 74, 01307 Dresden, Germany; heike.meissner@uniklinikum-dresden.de
* Correspondence: izadzi@amu.edu.pl (I.D.); herehr@amu.edu.pl (H.E.)

**Abstract:** Aminopolysaccharide chitin is one of the main structural biopolymers in sponges that is responsible for the mechanical stability of their unique 3D-structured microfibrous and porous skeletons. Chitin in representatives of exclusively marine Verongiida demosponges exists in the form of biocomposite-based scaffolds chemically bounded with biominerals, lipids, proteins, and bromotyrosines. Treatment with alkalis remains one of the classical approaches to isolate pure chitin from the sponge skeleton. For the first time, we carried out extraction of multilayered, tube-like chitin from skeletons of cultivated *Aplysina aerophoba* demosponge using 1% LiOH solution at 65 °C following sonication. Surprisingly, this approach leads not only to the isolation of chitinous scaffolds but also to their dissolution and the formation of amorphous-like matter. Simultaneously, isofistularin-containing extracts have been obtained. Due to the absence of any changes between the chitin standard derived from arthropods and the sponge-derived chitin treated with LiOH under the same experimental conditions, we suggest that bromotyrosines in *A. aerophoba* sponge represent the target for lithium ion activity with respect to the formation of LiBr. This compound, however, is a well-recognized solubilizing reagent of diverse biopolymers including cellulose and chitosan. We propose a possible dissolution mechanism of this very special kind of sponge chitin.

**Keywords:** chitin; marine sponges; *Aplysina aerophoba*; dissolution; bromotyrosines

**Citation:** Dziedzic, I.; Voronkina, A.; Pajewska-Szmyt, M.; Kotula, M.; Kubiak, A.; Meissner, H.; Duminis, T.; Ehrlich, H. The Loss of Structural Integrity of 3D Chitin Scaffolds from *Aplysina aerophoba* Marine Demosponge after Treatment with LiOH. *Mar. Drugs* **2023**, *21*, 334. https://doi.org/10.3390/md21060334

Academic Editor: Azizur Rahman

Received: 26 April 2023
Revised: 25 May 2023
Accepted: 28 May 2023
Published: 30 May 2023



## 1. Introduction

Chitin is one of the fundamental and most abundant structural polysaccharides in nature. In contrast to cellulose, its distribution and isomorphism belong to uni- and multicellular organisms. This polysaccharide has been identified within various skeletal structures of unicellular and multicellular organisms [1], including fungi [2], protists [3], diatoms [4], sponges [5–8], molluscs [9,10], arthropods [11–15] and fish [16]. N-acetyl-D-glucosamine units linked by β-(1-4)-glycosidic bonds [17] are the principal molecular fingerprints found in three polymorphic forms of chitin—α, β and γ—which exhibit different arrangement of the polymeric chains [18]. Chitin (and its biocomposites with diverse pigments, proteins, and lipids as well as mineral-based phases [19–21]) usually provides the stiffness and rigidification of the corresponding exoskeletal structures [5].

Traditionally, chitin is characterized as nontoxic, biocompatible, biodegradable, and physiologically inert [22]. Moreover, its fibers are nonallergenic, antibacterial, deodorizing, and moisture-controlling. On the account of these properties, chitin has found applications in the food industry, biomedicine, tissue engineering, wound-dressing material, and controlled drug release, among others [23,24]. It can also be used for the adsorption of industrial pollutants and in the paper-making process [17,22]. Another highly interesting application of chitin is shell biorefinery, where crustacean shell waste can be utilized to produce organonitrogen chemicals for the production of agrochemicals or pharmaceutical products [25–27]. Chitin can be chemically transformed to its deacetylated derivative called chitosan. In contrast to chitin, this industrially-produced biopolymer is soluble in aqueous acidic solutions, which opens up broad possibilities for its applications (see for overview [28]).

One of the new and recently investigated sources of naturally pre-structured chitin are representatives of demosponges (class in the phylum Porifera). For example, selected demosponges of the order Verongiida possess the unique skeletons in the form of three-dimensional (3D) flat or cylindrical chitin scaffolds [8], which are characterized by their mechanical stability as well as their ability to swell due to capillary effects within their microtubular structures [18]. Together with structural rigidity, this makes chitinous scaffolds remarkable candidates especially for applications in tissue engineering and biomedicine [1,24,29–33]. Chitin-based scaffolds of sponges are both chemically stable and thermostable up to 400 °C; this also makes them commonly used objects for extreme biomimetics [34,35] and the development of novel composites and biomaterials [36–40].

Structural biopolymers (i.e. cellulose, spongin, silk) are mostly insoluble. This represents one of the limiting factors for their practical applications in diverse technologies. Additionally, chitin is insoluble in most common solvents [18]. This fact makes it difficult to develop methods for processing and using this relevant polymer [17]. The problem with chitin solubilization is its high crystallization and strong inter- and intramolecular hydrogen bonds [41]. This polysaccharide can be only dissolved in solvents that destroy the hydrogen bonds (H-bonds). Furthermore, most of these solvents are toxic, mutagenic, or corrosive [42]. In the Table 1, examples of already-reported chitin solvents are represented.

In the first study on chitin solvents [43–45], the complex between chitin and LiCl that coordinated with the acetyl group was obtained. The complex was soluble in N-methyl-2-pyrrolidone and dimethylacetamide. For the dissolution of chitin chains, such carboxylic acids as formic, dichloroacetic, and trichloroacetic [43–45] have also been used previously.

**Table 1.** Overview of chitin solvents.

| Solvent | Advantages | Disadvantages | Reference |
|---|---|---|---|
| 2-chloroethanol and mineral acid | Dissolving chitin rapidly at room or mildly elevated temperature | Hydrolytic degradation occurs | [45] |
| Carboxylic acids (formic, dichloroacetic, trichloroacetic) | Dissolving chitin rapidly, usually at room or mildly elevated temperature | Chitin is degrading slowly; solutions of chitin in formic acid are unstable | [43,44,46] |
| Concentrated phosphoric acid | Dissolving chitin rapidly at room temperature | Chitin is hydrolyzed after a long time in the acid at room temperature | [47] |
| Hexafluoroacetone sesquihydrate | The solutions formed may be wet or dry spun into filaments, or cast into films or solid articles | Toxicity | [48] |
| Hexafluoro-2-propanol | No chitin degradation occurs | Toxicity | [49] |
| $CaCl_2 \cdot 2H_2O$-saturated methanol | Clear chitin solution easy to regenerate chitin into diverse forms | Chitin solubility depends on the degree of deacetylation and molecular weight | [50,51] |
| LiCl/N-methyl-2-pyrrolidone (NMP) | Non-degrading solvent | Toxicity | [43,46,52,53] |

**Table 1.** *Cont.*

| Solvent | Advantages | Disadvantages | Reference |
|---|---|---|---|
| LiCl/dimethylacetamide (DMA) | Non-degrading solvent | Not all species of chitin can be dissolved; toxicity | [43,46,52,53] |
| LiSCN | No hydrolysis | High temperatures required | [46,54] |
| LiI | No hydrolysis | High temperatures required | [54] |
| LiCl/DMF | Relatively short time (1 h) | Toxicity | [52,55] |
| NaOH/crushed ice or freezing | Chitin in alkali is stable with respect to degradation | Hydrolysis occurs | [52,56–59] |
| NaOH/urea | Little effect on the chitin structure; retaining the degree of deacetylation | Temperature not higher than −20 °C | [52,60] |
| KOH/urea | Good chitin solubility (~80%) | Deacetylation occurs (ca. 12.5%); Low temperatures required (−25 °C) | [41] |
| Deep eutectic solvents | No structural degradation | High temperatures required; depolymerization occurs | [61] |
| Ionic liquids | Dissolve chitin of all polymorphic forms; green solvents | Elevated temperatures required | [42,62] |

Solvents for dissolving chitin are often toxic or can cause hydrolysis, depolymerization, or structural degradation (see Table 1), so the challenge of developing a novel method for dissolving chitin remains important. Usually, chemical isolation of chitin scaffolds from corresponding marine sponges is based on an application of up to 10% concentrated NaOH, or $Ba(OH)_2$ (see for overview [8,63]). Any reports on the dissolution of such structures being located in these reagents during more than 12 months have been published to our best knowledge. However, we have recently started experiments by isolating chitin scaffolds from *Aplysina aerophoba* demosponge (Figure 1) cultivated under marine ranching conditions [64] using lithium hydroxide solution (LiOH).

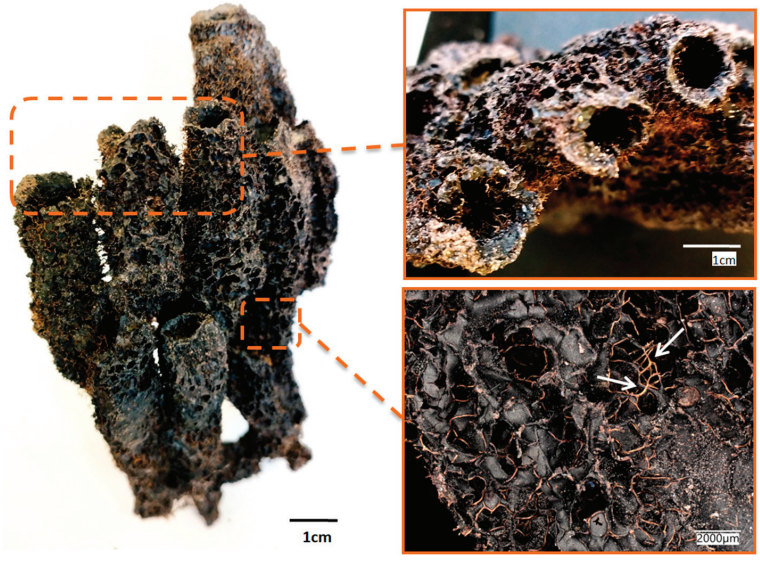


**Figure 1.** Image of the dried fragment of the *A. aerophoba* sponge with finger-like bioarchitecture. The chitin-based skeletal microfibers became visible (arrows) during the drying of the sponge body.

For this purpose, the solution of 1% LiOH was used and the process was conducted with the assistance of corresponding ultrasound treatment. Surprisingly, this simple method results in the dissolution of chitinous scaffolds and obtaining of both chitinous amorphous-like matter and bromotyrosines-containing extract. For the first time, we describe this methodology (see Figure 12) and propose a possible dissolution mechanism of this very special kind of chitin.

## 2. Results

Our primary aim was to isolate 3D chitin scaffolds from cultivated *A. aerophoba* sponge (Figure 2a) using a 1% LiOH solution similar to the classical approach reported by us previously [30,65,66]. However, during the procedure, it was observed that the amount of the obtained scaffolds was smaller than expected and the structural integrity of the scaffolds was significantly decreased (Figure 2b). The reason for this was the dissolution of chitin scaffolds in this solvent under the conditions used in the study (see Figure 12).

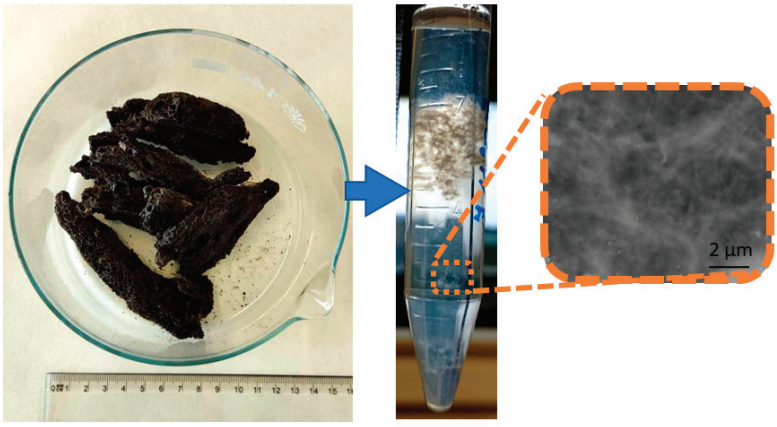


**Figure 2.** The sample of *A. aerophoba* sponge before the experiment (**a**) (see also Figure 1) and after insertion into 1% LiOH solution when disintegrated chitin scaffolds have been obtained (**b**). SEM image (**c**) shows non-regular microfibrous matter without typical microarchitecture observed with chitin scaffolds.

### *2.1. Digital Microscopy*

In a digital microscopic image (Figure 3) of the partially dissolved scaffold, the residual, pigmented chitin fibers (Figure 3b, arrows) were seen with the surrounding enigmatic structure. To examine this structure, the solution in which the scaffolds were sonicated was dialyzed and lyophilized. The product is shown in Figure 3a,c,d, and it had the structure of a thin (ca. 1 mm) film. Chitin fibers cannot be observed in these samples.

The process of the dissolution of the chitinous fibers is visualized in Figure 4 as the comparison of the digital microscopy images of the chitinous scaffolds of *A. aerophoba* demosponge obtained under similar experimental conditions after treatment with 10% NaOH (Figure 4a,c,e), with the same partially dissolved in 1% LiOH. We have observed the loss of structural integrity of the tubular structure of the scaffold during its layer-by-layer dissolution in LiOH (Figure 4b,d,f).

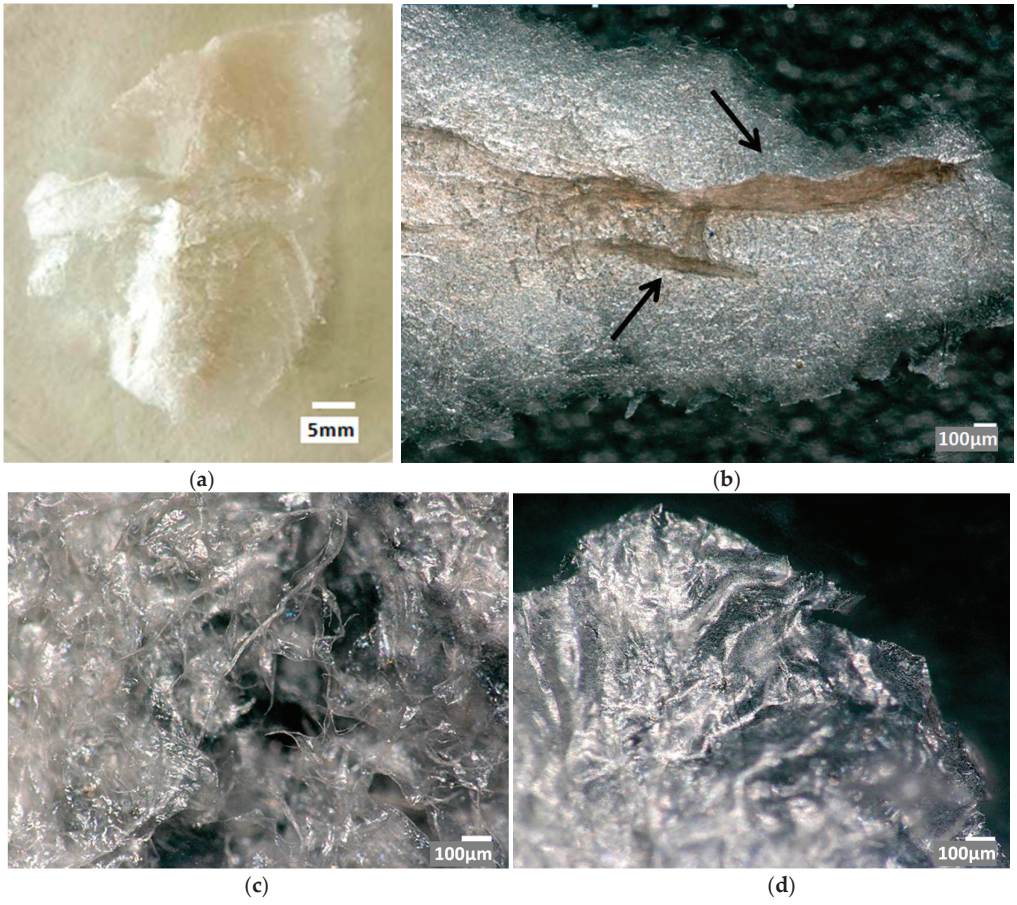


(**a**) (**b**)

(**c**) (**d**)

**Figure 3.** Dissolved and next dialyzed and lyophilized chitin of *A. aerophoba* sponge (**a**) after LiOH treatment. Digital microscopy images represent the partially dissolved chitin scaffold (**b**), where a few residual, pigmented chitinous microfibers (arrows) are still visible, and the finally-formed film (**c**,**d**).

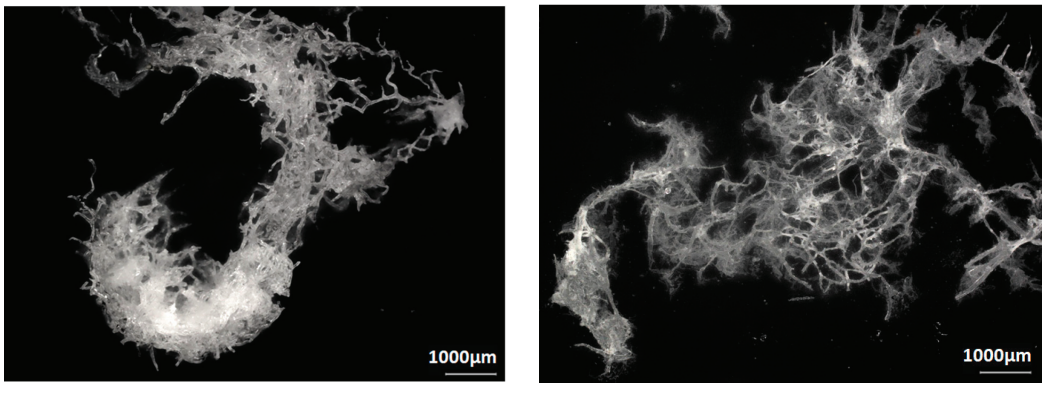


(**a**) (**b**)

**Figure 4.** *Cont*.

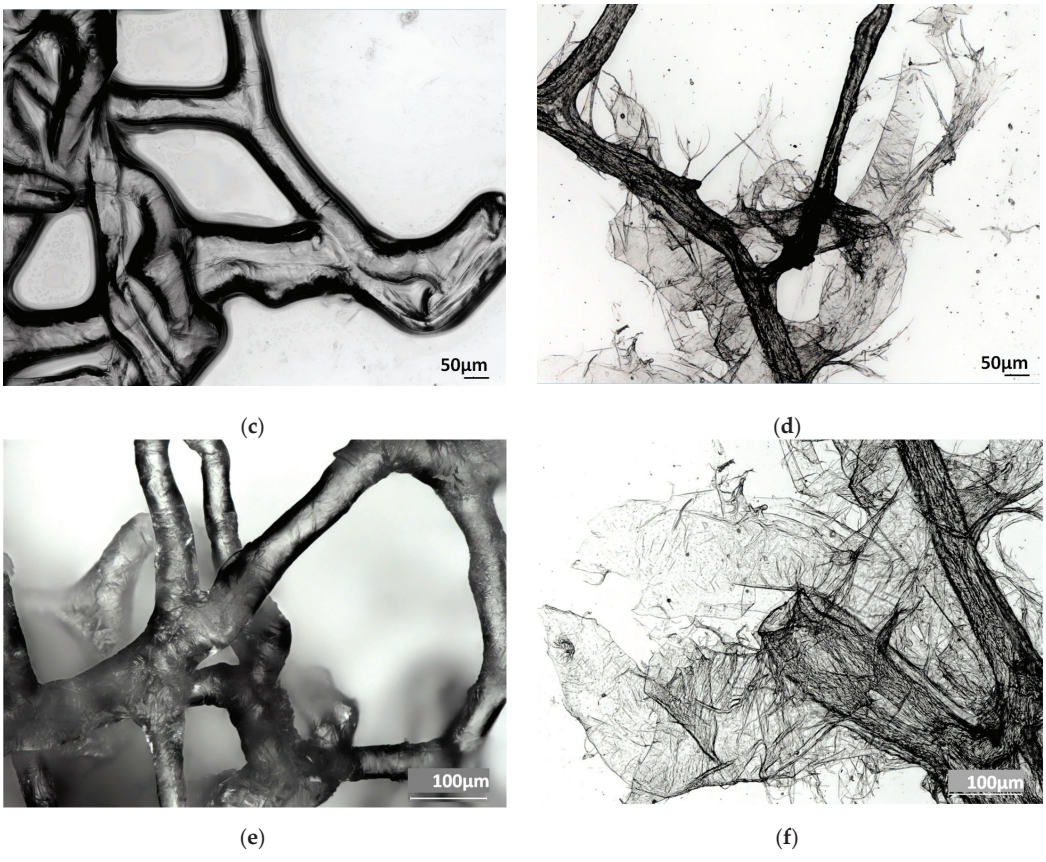


**Figure 4.** Digital microscopy imagery of isolated chitin scaffolds of *A. aerophoba* demosponge origin after 10% NaOH treatment (**a**,**c**,**e**) vs. chitin fibers partially dissolved in 1% LiOH (**b**,**d**,**f**).

### *2.2. Fourier Transformed Infrared Spectroscopy (FTIR)*

Infrared spectroscopy remains a well-recognized analytical method for the characterization of polysaccharides, including both chitin and chitosan [18]. Figure 5 shows the FTIR spectra of chitin and chitosan standards in comparison to an LiOH-treated sponge chitin sample. All characteristic bands attributed to chitin can be seen in the spectrum of the LiOH-treated samples. The spectrum of the chitosan standard and the LiOH-treated sponge samples differ significantly, so no deacetylation occurred during the process used in the study. No shift of the bands indicates the chemical stability of the polysaccharide [61]. Since there are no noticeable differences in the FTIR spectra of chitin standard and dissolved chitin. We emphasize that the dissolution of chitin in LiOH does not cause any chemical modification of the biopolymer on a molecular level.

In the spectra of dissolved chitin, the amide bands attributed to the CONH group vibrational modes appeared at 1627 $cm^{-1}$ (amide I), 1557 $cm^{-1}$ (amide II) and between 1309 and 1203 $cm^{-1}$ (amide III). The presence of the amide I doublet is related to the crystalline structure of chitin. The loss of sharpness in this region indicates the loss in crystallinity after the dissolution process. Four strong bands ascribed to the C–O–C and C–O stretching modes appeared at 1154, 1112, 1067, and 1028 $cm^{-1}$. The vibrational absorption band at 1375 $cm^{-1}$ was interpreted as the methyl group rocking. These bands were identical to or very close to the reference spectrum of α-chitin [6,18,67–69]. The assignment of the bands is presented in the Table 2.

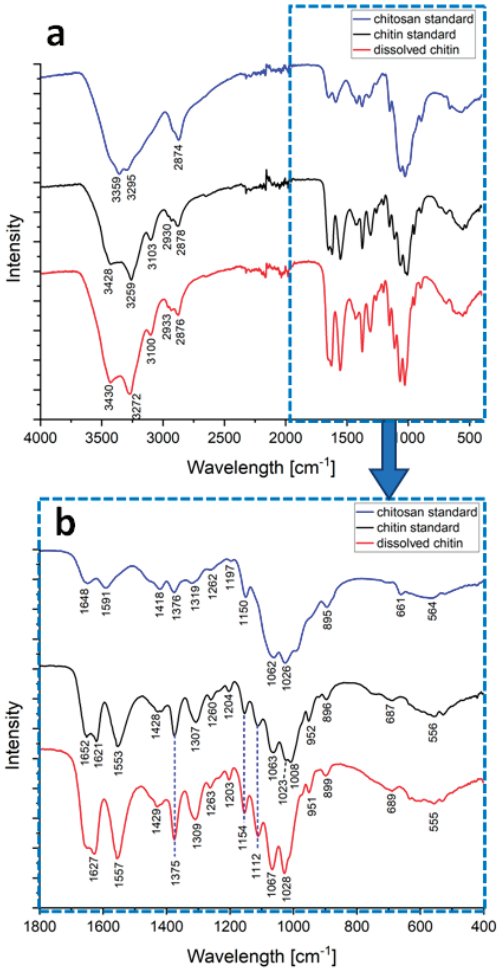


**Figure 5.** FTIR spectra of chitin and chitosan standards and in LiOH-dissolved sponge chitin in the range (**a**) 400—4000 $cm^{-1}$ and (**b**) 400—1800 $cm^{-1}$.

**Table 2.** Wavenumbers from the FTIR spectra of chitin and chitosan standards and dissolved chitin and its assignments [6,18,67–69].

| Chitosan Standard ($cm^{-1}$) | Chitin Standard ($cm^{-1}$) | Dissolved Chitin ($cm^{-1}$) | Peak Assignment |
|---|---|---|---|
| 3359 | 3428 | 3430 | O–H stretching |
| 3295 | 3259 | 3272 | N–H stretching |
| - | 3103 | 3100 | N–H stretching |
| - | 2930 | 2933 | $CH_x$ stretching |
| 2874 | 2878 | 2876 | $CH_x$ stretching |
| 1648 | 1652 | - | Amide I |
| - | 1621 | 1627 | Amide I |
| 1591 | 1553 | 1557 | Amide II |
| 1418 | 1428 | 1429 | $CH_2$ bending |
| 1376 | 1375 | 1375 | $CH_3$ deformation |
| 1320 | 1308 | 1309 | Amide III |
| 1262 | 1260 | 1263 | Amide III |
| 1197 | 1204 | 1203 | Amide III |

**Table 2.** *Cont.*

| Chitosan Standard ($cm^{-1}$) | Chitin Standard ($cm^{-1}$) | Dissolved Chitin ($cm^{-1}$) | Peak Assignment |
|---|---|---|---|
| 1150 | 1154 | 1154 | C–O–C, C–O stretching |
| - | 1112 | 1112 | C–O–C, C–O stretching |
| 1062 | 1063 | 1067 | C–O–C, C–O stretching |
| 1026 | 1023 | 1028 | C–O–C, C–O stretching |
| - | 1008 | - | C–O stretch in phase ring |
| - | 952 | 951 | $CH_3$ wagging |
| 895 | 896 | 899 | CH ring stretching |

### *2.3. X-ray Diffraction (XRD)*

The XRD patterns of chitin and chitosan standards and dissolved chitin are shown in Figure 6. The chitosan standard pattern shows two major peaks at 2θ = 11.16° and 20.26° related to the (020) and (200) crystallographic planes, respectively [18]. The XRD pattern of the chitin standard presents characteristic peaks at 9.31°, 12.69°, 19.27°, 20.55°, 23.33° and 26.31° corresponding to the reflections (020), (021), (110), (120), (130) and (013), respectively. After the dissolution process, the peaks at 20.55° and 23.33° disappeared. Dissolved chitin displays the major α-chitin diffraction peaks at 2θ = 9.03° and 19.65° corresponding to the α-type chitin crystallographic plane (020) and (110), respectively. Two minor peaks at 2θ = 12.50° and 26.81° are also visible and can be attributed to the reflections (021) and (013), respectively. These reflections are broad and localized at characteristic positions for α-chitin [18,65]. Combining the XRD results with the SEM images (Figure 6) shows the presence of nanofibers and suggests a nanocrystalline organization of the obtained sample [65]. Broadening of the XRD signals may arise from increased surface areas exposing chains of polysaccharides [65,70]. The peaks in the dissolved chitin spectrum are wider when compared to the reference standard. That may indicate a decrease in the crystallinity of chitin. The presence of a minor peak around 70° and the intensity of the peak associated with the reflection (020) in the dissolved chitin spectrum may be due to impurities. It is expected that the intra- and intermolecular hydrogen bonds are broken in the solution [61]. Since the spectra of the dissolved chitin are similar to those of the reference α-chitin standard and different from the chitosan standard spectrum, no chemical modifications occurred, which validates the FTIR analysis.

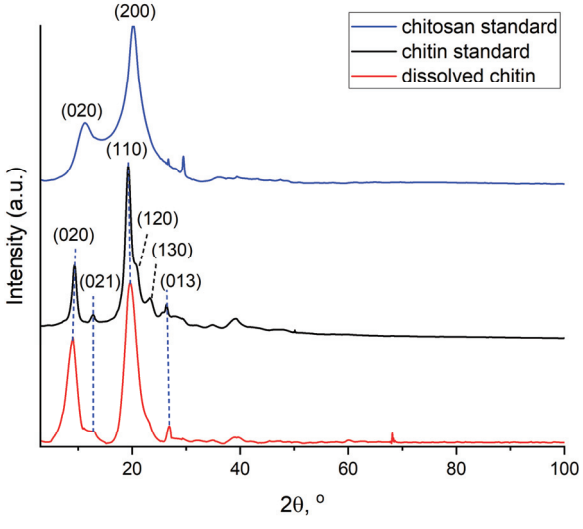


**Figure 6.** Normalized XRD spectra of chitin and chitosan standards in comparison to dissolved *A. aerophoba* sponge chitin.

*2.4. Scanning Electron Microscopy (SEM)*

Figure 7 presents SEM images of the sponge chitin fibers isolated after NaOH treatment (a, c) and those after dissolution in LiOH solution (b, d). The difference in the structural integrity is clearly visible. The surface of the NaOH-treated chitin scaffold is rough and monolithic (Figure 7a,c). The micrograph of the dissolved sponge chitin after freeze-drying presents a structure consisting of smooth layers (Figure 7b). A closer look at the apparently disintegrated smooth surface reveals the presence of chitin nanofibers (Figure 7d).

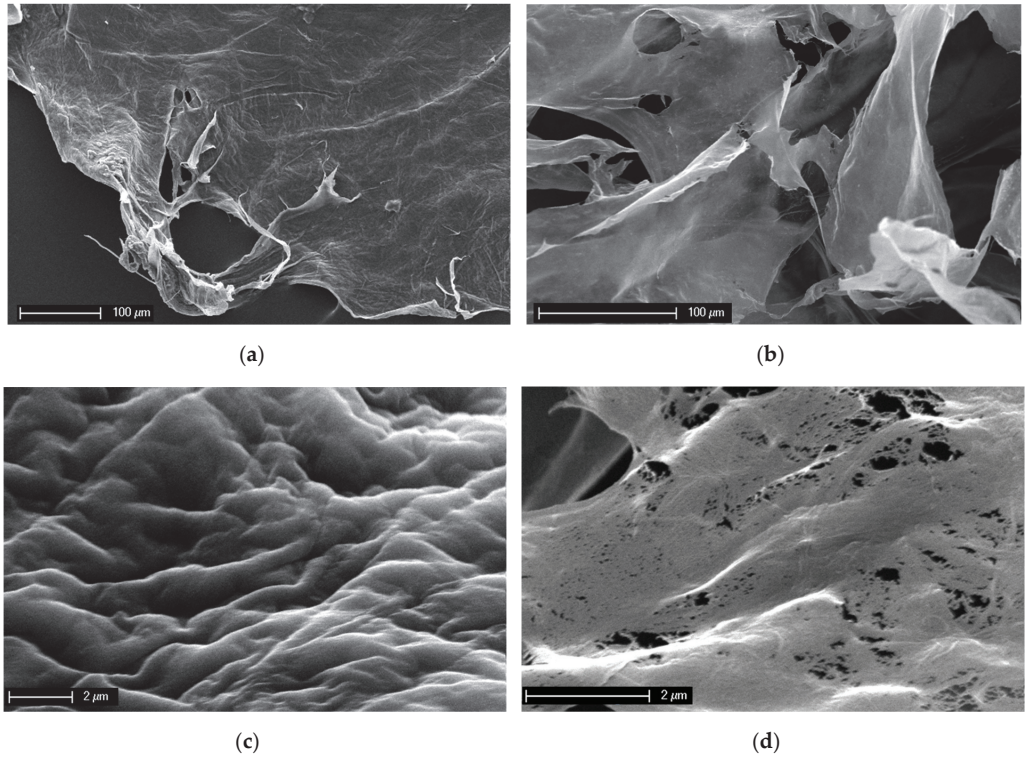


(**a**) (**b**)

(**c**) (**d**)

**Figure 7.** SEM images of the *A. aerophoba* chitin scaffold after NaOH treatment (**a**,**c**) and after dissolution in LiOH (**b**,**d**). The destruction of the structural integrity after insertion into LiOH solution on the microlevel is clearly visible.

*2.5. Control Test*

In order to conduct the control test with respect to the special activity of LiOH on selected sources of chitin, the samples of snow crab chitin and amorphous chitin standards were sonicated in the lithium hydroxide solution under the same conditions as in experiments with *A. aerophoba* sponge. After 24 days of treatment, we observed that only the chitin isolated from *A. aerophoba* sponge dissolved, while the rest of the chitin samples under the study remained stable (Figure 8). In contrast to the chitin reference standard derived from arthropods, only the chitin isolated from *A. aerophoba* sponge contained bromine in the form of bromotyrosines (for details, see [21,24,63]). The residual amount of Br detected in this partially dissolved chitin by EDX analysis ranged between 0.17 and 0.25 weight percent. Thus, we suggest that the observed phenomenon of this sponge chitin dissolution is based on a possible interaction between Li and Br ions that lead to the formation of LiBr, which is recognized as a well-known reagent for the dissolution of biopolymers, including those based on polysaccharides [71–74].

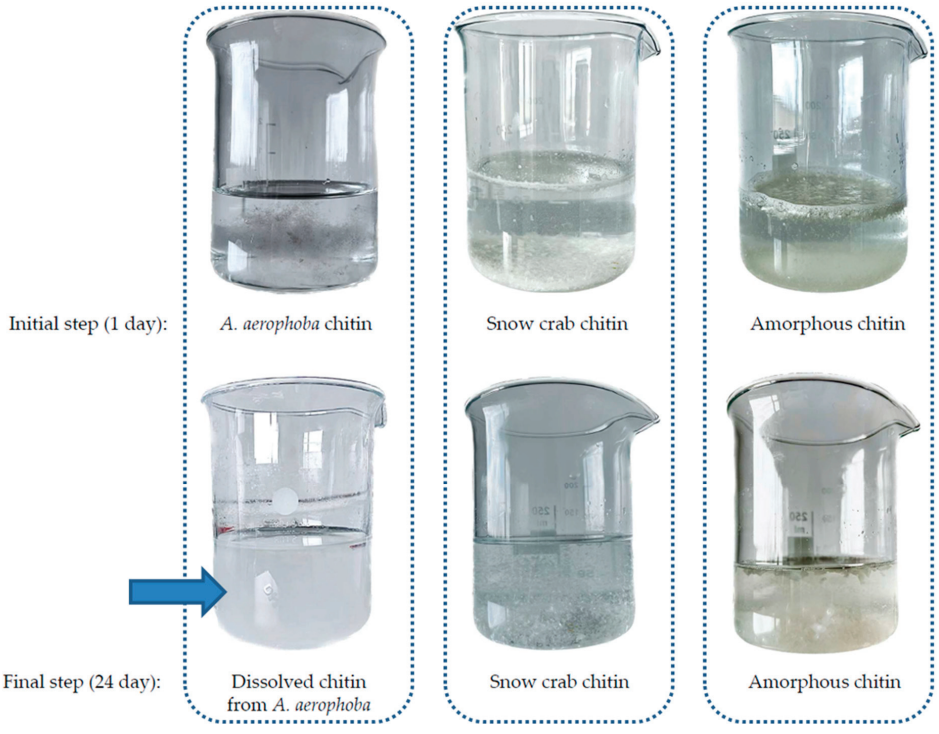


**Figure 8.** Comparison of different chitin samples before and after the LiOH-procedure. Only in the case of *A.aerophoba* sponge chitin was the milky suspension (arrow) obtained. The structural peculiarities of this phase are represented in the Figure 7d.

### *2.6. CFW Staining and Fluorescence Microscopy for Chitin Identification*

Additionally, in order to confirm the presence of chitin in the partially dissolved in 1% LiOH solution *A. aerophoba* skeletal scaffolds, Calcofluor white staining was used. This technique was already used for chitin identification in scaffolds of various species of marine sponges including *A. aerophoba* [64], *A. archeri*, *Ianthella basta* [75], *Ianthella labirintus* [76], etc. The mechanism of the method relies on the compound forming with a strong fluorescence in the blue field of the spectra, while CFW binds the β-glycoside groups of chitin. Both the partially LiOH-dissolved fibers of the sponge chitin scaffold (Figure 9b) and the dried film of the finally-obtained and lyophilized samples (Figure 9d) showed strong blue fluorescence under exceptionally low light exposure time (Figure 9a,c).

### *2.7. Bromotyrosines-Based Extracts*

Simultaneously with the isolation of chitin scaffolds, this kind of LiOH treatment leads to the formation of a dark brownish colored, bromotyrosine-containing extract (Figures 10a and 12). After dialysis and drying, it creates a black or brown crystalline-like phase (Figure 10b,c). Figure 10d,e show the FTIR spectra of the obtained *A. aerophoba* extract compared with that of the Isofistularin-3 standard, one of the most well-known bromotyrosines isolated from this verongiid sponge [64,77]. Bands in the range 2840–3500 $cm^{-1}$ are similar on both spectra and show the presence of the hydroxyl (3272 $cm^{-1}$) and $CH_x$ groups (2957, 2924, 2853 $cm^{-1}$). Above 3000 $cm^{-1}$, the band originating from C–H stretching also occurs. The bands at 1639 and 1539 $cm^{-1}$ may be the result of the presence of the amide bond. The peak at 1455 $cm^{-1}$ can be attributed to the aromatic ring stretch. The bands at 1159 and 1037 $cm^{-1}$ may be related to the C–O stretching vibrations. Aliphatic bromo compounds exhibit a band at the frequency between 600–700 $cm^{-1}$, but if several bromine

atoms are present, the interpretation is not evident. In the case of brominated aromatic compounds, the presence of the halogen cannot be detected directly [78].

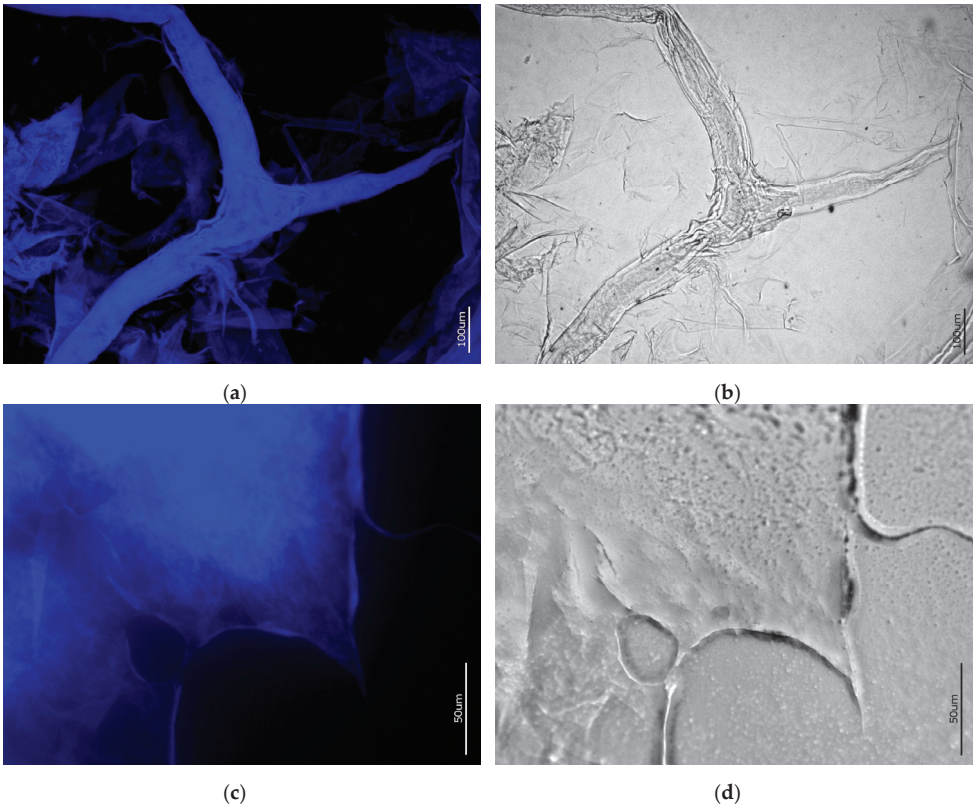


**Figure 9.** CFW-stained samples of (**a**,**b**) partially dissolved chitin fibers; (**c**,**d**) dried film of the obtained lyophylisate. Images (**a**,**c**) were obtained via the DAPI channel, images (**b**,**d**)—using bright field conditions. Light exposure time: (**a**) 1/6800 s; (**c**) 1/1100 s.

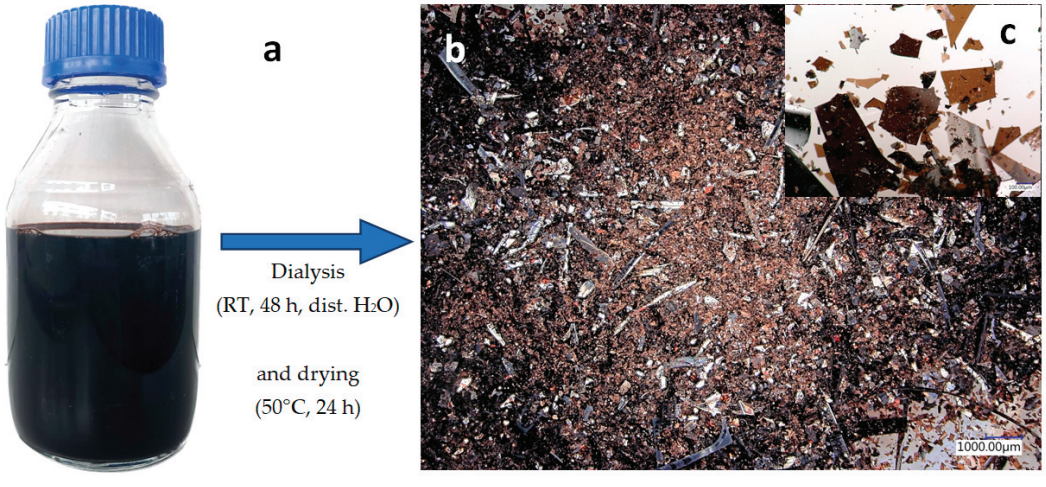


**Figure 10.** *Cont.*

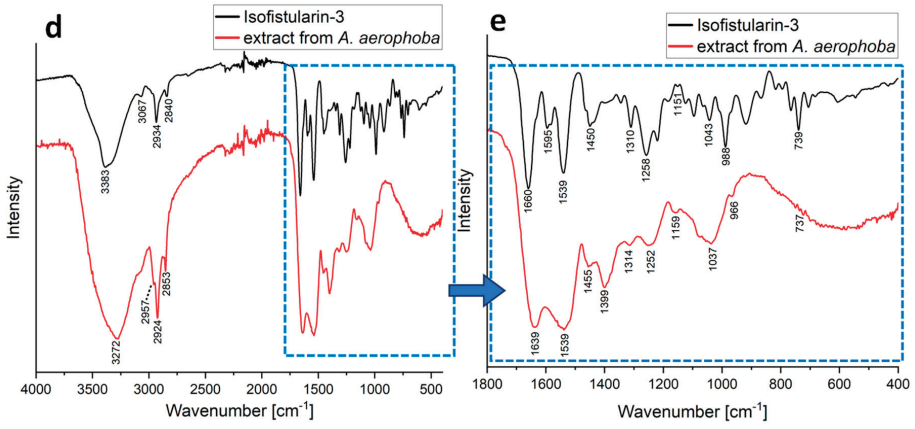


**Figure 10.** Bromotyrosine-containing extract (**a**) obtained during the chitin dissolution procedure based on LiOH treatment. (**b**) Digital microscopy image of the dialyzed and dried extract, (**c**) image in higher magnification. (**d**) Comparative FTIR spectra of the obtained dialyzed and dried extract and the Isofistularin-3 standard in the range 400–4000 $cm^{-1}$ and (**e**) in the range 400–1800 $cm^{-1}$.

Isofistularin-3 standard exhibits peaks characteristic for this compound (3383, 2934, 1660, 1595, 1539, 1450, and 1258 $cm^{-1}$), which are consistent with the literature [79–81]. The bands at 3383, 2934, 1660 and 1539 $cm^{-1}$ can be attributed to the hydroxyl groups [81].

In the fingerprint region, both the isofistularin-3 standard and the spectra for the extract preparation exhibit very similar peaks. These are the peaks at 1450, 1310, 1258, 1151, 1043, and 739 $cm^{-1}$ in the isofistularin-3 standard spectrum, which correspond well to the peaks in the spectrum of the *A. aerophoba* extract at 1455, 1314, 1252, 1159, 1037 and 737 $cm^{-1}$. The band at 1539 $cm^{-1}$ is located in the same position on both spectra.

## 3. Discussion

Despite the numerous publications regarding the features of 3D sponge chitin matrices since the first experimental data obtained in 2007 [6], many questions remain open. For example, there is still a lack of information concerning the mechanical properties of the chitinous scaffolds isolated from the sponges. However, these properties are based on structural features of multi-layered, tube-like sponge chitin, where fibrous formations are strongly interconnected within a 3D skeletal construct. Only recently, Machalowski and co-workers [82] presented the following data. The overall macro-scale compressive modulus of chitinous scaffolds isolated from *A. fistularis* marine demosponge that belongs to verongiids has been calculated as ~0.5 kPa. Nothing is known about the possible role of bromotyrosines as cross-linking agents between the chitinous skeletal nanofibers, even though these specific halogenated amino acids are recognized as identification markers for chitin derived from sponges in the Verongiida order [21,63,77]. However, 3,5-dibromotyrosines have previously been reported as cross-linking agents in the cuticle of the Atlantic horseshoe crab (*Limulus polyphemus*) [83], as well as within an operculum scleroprotein from the large whelk *Buccinum undatum* [84].

Additionally, the thermal stability of poriferan chitin [85], as well as its resistance to dissolution in alkalis such as NaOH and $Ba(OH)_2$ [8,63], remains to be investigated. Therefore, the phenomenon of dissolution of the chitin matrix from a well-studied *A. aerophoba* sponge during its treatment with low concentrated lithium hydroxide, despite its obviousness, led to the emergence of a logical question about the mechanism of the possible effect of this compound on such a specific chitin.

During the dissolution experiments in this study, it was observed that pigmented, bromotyrosine-containing microfibers of *A. aerophoba* chitin "disappeared", being transformed into amorphous-like matter (Figure 3b). Consequently, we suggest that lithium

hydroxide reacted with the bromotyrosine bromine from the *A. aerophoba* sponge, giving lithium bromide, which finally dissolved the scaffold. A schematic presentation of the process is shown in the Figure 11. The concentration of isofistularin as the main possible source of bromine in this species can reach up to 55 mg per 1 g of dried sponge [64]. It can be suggested that bromotyrosines-based cross-links may be responsible for the interconnectivity of chitinous nanolayers, which form corresponding skeletal microtubes (see Figure 4d,f). None of the already studied alkalis, except for lithium hydroxide here, led to the separation of such tubular structures and their subsequent transformation into membrane-like formations.

Therefore, lithium bromide solution can be a promising candidate for the dissolution of such special chitin as that from *A. aerophoba* demosponge. Moreover, this is confirmed by the fact that other natural polymers that have a limited number of solvents due to the occurrence of hydrogen bonds, such as silk, can be successfully dissolved in lithium bromide, giving an aqueous silk solution. This is due to the fact that LiBr is a chaotropic salt, which can break the inter- and intramolecular H-bonds and dissolve the silk fibers at high concentrations [73]. Feng et al. used lithium bromide solution to dissolve both silk fibroin and cellulose to produce porous sponges with a 3D nanofibrous structure [72]. It was reported that cellulose dissolution in lithium bromide solution causes a decrease in its crystallinity and that it can be dissolved in an aqueous LiBr solution producing cellulose nanofibrils. Upon heating the LiBr solution, the cellulose undergoes complete dissolution [71,86]. The dissolution of chitin in LiBr under diverse, selected conditions has been also reported (for details see [87,88]).

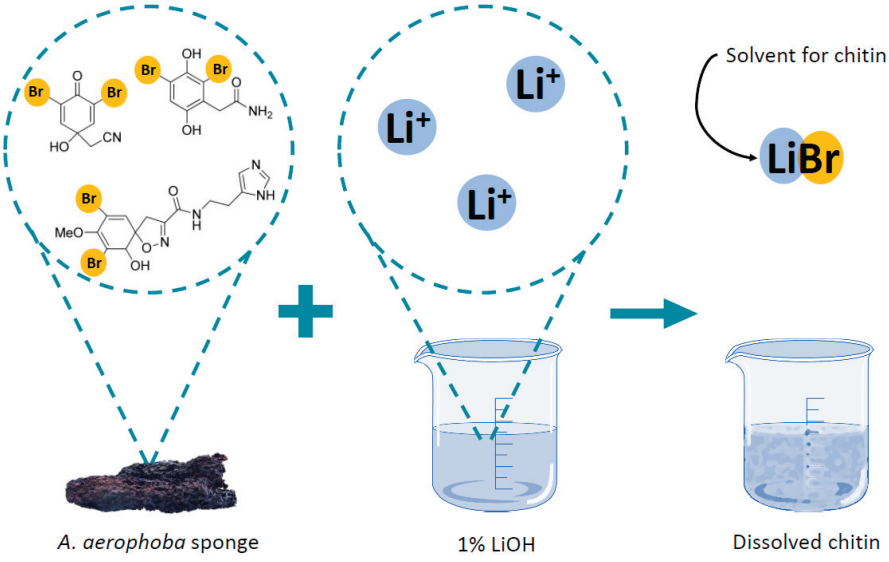


**Figure 11.** Schematic view of the dissolution mechanism of chitin in *A. aerophoba*. The molecules of selected bromotyrosines have been adapted from [89].

Chitosan can also be dissolved in the aqueous solution of lithium bromide. This process does not induce significant differences in the crystallinity [86].

Traditionally, the main advantage of poriferan chitin is based on its structural integrity on the 3D level and, consequently, the suitability of its application in cell and tissue engineering [31]. The insertion of *A. aerophoba* demosponge (as a renowned source of such ready-to-use chitin [1]) into 1% solution of LiOH at 65 °C leads to the destruction of 3D chitinous constructs; however, it also opens the door for obtaining chitinous film-like structures with nanofibrous architecture (Figure 7d). Despite the loss of the initial tube-like 3D architecture (see Figure 4c,d), sponge chitin still possesses the chemical nature of

*alpha*-chitin. No evidence concerning the possible formation of chitosan under conditions used in this study can be shown. Definitively, open questions such as the kinetics of sponge-derived chitin dissolution depending on LiOH concentrations and the temperature of the corresponding reactions will be studied in the near future. In addition, the structural features of LiOH-isolated chitin on the nano-level using TEM and HR-TEM approaches are being planned together with nanoindentation studies.

Intriguingly, the application of LiOH in our case also opens the perspective for optimization of the bromotyrosine isolation method, especially for such a biologically active antitumor drug as isofistularin-3 [77]. Today, the price of 1 g isofistularin-3 is 150,000$ [64]. Due to the cultivation of *A. aerophoba* sponges under marine ranching conditions [90], the isolation of this compound can lead to interesting changes in marine pharmacology and the marine bioeconomy of sponges as well.

## 4. Materials and Methods

### *4.1. Sample Collection*

Cultivated *A. aerophoba* sponge was collected in the Adriatic Sea (Kotor Bay, Montenegro) from the marine aquaculture facility from the depths of 3–5 m by scuba diving. Sponge samples were put in Ziploc bags underwater, brought to the laboratory, and washed with water to remove salts. Selected specimens were air-dried for 7 days prior to further treatment and stored in Ziploc plastic bags.

### *4.2. Isolation of Chitin Scaffolds*

Samples of dried *A. aerophoba* sponge were carefully cut to produce square-shaped scaffolds with sizes of about $2 \times 2 \times 2$ cm. The isolation of chitin scaffolds was accomplished using the previously reported method based on NaOH treatment [30,64]. The isolation procedure was repeated three times to obtain colorless scaffolds.

### *4.3. Dissolution of A. aerophoba Chitin in LiOH*

*A. aerophoba* sponges were purified from other marine (not sponge) material using scissors. They were put into 500 mL of distilled water and sonicated for 1 h at room temperature. The sponges were dried using paper and inserted into ca. 500 mL of 20% acetic acid, after that, the content was sonicated for 2 h at 40 °C. The acetic acid solution was changed for a fresh portion and the samples were sonicated for another 2 h. The sponges were rinsed in distilled water till pH = 6.5. After that, the sponges were put into 500 mL of 1% LiOH (Sigma Aldrich, St. Louis, MO, USA) solution and sonicated at 50–55 °C for 50 h. The obtained scaffolds were rinsed in water and put for ca. 20 h in 20% acetic acid to remove residual calcium carbonate debris. The scaffolds were put into fresh 100 mL 1% LiOH solution and sonicated for 15 h at up to 65 °C and changed into the 1% LiOH solution for a fresh portion every day (ca. 100 mL). Next, the solution was dialyzed using membrane with the molecular weight cut-off 14 kDa (Carl Roth GmbH, Karlsruhe, Germany) in distilled water for 48 h at room temperature by changing the water every 2 h and checking the pH. Finally, the solution was lyophilized with Alpha 1–2 LDplus freeze dryer (Martin Christ GmbH, Osterode am Harz, Germany) during 24 h at −35 °C. The scheme of the procedure used in the study is presented in the Figure 12.

### *4.4. Chemicals*

Lithium hydroxide monohydrate (pure p.a.) and glacial acetic acid (pure p.a.) were purchased from Chempur (Piekary Śląskie, Poland). The chitosan standard with molecular weight ~200,000 and deacetylation degree $\geq$ 90% was purchased from Pol-Aura (Poznań, Poland). Snow crab chitin was obtained from INTIB GmbH (Freiberg, Germany). Amorphous chitin was obtained from Prof. Rangzami Yajakumar (Amrita University, Bengaluru, Karnataka, India).

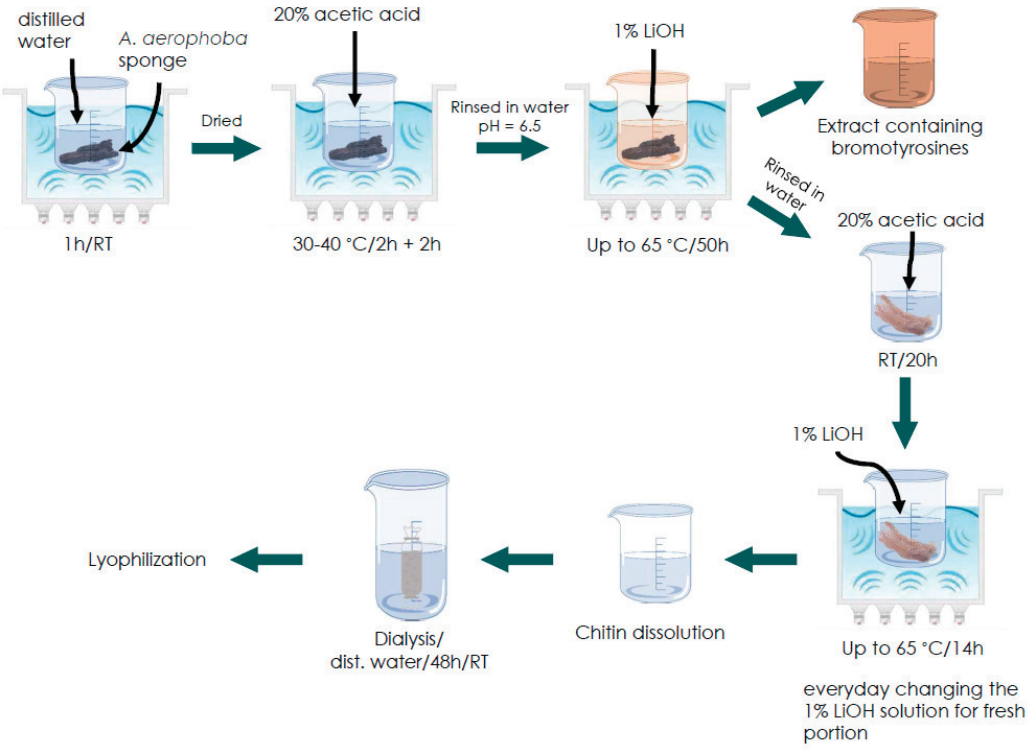


**Figure 12.** Schematic presentation of the *A. aerophoba* sponge chitin dissolution procedure in LiOH.

*4.5. FTIR Spectroscopy*

Fourier transformed infrared spectra of all the samples were recorded with the Nicolet iS50 FTIR spectrometer (Thermo Scientific, Inc., Waltham, MA, USA). Each analysis was performed using a built-in attenuated total reflectance (ATR) accessory. The measurements were carried out in the wavelength range of 4000–400 $cm^{-1}$. Postprocessing of the recorded spectra was performed with OriginLab 2023 (OriginPro, Version 2023. OriginLab Corporation, Northampton, MA, USA).

*4.6. X-ray Diffraction*

The X-ray diffraction analysis was performed with the powder diffractometer SmartLab Rigaku, Japan with a CuK alpha lamp, in the 2θ range of 3–80°, scan step 0.01, scan speed 4°/min.

*4.7. Digital Microscopy*

The organic-free samples of the pure chitin scaffolds, partially dissolved scaffolds, and the film of lyophilized dissolved chitin from *A. aerophoba* were observed with the advanced imaging systems consisting of a VHX-6000 digital microscope (Keyence, Osaka, Japan) and VH-Z20R zoom lenses (magnification up to 200×) as well as Keyence VHX-7000 digital optical microscope with zoom lenses VHX E20 (magnification up to 100×) and VHX E100 (magnification up to 500×) (Keyence, Osaka, Japan).

*4.8. Scanning Electron Microscopy (SEM) with Energy Dispersive X-ray Analysis (EDX)*

The analyses were performed using the scanning electron microscope Quanta 250 FEG (FEI Ltd., Brno, Czech Republic) correlated with an energy dispersive X-ray spectrometer EDX Team Software. Additionally, selected samples were analyzed using SEM images with

a scanning electron microscope (XL 30 ESEM, Philips, Amsterdam, The Netherlands). Prior to scanning, the samples were coated with a gold layer using the Cressington Sputtercoater 108 auto, Crawley (GB) (sputtering time 45 s).

### *4.9. Calcofluor White (CFW) Staining*

CFW staining was used for the identification of β-(1-3) and β-(1-4) linked polysaccharides, including chitin. Samples were placed into a few drops of 0.1 M KOH-glycerine-water solution (solution A) and then a few drops of 0.1% CFW solution (Fluorescent Brightener M2R, Sigma-Aldrich, St. Louis, MO, USA) were added. The samples were placed in the dark place for 24 h. Afterwards, samples were rinsed three times with distilled water and dried at room temperature.

### *4.10. Fluorescent Microscopy*

For fluorescence microscopy, the digital fluorescence microscope Keyence BZ9000 (Keyence, Osaka, Japan) was used. Fluorescence microscopy images were obtained using zoom lenses CFI Plan Apo 10×, CFI Plan Apo 40× through the DAPI channel (Ex/Em = 360/460 nm). The bright field regime was used for comparison.

**Author Contributions:** Conceptualization, H.E. and M.P.-S.; methodology, H.E., I.D., A.V. and H.M.; software, I.D., A.V. and H.M.; investigation, I.D., A.V., M.K., A.K., H.M. and T.D.; resources, H.E.; writing—original draft preparation, I.D., A.V., H.E., T.D. and M.P.-S.; writing—review and editing, H.E. and T.D.; visualization, I.D. and A.V.; supervision, H.E.; project administration, M.P.-S.; funding acquisition, H.E. All authors have read and agreed to the published version of the manuscript.

**Funding:** This research was funded by the National Science Centre within the framework of the project OPUS 19 grant of National Science Centre, Poland (2020/37/B/ST5/01909) and project MAESTRO 12 (2020/38/A/ST5/00151). A.V. was founded by VW Foundation (Funding for Refugee Scholars and Scientists from Ukraine, Personal Ref. No. 05020407B, TU Bergakademie Freiberg, Germany).

**Institutional Review Board Statement:** Not applicable.

**Data Availability Statement:** The original data presented in the study are included in the article; further inquiries can be directed to the corresponding author.

**Acknowledgments:** We would like to thank INTIB GmbH as well as BromMarin GmbH (Freiberg, Germany) for sponge specimens and technical support.

**Conflicts of Interest:** The authors declare no conflict of interest. The funders had no role in the design of the study; in the collection, analyses, or interpretation of data; in the writing of the manuscript; or in the decision to publish the results.

## References

1. Ehrlich, H. Chitin of Poriferan Origin as a Unique Biological Material. In *Blue Biotechnology*; John Wiley & Sons, Ltd.: Hoboken, NJ, USA, 2018; Volume 1, pp. 821–854. ISBN 978-3-527-80171-8.
2. Muzzarelli, R.; Boudrant, J.; Meyer, D.; Manno, N.; DeMarchis, M.; Paoletti, M. Current Views on Fungal Chitin/Chitosan, Human Chitinases, Food Preservation, Glucans, Pectins and Inulin: A Tribute to Henri Braconnot, Precursor of Thecarbohydrate Polymers Science, on the Chitin Bicentennial. *Carbohydr. Polym.* **2012**, *87*, 995–1012. [CrossRef]
3. Campos-Góngora, E.; Ebert, F.; Willhoeft, U.; Said-Fernández, S.; Tannich, E. Characterization of Chitin Synthases from Entamoeba. *Protist* **2004**, *155*, 323–330. [CrossRef]
4. Brunner, E.; Richthammer, P.; Ehrlich, H.; Paasch, S.; Simon, P.; Ueberlein, S.; van Pée, K.-H. Chitin-Based Organic Networks: An Integral Part of Cell Wall Biosilica in the Diatom Thalassiosira Pseudonana. *Angew. Chem. Int. Ed. Engl.* **2009**, *48*, 9724–9727. [CrossRef]
5. Ehrlich, H. Chitin and Collagen as Universal and Alternative Templates in Biomineralization. *Int. Geol. Rev.* **2010**, *52*, 661–699. [CrossRef]
6. Ehrlich, H.; Maldonado, M.; Spindler, K.-D.; Eckert, C.; Hanke, T.; Born, R.; Goebel, C.; Simon, P.; Heinemann, S.; Worch, H. First Evidence of Chitin as a Component of the Skeletal Fibers of Marine Sponges. Part I. Verongidae (Demospongia: Porifera). *J. Exp. Zool. B Mol. Dev. Evol.* **2007**, *308*, 347–356. [CrossRef] [PubMed]
7. Klinger, C.; Żółtowska-Aksamitowska, S.; Wysokowski, M.; Tsurkan, M.V.; Galli, R.; Petrenko, I.; Machałowski, T.; Ereskovsky, A.; Martinović, R.; Muzychka, L.; et al. Express Method for Isolation of Ready-to-Use 3D Chitin Scaffolds from Aplysina Archeri (Aplysineidae: Verongiida) Demosponge. *Mar. Drugs* **2019**, *17*, 131. [CrossRef] [PubMed]

8. Żółtowska, S.; Klinger, C.; Petrenko, I.; Wysokowski, M.; Joseph, Y.; Jesionowski, T.; Ehrlich, H. Methods of Isolating Chitin from Sponges (Porifera). In *Chitin and Chitosan: Properties and Applications*; John Wiley & Sons, Ltd.: Hoboken, NJ, USA, 2019; pp. 35–59. ISBN 978-1-119-45046-7.
9. Peters, W. Occurrence of Chitin in Mollusca. *Comp. Biochem. Physiol. Part B Comp. Biochem.* **1972**, *41*, 541–550. [CrossRef]
10. Weiss, I.M.; Schönitzer, V. The Distribution of Chitin in Larval Shells of the Bivalve Mollusk Mytilus Galloprovincialis. *J. Struct. Biol.* **2006**, *153*, 264–277. [CrossRef] [PubMed]
11. Giraud-Guille, M.-M.; Chanzy, H.; Vuong, R. Chitin Crystals in Arthropod Cuticles Revealed by Diffraction Contrast Transmission Electron Microscopy. *J. Struct. Biol.* **1990**, *103*, 232–240. [CrossRef]
12. Jabeen, F.; Younis, T.; Sidra, S.; Muneer, B.; Nasreen, Z.; Saleh, F.; Mumtaz, S.; Saeed, R.F.; Abbas, A.S. Extraction of Chitin from Edible Crab Shells of *Callinectes Sapidus* and Comparison with Market Purchased Chitin. *Braz. J. Biol.* **2021**, *83*, e246520. [CrossRef] [PubMed]
13. Percot, A.; Viton, C.; Domard, A. Optimization of Chitin Extraction from Shrimp Shells. *Biomacromolecules* **2003**, *4*, 12–18. [CrossRef] [PubMed]
14. Rødde, R.; Einbu, A.; Varum, K. A Seasonal Study of the Chemical Composition and Chitin Quality of Shrimp Shells Obtained from Northern Shrimp (Pandalus Borealis). *Carbohydr. Polym.* **2008**, *71*, 388–393. [CrossRef]
15. Xie, J.; Xie, W.; Yu, J.; Xin, R.; Shi, Z.; Song, L.; Yang, X. Extraction of Chitin From Shrimp Shell by Successive Two-Step Fermentation of Exiguobacterium Profundum and Lactobacillus Acidophilus. *Front. Microbiol.* **2021**, *12*, 677126. [CrossRef] [PubMed]
16. Wagner, G.P.; Lo, J.; Laine, R.; Almeder, M. Chitin in the Epidermal Cuticle of a Vertebrate (Paralipophrys Trigloides, Blenniidae, Teleostei). *Experientia* **1993**, *49*, 317–319. [CrossRef]
17. Rinaudo, M. Chitin and Chitosan: Properties and Applications. *Prog. Polym. Sci.* **2006**, *31*, 603–632. [CrossRef]
18. Tsurkan, M.V.; Voronkina, A.; Khrunyk, Y.; Wysokowski, M.; Petrenko, I.; Ehrlich, H. Progress in Chitin Analytics. *Carbohydr. Polym.* **2021**, *252*, 117204. [CrossRef] [PubMed]
19. Kertmen, A.; Petrenko, I.; Schimpf, C.; Rafaja, D.; Petrova, O.; Sivkov, V.; Nekipelov, S.; Fursov, A.; Stelling, A.L.; Heimler, K.; et al. Calcite Nanotuned Chitinous Skeletons of Giant Ianthella Basta Marine Demosponge. *Int. J. Mol. Sci.* **2021**, *22*, 12588. [CrossRef]
20. Machałowski, T.; Wysokowski, M.; Żółtowska-Aksamitowska, S.; Bechmann, N.; Binnewerg, B.; Schubert, M.; Guan, K.; Bornstein, S.R.; Czaczyk, K.; Pokrovsky, O.; et al. Spider Chitin. The Biomimetic Potential and Applications of Caribena Versicolor Tubular Chitin. *Carbohydr. Polym.* **2019**, *226*, 115301. [CrossRef]
21. Muzychka, L.; Voronkina, A.; Kovalchuk, V.; Smolii, O.B.; Wysokowski, M.; Petrenko, I.; Youssef, D.T.A.; Ehrlich, I.; Ehrlich, H. Marine Biomimetics: Bromotyrosines Loaded Chitinous Skeleton as Source of Antibacterial Agents. *Appl. Phys. A* **2021**, *127*, 15. [CrossRef]
22. Kertmen, A.; Ehrlich, H. Patentology of Chitinous Biomaterials. Part I: Chitin. *Carbohydr. Polym.* **2022**, *282*, 119102. [CrossRef]
23. Anitha, A.; Sowmya, S.; Kumar, P.T.S.; Deepthi, S.; Chennazhi, K.P.; Ehrlich, H.; Tsurkan, M.; Jayakumar, R. Chitin and Chitosan in Selected Biomedical Applications. *Prog. Polym. Sci.* **2014**, *39*, 1644–1667. [CrossRef]
24. Kovalchuk, V.; Voronkina, A.; Binnewerg, B.; Schubert, M.; Muzychka, L.; Wysokowski, M.; Tsurkan, M.V.; Bechmann, N.; Petrenko, I.; Fursov, A.; et al. Naturally Drug-Loaded Chitin: Isolation and Applications. *Mar. Drugs* **2019**, *17*, 574. [CrossRef] [PubMed]
25. Chen, X.; Song, S.; Li, H.; Gözaydın, G.; Yan, N. Expanding the Boundary of Biorefinery: Organonitrogen Chemicals from Biomass. *Acc. Chem. Res.* **2021**, *54*, 1711–1722. [CrossRef] [PubMed]
26. Dai, J.; Li, F.; Fu, X. Towards Shell Biorefinery: Advances in Chemical-Catalytic Conversion of Chitin Biomass to Organonitrogen Chemicals. *ChemSusChem* **2020**, *13*, 6498–6508. [CrossRef] [PubMed]
27. Ma, X.; Gözaydın, G.; Yang, H.; Ning, W.; Han, X.; Poon, N.Y.; Liang, H.; Yan, N.; Zhou, K. Upcycling Chitin-Containing Waste into Organonitrogen Chemicals via an Integrated Process. *Proc. Natl. Acad. Sci. USA* **2020**, *117*, 7719–7728. [CrossRef] [PubMed]
28. Kertmen, A.; Dziedzic, I.; Ehrlich, H. Patentology of Chitinous Biomaterials. Part II: Chitosan. *Carbohydr. Polym.* **2023**, *301*, 120224. [CrossRef]
29. Ehrlich, H. 2—Biomimetic Potential of Chitin-Based Composite Biomaterials of Poriferan Origin. In *Biomimetic Biomaterials*; Ruys, A.J., Ed.; Woodhead Publishing Series in Biomaterials; Woodhead Publishing: Amsterdam, The Netherlands, 2013; pp. 46–66. ISBN 978-0-85709-416-2.
30. Ehrlich, H.; Steck, E.; Ilan, M.; Maldonado, M.; Muricy, G.; Bavestrello, G.; Kljajic, Z.; Carballo, J.L.; Schiaparelli, S.; Ereskovsky, A.; et al. Three-Dimensional Chitin-Based Scaffolds from Verongida Sponges (Demospongiae: Porifera). Part II: Biomimetic Potential and Applications. *Int. J. Biol. Macromol.* **2010**, *47*, 141–145. [CrossRef] [PubMed]
31. Mutsenko, V.; Gryshkov, O.; Rogulska, O.; Lode, A.; Petrenko, A.Y.; Gelinsky, M.; Glasmacher, B.; Ehrlich, H. Chitinous Scaffolds from Marine Sponges for Tissue Engineering. In *Marine-Derived Biomaterials for Tissue Engineering Applications*; Choi, A.H., Ben-Nissan, B., Eds.; Springer Series in Biomaterials Science and Engineering; Springer: Singapore, 2019; pp. 285–307. ISBN 978-9-81-138855-2.
32. Mutsenko, V.V.; Bazhenov, V.V.; Rogulska, O.; Tarusin, D.N.; Schütz, K.; Brüggemeier, S.; Gossla, E.; Akkineni, A.R.; Meißner, H.; Lode, A.; et al. 3D Chitinous Scaffolds Derived from Cultivated Marine Demosponge Aplysina Aerophoba for Tissue Engineering Approaches Based on Human Mesenchymal Stromal Cells. *Int. J. Biol. Macromol.* **2017**, *104*, 1966–1974. [CrossRef]

33. Mutsenko, V.V.; Gryshkov, O.; Lauterboeck, L.; Rogulska, O.; Tarusin, D.N.; Bazhenov, V.V.; Schütz, K.; Brüggemeier, S.; Gossla, E.; Akkineni, A.R.; et al. Novel Chitin Scaffolds Derived from Marine Sponge Ianthella Basta for Tissue Engineering Approaches Based on Human Mesenchymal Stromal Cells: Biocompatibility and Cryopreservation. *Int. J. Biol. Macromol.* **2017**, *104*, 1955–1965. [CrossRef]
34. Ehrlich, H.; Wysokowski, M.; Jesionowski, T. The Philosophy of Extreme Biomimetics. *SMT* **2022**, *32*, e00447. [CrossRef]
35. Wysokowski, M.; Petrenko, I.; Galli, R.; Schimpf, C.; Rafaja, D.; Hubalkova, J.; Aneziris, C.G.; Dyshlovoy, S.; von Amsberg, G.; Meissner, H.; et al. Extreme Biomineralization: The Case of the Hypermineralized Ear Bone of Gray Whale (Eschrichtius Robustus). *Appl. Phys. A* **2020**, *126*, 1–13. [CrossRef]
36. Ehrlich, H.; Simon, P.; Motylenko, M.; Wysokowski, M.; Bazhenov, V.V.; Galli, R.; Stelling, A.L.; Stawski, D.; Ilan, M.; Stöcker, H.; et al. Extreme Biomimetics: Formation of Zirconium Dioxide Nanophase Using Chitinous Scaffolds under Hydrothermal Conditions. *J. Mater. Chem. B* **2013**, *1*, 5092–5099. [CrossRef] [PubMed]
37. Machałowski, T.; Czajka, M.; Petrenko, I.; Meissner, H.; Schimpf, C.; Rafaja, D.; Ziętek, J.; Dzięgiel, B.; Adaszek, Ł.; Voronkina, A.; et al. Functionalization of 3D Chitinous Skeletal Scaffolds of Sponge Origin Using Silver Nanoparticles and Their Antibacterial Properties. *Mar Drugs* **2020**, *18*, 304. [CrossRef]
38. Petrenko, I.; Bazhenov, V.V.; Galli, R.; Wysokowski, M.; Fromont, J.; Schupp, P.J.; Stelling, A.L.; Niederschlag, E.; Stöker, H.; Kutsova, V.Z.; et al. Chitin of Poriferan Origin and the Bioelectrometallurgy of Copper/Copper Oxide. *Int. J. Biol. Macromol.* **2017**, *104*, 1626–1632. [CrossRef] [PubMed]
39. Wysokowski, M.; Motylenko, M.; Beyer, J.; Makarova, A.; Stöcker, H.; Walter, J.; Galli, R.; Kaiser, S.; Vyalikh, D.; Bazhenov, V.V.; et al. Extreme Biomimetic Approach for Developing Novel Chitin-$GeO_2$ Nanocomposites with Photoluminescent Properties. *Nano Res.* **2015**, *8*, 2288–2301. [CrossRef]
40. Wysokowski, M.; Behm, T.; Born, R.; Bazhenov, V.V.; Meißner, H.; Richter, G.; Szwarc-Rzepka, K.; Makarova, A.; Vyalikh, D.; Schupp, P.; et al. Preparation of Chitin–Silica Composites by In Vitro Silicification of Two-Dimensional Ianthella Basta Demosponge Chitinous Scaffolds under Modified Stöber Conditions. *Mater. Sci. Eng. C* **2013**, *33*, 3935–3941. [CrossRef] [PubMed]
41. Gong, P.; Wang, J.; Liu, B.; Ru, G.; Feng, J. Dissolution of Chitin in Aqueous KOH. *Cellulose* **2016**, *23*, 1705–1711. [CrossRef]
42. Jaworska, M.M.; Kozlecki, T.; Gorak, A. Review of the Application of Ionic Liquids as Solvents for Chitin. *J. Polym. Eng.* **2012**, *32*, 67–69. [CrossRef]
43. Austin, P.R. Chitin Solvents and Solubility Parameters. In *Chitin, Chitosan, and Related Enzymes*; Zikakis, J.P., Ed.; Academic Press: Cambridge, MA, USA, 1984; pp. 227–237. ISBN 978-0−12-780950-2.
44. Austin, P.R. Solvents for and Purification of Chitin 1975. U.S. Patent US4062921A, 13 December 1977.
45. Austin, P.R. Purification of Chitin 1975. U.S. Patent 3879377, 22 April 1975.
46. Gagnaire, D.; Saint-Germain, J.; Vincendon, M. NMR Studies of Chitin and Chitin Derivatives. *Makromol. Chem.* **1982**, *183*, 593–601. [CrossRef]
47. Vincendon, M. Regenerated Chitin from Phosphoric Acid Solutions. *Carbohydr. Polym.* **1997**, *32*, 233–237. [CrossRef]
48. Capozza, R.C. Spinning and Shaping Poly-(N-Acetyl-D-Glucosamine) 1975. U.S. Patent US3988411A, 26 October 1976.
49. Rolandi, M.; Rolandi, R. Self-Assembled Chitin Nanofibers and Applications. *Adv. Colloid Interface Sci.* **2014**, *207*, 216–222. [CrossRef] [PubMed]
50. Tokura, S.; Nishimura, S.-I.; Sakairi, N.; Nishi, N. Biological Activities of Biodegradable Polysaccharide. *Macromol. Symp.* **1996**, *101*, 389–396. [CrossRef]
51. Tamura, H.; Nagahama, H.; Tokura, S. Preparation of Chitin Hydrogel Under Mild Conditions. *Cellulose* **2006**, *13*, 357–364. [CrossRef]
52. Hu, X.; Du, Y.; Tang, Y.; Wang, Q.; Feng, T.; Yang, J.; Kennedy, J.F. Solubility and Property of Chitin in NaOH/Urea Aqueous Solution. *Carbohydr. Polym.* **2007**, *70*, 451–458. [CrossRef]
53. Vincendon, M. 1H NMR Study of the Chitin Dissolution Mechanism. *Makromol. Chem.* **1985**, *186*, 1787–1795. [CrossRef]
54. Clark, G.L.; Smith, A.F. X-ray Diffraction Studies of Chitin, Chitosan, and Derivatives. *J. Phys. Chem.* **1936**, *40*, 863–879. [CrossRef]
55. Chen, X.; Ling Chew, S.; Kerton, F.M.; Yan, N. Direct Conversion of Chitin into a N-Containing Furan Derivative. *Green Chem.* **2014**, *16*, 2204–2212. [CrossRef]
56. Sannan, T.; Kurita, K.; Iwakura, Y. Studies on Chitin, 1. Solubility Change by Alkaline Treatment and Film Casting. *Makromol. Chem.* **1975**, *176*, 1191–1195. [CrossRef]
57. Sannan, T.; Kurita, K.; Iwakura, Y. Studies on Chitin, 2. Effect of Deacetylation on Solubility. *Makromol. Chem.* **1976**, *177*, 3589–3600. [CrossRef]
58. Einbu, A.; Naess, S.N.; Elgsaeter, A.; Vårum, K.M. Solution Properties of Chitin in Alkali. *Biomacromolecules* **2004**, *5*, 2048–2054. [CrossRef]
59. Feng, F.; Liu, Y.; Hu, K. Influence of Alkali-Freezing Treatment on the Solid State Structure of Chitin. *Carbohydr. Res.* **2004**, *339*, 2321–2324. [CrossRef] [PubMed]
60. Chang, C.; Chen, S.; Zhang, L. Novel Hydrogels Prepared via Direct Dissolution of Chitin at Low Temperature: Structure and Biocompatibility. *J. Mater. Chem.* **2011**, *21*, 3865–3871. [CrossRef]
61. Sharma, M.; Mukesh, C.; Mondal, D.; Prasad, K. Dissolution of α-Chitin in Deep Eutectic Solvents. *RSC Adv.* **2013**, *3*, 18149–18155. [CrossRef]

62. Shamshina, J.L. Chitin in Ionic Liquids: Historical Insights into the Polymer's Dissolution and Isolation. A Review. *Green Chem.* **2019**, *21*, 3974–3993. [CrossRef]
63. Ueberlein, S.; Machill, S.; Niemann, H.; Proksch, P.; Brunner, E. The Skeletal Amino Acid Composition of the Marine Demosponge Aplysina Cavernicola. *Mar. Drugs* **2014**, *12*, 4417–4438. [CrossRef] [PubMed]
64. Binnewerg, B.; Schubert, M.; Voronkina, A.; Muzychka, L.; Wysokowski, M.; Petrenko, I.; Djurović, M.; Kovalchuk, V.; Tsurkan, M.; Martinovic, R.; et al. Marine Biomaterials: Biomimetic and Pharmacological Potential of Cultivated Aplysina Aerophoba Marine Demosponge. *Mater. Sci. Eng. C* **2020**, *109*, 110566. [CrossRef] [PubMed]
65. Brunner, E.; Ehrlich, H.; Schupp, P.; Hedrich, R.; Hunoldt, S.; Kammer, M.; Machill, S.; Paasch, S.; Bazhenov, V.V.; Kurek, D.V.; et al. Chitin-Based Scaffolds Are an Integral Part of the Skeleton of the Marine Demosponge Ianthella Basta. *J. Struct. Biol.* **2009**, *168*, 539–547. [CrossRef]
66. Ehrlich, H.; Ilan, M.; Maldonado, M.; Muricy, G.; Bavestrello, G.; Kljajic, Z.; Carballo, J.L.; Schiaparelli, S.; Ereskovsky, A.; Schupp, P.; et al. Three-Dimensional Chitin-Based Scaffolds from Verongida Sponges (Demospongiae: Porifera). Part I. Isolation and Identification of Chitin. *Int. J. Biol. Macromol.* **2010**, *47*, 132–140. [CrossRef]
67. Dziedzic, I.; Kertmen, A. Methods of Chitosan Identification: History and Trends. *Lett. Appl. NanoBioSci.* **2023**, *12*, 94. [CrossRef]
68. Fernandes Queiroz, M.; Melo, K.R.T.; Sabry, D.A.; Sassaki, G.L.; Rocha, H.A.O. Does the Use of Chitosan Contribute to Oxalate Kidney Stone Formation? *Mar. Drugs* **2015**, *13*, 141–158. [CrossRef]
69. Lu, Y.; Sun, Q.; She, X.; Xia, Y.; Liu, Y.; Li, J.; Yang, D. Fabrication and Characterisation of α-Chitin Nanofibers and Highly Transparent Chitin Films by Pulsed Ultrasonication. *Carbohydr. Polym.* **2013**, *98*, 1497–1504. [CrossRef] [PubMed]
70. Fan, Y.; Saito, T.; Isogai, A. Preparation of Chitin Nanofibers from Squid Pen β-Chitin by Simple Mechanical Treatment under Acid Conditions. *Biomacromolecules* **2008**, *9*, 1919–1923. [CrossRef] [PubMed]
71. Cheng, G.; Wang, X.; Wu, M.; Wu, S.; Cheng, L.; Zhang, X.; Dai, F. Insignificant Difference in Biocompatibility of Regenerated Silk Fibroin Prepared with Ternary Reagent Compared with Regenerated Silk Fibroin Prepared with Lithium Bromide. *Polymers* **2022**, *14*, 3903. [CrossRef]
72. Feng, Y.; Li, X.; Zhang, Q.; Ye, D.; Li, M.; You, R.; Xu, W. Fabrication of Porous Silk Fibroin/Cellulose Nanofibril Sponges with Hierarchical Structure Using a Lithium Bromide Solvent System. *Cellulose* **2019**, *26*, 1013–1023. [CrossRef]
73. Li, C.; Wu, J.; Shi, H.; Xia, Z.; Sahoo, J.K.; Yeo, J.; Kaplan, D.L. Fiber-Based Biopolymer Processing as a Route toward Sustainability. *Adv. Mater.* **2022**, *34*, 2105196. [CrossRef] [PubMed]
74. Zhang, X.; Xiao, N.; Wang, H.; Liu, C.; Pan, X. Preparation and Characterization of Regenerated Cellulose Film from a Solution in Lithium Bromide Molten Salt Hydrate. *Polymers* **2018**, *10*, 614. [CrossRef] [PubMed]
75. Nowacki, K.; Galiński, M.; Fursov, A.; Voronkina, A.; Meissner, H.; Petrenko, I.; Stelling, A.L.; Ehrlich, H. Electrolysis as a Universal Approach for Isolation of Diverse Chitin Scaffolds from Selected Marine Demosponges. *Mar. Drugs* **2022**, *20*, 665. [CrossRef] [PubMed]
76. Schubert, M.; Binnewerg, B.; Voronkina, A.; Muzychka, L.; Wysokowski, M.; Petrenko, I.; Kovalchuk, V.; Tsurkan, M.; Martinovic, R.; Bechmann, N.; et al. Naturally Prefabricated Marine Biomaterials: Isolation and Applications of Flat Chitinous 3D Scaffolds from Ianthella Labyrinthus (Demospongiae: Verongiida). *Int. J. Mol. Sci.* **2019**, *20*, 5105. [CrossRef]
77. Bechmann, N.; Ehrlich, H.; Eisenhofer, G.; Ehrlich, A.; Meschke, S.; Ziegler, C.G.; Bornstein, S.R. Anti-Tumorigenic and Anti-Metastatic Activity of the Sponge-Derived Marine Drugs Aeroplysinin−1 and Isofistularin-3 against Pheochromocytoma In Vitro. *Mar. Drugs* **2018**, *16*, 172. [CrossRef]
78. Coates, J. Interpretation of Infrared Spectra, A Practical Approach. In *Encyclopedia of Analytical Chemistry*; John Wiley & Sons, Ltd.: Hoboken, NJ, USA, 2006; ISBN 978-0-470-02731-8.
79. Gopichand, Y.; Schmitz, F.J. Marine Natural Products: Fistularin−1, -2 and -3 from the Sponge Aplysina Fistularis Forma Fulva. *Tetrahedron Lett.* **1979**, *20*, 3921–3924. [CrossRef]
80. Cimino, G.; De Rosa, S.; De Stefano, S.; Self, R.; Sodano, G. The Bromo-Compounds of the True Sponge Verongia Aerophoba. *Tetrahedron Lett.* **1983**, *24*, 3029–3032. [CrossRef]
81. AYDOĞMUŞ, Z.; ERSOY, N.; İMRE, S. Chemical Investigation of the Sponge Verongia Aerophoba. *Turk. J. Chem.* **1999**, *23*, 339–344.
82. Machałowski, T.; Rusak, A.; Wiatrak, B.; Haczkiewicz-Leśniak, K.; Popiel, A.; Jaroszewicz, J.; Żak, A.; Podhorska-Okołów, M.; Jesionowski, T. Naturally Formed Chitinous Skeleton Isolated from the Marine Demosponge Aplysina Fistularis as a 3D Scaffold for Tissue Engineering. *Materials* **2021**, *14*, 2992. [CrossRef] [PubMed]
83. Welinder, B.S. Halogenated Tyrosines from the Cuticle of *Limulus Polyphemus* (L.). *Biochim. Biophys. Acta Gen. Subj.* **1972**, *279*, 491–497. [CrossRef] [PubMed]
84. Hunt, S.; Breuer, S.W. Chlorinated and Brominated Tyrosine Residues in Molluscan Scleroprotein. *Biochem. Soc. Trans.* **1973**, *1*, 215–216. [CrossRef]
85. Wysokowski, M.; Petrenko, I.; Stelling, A.L.; Stawski, D.; Jesionowski, T.; Ehrlich, H. Poriferan Chitin as a Versatile Template for Extreme Biomimetics. *Polymers* **2015**, *7*, 235–265. [CrossRef]
86. Kim, U.-J.; Kim, D.; You, J.; Choi, J.W.; Kimura, S.; Wada, M. Preparation of Cellulose-Chitosan Foams Using an Aqueous Lithium Bromide Solution and Their Adsorption Ability for Congo Red. *Cellulose* **2018**, *25*, 2615–2628. [CrossRef]
87. Gözaydın, G.; Song, S.; Yan, N. Chitin Hydrolysis in Acidified Molten Salt Hydrates. *Green Chem.* **2020**, *22*, 5096–5104. [CrossRef]

88. Gözaydın, G.; Sun, Q.; Oh, M.; Lee, S.; Choi, M.; Liu, Y.; Yan, N. Chitin Hydrolysis Using Zeolites in Lithium Bromide Molten Salt Hydrate. *ACS Sustain. Chem. Eng.* **2023**, *11*, 2511–2519. [CrossRef]
89. Carnovali, M.; Ciavatta, M.L.; Mollo, E.; Roussis, V.; Banfi, G.; Carbone, M.; Mariotti, M. Aerophobin−1 from the Marine Sponge Aplysina Aerophoba Modulates Osteogenesis in Zebrafish Larvae. *Mar. Drugs* **2022**, *20*, 135. [CrossRef]
90. Ehrlich, H.; Bazhenov, V.; Meschke, S.; Bürger, M.; Ehrlich, A.; Petovic, S.; Durovic, M. Marine Invertebrates of Boka Kotorska Bay Unique Sources for Bioinspired Materials Science. In *The Boka Kotorska Bay Environment*; Joksimović, A., Djurović, M., Semenov, A.V., Zonn, I.S., Kostianoy, A.G., Eds.; The Handbook of Environmental Chemistry; Springer International Publishing: Cham, Switzerland, 2016; pp. 313–334, ISBN 978-3-319-51614-1.

*marine drugs*

MDPI

*Article*

# Proteomic and Transcriptomic Analyses to Decipher the Chitinolytic Response of *Jeongeupia* spp.

**Nathanael D. Arnold, Daniel Garbe and Thomas B. Brück ***

TUM School of Natural Sciences, Department of Chemistry, Technical University of Munich, Werner-Siemens Chair for Synthetic Biotechnology (WSSB), Lichtenbergstr. 4, 85748 Garching, Germany; nathanael.arnold@tum.de (N.D.A.); daniel.garbe@tum.de (D.G.)
* Correspondence: brueck@tum.de

**Abstract:** In nature, chitin, the most abundant marine biopolymer, does not accumulate due to the action of chitinolytic organisms, whose saccharification systems provide instructional blueprints for effective chitin conversion. Therefore, discovery and deconstruction of chitinolytic machineries and associated enzyme systems are essential for the advancement of biotechnological chitin valorization. Through combined investigation of the chitin-induced secretome with differential proteomic and transcriptomic analyses, a holistic system biology approach has been applied to unravel the chitin response mechanisms in the Gram-negative *Jeongeupia wiesaeckerbachi*. Hereby, the majority of the genome-encoded chitinolytic machinery, consisting of various glycoside hydrolases and a lytic polysaccharide monooxygenase, could be detected extracellularly. Intracellular proteomics revealed a distinct translation pattern with significant upregulation of glucosamine transport, metabolism, and chemotaxis-associated proteins. While the differential transcriptomic results suggested the overall recruitment of more genes during chitin metabolism compared to that of glucose, the detected protein-mRNA correlation was low. As one of the first studies of its kind, the involvement of over 350 unique enzymes and 570 unique genes in the catabolic chitin response of a Gram-negative bacterium could be identified through a three-way systems biology approach. Based on the cumulative data, a holistic model for the chitinolytic machinery of *Jeongeupia* spp. is proposed.

**Keywords:** chitinase; transcriptomics; proteomics; omics; chitin; chitinolytic; glycosidic hydrolase family 18; lytic polysaccharide monooxygenase

**Citation:** Arnold, N.D.; Garbe, D.; Brück, T.B. Proteomic and Transcriptomic Analyses to Decipher the Chitinolytic Response of *Jeongeupia* spp. *Mar. Drugs* **2023**, *21*, 448. https://doi.org/10.3390/md21080448

Academic Editor: Azizur Rahman

Received: 25 July 2023
Revised: 12 August 2023
Accepted: 13 August 2023
Published: 15 August 2023



## 1. Introduction

Chitin, the most abundant marine polysaccharide, is composed of β-1,4-glycosidic linked *N*-acetylglucosamine, and to a lesser extent glucosamine monomers. Representing one of the major components of crustacean and insect exoskeletons, radulae of mollusks, and algal and fungal cell walls, $10^9$–$10^{11}$ t are estimated to be biosynthesized annually [1].

In addition to its biodegradability and biocompatibility, chitin and even more so the deacetylated, biologically active form, chitosan, exhibit antimicrobial, antitumoral, and anti-inflammatory properties, rendering them invaluable products for e.g., the biomedical, cosmetic, food, textile, and paper industries [2,3].

With increasing demand for seafood and the rapid growth of its respective industries, crustacean shell waste streams (originating from shrimp, crab, prawn, or lobster fisheries) have a lasting negative impact on ecosystems when disposed of in vast amounts into the ocean or landfills, as commonly practiced [4,5]. Its rigid, crystalline structure renders chitin insoluble, therefore requiring multimodal enzymatic conversion into smaller chitooligosaccharides (COS) to be metabolized by marine or soil organisms. Biological degradation of recalcitrant crustacean shell waste is delayed by calcium carbonate naturally interspersed in between the chitin scaffold, thereby decreasing the surface area for enzymes to act upon, as reflected in the low bioconversion rates of environmental microorganisms [6]. Chitin

content and enzymatically relevant physiochemical characteristics, such as the degree of acetylation or solubility, are heavily dependent on the shell waste source material [7]. Crab and lobster exoskeletons naturally contain more calcium carbonate [8,9] in contrast to shrimp [10] or prawns. Furthermore, distinct chitin allomorphs are present, including the predominant and structurally more robust α-isoform, alongside the less common β-isoform found, for instance, in squid pens [11], each requiring different compositions of enzyme cocktails to be hydrolyzed.

Chemical chitin extraction methods are commonly applied on an industrial scale, being both economical and effective [12]. However, they result in hazardous waste streams and unspecific, complex product spectra, which fashion them inapt for high-tech applications and environment-friendly mass production [13].

Therefore, biotechnological extraction methods [14] and enzymatic hydrolysis of shell waste streams are clearly favorable. However, slower conversion rates, higher production costs, and reusability still pose challenges to overcome at an industrial scale, which is why the investigation of novel chitinases is of utter importance.

Vast chitin accumulations in both soil and marine sediments are prevented by chitinolytic organisms, which have evolved sophisticated systems to compete for and exploit the recalcitrant polysaccharide as a carbon and nitrogen source [1]. They are equipped with the enzymatic tools to sense chitin, adhere to it, secrete hydrolases and import the degraded chitooligomers for catabolic assimilation [15]. The chitinolytic machinery—that is all enzymes involved in chitin metabolism—was estimated to comprise up to 100 enzymes and is yet to be understood in its entirety [16–18].

In this study, we used our previously isolated and genome-sequenced bacterium *Jeongeupia wiesaeckerbachi* [19], which is closely related to *Jeongeupia naejangsanensis* [20]. Due to the high-resolution genome data available in our group, we chose this microorganism as a model to investigate and characterize its extensive chitinolytic machinery for the first time, using a three-way systems biology approach: First, the most abundant extracellular chitin-active (interacting with chitin or COS molecules) enzymes were identified through LC-MS/MS analysis of the average secretome with colloidal chitin and crab shell chitin as inducers of the chitinolytic enzyme machinery, respectively. Results were critically evaluated by means of combined in silico signal peptide analyses through SignalP 6.0 and SecretomeP 2.0, considering classical and non-classical secretion pathways, respectively. To illuminate the catabolic adaptations in response to chitin intracellularly, comparative proteomic and transcriptomic analyses were conducted. Applying glucose and chitin minimal growth conditions, distinct mRNA and protein expression patterns were revealed through next-generation sequencing and mass spectrometry, respectively, suggesting the involvement of over 600 transcripts and 200 enzymes in the intracellular chitin response of *J. wiesaeckerbachi*. Based on these cumulative results, we propose a simplified holistic model for the chitinolytic machinery of the Gram-negative genus *Jeongeupia* that is exceedingly more complex than previously assumed. The primary gene sequences provided by our synergistic systems biology approach provide the basis for further biochemical enzyme characterizations using a recombinant enzyme production approach.

## 2. Results and Discussion

### *2.1. Extracellular Proteomics*

#### 2.1.1. Predicted Chitinolytic Machinery of *J. wiesaeckerbachi* and Subcellular Localization

When cultivated in minimal media with chitin as the exclusive carbon source, *Jeongeupia wiesaeckerbachi* secretes chitinolytic enzymes, which break down the environmental chitin and allow for its import and assimilation. Although this strategy is well described in both fungi and bacteria [21,22], a multitude of export pathways have been identified for the latter, with the Sec and Tat systems noted as major facilitators [23–25]. As previously demonstrated [19], the investigated strain's genome contains 13 glycoside hydrolases of family 18 (GH18) [26,27], which imply not only chitinases (EC 3.2.1.14) of classes III and V

but also non-catalytic, accessory proteins. Furthermore, six β-N-acetyl-hexosaminidases, three of which could be attributed to either the GH3 or GH20 family, three GH19 chitinases, and a single lytic polysaccharide monooxygenase (LPMO, AA10; formerly CBM33) are present on a genetic level. An analysis using SignalP 6.0 [28] revealed that only two out of the 13 GH18 did not exhibit an N-terminal signal sequence (gene IDs 635 and 1746), whereas another two signal peptides predictions had comparably lower confidence values of 46% (gene ID 371) and 76% (gene ID 1841), respectively (Table S1). Regarding the residual putative chitinolytic system, the LPMO, two of the three GH19 (gene IDs 1077 and 302) and merely one of the six β-N-acetyl-hexosaminidases (gene ID 1731) likewise present a leader sequence at their respective N-termini. In conclusion, only 8 out of the 23 enzymes, which form the predicted chitinolytic machinery, do not display a localization signal at all, with two additional inconclusive proteins. Further, all enzymes are predicted to be translocated by the standard secretory Sec-pathway and preprocessed by the leader peptidase I, except for one GH18 (gene ID 2137), which is predicted to be a lipopeptide with a leader peptidase II specific signal peptide instead. In silico analysis using the NetGPI 1.1 glycosylphosphatidyl-inositol anchoring prediction tool revealed no attachment of any of the chitinolytic enzymes to the bacterial cell surface [29].

#### 2.1.2. The Vast Majority of the Chitinolytic System Was Detected Extracellularly

As expected, there was a complete absence of proteins in the culture supernatant when *J. wiesaeckerbachi* was cultured on glucose as a carbon source. This was confirmed by SDS-PAGE and spectrophotometry (results not shown). Due to the absence of proteins, these glucose control samples were rejected as impracticable for the secretome analysis. By contrast, the secreted enzyme amounts were significantly increased when chitin-based substrates were added as an inducing carbon substrate in the medium. Here, protein samples were isolated, purified, and subjected to mass spectrometric-based proteomic analysis. In this instance, all detected peptides were regarded as potentially relevant. To introduce a control mechanism, which might minimize the effects of cell lysis during cultivation and sample preparation, only proteins that were verified in all samples were taken into consideration for subsequent bioinformatic evaluations.

The assessment of the extracellular proteins of three biological *Jeongeupia wieaeckerbachi* replicates in minimal media with colloidal chitin and one sample with unbleached crab shell chitin revealed that peptide fragments of 8 out of the 13 GH18 were abundant extracellularly in all samples (Table 1). If the substrates are regarded separately, a minimum of eleven GH18 were present in the (crab α-chitin derived) colloidal chitin-supplied triplicates' supernatant, while the unbleached α-chitin from decalcified crab shells only induced the secretion of eight chitinases. This observation is consistent with investigations of the *Cellvibrio japonicus* Ueda107 secretome, which recruits fewer enzymes for α-chitin vs. β-chitin conversion [30]. However, in this study, we utilized two different α-chitin derived substrates with varying degrees of crystallinity. Furthermore, half of the commonly secreted chitinases were among the top 10 most significant proteins, on average, emphasizing their importance in the metabolic response to a chitin-rich environment. Interestingly, both GH18 without a predicted signal peptide were among the commonly secreted enzymes in minimal media with chitin (gene IDs 635 and 1746), indicating a potential non-classical export mechanism [28,31].

Other chitinoplastic (chitin structure-altering) or chitin-active enzymes shared between all secretome replicates involve a putative chitobiose transport system substrate-binding protein (chiE), a FAD-binding oxidoreductase predicted as being AA7 (chitooligosaccharide oxidase (EC 1.1.3.-)) by dbCAN 3.0 [32], a glucosamine kinase, a hexosaminidase, and one lytic polysaccharide monooxygenase (Table 1, lower half). The latter is known to be a crucial, copper-dependent and oxygen-driven auxiliary enzyme for hydrolysis of recalcitrant substrates, such as cellulose and chitin [33–37].

**Table 1.** Top 10 most significant extracellular proteins on average, detected in all four samples with chitin as exclusive carbon and nitrogen source. Additionally, chitinoplastic enzymes among the commonly secreted proteins (386 in total) are provided with their respective significance rank in the lower half of the table.

| Rank | Gene ID | Significance Score −10logP (Average) | Annotation (PGAP and dbCAN 3.0) | Complementary Annotation (KO) |
|---|---|---|---|---|
| **1** | pgaptmp_000837 | 631.37 | glycosyl hydrolase family 18 protein | E3.2.1.14; chitinase [EC:3.2.1.14] |
| **2** | pgaptmp_001746 | 602.58 | glycosyl hydrolase family 18 protein | E3.2.1.14; chitinase [EC:3.2.1.14] |
| **3** | pgaptmp_002871 | 595.18 | branched-chain amino acid ABC transporter substrate-binding protein | livK; branched-chain amino acid transport system substrate-binding protein |
| **4** | pgaptmp_001064 | 582.92 | TonB-dependent receptor | xylulose-5-phosphate/fructose-6-phosphate phosphoketolase |
| **5** | pgaptmp_000389 | 582.37 | glycosyl hydrolase family 18 protein | E3.2.1.14; chitinase [EC:3.2.1.14] |
| **6** | pgaptmp_000021 | 560.63 | MBL fold metallo-hydrolase | sdsA1; linear primary-alkylsulfatase [EC:3.1.6.21] |
| **7** | pgaptmp_002723 | 550.72 | TonB-dependent siderophore receptor | TC.FEV.OM; iron complex outermembrane recepter protein |
| **8** | pgaptmp_000441 | 548.21 | sugar ABC transporter substrate-binding protein | chiE; putative chitobiose transport system substrate-binding protein |
| **9** | pgaptmp_001471 | 525.48 | porin | NA |
| **10** | pgaptmp_000366 | 523.85 | glycosyl hydrolase family 18 protein | E3.2.1.14; chitinase [EC:3.2.1.14] |
| **49** | pgaptmp_002996 | 394,47 | FAD-binding oxidoreductase (AA7) | NA |
| **56** | pgaptmp_001732 | 385.83 | glycosyl hydrolase family 18 protein | E3.2.1.14; chitinase [EC:3.2.1.14] |
| **57** | pgaptmp_000635 | 384.40 | glycosyl hydrolase family 18 protein | E3.2.1.14; chitinase [EC:3.2.1.14] |
| **58** | pgaptmp_000444 | 383.76 | ATPase | gspK; glucosamine kinase [EC:2.7.1.8] |
| **91** | pgaptmp_003083 | 326.35 | glycosyl hydrolase family 18 protein | E3.2.1.14; chitinase [EC:3.2.1.14] |
| **107** | pgaptmp_000269 | 308.55 | carbohydrate-binding domain-containing protein (GH20) | HEXA_B; hexosaminidase [EC:3.2.1.52] |
| **134** | pgaptmp_000148 | 284.47 | lytic polysaccharide monooxygenase | cpbD; chitin-binding protein |
| **198** | Pgaptmp_000371 | 238.27 | glycosyl hydrolase family 18 protein | NA |

#### 2.1.3. The Lytic Polysaccharide Monooxygenase of the Auxiliary Activity Enzyme Family 10 Seems to Play a Minor Role in α-Chitin Hydrolysis of *Jeongeupia* spp.

Surprisingly, the LPMO's significance score (or final peptide score, −10logP) provided by the MS/MS peptide identification software PEAKS [38] was rather low, with an average significance rank of 134 throughout all samples. The relatively low LPMO abundance is in concordance with a study by Mekasha et al. [34], which investigated optimal enzyme ratios for a *Serratia marcescens*-based chitin saccharification cocktail. According to the study, 15% of the auxiliary monooxygenase is optimal for shrimp or β-chitins, whereas 2% is ideal when hydrolyzing crab or α-chitins, the latter of which applies to this study's substrates. Interestingly, the significance score of the LPMO was considerably lower in the unbleached crab shell chitin sample (−10logP of 127.55), compared to those with crab chitin-derived colloidal chitin (−10logP of 245–407). These findings are consistent with the results of the aforementioned study [34], where the LPMO appeared only moderately

relevant for α-, as opposed to the generally preferred β-chitin conversion [39]. The exact opposite was reported for chitinase synergy experiments in *Streptomyces griseus*, where the *Sg*LMPO10F exhibited enhanced activity levels on the more stable and crystalline α-chitin over β-chitin [39], resulting in a 30-fold increased substrate solubility. Consequently, the substrate specificity of lytic chitin monooxygenases must be assessed for every enzyme variant. Hereby, the identity of the only surface-protruding aromatic residue in the binding cleft, either Tyrosine (for β-chitin) or Tryptophan (for α-chitin), is reported to influence substrate binding strength [40].

*Jeongeupia wiesaeckerbachi's* LPMO was more abundant in the amorphous, colloidal chitin-induced secretomes compared to the more crystalline, unbleached crab shell growth conditions. However, no assertions regarding its activity levels can be made, which will be the focus of future work in our lab. Whether the low LPMO abundance in the crab shell-induced secretome is correlated with the enzyme's low specificity and activity towards α-chitin, or if inhibitory effects of secondary compounds in the unbleached crab shells on chemotaxis and related signal cascades came into effect, remains unclear, but this might prompt relevant questions for industrial applications of unprocessed crustacean waste.

#### 2.1.4. Promising Candidate Proteins for Recombinant Expression Studies

Apart from the obviously chitinoplastic enzymes, a branched-chain amino acid ABC transporter substrate-binding protein (BCAA-ABC-SBP), two TonB-dependent (siderophore) receptors, a class B metal beta-lactamase (MBL) fold metallo-hydrolase, and a porin were present in the top 10 most significant extracellular proteins. Among these, the porin's function as an outer membrane channel is the most obvious. Knock-out experiments would have to show which (potentially chitinolytic) enzymes would not be present in the secretome anymore and thus are transported through that specific porin. According to domain analysis with InterProScan [41,42], the two as TonB-dependent receptors annotated proteins exhibit large β-barrel domains and might represent ligand gated channels or porins, thus serving as secretion facilitators. The BCAA-ABC-SBP is predicted to have high similarity to the Ile/Leu/Val-binding ABC transporter subunit. It might be upregulated and secreted due to the presence of amido-residues in the environment (media). Unspecific binding to, and import of, *N*′*N*′-diacetylchitobiose is possible [16,43], but a role in chemotaxis, pathogenicity, export, o surface motility cannot be eliminated entirely for the superfamily of ABC transporters [44–46]. The involvement of the MBL fold-metallo hydrolase in chitinoplastic activities would have to be studied with knockout or expression experiments since typical functions of this superfamily comprise totally different hydrolytic activities such as alkylsulfatase, as suggested by KEGG annotation and InterProScan results (Table 1).

#### 2.1.5. In Silico Analyses May Aid in Reduction of Cell-Lysis Derived False-Positives

A similar, abovementioned study from Tuveng et al. [30] investigated the secretome of *C. japonicus* on α- and β-chitin-rich biomass with a sophisticated method to ensure cell-free secretomes [47]. With approximately 400 secreted enzymes, depending on the substrate, the secretome was comparable in size to this study, with 386 proteins shared by all samples, although we could not methodically eliminate cell lysis. To compensate for this, we followed the example of Tuveng et al. and conducted an in-silico signal peptide analysis of the putative secretome, thus verifying or challenging their extracellular localization.

In this bioinformatic analysis, we applied the SecretomeP 2.0 and SignalP 6.0 [28,48] software packages, which revealed (Figure 1) that 38% were predicted to be translocated via the classical pathways Sec, TAT, or Pilin, and 12% were predicted to be exported by non-classical pathways, when removing all proteins with a secP score of >0.5 that were also predicted to be secreted classically. In other words, only 50% of the presented minimal chitin-secretome, shared by all samples independent of the supplied chitin form, could be confirmed to be secreted with biocomputational tools, when placing more weight on the SignalP 6.0 algorithm [28] for all five classical secretion pathways over SecretomeP 2.0 [48]. This approach can be justified by the fact that N-terminal secretory signal peptides can

be predicted more reliably due to the presence of conserved motifs, which non-classically secreted proteins lack altogether. These are predicted by SecretomeP 2.0 based on specific, pathway-independent protein features instead, including amino acid composition, secondary structure, and degree of predicted structural disorder [48]. Since this represents a more complex task, with substantially less experimentally verified data to feed the neural network, the margin for error in non-classical translocation prediction is naturally higher compared to that of N-terminal signal peptide prediction tools [49].

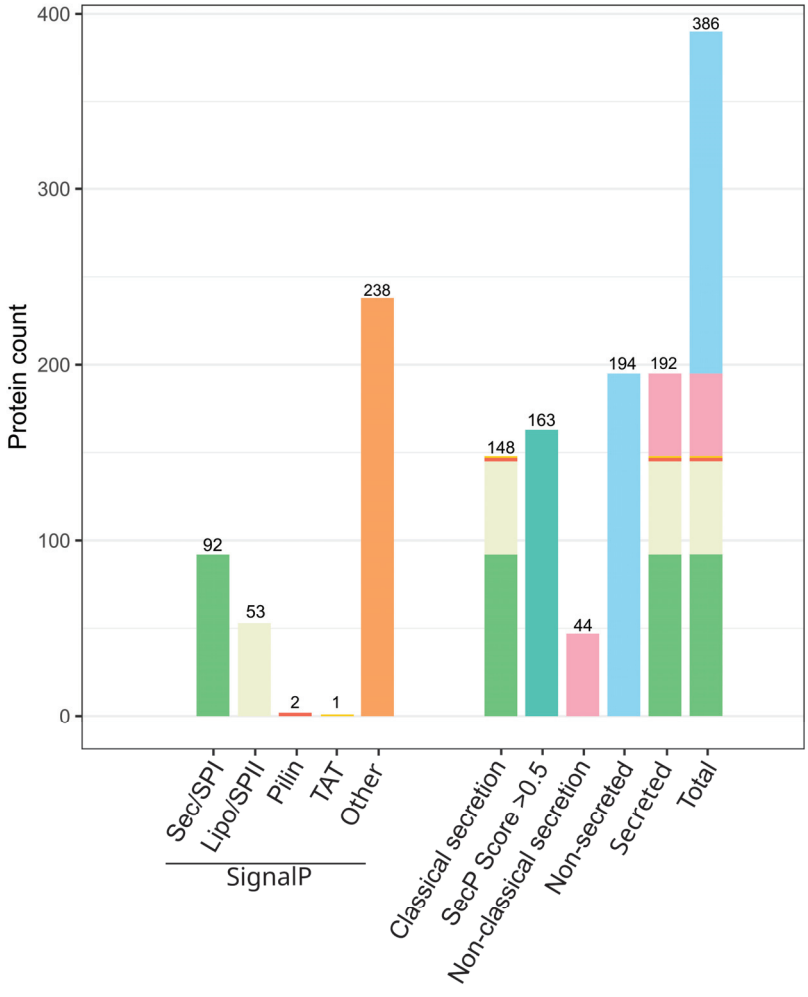


**Figure 1.** Predicted signal peptides of *Jeongeupia wiesaeckerbachi* in the chitin-induced extracellular proteome. Enzymes predicted to be translocated with the classical secretory pathways Sec, TAT, and Pilin or non-classical pathways ("Other") by SignalP 6.0 are illustrated on the left side. The sum of all classically secreted enzymes (SignalP), non-classically secreted enzymes predicted by SecretomeP 2.0 with scores of >0.5, and actual non-classically secreted enzymes through comparison of the two algorithms are on the right. Non-secreted enzymes are assembled by the total minimal chitin induced proteome count (386) subtracted by the sum of all classical (148) and non-classical (44) translocated enzymes.

However, secondary or even tertiary functions of cytosolic or periplasmatic enzymes are described in the literature as so-called moonlighting proteins, which can be accompanied by an unexpected localization inside or outside the cell [50]. For instance, the nucleosome protein histone H1, widely known for its involvement in chromatin structuring, can also function as a thyroglobulin receptor on the outer membrane surface of macrophages [51]. Factoring this phenomenon and potentially unknown secretory mechanisms into the description of the current dataset, probably an excess of 50% of the commonly detected extracellular proteins are exported. Furthermore, while additional analysis with LipoP 1.0 predicted 207/386 of the secretome to be localized in the cytosol [52], it assigned generally low confidence scores of 0.2 for all of these proteins. Of the two previously mentioned GH18 without a signal peptide, one of the two (gene ID 1746) could be confirmed as non-classically exported, hinting at yet-to-be-elucidated translocation pathways that evade our current knowledge and descriptive factors.

We then investigated whether the top 10 most significant proteins found in the secretome (Table 1) were real hits or false positives due to cell lysis events. Deploying the SignalP 6.0 [28] results for classical secretion pathways and our SignalP 6.0-corrected SecretomeP 2.0 [48] prediction results for non-classical secretion pathways (Figure 1), we concluded that all detected extracellular proteins were real hits. Especially the five non-chitin utilization-associated proteins comprising a BCAA-ABC-SBP (gene ID 2871), two TonB-dependent (siderophore) receptors (gene IDs 1064 and 2723), a class B metal beta-lactamase (MBL) fold metallo-hydrolase (gene ID 21), and a porin (gene ID 1471) had to be verified to confirm the validity of the dataset. According to SignalP 6.0 [28], four out of these five proteins are predicted to be secreted by means of the classical SEC pathway. To this end, three proteins (gene IDs 21, 1064, and 1471) were anticipated to be guided outside the bacterial cell with a signal peptide of type I, except for the BCAA-ABC-SBP, being directed by a lipoprotein signal peptide of type II. In contrast, the TonB-dependent siderophore receptor (gene ID 2723) was predicted by SecretomeP 2.0 [48] to be exported non-conventionally. Of the chitin utilization-associated proteins, including four glycosyl hydrolase family 18 proteins (gene IDs 366, 389, 837, and 1746) and the sugar ABC transporter substrate-binding protein (gene ID 441), all proteins were predicted to be exported classically with a signal peptide of type I, except for the non-classically exported GH18 (gene ID 1746), as mentioned above.

#### 2.1.6. Highly Abundant Chitinases Exhibit Two Carbohydrate-Binding Modules

Lorentzen et al. discovered a Gram-negative bacterium in an abandoned ant hill with an unprecedentedly rich chitinase arsenal [53]. During investigation of its secretome, they observed that an increased fraction (93%) of upregulated chitinases contained two carbohydrate-binding modules of the Pfam family 5/12 (CBM5/12). Interestingly, this aligns well with our results, where 3 out of the 4 top 10 most abundant GH18 in the minimal secretome also exhibited one CBM5 and one CBM12, each. For the remaining chitinases or enzymes of hitherto unknown functions, no correlation between the amount of CBM5/12 and abundance could be determined.

### *2.2. Differential Intracellular Protein Expression Using Chitin and Glucose Media*

#### 2.2.1. The Intracellular Chitin Response Specializes in Glucosamine Utilization and Cell Maintenance over Hydrolysis

Investigation of the intracellular proteome of *Jeongeupia wiesaeckerbachi* unraveled distinct expression patterns when either chitin or glucose was used as respective carbon sources (Figure 2). A total of 203 putative proteins, depicted in the heatmap or volcano plot, were upregulated at least two-fold with a significance value of 20% and above, corresponding to a $p$-value of $<0.05$, with chitin.

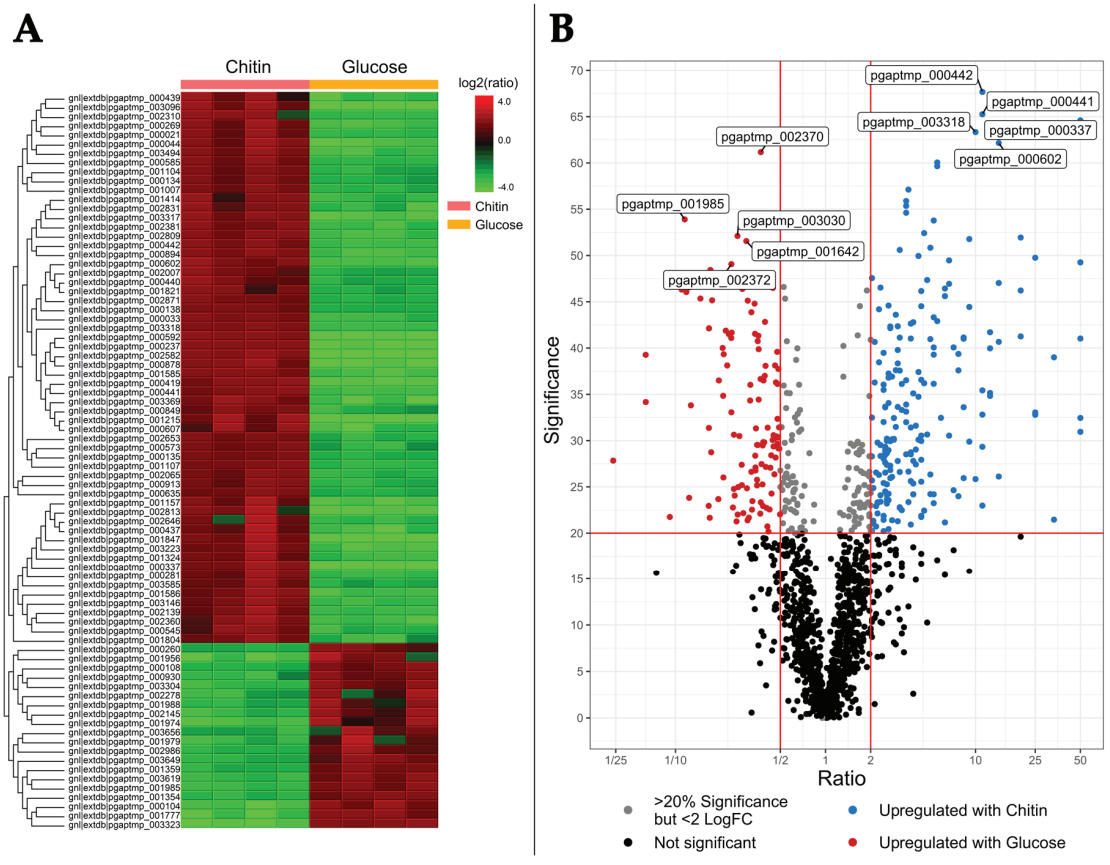


**Figure 2.** Heatmap (**A**) and volcano plot (**B**) of the differential intracellular proteomic analysis of *Jeongeupia wiesaeckerbachi* with chitin and glucose minimal media. (**A**) The heatmap was generated with PEAKS studios with the following parameters: Fold Change >2, Significance >20, Significance method ANOVA. Upregulated proteins are depicted in red and downregulated proteins in green. (**B**) Volcano plot of the same dataset. Dots in red represent proteins with a fold change >2 and a significance of >20% under glucose media; blue dots represent proteins, which are upregulated under chitin media conditions applying the same statistic thresholds. The top 5 most significant proteins are labelled with their respective gene ID. Refer to Table 2 for detailed information on gene functions.

Strikingly, the five topmost significantly expressed proteins could be linked to chitobiose import, chemotaxis, nitrogen metabolism, and a PrkA family protein serine kinase, the latter of which has been reported to be involved in carbon catabolite repression through mediation of the concomitant signal transduction as well as general stress response [54,55] (Table 2, top).

Closer inspection of the five topmost upregulated proteins in a colloidal chitin-rich environment uncovered a short chain hydrogenase/oxidoreductase [56], an inclusion body family protein, indicating high expression stress, which in turn results in misfolded enzymes [57,58]. Moreover, a substrate-binding protein was detected, which might be related to signal transduction or chemotaxis [59]. Additionally, two proteins of unknown function (Table 2, middle section) could be assigned; these represent promising targets for expression and characterization studies.

**Table 2.** Top 5 most significantly and top 5 most variably expressed proteins in the intracellular differential proteomics analysis of *Jeongeupia wiesaeckerbachi* with chitin as sole carbon and nitrogen source. Additionally, glucosamine metabolism-related proteins, which were upregulated in chitin medium are listed. Refer to Heatmap and volcano plot for a more holistic view of the data (Figure 2).

| Gene ID | Significance | Log2 Fold Change | Annotation (PGAP and dbCAN3.0) | Complementary Annotation (KO) |
|---|---|---|---|---|
| pgaptmp_000442 | 67.67 | 11.11 | sugar ABC transporter substrate-binding protein | chiE; putative chitobiose transport system substrate-binding protein |
| pgaptmp_000441 | 65.26 | 11.11 | sugar ABC transporter substrate-binding protein | chiE; putative chitobiose transport system substrate-binding protein |
| pgaptmp_000337 | 64.6 | 50 | nitrate reductase subunit beta | Identical |
| pgaptmp_003318 | 63.33 | 10 | PrkA family serine protein kinase | identical |
| pgaptmp_000602 | 62.16 | 14.29 | methyl-accepting chemotaxis protein | identical |
| pgaptmp_001215 | 49.26 | 50 | SDR family oxidoreductase | NA |
| pgaptmp_002582 | 41.03 | 50 | inclusion body family protein | aidA; nematocidal protein AidA |
| pgaptmp_001847 | 32.45 | 50 | substrate-binding domain-containing protein | rbsB; ribose transport system substrate-binding protein |
| ggaptmp_000878 | 30.95 | 50 | hypothetical protein | NA |
| pgaptmp_000237 | 39 | 33.33 | hypothetical protein | NA |
| pgaptmp_000269 | 47.03 | 14.29 | carbohydate-binding domain-containing protein (GH20) | HEXA_B; hexosaminidase [EC:3.2.1.52] |
| pgaptmp_000439 | 29.33 | 11.11 | carbohydrate ABC transporter permease | chiG; putative chitobiose transport system permease protein |
| pgaptmp_000437 | 25.84 | 10 | polysaccharide deacetylase family protein | pgdA; peptidoglycan-*N*-acetylglucosamine deacetylase [EC:3.5.1.104] |
| pgaptmp_000281 | 41.14 | 8.33 | polysaccharide deacetylase family protein | NA |
| pgaptmp_001323 | 29.95 | 8.33 | beta-*N*-acetylhexosaminidase (GH3) | nagZ; beta-*N*-acetylhexosaminidase [EC:3.2.1.52] |
| pgaptmp_000635 | 60.05 | 5.56 | glycoside hydrolase family 18 protein | chitinase [EC:3.2.1.14] |
| pgaptmp_002871 | 59.65 | 5.56 | branched-chain amino acid ABC transporter substrate-binding protein | identical |
| pgaptmp_000440 | 39.29 | 5.26 | Sugar ABC transporter permease | chiF; putative chitobiose transport system permease protein |
| pgaptmp_003368 | 4.62 | 1.30 | *N*-acetylglucosamine-specific PTS transporter subunit IIBC | nagE; *N*-acetylglucosamine PTS system EIICBA or EIICB component [EC:2.7.1.193] |

Further, glucosamine metabolism-related enzymes, which were upregulated intracellularly by *Jeongeupia wiesaeckerbachi* under chitin induction, included four transport proteins, two hexosaminidases, two polysaccharide deacetylases, and a single chitinase belonging to GH18 (Protein accession number 635), which was also detected extracellularly despite its lack of a signal peptide, indicating a potential moonlighting function or an unconventional translocation pathway [50].

### 2.2.2. Comparison of Intra- and Extracellular Chitin-Induced Proteomics

The datasets of the significantly and at least two-fold upregulated intracellular proteins and all extracellular proteins in the chitin-rich environment were functionally annotated and classified according to GO-terms with BlastKOALA [60] and subsequently compared (Figure 3). Thereby, approximately 71% of the proteins could be annotated and assigned to the appropriate functional category, while 29% enzymes are of an as-yet unknown function.

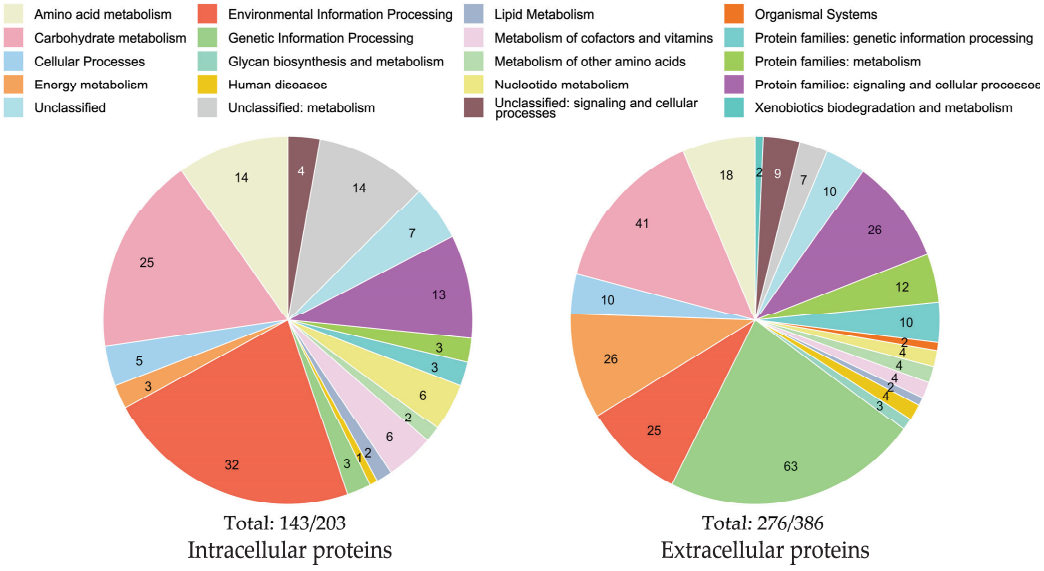


**Figure 3.** Functional classification of intra- and extracellular proteins of *Jeongeupia wiesaeckerbachi* under chitin conditions according to GO-terms. Both datasets were gathered in quadruplicates. Intracellular proteomics data were evaluated differentially to glucose-supplied cells, with significance values >20% and >2 log2 fold changes; refer to the heatmap (Figure 2). Extracellular proteins depicted were shared amongst all samples. Category counts are shown in each individual pie chart. Totals under the pie charts refer to the annotated fractions of the total protein entries submitted to BlastKOALA, with 203 intracellularly and 386 extracellularly, corresponding to approximately 70% annotated proteins each.

The extracellular proteome exhibited a larger fraction of genetic information processing and energy metabolism proteins, whereas the intracellular proteome possessed a higher fraction of environmental information processing proteins.

It is important to note that although the total number of extracellular proteins is higher than that of intracellular proteins in Figure 3, this can be ascribed to the differences in statistical methodology. The intracellular colloidal chitin-induced proteomics data were evaluated differentially to glucose negative controls, with strict statistical thresholds of >2 log fold changes and >20% significance values, whereas all detected extracellular proteins shared among every sample were considered. Expectedly, when inspecting total MS/MS protein detection counts, the number of common intracellular proteins far exceeded that of extracellular proteins with 1475 opposed to 386.

### 2.2.3. Challenges and Benefits of Biocomputational Approaches

Data evaluation and statistical methodology heavily influence the results of system biology experiments. If the dataset were evaluated with a laxer threshold, considering every intracellular protein to be upregulated 1.2-fold (or 20%) instead of 2-fold (or 100%) for example, a total of 257 proteins instead of 203 could be considered. Subsequently, this

would translate to approximately 21% more proteins to be considered as either influenced by or directly involved in the intracellular chitin metabolism of *J. wiesaeckerbachi*, exemplifying the difficulty of bioinformatic data evaluation. Hence, subsequent experimental validation is required to conclude the precise role of individual proteins. However, wet lab approaches are inherently slow and costly. Additionally, when looking at complex systems, such as the chitinolytic machinery, which appears to consist of an interplay of over 200 intracellular proteins, knock-out mutant guided experimental validation, for example, would be unfeasible to achieve in a time- and cost-efficient manner.

### *2.3. Differential Transcriptomics*

#### 2.3.1. Distinct Transcription Patterns Highlight the Increased Burden of the Metabolic Chitin Response

Illumina Novaseq 6000-guided cDNA-library sequencing of *Jeongeupia wiesaeckerbachi* culture duplicates in glucose or colloidal chitin minimal media yielded 18.65–21.71 million high quality reads. On average, 93.8% of these were unique reads and 96.8% could be mapped to the provided genome. Please refer to Table S2 for detailed information on the sequencing metrics.

Biocomputational evaluation of the differential transcriptomes revealed distinct transcription patterns in response to the respective carbon sources, as evident in the heatmap (Figure 4A). The volcano plot (Figure 4B) visualization serves to elucidate the three core statements of the dataset, that an increased gene count was upregulated more significantly and at higher expression rates with chitin compared to glucose substrate.

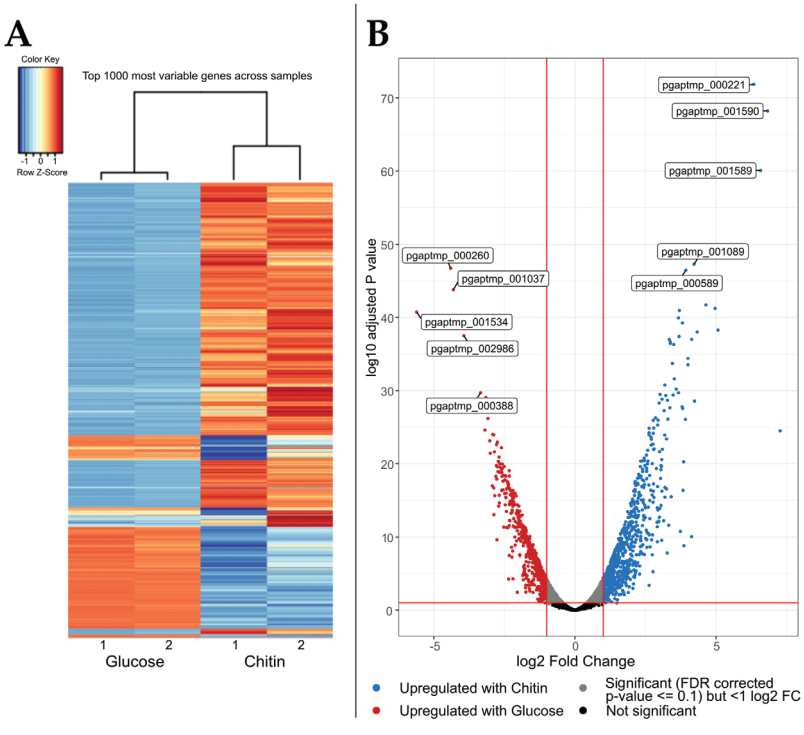


**Figure 4.** Differential transcriptomics results of *Jeongeupia wiesaeckerbachi* supplied with glucose or chitin. (**A**) Heatmap of the top 1000 most variable transcripts detected in duplicates, (**B**) Volcano plot of the differential transcriptomic dataset. The respective top 5 most significantly transcribed genes in glucose (red dots) or chitin (blue dots) media are labelled with their gene accession number.

In total, 600 transcripts were upregulated at least 20% or 1.2-fold and with an adjusted *p*-value of <0.1 with chitin in contrast to 468 with glucose as the carbon source. The increased gene recruitment, paired with the extraordinarily abundant chitinolytic machinery of the investigated organism [19], leaves room for speculation regarding whether the *Jeongeupia* genus specializes in chitin as a primary carbon source. In contrast to D-glucose, chitin exhibits a more rigid, less accessible and acetylated structure, which plainly requires more enzymes for degradation, deacetylation, and finally, assimilation. Moreover, terrestrial bacteria compete with fungi for soil nutrients, and co-evolution lead to the development of antagonistic mechanisms, such as antibiotics in fungi and cell-wall targeting chitinases in bacteria [61].

When explicitly looking at the five topmost significantly upregulated transcripts (Table 3), no obviously chitinoplastic genes are listed. Rather, a general NirD/YgiW/YdeI family stress tolerance protein encoding gene, two type IVb pilin encoding genes, an inner membrane FtsX-like permease, and a protein of unknown function were detected. YgiW is known to convey hydrogen-peroxide resistance in *E. coli*, but it functions as a general stress response protein to external stimuli [62]. In *Jeongeupia* spp., it might play a central role in the chitin stress response, rendering it a promising target for knockout experiments.

**Table 3.** Top 5 most variable transcripts of *Jeongeupia wiesaeckerbachi* in minimal media with colloidal chitin as exclusive carbon source. Transcripts were sorted according to the five lowest FDR (false discovery rate) corrected *p*-values. Additionally, all detected glycosyl hydrolase genes, which were upregulated under chitin media conditions, are listed. Refer to Table S3 in the Supplementary Data for more information on differentially upregulated glucose transcripts.

| Carbon Source | Rank | Adjusted *p*-Value | log2 Fold Change | Gene ID | Annotation (PGAP and dbCAN3.0) |
|---|---|---|---|---|---|
| Chitin | 1 | $1.44 \times 10^{-72}$ | 6.34 | pgaptmp_000221 | NirD/YgiW/YdeI family stress tolerance protein |
| | 2 | $6.13 \times 10^{-69}$ | 6.83 | pgaptmp_001590 | Flp family type IVb pilin |
| | 3 | $8.63 \times 10^{-61}$ | 6.58 | pgaptmp_001589 | Flp family type IVb pilin |
| | 4 | $5.63 \times 10^{-48}$ | 4.22 | pgaptmp_001089 | FtsX-like permease family protein |
| | 5 | $3.56 \times 10^{-47}$ | 3.93 | pgaptmp_000589 | hypothetical protein |
| Chitin | 26 | $2.02 \times 10^{-34}$ | 3.45 | pgaptmp_000680 | peptidoglycan-binding protein (GH19) |
| | 52 | $1.15 \times 10^{-26}$ | 2.77 | pgaptmp_000371 | glycosyl hydrolase family 18 protein |
| | 102 | $4.18 \times 10^{-20}$ | 2.54 | pgaptmp_000306 | carbohydate-binding domain-containing protein (GH20) |
| | 294 | $8.38 \times 10^{-13}$ | 1.80 | pgaptmp_000836 | glycosyl hydrolase family 18 protein |
| | 309 | $2.1 \times 10^{-12}$ | 1.90 | pgaptmp_001841 | glycosyl hydrolase family 18 protein |
| | 348 | $1.08 \times 10^{-11}$ | 2.25 | pgaptmp_002137 | glycosyl hydrolase family 18 protein |
| | 448 | $4.33 \times 10^{-10}$ | 2.92 | pgaptmp_000372 | glycosyl hydrolase family 18 protein |
| | 453 | $4.9 \times 10^{-10}$ | 1.66 | pgaptmp_000302 | chitinase (GH19) |
| | 678 | $2.83 \times 10^{-7}$ | 1.32 | pgaptmp_001746 | glycosyl hydrolase family 18 protein |

Type IV pili (T4P) are multifunctional protein filaments, populating the surface of many bacteria and archaea [63]. Through rapid assembly and disassembly, T4P enable twitching motility for directed movement towards substrates upon external stimuli but are also involved in the Type II secretion system, DNA uptake, and biofilm formation [64]. The FtsX-like permease family are predicted transmembrane proteins that can release, for example, lipoproteins from the cytosol to the periplasm in an ATP-dependent manner (refer to UniProt accession P57382). Nonetheless, six out of the thirteen genome-encoded GH18 [19] were upregulated during exposure to colloidal chitin, albeit on surprisingly low ranks, underpinning the intra- and extracellular proteomic results. In addition, two of the three GH19 type chitinases and one of the three GH20 hexosaminidases exhibited increased transcript rates.

2.3.2. Low Protein-mRNA Correlation between the Intracellular Datasets

The inquiry for the top hits shared between the proteomic and transcriptomic datasets revealed intriguingly little correlation between upregulated transcripts and detected protein levels.

Refer to Table A1 in the Appendix A for the extensive evaluation results and Table S3 in the Supplementary Data for the most significantly upregulated genes with glucose.

The discrepancy between mRNA and protein abundancies is a well-reported challenge in the systems biology domain and has been subject of intense scientific discussions [65].

With correlation coefficients of about 0.77 in *E. coli*, where one mRNA molecule corresponds to $10^2$–$10^4$ respective protein molecules, transcript concentrations were long thought to be unreliable proxies for the prediction of corresponding protein levels and activities [66,67]. Variations of mRNA levels reflect approximately 29% of variations in cellular protein concentration [68]. Translation of genes into proteins, with mRNAs as mediating templates, is an immensely complex process with a multitude of influencing factors: (1) sequence-based translation efficiency, influenced by codon bias or chromatin structure, (2) translation rate modulation through genetic regulatory elements including feedback repression, (3) highly dissimilar protein turnover rates, which are dependent on the ubiquitin–proteasome pathway and temperature, among other things, (4) protein synthesis delay, (5) protein transport, disconnecting measured transcript and enzyme levels through spatial separation in a given compartment, and (6) transcript measurement noise on a methodological level [65,67,69].

When comparing proteome and transcriptome datasets regarding their validity, proteins are more closely related to the phenotype of a cell as a functional expression of its origin gene. Additionally, they are more robust ex vivo, immune to non-functional mRNA artefacts, and outperform transcriptomics in gene function prediction. Nonetheless, transcript concentrations still offer valuable information about imminent protein biosynthesis requirements of a cell [70].

2.3.3. Chitin Metabolism Transcript Upregulation Is Time Dependent

A similar study from Monge et al. concerning the chitinolytic system of *C. japonicus* revealed strong upregulation of chitin degradation-implicated transcripts [71], occupying the top seven most strongly upregulated gene ranks. According to the authors, the upregulation of chitinoplastic genes was more pronounced in the exponential growth phase than the early stationary phase. The latter finding provides a methodological explanation for the relatively low fold changes and adjusted *p*-value rankings of *J. wiesaeckerbachi's* chitin conversion-related mRNAs. In this study, cultures for transcriptomic investigation were grown on minimal colloidal chitin medium for three days when the majority of the insoluble substrate particles were hydrolyzed, which interfered with RNA extraction. Furthermore, sufficient biomass and concomitant RNA yields, required by the external RNA-sequencing provider Eurofins Genomics, cannot be achieved earlier under these growth conditions. Therefore, the cells were most likely in the (mid to late) stationary phase when relevant transcripts were already degraded. In *E. coli*, mRNA is degraded within 5–10 min [66], therefore transcript levels resemble the recent transcription activity whereas protein levels reflect the accumulated long-term expression. It is further reported that different proteins have distinct optimal concentrations in the cell, which might have been reached and transcription thereof inhibited at this point in time, since protein residence times often exceed that of a cell life cycle anyway [72,73].

Saito et al. conducted a study on the co-transcriptional regulation of chitinase genes in the genome of *Streptomyces coelicolor* A3(2) with Northern blot hybridization, using labelled anti-sense RNAs [74]. Their results demonstrated that colloidal chitin-induced chitinase transcription reaches a maximum after 4 h, emphasizing the importance of temporal expression patterns. Interestingly, only five of the eight genome-encoded chitinase mRNAs could be detected experimentally in varying concentrations, deploying either colloidal chitin or chitobiose. This is in accordance with the several non-traceable chitinolytic

machinery-implicated transcripts or proteins of *J. wiesaeckerbachi*, suggesting either specific substrate dependence, non-functionality, or even superfluity of certain genes. In a follow-up study, Saito et al. elaborated that the multiplicity of chitinases in *Streptomyces* spp. has developed through domain deletion and gene duplication [75], which might be extrapolated to other chitinase-rich genera like *Jeongeupia* [19,76].

Pathways connected with high protein cost, such as the chitinolytic machinery, are tightly regulated by fine-tuned transcriptional programs to not unnecessarily waste cellular energy and resources [77]. A GntR family transcription factor [78], annotated as *N*-acetylglucosamine utilization regulator by the KO database, is located just upstream (gene ID 443) of the chitobiose transport system genes (gene IDs 439–442). It was neither found to be upregulated in our transcriptome, which captured the RNA concentrations after three days, nor in the intracellular proteome within the same time frame. Nonetheless, the chitobiose transport proteins under the control of the *N*-acetylglucosamine utilization regulator were upregulated significantly intracellularly Table 2). Again, this emphasizes the temporal delay between transcription and protein synthesis of genetic regulators and their target proteins, as well as protein longevity, given sufficiently low turnover-rates.

The search for additional transcripts involved in gene regulation uncovered 18 upregulated mRNAs in total (Table S4), with 6 >2-fold upregulated mRNAs under colloidal chitin growth conditions after three days of cultivation. Among them are two transcriptional regulators of the families Rrf2 and GntR (gene IDs 2638 and 2797), two $\sigma^{70}$ family RNA polymerase factors (gene IDs 299 and 2681), one anti $\sigma^{70}$ factor (gene ID 300), and one hypothetical transcription factor (gene ID 237) according to SWISS-MODEL [79], which was also upregulated 33-fold in the intracellular chitin-induced proteome.

## 3. Materials and Methods

### *3.1. Chemicals and Consumables*

All chemicals were supplied from Sigma-Aldrich (Darmstadt, Germany), and general consumables were obtained from VWR (Darmstadt, Germany). All necessary buffers and enzymes for next-generation genome sequencing were shipped from Pacific Biosciences (Menlo Park, CA, USA). High molecular weight DNA was extracted with the Quick-DNA™ HMW MagBead Kit from Zymo Research (Freiburg, Germany). HMW gDNA shearing was conducted with g-TUBEs (Covaris, Woburn, MA, USA).

### *3.2. Colloidal Chitin and Media Preparation*

Colloidal chitin (CC) was prepared according to Murthy and Bleakley [80] with slight modifications. A total of 20 g of crab shell chitin powder (Sigma-Aldrich) was incrementally added to 150 mL 37% HCl under moderate stirring, increasing the viscosity of the solution. When the viscosity decreased sufficiently, more chitin was carefully added. The slur was then incubated for 2–3 h at room temperature under moderate stirring, evading the formation of foam. Afterwards, the non-viscous, fully dissolved chitin of an intense brown color was slowly poured into 2 L of ice-cold deionized water (di$H_2O$) in a 5 L glass beaker and vigorously stirred, rapidly swelling to white colloidal chitin. The solution was incubated overnight at 4 °C without stirring and neutralized the following day through the addition of excessive amounts of di$H_2O$ and subsequent centrifugation in a Beckman JLA8.1000 rotor for 15 min at 10,000× *g* until a supernatant pH of 5 was reached. CC was harvested and kept in the refrigerator until its utilization for liquid chitinase screening media (CSM) or agar plates. The recipe was adapted and modified from [81,82]: 20 g/L (2% *w*/*v*) CC, 0.7 g/L $K_2HPO_4$, 0.3 g/L $KH_2PO_4$, 0.5 g/L $MgSO_4 \cdot 5H_2O$, 10 mg/L $FeSO_4 \cdot 7H_2O$, and 20 g/L agar (optional), adjusting to pH 6.5 for plates or 7 for liquid medium. After autoclaving, 1 mg/L $ZnSO_4$ and $MnCl_2$ were added from sterile filtrated stock solutions prior to the pouring of agar plates/inoculation of liquid media.

### *3.3. Bacterial Strains*

The previously described chitinolytic bacterium *Jeongeupia wiesaeckerbachi* retrieved from environmental samples was utilized for all experiments; its genome is available on NCBI, under the BioSample accession ID SAMN35557021.

### *3.4. Proteomics*

#### 3.4.1. Culture Conditions

I. Precultures

*Jeongeupia wiesaeckerbachi* was streaked out onto CSM-agar (pH 6.5, 2% CC (*w*/*v*)) from axenic cryostocks. The precultures were prepared by placing one colony each into 150 mL baffled shaking flasks holding 20 mL tryptic soy broth. Cultivations were carried out in an incubation shaker (New Brunswick Innova 44, Eppendorf, Hamburg, Germany) at 28 °C and 120 rpm overnight. Cell densities were determined spectrophotometrically, measuring the absorption at 600 nm wavelength in 2 mL cuvettes (Nano Photometer NP80, IMPLEN, Munich, Germany).

II. Intracellular Protein Investigation

The main cultures were prepared in 500 mL baffled shaking flasks holding 50 mL of either CSM (pH 7, 2% CC (*w*/*v*)) or modified CSM with 0.5% (*w*/*v*) glucose and 1% (*w*/*v*) $NH_4Cl$ instead of colloidal chitin. Sufficient bacterial cell amounts were washed twice in sterile phosphate buffered saline (PBS) prior to media inoculation to an OD600 of 0.05. Cultivation parameters identical to those of the precultures (28 °C, 120 rpm) were selected, with incubation times of one (glucose-fed) or three days (chitin-fed), respectively, to acquire enough cell mass. Both carbon sources (glucose or colloidal chitin) were tested in biological quadruplicates, equating to eight samples in total.

III. Extracellular Protein Investigation

In order to examine the enzymes secreted into the culture medium, 500 mL CSM in 5 L baffled shaking flasks was inoculated with *Jeongeupia wiesaeckerbachi* to an OD600 of 0.05 in biological triplicates. Additionally, one flask was prepared with CSM containing 2% (*w*/*v*) processed crab shell chitin (unbleached) instead of CC as the sole C and N source. After three days at 28 °C and 120 rpm, the cultures were centrifuged at 10,000× *g* for 10 min. The supernatants were sterile filtered with a 0.22 µm syringe filter and concentrated using a tangential flow filter membrane (MWCO 10 kDa; Omega 10K Membrane, Pall Cooperation, New York, NY, USA) and a peristaltic pump (Masterflex P/S Model 910-0025, Thermo Scientific, Menlo Park, CA, USA) to a volume of 10–15 mL. Afterwards, 10 kDa MWCO centrifugal filter units (Centriprep, Merck Millipore, Darmstadt, Germany) were applied to further concentrate the secreted crude enzyme mixes to a final volume of approximately 1 mL per sample. Protein concentrations were measured with a photometer based on 260/280 nm absorption ratios (Nano Photometer NP80, IMPLEN, Munich, Germany). Of these protein extracts, 15 µL were transferred into a new reaction tube, mixed with 5 µL 4 × SDS-sample buffer, and boiled for 5 min at 95 °C.

#### 3.4.2. Whole Cell Protein Extraction

The protocol for protein extract and precipitation was slightly modified from Engelhart-Straub and Cavelius [83]. Bacterial cultures were harvested through centrifugation at 8000× *g* for 10 min, and the media supernatant was discarded. The cells were subsequently washed twice with 5 mL of sterile PBS, resuspended in 600 µL PBS, and transferred to 2 mL micro reaction tubes. Afterwards, cell lysis was induced by horizontal vigorous shaking (Vortex Genie 2, Scientific Industries, Bohemia, NY, USA) for 30 min with fine glass beads, supported by 1:3 (*v*/*v*) Protein Extraction Reagent Type 4 (Sigma-Aldrich, St. Louis, MO, USA). After centrifugation at 14,000× *g* for 30 min, protein precipitation was achieved through the addition of 1:1 (*v*/*v*) 20% trichloroacetic acid in HPLC-grade acetone (*w*/*v*), supplemented with 10 mM DL-1,4-Dithiothreitol (DTT). The samples were vigorously vortexed and then incubated at −20 °C for one hour. Following centrifugation at 14,000× *g* for 10 min at 4 °C, the protein pellets were washed twice with HPLC-grade

acetone supplemented with 10 mM DTT and air dried under a sterile bench. Lastly, the protein pellets were resuspended in 450 µL 8 M urea with 10 mM DTT and homogenized with a micro pestle suitable for 2 mL micro reaction tubes. Of this protein extract, 15 µL were transferred into a new reaction tube, mixed with 5 µL 4 × SDS-sample buffer, and boiled for 5 min at 95 °C.

#### 3.4.3. Tryptic In-Gel Digestion and LC-MS/MS Analysis

The extracted proteins from whole cells were resolved by SDS-PAGE and subsequently digested with trypsin. The resulting peptides were then separated by reversed-phase chromatography and detected with a mass spectrometer as described next.

The tryptic in-gel digestion protocol and LC-MS/MS analysis with a timsTOF Pro mass spectrometer, coupled with a NanoElute LC System (Bruker Daltonik GmbH, Bremen, Germany) equipped with an Aurora column (250 × 0.075 mm, 1.6 µm; IonOpticks, Melbourne, Australia), were adapted from Fuchs et al. and Engelhart-Straub and Cavelius [83,84]: One-dimensional 12% SDS PAGEs with short stacking gels were deployed to transfer 10 µL of each whole cell protein extract into the resolving gel matrix. Hereby, it is crucial to leave several empty wells between the different conditions (glucose/chitin) to prevent sample migration. Refer to the Supplementary Materials for the full protocol.

The mobile phase consisted of two solvents for reverse-phase chromatography: (A) 0.1% formic acid and 2% acetonitrile in water and (B) 0.1% formic acid in acetonitrile, which was added linearly with a constant flow rate 0.4 µL/min. Both separation cycles started at 2% of B ($v/v$). For the less complex extracellular protein mixtures, a short gradient was carried out: t = 25 min and 17% B ($v/v$), t = 27 min and 25% B, t = 30 min and 37% B, with t = 33 min and a hold at 95% B for 10 more minutes. In case of the more complex intracellular protein compositions, a longer separation cycle of 100 min was selected: t = 60 min and 17% B, t = 90 min and 25% B, t = 100 min and 37% B, and t = 110 min and 95% B with a hold at 95% B for 10 more minutes. The oven temperature was kept at a constant 50 °C during measurements.

#### 3.4.4. Bioinformatic Analysis

The PEAKS studio software (v.10.6, build 20201221) was utilized for evaluation of the MS/MS tandem spectrometry data of tryptic digested peptides, deploying the annotated genome of *Jeongeupia wiesaeckerbachi* (BioSample accession ID SAMN35557021) as the reference for protein identification [38]. The following "*Database search*" parameters were applied: a precursor mass of 25 ppm using monoisotopic mass and a fragment ion of 0.05 Da for the error tolerance; trypsin as a digestion enzyme; a maximum of two missed cleavages per peptide; a maximum of three variable PTM (post-translational modification) per peptide and estimation of FDR (false discovery rate) with decoy fusion was allowed. For the protein identification, 1.0% FDR with at least one unique peptide per protein was selected. The intracellular glucose and colloidal chitin sample groups were differentially quantified with PEAKSQ, applying a mass error tolerance of 20.0 ppm, an ion mobility tolerance of 0.05 Da, and a retention time shift tolerance of 6 min (auto detect). The fold change and significance were set to 2 and 20, respectively. All proteins were exported and utilized for manual evaluation and plot creation.

The R-Studio software with the ggplot2 package served as the main tool for the creation of plots, if not stated otherwise [24,25].

The functional characterization of both the secreted and intracellular proteomes was conducted with the browser-based BlastKOALA (KEGG Orthology And Links Annotation) tool on the KEGG server [60], utilizing the taxonomy ID (taxid) 885864 or the option "Prokaryote" since the latest update as of May 2023. Carbohydrate-active enzymes (CAZymes) and carbohydrate-binding modules (CBM) in the proteomes and the transcriptome were predicted with the browser based tool dbCAN 3.0, using the HMMER:dbCAN (E-Value < $10^{-15}$, coverage > 0.35), DIAMOND: CAZy (E-Value < $10^{-102}$) and HMMER: dbCAN-sub (E-Value < $10^{-15}$, coverage > 0.35) options [32].

### *3.5. Differential Transcriptomics*

#### 3.5.1. Culture Conditions

Like during the investigation of the intracellular proteins (see 3.4.1, II), the main cultures were prepared in 500 mL baffled shaking flasks holding 50 mL of either CSM (pH 7, 2% CC (*w*/*v*)) or modified CSM, with 0.5% (*w*/*v*) glucose and 1% (*w*/*v*) $NH_4Cl$ instead of colloidal chitin. Sufficient bacterial cell amounts were washed twice in sterile phosphate buffered saline (PBS) prior to media inoculation to an OD600 of 0.05. Cultivation parameters identical to those of the precultures (28 °C, 120 rpm) were selected, with incubation times of one (glucose-fed) or three days (chitin-fed), respectively, to acquire enough cell mass.

#### 3.5.2. RNA Extraction and Quality Control

Bacterial cells were harvested via centrifugation at 6800× *g* for 10 min. Total cell RNA was isolated according to the recommendations of the SV total RNA Isolation System Kit (Promega, Madison, WI, USA). Purity and quantity of the obtained RNA were assessed per photometer based 260/280 nm absorption ratios (Nano Photometer NP80, IMPLEN, Munich, Germany). Furthermore, quality numbers were evaluated with the Qubit 4 fluorometer and the Qubit RNA IQ Assay-Kit (Thermo Fisher Scientific; Waltham, MA, USA). The experiment was performed in biological triplicates, but only two samples per condition (chitin- or glucose-containing media) were analyzed.

#### 3.5.3. Next Generation Sequencing and Bioinformatic Analysis

The EuroFins Genomics Europe Sequencing GmbH (Constance, Germany) performed rRNA depletion, cDNA library construction, next-generation sequencing with the Illumina NovaSeq platform (6000 S4 PE150 XP mode), and the following bioinformatic analyses. Raw sequencing data were cleansed of rRNA reads with RiboDetector [85]. Adapter trimming, quality filtering, and per-read quality pruning were executed with fastp [86]. High quality reads were aligned to the provided *J. wiesaeckerbachi* genome with STAR [87]. Gene-wise quantification was achieved by evaluating transcriptome alignments by means of the software featureCounts [88]. Differential gene expression analysis between the glucose-fed and chitin-fed sample groups was performed using the R/Bioconductor package edgeR [89]. Variant calling for SNP and InDel assessment was conducted with Sentieon's HaplotypeCaller [90]. Details on the applied software and command line parameters can be found in the Supplementary Materials (Table S5).

## 4. Conclusions

### *4.1. Chitin-Metabolism Causes Profound Genetic Changes*

Through a combination of intracellular and extracellular proteomic analyses, the involvement of 360 unique enzymes within the chitin metabolism of the Gram-negative bacteria genus *Jeongeupia* could be demonstrated, deepening our understanding of natural chitin saccharification systems. Considering all genes with >2-fold increased differential expression rates and with significance values of >20% (proteomics) or adjusted *p*-values of <0.001 (transcriptomics), respectively, 203 intracellular proteins and 244 transcripts (pseudo gene-adjusted) could be detected. The addition of the 192 extracellular enzymes that were both monitored among all samples and confirmed in silico to be secreted, followed by the removal of redundant hits, produces a total of 577 unique genes that were reliably induced by chitin substrates.

Our previously reported dbCAN 3.0-mediated CAZyme prediction [19,32] disclosed the existence of thirteen GH18, three GH19, three GH20, and a single LPMO (AA10) in the genome of *Jeongeupia wiesaeckerbachi*. Twelve of those thirteen GH18 (all but gene ID 1841), one GH19 chitinase (gene ID 302), one GH3 hexosaminidase (gene ID 1323), and all three GH20 hexosaminidases (gene IDs 269, 306 and 1731), in addition to the LPMO (gene ID 148), could be detected in extracellular proteomic samples on colloidal chitin. Intriguingly, the GH20 were secreted on both crab shell and colloidal chitin substrate, while the GH19

was only detected in colloidal chitin samples. These results were confirmed and elaborated through the detection of two GH19 transcripts (gene IDs 302 and 680) in addition to two GH20 transcripts (gene IDs 269 and 306). Overall, only a single GH19 chitinase (gene ID 1077) and two of the three GH3 hexosaminidase (gene IDs 308 and 872) genes of the previously in silico-predicted chitinolytic machinery could not be experimentally verified to be at least transcribed or translated in an enhanced manner under chitinase-inducing growth conditions. Remarkably, most of the chitinolytic system was secreted, or at least exclusively found extracellularly, whereas only a single GH18 (gene ID 635), two GH3 hexosaminidases (gene IDs 308 and 1323), and a single GH20 hexosaminidase (gene ID 269) could be confirmed in the intracellular proteome.

### *4.2. Potential Role of Redox Enzymes in Chitin Hydrolysis*

Despite the LPMO's well-understood function to promote the efficiency of synergistic chitinases on a crystalline substrate [35,91–94], there are reports where its activity is uncoupled and may play a role in virulence instead [95–97]. Similarly, the *Jeongeupia wiesaeckerbachi* LPMO of family AA10 (gene ID 148) was merely among the top 150 most significant secreted proteins on average and was ranked considerably lower in the crab shell chitin sample (opposed to colloidal chitin), specifically. Notably, two additional predicted AA proteins of families 2 and 7 (gene IDs 1157 and 2996, respectively) were more abundant throughout all the secretome samples, independent of the respective substrate. Aside from that, a third FAD-dependent oxidoreductase (gene ID 1920) was detected extracellularly with amorphous chitin, but not crab chitin, suggesting substrate-specific expression. On an intracellular level, an additional oxidoreductase of the SDR (short-chain dehydrogenases/reductases) family (gene ID 1215) was upregulated 50-fold, indicating a general importance of electron transfer chains for bacterial chitin metabolism. Apart from the redox chemistry catalyzing enzymes and the obvious chitinoplastic GH18/19/20 and LPMOAA10 enzymes, two >8-fold upregulated polysaccharide deacetylases (gene IDs 281 and 437), as detected in the intracellular proteome, could represent promising targets for characterization studies. Since the deacetylated form of chitin, chitosan, is the desired molecule for most industrial applications, a strong interest in the targeted and sustainable enzymatic conversion persists. CAZyme prediction of the collective upregulated proteome and transcriptome (>20% increase) dataset unraveled several additional CBM5/12 exhibiting enzymes, which are hallmarks for chitin-active proteins (Table A2; refer to Table S6 for a comprehensive list). Furthermore, the CBM50 or LysM domains have been reported to be involved in penta-*N*-acetyl-chitopentaose (pentamer of *N*-acetylglucosamines) binding [98]. Lastly, some of the secretome-detected GH23 enzymes are of particular interest, being a family of hydrolases that can comprise chitinase activities (EC 3.2.1.14) [99].

### *4.3. Chitin-Rich Environments Prompt a Multitude of Methyl-Accepting Chemotaxis and Motility Proteins*

In *Vibrio cholerae*, a single regulatory noncanonical histidine sensor kinase ChiS was identified to orchestrate the catabolic chitin response [16,100,101]. However, genome-wide protein sequence alignment with ChiS did yield no feasible homologies. With the *Vibrio cholerae* chitinolytic signal transduction cascade as a role model, an inquiry into highly transcribed or translated two-component sensor histidine kinases yielded a noteworthy amount of methyl-accepting chemotaxis proteins (MCP) or aspartate receptors, with high log2 fold changes and significance. MCPs are the most common bacterial receptors and mediate transmembrane signal transduction of environmental cues as part of a multiprotein complex, ultimately leading to chemotaxis towards a more favorable environment [102,103]. Hereby, a correlation between genome complexity, habitat, and the amount of genome-encoded MCPs (gene IDs 602, 1841, 3352, 246, 3077, 2218; upregulated 14-, 5-, 3-, 2-, 3.5-, and 1.5-fold, respectively) was observed [104]. Through propagation of conformational changes over receptor-modulating enzymes like CheR (gene ID 36, 12-fold upregulated) and a receptor-coupling protein CheW (gene ID 1614, 2.5-fold upregulated), MCPs control

the sensor histidin kinase CheA (gene ID 138, upregulated 5-fold), which subsequently phosphorylates the flagellar-motor receptors CheV and CheY (genes ID 134 and 135; upregulated 5- and 5.5-fold, respectively) [105,106]. Furthermore, a putative transcription factor (gene ID 237) was upregulated 33-fold with high significance in the intracellular proteome, suggesting a central role in chitin adaptation.

Light microscopy imaging (not shown) revealed dense colloidal chitin particle colonization through bacterial cells, implying chemotaxis and possibly pili-mediated twitching motility, as suggested by the transcriptomics data set. Conceivably, *Jeongeupia wiesaeckerbachi* follows a common strategy to secure the released glucosamines against competing soil bacteria and fungi through the abbreviation of transport routes and immediate substrate-binding and import [15].

### *4.4. Schematic Summary of the Cumulative Systems Biology Approach*

Based on our combined omics results, we propose a holistic model for the chitinolytic machinery of *Jeongeupia* spp., trying to factor in the most relevant findings for chitin metabolism (Figure 5). In light of the approximately 550 upregulated genes induced through chitin substrates, the schematic does not claim to be more than a mere approximation of reality. Nevertheless, it does provide an overview of the putatively involved main enzymes and avails to appreciate the complex interplay of gene transcription, protein translation, and signal transduction, which assembles the catabolic chitin response of chitinolytic bacteria.

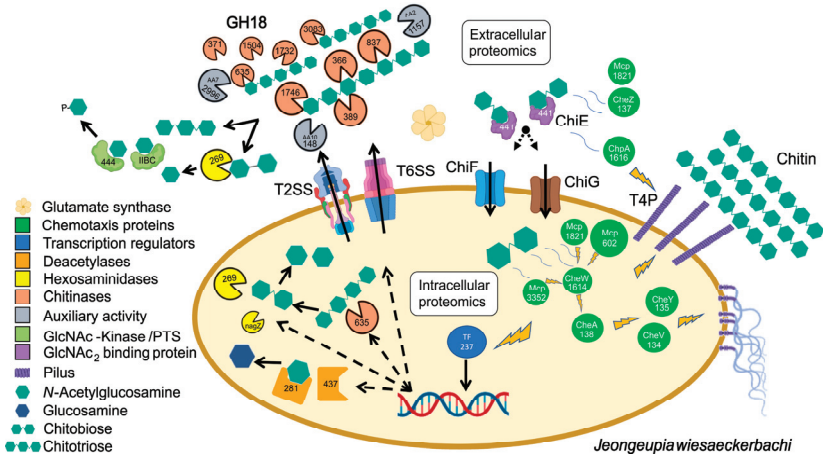


**Figure 5.** Schematic illustration of the proposed chitinolytic machinery of *Jeongeupia wiesaeckerbachi*. Extracellular proteins, depicted outside the bacteria cell, were detected in all triplicates cultivated in minimal media with colloidal chitin and a single sample cultivated with unbleached, decalcified crab shells. Intracellular proteins, illustrated inside the bacteria cell, were differentially upregulated with chitin minimal media compared to on glucose cultivated cells. Lightning bolts indicate signal transduction. Larger symbols indicate a higher significance or fold-change compared to enzymes of the same classification. Figure created with BioRender and Inkscape.

**Supplementary Materials:** The following supporting information can be downloaded at https://www.mdpi.com/article/10.3390/md21080448/s1. Table S1: Signal peptide prediction of the *J. wiesaeckerbachi* chitinolytic machinery with SignalP 6.0. Table S2: Sequencing and mapping metrics per sample. Figure S1: Principal Component Analysis (PCA) plot of the differential transcriptomics samples of *Jeongeupia wiesaeckerbachi*. Table S3: Top 5 most variable transcripts of *Jeongeupia wiesaeckerbachi* in minimal media with glucose as exclusive carbon source. Table S4: Differentially upregulated *J. wiesaeckerbachi* transcripts involved in gene regulation under minimal colloidal chitin growth conditions compared to minimal glucose media-derived samples, from highest to

lowest log2 fold changes. Table S5: Bioinformatic transcriptomics analysis parameters as performed and provided by Eurofins Genomics. Table S6: CAZyme prediction of the collective >1.2-fold upregulated proteomic and transcriptomic results of *J. wiesaeckerbachi* with chitin substrate, mediated by dbCAN 3.0.

**Author Contributions:** Conceptualization, N.D.A., D.G., and T.B.B.; methodology, N.D.A.; software, N.D.A.; validation, N.D.A.; formal analysis, N.D.A.; investigation, N.D.A.; resources, T.B.B.; data curation, N.D.A.; writing—original draft preparation, N.D.A.; writing—review and editing, D.G. and T.B.B.; visualization, N.D.A.; supervision, D.G. and T.B.B.; project administration, D.G.; funding acquisition, T.B.B. All authors have read and agreed to the published version of the manuscript.

**Funding:** This research was funded by the German Ministry for Education and Research (BMBF) with the grant number 031B0838B in the framework of the Canadian/German BMBF bioeconomy international project ChitoMat (Holistic chitin conversion to materials for 3D printing application and performance animal feed additives).

**Data Availability Statement:** All data are provided in full in the results section, the Appendix A, or Supplementary Materials of this paper. All raw datasets generated and/or analyzed during the current study are publicly available in the Zenodo online repository with the https://doi.org/10.5281/zenodo.8184099.

**Acknowledgments:** We would like to acknowledge and thank our ChitoMat project partners at the Fraunhofer Institute for Interfacial Engineering and Biotechnology IGB, the Atlantic Veterinary College and Atlantic Biofabrication Laboratory at the University of Prince Edward Island and CigalaTech for their fruitful cooperation. A special thanks to Steven Reisse, former CEO of CigalaTech, for kindly providing us with decalcified, unbleached crab shell chitin material. Thanks to Zora Rerop and Manfred Ritz for their endless patience and valuable advice on biocomputational questions and Nadim Ahmad for proofreading.

**Conflicts of Interest:** The authors declare no conflict of interest. The funders had no role in the design of the study; in the collection, analyses, or interpretation of data; in the writing of the manuscript; or in the decision to publish the results.

## Appendix A

**Table A1.** Evaluation of the *J. wiesaeckerbachi* transcriptomic dataset regarding correlations with the intracellular (IC) proteomic dataset and miscellaneous proteins of interest. The "Annotation" color code depicts: (1) transcripts whose proteins were detected with high log2 fold changes or significance values in the IC proteomics (yellow), (2) glucosamine metabolism transcripts (light blue), (3) chemotaxis transcripts (light green) or (4) hydrolase transcripts (light red) with their adjusted *p*-value dependent ranking and log2 fold change. Hereby, correlations with the IC proteomics (yellow) overruled the other colors, descriptive of predicted protein function. The "Rank" color code depicts: (1) chitin upregulated transcripts (green) and (2) glucose upregulated transcripts (red).

| Rank | Protein Accession Identifier | log2Fold Change | Adjusted *p*-Value | Annotation (PGAP and dbCAN 3.0) |
|---|---|---|---|---|
| 7 | pgaptmp_002582 | 4.04 | $4.84 \times 10^{-46}$ | inclusion body family protein |
| 26 | pgaptmp_000680 | 3.45 | $2.02 \times 10^{-34}$ | peptidoglycan-binding protein (GH19) |
| 34 | pgaptmp_002996 | 3.48 | $4 \times 10^{-30}$ | FAD binding oxidoreductase (AA7) |
| 52 | pgaptmp_000371 | 2.77 | $1.15 \times 10^{-26}$ | glycosyl hydrolase family 18 protein (GH18) |
| 66 | pgaptmp_003576 | 2.71 | $4.4 \times 10^{-24}$ | methyl-accepting chemotaxis protein |
| 69 | pgaptmp_001506 | 2.77 | $2.06 \times 10^{-23}$ | PAS domain-containing methyl-accepting chemotaxis protein |
| 102 | pgaptmp_000306 | 2.54 | $4.18 \times 10^{-20}$ | carbohydate-binding domain-containing protein (GH20) |
| 105 | pgaptmp_001215 | 2.40 | $5.45 \times 10^{-20}$ | SDR family oxidoreductase |
| 127 | pgaptmp_003096 | 3.04 | $1.03 \times 10^{-18}$ | DUF1631 domain-containing protein |
| 169 | pgaptmp_002942 | 2.09 | $4.56 \times 10^{-17}$ | cellulase family glycosylhydrolase |
| 228 | pgaptmp_003580 | 2.47 | $4.69 \times 10^{-15}$ | hydrolase |

**Table A1.** *Cont.*

| Rank | Protein Accession Identifier | log2Fold Change | Adjusted *p*-Value | Annotation (PGAP and dbCAN 3.0) |
|---|---|---|---|---|
| 239 | pgaptmp_001847 | 2.20 | $1.4 \times 10^{-14}$ | substrate-binding domain-containing protein |
| 294 | pgaptmp_000836 | 1.80 | $8.38 \times 10^{-13}$ | glycosyl hydrolase family 18 protein (GH18) |
| 309 | pgaptmp_001841 | 1.90 | $2.1 \times 10^{-12}$ | glycosyl hydrolase family 18 protein (GH18) |
| 314 | pgaptmp_000237 | 2.21 | $2.66 \times 10^{-12}$ | hypothetical protein |
| 348 | pgaptmp_002137 | 2.25 | $1.08 \times 10^{-11}$ | glycosyl hydrolase family 18 protein (GH18) |
| 370 | pgaptmp_000470 | 1.69 | $2.48 \times 10^{-11}$ | N-acetylglucosamine-6-phosphate deacetylase |
| 394 | pgaptmp_000419 | 2.06 | $8.64 \times 10^{-11}$ | glutamine amidotransferase |
| 438 | pgaptmp_000602 | 1.60 | $2.97 \times 10^{-10}$ | methyl-accepting chemotaxis protein |
| 448 | pgaptmp_000372 | 2.92 | $4.33 \times 10^{-10}$ | glycosyl hydrolase family 18 protein (GH18) |
| 453 | pgaptmp_000302 | 1.66 | $4.9 \times 10^{-10}$ | chitinase (GH19) |
| 507 | pgaptmp_000337 | 1.64 | $3.04 \times 10^{-9}$ | nitrate reductase subunit beta |
| 521 | pgaptmp_001552 | 1.43 | $4.87 \times 10^{-9}$ | FAD-dependent monooxygenase |
| 589 | pgaptmp_002133 | 1.37 | $3.47 \times 10^{-8}$ | alpha/beta hydrolase-fold protein |
| 678 | pgaptmp_001746 | 1.32 | $2.83 \times 10^{-7}$ | glycosyl hydrolase family 18 protein (GH18) |
| 691 | pgaptmp_000878 | 1.84 | $3.37 \times 10^{-7}$ | hypothetical protein |
| 869 | pgaptmp_003318 | 1.82 | $5.51 \times 10^{-6}$ | PrkA family serine protein kinase |
| 981 | pgaptmp_002310 | 1.04 | $2.73 \times 10^{-5}$ | basic amino acid ABC transporter substrate-binding protein |
| 1057 | pgaptmp_000437 | 1.15 | $6.33 \times 10^{-5}$ | polysaccharide deacetylase family protein |
| 1334 | pgaptmp_001731 | −0.93 | $8.50 \times 10^{-4}$ | carbohydate-binding domain-containing protein (GH20) |
| 1353 | pgaptmp_001323 | −0.94 | $9.96 \times 10^{-4}$ | beta-N-acetylhexosaminidase (GH3) |
| 1512 | pgaptmp_001504 | −0.79 | $2.89 \times 10^{-3}$ | glycosyl hydrolase family 18 protein (GH18) |
| 1900 | pgaptmp_000440 | −0.60 | $2.47 \times 10^{-2}$ | sugar ABC transporter permease |
| 3390 | pgaptmp_000441 | −0.03 | $9.32 \times 10^{-1}$ | sugar ABC transporter substrate-binding protein |

**Table A2.** Promising chitinoplastic candidate CAZymes of the collective >1.2-fold upregulated proteomic and transcriptomic results of *J. wiesaeckerbachi* with chitin substrates, predicted by dbCAN 3.0. AA = auxiliary activity, CBM = carbohydrate binding module, CE = carbohydrate esterase, EC = extracellular proteomics, IC = intracellular proteomics, GH = glycosyl hydrolase family, GT = glycosyltransferase, T = transcriptomics. The two sequence homology-based function prediction tools HMMER and DIAMOND are deployed by dbCAN 3.0 with the following parameters: HMMER:dbCAN (E-Value < $10^{-15}$, coverage > 0.35), DIAMOND: CAZy (E-Value < $10^{-102}$) HMMER: dbCAN-sub (E-Value < $10^{-15}$, coverage > 0.35). SignalP predicts prokaryotes signal peptides of the conventional Sec and TAT translocons, processed with either SPI, SPII or SPIII leader peptidases, respectively.

| Gene ID | HMMER | dbCAN_sub | DIAMOND | SignalP | Dataset |
|---|---|---|---|---|---|
| pgaptmp_000203 | N | N | CBM12+CBM5 | Y(1–21) | EC |
| pgaptmp_000437 | CE4(62–182) | CE4_e257 | CE4 | Y(1–21) | IC/EC |
| pgaptmp_000464 | N | N | CBM50+GH25 | N | IC |
| pgaptmp_001157 | N | AA2_e1 | AA0 | N | IC/EC |
| pgaptmp_001255 | N | CBM12_e3 | N | Y(1–28) | IC/EC |
| pgaptmp_001722 | GH23(474–603) | GH23_e952 | GH23 | Y(1–19) | EC |
| pgaptmp_001840 | N | N | CBM12 | Y(1–21) | T/EC |
| pgaptmp_001854 | N | CBM5_e49 | CBM5 | Y(1–24) | T/EC |
| pgaptmp_002133 | CE1(152–377) | N | CBM5 | Y(1–27) | T |
| pgaptmp_002212 | CE2(195–406) | CBM5_e51+CE2_e8 | CBM5+CE2 | Y(1–21) | T |
| pgaptmp_002996 | AA7(31–458) | AA7_e0 | N | N | T/EC |
| pgaptmp_003133 | N | CBM50_e508 | CBM50 | Y(1–26) | IC/EC |
| pgaptmp_003266 | GH23(302–444) | GH23_e322 | GH23 | N | IC |
| pgaptmp_003309 | GH23(334–469) | GH23_e69 | GH23 | Y(1–32) | T |
| pgaptmp_003521 | N | N | CBM50 | Y(1–24) | IC |
| pgaptmp_003567 | N | CBM50_e665 | N | N | EC |

## References


1. Gooday, G.W. *The Ecology of Chitin Degradation BT-Advances in Microbial Ecology*; Marshall, K.C., Ed.; Springer: Boston, MA, USA, 1990; pp. 387–430. ISBN 978-1-4684-7612-5.
2. Younes, I.; Hajji, S.; Frachet, V.; Rinaudo, M.; Jellouli, K.; Nasri, M. Chitin Extraction from Shrimp Shell Using Enzymatic Treatment. Antitumor, Antioxidant and Antimicrobial Activities of Chitosan. *Int. J. Biol. Macromol.* **2014**, *69*, 489–498. [CrossRef] [PubMed]
3. Rinaudo, M. Chitin and Chitosan: Properties and Applications. *Prog. Polym. Sci.* **2006**, *31*, 603–632. [CrossRef]
4. FAO. *The State of World Fisheries and Aquaculture 2022*; Food & Agriculture Organization: Rome, Italy, 2022; ISBN 9789251363645.
5. Yan, N.; Chen, X. Don't Waste Seafood Waste: Turning Cast-off Shells into Nitrogen-Rich Chemicals Would Benefit Economies and the Environment. *Nature* **2015**, *524*, 155–157. [CrossRef]
6. Xie, X.H.; Fu, X.; Yan, X.Y.; Peng, W.F.; Kang, L.X. A Broad-Specificity Chitinase from Penicillium Oxalicum K10 Exhibits Antifungal Activity and Biodegradation Properties of Chitin. *Mar. Drugs* **2021**, *19*, 356. [CrossRef] [PubMed]
7. Mohan, K.; Muralisankar, T.; Jayakumar, R.; Rajeevgandhi, C. A Study on Structural Comparisons of α-Chitin Extracted from Marine Crustacean Shell Waste. *Carbohydr. Polym. Technol. Appl.* **2021**, *2*, 100037. [CrossRef]
8. Aklog, Y.F.; Egusa, M.; Kaminaka, H.; Izawa, H.; Morimoto, M.; Saimoto, H.; Ifuku, S. Protein/$CaCO_3$/Chitin Nanofiber Complex Prepared from Crab Shells by Simple Mechanical Treatment and Its Effect on Plant Growth. *Int. J. Mol. Sci.* **2016**, *17*, 1600. [CrossRef] [PubMed]
9. Boßelmann, F.; Romano, P.; Fabritius, H.; Raabe, D.; Epple, M. The Composition of the Exoskeleton of Two Crustacea: The American Lobster Homarus Americanus and the Edible Crab Cancer Pagurus. *Thermochim. Acta* **2007**, *463*, 65–68. [CrossRef]
10. Rødde, R.H.; Einbu, A.; Vårum, K.M. A Seasonal Study of the Chemical Composition and Chitin Quality of Shrimp Shells Obtained from Northern Shrimp (*Pandalus borealis*). *Carbohydr. Polym.* **2008**, *71*, 388–393. [CrossRef]
11. Tharanathan, R.N.; Kittur, F.S. Chitin—The Undisputed Biomolecule of Great Potential. *Crit. Rev. Food Sci. Nutr.* **2003**, *43*, 61–87. [CrossRef]
12. Kerton, F.M.; Liu, Y.; Omari, K.W.; Hawboldt, K. Green Chemistry and the Ocean-Based Biorefinery. *Green Chem.* **2013**, *15*, 860–871. [CrossRef]
13. Pacheco, N.; Garnica-Gonzalez, M.; Gimeno, M.; Bárzana, E.; Trombotto, S.; David, L.; Shirai, K. Structural Characterization of Chitin and Chitosan Obtained by Biological and Chemical Methods. *Biomacromolecules* **2011**, *12*, 3285–3290. [CrossRef]
14. Arbia, W.; Arbia, L.; Adour, L.; Amrane, A. Chitin Extraction from Crustacean Shells Using Biological Methods—A Review. *Food Technol. Biotechnol.* **2013**, *51*, 12–25.
15. Keyhani, N.O.; Roseman, S. Physiological Aspects of Chitin Catabolism in Marine Bacteria. *Biochim. Biophys. Acta-Gen. Subj.* **1999**, *1473*, 108–122. [CrossRef] [PubMed]
16. Li, X.; Roseman, S. The Chitinolytic Cascade in Vibrios Is Regulated by Chitin Oligosaccharides and a Two-Component Chitin Catabolic Sensor/Kinase. *Proc. Natl. Acad. Sci. USA* **2004**, *101*, 627–631. [CrossRef]
17. Souza, C.P.; Almeida, B.C.; Colwell, R.R.; Rivera, I.N.G. The Importance of Chitin in the Marine Environment. *Mar. Biotechnol.* **2011**, *13*, 823–830. [CrossRef] [PubMed]
18. Roseman, S. A Conversation with Saul Roseman. *Biochem. Biophys. Res. Commun.* **2003**, *300*, 5–8. [PubMed]
19. Arnold, N.D.; Garbe, D.; Brück, T.B. Isolation, Biochemical Characterization, and Sequencing of Two High-Quality Genomes of a Novel Chitinolytic Jeongeupia Species. *MicrobiologyOpen* **2023**, *12*, e1372. [CrossRef]
20. Yoon, J.H.; Choi, J.H.; Kang, S.J.; Choi, N.S.; Lee, J.S.; Song, J.J. Jeongeupia Naejangsanensis Gen. Nov., Sp. Nov., a Cellulose-Degrading Bacterium Isolated from Forest Soil from Naejang Mountain in Korea. *Int. J. Syst. Evol. Microbiol.* **2010**, *60*, 615–619. [CrossRef]
21. Lopes, M.A.; Gomes, D.S.; Koblitz, M.G.B.; Pirovani, C.P.; de Mattos Cascardo, J.C.; Góes-Neto, A.; Micheli, F. Use of Response Surface Methodology to Examine Chitinase Regulation in the Basidiomycete Moniliophthora Perniciosa. *Mycol. Res.* **2008**, *112*, 399–406. [CrossRef]
22. Itoh, T.; Kimoto, H. Bacterial Chitinase System as a -Model of Chitin Biodegradation. In *Targeting Chitin-Containing Organisms*; Springer: Singapore, 2019; Volume 1142, pp. 131–151. ISBN 978-981-13-7317-6.
23. Trost, M.; Wehmhöner, D.; Kärst, U.; Dieterich, G.; Wehland, J.; Jänsch, L. Comparative Proteome Analysis of Secretory Proteins from Pathogenic and Nonpathogenic Listeria Species. *Proteomics* **2005**, *5*, 1544–1557. [CrossRef]
24. Hamilton, J.J.; Marlow, V.L.; Owen, R.A.; Costa, M.d.A.A.; Guo, M.; Buchanan, G.; Chandra, G.; Trost, M.; Coulthurst, S.J.; Palmer, T.; et al. A Holin and an Endopeptidase Are Essential for Chitinolytic Protein Secretion in Serratia Marcescens. *J. Cell Biol.* **2014**, *207*, 615–626. [CrossRef]
25. Freudl, R. Signal Peptides for Recombinant Protein Secretion in Bacterial Expression Systems. *Microb. Cell Factories* **2018**, *17*, 52. [CrossRef]
26. Davies, G.; Henrissat, B. Structures and Mechanisms of Glycosyl Hydrolases. *Structure* **1995**, *3*, 853–859. [CrossRef]
27. Cantarel, B.L.; Coutinho, P.M.; Rancurel, C.; Bernard, T.; Lombard, V.; Henrissat, B. The Carbohydrate-Active EnZymes Database (CAZy): An Expert Resource for Glycogenomics. *Nucleic Acids Res.* **2009**, *37*, D233–D238. [CrossRef] [PubMed]
28. Teufel, F.; Armenteros, J.J.A.; Johansen, A.R.; Gíslason, M.H.; Pihl, S.I.; Tsirigos, K.D.; Winther, O.; Brunak, S.; von Heijne, G.; Nielsen, H. SignalP 6.0 Predicts All Five Types of Signal Peptides Using Protein Language Models. *Nat. Biotechnol.* **2022**, *40*, 1023–1025. [CrossRef] [PubMed]

29. Gíslason, M.H.; Nielsen, H.; Armenteros, J.J.A.; Johansen, A.R. Prediction of GPI-Anchored Proteins with Pointer Neural Networks. *Curr. Res. Biotechnol.* **2021**, *3*, 6–13. [CrossRef]
30. Tuveng, T.R.; Arntzen, M.Ø.; Bengtsson, O.; Gardner, J.G.; Vaaje-Kolstad, G.; Eijsink, V.G.H. Proteomic Investigation of the Secretome of Cellvibrio Japonicus during Growth on Chitin. *Proteomics* **2016**, *16*, 1904–1914. [CrossRef]
31. Wang, G.; Chen, H.; Xia, Y.; Cui, J.; Gu, Z.; Song, Y.; Chen, Y.Q.; Zhang, H.; Chen, W. How Are the Non-Classically Secreted Bacterial Proteins Released into the Extracellular Milieu? *Curr. Microbiol.* **2013**, *67*, 688–695. [CrossRef]
32. Zheng, J.; Ge, Q.; Yan, Y.; Zhang, X.; Huang, L.; Yin, Y. DbCAN3: Automated Carbohydrate-Active Enzyme and Substrate Annotation. *Nucleic Acids Res.* **2023**, *51*, gkad328. [CrossRef]
33. Forsberg, Z.; Nelson, C.E.; Dalhus, B.; Mekasha, S.; Loose, J.S.M.; Crouch, L.I.; Røhr, Å.K.; Gardner, J.G.; Eijsink, V.G.H.; Vaaje-Kolstad, G. Structural and Functional Analysis of a Lytic Polysaccharide Monooxygenase Important for Efficient Utilization of Chitin in Cellvibrio Japonicus. *J. Biol. Chem.* **2016**, *291*, 7300–7312. [CrossRef]
34. Mekasha, S.; Byman, I.R.; Lynch, C.; Toupalová, H.; Anděra, L.; Næs, T.; Vaaje-Kolstad, G.; Eijsink, V.G.H. Development of Enzyme Cocktails for Complete Saccharification of Chitin Using Mono-Component Enzymes from Serratia Marcescens. *Process Biochem.* **2017**, *56*, 132–138. [CrossRef]
35. Hemsworth, G.R.; Johnston, E.M.; Davies, G.J.; Walton, P.H. Lytic Polysaccharide Monooxygenases in Biomass Conversion. *Trends Biotechnol.* **2015**, *33*, 747–761. [CrossRef] [PubMed]
36. Müller, G.; Várnai, A.; Johansen, K.S.; Eijsink, V.G.H.; Horn, S.J. Harnessing the Potential of LPMO-Containing Cellulase Cocktails Poses New Demands on Processing Conditions. *Biotechnol. Biofuels* **2015**, *8*, 187. [CrossRef]
37. Bissaro, B.; Røhr, Å.K.; Müller, G.; Chylenski, P.; Skaugen, M.; Forsberg, Z.; Horn, S.J.; Vaaje-Kolstad, G.; Eijsink, V.G.H. Oxidative Cleavage of Polysaccharides by Monocopper Enzymes Depends on $H_2O_2$. *Nat. Chem. Biol.* **2017**, *13*, 1123–1128. [CrossRef]
38. Ma, B.; Zhang, K.; Hendrie, C.; Liang, C.; Li, M.; Doherty-Kirby, A.; Lajoie, G. PEAKS: Powerful Software for Peptide de Novo Sequencing by Tandem Mass Spectrometry. *Rapid Commun. Mass Spectrom.* **2003**, *17*, 2337–2342. [CrossRef]
39. Nakagawa, Y.S.; Kudo, M.; Loose, J.S.M.; Ishikawa, T.; Totani, K.; Eijsink, V.G.H.; Vaaje-Kolstad, G. A Small Lytic Polysaccharide Monooxygenase from *Streptomyces* Griseus Targeting α- And β-Chitin. *FEBS J.* **2015**, *282*, 1065–1079. [CrossRef] [PubMed]
40. Vaaje-Kolstad, G.; Houston, D.R.; Riemen, A.H.K.; Eijsink, V.G.H.; van Aalten, D.M.F. Crystal Structure and Binding Properties of the Serratia Marcescens Chitin-Binding Protein CBP21. *J. Biol. Chem.* **2005**, *280*, 11313–11319. [CrossRef]
41. Jones, P.; Binns, D.; Chang, H.-Y.; Fraser, M.; Li, W.; McAnulla, C.; McWilliam, H.; Maslen, J.; Mitchell, A.; Nuka, G.; et al. InterProScan 5: Genome-Scale Protein Function Classification. *Bioinformatics* **2014**, *30*, 1236–1240. [CrossRef]
42. Blum, M.; Chang, H.-Y.; Chuguransky, S.; Grego, T.; Kandasaamy, S.; Mitchell, A.; Nuka, G.; Paysan-Lafosse, T.; Qureshi, M.; Raj, S.; et al. The InterPro Protein Families and Domains Database: 20 Years On. *Nucleic Acids Res.* **2021**, *49*, D344–D354. [CrossRef]
43. Liu, H.; Cheng, M.; Zhao, S.; Lin, C.; Song, J.; Yang, Q. ATP-Binding Cassette Transporter Regulates *N*,*N*′-Diacetylchitobiose Transportation and Chitinase Production in Trichoderma Asperellum T4. *Int. J. Mol. Sci.* **2019**, *20*, 2412. [CrossRef]
44. Zeng, Y.; Charkowski, A.O. The Role of ATP-Binding Cassette Transporters in Bacterial Phytopathogenesis. *Phytopathology®* **2020**, *111*, 600–610. [CrossRef]
45. Dassa, E.; Bouige, P. The ABC of ABCs: A Phylogenetic and Functional Classification of ABC Systems in Living Organisms. *Res. Microbiol.* **2001**, *152*, 211–229. [CrossRef] [PubMed]
46. Davidson, D.A.; Elie, D.; Cedric, O.; Jue, C. Structure, Function, and Evolution of Bacterial ATP-Binding Cassette Systems. *Microbiol. Mol. Biol. Rev.* **2008**, *72*, 317–364. [CrossRef] [PubMed]
47. Bengtsson, O.; Arntzen, M.Ø.; Mathiesen, G.; Skaugen, M.; Eijsink, V.G.H. A Novel Proteomics Sample Preparation Method for Secretome Analysis of Hypocrea Jecorina Growing on Insoluble Substrates. *J. Proteom.* **2016**, *131*, 104–112. [CrossRef] [PubMed]
48. Bendtsen, J.D.; Kiemer, L.; Fausbøll, A.; Brunak, S. Non-Classical Protein Secretion in Bacteria. *BMC Microbiol.* **2005**, *5*, 58. [CrossRef] [PubMed]
49. Choo, K.H.; Tan, T.W.; Ranganathan, S. A Comprehensive Assessment of N-Terminal Signal Peptides Prediction Methods. *BMC Bioinform.* **2009**, *10*, S2. [CrossRef] [PubMed]
50. Jeffery, C.J. Mass Spectrometry and the Search for Moonlighting Proteins. *Mass Spectrom. Rev.* **2005**, *24*, 772–782. [CrossRef]
51. Brix, K.; Summa, W.; Lottspeich, F.; Herzog, V. Extracellularly Occurring Histone H1 Mediates the Binding of Thyroglobulin to the Cell Surface of Mouse Macrophages. *J. Clin. Investig.* **1998**, *102*, 283–293. [CrossRef]
52. Juncker, A.S.; Willenbrock, H.; Von Heijne, G.; Brunak, S.; Nielsen, H.; Krogh, A. Prediction of Lipoprotein Signal Peptides in Gram-Negative Bacteria. *Protein Sci.* **2003**, *12*, 1652–1662. [CrossRef]
53. Lorentzen, S.B.; Arntzen, M.; Hahn, T.; Tuveng, T.R.; Sørlie, M.; Zibek, S.; Vaaje-Kolstad, G.; Eijsink, V.G.H. Genomic and Proteomic Study of Andreprevotia Ripae Isolated from an Anthill Reveals an Extensive Repertoire of Chitinolytic Enzymes. *J. Proteome Res.* **2021**, *20*, 4041–4052. [CrossRef]
54. Liu, X.; Luo, Y.; Li, Z.; Wei, G. Functional Analysis of PrkA-a Putative Serine Protein Kinase from Mesorhizobium Alhagi CCNWXJ12-2-in Stress Resistance. *BMC Microbiol.* **2016**, *16*, 227. [CrossRef]
55. Galinier, A.; Kravanja, M.; Engelmann, R.; Hengstenberg, W.; Kilhoffer, M.C.; Deutscher, J.; Haiech, J. New Protein Kinase and Protein Phosphatase Families Mediate Signal Transduction in Bacterial Catabolite Repression. *Proc. Natl. Acad. Sci. USA* **1998**, *95*, 1823–1828. [CrossRef]

56. Kavanagh, K.L.; Jörnvall, H.; Persson, B.; Oppermann, U. Medium- and Short-Chain Dehydrogenase/Reductase Gene and Protein Families: The SDR Superfamily: Functional and Structural Diversity within a Family of Metabolic and Regulatory Enzymes. *Cell. Mol. Life Sci.* **2008**, *65*, 3895–3906. [CrossRef] [PubMed]
57. Balch, W.E.; Morimoto, R.I.; Dillin, A.; Kelly, J.W. Adapting Proteostasis for Disease Intervention. *Science* **2008**, *319*, 916–919. [CrossRef] [PubMed]
58. Bhatwa, A.; Wang, W.; Hassan, Y.I.; Abraham, N.; Li, X.-Z.; Zhou, T. Challenges Associated With the Formation of Recombinant Protein Inclusion Bodies in Escherichia Coli and Strategies to Address Them for Industrial Applications. *Front. Bioeng. Biotechnol.* **2021**, *9*, 630551. [CrossRef] [PubMed]
59. Matilla, M.A.; Ortega, Á.; Krell, T. The Role of Solute Binding Proteins in Signal Transduction. *Comput. Struct. Biotechnol. J.* **2021**, *19*, 1786–1805. [CrossRef]
60. Kanehisa, M.; Sato, Y.; Morishima, K. BlastKOALA and GhostKOALA: KEGG Tools for Functional Characterization of Genome and Metagenome Sequences. *J. Mol. Biol.* **2016**, *428*, 726–731. [CrossRef]
61. de Boer, W.; Folman, L.B.; Summerbell, R.C.; Boddy, L. Living in a Fungal World: Impact of Fungi on Soil Bacterial Niche Development. *FEMS Microbiol. Rev.* **2005**, *29*, 795–811. [CrossRef]
62. Lee, J.; Hiibel, S.R.; Reardon, K.F.; Wood, T.K. Identification of Stress-related Proteins in Escherichia Coli Using the Pollutant Cis-dichloroethylene. *J. Appl. Microbiol.* **2010**, *108*, 2088–2102. [CrossRef]
63. Giltner, C.L.; Nguyen, Y.; Burrows, L.L. Type IV Pilin Proteins: Versatile Molecular Modules. *Microbiol. Mol. Biol. Rev.* **2012**, *76*, 740–772. [CrossRef]
64. Craig, L.; Forest, K.T.; Maier, B. Type IV Pili: Dynamics, Biophysics and Functional Consequences. *Nat. Rev. Microbiol.* **2019**, *17*, 429–440. [CrossRef] [PubMed]
65. Maier, T.; Güell, M.; Serrano, L. Correlation of MRNA and Protein in Complex Biological Samples. *FEBS Lett.* **2009**, *583*, 3966–3973. [CrossRef] [PubMed]
66. Taniguchi, Y.; Choi, P.J.; Li, G.-W.; Chen, H.; Babu, M.; Hearn, J.; Emili, A.; Xie, X.S. Quantifying, *E. coli* Proteome and Transcriptome with Single-Molecule Sensitivity in Single Cells. *Science* **2010**, *329*, 533–538. [CrossRef] [PubMed]
67. Vogel, C.; Marcotte, E.M. Insights into the Regulation of Protein Abundance from Proteomic and Transcriptomic Analyses. *Nat. Rev. Genet.* **2012**, *13*, 227–232. [CrossRef]
68. Delogu, F.; Kunath, B.J.; Evans, P.N.; Arntzen, M.; Hvidsten, T.R.; Pope, P.B. Integration of Absolute Multi-Omics Reveals Dynamic Protein-to-RNA Ratios and Metabolic Interplay within Mixed-Domain Microbiomes. *Nat. Commun.* **2020**, *11*, 4708. [CrossRef]
69. Liu, Y.; Beyer, A.; Aebersold, R. On the Dependency of Cellular Protein Levels on MRNA Abundance. *Cell* **2016**, *165*, 535–550. [CrossRef]
70. Buccitelli, C.; Selbach, M. MRNAs, Proteins and the Emerging Principles of Gene Expression Control. *Nat. Rev. Genet.* **2020**, *21*, 630–644. [CrossRef]
71. Monge, E.C.; Tuveng, T.R.; Vaaje-Kolstad, G.; Eijsink, V.G.H.; Gardner, J.G. Systems Analysis of the Glycoside Hydrolase Family 18 Enzymes from Cellvibrio Japonicus Characterizes Essential Chitin Degradation Functions. *J. Biol. Chem.* **2018**, *293*, 3849–3859. [CrossRef]
72. Dekel, E.; Alon, U. Optimality and Evolutionary Tuning of the Expression Level of a Protein. *Nature* **2005**, *436*, 588–592. [CrossRef]
73. KOCH, A.L.; LEVY, H.R. Protein Turnover in Growing Cultures of Escherichia Coli. *J. Biol. Chem.* **1955**, *217*, 947–957. [CrossRef]
74. Saito, A.; Ishizaka, M.; Francisco, J.; Fujii, T.; Miyashita, K. Transcriptional Co-Regulation of Five Chitinase Genes Scattered on the *Streptomyces* Coelicolor A3(2) Chromosome. *Microbiology* **2000**, *146*, 2937–2946. [CrossRef]
75. Saito, A.; Fujii, T.; Miyashita, K. Distribution and Evolution of Chitinase Genes in *Streptomyces* Species: Involvement of Gene-Duplication and Domain-Deletion. *Antonie Van Leeuwenhoek* **2003**, *84*, 7–15. [CrossRef] [PubMed]
76. Bai, Y.; Eijsink, V.G.H.; Kielak, A.M.; van Veen, J.A.; de Boer, W. Genomic Comparison of Chitinolytic Enzyme Systems from Terrestrial and Aquatic Bacteria. *Environ. Microbiol.* **2016**, *18*, 38–49. [CrossRef]
77. Wessely, F.; Bartl, M.; Guthke, R.; Li, P.; Schuster, S.; Kaleta, C. Optimal Regulatory Strategies for Metabolic Pathways in Escherichia Coli Depending on Protein Costs. *Mol. Syst. Biol.* **2011**, *7*, 515. [CrossRef]
78. Suvorova, I.A.; Korostelev, Y.D.; Gelfand, M.S. GntR Family of Bacterial Transcription Factors and Their DNA Binding Motifs: Structure, Positioning and Co-Evolution. *PLoS ONE* **2015**, *10*, e0132618. [CrossRef]
79. Waterhouse, A.; Bertoni, M.; Bienert, S.; Studer, G.; Tauriello, G.; Gumienny, R.; Heer, F.T.; de Beer, T.A.P.; Rempfer, C.; Bordoli, L.; et al. SWISS-MODEL: Homology Modelling of Protein Structures and Complexes. *Nucleic Acids Res.* **2018**, *46*, W296–W303. [CrossRef]
80. Murthy, N.; Bleakley, B. Simplified Method of Preparing Colloidal Chitin Used For Screening of Chitinase- Producing Microorganisms. *Internet J. Microbiol.* **2012**, *10*, e2bc3. [CrossRef]
81. Lee, H.-S.; Lee, H.-J.; Choi, S.-W.; Her, S.; Oh, D.-H. Purification and Characterization of Antifungal Chitinase from *Pseudomonas* Sp. YHS-A2. *J. Microbiol. Biotechnol.* **1997**, *7*, 107–113.
82. Singh, P.P.; Shin, Y.C.; Park, C.S.; Chung, Y.R. Biological Control of Fusarium Wilt of Cucumber by Chitinolytic Bacteria. *Phytopathology* **1998**, *89*, 92–99. [CrossRef]
83. Engelhart-Straub, S.; Cavelius, P.; Hölzl, F.; Haack, M.; Awad, D.; Brueck, T.; Mehlmer, N. Effects of Light on Growth and Metabolism of Rhodococcus Erythropolis. *Microorganisms* **2022**, *10*, 1680. [CrossRef]

84. Fuchs, T.; Melcher, F.; Rerop, Z.S.; Lorenzen, J.; Shaigani, P.; Awad, D.; Haack, M.; Prem, S.A.; Masri, M.; Mehlmer, N.; et al. Identifying Carbohydrate-Active Enzymes of Cutaneotrichosporon Oleaginosus Using Systems Biology. *Microb. Cell Factories* **2021**, *20*, 205. [CrossRef] [PubMed]
85. Deng, Z.-L.; Münch, P.C.; Mreches, R.; McHardy, A.C. Rapid and Accurate Identification of Ribosomal RNA Sequences via Deep Learning. *Nucleic Acids Res.* **2022**, *50*, e60. [CrossRef] [PubMed]
86. Chen, S.; Zhou, Y.; Chen, Y.; Gu, J. Fastp: An Ultra-Fast All-in-One FASTQ Preprocessor. *Bioinformatics* **2018**, *34*, i884–i890. [CrossRef]
87. Dobin, A.; Davis, C.A.; Schlesinger, F.; Drenkow, J.; Zaleski, C.; Jha, S.; Batut, P.; Chaisson, M.; Gingeras, T.R. STAR: Ultrafast Universal RNA-Seq Aligner. *Bioinformatics* **2013**, *29*, 15–21. [CrossRef]
88. Liao, Y.; Smyth, G.K.; Shi, W. FeatureCounts: An Efficient General Purpose Program for Assigning Sequence Reads to Genomic Features. *Bioinformatics* **2014**, *30*, 923–930. [CrossRef] [PubMed]
89. Robinson, M.D.; McCarthy, D.J.; Smyth, G.K. EdgeR: A Bioconductor Package for Differential Expression Analysis of Digital Gene Expression Data. *Bioinformatics* **2010**, *26*, 139–140. [CrossRef]
90. Sentieon Sentieon Provides Complete Solutions for Secondary Dna/Rna Analysis for a Variety of Sequencing Platforms, Including Short and Long Reads. Available online: https://www.sentieon.com/ (accessed on 24 July 2023).
91. Sun, X.; Li, Y.; Tian, Z.; Qian, Y.; Zhang, H.; Wang, L. A Novel Thermostable Chitinolytic Machinery of *Streptomyces* Sp. F-3 Consisting of Chitinases with Different Action Modes. *Biotechnol. Biofuels* **2019**, *12*, 136. [CrossRef]
92. Vaaje-Kolstad, G.; Bøhle, L.A.; Gåseidnes, S.; Dalhus, B.; Bjørås, M.; Mathiesen, G.; Eijsink, V.G.H. Characterization of the Chitinolytic Machinery of Enterococcus Faecalis V583 and High-Resolution Structure of Its Oxidative CBM33 Enzyme. *J. Mol. Biol.* **2012**, *416*, 239–254. [CrossRef]
93. Vaaje-Kolstad, G.; Westereng, B.; Horn, S.J.; Liu, Z.; Zhai, H.; Sørlie, M.; Eijsink, V.G.H. An Oxidative Enzyme Boosting the Enzymatic Conversion of Recalcitrant Polysaccharides. *Science* **2010**, *330*, 219–222. [CrossRef]
94. Vaaje-Kolstad, G.; Horn, S.J.; van Aalten, D.M.F.; Synstad, B.; Eijsink, V.G.H. The Non-Catalytic Chitin-Binding Protein CBP21 from Serratia Marcescens Is Essential for Chitin Degradation. *J. Biol. Chem.* **2005**, *280*, 28492–28497. [CrossRef]
95. Paspaliari, D.K.; Loose, J.S.M.; Larsen, M.H.; Vaaje-Kolstad, G. Listeria Monocytogenes Has a Functional Chitinolytic System and an Active Lytic Polysaccharide Monooxygenase. *FEBS J.* **2015**, *282*, 921–936. [CrossRef] [PubMed]
96. Leisner, J.J.; Larsen, M.H.; Jørgensen, R.L.; Brøndsted, L.; Thomsen, L.E.; Ingmer, H. Chitin Hydrolysis by *Listeria* Spp., Including *L. monocytogenes*. *Appl. Environ. Microbiol.* **2008**, *74*, 3823–3830. [CrossRef]
97. Chaudhuri, S.; Gantner, B.N.; Ye, R.D.; Cianciotto, N.P.; Freitag, N.E. The Listeria Monocytogenes ChiA Chitinase Enhances Virulence through Suppression of Host Innate Immunity. *mBio* **2013**, *4*, e00617-12. [CrossRef]
98. Ohnuma, T.; Onaga, S.; Murata, K.; Taira, T.; Katoh, E. LysM Domains from Pteris Ryukyuensis Chitinase-A: A Stability Study and Characterization of the Chitin-Binding Site. *J. Biol. Chem.* **2008**, *283*, 5178–5187. [CrossRef]
99. Arimori, T.; Kawamoto, N.; Shinya, S.; Okazaki, N.; Nakazawa, M.; Miyatake, K.; Fukamizo, T.; Ueda, M.; Tamada, T. Crystal Structures of the Catalytic Domain of a Novel Glycohydrolase Family 23 Chitinase from Ralstonia Sp. A-471 Reveals a Unique Arrangement of the Catalytic Residues for Inverting Chitin Hydrolysis. *J. Biol. Chem.* **2013**, *288*, 18696–18706. [CrossRef] [PubMed]
100. Klancher, C.A.; Yamamoto, S.; Dalia, T.N.; Dalia, A.B. ChiS Is a Noncanonical DNA-Binding Hybrid Sensor Kinase That Directly Regulates the Chitin Utilization Program in Vibrio Cholerae. *Proc. Natl. Acad. Sci. USA* **2020**, *117*, 20180–20189. [CrossRef] [PubMed]
101. Hunt, D.E.; Gevers, D.; Vahora, N.M.; Polz, M.F. Conservation of the Chitin Utilization Pathway in the Vibrionaceae. *Appl. Environ. Microbiol.* **2008**, *74*, 44–51. [CrossRef] [PubMed]
102. Salah Ud-Din, A.I.M.; Roujeinikova, A. Methyl-Accepting Chemotaxis Proteins: A Core Sensing Element in Prokaryotes and Archaea. *Cell. Mol. Life Sci.* **2017**, *74*, 3293–3303. [CrossRef] [PubMed]
103. Yeh, J.I.; Biemann, H.-P.; Privé, G.G.; Pandit, J.; Koshland Jr, D.E.; Kim, S.-H. High-Resolution Structures of the Ligand Binding Domain of the Wild-Type Bacterial Aspartate Receptor. *J. Mol. Biol.* **1996**, *262*, 186–201. [CrossRef]
104. Ashby, M.K. Survey of the Number of Two-Component Response Regulator Genes in the Complete and Annotated Genome Sequences of Prokaryotes. *FEMS Microbiol. Lett.* **2004**, *231*, 277–281. [CrossRef]
105. Yu, E.W.; Koshland, J. Propagating Conformational Changes over Long (and Short) Distances in Proteins. *Proc. Natl. Acad. Sci. USA* **2001**, *98*, 9517–9520. [CrossRef] [PubMed]
106. Alexander, R.P.; Zhulin, I.B. Evolutionary Genomics Reveals Conserved Structural Determinants of Signaling and Adaptation in Microbial Chemoreceptors. *Proc. Natl. Acad. Sci. USA* **2007**, *104*, 2885–2890. [CrossRef] [PubMed]

*marine drugs*

MDPI

*Article*

# Spongin as a Unique 3D Template for the Development of Functional Iron-Based Composites Using Biomimetic Approach In Vitro

**Anita Kubiak [1,2,*], Martyna Pajewska-Szmyt [2], Martyna Kotula [1,2], Bartosz Leśniewski [1,2], Alona Voronkina [3,4], Parvaneh Rahimi [3], Sedigheh Falahi [3], Korbinian Heimler [5], Anika Rogoll [5], Carla Vogt [5], Alexander Ereskovsky [6], Paul Simon [7], Enrico Langer [8], Armin Springer [9,10], Maik Förste [11], Alexandros Charitos [11], Yvonne Joseph [3], Teofil Jesionowski [12] and Hermann Ehrlich [2,12,*]**

1 Faculty of Chemistry, Adam Mickiewicz University, Uniwersytetu Poznańskiego 8, 61-614 Poznan, Poland; markot6@amu.edu.pl (M.K.); barles5@amu.edu.pl (B.L.)
2 Center of Advanced Technology, Adam Mickiewicz University, Uniwersytetu Poznańskiego 10, 61-614 Poznan, Poland; mpszmyt@amu.edu.pl
3 Institute of Electronic and Sensor Materials, TU Bergakademie Freiberg, Gustav-Zeuner-Str. 3, 09599 Freiberg, Germany; voronkina@vnmu.edu.ua (A.V.); parvaneh.rahimi@esm.tu-freiberg.de (P.R.); sedigheh.falahi@doctorand.tu-freiberg.de (S.F.); yvonne.joseph@esm.tu-freiberg.de (Y.J.)
4 Department of Pharmacy, National Pirogov Memorial Medical University, Vinnytsya, Pyrogov Street. 56, 21018 Vinnytsia, Ukraine
5 Institute of Analytical Chemistry, TU Bergakademie Freiberg, Leipziger Str. 29, 09599 Freiberg, Germany; korbinian.heimler@chemie.tu-freiberg.de (K.H.); anika.rogoll@chemie.tu-freiberg.de (A.R.); carla.vogt@chemie.tu-freiberg.de (C.V.)
6 IMBE, CNRS, IRD, Aix Marseille University, Station Marine d'Endoume, Rue de la Batterie des Lions, 13007 Marseille, France; alexander.ereskovsky@imbe.fr
7 Max Planck Institute for Chemical Physics of Solids, Nöthnitzer Str. 40, 01187 Dresden, Germany; simon@cpfs.mpg.de
8 Institute of Semiconductors and Microsystems, TU Dresden, Nöthnitzer Str. 64, 01187 Dresden, Germany; enrico.langer@tu-dresden.de
9 Department Life, Light & Matter, University of Rostock, Albert-Einstein-Str. 25, 18059 Rostock, Germany; armin.springer@med.uni-rostock.de
10 Medical Biology and Electron Microscopy Centre, Rostock University Medical Center, Strempelstr. 14, 18057 Rostock, Germany
11 Institute for Nonferrous Metallurgy and Purest Materials (INEMET), TU Bergakademie Freiberg, Leipziger Str. 34, D-09599 Freiberg, Germany; maik.foerste@inemet.tu-freiberg.de (M.F.); alexandros.charitos@inemet.tu-freiberg.de (A.C.)
12 Faculty of Chemical Technology, Institute of Chemical Technology and Engineering, Poznan University of Technology, Berdychowo 4, 60-965 Poznan, Poland; teofil.jesionowski@put.poznan.pl
* Correspondence: anikub@amu.edu.pl (A.K.); herehr@amu.edu.pl (H.E.)

**Citation:** Kubiak, A.; Pajewska-Szmyt, M.; Kotula, M.; Leśniewski, B.; Voronkina, A.; Rahimi, P.; Falahi, S.; Heimler, K.; Rogoll, A.; Vogt, C.; et al. Spongin as a Unique 3D Template for the Development of Functional Iron-Based Composites Using Biomimetic Approach In Vitro. *Mar. Drugs* **2023**, *21*, 460. https://doi.org/10.3390/md21090460

Academic Editor: Azizur Rahman

Received: 11 July 2023
Revised: 20 August 2023
Accepted: 21 August 2023
Published: 22 August 2023



**Abstract:** Marine sponges of the subclass Keratosa originated on our planet about 900 million years ago and represent evolutionarily ancient and hierarchically structured biological materials. One of them, proteinaceous spongin, is responsible for the formation of 3D structured fibrous skeletons and remains enigmatic with complex chemistry. The objective of this study was to investigate the interaction of spongin with iron ions in a marine environment due to biocorrosion, leading to the occurrence of lepidocrocite. For this purpose, a biomimetic approach for the development of a new lepidocrocite-containing 3D spongin scaffold under laboratory conditions at 24 °C using artificial seawater and iron is described for the first time. This method helps to obtain a new composite as "Iron-Spongin", which was characterized by infrared spectroscopy and thermogravimetry. Furthermore, sophisticated techniques such as X-ray fluorescence, microscope technique, and X-Ray diffraction were used to determine the structure. This research proposed a corresponding mechanism of lepidocrocite formation, which may be connected with the spongin amino acids functional groups. Moreover, the potential application of the biocomposite as an electrochemical dopamine sensor is proposed. The conducted research not only shows the mechanism or sensor properties of "Iron-spongin" but also opens the door to other applications of these multifunctional materials.

**Keywords:** *Hippospongia communis*; sponge; biocorrosion; lepidocrocite; sensor; dopamine; biomineralization; biomaterials; biomimetics

## 1. Introduction

Marine sponges are a resourceful provider of a large diversity of biologically active compounds and biological materials, including chitin and spongin [1,2]. Proteinaceous spongin in the form of 3D porous network-like scaffolds is recognized as a renewable marine biomaterial due to its ability of selected demosponges (mostly bath sponges) to grow under marine ranching conditions [3]. It consists mainly of protein-derived collagen of still unknown type [4], a significant amount of sulfur (up to 5%) similar to keratins, unique halogenated amino acids, xylose, as well as traces of calcium carbonates and silica [5–8]. This biopolymer is characterized by a complex hierarchical structure based on interconnected nano- and micro-fibers [9–12]. Such a composition gives this marine biomaterial special resistance to a wide range of acids and enzymes as well as specific structural and mechanical features [13]. Consequently, there are numerous fields of spongin's applications in the form of ready-to-use scaffolds, including tissue engineering and biomedicine [14], as well as bioinspired material science [15–18].

In addition, spongin's range of applications in extreme biomimetics [19] is enhanced due to its thermal stability of up to 300 °C [6]. Three-dimensional spongin scaffolds can also be carbonized at high temperatures under anaerobic conditions. Carbonization at 1200 °C confirms the preservation of spongin scaffold morphology in the formed graphite [20]. All these features mark a breakthrough opportunity in modern materials science with respect to spongin-based scaffolding strategies [20–31].

Biomimetics is the science-driven imitation of the natural phenomena, processes, and fascinating architectural principles of natural materials using a wide range of modern tools [22]. It is an interdisciplinary direction in the creation of new materials with unique properties for broad practical applications, where special priority is given to renewable biopolymers such as spongin, which precludes the deliberate depletion of natural resources. By combining inorganic compounds (e.g., iron (III) chloride [20], titanium (IV) oxide [24], manganese (IV) oxide [23], and copper (II) tetraamine chloride [19,22]) and spongin using a nature-inspired biomimetic approach, it can provide highly attractive solutions to current technological challenges and lead to the development of new advanced, sustainable, and biodegradable composite materials [32].

Intriguingly, the skeletons of selected species of spongin-based bath sponges represent examples of naturally occurring iron-containing 3D composites formed due to the corrosion of artificial iron constructs found in marine environments (Figure 1). The biocorrosion of metal structures in seawater is the cause of elevated iron ion concentrations in water [33]. Consequently, iron ions are involved in biomineralization, which results, as an example, in the formation of a unique iron-based mineral phase, lepidocrocite, on the organic part of the three-dimensional skeleton of the marine sponge–sponging (see for an overview [5]) (Figure 1). Crystalline lepidocrocite (γ-FeOOH) is an iron oxide–hydroxide mineral with magnetic properties [34]. It is red to reddish-brown in color and has a sub-metallic luster. Lepidocrocite is commonly found on rusted metal structures underwater, in soils, and in iron ore deposits [35,36]. It is stable over a wide range of temperatures (10–60 °C) and pH (4.0–8.0) [37]. Previously, lepidocrocite as a mineral was applied as a sensor, catalyst [38–40], and adsorbent of diverse pollutants [37,41] and pigments [42].

Diverse methods for the synthesis of lepidocrocite without the presence of organic matrices were proposed previously. For example, this mineral phase can be obtained by the oxidation of $FeCl_2$ with $NaClO_3$ under slow heating of a common solution from 20 to 75 °C [43]. The "Process for the preparation of synthetic lepidocrocite" where this compound "can be produced by reacting an aqueous iron (II) chloride solution with

aqueous alkali metal hydroxides with simultaneous oxidation with atmospheric oxygen" has been patented [44].

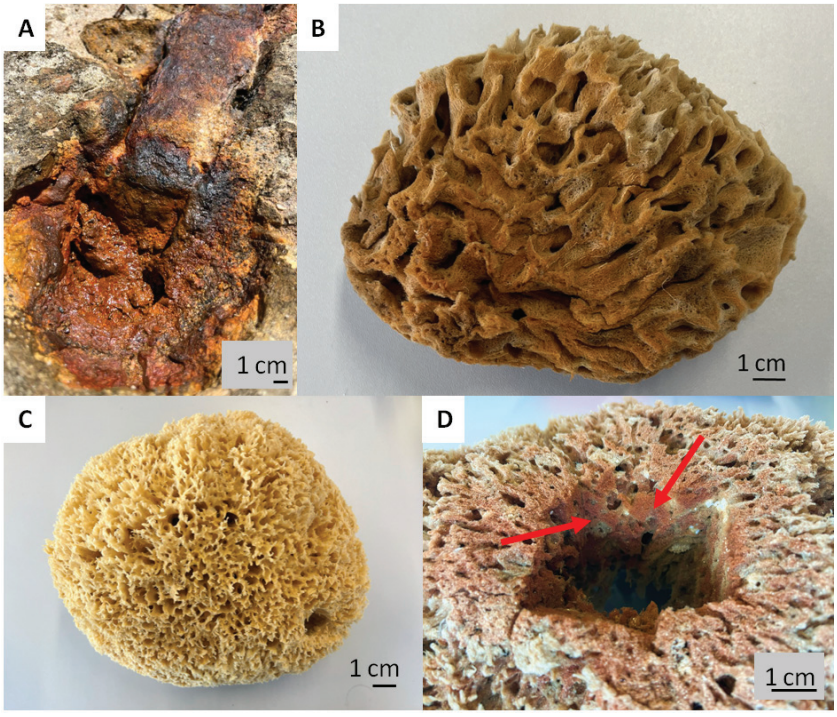


**Figure 1.** Corrosion of artificial iron-based tools after contact with seawater: (**A**) remains to be the main source of iron ions in the aquatic environment surrounding the bath sponges. This leads to the development of a well-visible rusty coloration (**B**) due to the presence of the lepidocrocite mineral phase tightly attached to the organic spongin. A natural skeleton isolated from the marine demosponge *Hippospongia communis* growing with the absence of iron ions (**C**) is yellowish in color. This kind of iron-based biomineralization is also detectable deep within the sponge skeleton ((**D**), arrows).

In this study, inspired by the previously reported phenomenon of natural biomineralization of iron into lepidocrocite in demosponges [45–47], a biomimetic method for the development of lepidocrocite on spongin scaffolds using artificial seawater under laboratory conditions, is proposed. The reaction in an artificial seawater environment between a spongin template and iron ions is presented, which leads to the formation of a new 3D composite material called "Iron-Spongin" that resembles the size and shape of the original sponge skeleton. The corresponding mechanism for the possible formation of crystalline lepidocrocite on spongin is discussed. This simple biomimetic approach has led to obtaining a specific multifunctional material that can be readily fabricated with realistic prospects for large-scale application within the framework of the marine bioeconomy of sponges [2]. Moreover, for the first time, a potential application of this unique lepidocrocite-spongin composite as a sensor for dopamine (DA) detection is proposed.

## 2. Results

### *2.1. Confocal Micro X-ray Fluorescence (CMXRF)*

Preliminary experiments with the aim to obtain knowledge of the chemistry of naturally occurring rusty sponges were carried out using CMXRF techniques. Thus, corresponding measurements were performed for the samples of spongin scaffold with naturally

formed lepidocrocite ("Spongin Fe-natural") and the control sample of the spongin scaffold ("Spongin pure") (Table 1) with identical measurement parameters.

**Table 1.** CMXRF measurements (maximum voxel counts) for the elements identified in the samples.

| Sample/Signal Count Rates | Fe-Kα | Br-Kα | Ca-Kα | S-Kα | I-Lβ | Si-Kα |
|---|---|---|---|---|---|---|
| Spongin Fe-natural | 243.0 | 39.0 | 31.0 | 27.0 | 15.0 | - |
| Spongin pure (control) | 18.0 | 19.0 | 19.0 | 18.0 | 19.0 | 12.0 |

From the fluorescence spectra of sample 'Spongin Fe-natural' five main elements are identified: sulfur, calcium, iron, bromine, and iodine. All five elements are assigned to the spongin structure (Figure 2A). Due to the relatively high count rates for iron (Table 1), a representative 3D distribution image for this element could be generated, which is in very good structural agreement with the video image (view on the top) provided by the spectrometer camera (Figure 2A).

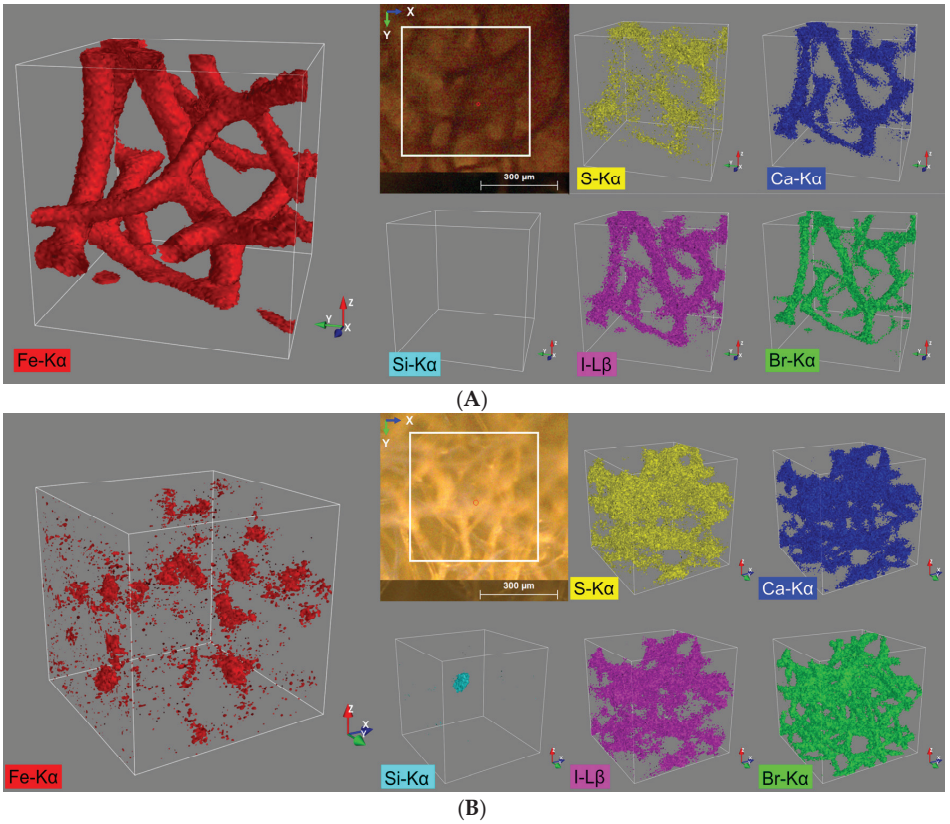


**Figure 2.** 3D distribution images of the elements S (Kα), Ca (Kα), Fe (Kα), Br (Kα), and I (Lβ) within an analysis volume of 500 µm × 500 µm × 500 µm of the (**A**) spongin with naturally formed lepidocrocite and (**B**) pure spongin (control).

For all the other four observed elements, far more diffuse elemental distribution images are obtained, caused by the overall lower signal count rates (Table 1). Nevertheless, the quality of the 3D reconstructions still allows assigning these elements to the spongin structure (Figure 2A). Even the distribution of S shows some correlation with the distribution of

the other elements, especially when measured at high sample densities (e.g., at conjunctions of the sponge strings). This result was rather unexpected since S with a relatively low Z number exhibits the lowest lateral resolution of the 5 elements detected in this sample (diameter of probing volume approx. 69.0 μm) together with a low fluorescence yield due to the high liability for absorption effects.

The same five elements and, additionally, silicon are identified from the fluorescence spectra of the control sample 'Spongin pure'. Only four of them (sulfur, calcium, iodine, and bromine) can be assigned to the spongin structure. Hereby, in contrast to the 'Spongin Fe-natural' sample, the most representative reconstruction of the spongin structure provides a 3D distribution image of bromine (Figure 2B, green). This is due to the relatively high fluorescence energy of bromine (Br Kα: 11.902 keV) and the coherent smaller excitation volume. The iron distribution (Figure 2B, red) for the control sample can also be assigned to the sponge structure, but it does not show a homogenous distribution throughout the sample and is distributed rather pointwise, and the absolute signal count rate for Fe in the control sample (compared to the 'Spongin Fe-natural' sample) is also much lower (Table 1). However, for all the observed elements, diffuse elemental distribution images (Figure 2B) were obtained. In particular, intensified silicon fluorescence radiation can be detected from a certain spot in the sample (Figure 2B, cyan). By matching it with the bromine distribution pattern, it seems to be located within the spongin structure and is probably a grain of sand (quartz) incorporated into the spongin structure (see example [48]).

### *2.2. Digital Microscopy*

In the images obtained with a digital microscope (Figure 3), a significant difference was observed in the appearance of the control sample and the "Iron-Spongin" sample after the ultrasound treatment. After 30 days of initiated corrosion, the spongin acquired a consistent rusty color, indicating the transformation of iron powder into an iron oxide form that was tightly bound to the organic matter.

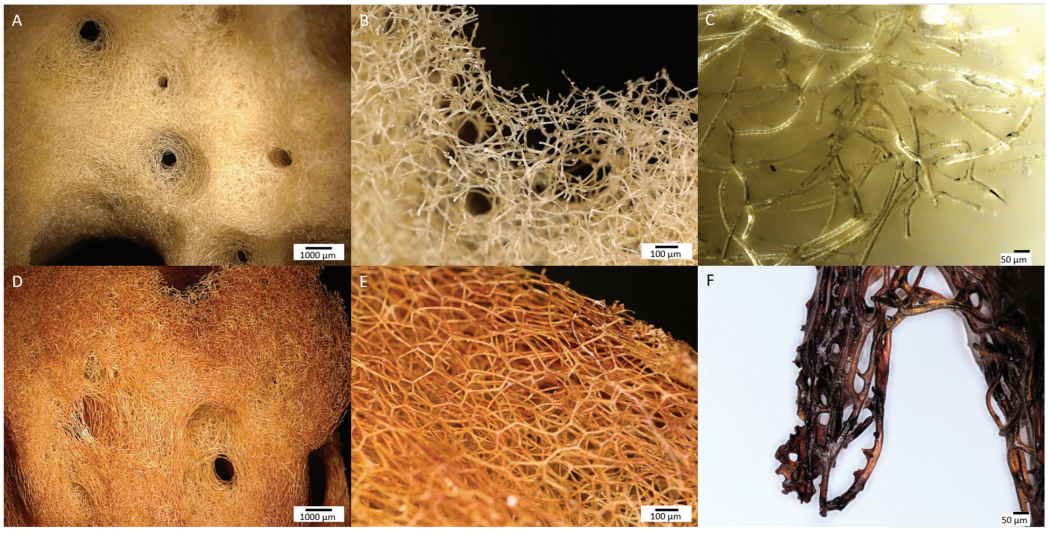


**Figure 3.** Digital microscopy imagery of two different samples of spongin from lower to higher magnifications (see the scale bars). (**A**–**C**) Control sample of spongin isolated from *H. communis* demosponge growing in a Fe-free environment remain to be yellowish in color. This biomaterial known as commercial, or bath sponge, found broad applications in human life. However, the same sponge material after induced corrosion of iron powder in artificial seawater for 30 days (**D**–**F**) becomes a rusty color that is still stable even after 2 h of ultrasonic treatment at 24 °C.

*2.3. Scanning Electron Microscopy (SEM) with Energy Dispersive X-ray Analysis (EDX)*

The SEM images in Figure 4 show the control sample and "Iron-Spongin" after ultrasonic treatment. In Figure 4A,B, a network of spongin microfibers is observed, which forms complex porous formations. An analysis of the SEM images confirmed that uniform deposition of iron oxide crystals occurred during the initiated corrosion. The SEM images in Figure 4C,D show spongin fibers densely covered with iron oxide clusters. In the approximation in Figure 4E,F, crystal-like structures can be clearly observed. The high quality of the inorganic coating may be due to the corrosion-initiated synthesis procedure, which took 30 days. Importantly, the unique porous structure with numerous iron oxide clusters was preserved even after ultrasonic treatment for 2 h.

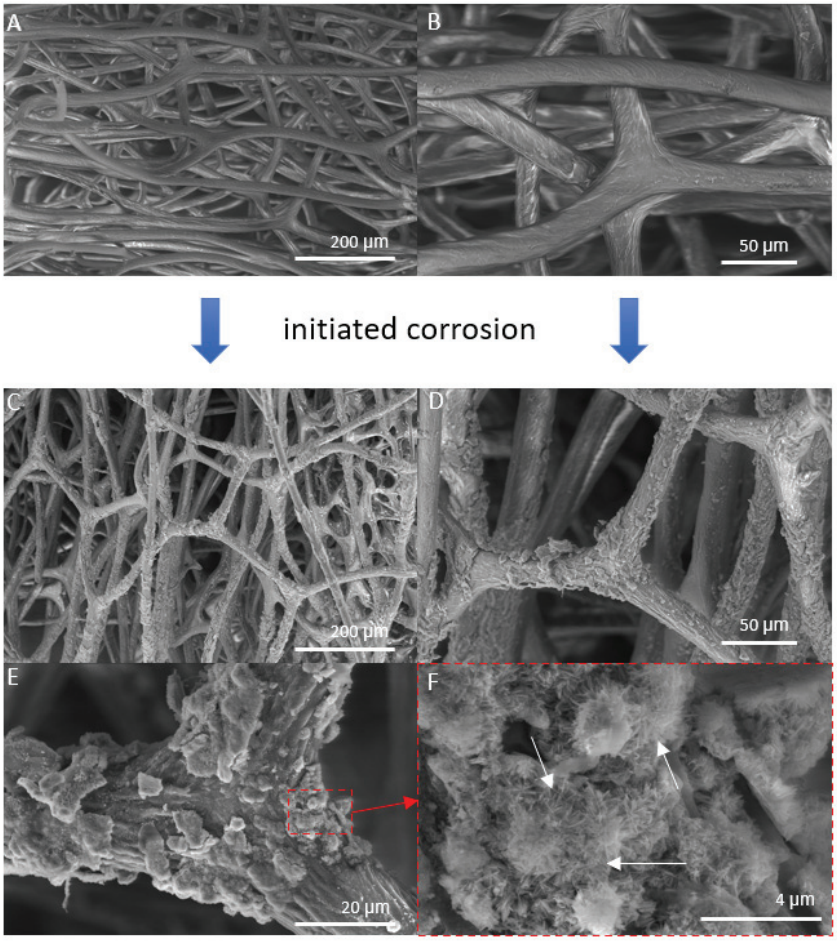


**Figure 4.** SEM images of iron-free spongin fibers with both lower (**A**) and higher (**B**) magnifications (scale bars represent 200 µm and 50 µm, respectively) (see also Figure 2A–C) drastically differ from that obtained after "Iron-Spongin" 3D composite, where the formation of crystalline phase (**C**–**F**) (scale bars represent 200 µm, 50 µm, 20 µm, and 4 µm, respectively) remains to be well visible even after ultrasonic treatment. (**F**) Arrows show needle-like crystals.

EDX analysis performed on an "Iron-Spongin after ultrasound treatment" material in the area with visible crystal-like structures showed a very high iron content (34.4 at%). In a control sample of spongin in seawater, the iron content was detected to be very low

(0.2 at%). This confirmed the formation of crystals during the initiated corrosion, consisting mainly of iron (Figure 5) (for details, see also Supplementary Materials, Figures S1–S8). The distribution of elements within the spongin fibers is shown in Figures 6 and 7. The results of the biomineralization are well visible both in the longitudinal (Figure 6A) and in the cross-section (Figures 6B and 7) of the fiber as two different (inner and outer) layers. The differences in the content of Fe and O in these layers are also noticeable (Figure 7).

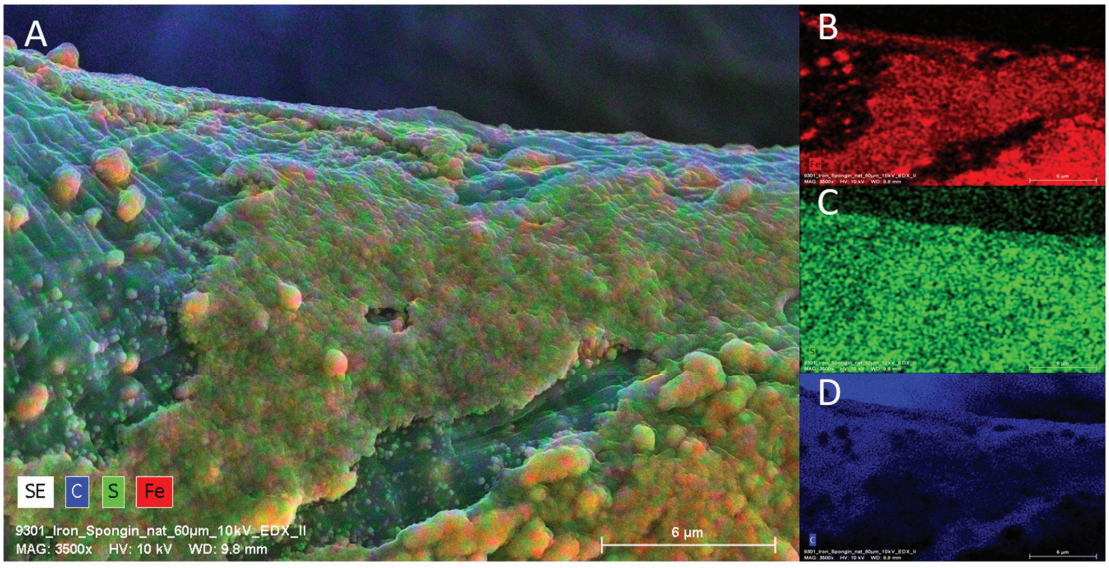


**Figure 5.** EDX Analysis (elemental mapping) of a single fiber of an "Iron-Spongin after ultrasound treatment" sample. Clearly visible is the presence of Fe and S on the surface of the scaffold strain (**A**). Fe is predominantly deposited in the crust-like structure (**B**), whereas sulfur is more or less equally distributed over the surface (**C**). C is present on the whole sample due to the organic compounds of the sample and of carbon coating used for SEM (**D**).

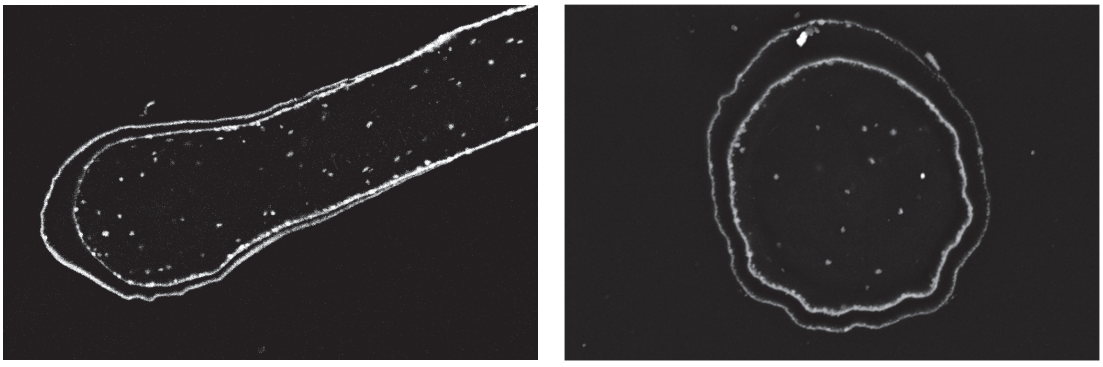

(**A**) (**B**)

**Figure 6.** Block face images of a single spongin fiber: longitudinal section (**A**) and cross-section (**B**). In both images, two different layers are distinguishable. According to the high contrast given in these layers, the presence of elements with higher atomic numbers—combined with elements origin from biological tissue—is most likely. Bars represent 10 µm.

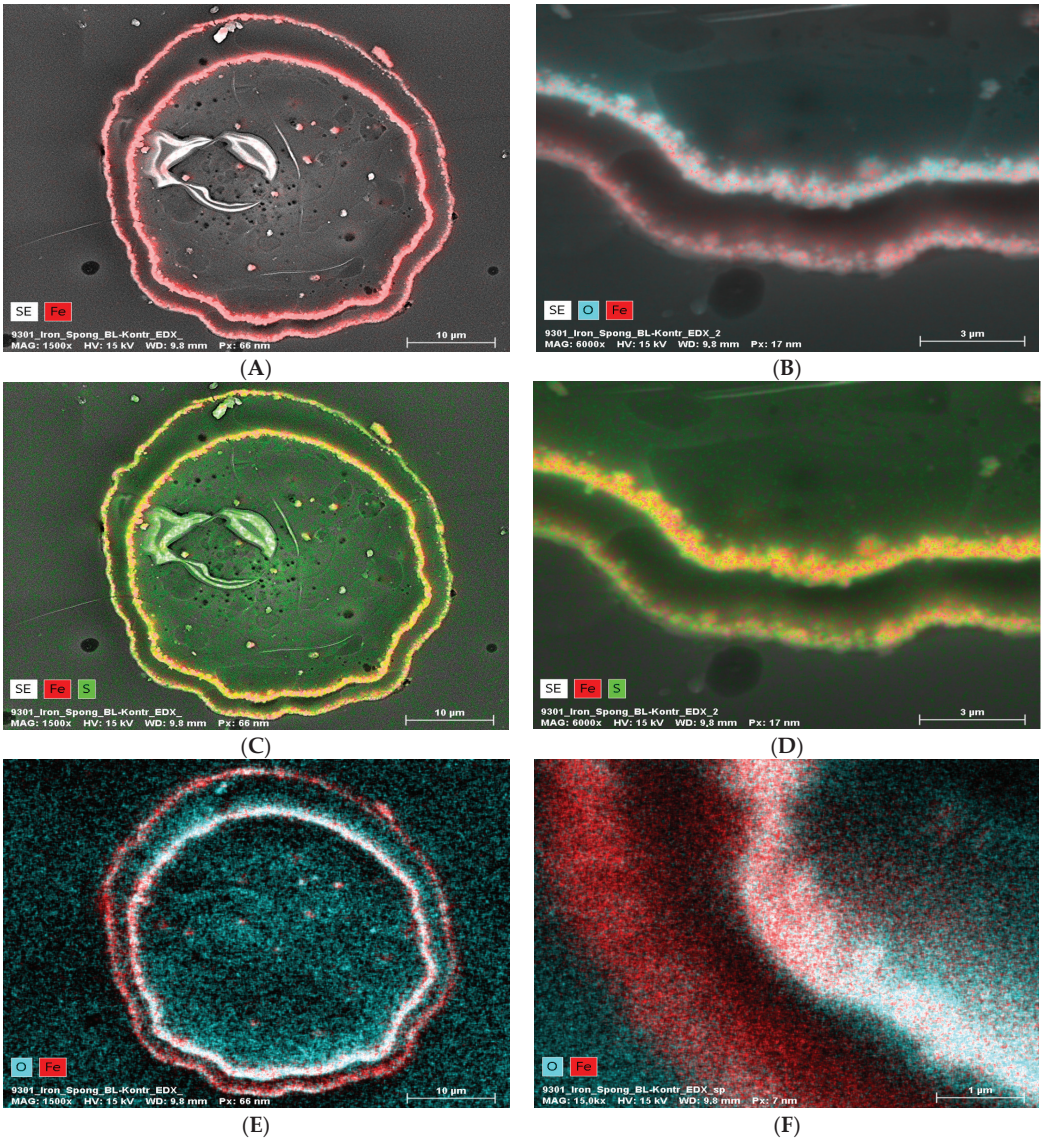


**Figure 7.** EDX analysis (elemental mapping) of a block face image cross-section of a single "Iron-Spongin after ultrasound treatment" fiber, whereby the element contents are colored in red for iron, blue for oxygen, and green for sulfur (in the case of red and green overlapping, a bright yellow color is observed). The presence of Fe and O in the two layers (**A**,**B**,**E**,**F**) is clearly visible. Sulfur seems more or less equally distributed over the cross-section (**C**,**D**). The inner layer seems to be higher in Fe and O combined with the outer layer (**B**,**E**,**F**).

### *2.4. High-Resolution Transmission Electron Microscopy (HR-TEM)*

HR-TEM analysis was used to confirm the presence of crystalline phase as lepidocrocite in the "Iron-Spongin after ultrasound treatment" sample. Figure 8A shows a cross-section of a selected section of the composite fiber with lath-like Fe-containing nanoparticles forming conglomerates inside the outer shell of the spongin fiber. This indicates the effective binding of the iron-containing phase to spongin during biomimetic-initiated corrosion

under laboratory conditions. The HR-TEM image shows that the particles consist of several nanocrystallites with crystallite sizes of 3–5 nm (Figure 8B). The calculated FFT of the HR-TEM image of the "Iron-Spongin after ultrasound treatment" sample consists of discrete diffraction spots of randomly oriented nanocrystals, reflecting the fine crystallinity of the particles (Figure 8C). An analysis of the reflections indicates that the majority of the particles can be attributed to the orthorhombic lepidocrocite phase (Amam space group [36] or Cmcm [49]). There are also interplane separations of 1.55 Å, 2.64 Å, and 2.66 Å consistent with the (110) and (100) planes of hexagonal feroxyhyte [50]. It is an unstable aqueous iron oxide that transforms spontaneously into goethite and is usually formed under high-pressure conditions on the ocean grounds [51]. For example, according to Vacelet and co-workers, lepidocrocite and a small amount of goethite are minerals that occur in the natural iron-rich skeletons of spongin-based *Spongia officinalis* marine demosponges [46].

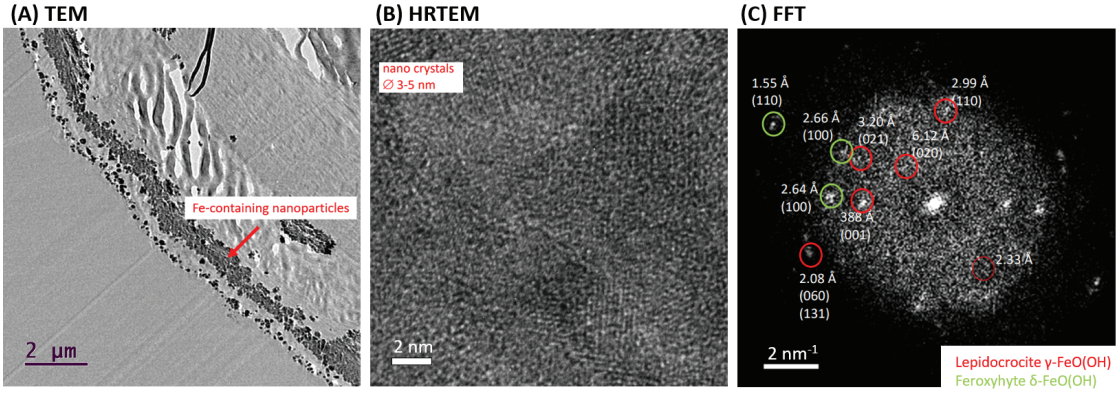


**Figure 8.** TEM overview (**A**) and high-resolution TEM (**B**) of Fe-containing nanoparticles on a selected nanofiber of "Iron-Spongin" composite investigated after ultrasound treatment. Calculated fast Fourier transform (FFT) with measurement of interplane separations indicating the occurrence of lepidocrocite and possible minor phase of feroxyhyte (**C**).

### *2.5. Fourier-Transform Infrared Spectroscopy*

In an attempt to identify the ferrous layer formed on the spongin scaffold under study, FTIR spectroscopy of the materials was performed to examine the presence of characteristic functional groups. Detailed studies were carried out for spongin control samples in seawater as well as "Iron-spongin", before and after ultrasound treatment (Figure 9A). Additional measurements were made for iron powder after 30 days in the seawater with and without the presence of the spongin scaffold (Figure 9B) (details of the bands present in the spectra, with their wave numbers and band assignments, are given in Supplementary Material, Table S1).

Most of the bands in the FTIR spectra of "Iron-Spongin" and "Iron-Spongin after ultrasound treatment" correspond to the bands in the spectrum of the control sample of spongin in seawater. The bands that occur only in the samples in the presence of corroded iron powder are 570, 740, 1021, and 1150 $cm^{-1}$ (Figure 9A). The band at 570 $cm^{-1}$ is characteristic of Fe-O vibrations in iron oxides [52,53]. The most intense band at 1021 $cm^{-1}$ in the FT-IR spectra is associated with lepidocrocite (γ-FeOOH) [54]. The bands at 1150 $cm^{-1}$ and 740 $cm^{-1}$ can also be assigned to OH deformation and bending in γ–FeOOH [55]. The high-intensity bands at 1021 $cm^{-1}$ and 740 $cm^{-1}$ may suggest that a well-crystallized lepidocrocite phase is strongly present.

The effect of spongin scaffold on iron corrosion in seawater was also investigated (Figure 9B). The band characteristic of iron oxides (570 $cm^{-1}$) and lepidocrocite (740, 1021, 1150 $cm^{-1}$) were observed only in the FTIR spectrum of the corroded iron powder after 30 days in seawater in the presence of the spongin scaffold.

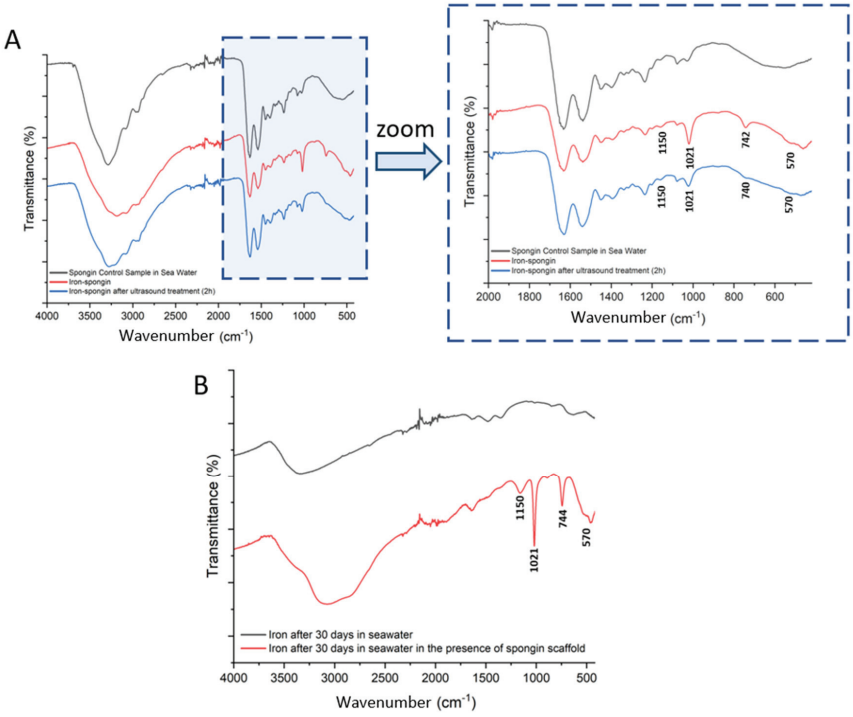


**Figure 9.** FTIR spectra of the samples: (**A**) spongin control sample and "Iron-Spongin after ultrasound treatment" along with an approximation in the range of 2000–420 $cm^{-1}$; (**B**) iron powder after 30 days insertion into seawater with and without the presence of spongin scaffold.

### *2.6. X-ray Diffraction*

The X-ray diffraction pattern of spongin under study is similar to that reported previously [15,22,24]. The treatment of spongin samples with iron powder using artificial seawater (see Section 4) causes the appearance of reflection characteristics for that of lepidocrocite [56], which confirms that this mineral phase is formed during the preparation of the "Iron-Spongin" composite. Further data analysis confirms the formation of lepidocrocite on both the "Iron-Spongin" sample and on "Iron-Spongin after ultrasound treatment". This is indicated by the peaks present in the XRD graphs of these samples at ~14°, ~27°, ~38°, ~47°, ~53°, ~61°, and ~68°, which correspond to the (020), (120), (111), (020), (151), (231), and (251) crystal planes, respectively (Figure 10). These peaks correspond to polymorphs of the iron oxyhydroxide lepidocrocite (γ-FeOOH) [57]. For comparison, a diffractogram of iron powder (Figure 10E) obtained after 30 days in seawater in the presence of spongin with lepidocrocite-characteristic reflections is included.

### *2.7. Thermogravimetric Analysis*

The thermal degradation of a control spongin sample in seawater and "Iron-Spongin after ultrasound treatment" was studied. Two weight losses occur during the thermal degradation of both samples (Figure 11). The first, a weight loss of about 5–8% in the 70–150 °C range, is related to the evaporation of physically adsorbed and hydrogen-bonded water from the spongin scaffold [12]. The second weight loss in the temperature range of 230–450 °C is about 63.2% for the control sample and about 44.8% for "Iron-Spongin after ultrasound treatment". This may be related to the decomposition of the protein matrix: the disintegration of the peptide bonds [12,25], and thermal degradation of disulfide bonds [12,58] and hydrogen bonds [12]. In the "Iron-Spongin after ultrasound treatment"

material, the thermal stability is higher than that of the control spongin sample. The difference in thermal stability can be attributed to the formation of bonds between spongin and iron and electrostatic interactions formed between the hydroxyl groups of spongin and lepidocrocite [29].

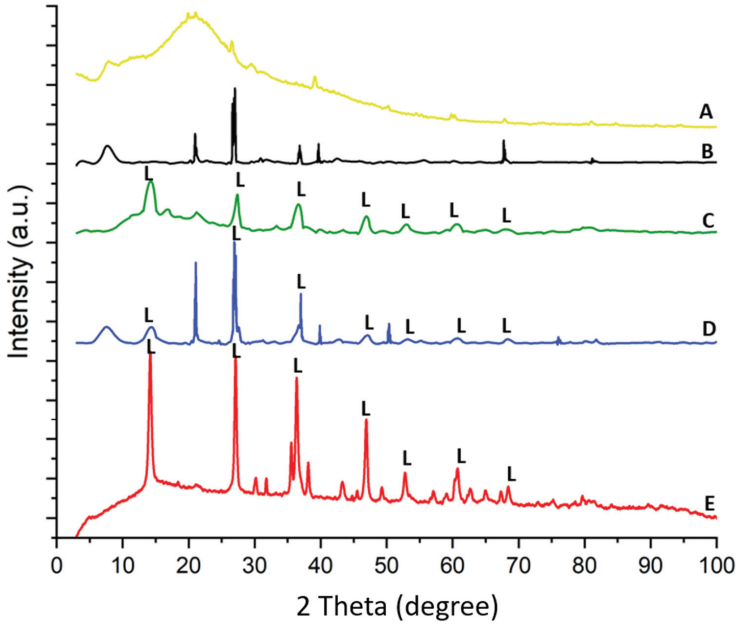


**Figure 10.** XRD patterns of (**A**) spongin, (**B**) spongin control sample after placement into seawater, (**C**) "Iron-Spongin", (**D**) "Iron-Spongin after ultrasound treatment", and (**E**) iron powder after placement in the seawater in the presence of spongin.

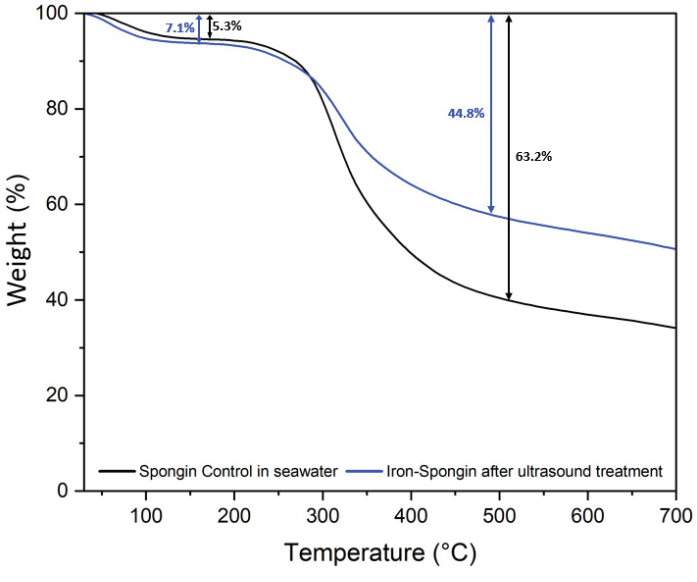


**Figure 11.** Thermogravimetric (TG) curves of spongin control sample in seawater and the "Iron-Spongin after ultrasound treatment".

### *2.8. Magnetic Properties*

The "Iron-Spongin after ultrasound treatment" is attracted by a neodymium magnet with a pull force of 192 N (see Supplementary Materials, Figure S9). It is well known that lepidocrocite is paramagnetic at room temperature with low field magnetic susceptibility [34,59,60]. Paramagnetism is the phenomenon whereby a material magnetizes in an external magnetic field in a direction consistent with the direction of the external field. This phenomenon occurs in all atoms and molecules with unpaired electrons, e.g., free atoms, free radicals, and transition metal compounds that contain ions with unfilled electron shells [61]. Paramagnetic materials have a relative magnetic permeability slightly greater than 1 (i.e., low positive magnetic susceptibility), and are therefore attracted to magnetic fields [62]. In contrast to the "Iron-Spongin after ultrasound treatment" represented here, all 35 naturally occurring rusty sponges (see Figures 1B,D and 15), which are approved for their magnetic features under the same experimental conditions, show no attachment to the neodymium magnet.

### *2.9. Dopamine Detection*

The application of spongin-based sensors remains to be in trend. In this study, we used the developed composite for the detection of DA. This compound is a vital catecholamine neurotransmitter found in mammals' central and peripheral nervous systems. It regulates a wide variety of neuronal functions, including emotion, behavior, cognition, learning, memory, and movement. In living systems, DA controls the transmission of signal messages to various domains of the brain and other parts of the body. In addition, DA receptors are vital targets for neuropsychiatric illnesses such as depression, Parkinson's, schizophrenia, and Huntington's [63,64]. Therefore, the quantitative detection of DA in biological and chemical systems is critical. Various analytical methods are used for the detection of DA, but each of them has some disadvantages. Among them, electrochemical methods have proven to be the most effective for the determination of DA in the presence of other biological molecules [65–68]. However, developing a simple, cost-effective, and compatible composite material as an electrode material for the selective detection of DA at low concentrations without interfering with other biologicals is challenging.

Herein, for the first time, a novel, low-cost, sensitive, and selective electrochemical sensor for the detection of DA based on carbon paste electrodes (CPE) modified with naturally occurring iron-spongin and biomimetic "Iron-Spongin after ultrasound treatment" is developed. The electrodes are denoted as N-Iron-Sp/CPE and B-Iron-Sp/CPE, respectively. The amperometric responses of N-Iron-Sp/CPE and B-Iron-Sp/CPE for the successive addition of different concentrations of DA in 0.1 M phosphate buffer pH 6.5 are given in Figure 12A. The oxidation reaction at each electrode was fast in reaching the dynamic equilibrium, producing a steady-state current within almost 10 s. To calculate the sensitivity of the electrodes, calibration curves were plotted (Figure 12B), which recorded the increase in the current with each subsequent addition of DA. The linear regression equation of DA oxidation for each of N-Iron-Sp/CPE and B-Iron-Sp/CPE was obtained between 5 μM to 1.3 mM with an equation of I (μA) = 28.104 CDA (mM) + 0.7336 ($R^2$ = 0.998) and I (μA) = 17.527 CDA (mM) + 0.4549 ($R^2$ = 0.9981), respectively. The sensitivity of N-Iron-Sp/CPE and B-Iron-Sp/CPE was found to be 0.22 μA $mM^{-1}$ $cm^{-2}$ and 0.14 μA $mM^{-1}$ $cm^{-2}$, respectively. The remarkable electrochemical behavior of each electrode toward DA sensing is ascribed to the excellent electrocatalytic performance of crystalline Fe-oxide tightly bound to the 3D spongin scaffold. The high electrocatalytic activity, low response time of 2 s, and high sensitivity of "Iron-Spongin" are attributed to its high concentration of active sites and facile charge transfer characteristics.

The specificity of the B-Iron-Sp/CPE sensor was evaluated in the presence of possible coexisting species (sucrose, glucose, sodium chloride (NaCl), and UA). The obtained results showed that the fabricated sensor diminished the influence of possible interfering species and exhibited excellent selectivity toward DA detection. The detection of DA in human urine has received interest in medical diagnostics due to the impacts of abnormal

concentrations of DA in regulating blood pressure, lipolysis, Huntington's disease, and Parkinson's disease. The detection of DA in human urine samples was performed using B-Iron-Sp/CPE to assess the practical applicability of the constructed DA sensor. A recovery of 93–115% was obtained for the studied sample, indicating the accuracy and reliability of the constructed sensor, which guaranteed its on-site applications.

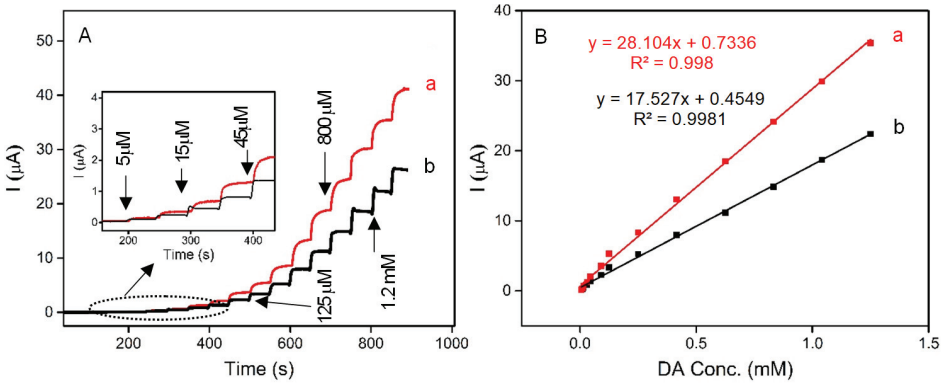


**Figure 12.** (**A**) Amperograms recorded in 0.1 M phosphate buffer pH 6.5 with the successive addition of DA (5 μM to 1.3 mM) at (a) N-Iron-Sp/CPE, and (b) B-Iron-Sp/CPE. (**B**) Calibration curve for the linear response of current vs. DA concentration.

## 3. Discussion

Lepidocrocite, as a biomineral, has been known since its discovery in the teeth of Chiton mollusc (Lowenstamm, 1967) [69]. Also, a microbial scenario of its formation, including the so-called forced biomineralization [70], is well documented in the literature. Bacterial biomineralization of lepidocrocite has been reported for diverse nitrate-reducing Fe(II)-oxidizing bacteria [71], as well as in denitrifying As(III)-oxidizing bacterium [72] under anaerobic conditions. Also, it was observed that iron oxyhydroxide crystallization could be directed during the cultivation of *Leptothrix* sp. bacterium [73]. The formation of strongly magnetic nanoscale particles due to lepidocrocite bioreduction by the iron-reducing bacterium *Shewanella putrefaciens* ATCC 8071 is described in [74]. In lithotrophic iron-oxidizing bacteria, such as *Gallionella ferruginea* or *Mariprofundus ferrooxydans*, up to 100 nm large lepidocrocite crystals nucleate on the surface of organic extracellular twisted ribbon-like stalks [75]. Maybe this phenomenon is based on the templating activity of bacterial exopolysaccharides, which are known as stabilizers of lepidocrocite. For example, iron oxyhydroxide–polysaccharide hybrid colloids with unusual pH stability of up to pH 13 are reported [76].

To the best of our knowledge, there are only two publications concerning the in vitro development of lepidocrocite-based composites using biopolymers as templates. For example, highly crystalline layers of lepidocrocite up to 125 nm large are obtained due to biomimetic mineralization of protein microtubules (MTs) with a diameter of 25 nm. It is suggested that MTs "can be used as scaffolds for the in situ production of high-aspect-ratio inorganic nanowires" [77]. In another paper, fibrillary collagen was used as a generic mineralization template for lepidocrocite [78]. The mineral phase was obtained both on and within the collagen fibrils after mixing them with $Fe(OH)_2$ and the addition of poly (aspartic acid) to promote the crystallization of lepidocrocite.

Based on the previous literature data [45–47,79] on the interactions between marine demosponges and iron, it was possible to design a nature-inspired biomimetic method for the mineralization of iron on spongin fibers. As early as 1968 [45], the existence of crystalline iron mineralization in the spongin fibers of *Ircinia fasciculate*, *Spongia graminea*, and *S. officinalis* marine sponges was first discovered. Then, it was proven that the reddish-

brown microgranules are formed of very fine crystallites of poorly organized lepidocrocite (Figure 13). It was also found that selected marine sponges grow only in the presence of iron ions [80], which are supplied to waters mainly from atmospheric sediments [81], hydrothermal vents [82], marginal sediments [83], artificial fertilization [84], groundwater discharges [85], and biocorrosion of artificial metal structures and shipwrecks [5,33,86]. The source of iron ions due to the biocorrosion of corresponding metallic constructs in seawater is crucial, especially when sponges use them as the substrate for attachment and growth [87]. Nevertheless, the mechanism of iron biomineralization on spongin fibers in nature, as well as under the laboratory conditions used in this study, is still not fully understood.

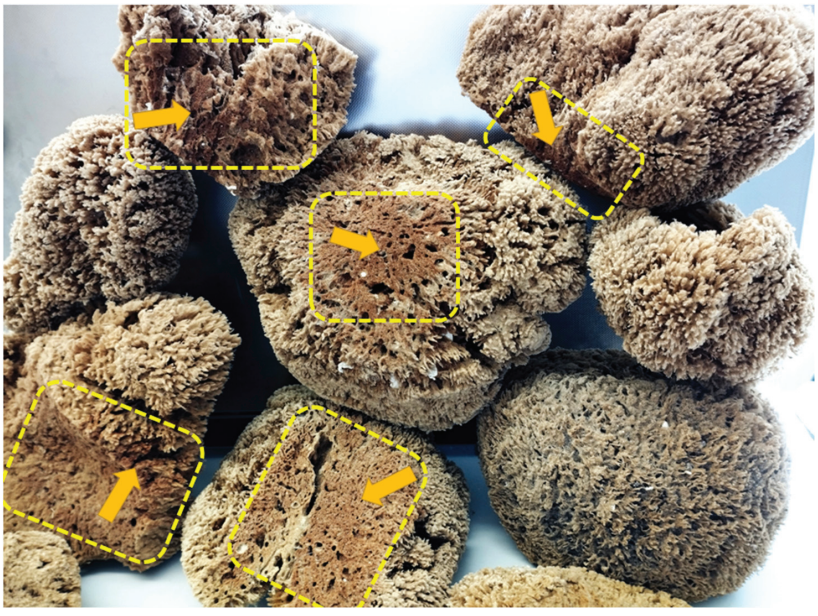

**Figure 13.** Rusty bath sponges represent a potential source of naturally occurring iron oxide-based 3D constructs, which can be useful in bioinspired material science and biomimetics. Well-defined lepidocrocite-containing locations within the sponge skeletons are marked in yellow.

The possible mechanism of lepidocrocite formation on spongin fibers may be associated with spongin amino acid sequences, including cysteine, histidine, lysine, or tyrosine [7,8]. Functional groups derived from amino acids (e.g., –SH, –OH, $–NH_2$, and –COOH) [22] and the presence of electron donor atoms (O, N, S) result in the ability to form complexes with iron ions [88]. A large group of Fe-S clusters of proteins is known; in most cases, the terminal ligands attached to iron are derived from thiol groups from cysteinyl residues [89–92]. Therefore, it is possible that cysteine/cysteine sulfur is involved in the formation of an iron-based crystalline mineral phase in spongins. Iron is a transition metal with well-known redox and ligand-binding properties [93]. It is capable of accepting and donating electrons, transitioning between the ferric ($Fe^{3+}$) and ferrous ($Fe^{2+}$) forms [94]. In seawater at pH 8.1, the $Fe^{2+}$ form is rapidly oxidized to the $Fe^{3+}$ form, so it exists mainly in the form of iron(III) oxyhydroxide, which has a very low solubility and a thermodynamically stable oxidation state [95–98]. Cornell and Schneider [99] demonstrated that in the presence of cysteine at pH 8.0, a fast transformation of non-crystalline iron(III) hydroxide into mainly crystalline lepidocrocite with a small amount of goethite occurs. Alkaline seawater conditions affect the surface chemistry of spongin—cysteine-derived thiol groups (SH–), which are converted to thiolate anions (RS–) [100]. Then, the interaction between cysteine and non-crystalline iron(III) hydroxide involves the oxidative dehydration of

cysteine, which can form disulfide bonds (S–S) to produce cysteine [101,102]. There is also a concomitant reduction in some interfacial ferric sites, transforming the solid iron phase into a compound with mixed-valence $Fe^{2+}/Fe^{3+}$. This compound dissolves more readily than the starting material, and the dissolution/precipitation mechanism then leads to more thermodynamically stable iron mineral phases, such as lepidocrocite (Figure 14) [103–105].

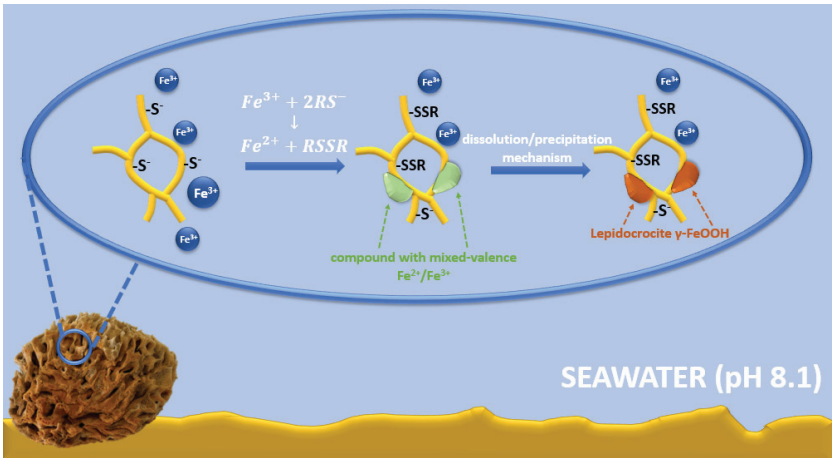


**Figure 14.** Schematic representation of the possible mechanism of lepidocrocite formation on spongin fibers.

Learning about the mechanism of iron mineralization in spongin fibers is essential to understanding the nature of the exceptional composite "Iron-Spongin". It is easy and simple to prepare, and it consists of a biodegradable and renewable source—spongin. By combining both components, lepidocrocite (magneticity, stability over a wide range of temperatures (10–60 °C), pH (4.0–8.0), and spongin (3D porous structure, high thermal stability, resistance to a wide range of acids and enzymes), a nature-inspired biomaterial with many remarkable features, are created.

In this study, it was shown that such a 3D composite can be used as a sensor for neurotransmitter detection. Many methods for quantifying neurotransmitters, such as DA, are available, but most of them have their limitations [106–109]. Recently, there has been increased attention on the use of electrochemical methods for neurotransmitter analysis due to their advantages, such as high sensitivity, simplicity of analysis, fast time response, and low cost of material consumption [110]. The electroanalysis method relies on an enzymatic or enzyme-free method for detecting neurotransmitters such as DA. The main disadvantage of enzymatic biosensors is the insufficient stability of the enzymes used to develop these sensors. Their shortcomings create a real need for the development of non-enzymatic sensors. Non-enzymatic sensors generally detect chemical or biological substances through their redox activity. Electrochemical sensors based on metal oxides, such as iron, are ideal for the electroanalysis of neurotransmitters because of their simplicity, low cost, fast response, and good portability [111,112]. In their application, the electrochemical detection of specific analytes is enabled by the behavior of semiconductors, while the separation of analytes is achieved by magnetic properties. Lepidocrocite, which has magnetic properties combined with spongin, provides a large surface area and a well-developed 3D structure that seems to possess the potential for use as a DA sensor. Various magnetic iron oxide nanoparticles [113–115] have been proven to be excellent non-enzymatic materials for DA sensing. Previous electrochemical studies of lepidocrocite have shown its high sensitivity and selectivity in detecting DA [116]. In our study, the "Iron-Spongin" composite as a non-enzymatic electrode showed high sensitivity toward DA detection, which was attributed to the excellent electrocatalytic performance of Fe-oxide adsorbed on the unique

3D spongin scaffold. The development of "Iron-Spongin" 3D constructs in this study will stimulate experiments on their application for sodium-ion batteries, or for photocatalytic hydrogen production, where heterostructured lepidocrocite titanate-carbon nanostructures have already been used recently [117,118]. Also, such composites as potential magnetic scaffolds [119] should be investigated in the future.

## 4. Materials and Methods

### *4.1. Materials*

Purified, acellular, and mineral-free spongin scaffolds of *Hippospongia communis* (Lamarck, 1814) marine demosponges were purchased from INTIB GmbH (Freiberg, Germany). InstantOcean®SeaSalt acquired from Spectrum Brands (Blacksburg, VA, USA) was used to prepare artificial seawater. Sodium hydroxide (analytical grade) purchased from EuroChem BGD (Tarnów, Poland) was used to prepare a 1 M (mol/L) NaOH solution. Iron powder 99.99% (with a particle size in the range of 25–100 μm) was acquired from Chempur (Piekary Śląskie, Poland). To prepare the artificial seawater, 18 g of sea salt was placed in a glass bottle and dissolved in 500 mL of distilled water. The pH of the solution was brought to pH 8.1 (the value present in natural seawater [120]) with 1 M NaOH solution. Dopamine (DA), paraffin oil, and sodium phosphate ($Na_2HPO_4$ and $NaH_2PO_4$) were purchased from Sigma-Aldrich (Burlington, MA, USA). Phosphate-buffered solution (PBS, 0.1 M, pH 6.5) was prepared using a mixture of stock solutions ($NaH_2PO_4$ and $Na_2HPO_4$) and employed as an electrolyte solution for amperometric measurements. Graphite powder was obtained from Merck (Darmstadt, Germany).

### *4.2. Samples Preparation*

Preparation of the "Iron-Spongin" Material

A fragment of spongin scaffold weighing 1.1 g and measuring 3 cm × 6 cm × 3 cm was placed in a 500 mL bottle of artificial seawater, and 3.5 g of iron powder was added. The whole content was shaken vigorously for one minute until the entire spongin scaffold was covered with iron powder. Then, it was stored in the lab for 30 days at room temperature. Similarly, a control sample without iron powder and a control sample of iron powder alone in seawater without the presence of the spongin scaffold were prepared. After this, the obtained "Iron-Spongin" material with rusty color was placed in an ultrasonic bath (Bandelin, Berlin, Germany) for 2 h at room temperature to remove excess iron powder that did not bond to the spongin scaffold (Figure 15). The dry mass of the "Iron-Spongin" samples was measured to be 1.967 ± 0.035 g prior to and 0.708 ± 0.040 g after ultrasonic treatment.

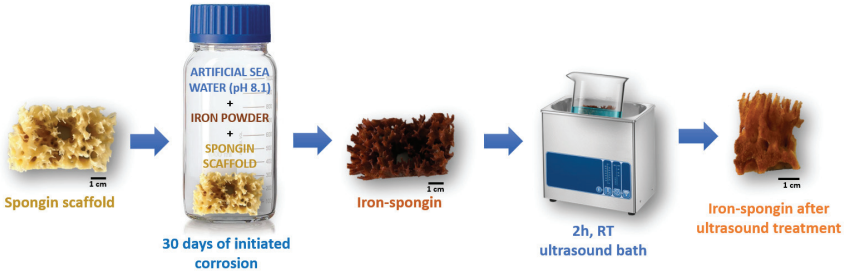


**Figure 15.** Schematic overview of the preparation of "Iron-Spongin" material using iron powder in artificial seawater with pH 8.1 at 24 °C.

The "Iron-Spongin" material, spongin control sample, iron from seawater alone, and iron from seawater and the presence of the sponge scaffold were then air-dried for further analysis.

*4.3. Characterisation Techniques*

4.3.1. Digital Microscopy

A control sample of spongin in seawater and iron-spongin after ultrasonic treatment was observed and analyzed using an advanced imaging system consisting of a VHX-6000 digital optical microscope (Keyence, Osaka, Japan) and VH-Z20R zoom lenses (magnification up to 200×), as well as a VHX-7000 digital optical microscope (Keyence, Osaka, Japan) and VHX-E20 (magnification up to 100×) and VHX-E100 (magnification up to 500×) zoom lenses.

4.3.2. Scanning Electron Microscopy (SEM) with Energy Dispersive X-ray Analysis (EDX)

For block-face analysis, the regions of interest (ROI) of TEM samples in resin blocks were trimmed using the Leica EM Trim 2 (Leica Microsystems, Wetzlar, Germany). In order to obtain a flat surface, the samples were cut with a Leica UC7 ultramicrotome using a diamond knife (Diatome, Nidau, Switzerland).

The samples were mounted on a heavy metal-free Al-SEM-carrier (co. PLANO, Wetzlar, Germany) with adhesive conductive carbon tape (Spectro Tabs, TED PELLA INC, Redding, CA, USA) and coated with carbon (5.0 nm thickness) under vacuum (CCU 010 HV-Coating Unit, Co. Safematic GmbH, Zizers, Switzerland).

The samples were analyzed using a field emission scanning electron microscope (SEM, MERLIN® VP Compact, Co. Zeiss, Oberkochen, Germany) equipped with an energy-dispersive X-ray (EDX) detector (XFlash 6/30, Co. Bruker, Berlin, Germany). Representative areas or defined lines of the samples were analyzed and mapped for elemental distribution based on the EDX-spectra data using QUANTAX ESPRIT Microanalysis software (version 2.0, Berlin, Germany) SEM images were taken from selected regions (the conditions are shown in the figures).

Comparative SEM-EDX analyses of the control sample and iron-spongin after ultrasound treatment were carried out using a scanning electron microscope (Quanta 250 FEG; FEI Ltd., Brno, Czech Republic) correlated with an energy-dispersive X-ray spectrometer (EDX Team Software) to determine the elemental composition and surface morphology of the samples studied.

Moreover, SEM and supplementary EDX measurements were carried out using a low-vacuum scanning electron microscope, JEOL JSM-6610LV, with a LaB6 cathode, which was also equipped with an energy-dispersive X-ray spectrometer (10 $mm^2$ Silicon Drift Detector (SDD) X-Flash 6∣10, Bruker Co., Berlin, Germany).

4.3.3. High-Resolution Transmission Electron Microscopy (HR-TEM)

Conventional TEM analysis was carried out using the FEI Tecnai F30-$G^2$ with Super-Twin lens (FEI) with a field emission gun at an acceleration voltage of 300 kV. The point resolution amounted to 2.0 Å, and the information limit was about 1.2 Å. The microscope was equipped with a wide-angle slow-scan CCD camera (MultiScan, 2k × 2k pixels; Gatan Inc., Pleasanton, CA, USA).

4.3.4. Transmission Electron Microscopy (TEM)

Selected fragments of "Iron-Spongin after ultrasonic treatment" were placed in distilled $H_2O$ for one night at room temperature (RT). Then, they were dehydrated in an ethanol series from 30% to 100% at RT and embedded in Araldite (Sigma-Aldrich, Burlington, MA, USA) epoxy embedding media according to the manufacturer's instructions. Ultra-thin sections (60–70 nm) were cut with an Ultramicrotome PowerTome XL (Boeckeler Instruments, Inc., Tucson, AZ, USA) equipped with a Druker International b.V (Amsterdam, the Netherlands) 45 diamond knife, double-stained with UranyLess (EMS), lead citrate, and lead citrate. Ultrathin sections were studied under Tecnai G2 20 TWIN (FEI Company, Alhambra, CA, USA) transmission electron microscope with an acceleration voltage of 200 kV.

4.3.5. Fourier-Transform Infrared Spectroscopy

FTIR spectra of the control and obtained samples were recorded using a Nicolet iS50 spectrometer (Thermo Fisher Scientific Co., Hillsboro, OR, USA). Each measurement was performed using a built-in attenuated total reflectance (ATR) accessory. The analysis was carried out in the wavelength range of 4000–400 $cm^{-1}$.

4.3.6. X-ray Diffraction

The X-ray studies of the examined materials were performed using a powder diffractometer (SmartLab Rigaku, Tokyo, Japan) with a Cu K-alpha X-ray tube, in the range of 3–80 (2 theta), scan step 0.01, and scan speed 4°/min.

4.3.7. Thermogravimetric Analysis

Thermogravimetric analysis (TG/DTG) was performed on a TGA/DSC1 Star Systemanalyzer (Mettler Toledo, Columbus, OH, USA) Measurements were carried out at a heating rate of 10 °C/min under nitrogen flow conditions (60 mL/min) in the temperature range of 30–700 °C.

4.3.8. Confocal Micro X-ray Fluorescence (CMXRF)

CMXRF measurements were performed with a modified commercial MXRF spectrometer (M4 TORNADO) by Bruker Nano GmbH, Berlin, Germany, which was equipped with a 30 W Rh-microfocus X-ray tube (50 kV, 600 μA), a polycapillary full lens in the excitation channel for X-ray focusing, and a 30 $mm^2$ silicon drift detector (SDD). Due to the modification, a polycapillary half lens was installed in the detection channel before a 60 $mm^2$ SDD. The confocal arrangement of both lenses resulted in a defined probing volume, providing three-dimensional resolved element analysis by lateral movement of the sample with an xyz-motorized sample stage. The calibration of the optics alignment was realized by the precise movement of the second lens by piezo actuators and tracking the signal intensity of a 2 μm thick Cu foil.

The CMXRF measurements were performed within a total sample volume of $500 \times 500 \times 500$ $\mu m^3$ and a global step size of 5 μm. A spot measurement time of 10 ms was utilized with five measurement cycles, resulting in a measurement time of 50 ms for each point and an overall measurement time of approximately 63 h. Additionally, with respect to the presence of light elements in the spongin samples, a vacuum of 20 mbar was applied for all the measurements.

For the first data evaluation of the 101 generated xy area mappings at varying z positions, the spectrometer corresponding software was utilized, providing the impulse count values for the element signals Si-Kα (1.740 keV), S-Kα (2.307 keV), Ca-Kα (3.691 keV), I-Lβ (4.239 keV), Fe-Kα (6.397 keV), and Br-Kα (11.902 keV). Due to the physical properties of the lenses used, quite different probing volume sizes need to be considered for the different fluorescence energies of the element lines. For the utilized setup, the probing volume sizes were calculated as a function of the energy by calibrating the characteristics of the spectrometer parameters [121]. Hereby, the following probing volume z-sizes can be expected in approximation: Si-Kα (77.2 μm), S-Kα (69.0 μm), Ca-Kα (55.6 μm), I-Lβ (51.8 μm), Fe-Kα (42.0 μm) and Br-Kα (31.4 μm).

The exported measurement datasets (containing information about the location coordinates x and y and the signal count values) were then further processed using in-house software (applied in references [122,123]), providing tools like the normalization of the xy mappings to a global signal maximum, generating RGB color-coded images and signal noise correction. The final stacking of the two-dimensional distribution datasets was carried out with the Python application Mayavi, achieving three-dimensional distribution images. For the three-dimensional reconstruction of the element distributions (Si (cyan), S (yellow), Ca (blue), I (magenta), Fe (red), and Br (green)) a volume module was used in combination with light and shade calculations for better visibility of the three-dimensional structure.

Due to the small size of the sponge structure (~30 μm) compared to the probing volume sizes (≥31.4 μm), weak signal values were excluded from the volume rendering by setting the RGB alpha value to zero.

Due to the properties of natural samples (varying density, elemental composition, and absorption due to the 3D structure) and different physical behaviors of the observed elements (fluorescence yield, sensitivity, and concentration), different alpha values were utilized for the volume reconstruction of each element and sample. Hereby, data points within the range of 1 to 10% of the global maximum count value were excluded, aiming for a less cluttered representation of the 3D elemental distributions. Therefore, the volume reconstructions depict only a qualitative approximation of the 3D elemental distribution. Further data processing is needed for the correction of the influences of probing volume size and absorption effects. Since these samples exhibit a quite complex three-dimensional structure and composition, the feasibility of these complex reconstruction tasks (both qualitatively and quantitatively) needs to be addressed in future work.

#### 4.3.9. Magnetic Properties

The magnetic properties of the obtained "Iron-Spongin" material were tested using a neodymium magnet with a pull force of 192 N, purchased from Mistral, Jaworzno, Poland.

### *4.4. Dopamine Detection*

For the sensor preparation, modified carbon paste electrodes (CPE) were fabricated by grinding graphite, paraffin oil as a binder, and a modifier in a mortar with a ratio of 65:15:20 (*w*/*w*/*w*) and a grinding time of 40 min. The components were homogenized to form a paste, which was then pressed into a holder with an inner diameter of 4 mm.

Amperometric measurements were carried out using a PalmSens 4 electrochemical analyzer with the software PSTrace 5.8 (PalmSens BV, Houten, the Netherlands) and a three-electrode setup including modified CPE as the working electrode, Ag/AgCl (3 M KCl) electrode as the reference, and a platinum wire as the counter electrode. The amperometric response of the different modified CPEs for the successive addition of DA in 0.1 M phosphate buffer pH 6.5 was recorded at a potential of 0.25 V.

## 5. Conclusions

This study focused on a better understanding of the interaction between biomaterial spongin and iron ions in marine environments due to biocorrosion, which led to the occurrence of the biomineral lepidocrocite. For this purpose, a biomimetic approach for the creation of a new lepidocrocite-containing 3D spongin scaffold using artificial seawater and iron powder under laboratory conditions at 24 °C is described for the first time. This simple method allowed obtaining a new composite called "Iron-Spongin". The limiting factors such as the concentration of iron ions, pH, and temperature should be studied in the future with the aim of finding optimal parameters for the development of functional lepidocrocite-based 3D composites on a large scale.

The discovery of rusty bath sponges in the industrial production of marine sponges, from both open ocean colonies and those grown in marine culture, is not uncommon. On the contrary, rusty sponges are found in mass quantities (Figure 13) and are rejected by the respective companies due to a lack of demand or use for traditional cosmetic purposes.

However, our work shows the possibility of further application of such rusty sponges in biomimetics and materials science. Consequently, the strategy for the use of these specific sponges must be changed drastically. This opens a way for the sustainable and correct use of sponges without the presence of substandard biomaterials. Intriguingly, technologies have been developed to grow sponges under marine ranching conditions on reinforced iron pins or plates to create iron-containing composites as functional materials.

**Supplementary Materials:** The following supporting information can be downloaded at: https://www.mdpi.com/article/10.3390/md21090460/s1, Figure S1: EDX measurements of pure spongin scaffold isolated from *Hippospongia communis* demosponge (control sample); Figure S2: SEM image of lepidocrocite nanoparticles formed on the surface of natural spongin scaffold of *H. communis*, described as rusty sponge; Figure S3: SEM image with spots of EDX measurements of the rusty natural spongin scaffold of *H. communis* (for measurements data see Figure S4); Figure S4: EDX measurements for the natural rusty spongin scaffold of *H. communis* (for spot locations, see Figure S3) and EDX measurements for the natural rusty spongin scaffold of *H. communis* (for spot locations, see Figure S3); Figure S5: SEM images of the "Iron-Spongin" scaffold with well-defined crystals of lepidocrocite. See also Figure S6; Figure S6: SEM image with spots of EDX measurements carried out on "Iron-Spongin" sample (for measurements data, see Figure S7).; Figure S7: EDX measurements for the "Iron-Spongin" scaffold (for spot locations, see Figure S6); Figure S8: Quantitative EDX analysis (line scan) of a block face image cross-section of a single "Iron-Spongin after ultrasound treatment" fiber; Table S1: Wavenumbers of the bands present in the spectra of the studied samples and their assignment; Figure S9. Magnetic properties of biomimetically created "Iron-Spongin after ultrasound treatment" sample; Video S1: 3D distribution of Fe on the natural spongin scaffold of *H. communis*, described as a rusty sponge.

**Author Contributions:** Conceptualization and project administration, H.E., A.S. and M.P.-S.; methodology, A.C., Y.J., H.E., P.R., A.S., A.R. and C.V.; investigation and formal analysis A.K., M.K., B.L., S.F., P.S., M.F., K.H., A.V., A.E. and E.L.; resources, H.E., M.P.-S., Y.J. and C.V.; writing—original draft preparation, H.E., A.K., A.V., K.H., S.F. and T.J.; writing—review and editing, H.E., A.V., A.K. and M.P.-S.; visualization, A.K., K.H., S.F., A.V. and A.E.; supervision, H.E., M.P.-S., P.R., C.V., A.S., A.C., Y.J. and T.J. All authors have read and agreed to the published version of the manuscript.

**Funding:** This research was funded by the National Science Centre (Poland) within the framework of the projects Maestro 12 (2020/38/A/ST5/00151) and OPUS 19 (2020/37/B/ST5/01909). A.V. was founded by VW Foundation (Funding for Refugee Scholars and Scientists from Ukraine, Personal Ref. No. 05020407B, TU Bergakademie Freiberg, Germany).

**Institutional Review Board Statement:** Not applicable.

**Data Availability Statement:** Not applicable.

**Acknowledgments:** The authors would like to thank Agnieszka Martyła for her assistance in interpreting the XRD results and Daria Tokina and Morphology Service of IMBE, Marseille, France, for technical support in specimen preparation for TEM. The electron microscopy studies were provided using the equipment of the Microscopy Core Facility of IMM, Marseille, France. Special thanks to Jean Vacelet for the discussions and motivation of our study.

**Conflicts of Interest:** The authors declare no conflict of interest. The funders had no role in the design of the study; in the collection, analyses, or interpretation of data; in the writing of the manuscript; or in the decision to publish the results.

## References

1. Maslin, M.; Gaertner-Mazouni, N.; Debitus, C.; Joy, N.; Ho, R. Marine sponge aquaculture towards drug development: An ongoing history of technical, ecological, chemical considerations and challenges. *Aquac. Rep.* **2021**, *21*, 100813. [CrossRef]
2. Binnewerg, B.; Schubert, M.; Voronkina, A.; Muzychka, L.; Wysokowski, M.; Petrenko, I.; Djurović, M.; Kovalchuk, V.; Tsurkan, M.; Martinovic, R.; et al. Marine Biomaterials: Biomimetic and Pharmacological Potential of Cultivated *Aplysina aerophoba* Marine Demosponge. *Mater. Sci. Eng. C* **2020**, *109*, 110566. [CrossRef] [PubMed]
3. Ehrlich, H. *Marine Biological Materials of Invertebrate Origin*; Springer International Publishing: Cham, Switzerland, 2019; Volume 13.
4. Ehrlich, H. Chitin and collagen as universal and alternative templates in biomineralization. *Int. Geol. Rev.* **2010**, *52*, 661–699. [CrossRef]
5. Kubiak, A.; Kotula, M.; Leśniewski, B.; Pajewska-Szmyt, M. Iron-Sponges Interrelations: From Biocorrosion to Nanostructured Biocomposites. *Lett. Appl. Nanobiosci.* **2022**, *12*, 64.
6. Petrenko, I.; Summers, A.P.; Simon, P.; Żółtowska-Aksamitowska, S.; Motylenko, M.; Schimpf, C.; Rafaja, D.; Roth, F.; Kummer, K.; Brendler, E.; et al. Extreme biomimetics: Preservation of molecular detail in centimeter-scale samples of biological meshes laid down by sponges. *Sci. Adv.* **2019**, *5*, eaax2805. [CrossRef]
7. Ehrlich, H.; Wysokowski, M.; Żółtowska-Aksamitowska, S.; Petrenko, I.; Jesionowski, T. Collagens of Poriferan Origin. *Mar. Drugs* **2018**, *16*, 79. [CrossRef]

8. Jesionowski, T.; Norman, M.; Żółtowska-Aksamitowska, S.; Petrenko, I.; Joseph, Y.; Ehrlich, H. Marine Spongin: Naturally Prefabricated 3D Scaffold-Based Biomaterial. *Mar. Drugs* **2018**, *16*, 88. [CrossRef]
9. Khrunyk, Y.; Lach, S.; Petrenko, I.; Ehrlich, H. Progress in Modern Marine Biomaterials Research. *Mar. Drugs* **2020**, *18*, 589. [CrossRef]
10. Ehrlich, H.; Maldonado, M.; Hanke, T.; Meissner, H.; Born, R.; Scharnweber, D.; Worch, H.; Vdi, V.D.I. Spongins: Nanostructural Investigations and Development of Biomimetic Material Model. *VDI Ber.* **2003**, *1803*, 287–292.
11. Tsurkan, D.; Wysokowski, M.; Petrenko, I.; Voronkina, A.; Khrunyk, Y.; Fursov, A.; Ehrlich, H. Modern scaffolding strategies based on naturally pre-fabricated 3D biomaterials of poriferan origin. *Appl. Phys. A* **2020**, *126*, 382. [CrossRef]
12. Żółtowska, S.; Koltsov, I.; Alejski, K.; Ehrlich, H.; Ciałkowski, M.; Jesionowski, T. Thermal decomposition behaviour and numerical fitting for the pyrolysis kinetics of 3D spongin-based scaffolds. The classic approach. *Polym. Test.* **2021**, *97*, 107148. [CrossRef]
13. Louden, D.; Inderbitzin, S.; Peng, Z.; de Nys, R. Development of a new protocol for testing bath sponge quality. *Aquaculture* **2007**, *271*, 275–285. [CrossRef]
14. Wang, Q.; Chen, J.; Wang, D.; Shen, M.; Ou, H.; Zhao, J.; Chen, M.; Yan, G.; Chen, J. Rapid Hemostatic Biomaterial from a Natural Bath Sponge Skeleton. *Mar. Drugs* **2021**, *19*, 220. [CrossRef] [PubMed]
15. Akbari, M.; Jafari, H.; Rostami, M.; Mahdavinia, G.R.; Sobhani nasab, A.; Tsurkan, D.; Petrenko, I.; Ganjali, M.R.; Rahimi-Nasrabadi, M.; Ehrlich, H. Adsorption of Cationic Dyes on a Magnetic 3D Spongin Scaffold with Nano-Sized $Fe_3O_4$ Cores. *Mar. Drugs* **2021**, *19*, 512. [CrossRef]
16. Falahi, S.; Jaafar, A.; Petrenko, I.; Zarejousheghani, M.; Ehrlich, H.; Rahimi, P.; Joseph, Y. High-Performance Three-Dimensional Spongin-Atacamite Biocomposite for Electrochemical Nonenzymatic Glucose Sensing. *ACS Appl. Bio. Mater.* **2022**, *5*, 873–880. [CrossRef] [PubMed]
17. Shahdost-Fard, F.; Faridfar, S.; Keihan, A.H.; Aghaei, M.; Petrenko, I.; Ahmadi, F.; Ehrlich, H.; Rahimi-Nasrabadi, M. Applicability of a Green Nanocomposite Consisted of Spongin Decorated $Cu_2WO_4(OH)_2$ and AgNPs as a High-Performance Aptasensing Platform in Staphylococcus aureus Detection. *Biosensors* **2023**, *13*, 271. [CrossRef]
18. Falahi, S.; Falahi, S.; Zarejousheghani, M.; Ehrlich, H.; Joseph, Y.; Rahimi, P. Electrochemical Sensing of Gallic Acid in Beverages Using a 3D Bio-Nanocomposite Based on Carbon Nanotubes/Spongin-Atacamite. *Biosensors* **2023**, *13*, 262. [CrossRef]
19. Ehrlich, H. *Extreme Biomimetics*; Springer International Publishing: Cham, Switzerland, 2017.
20. Szatkowski, T.; Wysokowski, M.; Lota, G.; Pęziak, D.; Bazhenov, V.V.; Nowaczyk, G.; Walter, J.; Molodtsov, S.L.; Stöcker, H.; Himcinschi, C.; et al. Novel nanostructured hematite–spongin composite developed using an extreme biomimetic approach. *RSC Adv.* **2015**, *5*, 79031–79040. [CrossRef]
21. Ehrlich, H.; Simon, P.; Motylenko, M.; Wysokowski, M.; Bazhenov, V.V.; Galli, R.; Stelling, A.L.; Stawski, D.; Ilan, M.; Stöcker, H.; et al. Extreme Biomimetics: Formation of zirconium dioxide nanophase using chitinous scaffolds under hydrothermal conditions. *J. Mater. Chem. B* **2013**, *1*, 5092–5099. [CrossRef]
22. Tsurkan, D.; Simon, P.; Schimpf, C.; Motylenko, M.; Rafaja, D.; Roth, F.; Inosov, D.S.; Makarova, A.A.; Stepniak, I.; Petrenko, I.; et al. Extreme Biomimetics: Designing of the First Nanostructured 3D Spongin-Atacamite Composite and Its Application. *Adv. Mater.* **2021**, *33*, 2101682. [CrossRef]
23. Szatkowski, T.; Kopczyński, K.; Motylenko, M.; Borrmann, H.; Mania, B.; Graś, M.; Lota, G.; Bazhenov, V.V.; Rafaja, D.; Roth, F.; et al. Extreme biomimetics: A carbonized 3D spongin scaffold as a novel support for nanostructured manganese oxide(IV) and its electrochemical applications. *Nano Res.* **2018**, *11*, 4199–4214. [CrossRef]
24. Szatkowski, T.; Siwińska-Stefańska, K.; Wysokowski, M.; Stelling, A.L.; Joseph, Y.; Ehrlich, H.; Jesionowski, T. Immobilization of Titanium(IV) Oxide onto 3D Spongin Scaffolds of Marine Sponge Origin According to Extreme Biomimetics Principles for Removal of C.I. Basic Blue 9. *Biomimetics* **2017**, *2*, 4. [CrossRef]
25. Norman, M.; Żółtowska-Aksamitowska, S.; Zgoła-Grześkowiak, A.; Ehrlich, H.; Jesionowski, T. Iron(III) Phthalocyanine Supported on a Spongin Scaffold as an Advanced Photocatalyst in a Highly Efficient Removal Process of Halophenols and Bisphenol A. *J. Hazard. Mater.* **2018**, *347*, 78–88. [CrossRef] [PubMed]
26. Norman, M.; Bartczak, P.; Zdarta, J.; Ehrlich, H.; Jesionowski, T. Anthocyanin dye conjugated with *Hippospongia communis* marine demosponge skeleton and its antiradical activity. *Dye. Pigment.* **2016**, *134*, 541–552. [CrossRef]
27. Norman, M.; Zdarta, J.; Bartczak, P.; Piasecki, A.; Petrenko, I.; Ehrlich, H.; Jesionowski, T. Marine Sponge Skeleton Photosensitized by Copper Phthalocyanine: A Catalyst for Rhodamine B Degradation. *Open Chem.* **2016**, *14*, 243–254. [CrossRef]
28. Norman, M.; Bartczak, P.; Zdarta, J.; Tomala, W.; Żurańska, B.; Dobrowolska, A.; Piasecki, A.; Czaczyk, K.; Ehrlich, H.; Jesionowski, T. Sodium Copper Chlorophyllin Immobilization onto *Hippospongia communis* Marine Demosponge Skeleton and Its Antibacterial Activity. *Int. J. Mol. Sci.* **2016**, *17*, 1564. [CrossRef] [PubMed]
29. Norman, M.; Bartczak, P.; Zdarta, J.; Tylus, W.; Szatkowski, T.; Stelling, A.L.; Ehrlich, H.; Jesionowski, T. Adsorption of C.I. Natural Red 4 onto Spongin Skeleton of Marine Demosponge. *Materials* **2014**, *8*, 96–116. [CrossRef]
30. Antecka, K.; Zdarta, J.; Zgola-Grzeskowiak, A.; Ehrlich, H.; Jesionowski, T. Degradation of bisphenols using immobilized laccase supported onto biopolymer marine sponge scaffolds: Effect of operational parameters on removal efficiency. *New Biotechnol.* **2018**, *44*, S163. [CrossRef]

31. Zdarta, J.; Norman, M.; Smułek, W.; Moszyński, D.; Kaczorek, E.; Stelling, A.L.; Ehrlich, H.; Jesionowski, T. Spongin-Based Scaffolds from *Hippospongia communis* Demosponge as an Effective Support for Lipase Immobilization. *Catalysts* **2017**, *7*, 147. [CrossRef]
32. Ehrlich, H.; Wysokowski, M.; Jesionowski, T. The philosophy of extreme biomimetics. *Sustain. Mater. Technol.* **2022**, *32*, e00447. [CrossRef]
33. Lherbette, M.; Regeard, C.; Marlière, C.; Raspaud, E. Biocorrosion on Nanofilms Induces Rapid Bacterial Motions via Iron Dissolution. *ACS Central Sci.* **2021**, *7*, 1949–1956. [CrossRef] [PubMed]
34. Vlasov, A.Y.; Gornushkina, N.A.; Petrov, M.I. Crystal structure and magnetic properties of lepidocrocite upon thermal transformation to hematite. *Sov. Phys. JETP* **1972**, *15*, 698–702. [CrossRef]
35. Cornell, R.M.; Schwertmann, U. *The Iron Oxides*; Wiley-VCH: Weinheim, Germany, 2003.
36. Ewing, F.J. The Crystal Structure of Lepidocrocite. *J. Chem. Phys.* **1935**, *3*, 420–424. [CrossRef]
37. Navarro, G.; Acevedo, R.; Soto, A.; Herane, M. Synthesis and characterization of lepidocrocite and its potential applications in the adsorption of pollutant species. *J. Phys. Conf. Ser.* **2008**, *134*, 012023. [CrossRef]
38. Zhong, D.; Feng, W.; Ma, W.; Liu, X.; Ma, J.; Zhou, Z.; Du, X.; He, F. Goethite and Lepidocrocite Catalyzing Different Double-Oxidant Systems to Degrade Chlorophenol. *Environ. Sci. Pollut. Res.* **2022**, *29*, 72764–72776. [CrossRef] [PubMed]
39. Shopska, M.; Paneva, D.; Kolev, H.; Kadinov, G.; Briančin, J.; Fabián, M.; Cherkezova-Zheleva, Z.; Mitov, I. Characterization and catalytic activity in CO oxidation of biogenic lepidocrocite layered on anodic alumina. *Catal. Today* **2019**, *357*, 436–441. [CrossRef]
40. Qin, M.; Lu, B.; Feng, S.; Zhen, Z.; Chen, R.; Liu, H. Role of exposed facets and surface OH groups in the Fenton-like reactivity of lepidocrocite catalyst. *Chemosphere* **2019**, *230*, 286–293. [CrossRef]
41. Farquhar, M.L.; Charnock, J.M.; Livens, F.R.; Vaughan, D.J. Mechanisms of Arsenic Uptake from Aqueous Solution by Inter-action with Goethite, Lepidocrocite, Mackinawite, and Pyrite: An X-ray Absorption Spectroscopy Study. *Environ. Sci. Technol.* **2002**, *36*, 1757–1762. [CrossRef]
42. Pfaff, G. Iron Oxide Pigments. *Phys. Sci. Rev.* **2021**, *6*, 535–548. [CrossRef]
43. Engel, G.; Hilsenbek, U. An Efficient Synthesis of Lepidocrocite (γ-FeOOH) by Homogeneous Precipitation. *Z Naturforsch B* **2006**, *61*, 342–345. [CrossRef]
44. Rudolf, P.D. Process for the Preparation of Synthetic Lepidocrocite. European Patent EP0040722A1, 2 December 1981.
45. Towe, K.M.; Rützler, K. Lepidocrocite Iron Mineralization in Keratose Sponge Granules. *Science* **1968**, *162*, 268–269. [CrossRef]
46. Vacelet, J.; Verdenal, B.; Perinet, G. The Iron Mineralization of *Spongia officinalis* L. (Porifera, Dictyoceratida) and Its Relationships with the Collagen Skeleton. *Biol. Cell.* **1988**, *62*, 189–198. [CrossRef]
47. Meldrum, F.C.; Heywood, B.R.; Dickson, D.P.; Mann, S. Iron Biomineralization in the Poriferan *Ircinia oros*. *J. Mar. Biol. Assoc.* **1995**, *75*, 993–996. [CrossRef]
48. Teragawa, C.K. Sponge dermal membrane morphology: Histology of cell-mediated particle transport during skeletal growth. *J. Morphol.* **1986**, *190*, 335–347. [CrossRef]
49. Oleś, A.; Szytuła, A.; Wanic, A. Neutron Diffraction Study of γ-FeOOH. *Phys. Status Solidi B* **1970**, *41*, 173–177. [CrossRef]
50. Ali, F.M.; Hmadeh, M.; O'Brien, P.G.; Perovic, D.D.; Ozin, G.A. Photocatalytic Properties of All Four Polymorphs of Nanostructured Iron Oxyhydroxides. *Chemnanomat* **2016**, *2*, 1047–1054. [CrossRef]
51. Chukhrov, F.; Zvyagin, B.B.; Gorshkov, A.I.; Yermilova, L.P.; Korovushkin, V.V.; Rudnitskaya, Y.S.; Yakubovskaya, N.Y. Feroxyhyte, a new modification of FeOOH. *Int. Geol. Rev.* **1977**, *19*, 873–890. [CrossRef]
52. Namduri, H.; Nasrazadani, S. Quantitative analysis of iron oxides using Fourier transform infrared spectrophotometry. *Corros. Sci.* **2008**, *50*, 2493–2497. [CrossRef]
53. Dong, X.; Li, L.; Zhao, C.; Liu, H.-K.; Guo, Z. Controllable synthesis of RGO/$Fe_xO_y$ nanocomposites as high-performance anode materials for lithium ion batteries. *J. Mater. Chem. A Mater.* **2014**, *2*, 9844–9850. [CrossRef]
54. Zhao, X.; Yuan, Z.; Wang, S.; Pan, Y.; Chen, N.; Tunc, A.; Cheung, K.; Alparov, A.; Chen, W.; Deevsalar, R.; et al. Iron(II)-activated phase transformation of Cd-bearing ferrihydrite: Implications for cadmium mobility and fate under anaerobic conditions. *Sci. Total Environ.* **2022**, *848*, 157719. [CrossRef]
55. Święch, D.; Paluszkiewicz, C.; Piergies, N.; Pięta, E.; Lelek-Borkowska, U.; Kwiatek, W. Identification of Corrosion Products on Fe and Cu Metals using Spectroscopic Methods. *Acta Phys. Pol. A* **2018**, *133*, 286–288. [CrossRef]
56. Christensen, H.; Christensen, A.N.; Turpeinen, U.; Andresen, A.F.; Smidsrød, O.; Pontchour, C.-O.; Phavanantha, P.; Pramatus, S.; Cyvin, B.N.; Cyvin, S.J. Hydrogen Bonds of Gamma-FeOOH. *Acta Chem. Scand.* **1978**, *32a*, 87–88. [CrossRef]
57. Liu, A.; Liu, J.; Pan, B.; Zhang, W. Formation of Lepidocrocite (γ-FeOOH) from Oxidation of Nanoscale Zero-Valent Iron (NZVI) in Oxygenated Water. *RSC Adv.* **2014**, *4*, 57377–57382. [CrossRef]
58. Wetzel, R.; Perry, L.J.; Baase, W.A.; Becktel, W.J. Disulfide bonds and thermal stability in T4 lysozyme. *Proc. Natl. Acad. Sci. USA* **1988**, *85*, 401–405. [CrossRef]
59. Hirt, A.M.; Lanci, L.; Dobson, J.; Weidler, P.; Gehring, A.U. Low-temperature magnetic properties of lepidocrocite. *J. Geophys. Res. Solid Earth* **2002**, *107*, EPM 5-1–EPM 5-9. [CrossRef]
60. Pope, D.J.; Clark, A.E.; Rosso, K.M.; Prange, M.P. Rethinking the magnetic properties of lepidocrocite: A density functional theory and cluster expansion study. *J. Appl. Phys.* **2020**, *128*, 103906. [CrossRef]
61. Spain, E.; Venkatanarayanan, A. Review of Physical Principles of Sensing and Types of Sensing Materials. In *Comprehensive Materials Processing*; Elsevier: Amsterdam, The Netherlands, 2014; Volume 13, pp. 5–46. [CrossRef]

62. Richter, C.; van der Pluijm, B.A. Separation of Paramagnetic and Ferrimagnetic Susceptibilities Using Low Temperature Magnetic Susceptibilities and Comparison with High Field Methods. *Phys. Earth Planet. Inter.* **1994**, *82*, 113–123. [CrossRef]
63. Channer, B.; Matt, S.M.; Nickoloff-Bybel, E.A.; Pappa, V.; Agarwal, Y.; Wickman, J.; Gaskill, P.J. Dopamine, Immunity, and Disease. *Pharmacol. Rev.* **2023**, *75*, 62–158. [CrossRef]
64. Li, M.; Zhou, L.; Sun, X.; Yang, Y.; Zhang, C.; Wang, T.; Fu, F. Dopamine, a co-regulatory component, bridges the central nervous system and the immune system. *Biomed. Pharmacother.* **2022**, *145*, 112458. [CrossRef]
65. Adekunle, A.S.; Agboola, B.O.; Pillay, J.; Ozoemena, K.I. Electrocatalytic detection of dopamine at single-walled carbon nanotubes-iron (III) oxide nanoparticles platform. *Sens. Actuators B Chem.* **2010**, *148*, 93–102. [CrossRef]
66. Anantha, M.S.; Kumar, S.R.K.; Anarghya, D.; Venkatesh, K.; Santosh, M.S.; Kumar, K.Y.; Muralidhara, H.B. ZnO@$MnO_2$ Nanocomposite Modified Carbon Paste Electrode for Electrochemical Detection of Dopamine. *Sens. Int.* **2021**, *2*, 100087. [CrossRef]
67. Gnahore, G.T.; Velasco-Torrijos, T.; Colleran, J. The Selective Electrochemical Detection of Dopamine Using a Sulfated β-Cyclodextrin Carbon Paste Electrode. *Electrocatalysis* **2017**, *8*, 459–471. [CrossRef]
68. Kokulnathan, T.; Anthuvan, A.J.; Chen, S.-M.; Chinnuswamy, V.; Kadirvelu, K. Trace level electrochemical determination of the neurotransmitter dopamine in biological samples based on iron oxide nanoparticle decorated graphene sheets. *Inorg. Chem. Front.* **2018**, *5*, 705–718. [CrossRef]
69. Lowenstam, H.A. Lepidocrocite, an Apatite Mineral, and Magnetite in Teeth of Chitons (Polyplacophora). *Science* **1967**, *156*, 1373–1375. [CrossRef] [PubMed]
70. Ehrlich, H.; Bailey, E.; Wysokowski, M.; Jesionowski, T. Forced Biomineralization: A Review. *Biomimetics* **2021**, *6*, 46. [CrossRef]
71. Larese-Casanova, P.; Haderlein, S.B.; Kappler, A. Biomineralization of lepidocrocite and goethite by nitrate-reducing Fe(II)-oxidizing bacteria: Effect of pH, bicarbonate, phosphate, and humic acids. *Geochim. Cosmochim. Acta* **2010**, *74*, 3721–3734. [CrossRef]
72. Lopez-Adams, R.; Fairclough, S.M.; Lyon, I.C.; Haigh, S.J.; Zhang, J.; Zhao, F.J.; Moore, K.L.; Lloyd, J.R. Elucidating Heterogeneous Iron Biomineralization Patterns in a Denitrifying As(III)-Oxidizing Bacterium: Implications for Arsenic Immobilization. *Environ. Sci. Nano* **2022**, *9*, 1076–1090. [CrossRef]
73. Shopska, M.G.; Paneva, D.G.; Kolev, H.G.; Kadinov, G.B.; Ilieva, R.; Iliev, M.; Cherkezova-Zheleva, Z.P.; Mitov, I.G. Bioinspired Synthesis of Lepidocrocite-Containing Material and Its Catalytic Behaviour in CO Oxidation. *Helv. Chim. Acta* **2017**, *100*, e1700172. [CrossRef]
74. Till, J.; Guyodo, Y.; Lagroix, F.; Ona-Nguema, G.; Brest, J. Magnetic comparison of abiogenic and biogenic alteration products of lepidocrocite. *Earth Planet. Sci. Lett.* **2014**, *395*, 149–158. [CrossRef]
75. Chan, C.S.; Fakra, S.C.; Emerson, D.; Fleming, E.J.; Edwards, K.J. Lithotrophic iron-oxidizing bacteria produce organic stalks to control mineral growth: Implications for biosignature formation. *ISME J.* **2010**, *5*, 717–727. [CrossRef]
76. Jones, F.; Cölfen, H.; Antonietti, M. Iron oxyhydroxide colloids stabilized with polysaccharides. *Colloid Polym. Sci.* **2000**, *278*, 491–501. [CrossRef]
77. Boal, A.K.; Headley, T.J.; Tissot, R.G.; Bunker, B.C. Microtubule-Templated Biomimetic Mineralization of Lepidocrocite. *Adv. Funct. Mater.* **2004**, *14*, 19–24. [CrossRef]
78. Oosterlaken, B.M.; Van Rijt, M.M.J.; Friedrich, H.; De With, G. Collagen Mineralization with Lepidocrocite via $Fe(OH)_2$ Addition. *CrystEngComm* **2022**, *24*, 1211–1217. [CrossRef] [PubMed]
79. Guan, L.L.; Sera, Y.; Adachi, K.; Nishida, F.; Shizuri, Y. Isolation and Evaluation of Nonsiderophore Cyclic Peptides from Marine Sponges. *Biochem. Biophys. Res. Commun.* **2001**, *283*, 976–981. [CrossRef] [PubMed]
80. Le Pennec, G.; Perovic, S.; Ammar, M.S.A.; Grebenjuk, V.A.; Steffen, R.; Brümmer, F.; Müller, W.E. Cultivation of primmorphs from the marine sponge *Suberites domuncula*: Morphogenetic potential of silicon and iron. *J. Biotechnol.* **2003**, *100*, 93–108. [CrossRef]
81. Borrione, I.; Aumont, O.; Nielsdóttir, M.C.; Schlitzer, R. Sedimentary and atmospheric sources of iron around South Georgia, Southern Ocean: A modelling perspective. *Biogeosciences* **2014**, *11*, 1981–2001. [CrossRef]
82. Lough, A.J.M.; Connelly, D.P.; Homoky, W.B.; Hawkes, J.A.; Chavagnac, V.; Castillo, A.; Kazemian, M.; Nakamura, K.-I.; Araki, T.; Kaulich, B.; et al. Diffuse Hydrothermal Venting: A Hidden Source of Iron to the Oceans. *Front. Mar. Sci.* **2019**, *6*, 329. [CrossRef]
83. Homoky, W.B.; Conway, T.M.; John, S.G.; König, D.; Deng, F.; Tagliabue, A.; Mills, R.A. Iron colloids dominate sedimentary supply to the ocean interior. *Proc. Natl. Acad. Sci. USA* **2021**, *118*, e2016078118. [CrossRef]
84. Smetacek, V.; Klaas, C.; Strass, V.H.; Assmy, P.; Montresor, M.; Cisewski, B.; Savoye, N.; Webb, A.; D'ovidio, F.; Arrieta, J.M.; et al. Deep carbon export from a Southern Ocean iron-fertilized diatom bloom. *Nature* **2012**, *487*, 313–319. [CrossRef]
85. Longhini, C.M.; Sá, F.; Neto, R.R. Review and synthesis: Iron input, biogeochemistry, and ecological approaches in seawater. *Environ. Rev.* **2019**, *27*, 125–137. [CrossRef]
86. Emerson, D. The role of iron-oxidizing bacteria in biocorrosion: A review. *Biofouling* **2018**, *34*, 989–1000. [CrossRef]
87. Salem, D.M.S.A.; Ismail, M.M.; Tadros, H.R.Z. Evaluation of the Antibiofilm Activity of Three Seaweed Species and Their Bio-synthesized Iron Oxide Nanoparticles ($Fe_3O_4$-NPs). *Egypt. J. Aquat. Res.* **2020**, *46*, 333–339. [CrossRef]
88. Zhou, Q.; Albert, O.; Deng, H.; Yu, X.-L.; Cao, Y.; Li, J.-B.; Huang, X. Effect of functional groups on the crystallization of ferric oxides/oxyhydroxides in suspension environment. *Front. Mater. Sci.* **2012**, *6*, 297–303. [CrossRef]
89. Ciofi-Baffoni, S.; Nasta, V.; Banci, L. Protein networks in the maturation of human iron-sulfur proteins. *Metallomics* **2018**, *10*, 49–72. [CrossRef] [PubMed]

90. Cardenas-Rodriguez, M.; Chatzi, A.; Tokatlidis, K. Iron-sulfur clusters: From metals through mitochondria biogenesis to disease. *J. Biol. Inorg. Chem.* **2018**, *23*, 509–520. [CrossRef]
91. Beinert, H.; Holm, R.H.; Münck, E. Iron-Sulfur Clusters: Nature's Modular, Multipurpose Structures. *Science* **1997**, *277*, 653–659. [CrossRef] [PubMed]
92. Kontoghiorghes, G.J.; Kontoghiorghe, C.N. Iron and Chelation in Biochemistry and Medicine: New Approaches to Controlling Iron Metabolism and Treating Related Diseases. *Cells* **2020**, *9*, 1456. [CrossRef] [PubMed]
93. Baker, H.M.; Anderson, B.F.; Baker, E.N. Dealing with iron: Common structural principles in proteins that transport iron and heme. *Proc. Natl. Acad. Sci. USA* **2003**, *100*, 3579–3583. [CrossRef]
94. Andrews, N.C. Iron Metabolism: Iron Deficiency and Iron Overload. *Annu. Rev. Genom. Hum. Genet.* **2003**, *1*, 75–98. [CrossRef]
95. Leigh-Smith, J.; Reichelt-Brushett, A.; Rose, A.L. The characterization of iron (III) in seawater and related toxicity to early life stages of scleractinian corals. *Environ. Toxicol. Chem.* **2018**, *37*, 1104–1114. [CrossRef]
96. Liu, X.; Millero, F.J. The solubility of iron in seawater. *Mar. Chem.* **2002**, *77*, 43–54. [CrossRef]
97. Muller, F.L.L. Exploring the Potential Role of Terrestrially Derived Humic Substances in the Marine Biogeochemistry of Iron. *Front. Earth Sci.* **2018**, *6*, 159. [CrossRef]
98. Gunnars, A.; Blomqvist, S.; Johansson, P.; Andersson, C. Formation of Fe(III) oxyhydroxide colloids in freshwater and brackish seawater, with incorporation of phosphate and calcium. *Geochim. Cosmochim. Acta* **2002**, *66*, 745–758. [CrossRef]
99. Cornell, R.; Schneider, W.; Giovanoli, R. Phase transformations in the ferrihydrite/cysteine system. *Polyhedron* **1989**, *8*, 2829–2836. [CrossRef]
100. Poole, L.B. The basics of thiols and cysteines in redox biology and chemistry. *Free. Radic. Biol. Med.* **2015**, *80*, 148–157. [CrossRef]
101. Cornell, R.M.; Giovanoli, R.; Schneider, W. Effect of Cysteine and Manganese on the Crystallization of Noncrystalline Iron(III) Hydroxide at pH 8. *Clays Clay Miner.* **1990**, *38*, 21–28. [CrossRef]
102. Li, J.; Shi, C.; Zeng, W.; Wang, Y.; Hong, Z.; Ma, Y.; Fang, L. Distinct roles of pH and organic ligands in the dissolution of goethite by cysteine. *J. Environ. Sci.* **2022**, *113*, 260–268. [CrossRef]
103. Caraballo, M.A.; Asta, M.P.; Perez, J.P.H.; Hochella, M.F. Past, Present and Future Global Influence and Technological Applica-tions of Iron-Bearing Metastable Nanominerals. *Gondwana Res.* **2022**, *110*, 283–304. [CrossRef]
104. O'loughlin, E.J.; Boyanov, M.I.; Flynn, T.M.; Gorski, C.A.; Hofmann, S.M.; Mccormick, M.L.; Scherer, M.M.; Kemner, K.M. Effects of Bound Phosphate on the Bioreduction of Lepidocrocite ($\gamma$-FeOOH) and Maghemite ($\gamma$-$Fe_2O_3$) and Formation of Secondary Minerals. *Environ. Sci. Technol.* **2013**, *47*, 9157–9166. [CrossRef]
105. Liu, H.; Li, P.; Zhu, M.; Wei, Y.; Sun, Y. Fe(II)-induced transformation from ferrihydrite to lepidocrocite and goethite. *J. Solid State Chem.* **2007**, *180*, 2121–2128. [CrossRef]
106. Khattar, R.; Mathur, P. 1-(Pyridin-2-ylmethyl)-2-(3-(1-(pyridin-2-ylmethyl)benzimidazol-2-yl) propyl) benzimidazole and its copper(II) complex as a new fluorescent sensor for dopamine (4-(2-aminoethyl)benzene-1,2-diol). *Inorg. Chem. Commun.* **2013**, *31*, 37–43. [CrossRef]
107. Carrera, V.; Sabater, E.; Vilanova, E.; Sogorb, M.A. A simple and rapid HPLC-MS method for the simultaneous determination of epinephrine, norepinephrine, dopamine and 5-hydroxytryptamine: Application to the secretion of bovine chromaffin cell cultures. *J. Chromatogr. B Biomed. Appl.* **2007**, *847*, 88–94. [CrossRef]
108. Leng, Y.; Xie, K.; Ye, L.; Li, G.; Lu, Z.; He, J. Gold-nanoparticle-based colorimetric array for detection of dopamine in urine and serum. *Talanta* **2015**, *139*, 89–95. [CrossRef]
109. Shen, J.; Sun, C.; Wu, X. Silver nanoprisms-based Tb(III) fluorescence sensor for highly selective detection of dopamine. *Talanta* **2017**, *165*, 369–376. [CrossRef]
110. Ratnam, K.V.; Manjunatha, H.; Janardan, S.; Naidu, K.C.B.; Ramesh, S. Nonenzymatic electrochemical sensor based on metal oxide, MO (M= Cu, Ni, Zn, and Fe) nanomaterials for neurotransmitters: An abridged review. *Sens. Int.* **2020**, *1*, 100047. [CrossRef]
111. Campbell, F.W.; Compton, R.G. The use of nanoparticles in electroanalysis: An updated review. *Anal. Bioanal. Chem.* **2010**, *396*, 241–259. [CrossRef]
112. Jackowska, K.; Krysinski, P. New trends in the electrochemical sensing of dopamine. *Anal. Bioanal. Chem.* **2013**, *405*, 3753–3771. [CrossRef]
113. Li, G.; Zhong, P.; Ye, Y.; Wan, X.; Cai, Z.; Yang, S.; Xia, Y.; Li, Q.; Liu, J.; He, Q. A Highly Sensitive and Stable Dopamine Sensor Using Shuttle-Like $\alpha$-$Fe_2O_3$ Nanoparticles/Electro-Reduced Graphene Oxide Composites. *J. Electrochem. Soc.* **2019**, *166*, B1552–B1561. [CrossRef]
114. Liu, X.; Zhu, F.; Wang, W.; Lei, J.; Yin, G. Synthesis of Single-Crystalline Iron Oxide Magnetic Nanorings as Electrochemical Biosensor for Dopamine Detection. *Int. J. Electrochem. Sci.* **2016**, *11*, 9696–9703. [CrossRef]
115. Peik-See, T.; Pandikumar, A.; Nay-Ming, H.; Hong-Ngee, L.; Sulaiman, Y. Simultaneous Electrochemical Detection of Dopamine and Ascorbic Acid Using an Iron Oxide/Reduced Graphene Oxide Modified Glassy Carbon Electrode. *Sensors* **2014**, *14*, 15227–15243. [CrossRef]
116. Moolayadukkam, S.; Vishwanathan, S.; Jun, B.; Lee, S.U.; Matte, H.S.S.R. Unveiling the effect of the crystalline phases of iron oxyhydroxide for highly sensitive and selective detection of dopamine. *Dalton Trans.* **2021**, *50*, 13497–13504. [CrossRef] [PubMed]
117. Saito, K.; Inaguma, K.; Ogawa, M.; Ha, P.T.; Akiyama, H.; Yamaguchi, S.; Minokoshi, H.; Ogasawara, M.; Kato, S. Lepidocrocite-Type Layered Titanate Nanoparticles as Photocatalysts for $H_2$ Production. *ACS Appl. Nano. Mater.* **2022**, *5*, 9053–9062. [CrossRef]

118. Barim, G.; Dhall, R.; Arca, E.; Kuykendall, T.R.; Yin, W.; Takeuchi, K.J.; Takeuchi, E.S.; Marschilok, A.C.; Doeff, M.M. Heterostructured Lepidocrocite Titanate-Carbon Nanosheets for Electrochemical Applications. *ACS Appl. Nano. Mater.* **2022**, *5*, 678–690. [CrossRef]
119. Paltanea, G.; Paltanea, V.M.; Antoniac, I.; Antoniac, A.; Nemoianu, I.V.; Robu, A.; Dura, H. A Review of Biomimetic and Biodegradable Magnetic Scaffolds for Bone Tissue Engineering and Oncology. *Int. J. Mol. Sci.* **2023**, *24*, 4312. [CrossRef] [PubMed]
120. Halevy, I.; Bachan, A. The geologic history of seawater pH. *Science* **2017**, *355*, 1069–1071. [CrossRef]
121. Förste, F.; Bauer, L.; Heimler, K.; Hansel, B.; Vogt, C.; Kanngießer, B.; Mantouvalou, I. Quantification Routines for Full 3D Elemental Distributions of Homogeneous and Layered Samples Obtained with Laboratory Confocal Micro XRF Spectrometers. *J. Anal. Spectrom* **2022**, *37*, 1687–1695. [CrossRef]
122. Kertmen, A.; Petrenko, I.; Schimpf, C.; Rafaja, D.; Petrova, O.; Sivkov, V.; Nekipelov, S.; Fursov, A.; Stelling, A.L.; Heimler, K.; et al. Calcite Nanotuned Chitinous Skeletons of Giant *Ianthella basta* Marine Demosponge. *Int. J. Mol. Sci.* **2021**, *22*, 12588. [CrossRef]
123. Voronkina, A.; Romanczuk-Ruszuk, E.; Przekop, R.E.; Lipowicz, P.; Gabriel, E.; Heimler, K.; Rogoll, A.; Vogt, C.; Frydrych, M.; Wienclaw, P.; et al. Honeycomb Biosilica in Sponges: From Understanding Principles of Unique Hierarchical Organization to Assessing Biomimetic Potential. *Biomimetics* **2023**, *8*, 234. [CrossRef]

*marine drugs*

MDPI

*Article*

# On the Mechanical Properties of Microfibre-Based 3D Chitinous Scaffolds from Selected Verongiida Sponges

**Tomas Duminis [1,*], Marcin Heljak [2], Wojciech Święszkowski [2], Alexander Ereskovsky [3], Izabela Dziedzic [1,4], Marek Nowicki [1], Martyna Pajewska-Szmyt [1], Alona Voronkina [5,6], Stefan R. Bornstein [7,8] and Hermann Ehrlich [1,*]**

1 Centre for Advanced Technologies, Adam Mickiewicz University, Uniwersytetu Poznańskiego 10, 61-614 Poznan, Poland; izadzi@amu.edu.pl (I.D.); marek.nowicki@amu.edu.pl (M.N.); mpszmyt@amu.edu.pl (M.P.-S.)
2 Faculty of Materials Science and Engineering, Warsaw University of Technology, ul. Wołoska 141, 02-507 Warsaw, Poland; marcin.heljak@pw.edu.pl (M.H.); wojciech.swieszkowski@pw.edu.pl (W.Ś.)
3 Institut Méditerranéen de Biodiversité et d'Écologie Marine et Continentale (IMBE), Aix Marseille Université, Station Marine d'Endoume, Rue de la Batterie des Lions, 13007 Marseille, France; alexander.ereskovsky@imbe.fr
4 Faculty of Chemistry, Adam Mickiewicz University, Uniwersytetu Poznańskiego 8, 61-614 Poznan, Poland
5 Department of Pharmacy, National Pirogov Memorial Medical University, Vinnytsya, Pirogov Str. 56, 21018 Vinnytsia, Ukraine; voronkina@vnmu.edu.ua
6 Institute of Electronics and Sensor Materials, TU Bergakademie Freiberg, Gustav Zeuner Str. 3, 09599 Freiberg, Germany
7 Department of Medicine III, Universitz Hospital Carl Gustav Carus, Technische Universitat Dresden, Fetschelstrasse 74, 01307 Dresden, Germany; stefan.bornstein@uniklinikum-dresden.de
8 Departmen of Experimental Diabetology, German Institute of Human Nutrition Potsdam-Rehbruecke, 14558 Nuthetal, Germany
* Correspondence: tomas.duminis@amu.edu.pl (T.D.); herehr@amu.edu.pl (H.E.)

**Citation:** Duminis, T.; Heljak, M.; Święszkowski, W.; Ereskovsky, A.; Dziedzic, I.; Nowicki, M.; Pajewska-Szmyt, M.; Voronkina, A.; Bornstein, S.R.; Ehrlich, H. On the Mechanical Properties of Microfibre-Based 3D Chitinous Scaffolds from Selected Verongiida Sponges. *Mar. Drugs* **2023**, *21*, 463. https://doi.org/10.3390/md21090463

Academic Editors: Leto-Aikaterini Tziveleka and Azizur Rahman

Received: 17 July 2023
Revised: 22 August 2023
Accepted: 22 August 2023
Published: 24 August 2023



**Abstract:** Skeletal constructs of diverse marine sponges remain to be a sustainable source of biocompatible porous biopolymer-based 3D scaffolds for tissue engineering and technology, especially structures isolated from cultivated demosponges, which belong to the Verongiida order, due to the renewability of their chitinous, fibre-containing architecture focused attention. These chitinous scaffolds have already shown excellent and promising results in biomimetics and tissue engineering with respect to their broad diversity of cells. However, the mechanical features of these constructs have been poorly studied before. For the first time, the elastic moduli characterising the chitinous samples have been determined. Moreover, nanoindentation of the selected bromotyrosine-containing as well as pigment-free chitinous scaffolds isolated from selected verongiids was used in the study for comparative purposes. It was shown that the removal of bromotyrosines from chitin scaffolds results in a reduced elastic modulus; however, their hardness was relatively unaffected.

**Keywords:** tissue scaffolds; *Aplysina aerophoba*; Verongiida; demosponges; mechanical properties; 3D scaffolds; chitin; bromotyrosine

## 1. Introduction

Quite frequently, the sheer complexity of producing a biocompatible 3D matrix; the high cost, which makes it unattractive for the industry; and the high risk of short- or long-term toxicity and chemical incompatibility between the different components in synthetic materials opens new areas of research for discovering alternative, nature-derived "ready-made" biomaterials.

Structural polysaccharide chitin has been recently recognised as such a kind of 3D structured biological material that is excellently applicable within the "scaffolding strategy" of modern biomaterialogy [1]. In particular, chitinous constructs isolated from diverse representatives of cultivated marine demosponges, which belong to the Verongiida order

(Figure 1), remain to be candidates with high potential in biomedicine [2,3] and bioinspired materials science [4].

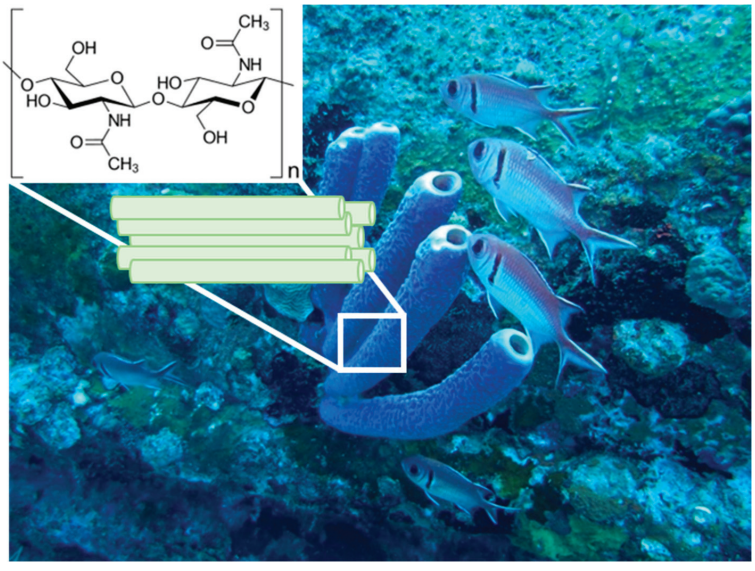


**Figure 1.** An underwater image of 30 cm-long marine demosponges belonging to the Verongiida order in their original environment. (Photograph courtesy: Dr. V. Ivanenko).

Chitin found in verongiids forms highly intricate tubular three-dimensional (3D) skeletal structures with fibre diameters of up to 120 μm [5] with a great potential in biomaterials science, which has already found applications as tissue scaffolds [6–8] and as local drug delivery devices [9,10]. Non-toxicity, cell adhesion, and proliferation for various cell types (i.e., murine fibroblasts Balb/3T3, human dermal fibroblasts NHDF, human keratinocytes HaCaT, and human neuronal cells SH-SY5Y) were recently reported by Machałowski et al. [11] for chitinous skeletons derived via alkali-acid treatment of an *Aplysina fistularis* marine demosponge.

Recently, systematic "express" methods [12] have been developed to isolate poriferan 3D scaffolds of chitin in less than an hour [13–15]. This has opened further investigations into the mechanical properties of these 3D scaffolds for potential exploitation in tissue engineering and technology. To our best knowledge, there is still only one publication [11] where compressive theoretical modulus of 0.5 kPa for poriferan chitin has been reported.

However, the mechanical properties of biomaterials, including chitin, are quite important, particularly if they are used to regenerate body areas which require load-bearing or stiffness, such as hard tissues including bone and tooth [16,17].

As with any other material, the physiochemical properties of chitin can usually be linked to the various structural parameters on a molecular level and the various arrangement modes, such as the size, distribution, and shape it takes up, e.g., hollow tubular capillaries or a homogenous matrix. Chitin is found in nature as α-chitin (anti-parallel chains), β-chitin (parallel chains), and γ-allomorph (anti-parallel and parallel chains) in respect to the position of the reducing terminus sugar molecule [18]. Chitin mostly exhibits a nano- and microfibril arrangement through H-bonding and a sheet structure.

The bonding in this special molecule is the key to understanding the physical properties of this natural polymer. Individual N-acetyl-D-glucosamine units are covalently bound to one another via the β-(1-4)-glycosidic linkages to form a polymer. Intermolecular H-bonding C-O. . .NH between the polymer chains significantly influences the mechanical properties of chitin [19].

The different polymorphs of chitin may exhibit slightly altered mechanical performances as a result of structural differences in the availability of sites for H-bonding. A highly significant study by Sawada et al. [20] reported corresponding neutron diffraction experiments and showed direct experimental evidence of hydrogen-bonding positions of anhydrous β-chitin and found that three major hydrogen bonds are intramolecular O3–H···O5 and intermolecular O6–H···O7 and N2–H···O7 [20].

It is noteworthy to mention that there are some critical differences between α-chitin and β-chitin [21]. It is generally accepted that both the α and β polymorphs of chitin exhibit a strong chain network dominated by intra-chain hydrogen bonds between the groups of C═O···NH and C═O···OH. In the α-chitin conformation, additional inter-chain hydrogen bonds bind the hydroxymethyl groups, which is absent in the β conformation due to differences in the chain alignment. The H-bonding in γ-allomorph is relatively similar to that of α-chitin. The extensive H-bonding is also confirmed by recent experimental studies [20] and theoretical simulations [22].

It has been recently postulated [23] using electron density functional theory and molecular dynamics simulations that the acetyl group found in chitin, as opposed to its deacetylated counterpart, chitosan, may play a very significant role in determining superior mechanical properties observed within chitin. The authors Cui et al. [23] postulated that this causes more high-occupancy H-bonds along the inter-sheet direction of the chitin model. Additionally, the van der Waals interaction within chitin crystals is significantly enlarged due to the larger molecular mass of the acetyl group, the authors explain, which is also responsible for the differences in the mechanical properties observed between chitin and chitosan. This report is consistent with the results of an experimental study examining β-chitin with a similar microfibril arrangement where the degree of deacetylation was also found to influence the mechanical properties, such as the maximum stress and Young's modulus, which decreased when reducing the deacetylation, and maximum elongation increased when decreasing the deacetylation [24].

A computational study by Wei and co-authors [21] revealed that the α-chitin crystal exhibits superior mechanical performance in response to tensile and shear loading. When a small-strain uniaxial tension is applied along the chain direction, the α-chitin crystal shows an elastic modulus at 48 GPa, almost twice as high as that of the β-chitin crystal at 27 GPa. Moreover, the shear modulus and strength of the α-chitin crystal are superior to those of the β-chitin crystal.

Besides chitin, diverse marine organisms, including sponges, also contain biominerals and pigments within their skeletal structure [19]. In the case of Verongiida order-related sponges, numerous bromotyrosines have been reported [25]. The biological role of these compounds was also suggested [26] to be protection against chitinase activity by microorganisms, which rely on the digestion of the chitinous matrix and use it as a source of carbon. Both the antiviral [27] and antibacterial activity of bromotyrosines are well-recognised [2]. The corresponding mechanisms of the aforementioned activities have been recently represented and discussed [10].

However, the role of this unique derivative of amino acid in the crosslinking of chitin in marine organisms, such as the Verongiida sponges, is poorly understood. Therefore, it can be suggested that the content of bromotyrosine, as well as the chemical interplay between chitin and bromotyrosine compounds, may play a very significant role in influencing the mechanical properties of chitin found in the verongiid sponges.

The mechanical properties of chitin films can be correlated to the amount of shrinkage from the gel to the final film [28]. Therefore, to retain flexibility, reduce dimensional distortion, and provide superior mechanical integrity in the dry state, it is important to manage the coagulation and shrinkage process during the preparation of chitin materials. For the production of flexible chitin films with thicknesses of 25–80 μm, cold-press processes (e.g., dissolution of chitin in dimethylacetamide-5% LiCl solution at 0 °C) have been used. To remove the solvent residue, the samples have been heated at 50 °C for 12 h and rinsed

in 95% ethanol. The Young's modulus of these flexible chitin films varied from 1240 to 3650 MPa, with a tensile strength between 38 and 60 MPa and transparency of up to 90% [28]. Chitin films with such mechanical properties have been suggested as very useful for wound dressing applications [28]. For a comparison of several mechanical properties between the relevant biomaterials, the reader is presented with Table 1.

**Table 1.** Comparison of mechanical properties between different biomaterials.

| | Biomaterial | Elastic Modulus (MPa) | Ultimate Tensile Strength (MPa) | Source |
|---|---|---|---|---|
| Chitin | Bush crickets' acoustic tracheae | 5200 | - | [29] |
| | Sheep crab exoskeleton (wet) | 518 ± 72 | 31.5 ± 5.4 | [30] |
| | Sheep crab exoskeleton (dry) | 764 ± 83 | 12.9 ± 1.7 | |
| | Commercial flake chitin films (solvent-casting) | 1240–3650 | 38–60 | [28] |
| | Philippine blue swimming crab chitin (solvent-casting) | - | 44.22 | [31] |
| Human Tissues | Human skin (back) | 98.97 ± 97 | 27.2 ± 9.3 | [32] |
| | Human femoral cancellous bone | 441 | 6.8 | [33] |

Duan et al. [34] recently developed strong chitin-based transparent films with gas-barrier properties. The creation of these chitin-based films was based on dissolving chitin in aqueous 11 wt% NaOH and 4 wt% urea at a low temperature. At a thickness of 800 nm, they demonstrated transmittance of 87% and possessed excellent tensile strength of up to 111 MPa.

The high mechanical strength and Young's modulus (higher than 150 GPa) of chitin-based materials is thought to be caused by the antiparallel extended crystal structure of chitin nanofibres. Due to such mechanical properties, chitin nanofibres can improve the mechanical properties of polylactide [35], poly (ε-caprolactone) [36,37], and acrylic resins [38,39].

Gadgey and Bahekar [31] recently used chitin from Philippine blue swimming crabs (*Portunus pelagicus*) and produced films using 5% (*w*/*v*) lithium chloride/N,N–dimethylacetamide (LiCl/DMAc) solvent. It was found that chitin polymer films have a tensile strength up to 44.22 MPa higher than the commercial plastic control samples which showed a tensile strength of 18.90 MPa. Moon et al. [40] recently analysed collagen/chitin composites produced using two polymorphs, α-chitin and β-chitin, and found that the β-chitin polymorph (parallel) exhibited much better mechanical properties due to the rearrangement of crystalline regions and formation of intermolecular hydrogen bonds with collagen.

Nonetheless, although the films developed from industrial, mostly crustacean chitin usually show good mechanical properties, they do not exhibit specifically interconnected microtubular 3D fibrous architectures. Consequently, the present investigations aim to understand the mechanical properties of alternative nature-derived 3D chitinous scaffolds isolated from the selected marine sponges, which possess α-chitin [19]. Based on molecular dynamics simulations, it has been reported that water can significantly influence the elasticity of simulated chitin-protein composites [41]. Therefore, the experiments herein were designed in a systematic way, having two types of samples: wet samples for the assessment of the elastic modulus (compressive) in the wet condition and dried embedded samples for the nanoindentation experiments. Both experiments assessed two types of samples: decellularized bromotyrosine-containing chitin scaffolds and decellularized and bromotyrosine-free chitin scaffolds. This was done to simultaneously determine the possible influence of bromotyrosines on the mechanical properties of poriferan chitin scaffolds.

## 2. Results

### *2.1. Monotonic Compression Test*

Figure 2 reports the stress–strain and the tangent modulus–strain curves for samples of chitinous scaffolds isolated from an *Aplysina aerophoba* demosponge cultivated under marine ranching conditions, tested under wet conditions.

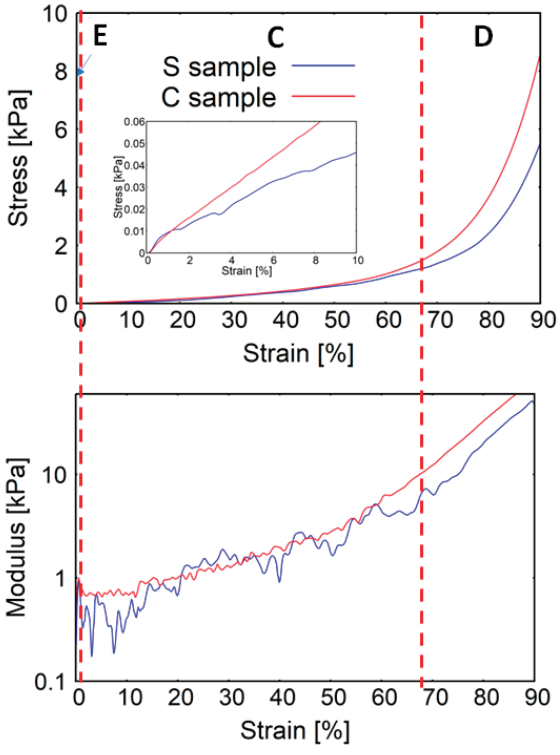


**Figure 2.** Stress–strain and modulus–strain curves of the investigated *A. aerophoba* sponge scaffolds. Three distinctive stages of compression were indicated: E—elastic stage, C—collapse stage, and D—densification stage. S samples (blue) correspond to bromotyrosine-containing samples and C (red) corresponds to bromotyrosine-free samples.

The elastic moduli characterising the samples were determined (Figure 3a). The elastic modulus of the S (bromotyrosine-containing) samples is slightly higher than that of the C (bromotyrosine-free) samples; however, the difference remains to be statistically non-significant. The collapse stages of C and S samples look distinctively different. The modulus–strain curve of the C sample is much smoother than in the case of the S samples. One can see that the stress notably increased when both samples of the scaffolds were compressed to more than 60% strain, which may indicate the densification stage presence. The smoothness of the tangent modulus–strain curves more explicitly manifests the densification of the scaffolds under study (Figure 2). One can see from Figure 3b that in the case of the C samples, the densification strain is significantly lower than in the case of the S samples. In Figure 4, stress–strain hysteresis curves are presented. Both of the investigated specimen groups were permanently distorted; however, they still had some residual ability to reshape. It is worth emphasizing that in the case of the S samples, the deformation is irreversible to a greater extent than in the case of the C samples (Figure 4), which could suggest that a significant number of sponge-like struts of S samples lost their continuity.

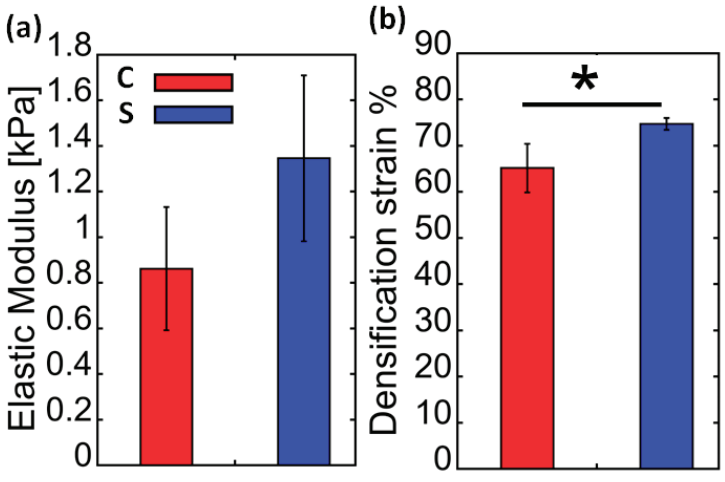


**Figure 3.** Comparison of elastic modulus (**a**) (compression) (MPa) and (**b**) densification strain (%) of bromotyrosine-containing (S, blue) and bromotyrosine-free (C, red) chitinous scaffolds isolated from *A. aerophoba* demosponge. * $p < 0.05$.

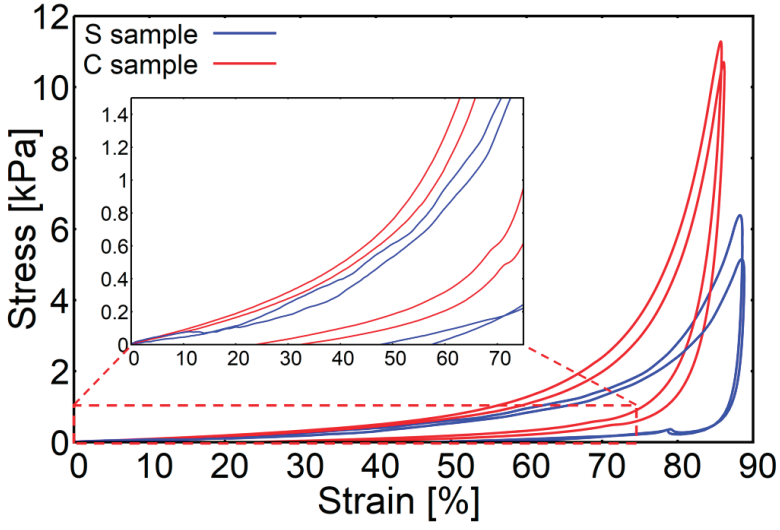


**Figure 4.** Loading–unloading hysteresis curves of the investigated chitinous scaffolds isolated from *A. aerophoba* demosponge. S samples (bromotyrosine-containing, blue), C samples (bromotyrosine-free, red).

### *2.2. Nanoindentation*

Figure 5 shows the results of the elastic modulus (nanoindentation) for the decellularised chitinous fibres isolated from the selected demosponge.

The value of the elastic modulus changes between samples by about four times, and the hardness value of the hardest sample (i.e., *A. archeri*.) is about 60% higher than for the sample with the lowest hardness (i.e., *Dendrilla* sp.) (Figure 6). This can be influenced by the dispersion of fibre sizes and the natural way of formation. Moreover, examining the fibres from a single sample, we observed significant scatter in the results between them. The standard deviations of the arithmetic mean have values ranging from 20 to 50% of the measured value. This is due to the high inhomogeneity of the tested material.

Figure 7 presents a summary of the nanoindentation hysteresis curves for one type of sample (several *A. aerophoba* fibres).

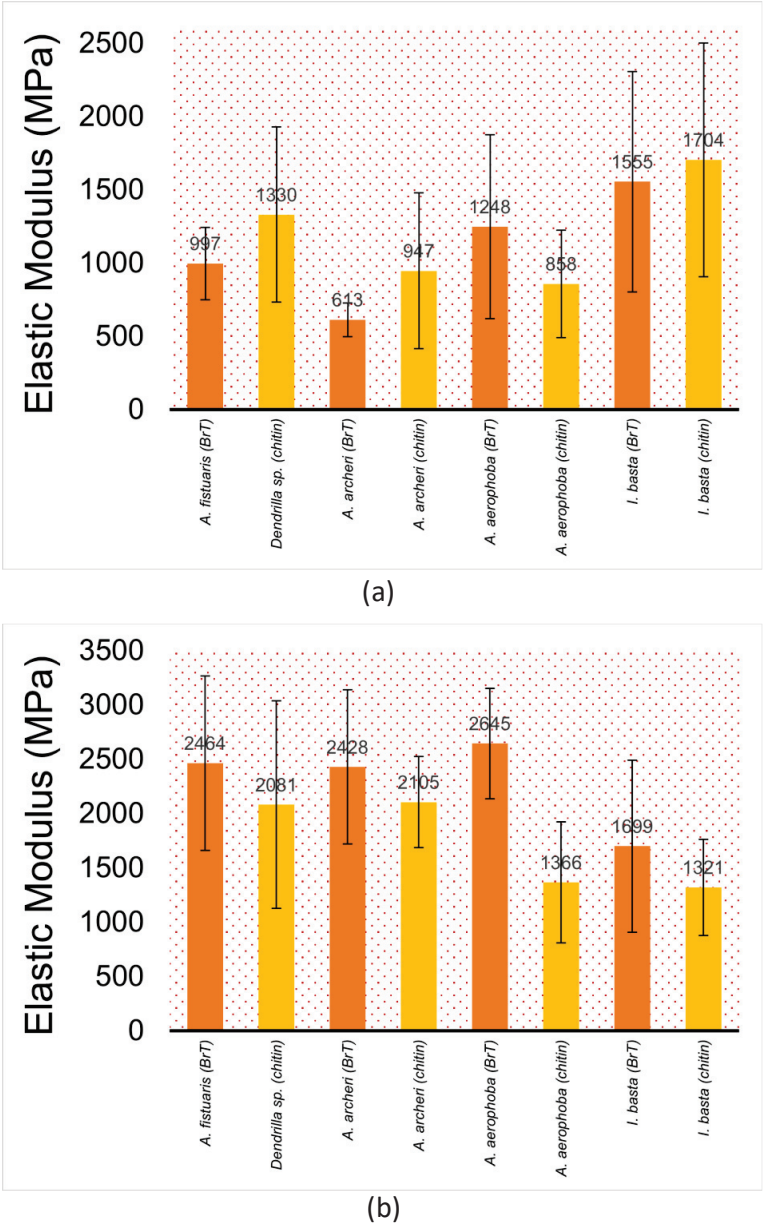


**Figure 5.** Elastic modulus (nanoindentation) in megapascals (MPa) of (**a**) 10 µm sections; (**b**) 1 µm sections of selected demosponges under study (from left to right: *A. fistularis*, *Dendrilla* sp., *A. archeri*, *A. aerophoba*, *Ianthella basta*) ± standard deviation. "BrT" denotes bromotyrosine-containing (orange). "Chitin" denotes sponge samples where bromotyrosines have been chemically removed (yellow).

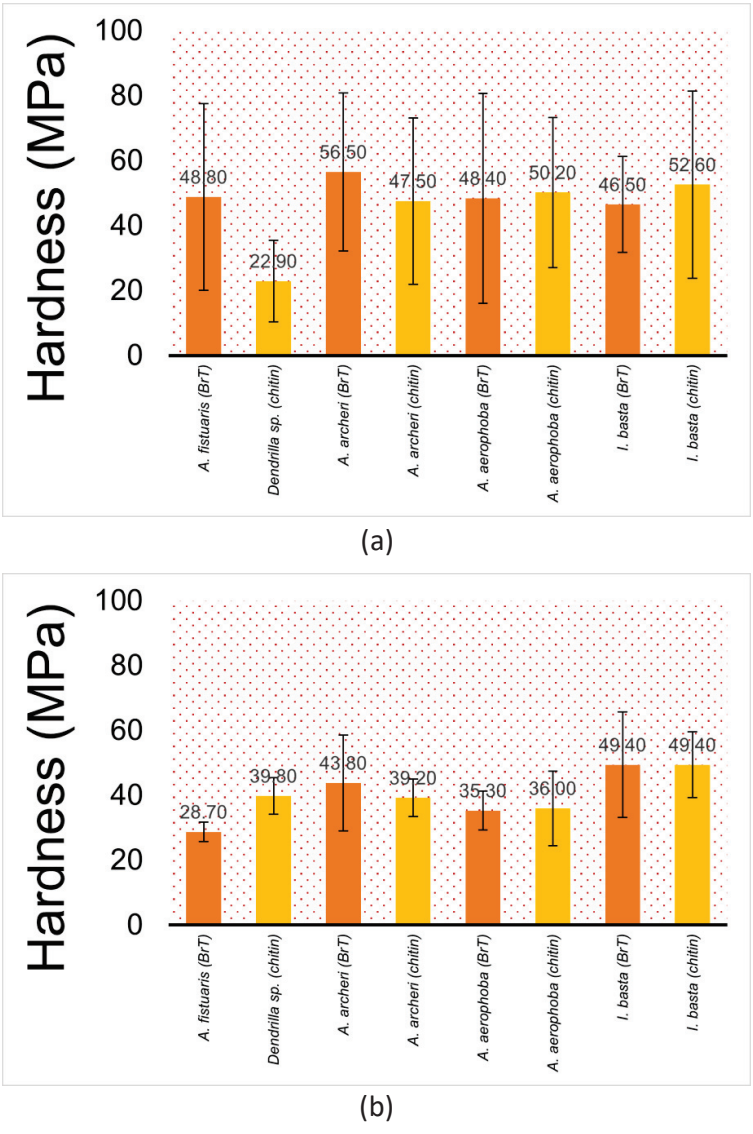


**Figure 6.** Hardness (nanoindentation) in megapascals (MPa) of (**a**) 10 µm sections; (**b**) 1 µm sections of selected decellularised fibres (from left to right: *A. fistularis*, *Dendrilla* sp., *A. archeri*, *A. aerophoba*, *I. basta*) ± standard deviation. "BrT" denotes bromotyrosine-containing (orange). "Chitin" denotes sponge samples where bromotyrosines have been chemically removed (yellow).

### *2.3. Scanning Electron Microscopy*

Figure 8 shows SEM images of mechanically pressed chitinous *A. aerophoba* sponge fibre samples at different magnifications: ×200, ×500, ×2000, and ×5000. The fibres exhibit random orientation and have a tendency to curve. Signs of shrinkage due to drying are visible. The average fibre diameter is around 59 ± 25.1 µm and varies greatly across a single fibre due to dehydration and uneven shrinkage. The porosity of the analysed samples was determined to be around 60% (pore size: 225 ± 96 µm).

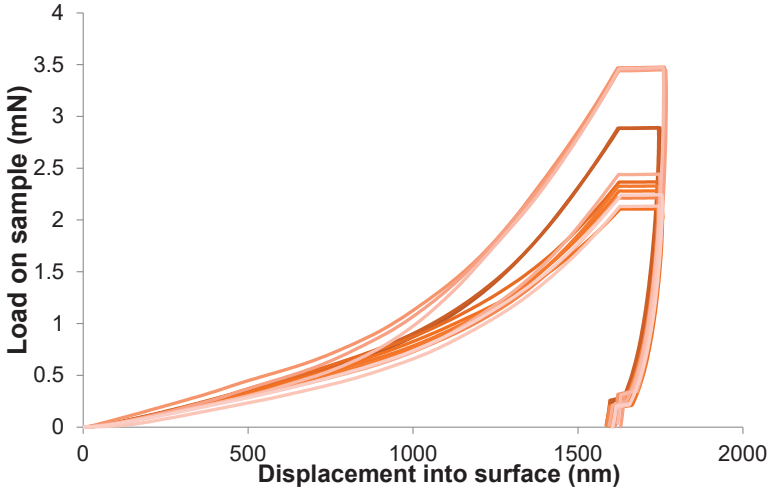


**Figure 7.** Indentation hysteresis curves for measurements on chitinous fibres of *A. aerophoba* demosponge origin.

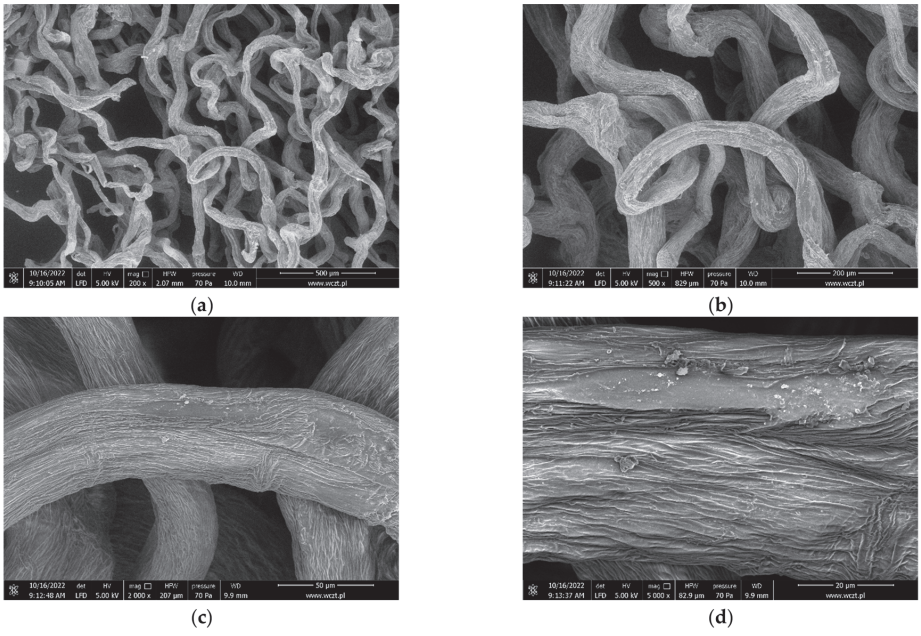


**Figure 8.** SEM images of the cell-free *A. aerophoba* chitin fibre scaffold's fibre after decellularisation (**a**) ×200, 500 µm; (**b**) ×500, 200 µm; (**c**) ×2000, 50 µm; and (**d**) ×5000, 20 µm.

### *2.4. Digital Optical Microscopy*

Figure 9 shows bromotyrosine-containing (pigmented) and bromotyrosine-free skeletal samples isolated from an *A. aerophoba* demosponge. The bromotyrosine-containing sample in Figure 9a,c shows a 3D porous microfibre architecture with characteristic brownish pigmentation [25]. Diverse bromotyrosines localised within the skeletal fibres of the sponge *A. aerophoba* have been already identified by us previously [2,10]. We also reported the elemental content of such bromotyrosine-containing and cell-free chitinous skeletal fibres

of this demosponge species analysed using EDX [42]. Not only Br, but also S, Cl, and traces of Ca have been identified by Nowacki and co-workers [42].

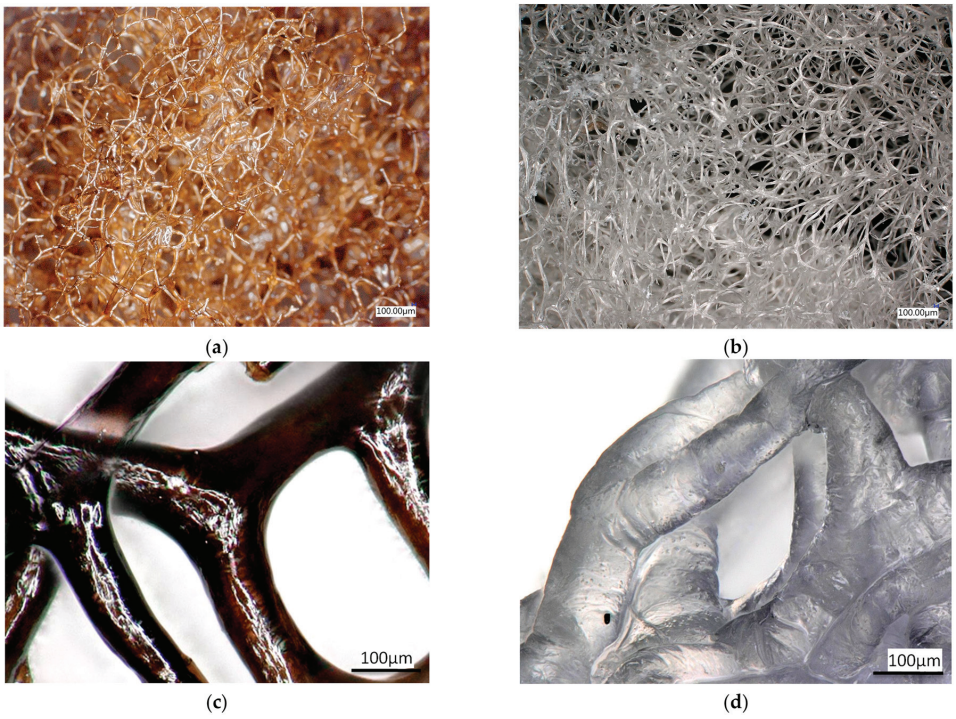


**Figure 9.** Digital microscopy images of the *A. aerophoba* chitin fibre scaffold after decellularisation. (**a**,**c**) Bromotyrosine-containing chitin scaffold, featuring a 3D porous network of microfibers. (**b**,**d**) Bromotyrosine-free chitin scaffold, featuring the same 3D porous network of microfibers.

Bromotyrosine-free samples in Figure 9b,d show a similar architecture; however, as a result of alkali treatment [25], the microfibres have lost pigmentation and appear translucent. This is typical for isolated chitinous fibre-based scaffolds reported previously for other verongiid species [13].

## 3. Discussion

Identifying subsequent stages of the compression of cellular materials that follow nonlinear elastic stress–strain behaviour could be facilitated when analysing the tangent modulus–strain curve instead of the stress–strain curve [43]. The initial trend of the compression behaviour is related to the adjustment and stabilization phases of the sample-vice system. This section of both considered curves is usually quite disturbed and does not indicate the mechanical behaviour of the spongious structure. Afterwards, usually three distinct regions can be identified [44]:

1. At a low-stress level, an elastic stage can be observed. The spongious structure is deformed, but it is still structurally stable. The stresses transferred between the spongious struts are insufficient to induce permanent structural modifications. In this region, a modulus peak is usually observed, indicating the transition from the stable phase toward the subsequent collapse stage;
2. During the collapse stage, the characteristic plateau in the case of both of the considered curves is present. The plateau is associated with the collapse of the pores. A series of local collapses percolate through the structure at some critical stress. In

particular, for an elastic foam, the plateau is due to elastic buckling, whereas, in the case of elastoplastic foams, it is due to the formation of plastic hinges [44]. Depending on the compressive mechanical behaviour of the cellular material, the plateau region can be characterised by a flat or slightly increasing slope stress plateau;

3. When the pores' closure is almost completed, spongious struts begin to interact together whereby a rapid increase of stress takes place. At the same time, an abrupt increase in the modulus is observed. This last region of the curve is called the densification stage. When analysing the tangent modulus–strain curve, one can observe that its densification region is smoother than the collapse region, which facilitates the accurate discrimination between them [41].

The mechanical properties of chitinous scaffolds (Figure 9) derived from Verongiida sponges have not been experimentally studied in the past. However, it was reported by Machałowski and co-authors [11] that the verongiid demosponge *A. fistularis* may show a compressive theoretical modulus of 0.5 kPa, which is comparable with the results presented in this study (Figure 3).

The mechanical properties of poriferan skeletons [45] and sponge-like materials of non-poriferan origin [46] are rarely studied comparatively, and only a handful of studies exist [47–49]. These can be contrasted by the type of organic matrix exhibited, such as proteinaceous spongin-based skeletons of commercial bath sponges [48], collagen sponges [50], wood sponges [51], as well as cellulose-based Luffa fruit (i.e., *Luffa aegyptiaca*) sponges [49]. A direct comparison between the mechanical properties of the sponges (Porifera) investigated in this study is not possible due to significant differences; however, as an example, *Rhopaloeides odorabile* marine sponges with spongin skeletons studied by Louden and co-workers [48] showed an elastic modulus of less than one megapascal (838.7 $\pm$ 53.5 kPa). On the contrary, cellulose-containing sponges isolated from the Luffa fruit, for example, showed a Young's modulus in the range 2–12 MPa, which is still well below the results presented in our study. This further confirms the unique nature and superior mechanical properties of the chitinous Verongiida demosponges under study. For example, the elastic modulus (nanoindentation) of the *A. aerophoba* demosponge skeleton, still containing bromotyrosines, is approximately 2.6 GPa (Figure 5), which is half of the bush crickets' *Mecopoda elongata* acoustic tracheae (5.2 GPa) [29] and scorpion (*Scorpio palmatus*) tarsus exoskeleton (5.4 GPa) [49]. However, this value falls within the range of, for example, chitin films [28,52,53] but below, for example, crustacean nanofibres isolated from the American lobster (*Homarus americanus)* (Young's modulus: 7.3 GPa) [54]. Such variations in the elastic modulus may be species-specific and are linked to different hierarchical arrangements and the chemical interplay between chitin and corresponding proteins as well as pigments [19].

A clear trend can be observed from Figures 3, 5 and 6 where the elastic modulus is influenced by whether the 3D scaffold sample contains bromotyrosines or is in the form of isolated, pigment-free chitin. A reduction in the elastic modulus is observed with chitin samples that have undergone alkali treatment [25] with respect to the extraction of all bromotyrosines [9]. This phenomenon is almost universally observed across all the chitin-based samples assessed in this study. However, this trend is not statistically significant.

Furthermore, another interesting phenomenon is observed: the hardness of sponge chitin samples that have undergone alkali treatment is relatively unchanged, which is a clear form of evidence that this kind of fibrous chitin is solely responsible for the material hardness observed in the samples studied. On the other hand, bromotyrosines in the skeletal chitinous fibres of the investigated sponges enhance their elasticity; however, they do not significantly contribute to their hardness. This can be explained by either the O-linked glycosylation bonding of bromotyrosines or hydrogen-bonding between chitin and bromotyrosines, or a mixture of both. Nonetheless, such a hypothesis would require future studies and confirmation by Nuclear Magnetic Resonance (NMR) spectroscopy.

The chitin samples of verongiid origin studied here undergo shrinking due to dehydration; however, they also undergo swelling once immersed in an aqueous medium [13]. The scaffolds studied here also exhibit "memory foam" properties, which is an attractive

property from a tissue engineering point of view [55]. Memory foam properties can be explained by the rotationally flexible hydrogen conformation between the chitin chains [56].

The 3D chitinous scaffolds of verongiid origin exhibit typical hysteresis curves (Figures 4 and 7) for brittle materials [57], with a sharp critical failure. However, upon the loss of bromotyrosines from the chitinous scaffold, a slight reduction in elasticity has been observed. The brittleness of the material is also confirmed by a very narrow elastic stage (Figure 2). Brittleness is very slightly more pronounced in the S samples (bromotyrosine-containing), which may be due to protein-reinforced matrix, i.e., chitin-bromotyrosine bonding. For example, previously [25], dibromotyrosines have been reported as crosslinking agents in cuticular structures of the Atlantic horseshoe crab (*Limulus polyphemus*) [58] as well as within scleroproteins found in the large whelk *Buccinum undatum* [59]. It has been recently found that proteins also play a role in the elastic properties of protein-chitin composites in the squid species of *Loligo vulgaris* and upon whole protein removal results in reduced elasticity [60]. This is also similar in the case of bush cricket *Mecopoda elongate* where dityrosine compounds cross-link protein resilin that results in significantly improved elasticity of the single taenidia fibres comprising the acoustic trachea, which the authors attributed to "*structural optimization between compliance and rigidity*" [29].

Nonetheless, renewable nanofibrillated cellulose (NFC) and nanofibrillated crustacean chitin (NFCh) nanoparticles comparable to chitinous sponge scaffolds were recently produced by wet-stretching and studied for mechanical properties as a function of macrofibre alignment where the investigating authors found that cellulose (elastic modulus: 33.7 GPa) outperformed chitin (elastic modulus: 12.6 GPa) and argued that this can be attributed to the higher axial modulus of cellulose I over α-chitin [61]. This study shows that the degree of alignment of microfibres can strongly influence the mechanical properties of chitin (see [62] for overview), which may also influence the mechanical properties of poriferan chitin observed in the present study.

It could be further postulated that based on the percentage reduction in the elastic modulus (Figure 5), it can be assumed with reasonable confidence that bromine and, therefore, protein content may be the highest in *A. aerophoba* (modulus reduction upon de-pigmentation, 48.35%), followed by *I. basta* (22.24%) and *A. archeri* (13.30%), which showed the least reduction upon de-pigmentation.

The mechanical properties observed in this study under wet conditions may not be suitable for immediate physiological load bearing; however, their dehydrated counterparts are comparable to human skin [32] and spongy bone [33]. This can explain why chitinous scaffolds of verongiid origin have already shown excellent and promising results in tissue engineering with respect to chondrocytes, cardiocytes, adipocytes, and diverse human mesenchymal stromal cells [6,7,11,63–65]. Nonetheless, bromotyrosine-containing skeletal matrices, such as those from *A. aerophoba* demosponge (Figure 9a,c), also have a great potential to be used as chemical catalysts and as templates which interact with metal ions through interaction with bromine and could serve in applications such as potential AgBr water filtration systems that have been recently investigated by Machałowski et al. [66]. Therefore, understanding the mechanical properties of these multiphase biomineralized [67] 3D constructs is quite essential.

We suggest that comparative studies on the mechanical properties of chitin fibres isolated from invertebrates, such as corals [68,69], coralline algae [70,71], as well as spiders [72,73] should be carried out in the near future, too.

## 4. Materials and Methods

### *4.1. Sample Preparation*

Selected sponge samples (*Dendrilla* sp.—order Dendroceratida and *Aplysina fistularis*, *Aplysina archeri*, *Aplysina aerophoba*, *Ianthella basta*—order Verongiida) purchased from INTIB GmbH and BromMarin GmbH, Freiberg, Germany were processed into two groups: bromotyrosine-containing (S) (decellularised) and chitin (C) (decellularised and bromotyrosine-free). Isolation of chitin scaffolds is described in more detail in [74]. Subse-

quently, the samples were stored in deionised water for compression testing and dried and embedded in a resin/sectioned (1 μm and 10 μm) for nanoindentation testing.

*4.2. Monotonic Compression Test*

The mechanical behaviour of specimens was investigated through monotonic compression tests. Hexahedral specimens with the approximate size of 10 mm × 10 mm × 4 mm were prepared. Monotonic compression tests were performed by means of a Q800 (TA Instruments, New Castle, DE, USA) instrument equipped with compression clamps enabled for testing in submersion. Specimens preloaded to 0.001 N were tested in native solution (deionised water, 10% methanol) and compressed at the constant strain rate of 5%/min. Following this, the unloading cycle was realized with the same strain rate. Tangent modulus–strain curves were determined based on the slope of the stress–strain curve at any specified strain. Experimental data were statistically analysed through one-way ANOVA and Tukey's multiple pairwise comparisons test calculated by Origin 8. A $p$-value of 0.05 was considered to be significantly different. Data are expressed as mean ± standard deviation ($n$ = 4).

*4.3. Nanoindentation*

Nanomechanical measurements were performed with an Agilent G200 nanoindenter. A DCMII measurement head was used, performing indentations with a maximum depth of 1600 nm. CSM mode was used during the measurements. The indenter used was made of diamond and had a Berkovich-type geometry. The instrument was calibrated before the measurement using the Oliver–Pharr method [75]. Measurements were made on fibres immobilized in resin, at the centre of the fibre cross-section. Each fibre type was analysed by indentation at several locations for several fibres ($n$ = 10) in a given series. The reported errors of the determined parameters are the standard deviations of the obtained results. Experimental data were statistically analysed through one-way ANOVA and Tukey's multiple pairwise comparisons test. A $p$-value of 0.05 was considered to be significantly different. Data are expressed as mean ± standard deviation ($n$ = 10).

*4.4. Scanning Electron Microscopy*

The analyses were performed using the scanning electron microscope Quanta 250 FEG (FEI Ltd., Prague, Czech Republic). The samples were dried and pressed prior to the analyses.

*4.5. Digital Optical Microscopy*

The samples were observed with the advanced imaging systems consisting of a VHX-6000 digital microscope (Keyence, Osaka, Japan) and VH-Z20R zoom lenses (magnification up to 200×) as well as a Keyence VHX-7000 digital optical microscope with zoom lenses VHX E20 (magnification up to 100×) and VHX E100 (magnification up to 500×) (Keyence, Osaka, Japan).

*4.6. Measurment of Porosity, Pore Size, and Fibre Diameter*

The program ImageJ was used in this study in order to conduct the different image analysis techniques for calculating the porosity, pore size, and fibre diameter. The analyses were performed on electron micrographs obtained from the SEM experiments. Briefly, the software was calibrated prior to the measurement by using the scale on the electron micrographs (Figure 8). Subsequently, the binary threshold was adjusted, and the readings were taken for the porosity measurements. Similarly, the fibre diameter and pore size were also determined using the calibrated scale and respective functionality in the software.

## 5. Conclusions

We conclude that the combined analyses of monotonic compression and nanoindentation tests show a clear, but statistically insignificant trend that the removal of bromoty-

rosines from chitin scaffolds results in a reduced elastic modulus, however, a relatively unaffected hardness of the 3D scaffold. This is irrespective of the sample testing condition. Our study provides further evidence that the hardness observed with the scaffolds is imparted mainly by the specificity of sponge chitin. The presented mechanical properties of the natural 3D chitin scaffolds isolated from the cultivated *A. aerophoba* and other sponges are crucial for their further use in tissue engineering.

**Author Contributions:** Conceptualization, H.E., T.D., M.H. and W.Ś.; methodology, H.E., I.D., M.H., M.N., A.E. and T.D.; software, T.D., M.H. and M.N.; investigation, T.D., I.D., M.H., H.E., A.E., A.V., W.Ś. and M.N.; resources, H.E.; writing—original draft preparation, T.D.; writing—review and editing, H.E., T.D., M.H. and S.R.B.; visualization, T.D. and M.H.; funding acquisition, H.E. and S.R.B.; administration: H.E., T.D., M.P.-S. and A.V. All authors have read and agreed to the published version of the manuscript.

**Funding:** This research was funded by the National Science Centre within the framework of the project OPUS 19 grant of National Science Centre, Poland (2020/37/B/ST5/01909) and project MAESTRO 12 (2020/38/A/ST5/00151). A.V. was founded by VW Foundation (Funding for Refugee Scholars and Scientists from Ukraine, Personal Ref. No. 05020407B, TU Bergakademie Freiberg, Germany).

**Institutional Review Board Statement:** Not applicable.

**Data Availability Statement:** The original data presented in the study are included in the article; further inquiries can be directed to the corresponding author.

**Acknowledgments:** We would like to thank INTIB GmbH as well as BromMarin GmbH (Freiberg, Germany) for sponge specimens and technical support. The authors acknowledge Ahmet Kertmen for technical assistance.

**Conflicts of Interest:** The authors declare no conflict of interest. The funders had no role in the design of the study, in the collection, analyses or interpretation of data, in the writing of the manuscript or in the decision to publish the results.

## References

1. Tsurkan, D.; Wysokowski, M.; Petrenko, I.; Voronkina, A.; Khrunyk, Y.; Fursov, A.; Ehrlich, H. Modern scaffolding strategies based on naturally pre-fabricated 3D biomaterials of poriferan origin. *Appl. Phys. A* **2020**, *126*, 382. [CrossRef]
2. Binnewerg, B.; Schubert, M.; Voronkina, A.; Muzychka, L.; Wysokowski, M.; Petrenko, I.; Djurović, M.; Kovalchuk, V.; Tsurkan, M.; Martinovic, R.; et al. Marine biomaterials: Biomimetic and pharmacological potential of cultivated *Aplysina aerophoba* marine demosponge. *Mater. Sci. Eng. C Mater. Biol. Appl.* **2020**, *109*, 110566. (In English) [CrossRef]
3. Khrunyk, Y.; Lach, S.; Petrenko, I.; Ehrlich, H. Progress in Modern Marine Biomaterials Research. *Mar. Drugs* **2020**, *18*, 589. [CrossRef]
4. Ehrlich, H.; Wysokowski, M.; Jesionowski, T. The philosophy of extreme biomimetics. *Sustain. Mater. Technol.* **2022**, *32*, e00447. [CrossRef]
5. Costa, G.; Violi, B.; Bavestrello, G.; Pansini, M.; Bertolino, M. *Aplysina aerophoba* (Nardo, 1833) (Porifera, Demospongiae): An unexpected miniaturised growth form from the tidal zone of Mediterranean caves: Morphology and DNA barcoding. *Eur. Zool. J.* **2020**, *87*, 73–81. [CrossRef]
6. Mutsenko, V.V.; Gryshkov, O.; Lauterboeck, L.; Rogulska, O.; Tarusin, D.N.; Bazhenov, V.V.; Schütz, K.; Brüggemeier, S.; Gossla, E.; Akkineni, A.R.; et al. Novel chitin scaffolds derived from marine sponge *Ianthella basta* for tissue engineering approaches based on human mesenchymal stromal cells: Biocompatibility and cryopreservation. *Int. J. Biol. Macromol.* **2017**, *104*, 1955–1965. (In English) [CrossRef]
7. Mutsenko, V.V.; Bazhenov, V.V.; Rogulska, O.; Tarusin, D.N.; Schütz, K.; Brüggemeier, S.; Gossla, E.; Akkineni, A.R.; Meißner, H.; Lode, A.; et al. 3D chitinous scaffolds derived from cultivated marine demosponge *Aplysina aerophoba* for tissue engineering approaches based on human mesenchymal stromal cells. *Int. J. Biol. Macromol.* **2017**, *104*, 1966–1974. (In English) [CrossRef]
8. Schubert, M.; Binnewerg, B.; Voronkina, A.; Muzychka, L.; Wysokowski, M.; Petrenko, I.; Kovalchuk, V.; Tsurkan, M.; Martinovic, R.; Bechmann, N.; et al. Naturally Prefabricated Marine Biomaterials: Isolation and Applications of Flat Chitinous 3D Scaffolds from *Ianthella labyrinthus* (Demospongiae: Verongiida). *Int. J. Mol. Sci.* **2019**, *20*, 5105. [CrossRef]
9. Kovalchuk, V.; Voronkina, A.; Binnewerg, B.; Schubert, M.; Muzychka, L.; Wysokowski, M.; Tsurkan, M.V.; Bechmann, N.; Petrenko, I.; Fursov, A.; et al. Naturally Drug-Loaded Chitin: Isolation and Applications. *Mar. Drugs* **2019**, *17*, 574. (In English) [CrossRef]

10. Muzychka, L.; Voronkina, A.; Kovalchuk, V.; Smolii, O.B.; Wysokowski, M.; Petrenko, I.; Youssef, D.T.A.; Ehrlich, I.; Ehrlich, H. Marine biomimetics: Bromotyrosines loaded chitinous skeleton as source of antibacterial agents. *Appl. Phys. A Mater. Sci. Process.* **2021**, *127*, 15. (In English) [CrossRef]
11. Machałowski, T.; Rusak, A.; Wiatrak, B.; Haczkiewicz-Leśniak, K.; Popiel, A.; Jaroszewicz, J.; Żak, A.; Podhorska-Okołów, M.; Jesionowski, T. Naturally Formed Chitinous Skeleton Isolated from the Marine Demosponge *Aplysina fistularis* as a 3D Scaffold for Tissue Engineering. *Materials* **2021**, *14*, 2992. [CrossRef]
12. Nowacki, K.; Galiński, M.; Fursov, A.; Voronkina, A.; Meissner, H.; Petrenko, I.; Stelling, A.L.; Ehrlich, H. Electrolysis as a Universal Approach for Isolation of Diverse Chitin Scaffolds from Selected Marine Demosponges. *Mar. Drugs* **2022**, *20*, 665. [CrossRef]
13. Klinger, C.; Żółtowska-Aksamitowska, S.; Wysokowski, M.; Tsurkan, M.V.; Galli, R.; Petrenko, I.; Machałowski, T.; Ereskovsky, A.; Martinović, R.; Muzychka, L.; et al. Express Method for Isolation of Ready-to-Use 3D Chitin Scaffolds from *Aplysina archeri* (Aplysineidae: Verongiida) Demosponge. *Mar. Drugs* **2019**, *17*, 131. [CrossRef] [PubMed]
14. Klinger, C.; Żółtowska, S.; Jesionowski, T. Isolation of Chitin from *Aplysina aerophoba* Using a Microwave Approach. *Prog. Chem. Appl. Chitin Deriv.* **2019**, *XXIV*, 61–74. [CrossRef]
15. Żółtowska, S.; Klinger, C.; Petrenko, I.; Wysokowski, M.; Joseph, Y.; Jesionowski, T.; Ehrlich, H. Methods of Isolating Chitin from Sponges (Porifera). In *Chitin and Chitosan: Properties and Applications*; John Wiley & Sons Ltd.: Hoboken, NJ, USA, 2019; pp. 35–59.
16. Duminis, T. Natural Polymers with Bioactive Glass Additives for Bone Regeneration: Chemistry and Trends. *Nat. Prod. J.* **2023**, *14*, e280423216342. [CrossRef]
17. Duminis, T.; Shahid, S.; Hill, R.G. Apatite glass-ceramics: A review. *Front. Mater.* **2017**, *3*, 59. [CrossRef]
18. Kaya, M.; Mujtaba, M.; Ehrlich, H.; Salaberria, A.M.; Baran, T.; Amemiya, C.T.; Galli, R.; Akyuz, L.; Sargin, I.; Labidi, J. On chemistry of γ-chitin. *Carbohydr. Polym.* **2017**, *176*, 177–186. [CrossRef]
19. Tsurkan, M.V.; Voronkina, A.; Khrunyk, Y.; Wysokowski, M.; Petrenko, I.; Ehrlich, H. Progress in chitin analytics. *Carbohydr. Polym.* **2021**, *252*, 117204. [CrossRef]
20. Sawada, D.; Nishiyama, Y.; Langan, P.; Forsyth, V.T.; Kimura, S.; Wada, M. Direct Determination of the Hydrogen Bonding Arrangement in Anhydrous β-Chitin by Neutron Fiber Diffraction. *Biomacromolecules* **2012**, *13*, 288–291. [CrossRef]
21. Wei, A.; Fu, J.; Guo, F. Mechanical properties of chitin polymorphs: A computational study. *J. Mater. Sci.* **2021**, *56*, 12048–12058. [CrossRef]
22. Deringer, V.L.; Englert, U.; Dronskowski, R. Nature, Strength, and Cooperativity of the Hydrogen-Bonding Network in α-Chitin. *Biomacromolecules* **2016**, *17*, 996–1003. [CrossRef]
23. Cui, J.; Yu, Z.; Lau, D. Effect of Acetyl Group on Mechanical Properties of Chitin/Chitosan Nanocrystal: A Molecular Dynamics Study. *Int. J. Mol. Sci.* **2016**, *17*, 61. [CrossRef]
24. Montroni, D.; Fermani, S.; Morellato, K.; Torri, G.; Naggi, A.; Cristofolini, L.; Falini, G. β-Chitin samples with similar microfibril arrangement change mechanical properties varying the degree of acetylation. *Carbohydr. Polym.* **2019**, *207*, 26–33. [CrossRef] [PubMed]
25. Dziedzic, I.; Voronkina, A.; Pajewska-Szmyt, M.; Kotula, M.; Kubiak, A.; Meissner, H.; Duminis, T.; Ehrlich, H. The Loss of Structural Integrity of 3D Chitin Scaffolds from *Aplysina aerophoba* Marine Demosponge after Treatment with LiOH. *Mar. Drugs* **2023**, *21*, 334. [CrossRef] [PubMed]
26. Brunner, E.; Ehrlich, H.; Schupp, P.; Hedrich, R.; Hunoldt, S.; Kammer, M.; Machill, S.; Paasch, S.; Bazhenov, V.V.; Kurek, D.V.; et al. Chitin-based scaffolds are an integral part of the skeleton of the marine demosponge *Ianthella basta*. *J. Struct. Biol.* **2009**, *168*, 539–547. (In English) [CrossRef]
27. Geahchan, S.; Ehrlich, H.; Rahman, M.A. The Anti-Viral Applications of Marine Resources for COVID-19 Treatment: An Overview. *Mar. Drugs* **2021**, *19*, 409. (In English) [CrossRef]
28. Yusof, N.L.B.M.; Lim, L.Y.; Khor, E. Flexible chitin films: Structural studies. *Carbohydr. Res.* **2004**, *339*, 2701–2711. [CrossRef] [PubMed]
29. Siamantouras, E.; Woodrow, C.; Celiker, E.; Cullen, D.A.; Hills, C.E.; Squires, P.E.; Montealegre-Z, F. Quantification of bush-cricket acoustic trachea mechanics using Atomic Force Microscopy nanoindentation. *Acta Biomater.* **2022**, *153*, 399–410. [CrossRef]
30. Chen, P.-Y.; Lin, A.Y.-M.; McKittrick, J.; Meyers, M.A. Structure and mechanical properties of crab exoskeletons. *Acta Biomater.* **2008**, *4*, 587–596. [CrossRef]
31. Gadgey, K.K.; Bahekar, A. Studies on extraction methods of chitin from crab shell and investigation of its mechanical properties. *Int. J. Mech. Eng. Technol.* **2017**, *8*, 220–231.
32. Gallagher, A.J.; Ní Annaidh, A.; Bruyère-Garnier, K. Dynamic tensile properties of human skin. In Proceedings of the 2012 IRCOBI Conference Proceedings, Dublin, Ireland, 12–14 September 2012; pp. 494–502.
33. Rohlmann, A.; Zilch, H.; Bergmann, G.; Kolbel, R. Material properties of femoral cancellous bone in axial loading—Part I: Time independent properties. *Arch. Orthop. Trauma. Surg.* **1980**, *97*, 95–102. [CrossRef] [PubMed]
34. Duan, B.; Chang, C.; Zhang, L. Structure and properties of films fabricated from chitin solution by coagulating with heating. *J. Appl. Polym. Sci.* **2014**, *131*, 1–7. [CrossRef]
35. Kim, J.; Ha, C.S.; Jo, N.J. Synthesis and properties of biodegradable chitin-graft-poly(L-lactide) copolymers. *Polym. Int.* **2002**, *51*, 1123–1128. [CrossRef]

36. Chen, B.; Sun, K.; Ren, T. Mechanical and viscoelastic properties of chitin fiber reinforced poly(ε-caprolactone). *Eur. Polym. J.* **2005**, *41*, 453–457. [CrossRef]
37. Jayakumar, R.; Tamura, H. Synthesis, characterization and thermal properties of chitin-g-poly(epsilon-caprolactone) copolymers by using chitin gel. *Int. J. Biol. Macromol.* **2008**, *43*, 32–36. (In English) [CrossRef] [PubMed]
38. Wysokowski, M.; Petrenko, I.; Stelling, A.L.; Stawski, D.; Jesionowski, T.; Ehrlich, H. Poriferan Chitin as a Versatile Template for Extreme Biomimetics. *Polymers* **2015**, *7*, 235–265. [CrossRef]
39. Ifuku, S.; Nogi, M.; Abe, K.; Yoshioka, M.; Morimoto, M.; Saimoto, H.; Yano, H. Preparation of Chitin Nanofibers with a Uniform Width as α-Chitin from Crab Shells. *Biomacromolecules* **2009**, *10*, 1584–1588. [CrossRef] [PubMed]
40. Moon, H.; Choy, S.; Park, Y.; Jung, Y.M.; Koo, J.M.; Hwang, D.S. Different Molecular Interaction between Collagen and α- or β-Chitin in Mechanically Improved Electrospun Composite. *Mar. Drugs* **2019**, *17*, 318. [CrossRef]
41. Yu, Z.; Lau, D. Molecular dynamics study on stiffness and ductility in chitin–protein composite. *J. Mater. Sci.* **2015**, *50*, 7149–7157. [CrossRef]
42. Nowacki, K.; Stępniak, I.; Machałowski, T.; Wysokowski, M.; Petrenko, I.; Schimpf, C.; Rafaja, D.; Langer, E.; Richter, A.; Ziętek, J.; et al. Electrochemical method for isolation of chitinous 3D scaffolds from cultivated *Aplysina aerophoba* marine demosponge and its biomimetic application. *Appl. Phys. A* **2020**, *126*, 368. [CrossRef]
43. Fu, Y.B.; Ogden, R.W. *Nonlinear Elasticity: Theory and Applications*; Cambridge University Press: Cambridge, UK, 2001.
44. Calabrese, L.; Bonaccorsi, L.; Bruzzaniti, P.; Gullì, G.; Freni, A.; Proverbio, E. Zeolite filled siloxane composite foams: Compression property. *J. Appl. Polym. Sci.* **2018**, *135*, 46145. [CrossRef]
45. Granito, R.N.; Custódio, M.R.; Rennó, A.C.M. Natural marine sponges for bone tissue engineering: The state of art and future perspectives. *J. Biomed. Mater. Res. B Appl. Biomater.* **2017**, *105*, 1717–1727. (In English) [CrossRef] [PubMed]
46. Chatzimitakos, T.G.; Stalikas, C.D. Sponges and Sponge-Like Materials in Sample Preparation: A Journey from Past to Present and into the Future. *Molecules* **2020**, *25*, 3673. (In English) [CrossRef] [PubMed]
47. Woesz, A.; Weaver, J.C.; Kazanci, M.; Dauphin, Y.; Aizenberg, J.; Morse, D.E.; Fratzl, P. Micromechanical properties of biological silica in skeletons of deep-sea sponges. *J. Mater. Res.* **2006**, *21*, 2068–2078. [CrossRef]
48. Louden, D.; Inderbitzin, S.; Peng, Z.; de Nys, R. Development of a new protocol for testing bath sponge quality. *Aquaculture* **2007**, *271*, 275–285. [CrossRef]
49. Shen, J.; Min Xie, Y.; Huang, X.; Zhou, S.; Ruan, D. Mechanical properties of luffa sponge. *J. Mech. Behav. Biomed. Mater.* **2012**, *15*, 141–152. [CrossRef] [PubMed]
50. Ghodbane, S.A.; Dunn, M.G. Physical and mechanical properties of cross-linked type I collagen scaffolds derived from bovine, porcine, and ovine tendons. *J. Biomed. Mater. Res. A* **2016**, *104*, 2685–2692. (In English) [CrossRef]
51. Wang, Z.; Lin, S.; Li, X.; Zou, H.; Zhuo, B.; Ti, P.; Yuan, Q. Optimization and absorption performance of wood sponge. *J. Mater. Sci.* **2021**, *56*, 8479–8496. [CrossRef]
52. Ofem, M.I.; Muhammed, M.; Umar, M. Mechanical properties of Dungeness crab based chitin. *Int. J. Sci. Eng. Res.* **2015**, *6*, 1737–1743.
53. Ifuku, S.; Saimoto, H. Chitin nanofibers: Preparations, modifications, and applications. *Nanoscale* **2012**, *4*, 3308–3318. [CrossRef] [PubMed]
54. Mushi, N.E.; Butchosa, N.; Salajkova, M.; Zhou, Q.; Berglund, L.A. Nanostructured membranes based on native chitin nanofibers prepared by mild process. *Carbohydr. Polym.* **2014**, *112*, 255–263. [CrossRef]
55. Wang, J.; Brasch, M.E.; Baker, R.M.; Tseng, L.F.; Peña, A.N.; Henderson, J.H. Shape memory activation can affect cell seeding of shape memory polymer scaffolds designed for tissue engineering and regenerative medicine. *J. Mater. Sci. Mater. Med.* **2017**, *28*, 151. (In English) [CrossRef]
56. Lv, S.; Cai, M.; Leng, F.; Jiang, X. Biodegradable carboxymethyl chitin-based hemostatic sponges with high strength and shape memory for non-compressible hemorrhage. *Carbohydr. Polym.* **2022**, *288*, 119369. (In English) [CrossRef]
57. Ross, C.T.F.; Case, T.J.; Chilver, A. *Strength of Materials and Structures*; Elsevier Science: Amsterdam, The Netherlands, 1999.
58. Welinder, B.S. Halogenated tyrosines from the cuticle of *Limulus polyphemus* (L.). *Biochim. Biophys. Acta* **1972**, *279*, 491–497. (In English) [CrossRef] [PubMed]
59. Hunt, S.; Breuer, S.W. Chlorinated and Brominated Tyrosine Residues in Molluscan Scleroprotein. *Biochem. Soc. Trans.* **1973**, *1*, 215–216. [CrossRef]
60. Montroni, D.; Sparla, F.; Fermani, S.; Falini, G. Influence of proteins on mechanical properties of a natural chitin-protein composite. *Acta Biomater.* **2021**, *120*, 81–90. [CrossRef]
61. Torres-Rendon, J.G.; Schacher, F.H.; Ifuku, S.; Walther, A. Mechanical Performance of Macrofibers of Cellulose and Chitin Nanofibrils Aligned by Wet-Stretching: A Critical Comparison. *Biomacromolecules* **2014**, *15*, 2709–2717. [CrossRef] [PubMed]
62. Mushi, N.E. A review on native well-preserved chitin nanofibrils for materials of high mechanical performance. *Int. J. Biol. Macromol.* **2021**, *178*, 591–606. (In English) [CrossRef]
63. Ehrlich, H. Chitin of poriferan origin as a unique biological material. In *Blue Biotechnology: Production and Use of Marine Molecules*; Wiley-VCH Verlag GmbH & Co. KGaA: Weinheim, Germany, 2018; Volume 2, pp. 821–854.
64. Mutsenko, V.; Gryshkov, O.; Rogulska, O.; Lode, A.; Petrenko, A.Y.; Gelinsky, M.; Glasmacher, B.; Ehrlich, H. Chitinous scaffolds from marine sponges for tissue engineering. In *Marine-Derived Biomaterials for Tissue Engineering Applications*; Springer: Singapore, 2019; pp. 285–307.

65. Ehrlich, H.; Steck, E.; Ilan, M.; Maldonado, M.; Muricy, G.; Bavestrello, G.; Kljajic, Z.; Carballo, J.; Schiaparelli, S.; Ereskovsky, A. Three-dimensional chitin-based scaffolds from Verongida sponges (Demospongiae: Porifera). Part II: Biomimetic potential and applications. *Int. J. Biol. Macromol.* **2010**, *47*, 141–145. [CrossRef]
66. Machałowski, T.; Czajka, M.; Petrenko, I.; Meissner, H.; Schimpf, C.; Rafaja, D.; Ziętek, J.; Dzięgiel, B.; Adaszek, Ł.; Voronkina, A.; et al. Functionalization of 3D Chitinous Skeletal Scaffolds of Sponge Origin Using Silver Nanoparticles and Their Antibacterial Properties. *Mar. Drugs* **2020**, *18*, 304. [CrossRef]
67. Ehrlich, H.; Simon, P.; Carrillo-Cabrera, W.; Bazhenov, V.V.; Botting, J.P.; Ilan, M.; Ereskovsky, A.V.; Muricy, G.; Worch, H.; Mensch, A.; et al. Insights into Chemistry of Biological Materials: Newly Discovered Silica-Aragonite-Chitin Biocomposites in Demosponges. *Chem. Mater.* **2010**, *22*, 1462–1471. [CrossRef]
68. Bo, M.; Bavestrello, G.; Kurek, D.; Paasch, S.; Brunner, E.; Born, R.; Galli, R.; Stelling, A.L.; Sivkov, V.N.; Petrova, O.V.; et al. Isolation and identification of chitin in the black coral *Parantipathes larix* (Anthozoa: Cnidaria). *Int. J. Biol. Macromol.* **2012**, *51*, 129–137. (In English) [CrossRef]
69. Nowacki, K.; Stępniak, I.; Langer, E.; Tsurkan, M.; Wysokowski, M.; Petrenko, I.; Khrunyk, Y.; Fursov, A.; Bo, M.; Bavestrello, G.; et al. Electrochemical Approach for Isolation of Chitin from the Skeleton of the Black Coral *Cirrhipathes* sp. (Antipatharia). *Mar. Drugs* **2020**, *18*, 297. (In English) [CrossRef] [PubMed]
70. Rahman, M.A.; Halfar, J. First evidence of chitin in calcified coralline algae: New insights into the calcification process of *Clathromorphum compactum*. *Sci. Rep.* **2014**, *4*, 6162. [CrossRef]
71. Baharlouei, P.; Rahman, A. Chitin and Chitosan: Prospective Biomedical Applications in Drug Delivery, Cancer Treatment, and Wound Healing. *Mar. Drugs* **2022**, *20*, 460. (In English) [CrossRef]
72. Machałowski, T.; Wysokowski, M.; Żółtowska-Aksamitowska, S.; Bechmann, N.; Binnewerg, B.; Schubert, M.; Guan, K.; Bornstein, S.R.; Czaczyk, K.; Pokrovsky, O.; et al. Spider Chitin. The biomimetic potential and applications of Caribena versicolor tubular chitin. *Carbohydr. Polym.* **2019**, *226*, 115301. [CrossRef] [PubMed]
73. Machałowski, T.; Wysokowski, M.; Tsurkan, M.V.; Galli, R.; Schimpf, C.; Rafaja, D.; Brendler, E.; Viehweger, C.; Żółtowska-Aksamitowska, S.; Petrenko, I.; et al. Spider Chitin: An Ultrafast Microwave-Assisted Method for Chitin Isolation from *Caribena versicolor* Spider Molt Cuticle. *Molecules* **2019**, *24*, 3736. [CrossRef]
74. Ehrlich, H.; Ilan, M.; Maldonado, M.; Muricy, G.; Bavestrello, G.; Kljajic, Z.; Carballo, J.L.; Schiaparelli, S.; Ereskovsky, A.; Schupp, P.; et al. Three-dimensional chitin-based scaffolds from Verongida sponges (Demospongiae: Porifera). Part I. Isolation and identification of chitin. *Int. J. Biol. Macromol.* **2010**, *47*, 132–140. [CrossRef]
75. Oliver, W.C.; Pharr, G.M. An improved technique for determining hardness and elastic modulus using load and displacement sensing indentation experiments. *J. Mater. Res.* **1992**, *7*, 1564–1583. [CrossRef]

marine drugs

MDPI

*Article*

# Chitosan from Marine Amphipods Inhibits the Wilt Banana Pathogen *Fusarium oxysporum* f. sp. Cubense Tropical Race 4

**Marc Roig-Puche [1], Federico Lopez-Moya [1,*], Miguel Valverde-Urrea [1], Pablo Sanchez-Jerez [2], Luis Vicente Lopez-Llorca [1,†] and Victoria Fernandez-Gonzalez [2,†]**

[1] Laboratory of Plant Pathology, Department of Marine Sciences and Applied Biology, University of Alicante, 03690 Alicante, Spain; marcpuche9919@gmail.com (M.R.-P.); mrvu1@gcloud.ua.es (M.V.-U.); lv.lopez@ua.es (L.V.L.-L.)

[2] Laboratory of Marine Biology, Department of Marine Sciences and Applied Biology, University of Alicante, 03690 Alicante, Spain; psanchez@ua.es (P.S.-J.); victoria.fernandez@ua.es (V.F.-G.)

* Correspondence: federico.lopez@ua.es

† These authors contributed equally to this work.

**Abstract:** In this work, we extracted chitosan from marine amphipods associated with aquaculture facilities and tested its use in crop protection. The obtained chitosan was 2.5 ± 0.3% of initial ground amphipod dry weight. The chemical nature of chitosan from amphipod extracts was confirmed via Raman scattering spectroscopy and Fourier transform infrared spectroscopy (FTIR). This chitosan showed an 85.7–84.3% deacetylation degree. Chitosan from biofouling amphipods at 1 mg·mL$^{-1}$ virtually arrested conidia germination (ca. sixfold reduction from controls) of the banana wilt pathogenic fungus *Fusarium oxysporum* f. sp cubense Tropical Race 4 (FocTR4). This concentration reduced (ca. twofold) the conidia germination of the biocontrol fungus *Pochonia chlamydosporia* (Pc123). Chitosan from amphipods at low concentrations (0.01 mg·mL$^{-1}$) still reduced FocTR4 germination but did not affect Pc123. This is the first time that chitosan is obtained from biofouling amphipods. This new chitosan valorizes aquaculture residues and has potential for biomanaging the diseases of food security crops such as bananas.

**Keywords:** amphipods; biofouling; fish farms; chitooligosacharides; Fourier transform infrared spectroscopy (FTIR); Raman; plant pathogenic fungi; banana disease; nematophagous fungi; *Pochonia chlamydosporia*

**Citation:** Roig-Puche, M.; Lopez-Moya, F.; Valverde-Urrea, M.; Sanchez-Jerez, P.; Lopez-Llorca, L.V.; Fernandez-Gonzalez, V. Chitosan from Marine Amphipods Inhibits the Wilt Banana Pathogen *Fusarium oxysporum* f. sp. Cubense Tropical Race 4. *Mar. Drugs* **2023**, *21*, 601. https://doi.org/10.3390/md21120601

Academic Editors: Azizur Rahman and Hermann Ehrlich

Received: 9 August 2023
Revised: 17 November 2023
Accepted: 20 November 2023
Published: 22 November 2023



## 1. Introduction

Since the publication of the Blue Growth strategy in 2012 by the European Commission [1], marine environments have been recognized as potential sources for innovation, economic growth, and job creation. This new sea economy aims to optimize the benefits of sustainably developing marine and maritime sectors [1]. Thus, aquaculture plays a key role in meeting our demand for fish and seafood of high nutritional value [2].

Offshore aquaculture has steadily increased in the marine environment over the last five decades. There is a need to address the challenges posed by this fast growth to provide strategies for the long-term sustainability and conservation of marine ecosystems [3]. The intensity of fish farm exploitation generates byproducts (waste). These wastes may accumulate on marine sediments and cause eutrophication [4]. Integrated multi-trophic aquaculture (IMTA) systems are devised to reduce these environmental impacts. IMTA systems co-culture species from different trophic levels, so by-products from a species become inputs for another [2,5]. Marine species that grow in aquaculture facilities forming biofouling communities can feed on fed waste, contributing to bioremediation [6]. Highly abundant crustacean amphipods in fish farms are suitable for co-culturing in IMTA systems [7].

The circular economy complements Blue Growth, aiming to create a restorative or regenerative industrial system through intention and design, replacing the concept of end-of-life with restoration [8]. It is based on an environmentalist mindset and proposes to change the motto "reduce, reuse and recycle" for a deep and lasting transformation [9]. The new paradigm is to turn waste into raw materials [10]. Thus, marine species that naturally grow in aquaculture facilities could be harvested and used to develop new biological products with applications in several industries, meaning an extra source of income [7].

Marine organisms are a new source of natural products, some with unusual chemical structures [11]. Chitin, one of the most abundant polymers in nature [12], can be found in marine crustaceans, insects, and fungi. Chitosan is a by-product of the partial deacetylation of chitin, primarily consisting of beta-1,4-glucosamine subunit polymers [13]. Chitosan is mostly obtained from by-products of fishing industries; it is a renewable, non-toxic, non-allergenic, antimicrobial, and biodegradable biopolymer [14]. Shellfish waste contains 14–35% chitin associated with proteins (30–40%), lipids, pigments, and calcium deposits (30–50%), and various technological alternatives have been developed for converting shellfish into useful products [15]. As a result, the large biomass of amphipods in aquaculture facilities could be used to produce chitin and chitosan, providing added value to fish farms.

Chitosan has countless applications, including cosmetics, medicine, and agriculture [13,16]. Chitosan from crustaceans has more antimicrobial properties than important worldwide plant pathogens such as *Fusarium oxysporum* or *Magnaporthe oryzae* [17–20]. Chitosan permeabilizes the plasma membrane of sensitive fungi, with membranes enriched in unsaturated free fatty acids. In contrast, biocontrol fungi (BCA) (mostly nematophagous and entomopathogenic fungi) tolerate chitosan. These BCAs develop infective structures on the exoskeletons and cuticles of their hosts. These structures are enriched in chitin and chitosan [21,22]. BCAs have glycosyl hydrolase families, mainly GH18 (chitinases) and GH 75 (chitosanases) expanded in their genomes [23,24]. These GHs can degrade chitin and chitosan.

In this study, we evaluated marine amphipods associated with aquaculture facilities as a new source of chitosan and its biotechnological use. Our aims are to: (a) extract chitin from amphipods and its conversion to chitosan, (b) characterize amphipod chitosan, and (c) test chitosan from amphipods on the spore germination of agriculturally important fungi: *Pochonia chlamydosporia*, a nematophagous fungus used in biological control; and *Fusarium oxysporum* f. sp. cubense Tropical Race 4 (FocTR4), an emerging and highly virulent fungal pathogen of banana plants.

## 2. Results

### *2.1. Chitosan Extraction*

Amphipod exoskeletons contain chitin that can be transformed into chitosan. Table 1 shows chitin/chitosan yields from amphipod samples. Biofouling amphipod's chitosan yield ($2.55 \pm 0.34\%$ ground amphipod dry weight) was similar to that from commercial turtle feed amphipods (2.43%). This was despite ca. 50 times more starting materials in the latter. Chitin yields were higher since this biopolymer is the source for chitosan extraction.

### *2.2. Spectroscopical Characterization of Chitin and Chitosan*

The chitin–chitosan Raman spectra from the 1500–1800 $cm^{-1}$ region showed a fluorescence background, with both lasers tested (785 and 1064 nm). They were, therefore, discarded. FTIR detected $NH_2$ (1) and N-acetyl groups (2), diagnostic for chitin (Figure 1a) and chitosan (Figure 1b–d) in all samples. This confirms that all samples analyzed were either chitin or chitosan. However, in chitin spectra (a), the intensity of band 1 (0.056) was much lower than band 2 (0.096). In contrast, there was little difference between the intensities of both bands for the rest of the samples (chitosan; b1: 0.056, b2: 0.051; c1: 0.062, c2: 0.060; and d1: 0.052, d2: 0.054). The spectra indicate that the b, c, and d samples underwent partial deacetylation, whereas sample a did not. The intensities corresponding to the N–H bonds of amide I and the O–H bond associated with the pyranose ring (5) were only clearly

observed in the b, c, and d spectra, indicating that the analyzed samples correspond to chitosan molecules. These bands are the most representative of this biopolymer. For sample a, this region was not observed with the same intensity, suggesting that the spectrum corresponds to chitin.

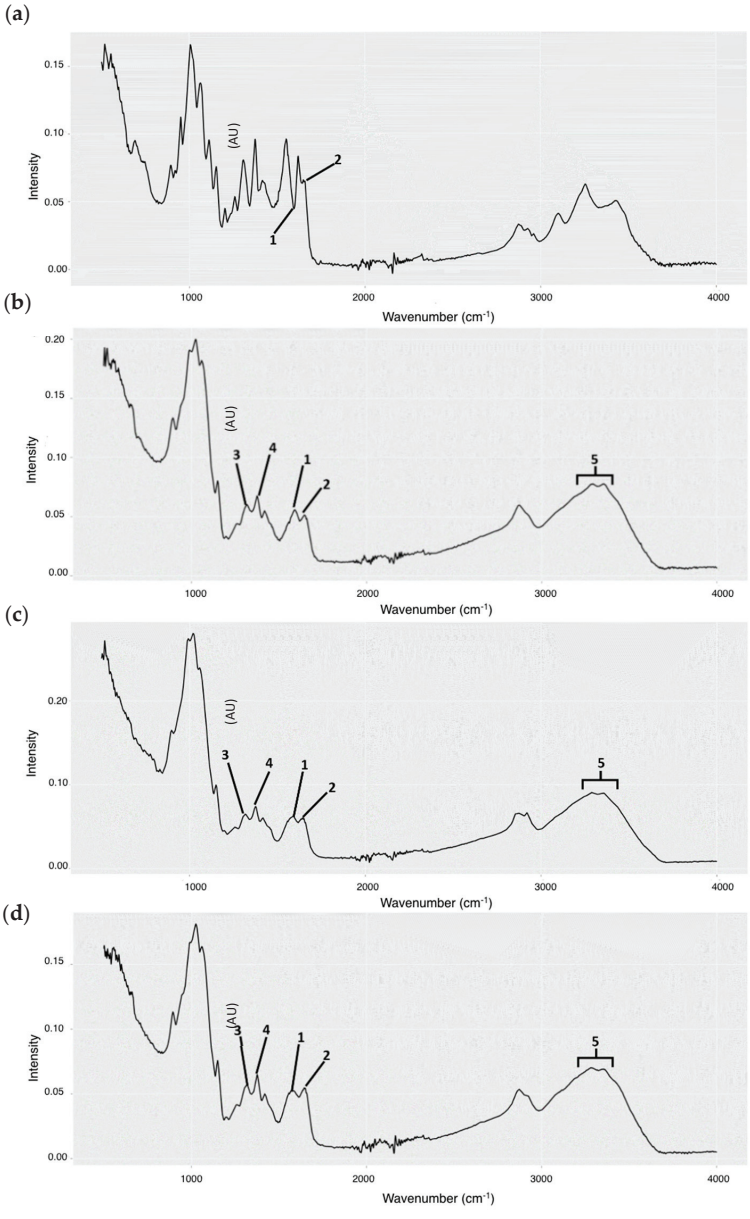


**Figure 1.** FTIR absorption spectra of chitin and chitosan: (**a**) Commercial chitin; (**b**) Commercial chitosan; (**c**) Biofouling amphipod chitosan (M4); and (**d**) Commercial amphipod (turtle feed) chitosan (M5). Group diagnostic bands: (1) $NH_2$ groups (1590 $cm^{-1}$); (2) residual N-acetyl groups (1650 $cm^{-1}$); (3) C–N amide III bond (1320 $cm^{-1}$); (4) $CH_3$ groups (1420 $cm^{-1}$); and (5) N–H amide I and O–H pyranose ring bonds (3200–3400 $cm^{-1}$). Intensity is measured in absorbance units (AU).

**Table 1.** Chitin and chitosan purification from amphipods in this work.

| Step | Sample Weight (g) | | | | |
|---|---|---|---|---|---|
| | **M1** | **M2** | **M3** | **M4** | **M5** |
| Ground-dried amphipods | 1.205 | 1.302 | 1.188 | 14.1 | 49.31 |
| Demineralization | 0.416 | 0.56 | 0.469 | 5.45 | 20.52 |
| Deproteinization | 0.156 | 0.151 | 0.121 | 2.955 | 2.85 |
| Chitin | 0.093 | 0.083 | 0.064 | 0.983 | 2.024 |
| Chitosan | 0.034 | 0.037 | 0.027 | 0.312 | 1.198 |
| Chitin Yield (%) | 7.72 | 6.37 | 5.39 | 6.97 | 4.1 |
| Chitosan Yield (%) | 2.82 | 2.84 | 2.27 | 2.21 | 2.43 |
| Biofouling Amphipods (M1–M4) Chitin Yield (% ± SD) | | | | 6.61± 0.98 | |
| Biofouling Amphipods (M1–M4) Chitosan Yield (% ± SD) | | | | 2.55 ± 0.34 | |

M1–4 chitosan from biofouling aquaculture amphipods. M5 chitosan from commercial amphipods (turtle food). SD indicates the standard deviation (in %) from the mean yield of chitin and chitosan in the biofouling aquaculture amphipod samples (M1–M4).

Deacetylation Degree (%DD)

Figure 1 (FTIR spectra) shows the intensity (in AU) of peaks corresponding to the $NH_2$ groups and the C–N bond of amide III (peaks 3 and 4, respectively). The %DD of chitosan extracted from amphipods and commercial chitosan (T8) were calculated from them (Table 2). All DDs were above 84%, confirming that these samples are chitosan.

**Table 2.** Chitosan N-deacetylation degree (DD).

| Chitosan Source | %DD |
|---|---|
| T8 | 85.2–(90.1 *) |
| M1 | 85.7 |
| M2 | 85.3 |
| M3 | 85.3 |
| M4 | 84.3 |
| M5 | 83.3 |

* %DD from (DD) data sheet provided by the manufacturer.

### *2.3. Effect of Chitosan on Spore Germination*

#### 2.3.1. *Pochonia chlamydosporia* Isolate 123

Chitosan from the biofouling amphipods and other sources had no significant ($p$-value < 0.05) effect on the conidia germination of the biocontrol fungus Pc123 at low concentrations (0.01 mg·mL$^{-1}$) (Figure 2). However, all chitosan samples significantly reduced (ca. twofold) Pc123 conidia germination at 1 mg·mL$^{-1}$. No differences ($p$-value < 0.05) in *P. chlamydosporia* conidia germination were found for 1 mg·mL$^{-1}$ chitosan from the three sources tested after 24 h and 48 h.

#### 2.3.2. *Fusarium oxysporum* f. sp. cubense Tropical Race 4

Chitosan from biofouling amphipods and other sources at 1 mg·mL$^{-1}$ virtually arrested the conidia germination (ca. sixfold reduction from controls, Figure 3) of the banana wilt pathogenic fungus FocTR4. Most chitosan reduced FocTR4 conidia germination even at a low concentration (0.01 mg·mL$^{-1}$). For *P. chlamydosporia,* no significant ($p$-value < 0.05) differences in FocTR4 spore germination were found for the tested three sources of chitosan.

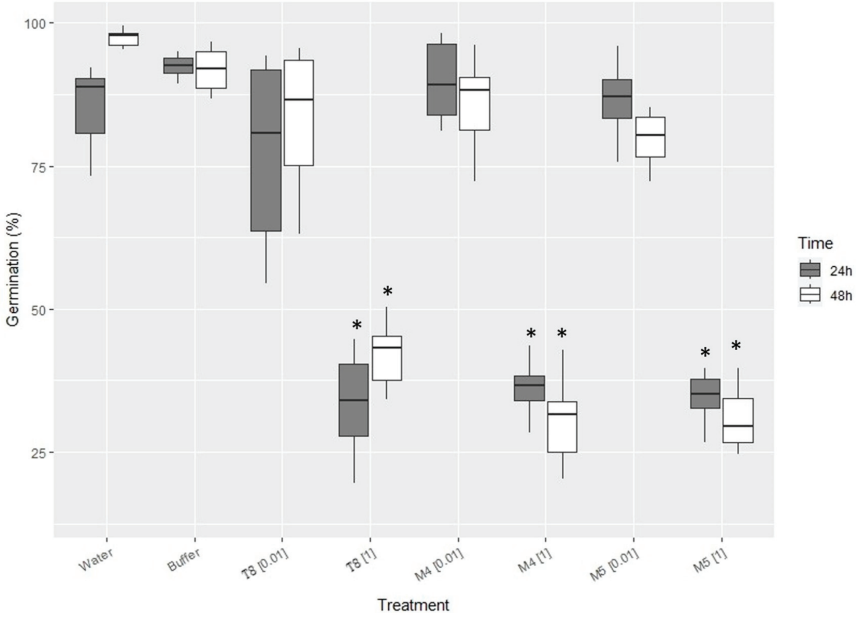


**Figure 2.** Effect of chitosan from biofouling amphipods and other sources on conidia germination of the nematophagous fungus *P. chlamydosporia*. Treatments: (T8) Commercial chitosan; (M4) Chitosan from biofouling amphipods; (M5) Chitosan from commercial (turtle feed) amphipods. (*) indicates significant differences from controls ($p < 0.05$).

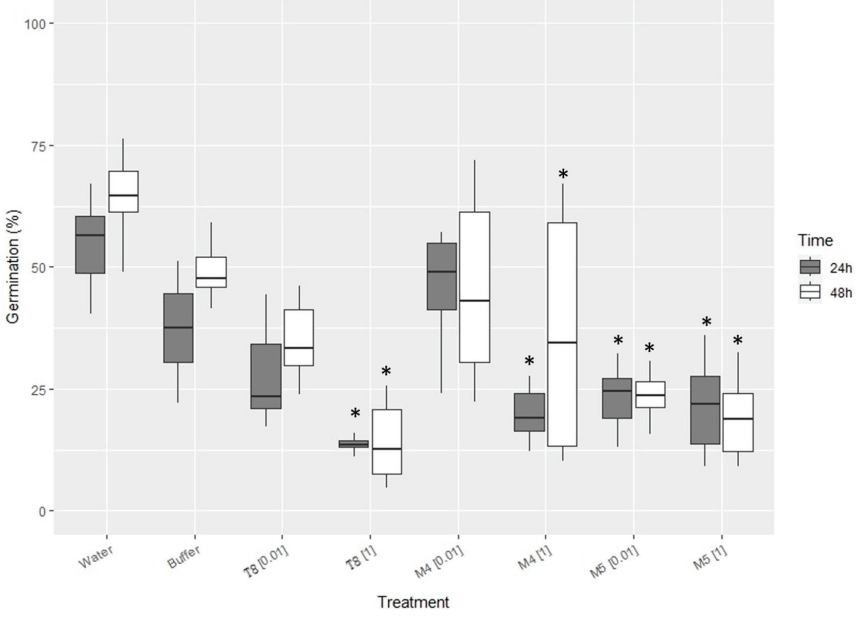


**Figure 3.** Effect of chitosan from biofouling amphipods and other sources on conidia germination of the phytopathogenic fungus FocTR4. Treatments: (T8) Commercial chitosan; (M4) Chitosan from biofouling amphipods; (M5) Chitosan from commercial (turtle feed) amphipods. (*) indicates significant differences from controls ($p < 0.05$).

## 3. Discussion

In our study, we have extracted and characterized chitosan from amphipods associated with biofouling in aquaculture facilities. Chitosan is often obtained from the exoskeletons of marine organisms, mainly crustaceans [25]. This uses waste from the seafood industry via a circular economy approach [15]. However, the current work is, to the best of our knowledge, the first report using amphipods associated with integrated aquaculture as a source for chitosan extraction.

The chitosan extraction yield from amphipods (2.2–2.8%) is significantly lower than that from the exoskeletons of larger crustaceans (e.g., crab, shrimp, or crayfish) [25]. Extraction yields ranging from 9.2 to 22.9% of the initial dry weight are reported, depending on the organism used as raw material.

Raman scattering spectroscopy can provide information on the chemical structures and physical shapes of molecules using characteristic spectral patterns [26]. However, sample fluorescence can be a major issue [27]. In this work, we have experienced that problem. Despite testing several lasers, we were unable to identify this polysaccharide in amphipod extracts using Raman spectroscopy. Fourier transform infrared spectroscopy (FTIR) is the most widely used spectroscopy technique to study vibration in molecules that avoids fluorescence problems. FTIR has allowed us to identify chitosan from amphipod samples. In our analyses, we detected the characteristic wavelengths [28], corroborating the fact that the amphipod extractions contained chitosan or chitin.

The essential parameter for chitosan characterization is the degree of N-deacetylation, determining the physiological and functional characteristics of the biopolymer [29]. Using FTIR data, we have estimated more than 80% of the degree of N-deacetylation of chitosan from biofouling amphipods and other sources, including commercial samples.

In our study, we have found that the conidia germination of the biocontrol fungus Pc123 is unaffected by low concentrations of chitosan from biofouling and commercial-fed amphipods. This agrees with previous studies using chitosan from large crustaceans [30]. However, 1 mg·mL$^{-1}$ causes a reduction from 100% of spore germination to ca. 50% of spore germination, as described using chitosan from crustaceans [30]. *P. chlamydosporia* is a chitosan-resistant fungus. Chitosan increases growth, sporulation, and pathogenicity to plant parasitic nematodes of this fungus [30–33]. On the other hand, our results indicate that chitosan from biofouling amphipods at 1 mg·mL$^{-1}$ can inhibit the germination of FocTR4, a wilt fungus highly pathogenic on bananas. According to our data, FocTR4 conidia germination seems more resistant than other *Fusarium* wilt pathogens, such as *Fusarium oxysporum* f. sp radicis-lycopersici, a tomato pathogen [33]. Chitosan treatment, applied as a soil drench, showed protection against several wilt diseases, including that caused by different *Fusarium* species on tomatoes [33]. In a recent study, chitosan inhibited *Fusarium spp*. involved in potato wilt [34]. In contrast, the biocontrol fungus Pc123 is tolerant to chitosan concentrations (0.01 mg·mL$^{-1}$), which significantly reduces the germination of Foc TR4. These results suggest that the combination of chitosan and biocontrol agents can help manage disease sustainably in banana and other crops. This has been shown for plant parasitic nematodes [31]. Chitosan has also been described as a plant defense elicitor inducing the expression of salicylic and jasmonic acid pathways in plants [35]. Our results on a new source of chitosan and its application with biocontrol agents and against pathogens and for plant defense induction could open new possibilities for its use in agriculture and other markets.

## 4. Conclusions

In this study, we promote the IMTA system, an environmentally friendly aquaculture procedure. We suggest using amphipods as secondary species to transform them into chitosan, a biopolymer used in numerous fields (e.g., medicine, industry, and agriculture). Chitosan extraction from amphipods is a good approach to valorizing biofouling from fisheries. This chitosan, from a new source, should be tested in future studies for applications that do not require large quantities, such as biomedicine. Methods for chitosan

extraction from amphipods should be optimized to maximize yields. However, at present, our results show that chitosan, obtained from amphipods associated with biofouling of aquaculture facilities, can arrest germination—and, therefore, the pathogenicity—of the wilt fungus FocTR4. This virulent new banana pathogen is expanding worldwide, but there are no efficient management methods. Ultimately, amphipod chitosan can help global food security. Our study, thus, contributes to economic sustainability via a new source of income for seafood and aquaculture (fish farms) companies, opening possibilities to generate blue and green circular economy industries.

## 5. Materials and Methods

### *5.1. Sample Collection and Preparation*

Samples were collected from a fish farm in the coastal waters of Murcia (Spain, 37°48.93′ N/0°41.73′ W) by scraping fouling organisms from shallow mooring ropes (1–10 m depths). Amphipods were extracted by introducing fouling samples into containers with fresh water for 3 min. Then, they were sieved through a 500 μm mesh and preserved in 70% ethanol. In the laboratory, the subsamples of at least 20% of the amphipod biomass samples were sorted, and amphipods were identified at a species level. The remaining samples were used for chitin/chitosan extraction and characterization. The species composition of amphipod samples is described in Table 3. We have also used amphipods from turtle foods (*Gammarus* spp. for turtle feed, Terra Viva) for comparison purposes.

**Table 3.** Taxonomic composition of amphipods causing biofouling.

| Genus/Species | Percentage (%) |
|---|---|
| *Jassa* spp. | 59.7 |
| *Ericthonius punctatus* | 27.7 |
| *Elasmopus rapax* | 5.5 |
| *Stenothoe* spp. | 5 |
| *Caprella equilibra* | 2.3 |

### *5.2. Chitosan Extraction*

Amphipod samples were dried at room temperature for 4 h and crushed in a mortar with liquid nitrogen until a homogeneous powder was obtained. Then, the sample was demineralized using a 0.5 M hydrochloric acid at a 1:30 $w/v$ ratio for 2 h at room temperature under constant stirring [36]. The sample was washed with deionized $H_2O$ to pH 7 and left to dry at 60 °C for 6 h. Protein removal was performed in a 0.5 M sodium hydroxide with a $w/v$ 1:40 for 19 h at room temperature under constant stirring. The chitin obtained was washed with deionized $H_2O$ to pH 7 and left to dry in an oven at 60 °C for 6 h. Chitin was bleached by shaking it in 2% sodium hypochlorite [25] at a 1:100 $w/v$ ratio for 10 min. The sample was washed with deionized $H_2O$ to neutral pH and left to dry in an oven at 60 °C for 6 h. Chitin was deacetylated with 50% sodium hydroxide in a 1:100 $w/v$ ratio at 100 °C for 2 h under constant stirring [37]. Finally, the obtained chitosan was washed with deionized $H_2O$ to a pH of 7 and dried at 60 °C for 6 h.

### *5.3. Chitosan Characterization*

Commercial chitosan (Marine BioProducts GmbH, Rosenheim, Germany), chitin (Sigma-Aldrich, St. Louis, MO, USA), and chitosan obtained from amphipods were subjected to Raman scattering spectroscopy, Fourier transform infrared spectroscopy (FTIR), and degree of deacetylation (%DD) calculation.

Raman scattering spectroscopy was used to detect the bond vibrations of the functional groups that make up chitosan and chitin samples to provide information on their chemical structures and physical forms [26]. NRS5100 Raman spectrometer was used. Both 785 nm and 1064 nm lasers were used. The latter usually generated fewer fluorescence emission artifacts. A study of the whole spectrum and another at the 1500–1800 $cm^{-1}$ region,

characteristic for differentiating chitin and chitosan, were carried out (Prof. A. C. Prieto, University of Valladolid, Spain. Personal communication).

FTIR analysis was carried out to characterize the obtained chitosan and compare them with chitin and commercial chitosan samples. This technique is based on the excitation of the molecules to be studied to observe the infrared absorption of the bonds they present, assigning the peaks corresponding to the bending and/or stretching of the bonds at wavelengths (in $cm^{-1}$) characteristic of the molecules under study. The characteristic bands used for chitosan are in the 3200–3400 $cm^{-1}$ region, corresponding to the N–H bond of amide I and the O–H bond associated with the pyranose ring, respectively [38]. The 1650 $cm^{-1}$ bands corresponding to the residual N-acetyl groups and the 1590 $cm^{-1}$ corresponding to the $NH_2$ groups were analyzed to differentiate the chitin and chitosan spectra [39]. When chitin is deacetylated, the intensity of the 1650 $cm^{-1}$ bands decays, while the 1590 $cm^{-1}$ band increases, indicating that the acetyl groups have been hydrolyzed and substituted by $NH_2$ groups [40]. Infrared spectra studies were carried out using the FT/IR-4700Type spectrophotometer (BRUKER, Billerica, MA, USA). The measurements were performed using the ATR PRO ONE mode of operation at an incidence angle of 45º, in the range of 500–4000 $cm^{-1}$. The number of scans was 3632, accumulating 16 scans per scan point, with a resolution of 4 $cm^{-1}$.

Chemically, chitin and chitosan are polyglucosamines distinguished only by the degree of acetylation, or the degree of deacetylation (one inverse of the other), of the amino groups. Chitin usually has a degree of deacetylation between 5 and 30% [28], whereas the %DD of chitosan must be greater than 50% to be considered such a molecule [41]. This parameter is one of the most important to determine the functional and physiological characteristics of the polymer. The spectra obtained in the FTIR study were used to calculate N-acetylation. The values obtained in the characteristic bands of amide III (1320 $cm^{-1}$) and, as a reference, the methyl groups (1420 $cm^{-1}$) were taken. Calculations of the degree of N-acetylation were obtained from the following equation [28]:

$$\%\ Degree\ of\ N-acetylation = 31.92 \times \frac{A_{1320}}{A_{1420}} - 12.2$$

The degree of N-deacetylation (DD) of chitin or chitosan is the complementary value demonstrated as follows [42]:

$$\%\ DD = 100 - Degree\ of\ N-acetylation$$

*5.4. Preparation of Chitosan Solutions*

Chitosan from a given source was dissolved in 0.25 M HCl under continuous stirring to obtain an initial concentration of 10 $mg{\cdot}mL^{-1}$, and pH was adjusted to 5.6 with 1 M and 0.1 M NaOH [17]. The obtained solution was dialyzed for salt removal for 48 h. The dialyzed chitosan was autoclaved (120 °C, 20 min) before use. We also prepared a 0.25 M HCl solution and adjusted it to pH 5.6 using 1 M and 0.1 M NaOH. This solution was dialyzed and autoclaved for chitosan [17].

*5.5. Effect of Chitosan on Spore Germination*

The fungal material used was strain Pc 123 of the nematophagous fungus *Pochonia chlamydosporia* 123 (Pc123, ATCC No. MYA-4875; CECT No.20929) isolated from eggs of *Heterodera avenae* in Seville. A further fungus used was a strain of *Fusarium oxysporum* f. sp. cubense Tropical Race 4 (FocTR4) (E.F. Smith) Snyder and Hansen, NRRL36114 (CBS 102025), isolated from the hybrid (*Musa acuminata* (AA) × *M. balbisiana* (BB)) *Pisang Manurung* (AAB) in Indonesia. The strain was acquired from the Institute of Fungal Biodiversity Westerdijk NL (authorization MiPAAF 31519, dated 6 December 2017), a former CBS collection of the Netherlands. Fungi were routinely grown on potato dextrose agar (PDA, Oxoid, Basingstoke, Hampshire, UK).

Conidia used for these experiments were collected from 2-week-old cultures of fungi growing in the media described above. The conidia were collected from the plates with 1 mL sterile distilled water, passed through a glass wool filter to remove hyphae, counted, and diluted to $1 \times 10^6$ conidia·mL$^{-1}$.

Three chitosan sources were used for experiments: commercial chitosan (T8, Biolog Heppe, GmbH Landsberg, Bremen, Germany), chitosan from aquaculture amphipods extracted as before (M4), and chitosan extracted for commercial amphipods (freeze-died natural *Gammarus* spp. for turtle feed, Terra Viva) (M5).

We designed moist chamber experiments in 9 cm diameter Petri dishes with autoclaved filter paper moistened with 1 mL of autoclaved distilled water to observe the effect of chitosan on Pc123 and FocTR4 conidia. We used 10 µ/L droplets with a concentration of $1 \times 10^6$ conidia·mL$^{-1}$ with chitosan at either 0.01 or 1 mg·mL$^{-1}$ on autoclaved microscopic glass slides. Controls consisting of autoclaved distilled water or HCl–NaOH buffer pH = 5.6 were also prepared.

For each treatment, 6 plates were prepared with 3 drops each. Three of the plates were incubated at room temperature and under 16 h light/8 h dark for 24 h and the other three for 48 h. After incubation, drops on slides were observed under an Olympus BH2 microscope (Olympus, Tokyo, Japan) with a Leica DFC 480 camera (Leica, Wetzlar, Germany). Observations were made at 20× magnification, observing a random field (with a total number of conidia of 200–800, approx.) and counting all germinated and non-germinated conidia, thus obtaining a germination percentage for each treatment and time.

### *5.6. Statistical Analysis*

To analyze the effect of chitosan on the germination of Pc123 and FocTR4, a two-factor ANOVA was performed by considering 'Time' (fixed and orthogonal) with two levels (24 h and 48 h) and 'Treatment' (fixed and orthogonal) with four levels ($H_2O$, Buffer, chitosan concentration (0.01) and (1) mg·mL$^{-1}$) on 3 samples to every level for each of the three-chitosan studied. The dependent variable was the germination percentage. Normality was tested with the Kolmogorov–Smirnov test. If normality was not met, as this study was balanced and $n > 30$, ANOVA was considered sufficiently robust. The homogeneity of variances was tested with Barlett's test. Data were transformed if necessary. However, if the homogeneity of variances was not met, a $p$-value of $\alpha < 0.01$ was considered significant. If significant differences were found in the ANOVA, an a posteriori test (Tukey HSD) was performed. All statistical analyses were carried out with the free software R v 4.1.2 [43].

**Author Contributions:** M.R.-P. planification of the study, experimental procedures, writing the manuscript, statistics, results interpretation. F.L.-M. planification of the study, writing the manuscript, editing, results interpretation. M.V.-U. writing the manuscript, statistics, results interpretation. P.S.-J. conception of idea, sampling work, writing the manuscript, editing. L.V.L.-L. conception of idea, planification of the study, writing the manuscript, editing, results interpretation, Funding acquisition. V.F.-G. conception of idea, planification of the study, sampling work, writing the manuscript, editing, results interpretation, Funding acquisition. All authors have read and agreed to the published version of the manuscript.

**Funding:** This project was funded by PID2020-119734RB-I00 (Spanish Ministry of Science and Innovation), EU H2020 MUSA no. 727624, and AIRAM (Biodiversity Foundation, Spanish Ministry for Ecological Transition, and the Demographic Challenge) projects.

**Institutional Review Board Statement:** Not applicable.

**Data Availability Statement:** The data that support the findings of this study are available from the corresponding author upon reasonable request.

**Acknowledgments:** Authors would like to thank Mateo Ballester and the PISCIALBA fish farm staff for their help. We are also grateful to Sanchez-Beresaluze and Carbonell-Garzón (UA Marine Biology research group) and the members of the UA Plant Pathology Laboratory for their technical help.

**Conflicts of Interest:** The authors declare no conflict of interest.

## References


1. Lillebø, A.I.; Pita, C.; Rodrigues, J.G.; Ramos, S.; Villasante, S. How can marine ecosystem services support the Blue Growth agenda? *Mar. Policy* **2017**, *81*, 132–142. [CrossRef]
2. FAO Agriculture Organization of the United Nations. Fisheries Department. The State of World Fisheries and Aquaculture, 2014 (Volume 3). Food and Agriculture Org. Available online: https://www.fao.org/3/i3720e/i3720e.pdf (accessed on 1 July 2023).
3. COM/2021/236 Final. Strategic Guidelines for a More Sustainable and Competitive EU Aquaculture for the Period 2021 to 2030. Communication from the Commission to the European Parliament, the Council, the European Economic and Social Committee and the Committee of the Regions. 2021. Available online: https://eur-lex.europa.eu/legal-content/ES/TXT/HTML/?uri=CELEX:52021DC0236&from=EN (accessed on 7 July 2023).
4. Kalantzi, I.; Karakassis, I. Benthic impacts of fish farming: Meta-analysis of community and geochemical data. *Mar. Pollut. Bull.* **2006**, *52*, 484–493. [CrossRef]
5. Rosa, J.; Lemos, M.F.; Crespo, D.; Nunes, M.; Freitas, A.; Ramos, F.; Leston, S. Integrated multitrophic aquaculture systems–Potential risks for food safety. *Trends Food Sci. Technol.* **2020**, *96*, 79–90. [CrossRef]
6. Gonzalez-Silvera, D.; Izquierdo-Gomez, D.; Fernandez-Gonzalez, V.; Martínez-López, F.J.; López-Jiménez, J.A.; Sanchez-Jerez, P. Mediterranean fouling communities assimilate the organic matter derived from coastal fish farms as a new trophic resource. *Mar. Pollut. Bul.* **2015**, *91*, 45–53. [CrossRef] [PubMed]
7. Fernandez-Gonzalez, V.; Toledo-Guedes, K.; Valero-Rodriguez, J.M.; Agraso, M.D.M.; Sanchez-Jerez, P. Harvesting amphipods applying the integrated multitrophic aquaculture (IMTA) concept in off-shore areas. *Aquaculture* **2018**, *489*, 62–69. [CrossRef]
8. MacArthur, E. *Towards the Circular Economy: Accelerating the Scale-Up across Global Supply Chains*; World Economic Forum: Cologny, Switzerland, 2014.
9. Lett, L.A. Las amenazas globales, el reciclaje de residuos y el concepto de economía circular. *Rev. Argent. Microbiol.* **2014**, *46*, 1–2. [CrossRef] [PubMed]
10. Martínez-Vázquez, R.M.; Milán-García, J.; de Pablo Valenciano, J. Challenges of the Blue Economy: Evidence and research trends. *Environ. Sci. Eur.* **2021**, *33*, 61. [CrossRef]
11. König, G.M.; Kehraus, S.; Seibert, S.F.; Abdel-Lateff, A.; Müller, D. Natural products from marine organisms and their associated microbes. *ChemBioChem* **2006**, *7*, 229–238. [CrossRef]
12. Cohen-Kupiec, R.; Chet, I. The molecular biology of chitin digestion. *Curr. Opin. Biotechnol.* **1998**, *9*, 270–277. [CrossRef]
13. Kumar, M.N.V.R. A review of chitin and chitosan applications. *React. Funct. Polym.* **2000**, *46*, 1–27. [CrossRef]
14. Pillai, C.K.S.; Paul, W.; Sharma, C.P. Chitin and chitosan polymers: Chemistry, solubility and fiber formation. *Prog. Polym. Sci.* **2009**, *34*, 641–678. [CrossRef]
15. Mármol, Z.; Páez, G.; Rincón, M.; Araujo, K.; Aiello, C.; Chandler, C.; y Gutiérrez, E. Quitina y Quitosano polímeros amigables. Una revisión de sus aplicaciones/Chitin and Chitosan friendly polymer. A review of their applications. *Rev. Tecnocientífica URU* **2013**, *1*, 53–58.
16. Zhao, D.; Yu, S.; Sun, B.; Gao, S.; Guo, S.; Zhao, K. Biomedical applications of chitosan and its derivative nanoparticles. *Polymers* **2018**, *10*, 462. [CrossRef] [PubMed]
17. Palma-Guerrero, J.; Jansson, H.B.; Salinas, J.; López-Llorca, L.V. Effect of chitosan on hyphal growth and spore germination of plant pathogenic and biocontrol fungi. *J. Appl. Microbiol.* **2008**, *104*, 541–553. [CrossRef] [PubMed]
18. Al-Hetar, M.Y.; Zainal Abidin, M.A.; Sariah, M.; Wong, M.Y. Antifungal activity of chitosan against *Fusarium oxysporum* f. sp. cubense. *J. Appl. Polym. Sci.* **2011**, *120*, 2434–2439. [CrossRef]
19. Lopez-Moya, F.; Martin-Urdiroz, M.; Oses-Ruiz, M.; Were, V.M.; Fricker, M.D.; Littlejohn, G.; Lopez-Llorca, L.V.; Talbot, N.J. Chitosan inhibits septin-mediated plant infection by the rice blast fungus *Magnaporthe oryzae* in a protein kinase C and Nox1 NADPH oxidase-dependent manner. *New Phytol.* **2021**, *230*, 1578–1593. [CrossRef]
20. Ren, J.; Tong, J.; Li, P.; Huang, X.; Dong, P.; Ren, M. Chitosan is an effective inhibitor against potato dry rot caused by *Fusarium oxysporum*. *Physiol. Mol. Plant. Pathol.* **2021**, *113*, 101601. [CrossRef]
21. Palma-Guerrero, J.; Huang, I.C.; Jansson, H.B.; Salinas, J.; Lopez-Llorca, L.V.; Read, N.D. Chitosan permeabilizes the plasma membrane and kills cells of *Neurospora crassa* in an energy dependent manner. *Fungal Genet. Biol. Fungal Genet. Biol.* **2009**, *46*, 585–594. [CrossRef]
22. Palma-Guerrero, J.; Lopez-Jimenez, J.A.; Pérez-Berná, A.J.; Huang, I.C.; Jansson, H.B.; Salinas, J.; Villalaín, J.; Read, N.D.; Lopez-Llorca, L.V. Membrane fluidity determines sensitivity of filamentous fungi to chitosan. *Mol. Microbiol.* **2010**, *75*, 1021–1032. [CrossRef]
23. Larriba, E.; Jaime, M.D.; Carbonell-Caballero, J.; Conesa, A.; Dopazo, J.; Nislow, C.; Martín-Nieto, J.; Lopez-Llorca, L.V. Sequencing and functional analysis of the genome of a nematode egg-parasitic fungus, *Pochonia chlamydosporia*. *Fungal Genet. Biol.* **2014**, *65*, 69–80. [CrossRef]
24. Aranda-Martinez, A.; Lenfant, N.; Escudero, N.; Zavala-Gonzalez, E.A.; Henrissat, B.; Lopez-Llorca, L.V. CAZyme content of *Pochonia chlamydosporia* reflects that chitin and chitosan modification are involved in nematode parasitism. *Env. Microbiol.* **2016**, *18*, 4200–4215. [CrossRef] [PubMed]
25. Kaya, M.; Dudakli, F.; Asan-Ozusaglam, M.; Cakmak, Y.S.; Baran, T.; Mentes, A.; Erdogan, S. Porous and nanofiber α-chitosan obtained from blue crab (*Callinectes sapidus*) tested for antimicrobial and antioxidant activities. *LWT-Food Sci. Technol.* **2016**, *65*, 1109–1117. [CrossRef]

26. Smith, E.; Dent, G. *Modern Raman Spectroscopy: A Practical Approach*; John Wiley and Sons: Hoboken, NJ, USA, 2019.
27. Agarwal, U.P. Analysis of cellulose and lignocellulose materials by Raman spectroscopy: A review of the current status. *Molecules* **2019**, *24*, 1659. [CrossRef]
28. Escobar Sierra, D.M.; Castro Ramírez, A.M.; y Vergara Castrillón, N.A. Determining the Relation between the Proportion of the Amino Group and the Degree of Deacetylation of Chitosan. *Rev. Cienc.* **2014**, *18*, 73–88.
29. Grifoll-Romero, L.; Pascual, S.; Aragunde, H.; Biarnés, X.; Planas, A. Chitin deacetylases: Structures, specificities, and biotech applications. *Polymers* **2018**, *10*, 352. [CrossRef]
30. Escudero, N.; Sebastiao, R.F.; Lopez-Moya, F.; Naranjo-Ortiz, M.A.; Marin-Ortiz, A.I.; Thornton, C.R.; Lopez-Llorca, L.V. Chitosan enhances parasitism of *Meloidogyne javanica* eggs by the nematophagous fungus *Pochonia chlamydosporia*. *Fungal Biol.* **2016**, *120*, 572–585. [CrossRef] [PubMed]
31. Escudero, N.; Lopez-Moya, F.; Ghahremani, Z.; Zavala-Gonzalez, E.A.; Alaguero-Cordovilla, A.; Ros-Ibañez, C.; Lopez-Llorca, L.V. Chitosan increases tomato root colonization by *Pochonia chlamydosporia* and their combination reduces root-knot nematode damage. *Front. Plant Sci.* **2017**, *8*, 1415. [CrossRef]
32. Lopez-Moya, F.; Suarez-Fernandez, M.; Lopez-Llorca, L.V. Molecular Mechanisms of Chitosan Interactions with Fungi and Plants. *Int. J. Mol. Sci.* **2019**, *20*, 332. [CrossRef]
33. Jabnoun-Khiareddine, H.; El-Mohamed, R.S.R.; Abdel-Kareem, F.; Aydi Ben Abdallah, R.; Gueddes-Chahed, M.; Daami-Remadi, M. Variation in chitosan and salicylic acid efficacy towards soil-borne and air-borne fungi and their suppressive effect of tomato wilt severity. *J. Plant Pathol. Microbiol.* **2015**, *6*, 325. [CrossRef]
34. Mejdoub-Trabelsi, B.; Touihri, S.; Ammar, N.; Riahi, A.; Daami-Remadi, M. Effect of chitosan for the control of potato diseases caused by *Fusarium* species. *J. Phytopathol.* **2020**, *168*, 18–27. [CrossRef]
35. Lopez-Moya, F.; Escudero, N.; Zavala-Gonzalez, E.A.; Esteve-Bruna, D.; Blázquez, M.A.; Alabadí, D.; Lopez-Llorca, L.V. Induction of auxin biosynthesis and WOX5 repression mediate changes in root development in *Arabidopsis* exposed to chitosan. *Sci. Rep.* **2017**, *7*, 16813. [CrossRef] [PubMed]
36. Cauchie, H.M. Chitin production by arthropods in the hydrosphere. *Hydrobiologia* **2002**, *470*, 63–95. [CrossRef]
37. Escobar Sierra, D.M.; Urrea Llano, C.A.; Gutiérrez Guerra, M.; y Zapata Ocampo, P.A. Producción de matrices de quitosano extraído de crustáceos. *Rev. Ing. Biomédica* **2011**, *5*, 20–25.
38. Queiroz, M.F.; Teodosio Melo, K.R.; Sabry, D.A.; Sassaki, G.L.; Rocha, H.A.O. Does the use of chitosan contribute to oxalate kidney stone formation? *Mar. Drugs* **2014**, *13*, 141–158. [CrossRef]
39. Kumari, S.; Rath, P.; Kumar, A.S.H.; y Tiwari, T.N. Extraction and characterization of chitin and chitosan from fishery waste by chemical method. *Environ. Technol. Innov.* **2015**, *3*, 77–85. [CrossRef]
40. Paulino, A.T.; Simionato, J.I.; Garcia, J.C.; Nozaki, J. Characterization of chitosan and chitin produced from silkworm crysalides. *Carbohydr. Polym.* **2006**, *64*, 98–103. [CrossRef]
41. Rinaudo, M. Chitin and chitosan: Properties and applications. *Prog. Polym. Sci.* **2006**, *31*, 603–632. [CrossRef]
42. Yen, M.T.; Yang, J.H.; Mau, J.L. Physicochemical characterization of chitin and chitosan from crab shells. *Carbohydr. Polym.* **2009**, *75*, 15–21. [CrossRef]
43. R Core Team. *R: A Language and Environment for Statistical Computing*; R Foundation for Statistical Computing: Vienna, Austria, 2020. Available online: https://www.R-project.org/ (accessed on 20 July 2023).

marine drugs

MDPI

*Article*

# Preparation and Antioxidant Activity of New Carboxymethyl Chitosan Derivatives Bearing Quinoline Groups

**Linqing Wang [1,2,3], Rui Guo [1,2,3], Xiaorui Liang [4], Yuting Ji [1,2,3], Jingjing Zhang [1,2,*], Guowei Gai [5] and Zhanyong Guo [1,2,3,*]**

[1] Key Laboratory of Coastal Biology and Bioresource Utilization, Yantai Institute of Coastal Zone Research, Chinese Academy of Sciences, Yantai 264003, China; linqingwang@yic.ac.cn (L.W.); guorui231@mails.ucas.ac.cn (R.G.); ytji@yic.ac.cn (Y.J.)
[2] Center for Ocean Mega-Science, Chinese Academy of Sciences, 7 Nanhai Road, Qingdao 266071, China
[3] University of Chinese Academy of Sciences, Beijing 100049, China
[4] School of Basic Sciences for Aviation Naval Aviation University, Yantai 264001, China; xrliang@yic.ac.cn
[5] Shandong Saline-Alkali Land Modern Agriculture Company, Dongying 257300, China; dyjwggw@126.com
* Correspondence: jingjingzhang@yic.ac.cn (J.Z.); zhanyongguo@hotmail.com (Z.G.); Tel.: +86-535-2109171 (Z.G.); Fax: +86-535-2109000 (Z.G.)

**Abstract:** A total of 16 novel carboxymethyl chitosan derivatives bearing quinoline groups in four classes were prepared by different synthetic methods. Their chemical structures were confirmed by Fourier-transform infrared spectroscopy (FTIR), nuclear magnetic resonance (NMR), and elemental analysis. The antioxidant experiment results in vitro (including DPPH radical scavenging ability, superoxide anion radical scavenging ability, hydroxyl radical scavenging ability, and ferric reducing antioxidant power) demonstrated that adding quinoline groups to chitosan (CS) and carboxymethyl chitosan (CMCS) enhanced the radical scavenging ability of CS and CMCS. Among them, both *N*, *O*-CMCS derivatives and *N*-TM-*O*-CMCS derivatives showed DPPH radical scavenging over 70%. In addition, their scavenging of superoxide anion radicals reached more than 90% at the maximum tested concentration of 1.6 mg/mL. Moreover, the cytotoxicity assay was carried out on L929 cells by the MTT method, and the results indicated that all derivatives showed no cytotoxicity (cell viability > 75%) except *O*-CMCS derivative 1a, which showed low cytotoxicity at 1000 μg/mL (cell viability 50.77 ± 4.67%). In conclusion, the carboxymethyl chitosan derivatives bearing quinoline groups showed remarkable antioxidant ability and weak cytotoxicity, highlighting their potential use in food and medical applications.

**Keywords:** antioxidant activity; carboxymethyl chitosan derivatives; quinoline

**Citation:** Wang, L.; Guo, R.; Liang, X.; Ji, Y.; Zhang, J.; Gai, G.; Guo, Z. Preparation and Antioxidant Activity of New Carboxymethyl Chitosan Derivatives Bearing Quinoline Groups. *Mar. Drugs* **2023**, *21*, 606. https://doi.org/10.3390/md21120606

Academic Editor: Azizur Rahman

Received: 16 October 2023
Revised: 17 November 2023
Accepted: 20 November 2023
Published: 24 November 2023



## 1. Introduction

Playing essential roles in combating intracellular microorganisms, reactive oxygen species (ROS) are natural byproducts of cellular oxidative metabolism [1–3]. However, excessive ROS adversely affects genetic material, proteins, and lipid membranes, leading to cellular senescence, carcinogenesis, and inflammation [4,5]. Therefore, removing excess ROS from the body can effectively delay cellular senescence, inhibit malignant tumors, and prevent inflammation. Research on antioxidants continues to find more efficient solutions for clearing excess reactive oxygen species in the body.

Quinoline, present in natural products, has various biological activities such as antioxidant, antibacterial, anti-inflammatory, and anti-tumor [6–8]. Runge isolated quinoline from coal tar in 1834 and named it "Leukol". Gerhardt officially named it "quinoline" in 1842 [9]. Subsequently, more and more researchers have shown great interest in this nitrogen-containing heterocyclic compound with unique molecular structure and biological activity. Douadi et al. synthesized a series of azoimine quinoline derivatives with excellent antioxidant, anti-inflammatory, and antimicrobial activities [10]. Mahajan's group

prepared a variety of novel thieno[2,3-*b*]quinoline-2-carboxylic acid derivatives, including β-diketone, pyrazole, and flavone. It was found that these derivatives exhibit a strong scavenging ability for the DPPH radical [11]. In addition, various drugs containing quinoline groups have been widely used in treating malaria, inflammation, and cancer. Such as quinine, quinidine, topotecan, and irinotecan.

Chitosan, a deacetylation product of chitin, has a broad application prospect in food packaging due to its antioxidant activity [12,13]. Carboxymethyl chitosan (CMCS) is a vital derivative with better water solubility and biological activity than chitosan [14,15]. Three types of carboxymethyl chitosan can be obtained through different preparation methods: *O*-carboxymethyl chitosan, *N*-carboxymethyl chitosan, and *N*, *O*-carboxymethyl chitosan. CMCS is vital in medical materials, food, environmental protection, and other fields [16–18]. Hashmi's group developed a Tacrolimus-loaded carboxymethyl chitosan medical scaffold with promising antibacterial activity for improving angiogenesis, fibroblast proliferation, and inflammation [19]. Zhao's team prepared a composite hydrogel containing oxidized pullulan polysaccharide and carboxymethyl chitosan that is injectable, self-healing, antibacterial, and pro-healing, making it suitable for protecting and treating open abdominal wounds [20]. In addition, Liu et al. used a self-assembling composite membrane made of carboxymethyl chitosan and zinc alginate to preserve refrigerated meat. The membrane demonstrated significant water resistance and antibacterial properties [21]. Sela's research group synthesized derivatives of carboxymethyl chitosan grafted with quercetin through a Schiff base reaction in one step. The derivatives demonstrated excellent antioxidant and antifungal activities. Moreover, they were found to be effective in slowing water loss and the browning of fresh-cut fruits. This discovery holds great importance in the field of food preservation [22]. Zhang et al. developed a sodium alginate/carboxymethyl chitosan composite hydrogel bead with high water absorption that effectively removes methylene blue dye from water bodies [23]. Although researchers' in-depth study of carboxymethyl chitosan has achieved good research results, carboxymethyl chitosan still has excellent development potential and broad development prospects in antioxidant, antibacterial, and anti-tumor [24–26].

In this thesis, CMCS was prepared and slightly modified according to existing reports [27–29]. We believe that quinoline groups can serve as the core backbone of multiple drugs with various biological activities. To test this hypothesis, we have systematically introduced quinoline groups into chitosan molecules through acylation reactions for the first time. We have also tested the antioxidant activity of CMCS derivatives. A total of 16 novel carboxymethyl chitosan derivatives bearing quinoline groups in four classes were prepared by different synthetic methods. These included four *O*-carboxymethyl chitosan derivatives bearing quinoline groups, four *N*-carboxymethyl chitosan derivatives bearing quinoline groups, four *N*, *O*-carboxymethyl chitosan derivatives bearing quinoline groups, and four *N*, *N*, *N*-trimethyl-*O*-carboxymethyl chitosan derivatives bearing quinoline groups. Their structures were characterized by FTIR and $^1$H NMR. In addition, their nitrogen and carbon contents were determined by elemental analysis, and their degree of substitution was calculated. In this study, carboxymethyl chitosan derivatives were tested for their antioxidant properties, such as their ability to scavenge DPPH, superoxide anion, and hydroxyl radicals, as well as their ferric-reducing antioxidant power. Additionally, the cytotoxicity of these derivatives to mouse fibroblasts was measured in vitro. The results indicated that most of the derivatives exhibited strong free radical scavenging ability while also showing low cytotoxicity.

## 2. Results and Discussion

### *2.1. Chemical Synthesis and Characterization*

Scheme 1 outlines the synthetic reaction for creating carboxymethyl chitosan derivatives with quinoline groups. Subsequently, FTIR (Figure 1) and $^1$H NMR (Figure 2) spectroscopy were used to characterize the chemical structures of all carboxymethyl chitosan derivatives. Additionally, Table 1 displays their yields and degrees of substitution (*DS*).

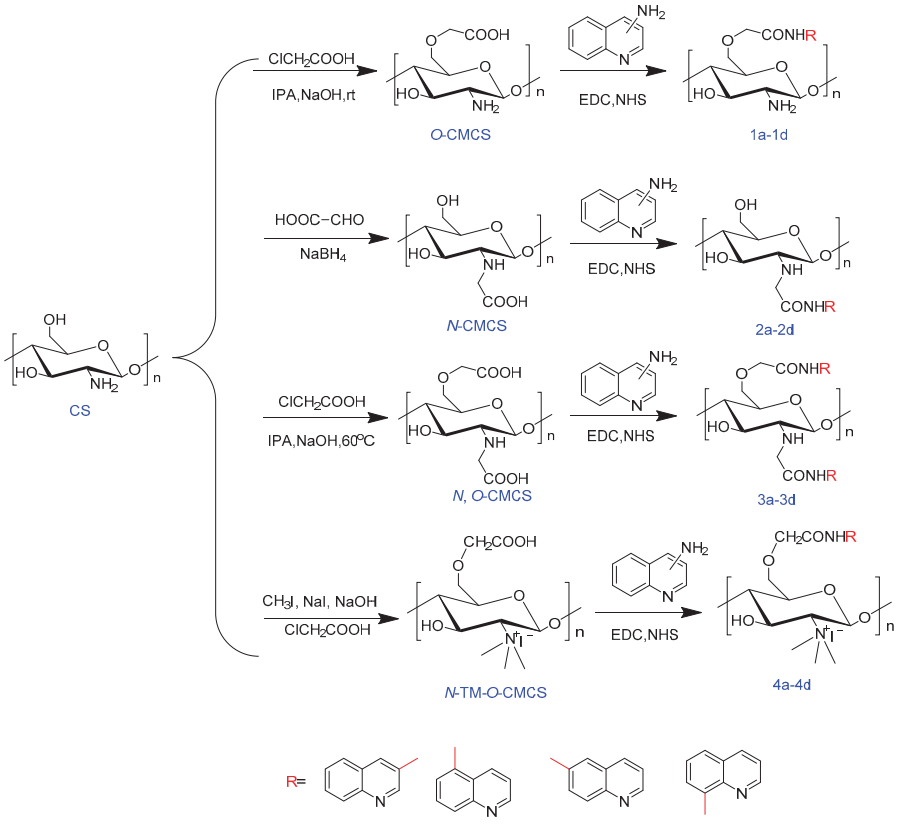


**Scheme 1.** Synthesis routes for carboxymethyl chitosan derivatives bearing quinoline groups.

**Table 1.** The yields and degrees of substitution of CMCS derivatives.

| Compounds | Yields (%) | Elemental Analyses (%) | | | Degrees of Substitution (%) | Deacetylation (%) |
|---|---|---|---|---|---|---|
| | | C | N | C/N | | |
| CS | | 34.86 | 6.13 | 5.68 | | 68.67 |
| *O*-CMCS | 70.23 | 35.96 | 5.57 | 6.46 | 45.00 | |
| *N*-CMCS | 77.73 | 32.36 | 4.62 | 7.00 | 76.33 | |
| *N*, *O*-CMCS | 51.37 | 33.62 | 3.55 | 9.48 | 87.75 | |
| *N*-TM-*O*-CMCS | 62.37 | 37.27 | 4.65 | 8.01 | 60.17 | |
| 1a | 45.36 | 34.76 | 6.30 | 5.52 | 28.35 | |
| 1b | 31.22 | 38.63 | 6.77 | 5.70 | 20.70 | |
| 1c | 42.86 | 38.67 | 6.64 | 5.83 | 16.38 | |
| 1d | 25.51 | 39.75 | 6.90 | 5.76 | 18.47 | |
| 2a | 41.25 | 34.82 | 5.37 | 6.48 | 9.80 | |
| 2b | 35.27 | 35.38 | 5.64 | 6.27 | 14.89 | |
| 2c | 40.16 | 35.62 | 5.79 | 6.16 | 18.28 | |
| 2d | 32.71 | 42.21 | 7.13 | 5.91 | 26.25 | |
| 3a | 25.64 | 38.15 | 5.23 | 7.29 | 15.84 | |
| 3b | 30.85 | 37.88 | 5.18 | 7.31 | 15.63 | |
| 3c | 16.79 | 39.11 | 5.35 | 7.31 | 15.63 | |
| 3d | 26.41 | 33.96 | 4.89 | 6.95 | 20.57 | |
| 4a | 26.15 | 42.02 | 6.04 | 6.95 | 16.85 | |
| 4b | 16.84 | 41.85 | 5.40 | 7.74 | 3.42 | |
| 4c | 33.14 | 38.82 | 5.28 | 7.36 | 9.31 | |
| 4d | 45.26 | 40.70 | 5.42 | 7.51 | 6.81 | |

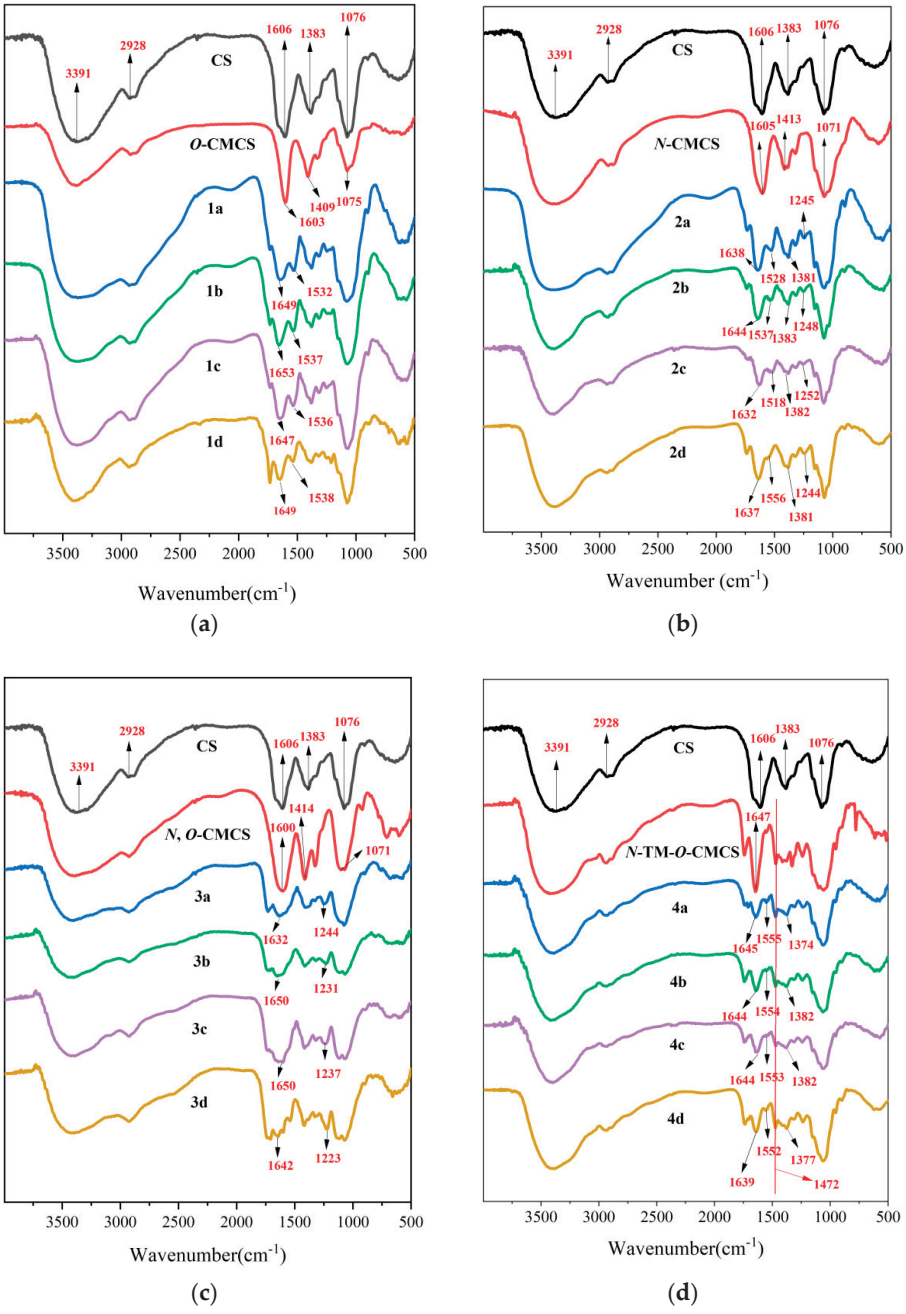


**Figure 1.** FTIR spectra of chitosan and CMCS derivatives ((**a**): *O*-CMCS derivatives, (**b**): *N*-CMCS derivatives, (**c**): *N*, *O*-CMCS derivatives, (**d**): *N*-TM-*O*-CMCS derivatives).

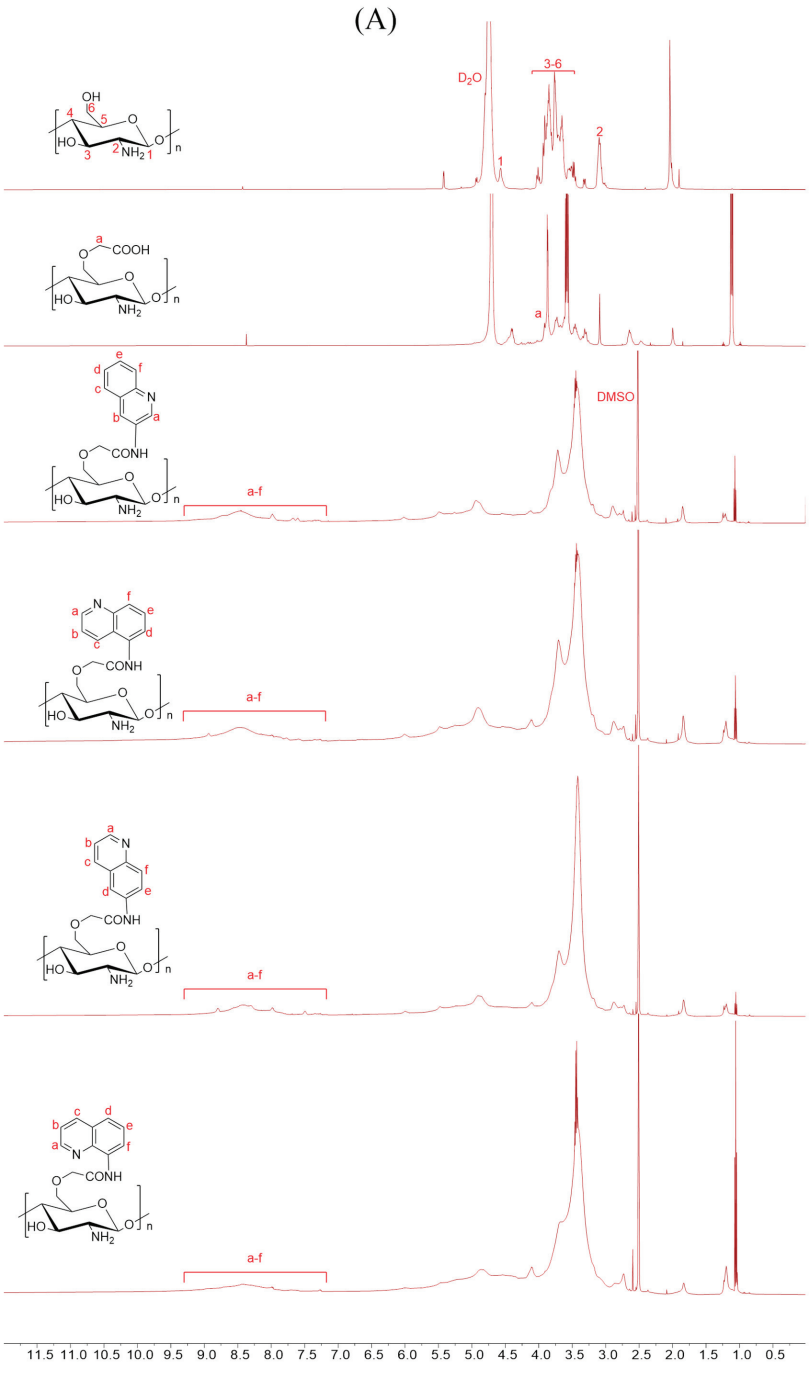


**Figure 2.** *Cont*.

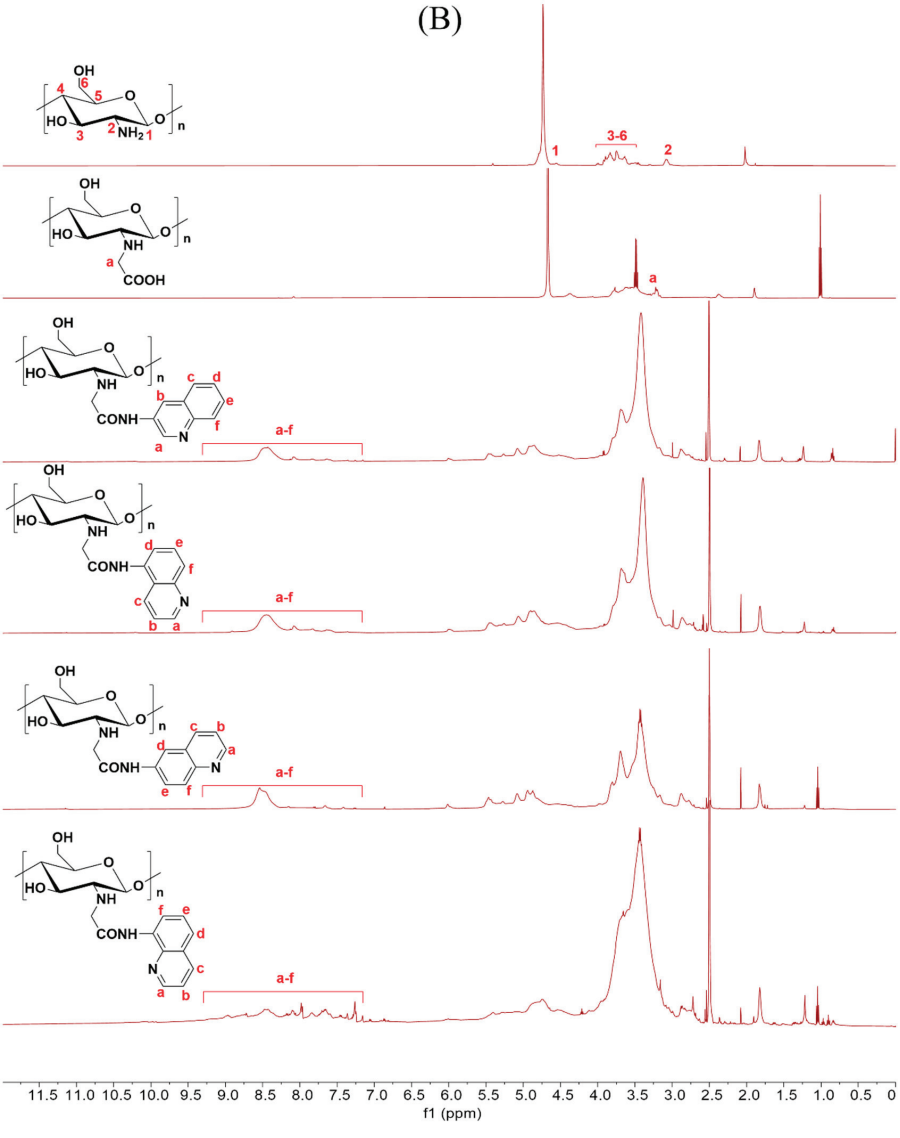


**Figure 2.** *Cont*.

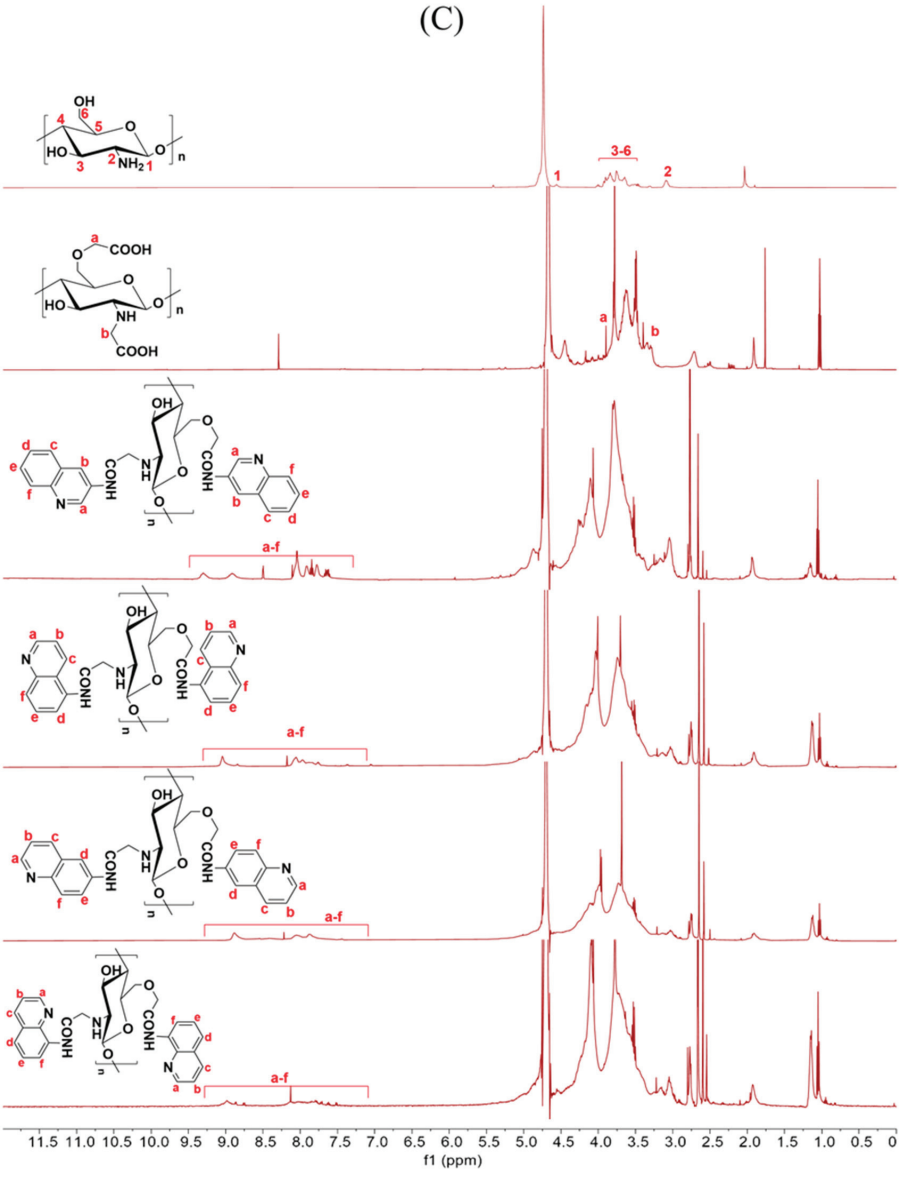


**Figure 2.** *Cont.*

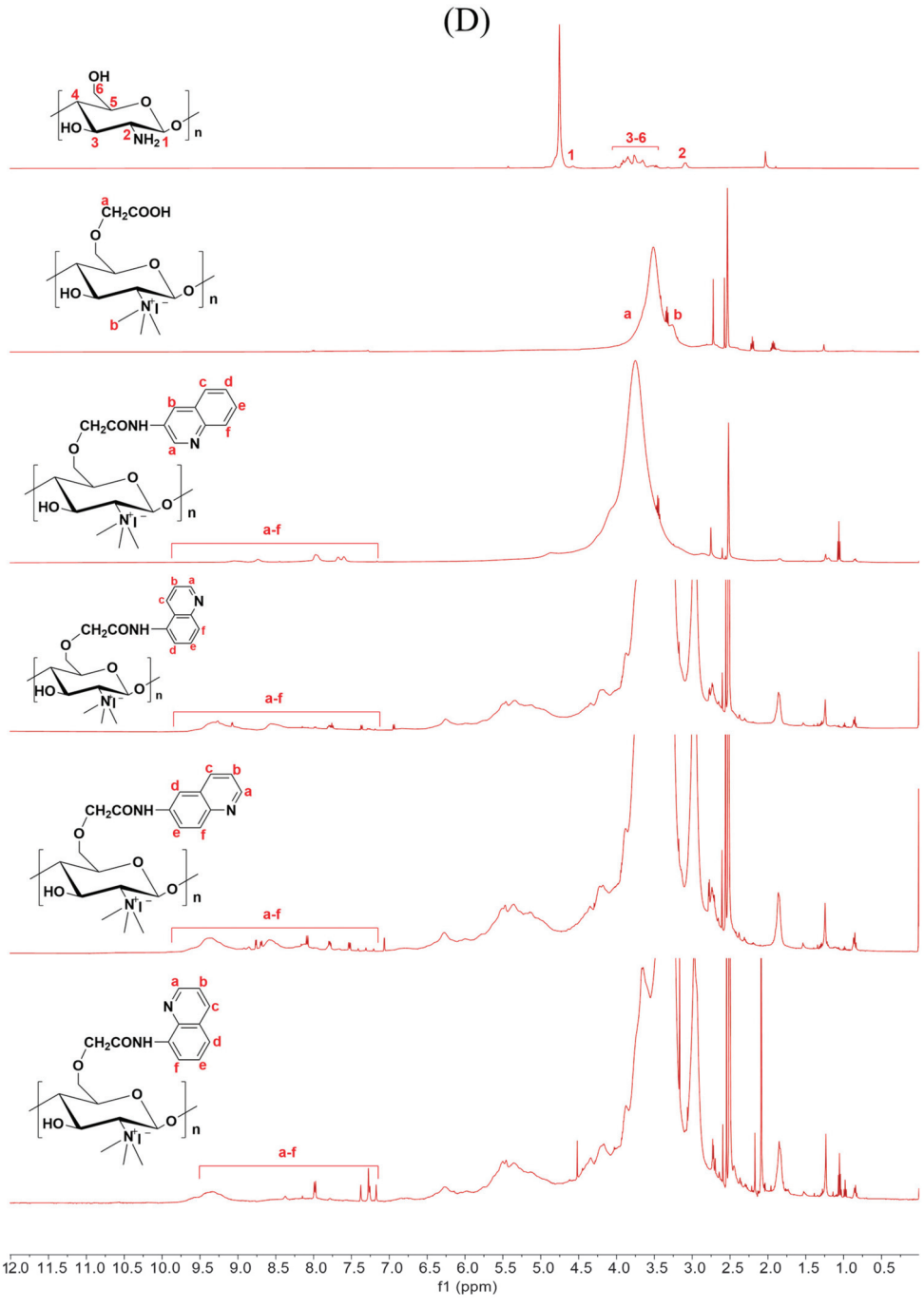


**Figure 2.** $^{1}$H NMR spectra of chitosan and CMCS derivatives ((**A**): *O*-CMCS derivatives, (**B**): *N*-CMCS derivatives, (**C**): *N*, *O*-CMCS derivatives, (**D**): *N*-TM-*O*-CMCS derivatives).

2.1.1. Yields and DS Analysis

The yields and the degrees of substitution of carboxymethyl chitosan derivatives are shown in Table 1. The deacetylation degree of chitosan was 68.67%. The DS values of *O*-CMCS derivatives were 28.35%, 20.70%, 16.38%, and 18.47%, respectively. The DS values of *N*-CMCS derivatives were 9.80%, 14.89%, 18.28%, and 26.25%, respectively. The DS values of *N*, *O*-CMCS derivatives were 15.84%, 15.63%, 15.63%, and 20.57%, respectively. The DS values of *N*-TM-*O*-CMCS derivatives were 16.85%, 3.42%, 9.31%, and 6.81%, respectively. Therefore, the changes in the content of C/N elements proved the success of the modification of CMCS.

2.1.2. FTIR Spectra Analysis

Evidence of chitosan derivative synthesis was explained by FTIR spectroscopy. Figure 1 displays the FTIR spectra of chitosan, carboxymethyl chitosan, and carboxymethyl chitosan derivatives with quinoline groups. In the FTIR spectrum of chitosan, the absorption peak near 3391 $cm^{-1}$ was attributed to the absorption peak generated by the stretching vibration of the O-H bond and N-H bond; the weak broad band peak appearing near 2928 $cm^{-1}$ was attributed to the vibration absorption peak of the C-H bond; and the absorption peak of the C2 amino group of chitosan appeared at 1606 $cm^{-1}$. Moreover, the absorption peak at 1076 $cm^{-1}$ is the stretching vibration peak of the C-O bond [30,31]. In the FTIR spectra of CMCS, the absorption peaks at around 1603, 1409, and 1075 $cm^{-1}$ are the asymmetric stretching vibration peaks of the carboxyl group [32,33]. Furthermore, in the spectrum of *N*-TM-*O*-CMCS, the peak at 1472 $cm^{-1}$ was attributed to the absorption peak of $N(CH_3)_3^+$ [34,35]. In the FTIR spectra of CMCS derivatives bearing quinoline groups, new absorption peaks appear in the 1647–1653 $cm^{-1}$ attachment and are thought to be characteristic of the amide bond [36]. The characteristic absorption peaks of the quinoline ring appear around 1518–1556 $cm^{-1}$, 1381–1383 $cm^{-1}$, and 1223–1252 $cm^{-1}$ [37–39]. In conclusion, the preliminary analysis proves the successful preparation of CMCS derivatives. More structural characteristics require verification by NMR.

2.1.3. $^1$H NMR Spectra Analysis

The correctness of the structure of the carboxymethyl chitosan derivatives bearing quinoline groups was further confirmed by $^1$H NMR spectroscopy. The chemical shifts of the hydrogen atoms [H1], [H2], and [H3]–[H6] in the chitosan molecule are 4.57 ppm, 3.10 ppm, and 3.50–4.01 ppm, respectively [30]. The hydrogen atom on the methylene group of the CMCS molecule has a chemical shift of approximately 3.30 ppm and 3.90 ppm [40]. The peak of the proton signal on the aromatic quinoline ring was observed between 7.10 and 9.50 ppm [41]. Thus, the successful synthesis of carboxymethyl chitosan derivatives bearing quinoline was further demonstrated by the $^1$H NMR data.

*2.2. Antioxidant Activity*

It has been reported that the occurrence of cardiovascular and cerebrovascular diseases such as cancer, premature aging, rheumatoid arthritis, and diabetes may be due to excessive ROS-mediated oxidative stress in the human body, which damages vital substances such as lipids, proteins, and DNA. Therefore, we chose to evaluate the antioxidant activity of CMCS derivatives by testing their ability to scavenge DPPH radical, superoxide anion radical, hydroxyl radical, and ferric reduction ability compared to Vc as a positive control (Figures 3–6).

It can be seen from Figure 3 that the chitosan raw material has a weak ability to scavenge DPPH radical, and its scavenging rate is only 26.07 $\pm$ 4.47% at the maximum tested concentration of 1.6 mg/mL. The ability of CMCS derivatives to scavenge DPPH radicals is higher than that of both CMCS and CS, and this ability increases with an increase in sample concentration. The *N*-CMCS derivative 2d has the highest scavenging ability due to the retention of the C6 hydroxyl group and a higher degree of substitution. At the tested concentration of 0.4 mg/mL, its DPPH radical scavenging index reached 100%.

The clearance rate of all CMCS derivatives is higher than 50% at the maximum tested concentration of 1.6 mg/mL. In particular, the *N*-TM-*O*-CMCS derivatives exhibit the most significant improvement compared to chitosan. Additionally, all other derivatives exhibit a scavenging effect exceeding 85%, except for the derivative 4a.

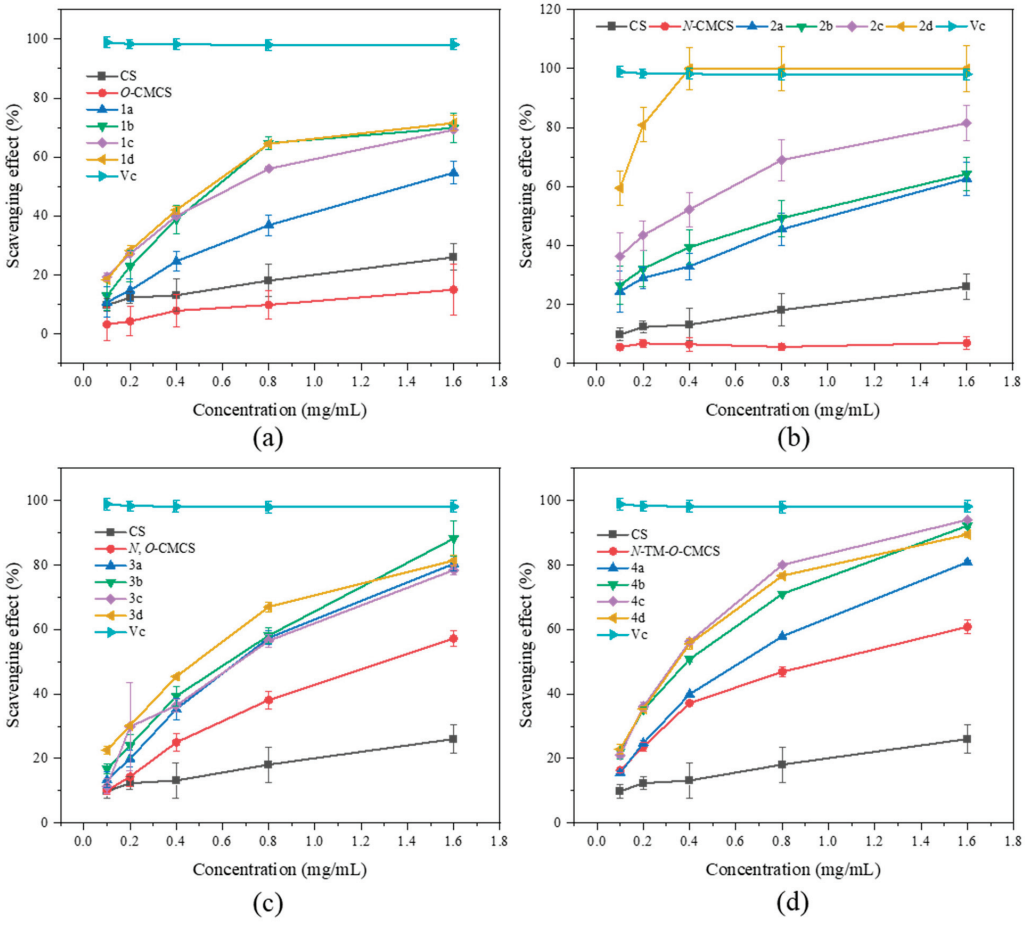


**Figure 3.** DPPH radical scavenging activity of chitosan and CMCS derivatives ((**a**): *O*-CMCS derivatives, (**b**): *N*-CMCS derivatives, (**c**): *N*, *O*-CMCS derivatives, (**d**): *N*-TM-*O*-CMCS derivatives).

In Figure 4, the superoxide anion-scavenging ability of CMCS derivatives is demonstrated. The scavenging capacity of all samples was found to increase with concentration. The scavenging ability of chitosan on superoxide anion-free radicals is significantly better than the scavenging ability of DPPH-free radicals. At a concentration of 1.6 mg/mL, chitosan shows a scavenging ability of 57.82 ± 1.79%. At the highest concentration tested (1.6 mg/mL), all derivatives, except *O*-CMCS derivatives, exhibited over 80% scavenging ability against superoxide anion radicals. In particular, the *N*-CMCS and *N*-TM-*O*-CMCS derivatives exhibit a scavenging ability that surpasses 90%. The results indicate that adding quinoline groups enhances CS's ability to scavenge superoxide anion radicals.

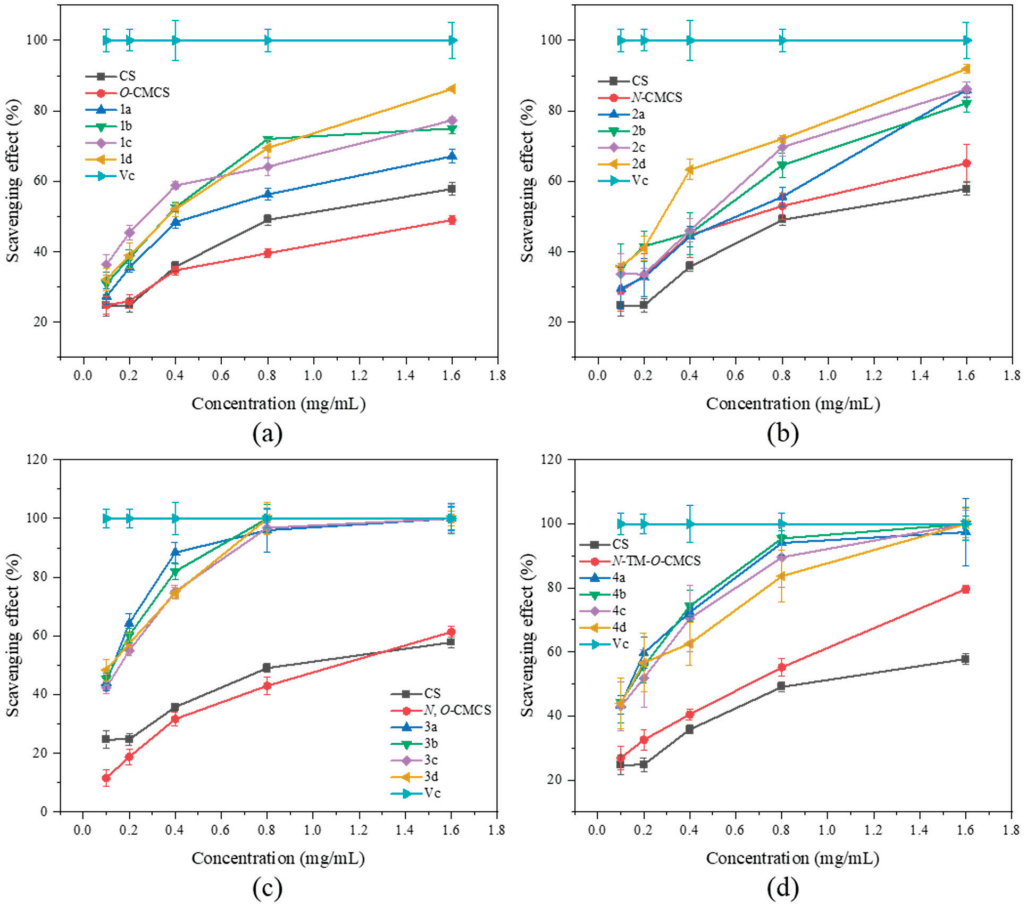


**Figure 4.** Superoxide anion radical scavenging activity of chitosan and CMCS derivatives ((**a**): *O*-CMCS derivatives, (**b**): *N*-CMCS derivatives, (**c**): *N*, *O*-CMCS derivatives, (**d**): *N*-TM-*O*-CMCS derivatives).

In Figure 5, it is demonstrated that CS, CMCS, and CMCS derivatives have the ability to scavenge hydroxyl radicals. Additionally, the scavenging ability of all the samples is directly proportional to their concentration. Furthermore, the scavenging ability of CMCS derivatives is found to be superior to that of both CS and CMCS. The derivatives have a slightly weaker ability to scavenge hydroxyl radicals than their ability to scavenge DPPH radicals and superoxide anion radicals. However, *N*, *O*-CMCS derivative 2b has a clearance rate of 85.24 ± 4.39% even at the maximum tested concentration of 1.6 mg/mL, while the clearance rates of other derivatives are less than 80%. Among the derivatives tested, *N*-TM-*O*-CMCS derivatives (4a–4d) demonstrated the highest ability to scavenge hydroxyl radicals, with values exceeding 50%. Specifically, the values were 74.71 ± 3.38%, 69.71 ± 3.26%, 59.06 ± 3.21%, and 57.49 ± 3.49%, respectively.

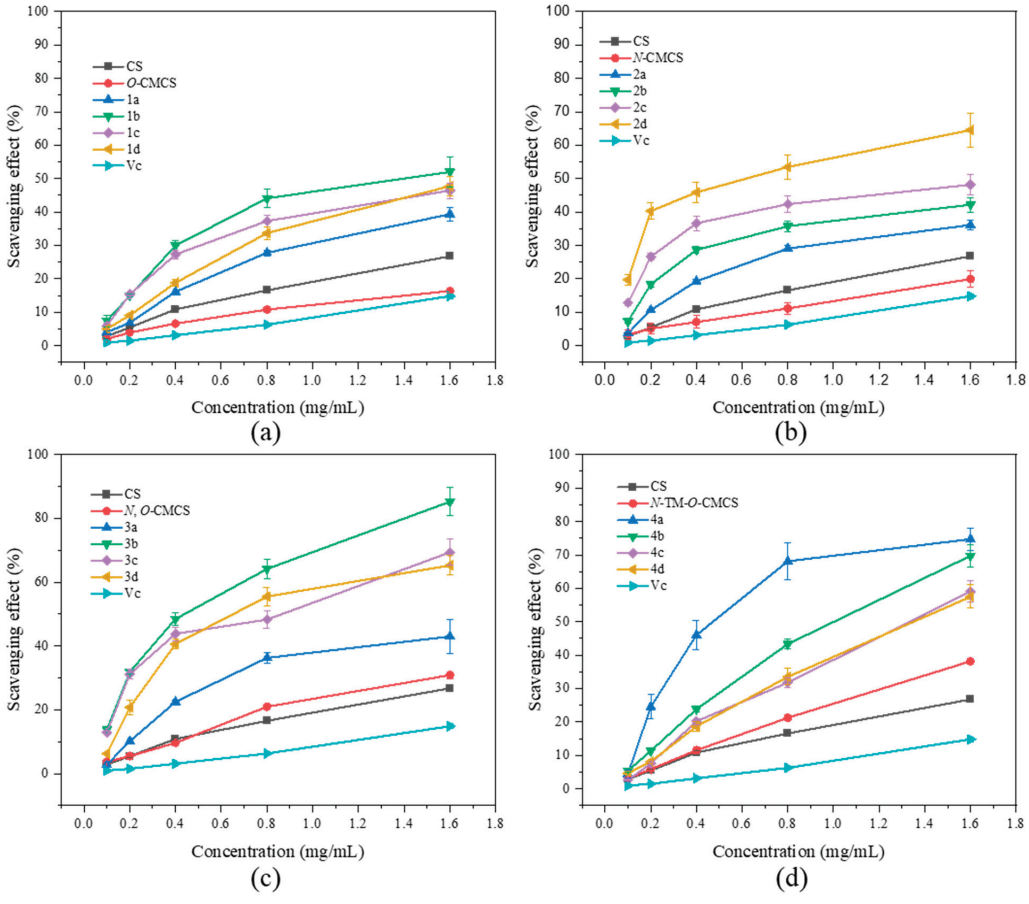


**Figure 5.** Hydroxyl radical scavenging activity of chitosan and CMCS derivatives ((**a**): *O*-CMCS derivatives, (**b**): *N*-CMCS derivatives, (**c**): *N*, *O*-CMCS derivatives, (**d**): *N*-TM-*O*-CMCS derivatives).

As shown in Figure 6, none of the CMCS derivatives show a significant increase in ferric-reducing antioxidant power. Among them, the *O*-CMCS derivative 2b demonstrates the highest reducing power, but it is only 1.53 ± 0.03 A, while all the other CMCS derivatives are all below 1.5 A. This suggests that adding quinoline groups has little effect on improving the ferric-reducing antioxidant power of CS.

### *2.3. Cytotoxicity Analysis*

Figure 7 shows the bar chart of the cell survival rate of L929 cells cultured with CS, CMCS, and CMCS derivatives for 24 h. Moreover, Figure 8 shows the cell morphology of L929 cells after 24 h of incubation in a sample solution at 1000 μg/mL. Except for *O*-CMCS and its derivatives 1a at high concentrations (1000 μg/mL), which show high cytotoxicity (cell survival rates of 58.46 ± 11.64% and 50.77 ± 4.67%), other derivatives exhibit low toxicity or no cytotoxicity. *O*-CMCS derivatives (1b–1d): 109.67 ± 5.67%, 99.73 ± 4.95%, and 105.46 ± 2.98%; *N*-CMCS derivatives (2a–2d): 94.51 ± 4.85%, 88.91 ± 9.78%, 78.58 ± 7.21%, and 100.32 ± 10.27%; *N*, *O*-CMCS derivatives (3a–3d): 91.16 ± 2.10%, 98.92 ± 1.57%, 82.48 ± 2.78%, and 96.01 ± 5.60%; *N*-TM-*O*-CMCS derivatives (4a–4d): 114.08 ± 2.53%, 84.90 ± 6.01%, 81.32 ± 7.28%, and 101.15 ± 5.69%. In conclusion, the introduction of

quinoline groups has little effect on the biocompatibility of CS. Therefore, CMCS derivatives bearing quinoline groups have a certain application potential as synthetic antioxidants.

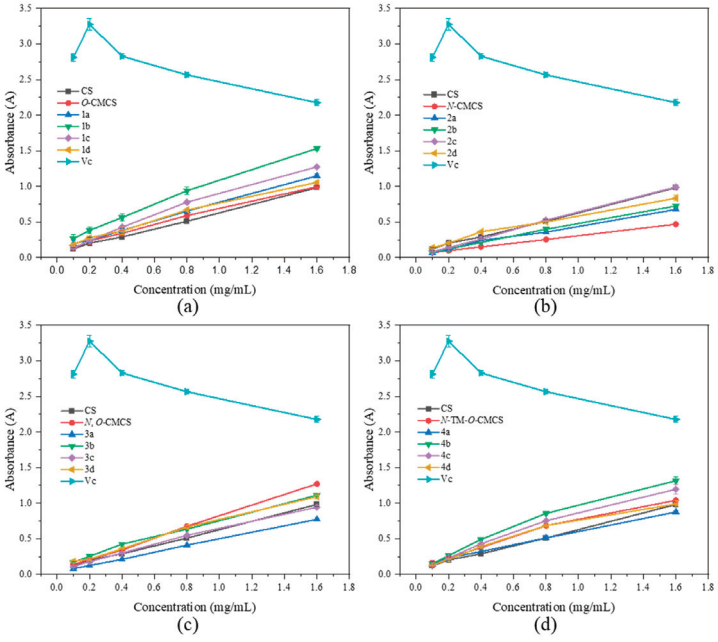


**Figure 6.** Ferric-reducing antioxidant power of chitosan and CMCS derivatives ((**a**): *O*-CMCS derivatives, (**b**): *N*-CMCS derivatives, (**c**): *N*, *O*-CMCS derivatives, (**d**): *N*-TM-*O*-CMCS derivatives).

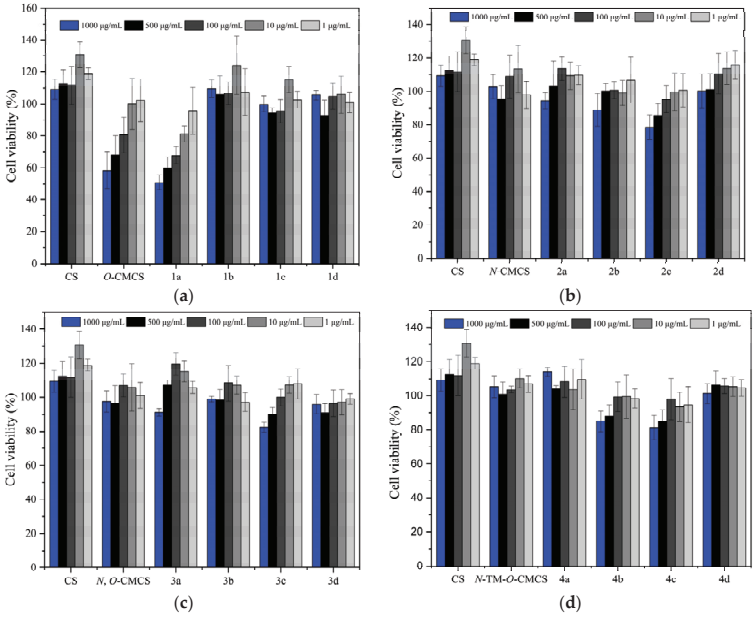


**Figure 7.** The cytotoxicity of chitosan and CMCS derivatives ((**a**): *O*-CMCS derivatives, (**b**): *N*-CMCS derivatives, (**c**): *N*, *O*-CMCS derivatives, (**d**): *N*-TM-*O*-CMCS derivatives).

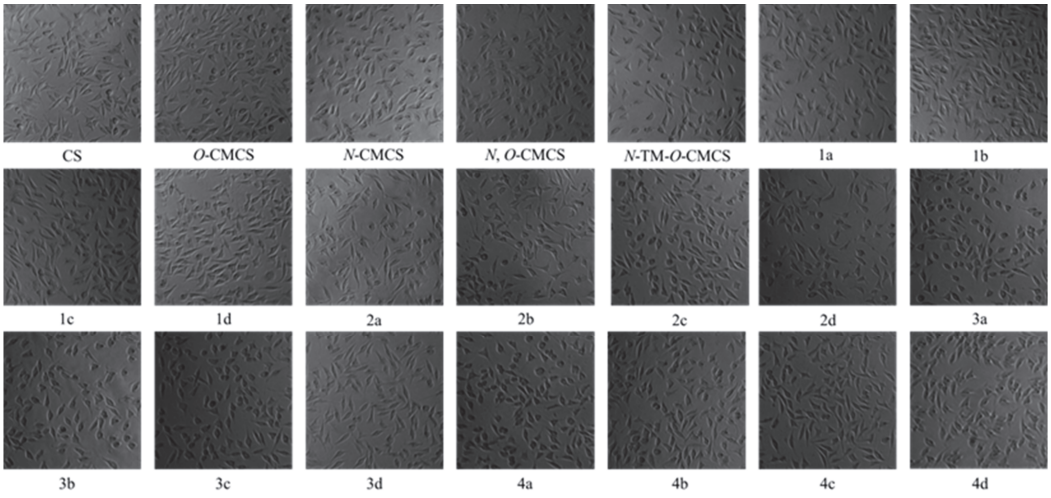


**Figure 8.** Pictures of L929 cells incubated for 24 h in sample solution at 1000 μg/mL.

## 3. Materials and Methods

### *3.1. Materials*

Golden-Shell Pharmaceutical Co., Ltd. (Zhejiang, China) supplied chitosan with a molecular weight of 5000–8000 Da and 68.67% deacetylation degree. Furthermore, 3-aminoquinoline, 5-aminoquinoline, 6-aminoquinoline, and 8-aminoquinoline were purchased from Sigma-Aldrich Chemical Corp. (Shanghai, China). 1-(3-Dimethylaminopropyl)-3-ethylcarbodiimide hydrochloride (EDC) and *N*-hydroxysuccinimide (NHS) were purchased from Shanghai Macklin Biochemical Co., Ltd. (Shanghai, China). Sodium hydroxide, glyoxylic acid monohydrate, isopropanol, chloroacetic acid, hydrochloric acid, sodium iodide, iodomethane, dimethyl sulfoxide (DMSO), acetone, ethanol, and *N*-methylpyrrolidone (NMP) were provided by Sinopharm Chemical Reagent Co., Ltd. (Shanghai, China). The reagents used in the experiment in this paper are analytically pure, and the experimental water is deionized water.

### *3.2. Preparation of Chitosan Derivatives*

#### 3.2.1. Synthesis of *O*-Carboxymethyl Chitosan (*O*-CMCS)

One gram of chitosan (6.2 mmol) was accurately weighed, and 10 mL of isopropyl alcohol was placed in a 100 mL reaction flask. Then, 2.5 mL of a 40% NaOH solution was slowly added dropwise, and the reaction was performed at room temperature for 1 h. Then, 23 mL of a 10% chloroacetic acid solution was added drop by drop. The reaction was performed at room temperature for 4 h. After the reaction, the system's pH value was adjusted to 5–6 with hydrochloric acid, and the system was poured into excess ethanol to precipitate a large amount of light yellow solid. The system underwent filtration and dialysis in deionized water for 48 h using a 500 Da cut-off molecular-weight dialysis bag. Subsequently, *O*-CMCS was obtained via vacuum freeze-drying.

#### 3.2.2. Synthesis of *N*-Carboxymethyl Chitosan (*N*-CMCS)

To synthesize *N*-CMCS, 2.0 g of chitosan (12.4 mmol) was dissolved in 20 mL of deionized water. Then, a solution containing 8.17 g of glyoxylic acid monohydrate (88.8 mmol) was added slowly. The reaction was performed at room temperature for 2.5 h. Next, NaOH was added to make the system's pH 10, and 4.7 g of sodium borohydride (124 mmol) was added in batches. The reaction continued at room temperature for 5 h. Once the reaction was complete, hydrochloric acid was added to make the system pH 5. The next step involved dialysis in deionized water for 48 h using a molecular weight intercep-

tion in a 500 Da dialysis bag. Finally, *N*-CMCS (white solid) was obtained after vacuum freeze-drying.

3.2.3. Synthesis of *N*, *O*-Carboxymethyl Chitosan (*N*, *O*-CMCS)

Four grams of chitosan (24.8 mmol) were added to 40 mL of isopropanol, and 10 mL of a 40% NaOH solution was added for 1 h. The reaction was heated to 60 °C, and 7.5 g of chloroacetic acid (79.4 mmol) was added, followed by a 5-hour reaction. At the end of the reaction, deionized water was added to dilute the system. The solution was then poured into excess ethanol and filtered to obtain a yellow solid. This solid was washed with ethanol three times and vacuum freeze-dried to obtain *N*, *O*-CMCS.

3.2.4. Synthesis of *N*, *N*, *N*-Trimethyl-*O*-Carboxymethyl Chitosan (*N*-TM-*O*-CMCS)

First, 1.61 g of chitosan (10 mmol) was dissolved in 40 mL of NMP, and 4.5 g of NaI (30 mmol), 15 mL of a 15% NaOH solution, and 15 mL of $CH_3I$ were slowly added under an ice bath. Then, the reaction was heated to 60 °C and refluxed for 2 h. After cooling to room temperature, the reaction solution was poured into excess ethanol and filtered to obtain a large amount of solid. The solid was dried in a vacuum and then dissolved in 10 mL of isopropanol. Next, 2.5 mL of a 40% NaOH solution was added drop by drop, and the reaction was allowed to proceed for 1 h. After that, 23 mL of a 10% chloroacetic acid solution was slowly added to the reaction at room temperature for 6 h. Excess acetone was added once the reaction was complete, and the system was filtered to obtain a brown solid. The filter cake was washed three times with acetone and dried under vacuum to obtain *N*-TM-*O*-CMCS.

3.2.5. Synthesis of Carboxymethyl Chitosan Derivatives Bearing Quinoline Groups (1a–1d, 2a–2d, 3a–3d, and 4a–4d)

According to the preparation method of *O*-carboxymethyl chitosan derivatives bearing quinoline groups (1a–1d), the rest of the carboxymethyl chitosan derivatives bearing quinoline groups (2a–2d, 3a–3d, and 4a–4d) were prepared in the same way. First, 1.0 g of *O*-CMCS (4.5 mmol), 1.0 g of EDC (4.5 mmol), and 0.55 g of NHS (4.5 mmol) were added to the reaction flask containing 20 mL of DMSO. Concentrated hydrochloric acid was added to make the system clear and transparent, and nitrogen was used to displace the air. The mixture was then allowed to react for 5 h at room temperature without light. Next, a solution of 1.97 g of aminoquinoline (13.7 mmol) in 20 mL of DMSO was added drop by drop. The reaction was conducted without light for 10 h at room temperature in a nitrogen atmosphere. After the reaction was completed, the reaction system was poured into excess acetone, filtered to obtain a large number of solids, and the filter cake was extracted by Soxhlet using ethanol for 48 h to obtain *O*-carboxymethyl chitosan derivatives bearing quinoline groups (1a–1d).

*3.3. Analytical Methods*

3.3.1. Fourier Transform Infrared Spectroscopy (FTIR)

FTIR analysis was carried out on a Nicolet iS 50 Fourier Transform Infrared Spectrometer (Thermo, Waltham, MA, USA), using transmittance modes at a resolution of 4.0 $cm^{-1}$ in the 4000–500 $cm^{-1}$ region. The tested samples were treated with the potassium bromide table method for observation with the accumulation of 16 scans at room temperature.

3.3.2. $^1$H Nuclear Magnetic Resonance Spectroscopy ($^1$H NMR)

$^1$H NMR was carried out on a Bruker AVIII-500 Spectrometer (Switzerland, provided by Bruker Tech. and Serv. Co., Ltd., Beijing, China) operating at 500 MHz to determine the chemical structures of the prepared carboxymethyl chitosan derivatives dissolved in $D_2O$ or DMSO. The detection temperature was 25 °C.

3.3.3. Degrees of Substitution (DS)

The elemental composition of the prepared samples was performed on a Vario EL III elemental analyzer. According to the ratio of carbon and nitrogen content, the degree of deacetylation (*DD*) of chitosan, the degree of substitution of intermediate products ($DS_1$), and the degree of substitution of carboxymethyl chitosan derivatives ($DS_2$) were calculated as follows:

$$DD = \frac{n_1 \times M_C - M_N \times W_{C/N}}{n_2 \times M_C}$$

$$DS_1 = \frac{W_{C/N} \times M_N - n_1 \times M_C + n_2 \times DD \times M_C}{n_3 \times M_C}$$

$$DS_2 = \frac{W_{C/N} \times M_N - n_1 \times M_C + n_2 \times DD \times M_C - n_3 \times DS_1 \times M_C}{n_4 \times M_C - n_1^* \times W_{C/N} \times M_N}$$

where $n_1$, $n_2$, $n_3$, $n_4$, and $n_1^*$ represent the number of carbon atoms in the chitin molecule, the number of carbon atoms in the acetyl group, the number of carbon atoms remaining in the chitosan molecule in the intermediate product, the number of carbon atoms in aminoquinoline, and the number of nitrogen atoms in aminoquinoline, $n_1 = 8$, $n_2 = 2$, $n_3 = 2$ or 4 or 5, respectively. $n_4 = 9$ or 18, $n_1^* = 2$ or 4; $M_C$ and $M_N$ represent the relative atomic masses of carbon and nitrogen, $M_C = 12$, $M_N = 14$. $W_{C/N}$ represents the ratio of carbon to nitrogen content in the sample.

*3.4. Antioxidant Assay In Vitro*

3.4.1. DPPH Radical Scavenging Activity

The DPPH radical scavenging ability of chitosan, carboxymethyl chitosan, and carboxymethyl chitosan derivatives was measured following Zhang's method with slight modifications [42]. All tested samples (chitosan, carboxymethyl chitosan, and carboxymethyl chitosan derivatives) were prepared in a series of 1 mL aqueous solutions of 0.3, 0.6, 1.2, 2.4, and 4.8 mg/mL, respectively. The reaction mixture, involving 1 mL of the test samples and 2 mL of DPPH-ethanol solution (180 μM), was incubated in the dark at room temperature for 20 min. To prepare the blank solution, 1.0 mL of deionized water was added instead of 1.0 mL of sample solution. Absolute ethanol was used as the control instead of the DPPH-ethanol solution. The DPPH radical scavenging activity was evaluated by measuring the absorbance at 517 nm. A triplicate measurement was taken for each test sample, and the scavenging rate of DPPH radical was calculated according to the following formula:

$$\text{Scavenging effect } (\%) = \left[1 - \frac{A_{sample\ 517\text{nm}} - A_{control\ 517\text{nm}}}{A_{blank\ 517\text{nm}}}\right] \times 100$$

where $A_{sample\ 517\text{nm}}$ represents the absorbance of samples at 517 nm, $A_{control\ 517\text{nm}}$ represents the absorbance of the control at 517 nm, and $A_{blank\ 517\text{nm}}$ represents the absorbance of the blank at 517 nm.

3.4.2. Superoxide Anion Radical Scavenging Activity

The superoxide anion radical scavenging activity assay of chitosan, carboxymethyl chitosan, and carboxymethyl chitosan derivatives was conducted according to the previous method with a minor adjustment [43]. Firstly, 36.57 mg reduced coenzyme I (NADH), 24.53 mg nitroblue tetrazolium (NBT), and 1.838 mg phenazine methyl sulfate (PMS) were weighed and dissolved in 100 mL of Tris-HCl buffer (16 mM, pH 8.2), respectively. All tested samples (chitosan, carboxymethyl chitosan, and carboxymethyl chitosan derivatives) were dissolved in deionized water and prepared into a series of 1.5 mL aqueous solutions of 0.20, 0.40, 0.80, 1.60, and 3.20 mg/mL. Subsequently, 0.50 mL of NADH, NBT, and PMS were added to various sample solutions. The mixture was evenly mixed and reacted for 5 min at room temperature in the dark. The absorbance was measured at 560 nm after the reaction. The blank group was replaced with deionized water, and the control group's

buffer was substituted with NADH. All experiments were conducted in triplicate, and the effects of scavenging superoxide anion radicals were calculated using the following formula:

$$\text{Scavenging effect } (\%) = \left[1 - \frac{A_{sample\ 560\text{nm}} - A_{control\ 560\text{nm}}}{A_{blank\ 560\text{nm}}}\right] \times 100$$

where $A_{sample\ 560\text{nm}}$ is the absorbance of the sample at 560 nm, $A_{control\ 560\text{nm}}$ is the absorbance of the blank group at 560 nm, and $A_{blank\ 560\text{nm}}$ is the absorbance of the control group at 560 nm.

#### 3.4.3. Hydroxyl Radical Scavenging Activity

Hydroxyl radical scavenging activity was performed using the previous method with slight modifications [44]. Firstly, 1.0 mL of samples at different concentrations (0.45, 0.90, 1.80, 3.60, and 7.20 mg/mL) were mixed with 0.5 mL of EDTA-$Fe^{2+}$ (220 μM). Then, 2.0 mL of phosphate buffer solution (pH = 7.4) containing safranine T (0.23 μM) and $H_2O_2$ (60 μM) was added to a final volume of 3.0 mL. Instead of using the sample solutions, 1.0 mL of deionized water was used for the blank group, and 1.0 mL of phosphate buffer solution was used for the control group instead of 3% hydrogen peroxide solution. The reaction mixture was shaken quickly and incubated in the dark for 30 min at 37 °C. Three replicates for every sample concentration were performed, and the absorbance was measured at 520 nm. To calculate the rate of hydroxyl radical scavenging, the following formula was used:

$$\text{Scavenging effect } (\%) = \left[\frac{A_{sample\ 520\ \text{nm}} - A_{blank\ 520\ \text{nm}}}{A_{control\ 520\ \text{nm}} - A_{blank\ 520\ \text{nm}}}\right] \times 100$$

where $A_{sample\ 520\ \text{nm}}$ is the absorbance of the sample group, $A_{control\ 520\ \text{nm}}$ is the absorbance of the control group, and $A_{blank\ 520\ \text{nm}}$ is the absorbance of the blank group.

#### 3.4.4. Ferric-Reducing Antioxidant Power

The ferric-reducing antioxidant power was conducted following the procedure outlined by Li [45]. Samples at different concentrations (0.60, 1.20, 2.40, 4.80, and 9.60 mg/mL) were mixed with potassium ferricyanide (1%, *w*/*v*) and incubated at 50 °C for 20 min. One milliliter of trichloroacetic acid solution (10%, *w*/*v*) was added after the reaction mixture was cooled to room temperature. After shaking, the mixture was centrifuged (3000 r/min) for 5 min to obtain the supernatant. Furthermore, 1.5 mL of the supernatant was mixed with 1.2 mL of deionized water and 0.3 mL of ferric chloride (0.1%, *w*/*v*). The mixture was shaken quickly and reacted for 10 min at 25 °C. All samples and the blank (deionized water) were performed in triplicate and measured at 700 nm. A higher absorbance value indicates a more substantial reduction in power.

### *3.5. Cytotoxicity Assay*

#### 3.5.1. Cell Preparation and Culturing

Briefly, L929 cells (fibroblasts) were cultured in Dulbecco's modified Eagle's medium (DMEM) supplemented with 10% fetal bovine serum at 37 °C and 5% $CO_2$.

#### 3.5.2. Cell Viability Assay

The cytotoxicity of chitosan, carboxymethyl chitosan, and carboxymethyl chitosan derivatives was investigated using the MTT assay [46]. L929 cells were cultured to the exponential growth phase and diluted into cell suspension at a density of 5–10 × $10^4$ cells/mL. Then, 100 μL of cell suspension was added to sterile 96-well plates and incubated at 37 °C with 5% $CO_2$ for 24 h. The samples with different final concentrations were added to the 96-well plates, and the cells were cultured for another 24 h. A total of five parallel tests were established for each sample concentration. Next, the culture medium was removed, and 100 μL of MTT solution was added to each well and incubated for 4 h at 37 °C. Fi-

nally, 150 μL of dimethyl sulfoxide (DMSO) was added to dissolve the crystals, and the absorbance of each well was measured at 490 nm. Cell viability was calculated using the following formula:

$$\text{Cell viability } (\%) = \frac{A_{sample\ 490\text{nm}} - A_{blank\ 490\text{nm}}}{A_{control\ 490\text{nm}} - A_{blank\ 490\text{nm}}} \times 100$$

where $A_{sample\ 490\text{nm}}$ is the absorbance of the samples at 490 nm, $A_{blank\ 490\text{nm}}$ is the absorbance of the blank at 490 nm, and $A_{control\ 490\text{nm}}$ is the absorbance of the negative control at 490 nm.

### *3.6. Statistical Analysis*

All experiments related to antioxidant activity and cytotoxicity were performed in triplicate. Data were reported as the mean ± standard deviation (SD) and analyzed by one-way analysis of variance. Significant differences ($p < 0.05$) between the means were determined using Scheffe's multiple range test. The data figures were prepared using OriginPro 2021 software (OriginLab Corporation, Northampton, MA, USA).

## 4. Discussion

According to the in-depth study, antioxidants provide significant protection against oxidative stress in various pathological processes. In addition, with the development of the economy, people have higher requirements for food preservation technology, and synthetic antioxidants are usually highly toxic and unsuitable as food additives and packaging materials. Chitosan and its derivatives, as natural polymers, have attracted much attention in the field of antioxidants because of their non-toxic and easy degradation characteristics. In this paper, the antioxidant activity of CMCS derivatives containing quinoline groups was preliminarily determined using different methods. The results showed that the prepared CMCS derivatives had good free radical scavenging ability, especially the *N*, *O*-carboxymethyl chitosan derivatives and *N*-TM-*O*-CMCS derivatives, which were generally better than *O*-CMCS derivatives and *N*-CMCS derivatives, which might be attributed to the unique structure of the quinoline ring. Its ring nitrogen atom has a pair of lone electrons, which can be used as an electron donor to convert reactive free radicals into stable products that quench free radicals. Therefore, modification of the amino group and hydroxyl group of chitosan may be more beneficial to improve its free radical scavenging ability. In addition, cytotoxicity experiments also preliminarily demonstrated that the prepared CMCS derivatives were safe and non-toxic. Although the preliminary experimental results can prove that CMCS derivatives have good antioxidant capacity and biocompatibility, which can provide theoretical support for applying CMCS derivatives in the food and pharmaceutical fields, more in-depth experiments are still needed to evaluate their antioxidant activity and cytotoxicity.

## 5. Conclusions

In this paper, 16 novel CMCS derivatives were successfully synthesized by EDC/NHS catalysis. Their chemical structures were characterized by FTIR, $^1$H NMR, and elemental analysis to confirm the successful introduction of the quinoline groups. Currently, there are only four in vitro antioxidant models available for testing the antioxidant activities of derivatives of carboxymethyl chitosan (CMCS). However, these models are still in the early experimental stage. To confirm the potential and application scope of CMCS derivatives as synthetic antioxidants in the future, more comprehensive research techniques are required. Additionally, the cytotoxic results suggested that the introduction of quinoline groups had a minimal impact on the biocompatibility of CS and CMCS. In summary, the CMCS derivatives synthesized in this study demonstrated outstanding antioxidant activity and biocompatibility. Ongoing studies are being conducted in our laboratory to explore the synthetic applications of these derivatives.

**Author Contributions:** Conceptualization, L.W. and Z.G.; methodology, L.W. and Z.G.; software, L.W., R.G., X.L., Y.J. and J.Z.; formal analysis, L.W., R.G., X.L., Y.J. and J.Z.; writing—original draft, L.W., J.Z. and Z.G.; writing—review and editing, L.W. and Z.G.; investigation, G.G.; supervision, Z.G.; funding acquisition, G.G., J.Z. and Z.G. All authors have read and agreed to the published version of the manuscript.

**Funding:** The authors thank the Natural Science Foundation of Shandong Province of China (ZR2021QD047), Shandong Key R&D Plan, Major Scientific and Technological Innovation Project (2022CXGC020413), and Science & Technology Specific Projects in the Agricultural High-Tech Industrial Demonstration Area of the Yellow River Delta (2022SZX01) for financial support of this work.

**Institutional Review Board Statement:** Not applicable.

**Informed Consent Statement:** Not applicable.

**Data Availability Statement:** All data contained in the manuscript are available from the authors.

**Acknowledgments:** We would like to thank the Institutional Center for the shared technologies and facilities of the Yantai Institute of Coastal Zone Research, the Chinese Academy of Sciences for their assistance with conventional $^{1}$H NMR, and the Yellow River Delta Saline-Alkali Agroecosystem Observation and Research Station for their valuable support during the experiment. And we would also like to thank the editors and reviewers for their helpful comments to improve this manuscript.

**Conflicts of Interest:** The authors declare no conflict of interest.

## References

1. Cardoso, M.A.; Gonçalves, H.M.R.; Davis, F. Reactive oxygen species in biological media are they friend or foe? Major In vivo and In vitro sensing challenges. *Talanta* **2023**, *260*, 124648. [CrossRef]
2. MohanKumar, S.M.J.; Murugan, A.; Palaniyappan, A.; MohanKumar, P.S. Role of cytokines and reactive oxygen species in brain aging. *Mech. Ageing Dev.* **2023**, *214*, 111855. [CrossRef]
3. Rosa, C.P.; Belo, T.C.A.; Santos, N.C.d.M.; Silva, E.N.; Gasparotto, J.; Corsetti, P.P.; de Almeida, L.A. Reactive oxygen species trigger inflammasome activation after intracellular microbial interaction. *Life Sci.* **2023**, *331*, 122076. [CrossRef]
4. Chasara, R.S.; Ajayi, T.O.; Leshilo, D.M.; Poka, M.S.; Witika, B.A. Exploring novel strategies to improve anti-tumour efficiency: The potential for targeting reactive oxygen species. *Heliyon* **2023**, *9*, e19896. [CrossRef]
5. Zhou, X.; Chen, Q.; Chen, L.; Liao, X.; Wang, Z.; Zhu, F. The effect of reactive oxygen species (ROS) in immunity and WSSV infection of *Scylla paramamosain*. *Fish Shellfish Immunol.* **2023**, *141*, 109075. [CrossRef]
6. Ali, M.M.A.; Suriyan, G.U.; Surya, K.J.; Mani, K.S. Synthesis of bioactive quinoline appended spiro pyrrolidines as antioxidants. *J. Heterocycl. Chem.* **2023**, *60*, 1558–1564. [CrossRef]
7. Harry, N.A.; Ujwaldev, S.M.; Anilkumar, G. Recent advances and prospects in the metal-free synthesis of quinolines. *Org. Biomol. Chem.* **2020**, *18*, 9775–9790. [CrossRef]
8. Zhang, X.; Chen, J.; Yong, S.; Zhao, Y. Acid/base-co-catalyzed cyclization of ketones with *o*-amino-benzylamines: Direct synthesis of quinoline compounds. *Tetrahedron Lett.* **2023**, *128*, 154700. [CrossRef]
9. Ambatkar, M.P.; Rarokar, N.R.; Khedekar, P.B. Clinical Use of COX-2 Inhibitors Containing Quinoline Heterocycle as a Selective Therapeutic Agents for Complementary Medicine. *Clin. Complement. Med. Pharmacol.* **2023**, *3*, 100102. [CrossRef]
10. Douadi, K.; Chafaa, S.; Douadi, T.; Al-Noaimi, M.; Kaabi, I. Azoimine quinoline derivatives: Synthesis, classical and electrochemical evaluation of antioxidant, anti-inflammatory, antimicrobial activities and the DNA/BSA binding. *J. Mol. Struct.* **2020**, *1217*, 128305. [CrossRef]
11. Mahajan, P.; Nikam, M.; Asrondkar, A.; Bobade, A.; Gill, C. Synthesis, Antioxidant, and Anti-Inflammatory Evaluation of Novel Thiophene-Fused Quinoline Based β-Diketones and Derivatives. *J. Heterocycl. Chem.* **2016**, *54*, 1415–1422. [CrossRef]
12. Bandiwadekar, C.R.; Jagdale, A.D.; Durge, A.S.; Pachpor, T.A.; Tupe, R.S. Evaluation of different sugars for glycation modifications of chitosan to improve its functionality for food preservation. *Food Hydrocoll.* **2023**, *145*, 109104. [CrossRef]
13. Kritchenkov, A.S.; Egorov, A.R.; Volkova, O.V.; Artemjev, A.A.; Kurliuk, A.V.; Anh Le, T.; Hieu Truong, H.; Le-Nhat-Thuy, G.; Van Tran Thi, T.; Van Tuyen, N.; et al. Novel biopolymer-based nanocomposite food coatings that exhibit active and smart properties due to a single type of nanoparticles. *Food Chem.* **2021**, *343*, 128676. [CrossRef]
14. Kang, H.; Jiang, B.; Song, C.; Huang, J.; Chu, L. Synthesis and fluorescent property of carboxymethyl chitosan with different degrees of carboxymethylation and its application for fluorescence turn-on detection of Cd(II) ion. *Int. J. Biol. Macromol.* **2023**, *250*, 126252. [CrossRef]
15. Nawaz, A.; Atif, M.; Naz, I.; Khan, A.; Naz, F.; Ali, N. Comparative robustness and sustainability of in-situ prepared antimony nanoarchitectonics in chitosan/synthesized carboxymethyl chitosan in environmental remediation perspective. *Int. J. Biol. Macromol.* **2023**, *235*, 123591. [CrossRef]

16. Fu, Y.; Li, C.; Xue, M.; Cao, Y.; Zhang, W.; Li, D. Liquid handling properties of carboxymethyl modified chitosan nonwovens for medical dressings. *J. Mol. Struct.* **2023**, *1292*, 136118. [CrossRef]
17. Geng, Y.; Xue, H.; Zhang, Z.; Panayi, A.C.; Knoedler, S.; Zhou, W.; Mi, B.; Liu, G. Recent advances in carboxymethyl chitosan-based materials for biomedical applications. *Carbohydr. Polym.* **2023**, *305*, 120555. [CrossRef]
18. Zidan, N.; Albalawi, M.A.; Alalawy, A.I.; Al-Duais, M.A.; Alzahrani, S.; Kasem, M.; Tayel, A.A.; Nagib, R.M. Active and smart antimicrobial food packaging film composed of date palm kernels extract loaded carboxymethyl chitosan and carboxymethyl starch composite for prohibiting foodborne pathogens during fruits preservation. *Eur. Polym. J.* **2023**, *197*, 112353. [CrossRef]
19. Al-Hashmi, S.; Vakilian, S.; Jamshidi-adegani, F.; Al-Kindi, J.; Al-Fahdi, F.; Al-Hatmi, A.M.S.; Al-Jahdhami, H.; Anwar, M.U.; Al-Wahaibi, N.; Shalaby, A.; et al. Development of a Tacrolimus-loaded carboxymethyl chitosan scaffold as an effective 3D-printed wound dressing. *J. Drug Delivery Sci. Technol.* **2023**, *86*, 104707. [CrossRef]
20. Zhao, Y.; Li, R.; Liu, Y.; Song, L.; Gao, Z.; Li, Z.; Peng, X.; Wang, P. An injectable, self-healable, antibacterial, and pro-healing oxidized pullulan polysaccharide/carboxymethyl chitosan hydrogel for early protection of open abdominal wounds. *Int. J. Biol. Macromol.* **2023**, *250*, 126282. [CrossRef]
21. Liu, W.; Kang, S.; Xue, J.; Chen, S.; Yang, W.; Yan, B.; Liu, D. Self-assembled carboxymethyl chitosan/zinc alginate composite film with excellent water resistant and antimicrobial properties for chilled meat preservation. *Int. J. Biol. Macromol.* **2023**, *247*, 125752. [CrossRef]
22. Sela, A.; Shkuri, N.; Tish, N.; Vinokur, Y.; Rodov, V.; Poverenov, E. Carboxymethyl chitosan-quercetin conjugate: A sustainable one-step synthesis and use for food preservation. *Carbohydr. Polym.* **2023**, *316*, 121084. [CrossRef]
23. Zhang, Z.; Abidi, N.; Lucia, L. Smart superabsorbent alginate/carboxymethyl chitosan composite hydrogel beads as efficient biosorbents for methylene blue dye removal. *J. Mater. Sci. Technol.* **2023**, *159*, 81–90. [CrossRef]
24. Cai, M.; Duan, Y.; Shi, T.; Su, J.; Chen, K.; Ma, D.; Wang, F.; Qin, J.; Wei, S.; Gao, Z. Multiple effects achieved with a single agent of *O*-carboxymethyl chitosan exhibiting cross-linking and antibacterial properties. *Prog. Org. Coat.* **2023**, *175*, 107345. [CrossRef]
25. Jiang, Z.; Han, B.; Li, H.; Li, X.; Yang, Y.; Liu, W. Preparation and anti-tumor metastasis of carboxymethyl chitosan. *Carbohydr. Polym.* **2015**, *125*, 53–60. [CrossRef]
26. Wei, Q.; Wang, Y.; Wang, H.; Qiao, L.; Jiang, Y.; Ma, G.; Zhang, W.; Hu, Z. Photo-induced adhesive carboxymethyl chitosan-based hydrogels with antibacterial and antioxidant properties for accelerating wound healing. *Carbohydr. Polym.* **2022**, *278*, 119000. [CrossRef]
27. Mi, Y.; Zhang, J.; Chen, Y.; Sun, X.; Tan, W.; Li, Q.; Guo, Z. New synthetic chitosan derivatives bearing benzenoid/heterocyclic moieties with enhanced antioxidant and antifungal activities. *Carbohydr. Polym.* **2020**, *249*, 116847. [CrossRef]
28. Chen, S.; Wu, Y.; Mi, F.; Lin, Y.; Yu, L.; Sung, H. A novel pH-sensitive hydrogel composed of *N*,*O*-carboxymethyl chitosan and alginate cross-linked by genipin for protein drug delivery. *J. Control. Release* **2004**, *96*, 285–300. [CrossRef]
29. Chang, J.; Liu, W.; Han, B.; Peng, S.; He, B.; Gu, Z. Investigation of the skin repair and healing mechanism of N-carboxymethyl chitosan in second-degree burn wounds. *Wound Repair Regen.* **2013**, *21*, 113–121. [CrossRef]
30. Hamdan, Y.A.; Elouali, S.; Eladlani, N.; Lefeuvre, B.; Oudadesse, H.; Rhazi, M. Investigation on Akis granulifera (Coleoptera, Sahlberg, 1823) as a potential source of chitin and chitosan: Extraction, characterization and hydrogel formation. *Int. J. Biol. Macromol.* **2023**, *252*, 126292. [CrossRef]
31. Hamodin, A.G.; Elgammal, W.E.; Eid, A.M.; Ibrahim, A.G. Synthesis, characterization, and biological evaluation of new chitosan derivative bearing diphenyl pyrazole moiety. *Int. J. Biol. Macromol.* **2023**, *243*, 125180. [CrossRef]
32. Bai, R.; Yong, H.; Zhang, X.; Liu, J.; Liu, J. Structural characterization and protective effect of gallic acid grafted *O*-carboxymethyl chitosan against hydrogen peroxide-induced oxidative damage. *Int. J. Biol. Macromol.* **2020**, *143*, 49–59. [CrossRef]
33. Zheng, J.; Li, K.; Li, Y.; Jiang, G. Preparation and characterization of carboxymethyl chitosan/κ-carrageenan/silver nanoparticles sponge for wound dressing. *Mater. Today Commun.* **2023**, *35*, 105818. [CrossRef]
34. Gu, H.; Chen, P.; Liu, X.; Lian, Y.; Xi, J.; Li, J.; Song, J.; Li, X. Trimethylated chitosan-coated flexible liposomes with resveratrol for topical drug delivery to reduce blue-light-induced retinal damage. *Int. J. Biol. Macromol.* **2023**, *252*, 126480. [CrossRef]
35. Zhang, J.; Tan, W.; Wang, G.; Yin, X.; Li, Q.; Dong, F.; Guo, Z. Synthesis, characterization, and the antioxidant activity of *N*,*N*,*N*-trimethyl chitosan salts. *Int. J. Biol. Macromol.* **2018**, *118*, 9–14. [CrossRef]
36. Wennman, M.; Pinon, A.C.; Svagan, A.J.; Hellberg, M.; Hedenqvist, M.S. A biobased binder of carboxymethyl cellulose, citric acid, chitosan and wheat gluten for nonwoven and paper. *Carbohydr. Polym.* **2024**, *323*, 121430. [CrossRef]
37. Janeoo, S.; Reenu; Saroa, A.; Kumar, R.; Kaur, H. Computational investigation of bioactive 2,3-diaryl quinolines using DFT method: FT-IR, NMR spectra, NBO, NLO, HOMO-LUMO transitions, and quantum-chemical properties. *J. Mol. Struct.* **2022**, *1253*, 132285. [CrossRef]
38. Khotele, N.B.; Dahule, H.K.; Dhoble, S.J. Synthesis and Characterization Red Emitting Iridium (III) Complex with 2-(4-cynophenyl)-4 Phenyl quinoline for PhOLEDs. *Mater. Today Proc.* **2018**, *5*, 22163–22170. [CrossRef]
39. Song, Z.; Chen, S.; Du, S.; Fan, C. Construction of high-performance $LiMn_{0.8}Fe_{0.2}PO_4$/C cathode by using quinoline soluble substance from coal pitch as carbon source for lithium ion batteries. *J. Alloys Compd.* **2022**, *927*, 166921. [CrossRef]
40. Lei, M.; Huang, W.; Sun, J.; Shao, Z.; Duan, W.; Wu, T.; Wang, Y. Synthesis, characterization, and performance of carboxymethyl chitosan with different molecular weight as additive in water-based drilling fluid. *J. Mol. Liq.* **2020**, *310*, 113135. [CrossRef]

41. Kumru, M.; Altun, A.; Kocademir, M.; Küçük, V.; Bardakçı, T.; Şaşmaz, İ. Combined experimental and quantum chemical studies on spectroscopic (FT-IR, FT-Raman, UV–Vis, and NMR) and structural characteristics of quinoline-5-carboxaldehyde. *J. Mol. Struct.* **2016**, *1125*, 302–309. [CrossRef]
42. Zhang, J.; Wang, L.; Tan, W.; Li, Q.; Dong, F.; Guo, Z. Preparation of chitosan-rosmarinic acid derivatives with enhanced antioxidant and anti-inflammatory activities. *Carbohydr. Polym.* **2022**, *296*, 119943. [CrossRef]
43. Ma, B.; Zhang, J.; Mi, Y.; Miao, Q.; Tan, W.; Guo, Z. Preparation of imidazole acids grafted chitosan with enhanced antioxidant, antibacterial and antitumor activities. *Carbohydr. Polym.* **2023**, *315*, 120978. [CrossRef]
44. Li, Q.; Li, Q.; Tan, W.; Zhang, J.; Guo, Z. Phenolic-containing chitosan quaternary ammonium derivatives and their significantly enhanced antioxidant and antitumor properties. *Carbohydr. Res.* **2020**, *498*, 108169. [CrossRef]
45. Li, Q.; Mi, Y.; Tan, W.; Guo, Z. Highly efficient free radical-scavenging property of phenolic-functionalized chitosan derivatives: Chemical modification and activity assessment. *Int. J. Biol. Macromol.* **2020**, *164*, 4279–4288. [CrossRef]
46. Cui, J.; Sun, Y.; Wang, L.; Tan, W.; Guo, Z. Preparation of chitosan derivatives containing aromatic five-membered heterocycles for efficient antimicrobial and antioxidant activities. *Int. J. Biol. Macromol.* **2023**, *247*, 125850. [CrossRef]

*marine drugs*

MDPI

*Article*

# Low-Molecular-Weight Fish Collagen Peptide (Valine-Glycine-Proline-Hydroxyproline-Glycine-Proline-Alanine-Glycine) Prevents Osteoarthritis Symptoms in Chondrocytes and Monoiodoacetate-Injected Rats

**Wonhee Cho [1,†], Jeongjin Park [2,†], Jinhee Kim [1], Minhee Lee [3], So Jung Park [4], Kyung Seok Kim [4], Woojin Jun [2], Ok-Kyung Kim [2,*] and Jeongmin Lee [1,3,*]**

[1] Department of Medical Nutrition, Kyung Hee University, Yongin 17104, Republic of Korea; wonhi1117@khu.ac.kr (W.C.); jinhee625@khu.ac.kr (J.K.)
[2] Division of Food and Nutrition and Human Ecology Research Institute, Chonnam National University, Gwangju 61186, Republic of Korea; pjj8425@hanmail.net (J.P.); wjjun@jnu.ac.kr (W.J.)
[3] Department of Food Innovation and Health, Kyung Hee University, Yongin 17104, Republic of Korea; miniclsrn@khu.ac.kr
[4] Suheung Co., Ltd., Seoul 02643, Republic of Korea; sjpark@suheung.com (S.J.P.); kskim1@suheung.com (K.S.K.)
* Correspondence: 20woskxm@jnu.ac.kr (O.-K.K.); jlee2007@khu.ac.kr (J.L.); Tel.: +82-62-530-1334 (O.-K.K.); +82-31-201-3838 (J.L.); Fax: +82-62-530-1339 (O.-K.K.); +82-31-204-8119 (J.L.)
† These authors contributed equally to this work.

**Abstract:** The objective of this study was to investigate the effect of low-molecular-weight fish collagen (valine-glycine-proline-hydroxyproline-glycine-proline-alanine-glycine; LMWCP) on $H_2O_2$- or LPS-treated primary chondrocytes and monoiodoacetate (MIA)-induced osteoarthritis rat models. Our findings indicated that LMWCP treatment exhibited protective effects by preventing chondrocyte death and reducing matrix degradation in both $H_2O_2$-treated primary chondrocytes and cartilage tissue from MIA-induced osteoarthritis rats. This was achieved by increasing the levels of aggrecan, collagen type I, collagen type II, TIMP-1, and TIMP-3, while simultaneously decreasing catabolic factors such as phosphorylation of Smad, MMP-3, and MMP-13. Additionally, LMWCP treatment effectively suppressed the activation of inflammation and apoptosis pathways in both LPS-treated primary chondrocytes and cartilage tissue from MIA-induced osteoarthritis rats. These results suggest that LMWCP supplementation ameliorates the progression of osteoarthritis through its direct impact on inflammation and apoptosis in chondrocytes.

**Keywords:** low-molecular-weight fish collagen; osteoarthritis; chondrocytes

**Citation:** Cho, W.; Park, J.; Kim, J.; Lee, M.; Park, S.J.; Kim, K.S.; Jun, W.; Kim, O.-K.; Lee, J. Low-Molecular-Weight Fish Collagen Peptide (Valine-Glycine-Proline-Hydroxyproline-Glycine-Proline-Alanine-Glycine) Prevents Osteoarthritis Symptoms in Chondrocytes and Monoiodoacetate-Injected Rats. *Mar. Drugs* **2023**, *21*, 608. https://doi.org/10.3390/md21120608

Academic Editor: Azizur Rahman

Received: 5 October 2023
Revised: 20 November 2023
Accepted: 25 November 2023
Published: 25 November 2023



## 1. Introduction

Osteoarthritis, a degenerative joint disease, manifests as joint pain arising from a combination of cartilage degradation and synovial inflammation. This disease is a complex degenerative joint disorder characterized by the progressive deterioration of articular cartilage, changes in subchondral bone, and alterations in other joint tissues [1,2]. While the factors contributing to osteoarthritis remain unknown, it predominantly emerges after the age of 60. The pathogenesis of osteoarthritis is multifaceted and involves a combination of mechanical, biochemical, and genetic factors [3–5].

Osteoarthritis arises from an imbalance between the breakdown and repair of joint tissues, particularly the articular cartilage. The articular cartilage, a specialized connective tissue, serves to cushion and distribute load within the joint. This cartilage is composed of chondrocytes embedded within an organized extracellular matrix (ECM) of collagen and aggrecan [6,7]. In osteoarthritis, a chronic cycle of cartilage degradation and inadequate

repair mechanisms leads to a net loss of the cartilage matrix. This process is driven by various molecular pathways, including the dysregulation of matrix metalloproteinases (MMPs), enzymes responsible for cartilage breakdown, and tissue inhibitors of metalloproteinases (TIMPs), which counteract MMP activity. Moreover, inflammation plays a key role in OA pathogenesis. Synovial inflammation, characterized by increased production of pro-inflammatory cytokines, chemokines, and mediators such as interleukin-1β (IL-1β), tumor necrosis factor-α (TNF-α), and prostaglandins, contributes to cartilage degradation and exacerbates joint damage. Additionally, activated immune cells and infiltrating macrophages further amplify the inflammatory response within the joint microenvironment [8–10].

Nonsteroidal anti-inflammatory drugs (NSAIDs) are frequently prescribed to alleviate the pain and inflammation associated with osteoarthritis. NSAIDs function by inhibiting cyclooxygenase (COX), thereby hindering the production of prostaglandins, which are crucial mediators in the inflammatory response. Nonetheless, NSAIDs are accompanied by gastrointestinal side effects [11,12]. Therefore, alternative remedies are often sought for the treatment of osteoarthritis due to their lower risk of side effects and minimal toxicity [13,14]. Collagen has recently garnered particular interest among researchers due to its multiple bioactive properties. However, the term "collagen" encompasses a variety of compounds with distinct structures, compositions, and origins, resulting in diverse properties and potential effects. Previous studies have proposed that collagen supplementation could promote the synthesis of connective tissue, especially cartilage ECM, mainly because collagen represents its major component. In fact, it has been demonstrated that certain peptides from hydrolyzed collagen are absorbed and accumulated in the cartilage [15–17]. Here, we investigated the effect of low-molecular-weight fish-derived type I collagen hydrolysate (LMWCP; valine-glycine-proline-hydroxyproline-glycine-proline-alanine-glycine), originating from tilapia, in primary chondrocytes and rats with monosodium iodoacetate (MIA)-induced osteoarthritis to identify mechanisms underlying the cartilage-regenerating properties of collagen.

## 2. Results

### *2.1. LMWCP Ameliorated Cell Damage and the Expression of Catabolic Factors in $H_2O_2$-Treated Chondrocytes*

LMWCP pretreatment ameliorated 200 μM $H_2O_2$-induced cell death (Figure 1A). The mRNA expression levels of anabolic factors, such as aggrecan, collagen type I, collagen type II, TIMP-1, and TIMP-3, were significantly decreased in the $H_2O_2$-treated chondrocytes compared to those in the normal control (NC). However, acetylsalicylic acid (PC) or LMWCP treatment significantly increased mRNA expression levels of these anabolic factors in the $H_2O_2$-treated chondrocytes ($p < 0.05$; Figure 1B–F). mRNA expression levels of catabolic factors, including MMP-3 and MMP-13, were significantly increased in the $H_2O_2$-treated chondrocytes compared to those in NC, while acetylsalicylic acid or LMWCP treatment significantly increased mRNA expression levels of these catabolic factors in the $H_2O_2$-treated chondrocytes ($p < 0.05$; Figure 1G,H).

The protein expression levels of catabolic factors, such as Smad3 phosphorylation, MMP-3, and MMP-9, in the $H_2O_2$-treated chondrocytes were investigated. The protein expression level of Smad3 phosphorylation was significantly decreased in the $H_2O_2$-treated chondrocytes compared to those in NC, but acetylsalicylic acid or LMWCP treatment significantly increased protein expression in the $H_2O_2$-treated chondrocytes. The protein expression levels of MMP-3 and MMP-9 were increased in the $H_2O_2$-treated chondrocytes compared to those in NC. However, acetylsalicylic acid or LMWCP treatment decreased the protein expression levels in the $H_2O_2$-treated SW982 cells (Figure 1I).

### *2.2. LMWCP Ameliorated Inflammation in LPS-Treated Chondrocytes*

The levels of pro-inflammatory cytokines, prostaglandin (PGE) 2, and NO were significantly increased in the LPS-treated chondrocytes compared with those in NC. However, acetylsalicylic acid or LMWCP treatment significantly decreased the levels of those factors

in the LPS-treated chondrocytes ($p < 0.05$; Figure 2A–E). The protein expression levels of phospho-IκBα/IκBα, phospho-p65/p65, and COX-2 were significantly increased in the LPS-treated chondrocytes compared with those in NC, whereas acetylsalicylic acid or LMWCP treatment significantly decreased the levels of those factors in the LPS-treated chondrocytes (Figure 2F).

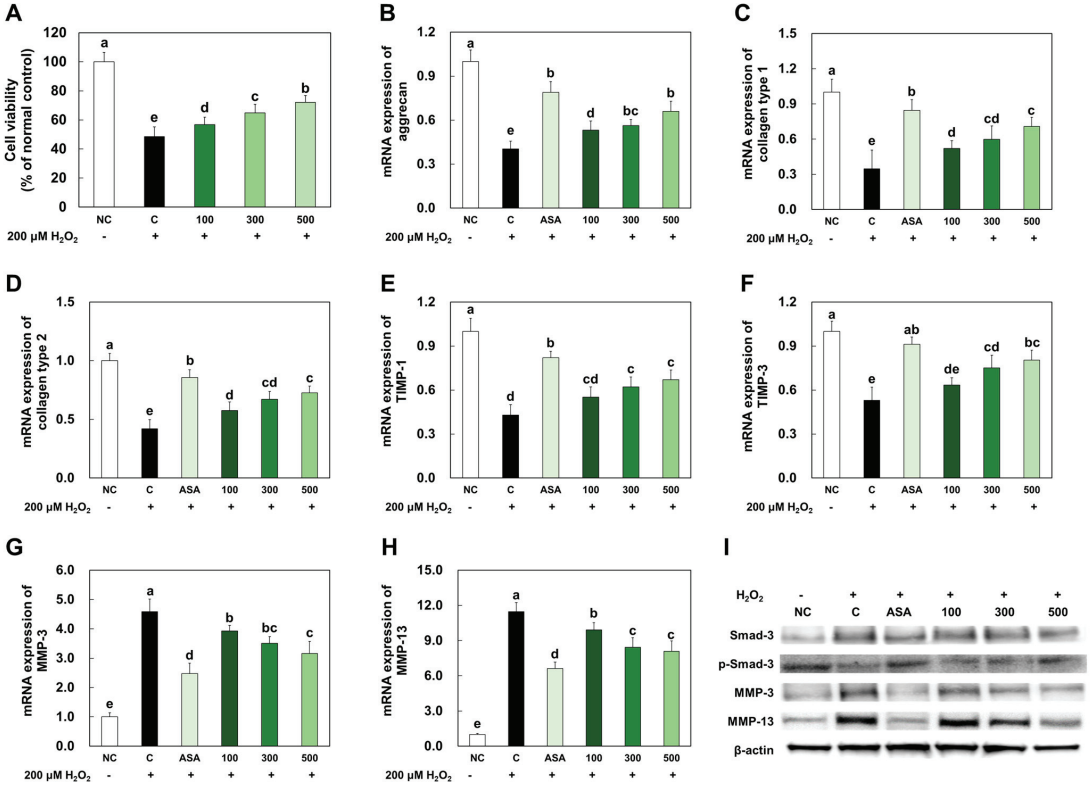


**Figure 1.** Effects of LMWCP on cell viability (**A**), mRNA expression of aggrecan (**B**), collagen type 1 (**C**), collagen type 2 (**D**), TIMP-1 (**E**), TIMP-3 (**F**), MMP-3 (**G**), MMP-13 (**H**), and protein expression of p-Smad-3, MMP-3, and MMP-13 (**I**) in $H_2O_2$-treated chondrocytes. NC: no treatment, C: 200 μM of $H_2O_2$ treatment, ASA: 200 μM of $H_2O_2$ and 10 μM acetylsalicylic acid, 100: 200 μM of $H_2O_2$ and 100 μg/mL of LMWCP, 300: 200 μM of $H_2O_2$ and 300 μg/mL of LMWCP, 500: 200 μM of $H_2O_2$ and 500 μg/mL of LMWCP. Values are presented as mean ± SD. Different letters (a > b > c > d > e) indicate a significant difference at $p < 0.05$ according to Duncan's multiple range test.

### *2.3. LMWCP Ameliorated Apoptosis in LPS-Treated Chondrocytes*

As illustrated in Figure 3, LPS treatment stimulated apoptosis signaling pathways, including the c-Jun N-terminal kinase (JNK)/c-Fos and c-Jun pathway, as well as the Fas-associated protein with death domain (FADD)/caspase8/Bax/caspase3 pathway in the primary chondrocytes. In the primary chondrocytes treated with acetylsalicylic acid or LMWCP, the expression of proteins involved in the apoptosis pathways was suppressed compared to those without treatment.

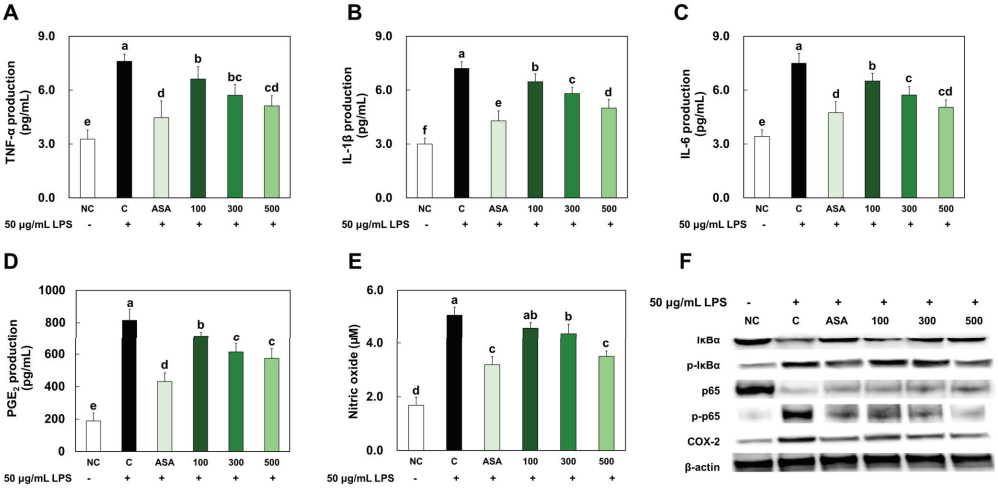


**Figure 2.** Effects of LMWCP on the production of TNF-α (**A**), IL-1β (**B**), and IL-6 (**C**), PGE2 (**D**), and nitric oxide (**E**) and the protein expression of p-IκBα, p-p65, and COX-2 (**F**) in LPS-treated chondrocytes. NC: no treatment, C: 200 μM of $H_2O_2$ treatment, ASA: 200 μM of $H_2O_2$ and 10 μM acetylsalicylic acid, 100: 200 μM of $H_2O_2$ and 100 μg/mL of LMWCP, 300: 200 μM of $H_2O_2$ and 300 μg/mL of LMWCP, 500: 200 μM of $H_2O_2$ and 500 μg/mL of LMWCP. Values are presented as mean ± SD. Different letters (a > b > c > d > e > f) indicate a significant difference at $p < 0.05$ by Duncan's multiple range test.

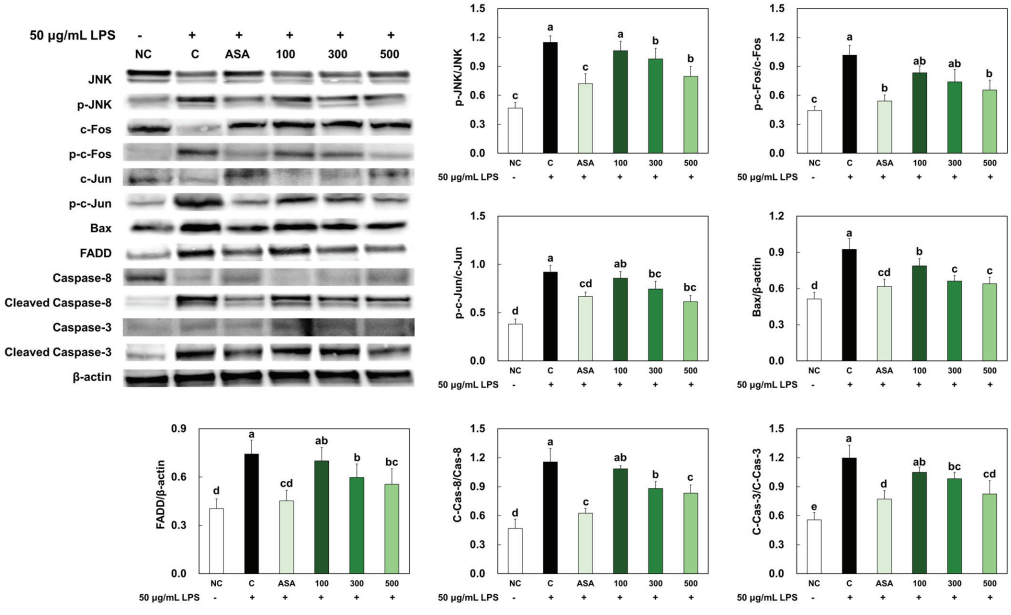


**Figure 3.** Effects of LMWCP on protein expression of apoptosis factors in LPS-treated chondrocytes. NC: no treatment, C: 200 μM of $H_2O_2$ treatment, ASA: 200 μM of $H_2O_2$ and 10 μM acetylsalicylic acid, 100: 200 μM of $H_2O_2$ and 100 μg/mL of LMWCP, 300: 200 μM of $H_2O_2$ and 300 μg/mL of LMWCP, 500: 200 μM of $H_2O_2$ and 500 μg/mL of LMWCP. Values are presented as mean ± SD. Different letters (a > b > c > d > e) indicate a significant difference at $p < 0.05$ by Duncan's multiple range test.

### *2.4. LMWCP Ameliorated Morphological Change of Cartilage Tissue in MIA-Injected Rats*

In the cartilage tissue of MIA-induced osteoarthritis rats, the observed morphological changes were characterized by a noticeable loss of luster and the presence of cartilage fibrillation and erosion. Additionally, MIA-induced osteoarthritis rats exhibited an irregular articular cartilage surface and cartilage matrix degradation, while the joints of non-induced osteoarthritis rats possessed a smooth articular cartilage surface. In contrast, the group treated with ibuprofen or LMWCP exhibited suppressed and morphological changes in the cartilage tissue and displayed an increase in cartilage surface volumes. This suggests that treatment with ibuprofen or LMWCP may have a protective effect on the integrity and structure of the cartilage tissue, potentially mitigating the degenerative changes associated with osteoarthritis (Figure 4).

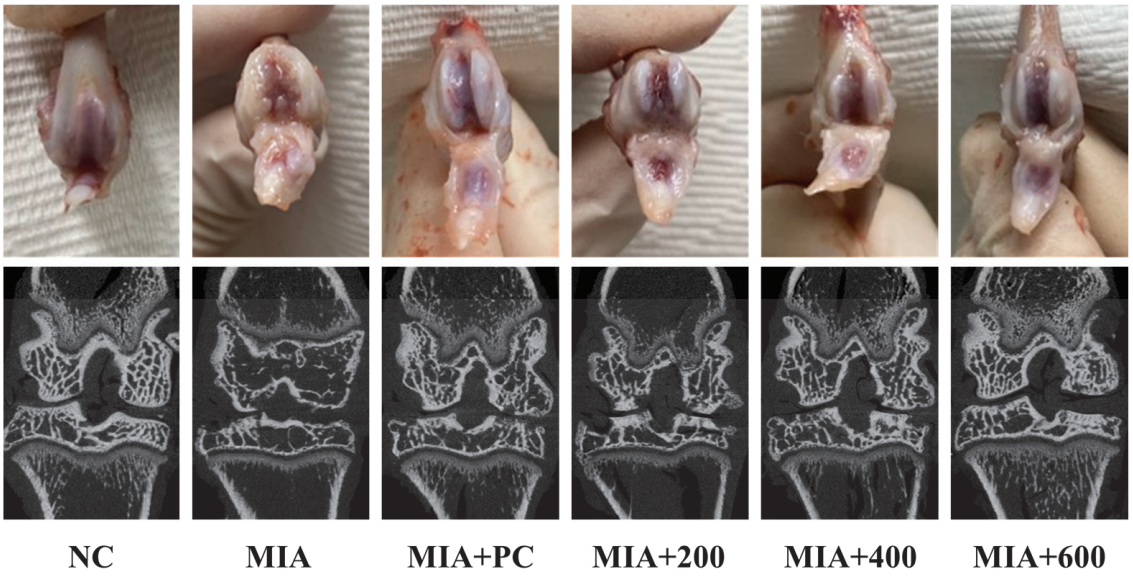


**Figure 4.** Effects of LMWCP on the morphological features of cartilage tissue from MIA-induced osteoarthritis rats. NC: saline injection, MIA: MIA injection, MIA + PC: MIA injection and 50 mg/kg BW of ibuprofen, MIA + 200: MIA injection and 200 mg/kg BW of LMWCP, MIA + 400: MIA injection and 400 mg/kg BW of LMWCP, MIA + 600: MIA injection and 600 mg/kg BW of LMWCP.

### *2.5. LMWCP Ameliorated Catabolic Factors Expression in Cartilage Tissue from MIA-Injected Rats*

The mRNA expression levels of the anabolic factors, aggrecan, collagen type I, collagen type II, TIMP-1, and TIMP-3, were significantly decreased in cartilage tissue from MIA-injected rats compared to those in normal rats (NC). However, mRNA expression levels of the anabolic factors were significantly increased in groups supplemented with ibuprofen or LMWCP compared to the group with MIA-induced osteoarthritis ($p < 0.05$; Figure 5A–E).

The protein expression level of Smad3 phosphorylation was significantly decreased, and MMP-3 and MMP-9 were increased in cartilage tissue from MIA-injected rats compared to those in normal control. However, ibuprofen or LMWCP supplementation significantly increased Smad3 phosphorylation and decreased MMP-3 and MMP-9 in cartilage tissue from MIA-injected rats compared to those in the MIA injection control ($p < 0.05$; Figure 5F,G).

### *2.6. LMWCP Ameliorated Inflammation in Cartilage Tissue from MIA-Injected Rats*

MIA injection increased the production of pro-inflammatory cytokines (TNF-α, IL-1β, and IL-6), PGE2, and NO in rats. However, ibuprofen or LMWCP supplementation significantly decreased the levels of these factors in cartilage tissue from MIA-induced osteoarthritis rats ($p < 0.05$; Figure 6A–E). MIA injection increased the protein expression levels of phospho-IκBα/IκBα, phospho-p65/p65, and COX-2 in cartilage tissue. However, ibuprofen or LMWCP treatment significantly decreased the levels of these factors in the LPS-treated chondrocytes (Figure 6F).

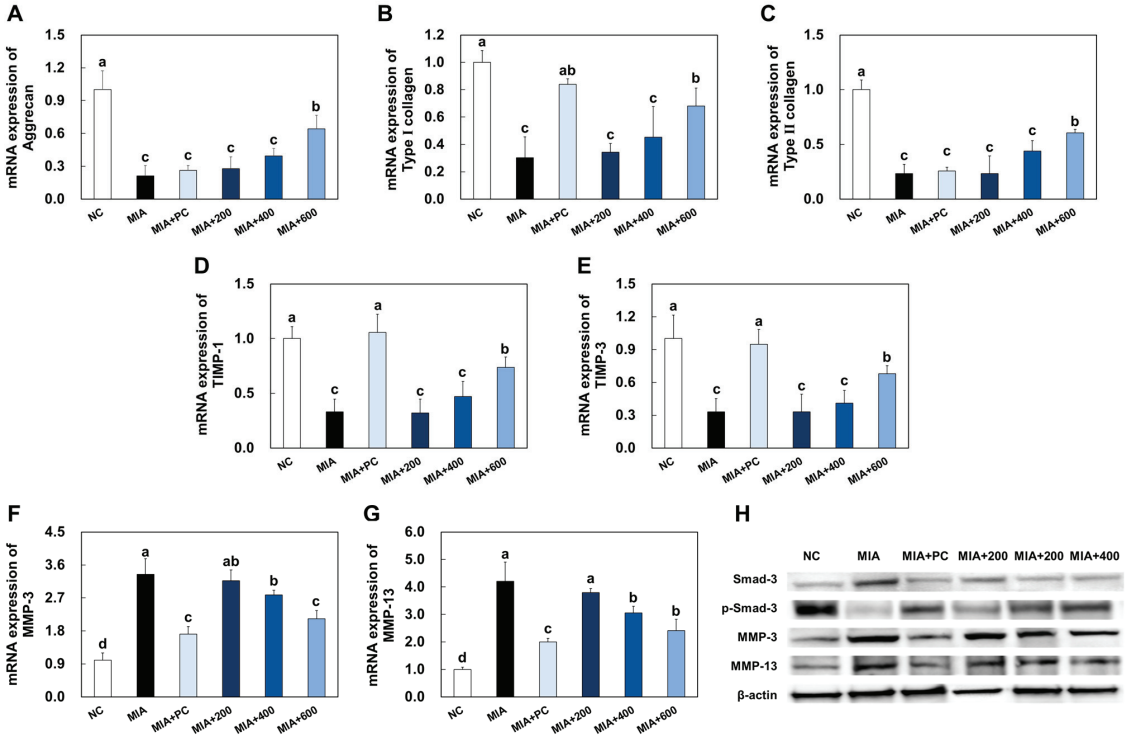


**Figure 5.** Effects of LMWCP on mRNA expression of aggrecan (**A**), collagen type 1 (**B**), collagen type 2 (**C**), TIMP-1 (**D**), TIMP-3 (**E**), MMP-3 (**F**), MMP-13 (**G**), and protein expression of p-Smad-3, MMP-3, and MMP-13 (**H**) in cartilage tissue from MIA-induced osteoarthritis rats. NC: saline injection, MIA: MIA injection, MIA + PC: MIA injection and 50 mg/kg BW of ibuprofen, MIA + 200: MIA injection and 200 mg/kg BW of LMWCP, MIA + 400: MIA injection and 400 mg/kg BW of LMWCP, MIA + 600: MIA injection and 600 mg/kg BW of LMWCP. All values are presented as mean ± SD. Different letters (a > b > c > d) indicate a significant difference at $p < 0.05$ according to Duncan's multiple range test.

### *2.7. LMWCP Ameliorated Apoptosis in Cartilage Tissue from MIA-Injected Rats*

MIA injection stimulated apoptosis signaling pathways, including the JNK/c-Fos and c-Jun pathway and the FADD/caspase8/Bax/caspase3 pathway, in cartilage tissue from rats. However, ibuprofen or LMWCP supplementation significantly suppressed these apoptosis signaling pathways in cartilage tissue from MIA-induced osteoarthritis rats ($p < 0.05$; Figure 7).

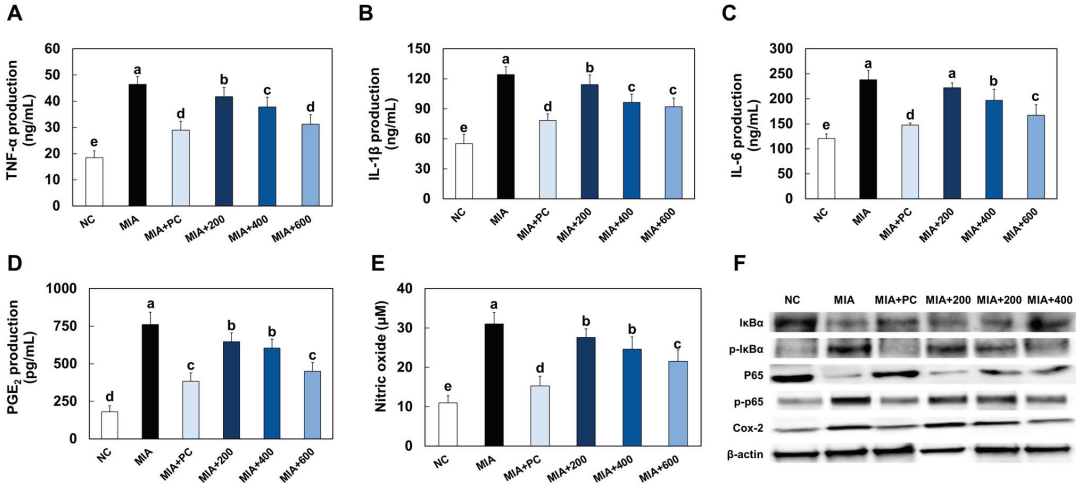


**Figure 6.** Effects of LMWCP on serum levels of TNF-α (**A**), IL-1β (**B**), and IL-6 (**C**), PGE2 (**D**), and nitric oxide (**E**) and protein expression of p-IκBα, p-p65, and COX-2 (**F**) in cartilage tissue from MIA-induced osteoarthritis rats. NC: saline injection, MIA: MIA injection, MIA + PC: MIA injection and 50 mg/kg BW of ibuprofen, MIA + 200: MIA injection and 200 mg/kg BW of LMWCP, MIA + 400: MIA injection and 400 mg/kg BW of LMWCP, MIA + 600: MIA injection and 600 mg/kg BW of LMWCP. Values are presented as mean ± SD. Different letters (a > b > c > d > e) indicate a significant difference at $p < 0.05$ by Duncan's multiple range test.

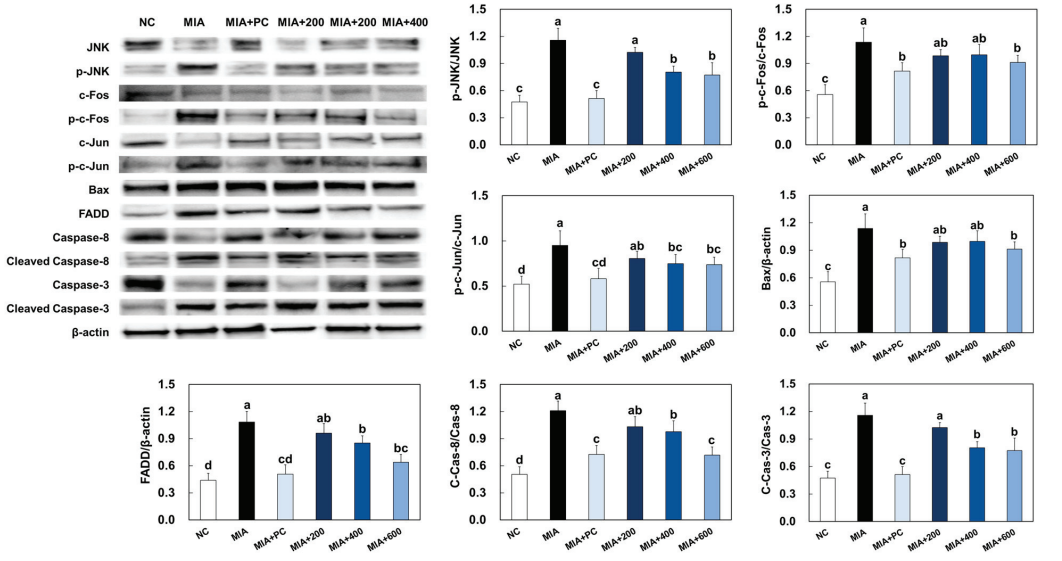


**Figure 7.** Effects of LMWCP on protein expression of apoptosis factors in cartilage tissue from MIA-induced osteoarthritis rats. NC: saline injection, MIA: MIA injection, MIA + PC: MIA injection and 50 mg/kg BW of ibuprofen, MIA + 200: MIA injection and 200 mg/kg BW of LMWCP, MIA + 400: MIA injection and 400 mg/kg BW of LMWCP, MIA + 600: MIA injection and 600 mg/kg BW of LMWCP. Values are presented as mean ± SD. Different letters (a > b > c > d) indicate a significant difference at $p < 0.05$ by Duncan's multiple range test.

## 3. Discussion

Various studies have investigated whether the intake of food-derived collagen influences collagen production in the body [15–19]. For example, Iwai et al. identified changes in the levels of collagen peptides in human blood after the oral ingestion of gelatin hydrolysates. The authors demonstrated that collagen-derived dipeptides, such as Pro-Hyp, and tripeptides, such as Pro-Hyp-Gly, were detected in the systemic blood within an hour after ingestion [18]. Yazaki et al. also investigated the levels of collagen-derived peptides in the blood after the ingestion of high tripeptide-containing collagen hydrolysate in humans and transiently identified 17 types of collagen-derived peptides, with a particular enrichment in Gly-Pro-Hyp. Additionally, the authors detected a higher enrichment of Pro-Hyp in the plasma and skin, derived from Gly-Pro-Hyp hydrolysis, upon administration of Gly-Pro-Hyp peptide in a mouse model [19]. These data suggest that dietary collagen affects the body's collagen composition. Therefore, our study aimed to investigate the inhibitory effect of LMWCP on osteoarthritis and compare it with positive controls using ibuprofen or acetylsalicylic acid.

Osteoarthritis is characterized by the progressive deterioration of articular cartilage, primarily driven by MMPs and inflammatory substances. Collagen, which constitutes approximately 30% of the body's total protein, forms the backbone of the extracellular matrix. Another vital component is aggrecan, a large proteoglycan that is indispensable for normal joint function. The overall quality of the extracellular matrix is crucial in maintaining the functional integrity of cartilage. Specifically, MMPs, known as collagenases, play a pivotal role in collagen breakdown, making them the primary mediators of this process. MMP-3, also known as stromelysins, primarily target non-collagen matrix proteins, whereas MMP-13, referred to as collagenases, primarily target interstitial collagens such as types I, II, and III. The activity of these MMPs is intricately regulated by TIMPs (tissue inhibitors of metalloproteinases) [20–23]. In our study, we observed an increase in MMPs, which was accompanied by a decrease in the mRNA expression levels of key components including aggrecan, collagen, and TIMPs, within the cartilage tissue of rats with MIA-induced osteoarthritis. However, following the administration of LMWCP, we noted a suppression of these factor changes in the cartilage tissue of rats with MIA-induced osteoarthritis. This suggests that LMWCP effectively inhibits the degradation of ECM (extracellular matrix) within the cartilage tissue.

Inflammation is a crucial factor in the development and progression of osteoarthritis. The mechanism of osteoarthritis, particularly in relation to inflammation, involves various elements, with a significant role played by the activation of nuclear factor-kappa B (NF-κB) and subsequent production of inflammatory cytokines. NF-κB is a protein complex that serves as a key regulator of immune and inflammatory responses. In osteoarthritis, NF-κB is frequently activated, often in response to factors like cytokines, including IL-1β and TNF-α, which stimulate the release of MMPs and other catabolic enzymes, thereby exacerbating osteoarthritis [24]. In our study, we have demonstrated that treatment with LMWCP effectively suppressed the phosphorylation of IκB and p65, as well as the production of inflammatory mediators in both the LPS-treated primary chondrocytes and the cartilage tissue of rats with MIA-induced osteoarthritis. These findings strongly suggest that LMWCP treatment provides a protective effect against inflammation in chondrocytes by inhibiting the NF-κB signaling pathways.

In the development of osteoarthritis, the molecular pathways that regulate chondrocyte apoptosis are influenced by various factors, including the activation of signaling cascades [25,26]. Two significant pathways implicated in this process are the JNK/c-Fos and c-Jun pathway, as well as the FADD/caspase8/Bax/caspase3 pathway. The JNK pathway is activated in response to various stress stimuli, including inflammation and oxidative stress, which are prevalent in osteoarthritis. This pathway leads to the activation of transcription factors such as c-Fos and c-Jun, which regulate the expression of genes involved in cell proliferation, differentiation, and apoptosis. In the context of osteoarthritis, the activation of JNK and subsequent upregulation of c-Fos and c-Jun can lead to increased

apoptotic signaling in chondrocytes, contributing to the degradation of articular cartilage. Additionally, the FADD pathway is a key pathway in the extrinsic apoptotic pathway activated by pro-inflammatory cytokines and oxidative stress in the osteoarthritic state. This pathway leads to the recruitment and activation of caspase-8, initiating a caspase cascade, which in turn activates downstream caspases, including caspase-3, a pivotal executioner caspase in apoptosis. These pathways collectively contribute to the initiation and execution of apoptosis in chondrocytes, ultimately leading to the degradation of articular cartilage observed in osteoarthritis [25–27].

Here, we demonstrated that LMWCP treatment suppressed the activation of the apoptosis pathway in both the LPS-treated primary chondrocytes and the cartilage tissue of rats with MIA-induced osteoarthritis. Therefore, our findings suggest that LMWCP supplementation can prevent the development of osteoarthritis through the suppression of apoptosis in chondrocytes. Although this study confirmed that LMWCP had a positive effect on joint health, it was not confirmed whether the ingested LMWCP was directly utilized for cartilage production, and therefore, additional studies are needed to clarify this.

## 4. Materials and Methods

### *4.1. Preparation of LMWCP*

The collagen used in this study was purified from fish scale collagen originating from tilapia (Oreochromis genus) gelatin, which was sourced from GELTECH in Busan, Korea. First, the dried tilapia scale was treated with HCl and then extracted with hot water. The extract was further purified by filtering and ion exchange. Then, the purified material was concentrated and sterilized. The resulting extract was heat-dried and milled, ready as gelatin for the next collagen production. Collagen production was initiated by melting the gelatin, followed by treatment with protease. Then, the solution was deodorized by treating it in an activated carbon tower. Subsequently, the gelatin was purified multiple times using pulp, carbon, and cartridge filters. The resulting crude peptides underwent high-temperature treatment (120 $\pm$ 5 °C) for 10–20 s to ensure sterilization. The products were then spray-dried at 170–230 °C and 150–230 bar, followed by sieving to achieve an average particle size of 50–150 µm. The low-molecular-weight fish collagen contained 0.93 mg/g of octapeptide (valine-glycine-proline-hydroxyproline-glycine-proline-alanine-glycine; LMWCP), with an average molecular weight of 667.7 Da.

### *4.2. Primary Culture of Chondrocytes*

Two Sprague-Dawley rats (6 weeks old, male) were obtained from SaeRon Bio in Uiwang, Korea, and were humanely euthanized by cervical dislocation. Cartilages were then isolated and incubated overnight in Hank's balanced salt solution (Hyclone Laboratories, Logan, UT, USA) containing 2 mg/mL collagenase (C0130, Sigma-Aldrich Co, St. Louis, MO, USA), and overnight in a shaker at 100 rpm. The obtained chondrocytes were seeded in 75T flasks and cultured in Dulbecco's minimal essential medium (Hyclone Laboratories) supplemented with 10% fetal bovine serum (Hyclone Laboratories), 100 mg/L penicillin-streptomycin (Hyclone Laboratories), and 2 mmol/L glutamine (Hyclone Laboratories). The cultures were maintained at 37 °C in a humid atmosphere with 5% $CO_2$. We performed medium replacement every three days, initiating subculturing when the culture reached approximately 80% confluence. Only cells with a passage number not exceeding 10 were employed for experimental purposes.

### *4.3. Animals and Induction of Osteoarthritis*

Sprague-Dawley rats (6 weeks old, male) were obtained from SaeRon Bio in Uiwang, Korea. These rats were acclimated in a controlled environment room, with conditions set at 23 $\pm$ 2 °C, a 12/12 h light/dark cycle, and a relative humidity of 50 $\pm$ 5%. Ethical approval for the experiments was granted by the Institutional Animal Care and Use Committee of Kyung Hee University (KHGASP-22-251). Prior to initiating the experiment, the rats were housed in cages for one week to acclimate to their surroundings. To induce osteoarthritis,

anesthesia was administered to all animals using a consistent concentration of isoflurane, and 60 mg/mL of MIA was injected into the articular space of the knee joints. The rats were divided into six groups, each consisting of eight rats, as follows: normal control (NC), 50 μL of saline was injected into both the left/right knee joint + AIN93G; MIA, 50 μL of MIA (60 mg/mL) was injected into both the left/right knee joint + AIN93G; MIA + PC, 50 μL of MIA (60 mg/mL) was injected into both the left/right knee joint + ibuprofen 20 mg/kg body weight (BW) in AIN93G; MIA + 200, 50 μL of MIA (60 mg/mL) was injected into both the left/right knee joint + LMWCP 200 mg/kg BW in AIN93G; MIA + 400, 50 μL of MIA (60 mg/mL) was injected into both the left/right knee joint + LMWCP 400 mg/kg BW in AIN93G; MIA + 600, 50 μL of MIA (60 mg/mL) was injected into both the left/right knee joint + LMWCP 600 mg/kg BW in AIN93G (Table 1). The rats were monitored for clinical signs of osteoarthritis on a weekly basis following the MIA injection, clinical signs were assessed by observing swelling in the knee joint of rats to determine the presence or absence of inflammation. After completion of the experiment (Figure 8), rats were anesthetized with isoflurane, followed by blood collection through the abdominal vena cava. Subsequently, the hearts were excised and euthanized, and both blood and knee joint tissues were stored at −70 °C until each experiment.

**Table 1.** Experimental groups ($n$ = 8).

| Group | Diet | Supplement | MIA |
|---|---|---|---|
| Normal control | AIN93G | – | – |
| MIA | AIN93G | – | + |
| MIA + PC | AIN93G | Ibuprofen 20 mg/kg BW | + |
| MIA + 200 | AIN93G | LMWCP 200 mg/kg BW | + |
| MIA + 400 | AIN93G | LMWCP 400 mg/kg BW | + |
| MIA + 600 | AIN93G | LMWCP 600 mg/kg BW | + |

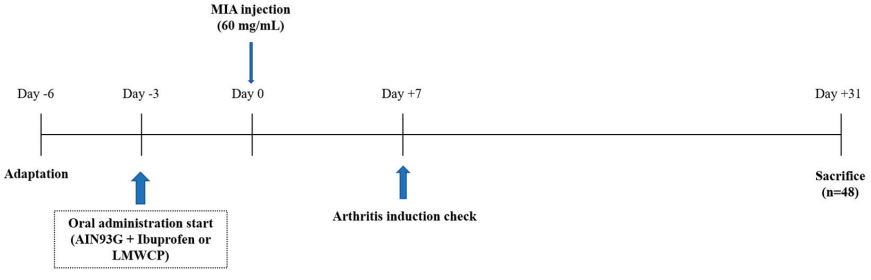


**Figure 8.** The experimental schedule.

### *4.4. Micro-CT and ELISA Analysis*

Micro-CT imaging of the formalin-fixed articular cartilage from rats was used to measure the roughness of the bone surface. Micro-CT image scanning was conducted using the Skyscan 1172® X-ray μCT scanning system (Bruker, Belgium). After standardized reconstruction of the scanned images, the data for each sample were obtained using the micro-CT software to orient each sample in the same manner. The levels of inflammatory cytokines (TNF-α, IL-1β, and IL-6), $PGE_2$, and nitric oxide were measured using an ELISA kit (R&D Systems, Minneapolis, MN, USA) according to the manufacturer's instructions.

### *4.5. Total RNA Extraction and Real-Time PCR*

Total RNA from chondrocytes and cartilage tissue was extracted using a commercial RNA extraction kit (QIAGEN, Gaithersburg, MD, USA), and the extracted RNA was assessed for ratio and concentration using Nano-drop. The cDNA was synthesized from purified total RNA (500 ng/mL) using the iScript™ cDNA Synthesis kit (Bio-Rad, Hercules, CA, USA). Real-time PCR was conducted using a CFX Connect™ Real Time System (Bio-

Rad) with the iScript™ Green Supermix, cDNA, and custom designed primers (Table 2) and the real-time PCR reactions run in duplicates. Data analysis was conducted using the CFX Manager™ 3.1 analysis software (Bio-Rad).

**Table 2.** Primer sets used for real-time RT-PCR.

| Gene | Forward Sequence (5′-3′) | Reverse Sequence (5′-3′) |
|---|---|---|
| GAPDH (NM_017008) | TGG CCT CCA AGG AGT AAG AAA C | CAG CAA CTG AGG GCC TCT CT |
| Aggrecan (NM_022190) | GAA GTG GCG TCC AAA CCA A | CGT TCC ATT CAC CCC TCT CA |
| Collagen Type I (NM_000088) | GAG CGG AGA GTA CTG GAT CGA | CTG ACC TGT CTC CAT GTT GCA |
| Collagen Type II (RATCOLLII) | GCA ACA GCA GGT TCA CGT ACA | TCG GTA CTC GAT GAT GGT CTT G |
| TIMP-1 (NM_053819) | ACA GCT TTC TGC AAC TCG GA | CGT CGA ATC CTT TGA GCA TC |
| TIMP-3 (RNU27201) | CTT CTG CAA CTC CGA CAT CGT | GGG GCA TCT TAC TGA ATC CTC |
| MMP-3 (NM_133523) | GAG TGT GGA TTC TGC CAT TGA G | TTA TGT CAG CCT CTC CTT CAG AGA |
| MMP-13 (NM_133530.1) | ACG TTC AAG GAA TCC AGT CT | GGA TAG GGC TGG GTC ACA CTT |

### *4.6. Western Blot*

Total protein from chondrocytes and cartilage tissue was extracted using 4X NuPAGE LDS sample buffer (Life Technologies, Gaithersburg, MD, USA). Protein samples containing 20~100 μg of protein from cells were separated by gel electrophoresis and transferred onto membranes. The membranes were blocked, followed by incubation with primary antibodies (Smad-3, p-Smad-3, MMP-3, MMP-13, IκBα, p-IκBα, p65, p-p65, COX-2, JNK, p-JNK, c-Fos, p-c-Fos, c-Jun, p-c-Jun, Bax, FADD, caspase-8, cleaved caspase-8, caspase-3, cleaved caspase-3, and β-actin and secondary antibodies (Table 3). Bands were captured using the ChemiDoc Imaging System (Bio-Rad, Hercules, CA, USA) and quantified with ImageJ software version 1.53e (National Institutes of Health, Bethesda, MD, USA).

**Table 3.** Antibodies used for Western blot analysis.

| Antibodies | Distributor |
|---|---|
| Smad3 | Cell signaling (#9523, Beverly, MA, USA) |
| p-Smad3 | Cell signaling (#9520) |
| MMP-3 | Abcam (ab53015) |
| MMP-13 | Abcam (ab39012) |
| IκBα | Cell signaling (#9242) |
| p-IκBα | Cell signaling (#2859) |
| p65 | Abcam (ab16502) |
| p-p65 | Cell signaling (#3031) |
| COX-2 | Cell signaling (#12282) |
| JNK | Cell signaling (#9252) |
| p-JNK | Cell signaling (#9251) |
| c-Fos | Cell signaling (#4384 |
| p-c-Fos | Cell signaling (#5348) |
| c-Jun | Cell signaling (#9165) |
| p-c-Jun | Cell signaling (#2361) |
| Bax | Cell signaling (#2772) |
| FADD | LSbio (LS-C766496, Settle, WA, USA) |
| Caspase-8 | Cell signaling (#4790) |
| Cleaved caspase-8 | Cell signaling (#8592) |
| Caspase-3 | Cell signaling (#9662) |
| Cleaved caspase-3 | Cell signaling (#9661) |
| β-actin | BETHYL (A300-491A, Waltham, MA, USA) |

MMP, matrix metallopeptidase; COX-2, cyclooxygenase-2; JNK, c-Jun N-terminal kinase; Host animal, Rabbit; Dilution for western blot, 1:1000.

### *4.7. Statistical Analysis*

The data were reported as mean ($n$ = 3 or 8) ± standard deviation (SD). Statistical analyses were conducted using Duncan's multiple range tests following a one-way analysis

of variance. All $p$-values < 0.05 were considered statistically significant, and the statistical analyses were carried out using SPSS software (SPSS PASW Statistic v.23.0, SPSS Inc., Chicago, IL, USA).

## 5. Conclusions

We demonstrated that LMWCP ameliorated osteoarthritis symptoms, including inflammation and degradation of articular cartilage in primary chondrocytes and rats with MIA-induced osteoarthritis. Our findings demonstrated that LMWCP supplementation has a beneficial effect in the treatment of osteoarthritis, as it suppresses the expression of catabolic factors. Moreover, LMWCP inhibited inflammation and apoptosis in both the LPS-treated primary chondrocytes and the cartilage tissue of rats with MIA-induced osteoarthritis. The study not only provides scientific evidence of the cartilage-regenerating effects of LMWCP but also offers insights into the mechanisms responsible for the anti-inflammatory and anti-osteoarthritis properties of LMWCP.

**Author Contributions:** Conceptualization, W.C., J.P., O.-K.K. and J.L.; methodology, W.C. and J.P.; validation, W.C. and J.P.; investigation, W.C., J.P., J.K., M.L., S.J.P., K.S.K., W.J., O.-K.K. and J.L.; writing—original draft preparation W.C., J.P., O.-K.K. and J.L. All authors have read and agreed to the published version of the manuscript.

**Funding:** This research received no external funding.

**Institutional Review Board Statement:** All animal experiments were approved by the Institutional Animal Care and Use Committee of Kyung Hee University (KHGASP-22-251).

**Data Availability Statement:** Data are contained within the article.

**Conflicts of Interest:** S.J.P. and K.S.K. are employed by the Suheung Co., Ltd. The remaining authors declare that the research was conducted in the absence of any commercial or financial relationships that could be construed as a potential conflict of interest.

## References

1. Arendt-Nielsen, L.; Eskehave, T.N.; Egsgaard, L.L.; Petersen, K.K.; Graven-Nielsen, T.; Hoeck, H.C.; Simonsen, O.; Siebuhr, A.S.; Karsdal, M.; Bay-Jensen, A.C. Association between experimental pain biomarkers and serologic markers in patients with different degrees of painful knee osteoarthritis. *Arthritis Rheumatol.* **2014**, *66*, 3317–3326. [CrossRef] [PubMed]
2. Di Francesco, M.; Fragassi, A.; Pannuzzo, M.; Ferreira, M.; Brahmachari, S.; Decuzzi, P. Management of osteoarthritis: From drug molecules to nano/micromedicines. *Wiley Interdiscip. Rev. Nanomed. Nanobiotechnology* **2022**, *14*, 1780. [CrossRef]
3. Martin, J.A.; Buckwalter, J.A. Roles of articular cartilage aging and chondrocyte senescence in the pathogenesis of osteoarthritis. *Iowa Orthop. J.* **2001**, *21*, 1–7. [PubMed]
4. Loeser, R.F.; Collins, J.A.; Diekman, B.O. Ageing and the pathogenesis of osteoarthritis. *Nat. Rev. Rheumatol.* **2016**, *12*, 412–420. [CrossRef] [PubMed]
5. Loeser, R.F. Aging and osteoarthritis: The role of chondrocyte senescence and aging changes in the cartilage matrix. *Osteoarthr. Cartil.* **2009**, *17*, 971–979. [CrossRef]
6. Giannoni, P.; Cancedda, R. Articular chondrocyte culturing for cell-based cartilage repair: Needs and perspectives. *Cells Tissues Organs* **2006**, *184*, 1–15. [CrossRef] [PubMed]
7. Camarero-Espinosa, S.; Rothen-Rutishauser, B.; Foster, E.J.; Weder, C. Articular cartilage: From formation to tissue engineering. *Biomater. Sci.* **2016**, *4*, 734–767. [CrossRef]
8. Sandell, L.J.; Aigner, T. Articular cartilage and changes in arthritis. An introduction: Cell biology of osteoarthritis. *Arthritis Res.* **2001**, *3*, 107–113. [CrossRef]
9. Aida, Y.; Maeno, M.; Suzuki, N.; Shiratsuchi, H.; Motohashi, M.; Matsumura, H. The effect of IL-1beta on the expression of matrix metalloproteinases and tissue inhibitors of matrix metalloproteinases in human chondrocytes. *Life Sci.* **2005**, *77*, 3210–3221. [CrossRef]
10. Bondeson, J.; Wainwright, S.D.; Lauder, S.; Amos, N.; Hughes, C.E. The role of synovial macrophages and macrophage-produced cytokines in driving aggrecanases, matrix metalloproteinases, and other destructive and inflammatory responses in osteoarthritis. *Arthritis Res. Ther.* **2006**, *8*, 187. [CrossRef]
11. Rovati, L.C.; Girolami, F.; D'Amato, M.; Giacovelli, G. Effects of glucosamine sulfate on the use of rescue non-steroidal anti-inflammatory drugs in knee osteoarthritis: Results from the Pharmaco-Epidemiology of GonArthroSis (PEGASus) study. *Semin. Arthritis Rheum.* **2016**, *45*, 34–41. [CrossRef]
12. Bannuru, R.R.; Vaysbrot, E.E.; Sullivan, M.C.; McAlindon, T.E. Relative efficacy of hyaluronic acid in comparison with NSAIDs for knee osteoarthritis: A systematic review and meta-analysis. *Semin. Arthritis Rheum.* **2014**, *43*, 593–599. [CrossRef]

13. Guan, V.X.; Mobasheri, A.; Probst, Y.C. A systematic review of osteoarthritis prevention and management with dietary phytochemicals from foods. *Maturitas* **2019**, *122*, 35–43. [CrossRef] [PubMed]
14. Cameron, M.; Gagnier, J.J.; Little, C.V.; Parsons, T.J.; Blümle, A.; Chrubasik, S. Evidence of effectiveness of herbal medicinal products in the treatment of arthritis. Osteoarthritis. *Phytother. Res.* **2009**, *23*, 1497–1515. [CrossRef] [PubMed]
15. Bello, A.E.; Oesser, S. Collagen hydrolysate for the treatment of osteoarthritis and other joint disorders: A review of the literature. *Curr. Med. Res. Opin.* **2006**, *22*, 2221–2232. [CrossRef] [PubMed]
16. Martínez-Puig, D.; Costa-Larrión, E.; Rubio-Rodríguez, N.; Gálvez-Martín, P. Collagen Supplementation for Joint Health: The Link between Composition and Scientific Knowledge. *Nutrients* **2023**, *15*, 1332. [CrossRef] [PubMed]
17. Cúneo, F.; Costa-Paiva, L.; Pinto-Neto, A.M.; Morais, S.S.; Amaya-Farfan, J. Effect of dietary supplementation with collagen hydrolysates on bone metabolism of postmenopausal women with low mineral density. *Maturitas* **2010**, *65*, 253–257. [CrossRef] [PubMed]
18. Iwai, K.; Hasegawa, T.; Taguchi, Y.; Morimatsu, F.; Sato, K.; Nakamura, Y.; Higashi, A.; Kido, Y.; Nakabo, Y.; Ohtsuki, K. Identification of food-derived collagen peptides in human blood after oral ingestion of gelatin hydrolysates. *J. Agric. Food Chem.* **2005**, *53*, 6531–6536. [CrossRef]
19. Yazaki, M.; Ito, Y.; Yamada, M.; Goulas, S.; Teramoto, S.; Nakaya, M.A.; Ohno, S.; Yamaguchi, K. Oral Ingestion of Collagen Hydrolysate Leads to the Transportation of Highly Concentrated Gly-Pro-Hyp and Its Hydrolyzed Form of Pro-Hyp into the Bloodstream and Skin. *J. Agric. Food Chem.* **2017**, *65*, 2315–2322. [CrossRef]
20. Maldonado, M.; Nam, J. The role of changes in extracellular matrix of cartilage in the presence of inflammation on the pathology of osteoarthritis. *Biomed. Res. Int.* **2013**, *2013*, 284873. [CrossRef]
21. Murphy, G.; Nagase, H. Progress in matrix metalloproteinase research. *Mol. Aspects Med.* **2008**, *29*, 290–308. [CrossRef] [PubMed]
22. Klatt, A.R.; Paul-Klausch, B.; Klinger, G.; Kühn, G.; Renno, J.H.; Banerjee, M.; Malchau, G.; Wielckens, K. A critical role for collagen II in cartilage matrix degradation: Collagen II induces pro-inflammatory cytokines and MMPs in primary human chondrocytes. *J. Orthop. Res.* **2009**, *27*, 65–70. [CrossRef]
23. Cui, N.; Hu, M.; Khalil, R.A. Biochemical and Biological Attributes of Matrix Metalloproteinases. *Prog. Mol. Biol. Transl. Sci.* **2017**, *147*, 1–73. [PubMed]
24. Choi, M.C.; Jo, J.; Park, J.; Kang, H.K.; Park, Y. NF-κB Signaling Pathways in Osteoarthritic Cartilage Destruction. *Cells* **2019**, *8*, 734. [CrossRef] [PubMed]
25. Hwang, H.S.; Kim, H.A. Chondrocyte Apoptosis in the Pathogenesis of Osteoarthritis. *Int. J. Mol. Sci.* **2015**, *16*, 26035–26054. [CrossRef]
26. Takács-Buia, L.; Iordachel, C.; Efimov, N.; Caloianu, M.; Montreuil, J.; Bratosin, D. Pathogenesis of osteoarthritis: Chondrocyte replicative senescence or apoptosis? *Cytometry B Clin. Cytom.* **2008**, *74*, 356–362. [CrossRef]
27. Zimmermann, K.C.; Green, D.R. How cells die: Apoptosis pathways. *J. Allergy Clin. Immunol.* **2001**, *108*, 99–103. [CrossRef]

marine drugs

MDPI

*Review*

# The Importance of Chitosan Coatings in Dentistry

**Anna Paradowska-Stolarz [1,*], Marcin Mikulewicz [1], Joanna Laskowska [1], Bożena Karolewicz [2] and Artur Owczarek [2,*]**

[1] Division of Dentofacial Anomalies, Department of Orthodontics and Dentofacial Orthopedics, Wroclaw Medical University, Krakowska 26, 50-425 Wroclaw, Poland; marcin.mikulewicz@umw.edu.pl (M.M.); j.laskowska@umw.edu.pl (J.L.)

[2] Department of Drug Forms Technology, Wroclaw Medical University, Borowska 211A, 50-556 Wroclaw, Poland; bozena.karolewicz@umw.edu.pl

* Correspondence: anna.paradowska-stolarz@umw.edu.pl (A.P.-S.); artur.owczarek@umw.edu.pl (A.O.); Tel.: +48-717840321 (A.O.)

**Abstract:** A Chitosan is a copolymer of N-acetyl-D-glucose amine and D-glucose amine that can be easily produced. It is a polymer that is widely utilized to create nanoparticles (NPs) with specific properties for applications in a wide range of human activities. Chitosan is a substance with excellent prospects due to its antibacterial, anti-inflammatory, antifungal, haemostatic, analgesic, mucoadhesive, and osseointegrative qualities, as well as its superior film-forming capacity. Chitosan nanoparticles (NPs) serve a variety of functions in the pharmaceutical and medical fields, including dentistry. According to recent research, chitosan and its derivatives can be embedded in materials for dental adhesives, barrier membranes, bone replacement, tissue regeneration, and antibacterial agents to improve the management of oral diseases. This narrative review aims to discuss the development of chitosan-containing materials for dental and implant engineering applications, as well as the challenges and future potential. For this purpose, the PubMed database (Medline) was utilised to search for publications published less than 10 years ago. The keywords used were "chitosan coating" and "dentistry". After carefully selecting according to these keywords, 23 articles were studied. The review concluded that chitosan is a biocompatible and bioactive material with many benefits in surgery, restorative dentistry, endodontics, prosthetics, orthodontics, and disinfection. Furthermore, despite the fact that it is a highly significant and promising coating, there is still a demand for various types of coatings. Chitosan is a semi-synthetic polysaccharide that has many medical applications because of its antimicrobial properties. This article aims to review the role of chitosan in dental implantology.

**Keywords:** chitosan; dentistry; preventive dentistry; coated materials; biocompatible

**Citation:** Paradowska-Stolarz, A.; Mikulewicz, M.; Laskowska, J.; Karolewicz, B.; Owczarek, A. The Importance of Chitosan Coatings in Dentistry. *Mar. Drugs* **2023**, *21*, 613. https://doi.org/10.3390/md21120613

Academic Editor: Azizur Rahman

Received: 14 August 2023
Revised: 15 November 2023
Accepted: 21 November 2023
Published: 26 November 2023



## 1. Introduction

Polymer coatings in dentistry are widely used and, recently, materials obtained from natural polymers have been widely treated as matrices for drug delivery, especially in surgery and periodontics [1–3]. The coatings may also be used in other dental specialities. In stainless steel corrosion, the elution of metallic ions from the surface of materials used in orthodontics, and which can be protected by coating, has been proven by Mikulewicz et al. [4]. This phenomenon has also been shown to influence gene expression [5]. In dentistry, coatings are used to improve the quality and properties of dental devices [6].

### *1.1. Chitosan Structure*

Chitosan, a naturally derived marine polymer with linear amino-polysaccharide structure, is widely used in dentistry. A D-glucosamine and N-acetyl glucosamine copolymer is obtained by deacetylation of the chitinous exoskeletons of crustaceans (also known as shellfish scaffolds). It also occurs naturally in mammalian cells. The main

characteristics of chitosan are biocompatibility, non-toxicity, regenerative properties, natural availability, and the possibility of chemical treatment. According to the Food and Drug Administration agency (FDA), it has biological activity properties and wide spectrum of usage against all types of bacteria, including Gram-positive and Gram-negative. Due to those conditions, it is used willingly to treat damages in the tissues of the oral cavity. Additionally, chitosan has elastane-like properties [1,7]. Chitosan represents a group of multifunctional excipients [8]. It is used as an auxiliary substance and an antimicrobial agent. This is especially important in current times due to the possible elimination of the SARS-CoV2 virus from saliva [9–11]. It is used in preventive and conservative dentistry, endodontics, periodontal procedures, surgery, prosthodontics and orthodontics [7,12,13]. Although widely used, it is still unclear whether chitosan could potentially be an allergen for humans [7]. Although chitosan is more frequently a drug carrier component and active formulation agent, the variety of its use changes [14]. It shows a high percentage of antimicrobial reactions, especially against *Streptococcus gordonii*, which is the first bacteria to colonise surfaces in the oral cavity [15].

In a linearly built chitosan molecule, the relationship between the present hydroxyl and amino groups forms hydrogen bounds that influence the structure and flexibility of the polymer chain. Chitosan is a copolymer of glucosamine and N-acetyl-D-glucose amine units as shown in Figure 1.

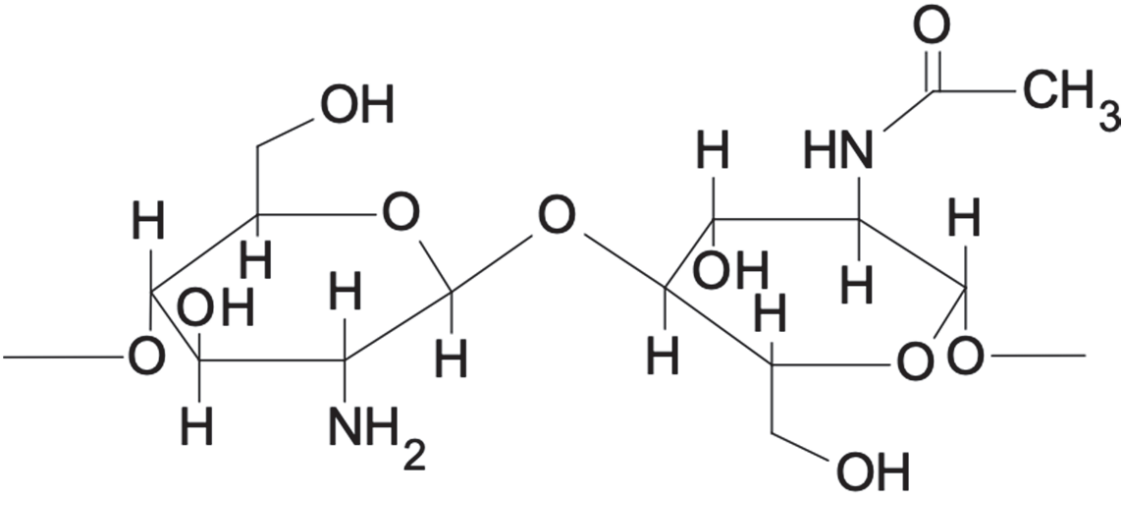


**Figure 1.** Chemical structure of chitosan.

Natural polymers and natural-based medicine are prominent topics of recent research. It is important to search for accessible materials which present biocompatibility and biocompetence. Chitosan is one of the natural materials which meets these criteria. The authors of the presented study are engaged in the two different fields of medicine–pharmacy (BK and AO) and dentistry (APS, MM and JL). We therefore tried to combine two points of view on chitosan: coatings–pharmaceutic and dental. We found this approach to be the advantageous to our research.

*1.2. General Use*

Chitosan belongs to the group of multifunctional polymers used in dentistry. It is used to design carriers and materials adapted to some specific conditions, as well as the specificity of the application site, which deliver active substances directly to diseased changed tissues. This includes intrapocket application and the release of the active substances in a timely manner. This specification allows for the improvement of the form of application and further development of therapeutic strategies. Its multifunctionality results from the function of the auxiliary substance that allows for the development of both the mucoadhesive carrier and the formulation component with biological activity. This phenomenon was confirmed in the biological activity tests, the mentioned antibacterial, haemostatic, but also antifungal and immunomodulating properties of the polymer and its derivatives, i.e., chitooligosaccharides. In the literature, chitosan, in addition to its antibacterial, antifungal, and anti-inflammatory properties mentioned before, is also reported to act as a biocompatible dental carrier that accelerates the process of periodontal regeneration. The biological activity of the polymer is caused by the cationic nature of the polymer and the interaction of the positively charged amino-group molecules with the negatively charged components of the Gram-negative bacteria cell membranes. As a result of the interaction, the properties of the cell membranes of the bacteria change-the transport of the nutrients inside the cell fluctuates, and its content starts leaking outside. Another explanation for the polymer activity is its penetration into the bacterial cell interior and binding to the DNA of the bacteria, which inhibits RNA transcription and, consequently, handicaps the protein synthesis. The biological activity of the polymer depends on its physicochemical properties, e.g., molecular weight, degree of polymerisation, degree of deacetylation, and also depends on the type of the microorganism. The properties of the polymer are crucial for its activity. It has been proven to react strongly against the bacteria responsible for creating dental plaque, including *Porphyronomas gingivalis, Prevotella intermedia,* and *Aggregatibacter actinomycetemcomitans* (*formerly Actinobacillus actinomycetemcomitans*). Due to all of these characteristics, polymers find many biological applications in materials and carriers used in the treatment of periodontitis, bone and tissue regeneration, drug delivery, and wound healing. However, the choice of appropriate molecular weight and degree of deacetylation affects the desired application properties as well as development of the carriers, e.g., matrices, bioadhesive tablets, films, microspheres, microparticles, nanoparticles, nanofibers, or gel forms.

*1.3. Molecular Interaction*

The use of chitosan in dentistry is also due to its increased induction of osteoblast growth and binding around polymer coated implants, which allows for the obtaining of bioactive surfaces ensuring osseointegration. Research has shown that chemical modifications of the polymer structure increase its antibacterial activity and osteoinductive properties. The polymer has the ability to bond to the metals surface, which can improve their mechanical strength and increase the durability of, e.g., titanium implants. Some researchers, however, emphasise that the adhesion of chitosan coatings to titanium surfaces is not suitable for clinical applications. Ferraresse et al. [16] proposed a chemical treatment of the titanium implant surface, using the method of 'direct coating', which is simply immersing the surface in an acid solution that allows a strong electrostatic attraction between the chitosan particles and the coated surface. In this condition, stable coatings are obtained mechanically and chemically, and chitosan-coated dental implants can have increased possibilities for osseointegration, which can lead to their commercial use. The preparation of the implant surface and bone preparation affects the stability and clinical success of the dental implant. To improve osseointegration, a number of methods of surface treatment and implant coatings have been tried, with promising results in coating them with chitosan. Chitosan coating can affect the surface that comes into contact with bone by changing the biological, mechanical and morphological

properties of the surface. For example, considering the mechanical properties, the chitosan coating changes the modulus of elasticity, thus reducing the mismatch of the implant surface with the bone of the alveolar process and reducing stress concentration areas [17,18]. In addition, chitosan coatings can potentially be used to release drugs, such as antibiotics, for local delivery around the implant area. Additionally, chitosan can prevent damage to the tooth surface by organic acids by buffering saliva pH in the mouth, preventing adhesion pathogens, and stimulating the structured regeneration of oral soft tissues.

### *1.4. Biomechanical Features*

Chitosan and chitosan-based coatings have relatively low stiffness and strength, especially in high humidity. Therefore, it is valid to obtain modified chitosan sol-gel preparations to improve their mechanical properties. The addition of chitosan improved the antibacterial activity of two types of subjects [9,19] of hybrid silica-chitosan coatings (50M50G and 45 M45G10T) and increased the proliferation rate of cells that grow on their surface. The proliferation indicators were the highest for coatings containing 5% and 10% chitosan. We can also conclude that the addition of chitosan and TEOS modulates the release of Si, which plays an important role in osteocompatibility. Tertiary coatings containing 5% and 10% chitosan have very good antibacterial properties [20]. They should be suitable for dental implants, as they protect against bone infection for a long time. The introduction of these materials into dental practice can increase the number of patients admitted to implantation.

A study by Tarsi et al. [21] showed that chitosan is an interesting candidate capable of preventing the adhesion of bacteria *Streptococcus mutans* to hydroxyapatite in teeth with tooth decay. This effect was attributed to the ability of chitosan to stimulate the orderly regeneration of soft tissues of the oral cavity, preventing the harmful effects of organic acids and the bactericidal effect. The desorption effect of chitosan was weaker when *Streptococcus mutans* adhered to saliva-coated hydroxyapatite in the presence of sucrose. These results indicate the possibility that the presence of small amounts of chitosan in the teeth, mouthwashes, or chewing gum may interfere with the bacterial colonisation of the surface of the teeth. The use of chitosan in dentistry is widespread and reflects many branches of this discipline. Table 1 presents examples of methodology and results of chitosan coatings used in dentistry. In summary, chitosan is a semisynthetic polysaccharide that has many medical applications due to its antimicrobial properties.

**Table 1.** Obtaining chitosan coating: methods and basic uses.

| Coating | Material | Results | References |
| --- | --- | --- | --- |
| Chitosan coatings (80.7% deacetylated polymer, 108 kDa) with incorporated tetracycline (20%) or digluconate chlorhexidine (0.02%) applied to the titanium implants in reactions silane | - Implants were covered with 3-aminopropyltriethoxysilane at pH 4.3, dried, then 2% glutaraldehyde was added for obtaining a reactive group aldehyde, which reacts with amino groups in chitosan particles<br>- Tetracycline or chlorhexidine was mixed with chitosan in 1% solution of acetic or formic acid<br>- The chitosan solutions were poured out on titanium surfaces coated with glutaric silane-aldehyde and dried in room temperature for ~3 days, rinsed by a 0.05M NaOH wash to neutralize the residual acid solvent<br>- The samples were sterilized with ethylene oxide at 38° C for 5 h | - The coatings released 89% of the tetracycline by 7 days and 100% of the chlorhexidine by 2 days<br>- The released tetracycline inhibited 95%-99.9% of pathogen growth up to 7 days without cytotoxicity to human cells<br>- The released chlorhexidine was active against pathogens for 1 to 2 days (56%–99.5% inhibition), and its cell toxicity was observed on the first day after the application. The potential for local delivering antimicrobial substances was observed; its purpose was to inhibit bacterial growth without toxic effects to host cells/tissues<br>- Release of tetracycline and chlorhexidine from the coatings were sufficient to stop bacterial growth for a few days, which can provide the necessary time for the normal host cells to stick to the implant surface and inhibit bacterial growth<br>- Chitosan coatings may be used as a local drug delivery system for antibiotics | Norowski et al. [22] |
| Chitosan coating (92.3% deacetylated polymer) | - 1% chitosan solution in 1% acetic acid was poured on ground titanium pins (rough ground titanium pins) covered with 3-aminopropyltriethoxysilane<br>- As controls uncoated titanium pins and coated with calcium phosphate were used<br>- In the tibias of 16 adult white male rabbits from New Zealand, 2 chitosan coated pins and 1 covered with phosphate calcium and uncoated were implanted<br>- After 2, 4, 8 and 12 weeks histologically an angle healing and bone formation were assessed | - Histological assessments of tissues in contact with chitosan coated spikes showed minimal inflammatory and typical response sequence of fibrous healing, bone formation followed by the development of the lamellar bone patterns of healing and development of bone connection with implant were assessed around chitosan-coated implants in a 12-week bone model, the tibia of the rabbit was similar to those in coated titanium pins and uncoated with calcium phosphate<br>- Chitosan coatings can offer benefits in drug and growth factor delivery, compared with traditional ones, coated with calcium phosphate and uncoated implants<br>- Chitosan coatings provide osseointegration of dental implants | Bumgardner et al. [23] |
| chitosan coating | - titanium implants coated with chitosan through dipping in the prepared polymer solution, then dried in a dryer at 25 °C in order to produce a uniform 50% relative humidity films to avoid cracking and shell deformation<br>- sterilized with gamma radiation | - In the jaws of dogs, four implants were put and 12 weeks after the surgery euthanasia was performed<br>- excised bone blocks were taken and assessed for with the help of computed microtomography and two parameters of the bone were measured: bone contact with the implant surface (BCIS) and bone area around the implant (PIBA)<br>- the results confirmed the suitability of the chitosan coatings on titanium surfaces in improving the osseointegration of dental implants | López-Valverde et al. [24] |
| Chitosan coated liposomes | - Liposomes prepared forLipid base: Egg-phosphatidylcholine, Nitrobenzoxadiazol-4-yl-phosphocholine, fluorescent phospholipid labelled with fatty acid and lipids, egg L-α-phosphatidylglycerol or Dioleyltrimethylammoniumpropane forming a lipid film by rotary evaporation of lipid solution in chloroform, then a phosphate film buffer was added (pH 6.8)<br>- Size reduction was obtained by extrusion of double-layer polycarbonate membranes at size 200 nm<br>- The coating was obtained through electrostatic deposition after mixing the liposomal dispersion with the solution polymer | - Positively charged liposomes showed higher adhesion ability to hydroxyapatite compared with liposomes negatively charged, but positively charged liposomes aggregated in artificial saliva<br>- Can be used in patients with reduced salivation | Pistone [25] |

**Table 1.** *Cont.*

| Coating | Material | Results | References |
| --- | --- | --- | --- |
| Titanium alloy implant (Ti6Al4V) coated chitosan | - Implants were covered with 3-iso-cyanopropyltriethoxy silane at pH 4.5–5.5, then 2% glutaraldehyde was added to give a reactive group aldehyde, which reacts with amino groups in the chitosan particles<br>- The implants were immersed in chitosan solution in acetic acid at 4 °C, then the excess water evaporated for more than 7 days<br>- The implants were rinsed with NaOH solution, then water | - Cell adhesion and proliferation of the fibroblasts for the implants have been improved, and simultaneously bacterial proliferation has been inhibited by the chitosan coating<br>- It has been shown that chitosan can be used as material for coating areas in periodontal healing of dental implants | Kalyoncuoglu et al. [26] |
| Chitosan and polycaprolactone (PCL) multilayers coating for metallic implants with incorporated vancomycin or daptomycin in microspheres with poly (methyl methacrylate) (PMMA) for treatment of periimplantitis | - cCoating produced with dip-coating technique | - Studies have shown that drug release in case for both types of drugs occurred by diffusion, and the release profile depended on the type of the drug, the pH of the solution, and whether the drug was incorporated directly into the film coating, or encapsulated in PMMA microspheres<br>- Coatings containing daptomycin directly incorporated into the films released 90% of substances after 1 day at pH 7.4 and after 4 days at pH 5.5<br>- Films with microspheres with incorporated daptomycin achieved 90% release after 2 days of treatment time at pH 5.5 and after 2 days at pH 7.4<br>- Coatings containing vancomycin directly incorporated into the films showed 90% of drug release after 20 h at pH 5.5 and 2 and 3 days respectively at pH 7.4<br>- Films containing daptomycin showed antibacterial activity against both MRSA and susceptible strains of *S. aureus*, which confirms the possibility of use of such films as coatings for the relief of *S. aureus* infections around the metal implant | Soares et al. [27] |
| Polylactic-co-glycolic acid (PLGA) nanoparticles coated with chitosan hydroxypropyltrimonium chloride as a carrier for rebamipid | - It was received positively charged nanoparticles with mean particle diameter of 97.0 ± 36.7 nm | - It was confirmed that the mucin adsorption capacity by nanoparticles coated with chitosan was 2.3 times higher than in uncoated nanoparticles<br>- Therapeutic efficacy of nanoparticles was evaluated in the treatment of a mouse model stomatitis, induced by cancer chemotherapy<br>- In the group administered with nanoparticles covered with chitosan, the ulcer area decreased significantly on the 9th, 11th and 13th day when compared to an untreated control group; additionally, the treatment period was significantly shortened by 3.6 days when compared to the group in which uncoated nanoparticles were administered<br>- Chitosan coated PLGA nanoparticles containing rebamipid may be beneficial in treatment of oral mucositis, resulting from cancer chemotherapy | Takeuchi et al. [28] |
| Gold nanoparticles (AuNP) coated chitosan-grafted thymol (CST) | - Implantation of thymol into the chitosan skeleton synthesized via adaptation of the Mannich reaction<br>- AuNP particles were obtained mostly in spherical shape and medium-sized 2.41–3.30 nm | - CST coating on the surface of nanoparticles has been successfully used against cariogenic bacteria in the mouth<br>- Electrostatic properties of CST used primarily for stabilization of the AuNP<br>- CST coating on the AuNP surface has potential to be used in fighting infections caused by cariogenic bacteria | Pakawat et al. [29] |

*1.5. Aims*

There are existing reviews on chitosan and its use in dentistry in general, while the literature is expected to focus on a more particular application in dental specialities. Existing reviews attempt to answer the question: What are the general results of dental treatments using chitosan and does the use of chitosan provide beneficial clinical results? [30] Furthermore, Hallmann et al. [31] evaluated chitosan's properties for use in dental implantology, and Qu et al. [32] investigated the use of chitosan as a biomaterial for the prevention and treatment of dental caries. Researchers believe that developing chitosan-based solutions in dental implantology, orthodontics, and prosthetics will improve clinical practice. The purpose of this review was to identify gaps in existing studies for potential future research.

## 2. Search Criteria

*Methods*

Pubmed (Medline) database was searched by key words "chitosan coatings" and "dentistry" in August 2022. The search was carried out according to the PRISMA guidelines. In total, 135 articles were found, among them 131 full text articles were selected. To gain the most recent data, the filter excluding papers published earlier than 10 years ago and English-written papers was used, which gave us a number of 112 papers in total. After including the words "Covid-19" or "SARS-CoV-2", no results were found for this investigation. We checked this because the pandemic was one of the most important topics of scientific research in the last 3 years. After skimming through the abstract, the papers that did not fit the topic were excluded, which gave us the final number of 92 papers. One of the articles was duplicated. Furthermore, the obtained full text articles were read, and additional articles were excluded, especially those concerning influence of chitosan coatings on the genome and compositions added to the dental materials. In the end, 23 papers were chosen that concerned the topic directly.

## 3. Biomedical Application of Chitosan Coatings

Chitosan is recognized as an exciting and promising excipient for the pharmaceutical industry. There is evidence that the addition of drugs, chitosan nanoparticles can improve absorption in the whole small intestine, increase survival time, reduce drug cardiotoxicity, reduce tumour cell dispersion, and even improve tumour cell destruction efficiency. Chitosan nanoparticles prevent proteins and DNA from being degraded by gastric enzymes and nucleases, thereby increasing the resident time in the gastrointestinal tract. This leads to greater control of drug release, improved protein biodegradation, and increased absorption of hydrophilic molecules by the epithelium layer. These possibilities have also been used for insulin, resulting in high drug entrapment efficiency, good stability, low outbreak, and consistent insulin release [33].

Moreover, chitosan-based nanoparticles are used to improve vaccine delivery due to their mucoadhesive and osmotic properties, which increase peptide adsorption and transport through the nasal epithelium. Chitosan nanoparticle glucuronidation significantly increased systemic (serum immunoglobulin G (IgG) titers), mucosal (secretory immunoglobulin A (IgA)), and cell-mediated (IL-2 and interferon- (IFN-)) immune responses. In addition, there is evidence that chitosan can stimulate an immune response on its own [34].

Furthermore, chitosan and its derivatives have been found to have haemostatic potential, antimicrobial activity, and biocompatibility. In addition, chitosan is effective in lowering plasma and liver lipid levels in rats fed high-fat diets and increasing lipase activities [35]. Furthermore, it prevented and improved the condition of hypercholesterolemia in rats fed a high-fat diet. Longer term feeding of chitosan resulted in a better hypolipidemic effect [36]. Chitosan induced the formation of granulation tissue or re-epithelialization in the early stages of wound healing, so it is commonly used as a wound care material [37].

## 4. Dental Application of Chitosan Coatings

### *4.1. Surgical Procedures*

Chitosan coatings, because of their properties in increasing tissue healing and stabilisation of implants and membranes, are mainly used in surgery, and they could be used in other dental specialities. This is thanks to its potential to increase healing and antiseptic activity. Chitosan coatings are used especially during dental implantation. The search for a perfect coating agent that has a bacteriostatic effect, which also results in greater implant stabilisation, was implemented. The most common problem with implant loss is periimplantitis around the metal part of the implant and the need for better osteointegration pairs with the need for an antimicrobial reaction. It has been proven that chitosan/AgNPs and chitosan/HA coatings protect the surface more effectively, especially when used on porous surfaces [38–40]. VEGF (vascular endothelial growth factor) plays a role in vascularization and osteoblastic differentiation as well as bone regeneration. These procedures are key factors in the osteointegration of dental implants. There are serious trials to add a chitosan coating to the implant surface to increase the osteointegrative process, although the results of this research have not been published yet [41]. The addition of other substances, however, increases osteointegration with implants [42]. The addition of chitosan is even more effective when the implant surface is under osteoblast formation [43]. Recent interest in the application of chitosan in dental implantology is also the key to the attention of other researchers, which is presented in the recent review by Hallmann et al. [31]. One of the most specific branches where chitosan coatings are used is dental and orofacial surgery. The substances and the use of chitosan-based coatings in surgery are presented in Table S1, [15,16,44–58] which is in the supplementary files.

### *4.2. Disinfection*

Chitosan finds a wide range of uses as a disinfection agent, especially when prosthetic restorations and devices should be disinfected to increase wound healing [50]. Recent studies show that alternative methods of disinfection are being researched [59]. Thanks to the possibility of creating a coating, chitosan might be beneficial in the use of that agent for a longer period of time when compared to conventional disinfection agents. Additionally, the addition of chitosan to hand sanitisers increases the bactericidal effect [60].

### *4.3. Dental Appliances*

Among dental appliances, we could find removable prostheses, orthodontic appliances, and occlusal splints [1]. The influence of the archwire coating on the properties of the archwire and what follows: friction, duration of treatment, and risk of complications is widely known [61]. When it comes to chitosan, the benefits of using coatings are quite large. Chitosan coating reduces friction and therefore helps achieve better final bracket expression and reduce treatment time [62]. It could also be beneficial due to the bactericidal activity, because the orthodontically treated patient may have some problems achieving perfect oral hygiene.

Chitosan coatings could be used in postoperative prosthodontics, where the denture is applied to the patient's mouth directly after the surgical procedure [63].

It had been proven that chitosan coating of the dental prostheses has its antifungal properties, especially against the most commonly observed in the oral cavity *Candida* spp. [64]. It may be extremely important not only on the surface of the appliance itself, but also when the impression is transferred between the dental office and the technician [59].

Except for antifungal, haemostatic and antibacterial properties, chitosan could be used to cover the tooth surfaces, e.g., as an ingredient of the toothpaste. As a coating on the surface of the tooth, it desensitises the tooth to external conditions, such as acids in food [61].

Although chitosan finds less obvious outside of surgical and periodontological procedures, the application of its coatings has been collected in Table 2.

**Table 2.** The use of chitosan coatings in other than surgery and periodontology specialities.

| | Use | Author (Reference) |
|---|---|---|
| Prosthodontics | Antifungal properties | Jung et al. [64] |
| Conservative dentistry | Desensitizer, used to coved tooth surfaces in tooth pastes | Cicciù [30] |
| Orthodontics | Helping with healing after miniimplants placement | Anggani [42] |
| | Lower friction and therefore faster tooth movement in fixed appliances; better root control movement; reduced treatment time; better anchorage; reduced risk of root resorption | Elhelbawy [62] |
| Endodontics | Improved reaction anti-bacterial species *Peptostreptococcus* and *Fusobacterium* | Asadi [65] |

### *4.4. Risk of Bias*

It was not possible to assess any univocal statistics among the examined papers, as the papers apply to different methods and applications. For this reason, the article was prepared as a narrative review.

## 5. Advantages and Limitations of Chitosan Coatings in Dentistry

Due to the many possibilities of the use of chitosan in dental applications, its use in general is beneficial. By binding those two substances, we could gain perfect novel drug carriers or create new drug formulations. Biodegradability, biocompatibility, antimicrobial activity, and low immunogenicity are properties that are advantageous in terms of the prevention and treatment of inflammatory diseases and can accelerate the development of biological materials for wound healing and osteointegration in dentistry. The mixture of natural polymers with nanomaterials could be a future design of dental materials. The fact that the material is naturally-based makes it interesting to the researchers and keeps on developing the new trends to its use, not only separately, but also as a part of materials and matrices used in clinic. One of the examples of that use was the addition of binding nanomaterials with chitosan in endodontic treatment. By binding those two substances, we could gain perfect novel drug carriers or create new drug formulations. Although the use of chitosan itself showed a beneficial effect in endodontic treatment, its application with nanomaterials also seems to have great possibilities [12,66]. This proves that the cooperation of material engineers, pharmacists and dentists is crucial to introducing new potential applications of chitosan.

The problem of the biocompatibility of dental materials used in dentistry is very large, especially due to the fact that this could prolong the retention of teeth in the dental socket. According to mimicking, this is the most natural way of healing with such materials [67,68]. Also, the trend to use more natural substances and the development of green dentistry make naturally-found substances like chitosan important [69]. The development of 3D printing in dentistry also adds new perspectives in the world today, as the materials are biocompatible and more precise in preparation [70]. In addition, the porous structure of the material creates a similar structure to natural matrices that mimics the adhesive properties of the cells. This structural construction emphasizes the three-dimensional distribution of the substance particles, creating a healing process and allowing for bone regeneration and new bone formation. The three-dimensional distribution refers not only to dentistry but also to all aspects of medicine and science [71–74]. Chitosan has many applications in almost every field because of its unique properties, but it also has some limitations. It is insoluble in water and most organic solvents, limiting its applications in a variety of fields. It is insoluble in water as a result of the presence of intermolecular and intramolecular H-bonding. It can only be dissolved in dilute acids like 1% acetic acid, formic acid, lactic acid, and so on. However, several modifications can be made to improve solubility [75].

## 6. Future Directions

Given that the surfaces of dental materials used after coating may change, one has to predict how to make the use of the dental materials as repeatable as possible. The nanostructure and microstructure of the materials changes. Even a 1 m layer of 1 μm of the coating can have an effect on properties and act in an antibacterial manner, which is a promising for dental implantology [76–78]. Other natural polymers could also be searched to be used as coatings, which could also be promising in the treatment of serious conditions, such as oral cancer [1,79]. Because of the high biocompatibility, the scaffolds could heal into the tissues and give great potential in tissue restorations. The experiments performed on rabbits show that Mg-CD/CH coated Ti-6Al-4V helps in bone regeneration procedures and reduces the bone defects. This could open the door to future bone scaffolds in tissue engineering and gives prospects for the production of novel bone substitutes [80]. Although chitosan is a very important and promising coating, different types of coatings to help heal and osteointegrate are still needed and being researched. Recent studies have hydroxyapatites (HAPs) are even more effective in fighting implant loss and that the bacteriostatic reaction is greater compared to chitosan [81]. Chitosan coatings could be added to help heal alveolar bone loss and during implantation to increase the possibility of implant adaptation and healing. In the authors' opinion, the studies with chitosan coatings should go into the fractal dimension analysis of bone to visualise the actual bone condition around the dental implant [81].

## 7. Conclusions

The study presented shows that chitosan has many applications in dentistry. Due to its antimicrobial effect and natural origin, it is a perfect natural disinfection agent. It is used not only in dental surgery, including implantology, but also in other dental specialities, including conservative dentistry, orthodontics, prosthetics etc. Chitosan is a multifactorial naturally-derived polymer that is very useful in pharmaceutical technology. Due to the multidisciplinary approach of this paper, we have shown that the cooperation between pharmacists and dentists might be useful in fully understanding the development of its use. Its natural origin makes chitosan a perfect candidate for multiple applications in the environmentally-conscious thinking of the world today.

**Supplementary Materials:** The following supporting information can be downloaded at: https://www.mdpi.com/article/10.3390/md21120613/s1, Table S1:Presentation of the substances and their activity in organism to chitosan-based coatings used in dental surgery.

**Author Contributions:** Conceptualization, A.P.-S. and A.O.; methodology, A.P.-S., A.O., M.M. and B.K.; validation, M.M. and B.K.; formal analysis, A.P.-S., A.O. and J.L.; investigation, A.P.-S., A.O. and J.L.; resources, A.P.-S. and A.O.; data curation, A.P.-S., A.O. and J.L.; writing—original draft preparation, A.P.-S. and A.O.; writing—review and editing, M.M. and B.K.; visualization, A.O.; supervision, A.P.-S.; project administration, A.P.-S. and A.O.; funding acquisition, A.P.-S. and A.O. All authors have read and agreed to the published version of the manuscript.

**Funding:** This research received no external funding.

**Data Availability Statement:** No new data were created or analyzed in this study. Data sharing is not applicable to this article.

**Conflicts of Interest:** The authors declare no conflict of interests.

## References

1. Paradowska-Stolarz, A.; Wieckiewicz, M.; Owczarek, A.; Wezgowiec, J. Natural Polymers for the Maintenance of Oral Health: Review of Recent Advances and Perspectives. *Int. J. Mol. Sci.* **2021**, *22*, 10337. [CrossRef] [PubMed]
2. Kida, D.; Karolewicz, B.; Junka, A.; Sender-Janeczek, A.; Duś, I.; Marciniak, D.; Szulc, M. Metronidazole-Loaded Porous Matrices for Local Periodontitis Treatment: In Vitro Evaluation and In Vivo Pilot Study. *Appl. Sci.* **2019**, *9*, 4545. [CrossRef]
3. Kida, D.; Zakrzewska, A.; Zborowski, J.; Szulc, M.; Karolewicz, B. Polymer-Based Carriers in Dental Local Healing-Review and Future Challenges. *Materials* **2021**, *14*, 3948. [CrossRef] [PubMed]

4. Mikulewicz, M.; Wołowiec, P.; Michalak, I.; Chojnacka, K.; Czopor, W.; Berniczei-Royko, A.; Vegh, A.; Gedrange, T. Mapping chemical elements on the surface of orthodontic appliance by SEM-EDX. *Med. Sci. Monit.* **2014**, *20*, 860–865. [CrossRef] [PubMed]
5. Kochanowska, I.E.; Chojnacka, K.; Pawlak-Adamska, E.; Mikulewicz, M. Metallic Orthodontic Materials Induce Gene Expression and Protein Synthesis of Metallothioneins. *Materials* **2021**, *14*, 1922. [CrossRef] [PubMed]
6. Kielan-Grabowska, Z.; Bącela, J.; Zięty, A.; Seremak, W.; Gawlik-Maj, M.; Kawala, B.; Borak, B.; Detyna, J.; Sarul, M. Improvement of Properties of Stainless Steel Orthodontic Archwire Using $TiO_2$:Ag Coating. *Symmetry* **2021**, *13*, 1734. [CrossRef]
7. Wieckiewicz, M.; Boening, K.W.; Grychowska, N.; Paradowska-Stolarz, A. Clinical Application of Chitosan in Dental Specialities. *Mini Rev. Med. Chem.* **2017**, *17*, 401–409. [CrossRef]
8. Grimling, B.; Karolewicz, B.; Nawrot, U.; Włodarczyk, K.; Górniak, A. Physicochemical and Antifungal Properties of Clotrimazole in Combination with High-Molecular Weight Chitosan as a Multifunctional Excipient. *Mar. Drugs* **2020**, *18*, 591. [CrossRef]
9. Atay, H.Y. Antibacterial Activity of Chitosan-Based Systems. In *Functional Chitosan*; Springer: Singapore, 2020; pp. 457–489. [CrossRef]
10. Duś-Ilnicka, I.; Krala, E.; Cholewińska, P.; Radwan-Oczko, M. The Use of Saliva as a Biosample in the Light of COVID-19. *Diagnostics* **2021**, *11*, 1769. [CrossRef]
11. Safarzadeh, M.; Sadeghi, S.; Azizi, M.; Rastegari-Pouyani, M.; Pouriran, R.; Haji Molla Hoseini, M. Chitin and chitosan as tools to combat COVID-19: A triple approach. *Int. J. Biol. Macromol.* **2021**, *183*, 235–244. [CrossRef]
12. Skoskiewicz-Malinowska, K.; Kaczmarek, U.; Malicka, B.; Walczak, K.; Zietek, M. Application of Chitosan and Propolis in Endodontic Treatment: A Review. *Mini Rev. Med. Chem.* **2017**, *17*, 410–434. [CrossRef] [PubMed]
13. Costa-Pinto, A.R.; Lemos, A.L.; Tavaria, F.K.; Pintado, M. Chitosan and Hydroxyapatite Based Biomaterials to Circumvent Periprosthetic Joint Infections. *Materials* **2021**, *14*, 804. [CrossRef] [PubMed]
14. Ganguly, A.; Ian, C.K.; Sheshala, R.; Sahu, P.S.; Al-Waeli, H.; Meka, V.S. Application of diverse natural polymers in the design of oral gels for the treatment of periodontal diseases. *J. Mater. Sci. Mater. Med.* **2017**, *28*, 39. [CrossRef] [PubMed]
15. Govindharajulu, J.P.; Chen, X.; Li, Y.; Rodriguez-Cabello, J.C.; Battacharya, M.; Aparicio, C. Chitosan-Recombinamer Layer-by-Layer Coatings for Multifunctional Implants. *Int. J. Mol. Sci.* **2017**, *18*, 369. [CrossRef] [PubMed]
16. de Lima, T.M.; Arias, L.S.; Afanaci, L.F.; Ferraresse, R.F.; de SNeto, F.N.; de Lima, B.H.; Straioto, F.G.; de Camargo, E.R.; Pessan, J.P.; Monteiro, D.R. Assembly and antifungal effect of a new fluconazole-carrier nanosystem. *Future Microbiol.* **2020**, *15*, 273–285. [CrossRef]
17. Aryaei, A.; Jayatissa, A.H.; Jayasuriya, A.C. Nano and micro mechanical properties of uncross-linked and cross-linked chitosan films. *J. Mech. Behav. Biomed. Mater.* **2012**, *5*, 82–89. [CrossRef]
18. Adamski, R.; Siuta, D. Mechanical, Structural, and Biological Properties of Chitosan/Hydroxyapatite/Silica Composites for Bone Tissue Engineering. *Molecules* **2021**, *26*, 1976. [CrossRef]
19. Gouveia, Z.; Perinpanayagam, H.; Zhu, J. Development of Robust Chitosan–Silica Class II Hybrid Coatings with Antimicrobial Properties for Titanium Implants. *Coatings* **2020**, *10*, 534. [CrossRef]
20. Praveen, M.; Aarthi, G.; Meenapriya, P.K.; Kumar, S.S.; Kumar, N.S.M.; Karunakaran, J.V. A Comparative Evaluation of Intraradicular Smear Removal Efficacy of 2% Chitosan (Low Molecular Weight), 4% Chitosan Citrate, and 10% Citric Acid when Used as Final Rinse in Irrigation Protocols: A Field Emission Scanning Electron Microscopic Study. *J. Pharm. Bioallied Sci.* **2017**, *9* (Suppl. S1), S73–S78. [CrossRef]
21. Tarsi, R.; Muzzarelli, R.A.; Guzman, C.A.; Pruzzo, C. Inhibition of Streptococcus mutansadsorption to hydroxyapatite by low-molecular-weight chitosans. *J. Dent. Res.* **1997**, *7*, 665–672. [CrossRef]
22. Norowski, P.A.; Courtney, H.S.; Babu, J.; Haggard, W.O.; Bumgardner, J.D. Chitosan Coatings Deliver Antimicrobials from Titanium Implants: A Preliminary Study. *Implant. Dent.* **2011**, *20*, 56–67. [CrossRef]
23. Bumgardner, J.D.; Chesnutt, B.M.; Yuan, Y.; Yang, Y.; Appleford, M.; Oh, S.; McLaughlin, R.; Elder, S.H.; Ong, J.L. The Integration of Chitosan-Coated Titanium in Bone: An In Vivo Study in Rabbits. *Implant. Dent.* **2007**, *16*, 66–79. [CrossRef] [PubMed]
24. López-Valverde, N.; López-Valverde, A.; Cortés, M.P.; Rodríguez, C.; Macedo De Sousa, B.; Aragoneses, J.M. Bone Quantification Around Chitosan-Coated Titanium Dental Implants: A Preliminary Study by Micro-CT Analysis in Jaw of a Canine Model. *Front. Bioeng. Biotechnol.* **2022**, *10*, 858786. [CrossRef] [PubMed]
25. Pistone, S.; Rykke, M.; Smistad, G.; Hiorth, M. Polysaccharide-coated liposomal formulations for dental targeting. *Int. J. Pharm.* **2017**, *516*, 106–115. [CrossRef] [PubMed]
26. Kalyoncuoglu, U.T.; Yilmaz, B.; Gungor, S.; Evis, Z.; Uyar, P.; Akca, G.; Kansu, G. Evaluation of the chitosan-coating effectiveness on a dental titanium alloy in terms of microbial and fibroblastic attachment and the effect of aging. *Mater. Technol.* **2015**, *49*, 925–931. [CrossRef]
27. Soares, Í.; Faria, J.; Marques, A.; Ribeiro, I.A.C.; Baleizão, C.; Bettencourt, A.; Ferreira, I.M.M.; Baptista, A.C. Drug Delivery from PCL/Chitosan Multilayer Coatings for Metallic Implants. *ACS Omega* **2022**, *7*, 23096–23106. [CrossRef]
28. Takeuchi, I.; Kamiki, Y.; Makino, K. Therapeutic efficacy of rebamipide-loaded PLGA nanoparticles coated with chitosan in a mouse model for oral mucositis induced by cancer chemotherapy. *Colloids Surf. B Biointerfaces* **2018**, *167*, 468–473. [CrossRef] [PubMed]
29. Chittratan, P.; Chalitangkoon, J.; Wongsariya, K.; Mathaweesansurn, A.; Detsri, E.; Monvisade, P. New Chitosan-Grafted Thymol Coated on Gold Nanoparticles for Control of Cariogenic Bacteria in the Oral Cavity. *ACS Omega* **2022**, *7*, 26582–26590. [CrossRef]

30. Cicciù, M.; Fiorillo, L.; Cervino, G. Chitosan Use in Dentistry: A Systematic Review of Recent Clinical Studies. *Mar. Drugs* **2019**, *17*, 417. [CrossRef]
31. Hallmann, L.; Gerngroß, M.D. Chitosan and its application in dental implantology. *J. Stomatol. Oral. Maxillofac. Surg.* **2022**, *123*, e701–e707. [CrossRef]
32. Qu, S.; Ma, X.; Yu, S.; Wang, R. Chitosan as a biomaterial for the prevention and treatment of dental caries: Antibacterial effect, biomimetic mineralization, and drug delivery. *Front. Bioeng. Biotechnol.* **2023**, *11*, 1234758. [CrossRef]
33. Feng, C.; Li, J.; Kong, M.; Liu, Y.; Cheng, X.J.; Li, Y.; Park, H.J.; Chen, X.G. Surface charge effect on mucoadhesion of chitosan based nanogels for local anti-colorectal cancer drug delivery. *Colloids Surf. B* **2015**, *128*, 439–447. [CrossRef] [PubMed]
34. Harde, H.; Agrawal, A.K.; Jain, S. Development of stabilized glucomannosylated chitosan nanoparticles using tandem crosslinking method for oral vaccine delivery. *Nanomedicine* **2014**, *9*, 2511–2529. [CrossRef] [PubMed]
35. Gheorghiță, D.; Moldovan, H.; Robu, A.; Bița, A.-I.; Grosu, E.; Antoniac, A.; Corneschi, I.; Antoniac, I.; Bodog, A.D.; Băcilă, C.I. Chitosan-Based Biomaterials for Hemostatic Applications: A Review of Recent Advances. *Int. J. Mol. Sci.* **2023**, *24*, 10540. [CrossRef] [PubMed]
36. Liu, S.H.; Cai, F.Y.; Chiang, M.T. Long-Term Feeding of Chitosan Ameliorates Glucose and Lipid Metabolism in a High-Fructose-Diet-Impaired Rat Model of Glucose Tolerance. *Mar. Drugs* **2015**, *13*, 7302–7313. [CrossRef]
37. Feng, P.; Luo, Y.; Ke, C.; Qiu, H.; Wang, W.; Zhu, Y.; Hou, R.; Xu, L.; Wu, S. Chitosan-Based Functional Materials for Skin Wound Repair: Mechanisms and Applications. *Front. Bioeng. Biotechnol.* **2021**, *9*, 650598. [CrossRef] [PubMed]
38. Pawłowski, Ł.; Bartmański, M.; Mielewczyk-Gryń, A.; Cieślik, B.M.; Gajowiec, G.; Zieliński, A. Electrophoretically Deposited Chitosan/Eudragit E 100/AgNPs Composite Coatings on Titanium Substrate as a Silver Release System. *Materials* **2021**, *14*, 4533. [CrossRef]
39. Kubasiewicz-Ross, P.; Fleischer, M.; Pitułaj, A.; Hadzik, J.; Nawrot-Hadzik, I.; Bortkiewicz, O.; Dominiak, M.; Jurczyszyn, K. Evaluation of the three methods of bacterial decontamination on implants with three different surfaces. *Adv. Clin. Exp. Med.* **2020**, *29*, 177–182. [CrossRef]
40. García-Cabezón, C.; Godinho, V.; Salvo-Comino, C.; Torres, Y.; Martín-Pedrosa, F. Improved Corrosion Behavior and Biocompatibility of Porous Titanium Samples Coated with Bioactive Chitosan-Based Nanocomposites. *Materials* **2021**, *14*, 6322. [CrossRef]
41. Leedy, M.R.; Jennings, J.A.; Haggard, W.O.; Bumgardner, J.D. Effects of VEGF-loaded chitosan coatings. *J. Biomed. Mater. Res. A* **2014**, *12*, 752–759. [CrossRef]
42. Anggani, H.S.; Perdana, R.G.; Siregar, E.; Bachtiar, E.W. The effect of coating chitosan on Porphyromonas gingivalis biofilm formation in the surface of orthodontic mini-implant. *J. Adv. Pharm. Technol. Res.* **2021**, *12*, 84–88. [CrossRef] [PubMed]
43. Alnufaiy, B.M.; Lambarte, R.N.A.; Al-Hamdan, K.S. The Osteogenetic Potential of Chitosan Coated Implant: An In Vitro Study. *J. Stem Cells. Regen. Med.* **2020**, *16*, 44–49. [CrossRef] [PubMed]
44. Karimi, S.; Salahinejad, E.; Sharifi, E.; Nourian, A.; Tayebi, L. Bioperformance of chitosan/fluoride-doped diopside nanocomposite coatings deposited on medical stainless steel. *Carbohydr. Polym.* **2018**, *202*, 600–610. [CrossRef]
45. Paulino-Gonzalez, A.D.; Sakagami, H.; Bandow, K.; Kanda, Y.; Nagasawa, Y.; Hibino, Y.; Nakajima, H.; Yokose, S.; Amano, O.; Nakaya, G.; et al. Biological Properties of the Aggregated Form of Chitosan Magnetic Nanoparticle. *In Vivo* **2020**, *34*, 1729–1738. [CrossRef]
46. Caldeirão, A.C.M.; Araujo, H.C.; Arias, L.S.; Ramírez Carmona, W.; Miranda, G.P.; Oliveira, S.H.P.; Pessan, J.P.; Monteiro, D.R. Nanocarriers of Miconazole or Fluconazole: Effects on Three-Species Candida Biofilms and Cytotoxic Effects In Vitro. *J. Fungi* **2021**, *7*, 500. [CrossRef] [PubMed]
47. Arias, L.S.; Pessan, J.P.; de Souza Neto, F.N.; Lima, B.H.R.; de Camargo, E.R.; Ramage, G.; Delbem, A.C.B.; Monteiro, D.R. Novel nanocarrier of miconazole based on chitosan-coated iron oxide nanoparticles as a nanotherapy to fight Candida biofilms. *Colloids Surf. B Biointerfaces* **2020**, *192*, 111080. [CrossRef]
48. Lin, M.H.; Wang, Y.H.; Kuo, C.H.; Ou, S.F.; Huang, P.Z.; Song, T.Y.; Chen, Y.C.; Chen, S.T.; Wu, C.H.; Hsueh, Y.H.; et al. Hybrid ZnO/chitosan antimicrobial coatings with enhanced mechanical and bioactive properties for titanium implants. *Carbohydr. Polym.* **2021**, *257*, 117639. [CrossRef]
49. Liu, W.C.; Ballenger, B.; Algarni, A.; Velez, M.; GChu, T.M. FTIR characterization and release of bovine serum albumin from bioactive glasses. *J. Appl. Biomater. Funct. Mater.* **2017**, *15*, e347–e355. [CrossRef]
50. Walczak, K.; Thiele, J.; Geisler, D.; Boening, K.; Wieckiewicz, M. Effect of Chemical Disinfection on Chitosan Coated PMMA and PETG Surfaces-An In Vitro Study. *Polymers* **2018**, *10*, 536. [CrossRef]
51. Chai, M.; An, M.; Zhang, X. Construction of a $TiO_2/MoSe_2$/CHI coating on dental implants for combating Streptococcus mutans infection. *Mater. Sci. Eng. C Mater. Biol. Appl.* **2021**, *129*, 112416. [CrossRef]
52. Campos, D.M.; Toury, B.; D'Almeida, M.; Attik, G.N.; Ferrand, A.; Renoud, P.; Grosgogeat, B. Acidic pH resistance of grafted chitosan on dental implant. *Odontology* **2015**, *103*, 210–217. [CrossRef] [PubMed]
53. Kalyoncuoglu, U.T.; Yilmaz, B.; Koc, S.G.; Evis, Z.; Arpaci, P.U.; Kansu, G. Investigation of surface structure and biocompatibility of chitosan-coated zirconia and alumina dental abutments. *Clin. Implant. Dent. Relat. Res.* **2018**, *20*, 1022–1029. [CrossRef] [PubMed]
54. Fernandes, R.C.; Damasceno, M.I.; Pimentel, G.; Mendonça, J.S.; Gelfuso, M.V.; da Silva Pereira, S.R.L.; Passos, V.F. Development of a membrane for guided tissue regeneration: An in vitro study. *Indian J. Dent. Res.* **2020**, 763–767. [CrossRef]

55. Yoon, S.W.; Kim, M.J.; Paeng, K.W.; Yu, K.A.; Lee, C.K.; Song, Y.W.; Cha, J.K.; Sanz, M.; Jung, U.W. Locally Applied Slow-Release of Minocycline Microspheres in the Treatment of Peri-Implant Mucositis: An Experimental In Vivo Study. *Pharmaceutics* **2020**, *1*, 668. [CrossRef] [PubMed]
56. Mukherjee, S.; Sharma, S.; Soni, V.; Joshi, A.; Gaikwad, A.; Bellare, J.; Kode, J. Improved osteoblast function on titanium implant surfaces coated with nanocomposite Apatite-Wollastonite-Chitosan- an experimental in-vitro study. *J. Mater. Sci. Mater. Med.* **2022**, *33*, 25. [CrossRef]
57. Tonglairoum, P.; Ngawhirunpat, T.; Rojanarata, T.; Panomsuk, S.; Kaomongkolgit, R.; Opanasopit, P. Fabrication of mucoadhesive chitosan coated polyvinylpyrrolidone/cyclodextrin/clotrimazole sandwich patches for oral candidiasis. *Carbohydr. Polym.* **2015**, *132*, 173–179. [CrossRef]
58. Takanche, J.S.; Kim, J.E.; Kim, J.S.; Lee, M.H.; Jeon, J.G.; Park, I.S.; Yi, H.K. Chitosan-gold nanoparticles mediated gene delivery of c-myb facilitates osseointegration of dental implants in ovariectomized rat. *Artif. Cells Nanomed. Biotechnol.* **2018**, *46* (Suppl. S3), S807–S817. [CrossRef]
59. Wezgowiec, J.; Wieczynska, A.; Wieckiewicz, M.; Czarny, A.; Malysa, A.; Seweryn, P.; Zietek, M.; Paradowska-Stolarz, A. Evaluation of Antimicrobial Efficacy of UVC Radiation, Gaseous Ozone, and Liquid Chemicals Used for Disinfection of Silicone Dental Impression Materials. *Materials* **2022**, *15*, 2553. [CrossRef]
60. Wulandari, I.O.; Pebriatin, B.E.; Valiana, V.; Hadisaputra, S.; Ananto, A.D.; Sabarudin, A. Green Synthesis of Silver Nanoparticles Coated by Water Soluble Chitosan and Its Potency as Non-Alcoholic Hand Sanitizer Formulation. *Materials* **2022**, *15*, 4641. [CrossRef]
61. Słonik, K.; Mikulewicz, M.; Sarul, M. Influence of Aesthetic Archwire Coatings on Bacterial Adhesion. *Coatings* **2022**, *12*, 1120. [CrossRef]
62. Elhelbawy, N.; Ellaithy, M. Comparative evaluation of Stainless-steel wires and brackets coated with nanoparticles of Chitosan or Zinc oxide upon friction: An in vitro study. *Int. Orthod.* **2021**, *9*, 274–280. [CrossRef]
63. Więckiewicz, M.; Wolf, E.; Walczak, K.; Meissner, H.; Boening, K. Chitosan Coating on Silica- Modified Polymethyl Methacrylate for Dental Applications. *Coatings* **2017**, *7*, 168. [CrossRef]
64. Jung, J.; Li, L.; Yeh, C.K.; Ren, X.; Sun, Y. Amphiphilic quaternary ammonium chitosan/sodium alginate multilayer coatings kill fungal cells and inhibit fungal biofilm on dental biomaterials. *Mater. Sci. Eng. C Mater. Biol. Appl.* **2019**, *104*, 109961. [CrossRef]
65. Asadi, S.; Mortezagholi, B.; Hadizadeh, A.; Borisov, V.; Ansari, M.J.; Shaker Majdi, H.; Nishonova, A.; Adelnia, H.; Farasati Far, B.; Chaiyasut, C. Ciprofloxacin-Loaded Titanium Nanotubes Coated with Chitosan: A Promising Formulation with Sustained Release and Enhanced Antibacterial Properties. *Pharmaceutics* **2022**, *14*, 1359. [CrossRef] [PubMed]
66. Diogo, P.; Amparo FFaustino, M.; Palma, P.J.; Rai, A.; Graça PM SNeves, M.; Miguel Santos, J. May carriers at nanoscale improve the Endodontic's future? *Adv. Drug Deliv. Rev.* **2023**, *195*, 114731. [CrossRef] [PubMed]
67. Rady, D.; Abdel Rahman, M.H.; El-Mallah, S.; Khalil, M.M. Biocompatibility assessment of different root-end filling materials implanted subcutaneously in rats: An in vivo study. *Dent. Med. Probl.* **2021**, *58*, 525–532. [CrossRef] [PubMed]
68. Palma, P.J.; Ramos, J.C.; Martins, J.B.; Diogenes, A.; Figueiredo, M.H.; Ferreira, P.; Viegas, C.; Santos, J.M. Histologic Evaluation of Regenerative Endodontic Procedures with the Use of Chitosan Scaffolds in Immature Dog Teeth with Apical Periodontitis. *J. Endod.* **2017**, *43*, 1279–1287. [CrossRef] [PubMed]
69. Mazur, M.; Ndokaj, A.; Bietolini, S.; Nisii, V.; Duś-Ilnicka, I.; Ottolenghi, L. Green dentistry: Organic toothpaste formulations. A literature review. *Dent. Med. Probl.* **2022**, *59*, 461–474. [CrossRef] [PubMed]
70. Paradowska-Stolarz, A.; Malysa, A.; Mikulewicz, M. Comparison of the Compression and Tensile Modulus of Two Chosen Resins Used in Dentistry for 3D Printing. *Materials* **2022**, *15*, 8956. [CrossRef] [PubMed]
71. Murphy, C.M.; O'Brien, F.J. Understanding the effect of mean pore size on cell activity in collagen-glycosaminoglycan scaffolds. *Cell Adh. Migr.* **2010**, *4*, 377–381. [CrossRef]
72. Palma, P.; Matos, S.; Ramos, J.; Guerra, F.; Figueiredo, M.; Kauser, J. New formulations for space provision and bone regeneration. *Biodental Eng. I* **2010**, *1*, 71–76.
73. Černý, M.; Petruš, J.; Chamradová, I. The Influence of Porosity on Mechanical Properties of PUR-Based Composites: Experimentally Derived Mathematical Approach. *Polymers* **2023**, *15*, 1960. [CrossRef] [PubMed]
74. Michurov, D.A.; Makhina, T.K.; Siracusa, V.; Bonartsev, A.P.; Lozinsky, V.I.; Iordanskii, A.L. Cryo-Structuring of Polymeric Systems. Poly(Vinyl Alcohol)-Based Cryogels Loaded with the Poly(3-hydroxybutyrate) Microbeads and the Evaluation of Such Composites as the Delivery Vehicles for Simvastatin. *Polymers* **2022**, *14*, 2196. [CrossRef] [PubMed]
75. Pardo-Castaño, C.; Bolaños, G. Solubility of chitosan in aqueous acetic acid and pressurized carbon dioxide-water: Experimental equilibrium and solubilization kinetics. *J. Supercrit. Fluids* **2019**, *151*, 63–74. [CrossRef]
76. Sarul, M.; Kozakiewicz, M.; Jurczyszyn, K. Surface Evaluation of Orthodontic Wires Using Texture and Fractal Dimension Analysis. *Materials* **2021**, *14*, 3688. [CrossRef] [PubMed]
77. Sarul, M.; Amm, E. Bioactive Coatings in Dentistry—What Is the Future? *Coatings* **2022**, *12*, 842. [CrossRef]
78. Wezgowiec, J.; Wieczynska, A.; Wieckiewicz, W.; Kulbacka, J.; Saczko, J.; Pachura, N.; Wieckiewicz, M.; Gancarz, R.; Wilk, K.A. Polish Propolis-Chemical Composition and Biological Effects in Tongue Cancer Cells and Macrophages. *Molecules* **2020**, *25*, 2426. [CrossRef]
79. Tsai, C.H.; Hung, C.H.; Kuo, C.N.; Chen, C.Y.; Peng, Y.N.; Shie, M.Y. Improved Bioactivity of 3D Printed Porous Titanium Alloy Scaffold with Chitosan/Magnesium-Calcium Silicate Composite for Orthopaedic Applications. *Materials* **2019**, *12*, 203. [CrossRef]

80. Alhazmi, A.S.; Syame, S.M.; Mohamed, W.S.; Hakim, A.S. Incorporation of Plant Extracted Hydroxyapatite and Chitosan Nanoparticles on the Surface of Orthodontic Micro-Implants: An In-Vitro Antibacterial Study. *Microorganisms* **2022**, *10*, 581. [CrossRef]
81. Jurczyszyn, K.; Kubasiewicz-Ross, P.; Nawrot-Hadzik, I.; Gedrange, T.; Dominiak, M.; Hadzik, J. Fractal dimension analysis a supplementary mathematical method for bone defect regeneration measurement. *Ann. Anat.* **2018**, *219*, 83–88. [CrossRef]

*marine drugs*

MDPI

*Article*

# The Characterization and Cytotoxic Evaluation of *Chondrosia reniformis* Collagen Isolated from Different Body Parts (Ectosome and Choanosome) Envisaging the Development of Biomaterials

**Miguel S. Rocha [1,2], Catarina F. Marques [1,2], Ana C. Carvalho [1,2], Eva Martins [1,2,†], Alexander Ereskovsky [3,4,5], Rui L. Reis [1,2] and Tiago H. Silva [1,2,*]**

[1] 3B's Research Group, I3Bs—Research Institute on Biomaterials, Biodegradables and Biomimetics, University of Minho, Headquarters of the European Institute of Excellence on Tissue Engineering and Regenerative Medicine, AvePark, Parque de Ciência e Tecnologia, Zona Industrial da Gandra, Barco, 4805-017 Guimaraes, Portugal; miguel.rocha@i3bs.uminho.pt (M.S.R.); catarina.marques@i3bs.uminho.pt (C.F.M.); anacpcarvalho@gmail.com (A.C.C.); eva.biotec@gmail.com (E.M.); rgreis@i3bs.uminho.pt (R.L.R.)
[2] ICVS/3B's–PT Government Associate Laboratory, 4806-909 Braga/Guimaraes, Portugal
[3] Institut Méditerranéen de Biodiversité et d'Ecologie Marine et Continentale (IMBE), Aix Marseille University, Avignon University, Centre National de la Recherche Scientifique (CNRS), Institut de Recherche pour le Développement (IRD), 13007 Marseille, France; alexander.ereskovsky@imbe.fr
[4] Faculty of Biology, Department of Embryology, Saint Petersburg State University, 199034 Saint Petersburg, Russia
[5] N.K. Koltzov Institute of Developmental Biology of Russian Academy of Sciences, 119334 Moscow, Russia
* Correspondence: tiago.silva@i3bs.uminho.pt
† Current address: CBQF—Centro de Biotecnologia e Química Fina—Laboratório Associado, Escola Superior de Biotecnologia, Universidade Católica Portuguesa, Rua de Diogo Botelho 1327, 4169-005 Porto, Portugal.

**Citation:** Rocha, M.S.; Marques, C.F.; Carvalho, A.C.; Martins, E.; Ereskovsky, A.; Reis, R.L.; Silva, T.H. The Characterization and Cytotoxic Evaluation of *Chondrosia reniformis* Collagen Isolated from Different Body Parts (Ectosome and Choanosome) Envisaging the Development of Biomaterials. *Mar. Drugs* **2024**, *22*, 55. https://doi.org/10.3390/md22020055

Academic Editor: Azizur Rahman

Received: 30 December 2023
Revised: 15 January 2024
Accepted: 19 January 2024
Published: 24 January 2024



**Abstract:** *Chondrosia reniformis* is a collagen-rich marine sponge that is considered a sustainable and viable option for producing an alternative to mammalian-origin collagens. However, there is a lack of knowledge regarding the properties of collagen isolated from different sponge parts, namely the outer region, or cortex, (ectosome) and the inner region (choanosome), and how it affects the development of biomaterials. In this study, a brief histological analysis focusing on *C. reniformis* collagen spatial distribution and a comprehensive comparative analysis between collagen isolated from ectosome and choanosome are presented. The isolated collagen characterization was based on isolation yield, Fourier-transformed infrared spectroscopy (FTIR), circular dichroism (CD), SDS-PAGE, dot blot, and amino acid composition, as well as their cytocompatibility envisaging the development of future biomedical applications. An isolation yield of approximately 20% was similar for both sponge parts, as well as the FTIR, CD, and SDS-PAGE profiles, which demonstrated that both isolated collagens presented a high purity degree and preserved their triple helix and fibrillar conformation. Ectosome collagen had a higher OHpro content and possessed collagen type I and IV, while the choanosome was predominately constituted by collagen type IV. In vitro cytotoxicity assays using the L929 fibroblast cell line displayed a significant cytotoxic effect of choanosome collagen at 2 mg/mL, while ectosome collagen enhanced cell metabolism and proliferation, thus indicating the latter as being more suitable for the development of biomaterials. This research represents a unique comparative study of *C. reniformis* body parts, serving as a support for further establishing this marine sponge as a promising alternative collagen source for the future development of biomedical applications.

**Keywords:** collagen; *C. reniformis*; marine sponges; ectosome; choanosome

## 1. Introduction

Collagen is widely known as the major structural protein of the human body and is present in various connective tissues, representing one-third of the total protein content [1].

Due to its particular characteristics, such as the presence of several proteoglycan binding domains, growth factors, and other cell signaling molecules, collagen is considered a great material for Tissue Engineering and Regenerative Medicine (TERM) applications [2–5]. Although the main industrial collagen sources for biomedical applications are still of mammalian origin, in recent decades, marine-origin collagens have been receiving growing attention and are now considered high-value materials. This alternative and promising source has several advantages when compared with its mammalian counterparts, namely the prevention of zoonosis transmission such as BSE (bovine spongiform encephalopathy) and FMD (Foot and mouth disease), as well as of immunogenic reactions [6,7]. Additionally, religious and ethical constraints regarding porcine or bovine derivatives, namely Hindu, Muslim, and Jewish cultures, are avoided while having a lower production cost and higher yields than recombinant collagen [8,9]. In fact, the high demand for marine collagen encouraged the search for environmentally friendly sources, either derived from sustainable origins or from fish by-product valorization [10–12]. Recently, many TERM approaches have already been successfully developed using marine-origin collagenous materials, ranging from wound healing to drug delivery, as well as cosmetics [10,11,13–16].

*Chondrosia reniformis* is a demosponge commonly found in the shallow waters of the Mediterranean Sea and the South-West cost of the Atlantic Ocean; it lacks endogenous spicules and is particularly rich in collagen [17]. Its body is constituted by two main distinct zones: the ectosome and the choanosome. The ectosome, or cortex, is the cortical zone of the sponge composed of a layer of exopinacocytes surrounding the densely interwoven bundles of fibrils of collagen; it is poorly irrigated by the incurrent aquiferous system canals [18]. The choanosome is the internal zone of the sponge, which contains the choanocyte chambers lined by choanocytes and is filled with a densely interlaced network of inner vessels surrounded by sheaths of cortical tissue that form a dense three-dimensional stroma [18].

Recently, an integrated mariculture method using *C. reniformis* was developed, enabling a sustainable and high-yielding marine collagen production process that is adaptable to seawater environments combined with organic matter sources such as fish culture or sewage outfall [12]. This progress makes this collagen-rich marine sponge one of the most promising collagen sources of the present time, as its mariculture has a positive effect on the surrounding marine environment while allowing for an environmentally friendly animal collection. Due to both its high collagen content and its ability to reversely modulate the mechanical properties of its mesohyl, research on this highly collagenous animal has been encouraged [19–23]. It has been described that *C. reniformis* possesses collagens similar to type I and type IV and that their distribution in ectosome and choanosome is distinct [24,25]. Type IV collagen was reported to be expressed mainly in the ectosome, while collagen that was isolated from the whole *C. reniformis* body presented similarities to bovine type I collagen, namely in the amino acid composition and infrared spectra [24,25]. Nevertheless, *C. reniformis* collagen isolation procedures, performed employing neutral buffer solutions or disaggregating solutions and using the sponge whole body or just the ectosome, always described the isolated intact fibrils as resembling collagen type I [19,24,26,27]. Other studies used a green extraction process based on water acidified with $CO_2$ for the high-yielding isolation of collagen/gelatin from the sponge's whole body, which presented similar properties to collagen isolated from other marine sources [20,28]. Nonetheless, despite these promising results, *C. reniformis* collagens have not been thoroughly characterized and are not commonly used for TERM applications, although some works have been developed [22,29,30]. In fact, previous studies focusing on this issue have employed collagen isolated from the whole cortex or from specific body parts (ectosome or choanosome), but no comparative study has ever been performed. The only study presented so far lacks a thorough assessment of the physicochemical properties of the isolated collagens and presents no data regarding possible cytotoxic effects [23].

In this work, we examined two distinct *C. reniformis* body parts—the ectosome and choanosome—via histology, focusing on their collagen content and spatial organization. Furthermore, collagen isolated from both body parts was studied in more detail to as-

sess its physicochemical properties as well as its biological performance. Following an established collagen isolation procedure, cytotoxicity assays using L929 cells employing different concentrations of collagen isolated separately from the ectosome and choanosome were performed for the first time, thus evaluating their suitability for the development of biomedical applications, particularly in tissue engineering strategies. These data are important as they can add value to collagen isolated from this sponge, which is considered a sustainable collagen source [12]. This study provides valuable information for the establishment of *C. reniformis* as an ecological and biomedically relevant source of collagen and is paramount for the future development of marine collagen-based biomaterials.

## 2. Results

### *2.1. Histological Characterization of C. reniformis*

Histology was performed to analyze the overall anatomy and microarchitecture of the *Chondrosia reniformis* mesohyl (Figure 1). Images of the transversal sections comprising the transition between ectosome and choanosome revealed differences regarding collagen content and organization (Figure 1). Hematoxylin and eosin (H&E) staining provided a general view of the sponge anatomy, allowing us to analyze the ectosome and choanosome structure and morphology (Figure 1A,B). It revealed a clear and easily distinguishable difference in the density of the extracellular matrix (ECM) between both body parts, as the ECM of the ectosome was denser than the choanosome (Figure 1A). Additionally, the areas surrounding the aquiferous system canals present in the choanosome had a higher ECM density than the rest of the tissue (Figure 1B). Moreover, some rock or sand debris was found incorporated exclusively in the outer zone of the sponge, a phenomenon that was previously reported (Figure 1A) [31].

Collagen-specific Masson's Trichrome staining showed that the ectosome was mostly constituted by collagen (stained blue), contrasting with choanosome, which had a much lower collagen content (Figure 1C). The highly collagenous extracellular framework present in the ectosome supports the sponge body and is similar to other metazoan taxa collagenous connective tissues [18]. In the choanosome, the collagen present that surrounds the canals provides stability to the sponge aquiferous system (Figure 1D). Picrosirius red staining, which allows for the visualization of the collagen fibrils' orientation, abundance, and thickness, showed that *C. reniformis*'s whole body consisted of densely interwoven bundles of collagen fibrils, although much more concentrated in the ectosome and around the aquiferous system canals (Figure 1E,F). Collagen fibers present in the ectosome and around the canals of the aquiferous system were bright yellow as they were larger and thicker, while collagen fibers present in the choanosome were thinner as they displayed a greenish color [32]. This observation agreed with Masson's Trichrome results, as it demonstrated that the ectosome and the areas surrounding the aquiferous system canals were the richest regions in collagen and presented thicker fibers. This may hint at different collagen types being present in the distinct regions. Despite being known to possess a mainly collagenous body, evidenced by the collagen fibrils being present throughout the entire *C. reniformis* mesohyl, it was clear that there were differences in collagen content depending on the body part. This might have an impact on collagen isolation procedures, as yields and isolated collagen purity may be affected.

### *2.2. Collagen Characterization*

Collagen has been widely used for biomedical applications; hence, it is imperative to isolate a high-purity and high-quality material with stable properties that match the requirements of the specific application intended before it can be validated and employed. Therefore, collagen isolated separately from the *C. reniformis* ectosome and choanosome was thoroughly characterized regarding its physicochemical properties.

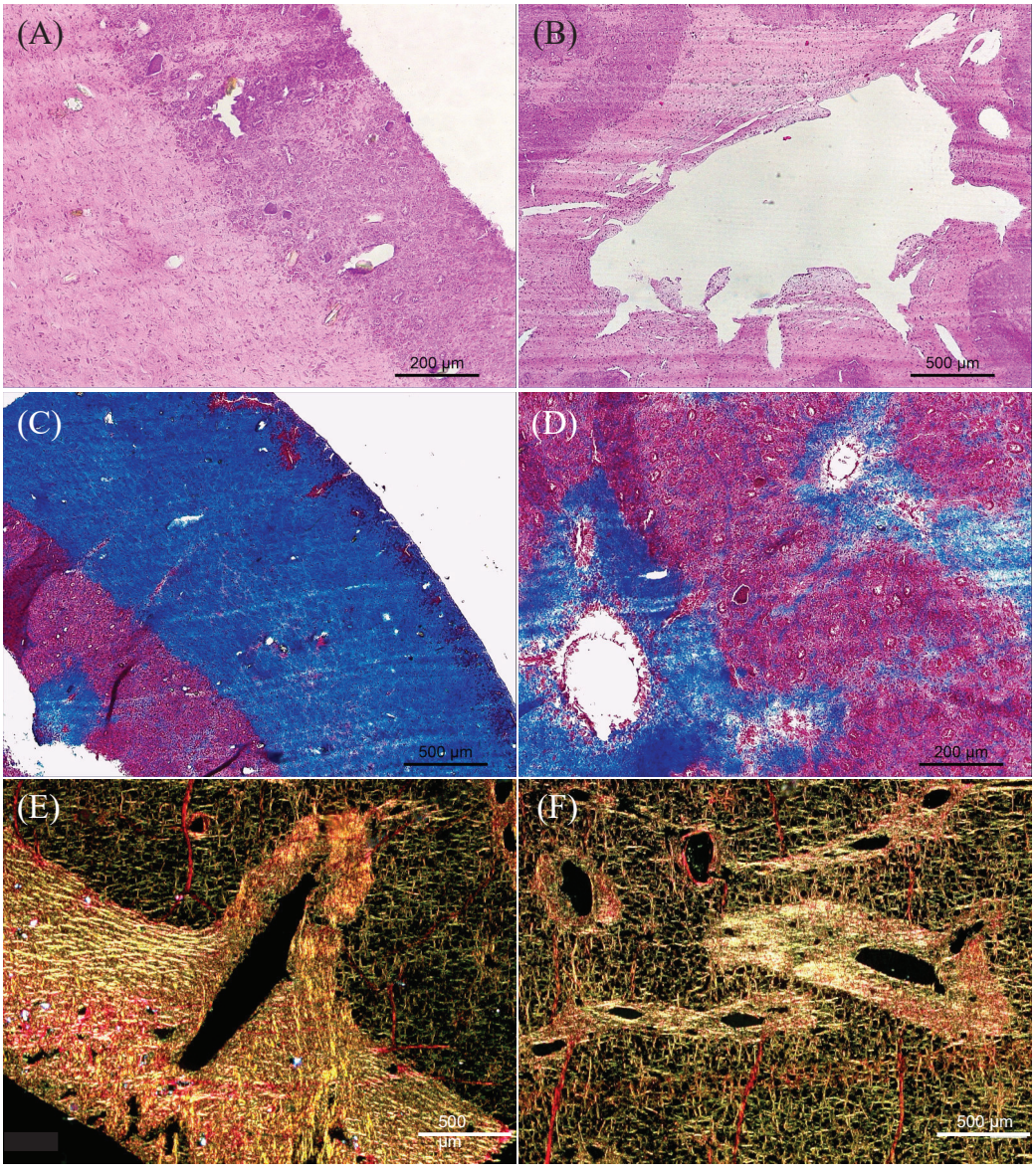


**Figure 1.** Histological cross-transversal sections of *C. reniformis* mesohyl on paraffin sections. (**A**) Section stained with H&E showing transition between ectosome (ec) on the right and choanosome (cho) on the left. (**B**) Section stained with H&E showing a big canal (ca) of aquiferous system present in the choanosome. (**C**) Section stained with Masson's trichome showing transition between ectosome (ec) on the right and choanosome (cho) on the left. (**D**) Section stained with Masson's trichome showing choanosome and some canals (ca) of aquiferous system. (**E**) Section stained with Picrosirius red showing transition between ectosome (ec), on the left, and choanosome (cho), on the right, and the presence of a canal (ca) of aquiferous system. (**F**) Section stained with Picrosirius red showing canals (ca) of aquiferous system present in the choanosome.

Fourier transform infrared (FTIR) spectra of collagen from *C. reniformis* ectosome and choanosome were very similar to each other, suggesting that their chemical composition was

identical (spectra and table in Figure 2A). Both FTIR spectra presented the peaks representing amide A, amide B, amide I, amide II, and amide III bonds, which are commonly associated with collagen and indicative of the secondary structure of different materials [20,26,28]. The amide A broadband is associated with N–H stretching, demonstrating the presence of intermolecular hydrogen bonds, while the amide B band represents the $CH_3$ asymmetrical stretch. The amide I peak is associated with the proteins' carbonyl group stretching vibrations (C=O), the amide II peak results from the N–H bending vibration coupled with the C–N stretching vibration, and the amide III band is related to C–H stretching. The band representing amide I is the most intense and sensitive, and it can be considered a useful marker for the analysis of the protein secondary structure, while the amide III band is considered a collagen fingerprint as it is credited to the characteristic collagen repeating tripeptide Gly-X-Y [33]. Taking this into account, in both spectra, the reference peaks of collagen were clearly visible.

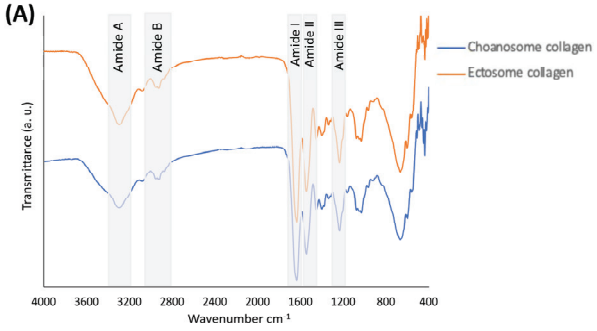


| Band | Range ($cm^{-1}$) | Ectosome collagen reference peak ($cm^{-1}$) | Choanosome collagen reference peak ($cm^{-1}$) |
|---|---|---|---|
| Amide A | 3200–3500 | 3296 | 3294 |
| Amide B | ≈ 2900 | 2878 | 2878 |
| Amide I | ≈ 1635 | 1636 | 1636 |
| Amide II | ≈ 1500 | 1545 | 1545 |
| Amide III | ≈ 1230 | 1234 | 1234 |

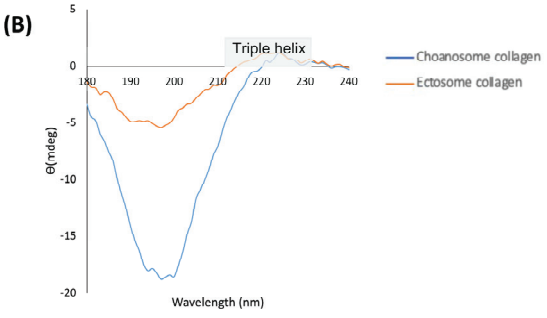


(C)

| Amino acid | Residues per 1000 total amino acid residues: Ectosome collagen | Choanosome collagen |
|---|---|---|
| Asp | 96 | 98 |
| Thr | 48 | 45 |
| Ser | 52 | 46 |
| Glu | 103 | 99 |
| **Gly** | **261** | **250** |
| Ala | 75 | 82 |
| Cys | 7 | 14 |
| Val | 32 | 33 |
| Met | 8 | 14 |
| Ile | 29 | 29 |
| Leu | 37 | 41 |
| Nleu | 8 | 7 |
| Tyr | 13 | 15 |
| Phe | 19 | 25 |
| OHlys | 10 | 9 |
| His | 7 | 8 |
| Lys | 21 | 25 |
| Arg | 45 | 46 |
| **OHpro** | **63** | **46** |
| Pro | 67 | 70 |
| **Total** | **1000** | |

**Figure 2.** (**A**) Fourier transform infrared (FTIR) spectra and reference peaks and peak assignments of ectosome (orange line) and choanosome (blue line) collagens. (**B**) Circular dichroism (CD) spectra of ectosome (orange line) and choanosome (blue line) collagens. (**C**) Amino acid content of ectosome and choanosome collagens.

Circular dichroism (CD) spectra of *C. reniformis* collagen from the ectosome and choanosome in the wavelength of 180 to 240 nm are shown in Figure 2B. This technique enabled us to evaluate the secondary structure of the isolated collagens and confirm if the isolation process did not denature the proteins. Both collagens spectra presented a negative peak around 200 nm and a positive peak around 225 nm, which is the characteristic profile of the collagen triple helix conformation [34–36]. Preservation of the characteristic

triple helix conformation is important since its loss by denaturation has an undesirable detrimental effect on the performance of biological molecules [37,38].

Figure 2C shows the results of the amino acid measurement of ectosome and choanosome collagens as the molar ratio of a given amino acid with regard to 1000 total amino acid residues, which is the approximate value of amino acids in each collagen alpha chain [8]. In both samples, the most abundant amino acid was glycine (Gly), accounting for roughly one-quarter, in line with the findings obtained previously [20,27]. Glutamic acid (Glu) and aspartic acid (Asp) were the second and third most abundant amino acids, respectively, in both samples. Additionally, OHpro, which results from the hydroxylation of proline and is a characteristic post-translation modification of collagen proteins used as a marker of collagen presence in protein extracts, was present more abundantly in ectosome collagen than in choanosome [39]. OHpro and Pro (pyrrolidine acids) are known to enhance the thermal stability of the triple helix conformation conferred by inter-chain hydrogen bonding between the carbonyl groups of the polypeptides, with marine-origin collagens typically exhibiting a lower denaturation temperature than terrestrial mammals collagens [40]. Moreover, the hydroxylation degree is a significant parameter to evaluate the collagen thermal stability and helix structure [41]. The hydroxylation degree of ectosome collagen (48.5%) was higher than choanosome collagen (39.7%), hinting at the higher thermal stability of this collagen molecule [42]. Thermal stability of the collagen triple helix conformation is paramount, as this protein is an essential structural compound that has the ability to support various connective tissues [8].

Both collagens were screened on an electrophoresis gel, which allowed the separation of protein chains by their molecular weight (Figure 3A). Observing the obtained SDS-PAGE profiles, it was possible to detect both samples on the high molecular region (stacking gel), as they were not able to penetrate the separating gel. This was due to the collagen's high molecular weight, around 300 kDa, as the collagen isolation process employed in this work preserved collagen in its fibrillar form [8,23,43]. Additionally, although Coomassie blue staining did not allow for the visualization of any bands (results not shown), the glycoprotein stain employed clearly dyed both samples, indicating that they were highly glycosylated. The low-molecular-weight bands present around 20 kDa were possibly collagen peptides resulting from hydrolysis or a low-concentration contaminant protein co-isolated with collagen. However, it is probable that these bands corresponded to collagen peptides since they were dyed as well demonstrating their highly glycosylated nature.

The isolated collagens were analyzed for the collagen types present in their constitution by dot blot, and the results are depicted in Figure 3B. Although *C. reniformis* has been described as possessing collagen types I and IV, antibodies specific to collagen types I, II, and IV were employed in this assay. The results confirmed the presence of collagen type I and IV in both body parts, while collagen type II was not detected, which is in accordance with previous reports [24,25]. Collagen type IV was present in high quantities in both samples, although it appeared to be present in a slightly higher quantity in the ectosome since the detection was moderately stronger than in the choanosome. Regarding collagen type I, ectosome had an evidently higher quantity when compared to choanosome, as it presented a heavy detection similar to collagen type IV, indicating that this body part was constituted by equal amounts of both collagen types. However, the amount of collagen type I detected in choanosome collagen appeared to be residual as the signal was barely detectable, indicating that it was mainly constituted by type IV collagen.

The collagen isolation yield of each sponge body part is evaluated and represented in Table 1. It was observed a recovery of around 20% of the total wet weight of the sponge tissue for collagen isolation procedures from both body parts, with no significant differences observed. Accordingly, on average, 0.2 g of collagen extract can be obtained from 1 g of dried *C. reniformis* employing this collagen isolation protocol. Although histology results point to the fact that ectosome is richer in collagen than choanosome, it had no effect on the final collagen isolation yield.

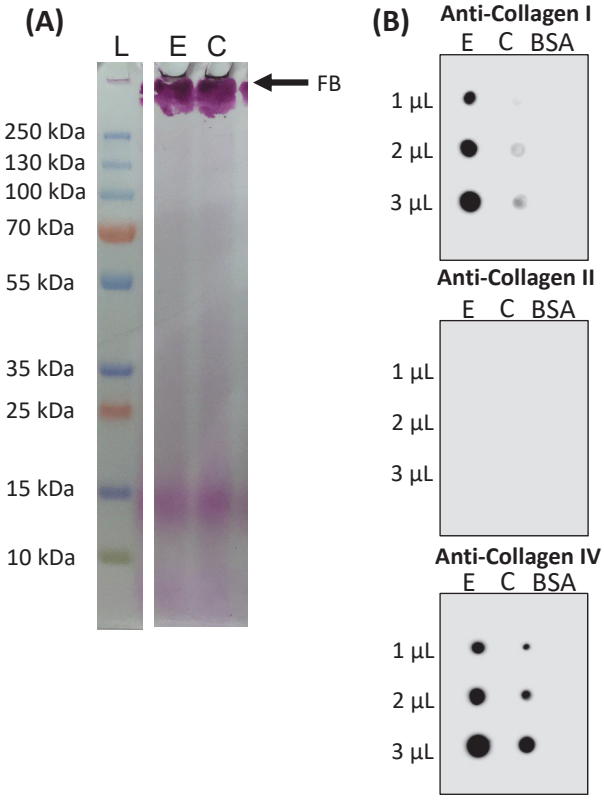


**Figure 3.** (**A**) Sodium dodecyl sulfate-polyacrylamide gel electrophoresis (SDS-PAGE) pattern of ectosome and choanosome collagens: L: protein marker; E: ectosome collagen; C: choanosome collagen; FB: fibrillar collagen. (**B**) Dot blot assay verifying the presence of collagen type I, II, and IV in the ectosome (E) and choanosome (C) collagens; bovine serum albumin (BSA) was used as negative control.

**Table 1.** Collagen isolation yields.

| *C. reniformis* **Collagen** | **Isolation Yield (%)** |
|---|---|
| Ectosome | 20.0 |
| Choanosome | 20.2 |

### *2.3. Collagen Biological Assessment*

After a thorough characterization of the physicochemical properties of the isolated collagens, a biological assessment was performed to understand if the previously detected differences between the collagens influence their biological performance. The cytotoxicity of both isolated collagens was evaluated by assessing the in vitro biological performance of fibroblast-like cells in contact with different collagen concentrations. The metabolic activity and viability of cells cultured in the presence of collagen dissolved in culture medium at different concentrations (0.25, 0.5, 1, and 2 mg/mL) were assessed via MTS and live/dead assays, respectively, and compared with cells cultured in culture medium without added collagen (Figures 4 and 5).

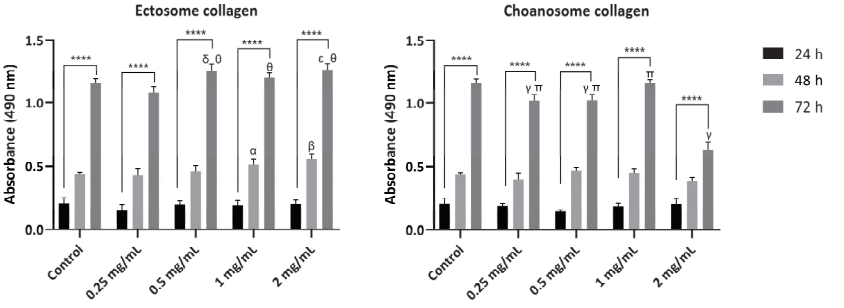


**Figure 4.** Metabolic activity of untreated L929 cells (control) and treated with ectosome and choanosome collagen dissolved at different concentrations (0.25 mg/mL, 0.5 mg/mL, 1 mg/mL, and 2 mg/mL) for 24 h, 48 h, and 72 h as determined by MTS assay. Data are mean ± standard deviation ($n = 3$, statistical significance for * $p \leq 0.05$; ** $p \leq 0.01$ and **** $p \leq 0.0001$, and symbols denote statistical differences: α (*) and β (****) compared with 48 h of control, δ (*), ε (**), and γ (****) compared with 72 h of control, θ (****) compared with 72 h of 0.25 mg/mL ectosome collagen, and π (****) compared with 72 h of 2 mg/mL choanosome collagen).

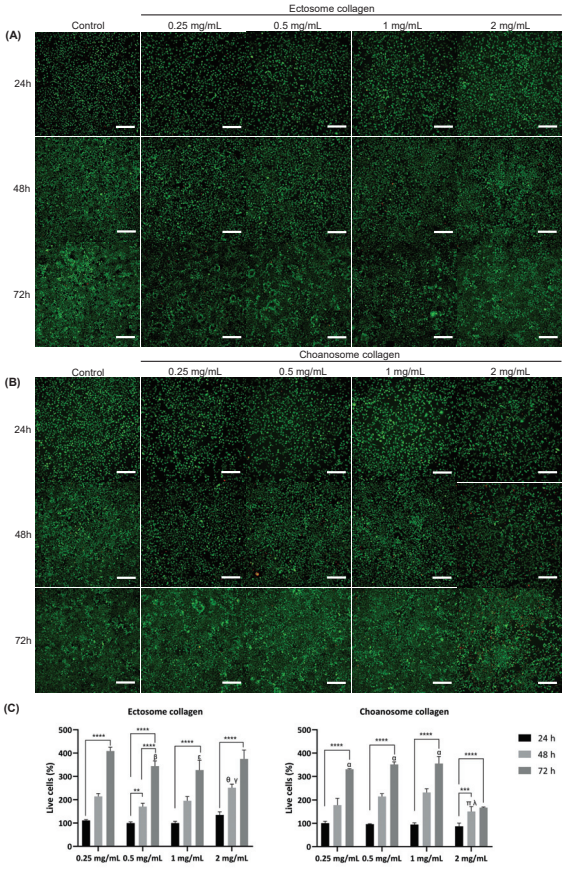


**Figure 5.** (**A**) Microscopy of live/dead assay of untreated L929 cells (control) and L929 cells treated with ectosome collagen dissolved at different concentrations (0.25 mg/mL, 0.5 mg/mL, 1 mg/mL,

and 2 mg/mL) for 24 h, 48 h, and 72 h. Viable cells were stained with calcein-AM (green), and dead cells with PI (red). Scale bar: 200 μm. (**B**) Microscopy of live/dead assay of untreated L929 cells (control) and L929 cells treated with choanosome collagen dissolved at different concentrations (0.25 mg/mL, 0.5 mg/mL, 1 mg/mL, and 2 mg/mL) for 24 h, 48 h, and 72 h. Viable cells were stained with calcein-AM (green) and dead cells with PI (red). Scale bar: 200 μm. (**C**) Quantitative analysis of fluorescence of viable cells (%) treated with ectosome and choanosome collagen at different concentrations (0.25 mg/mL, 0.5 mg/mL, 1 mg/mL, and 2 mg/mL) at 24 h, 48 h, and 72 h. Results are expressed as percentages relative to the control (viable cells of control at 24 h). Data are mean ± standard error ($n$ = 6, statistical significance for * $p \leq 0.05$; ** $p \leq 0.01$; *** $p \leq 0.001$ and **** $p \leq 0.0001$, and symbols denote statistical differences: β (*) and ε (**) compared with 72 h of 0.25 mg/mL ectosome collagen, θ (***) and γ (*) compared with 48 h of 0.5 mg/mL and 1 mg/mL ectosome collagen, respectively, α (****) compared with 72 h of 2 mg/mL choanosome collagen and π (***) and λ (****) compared with 48 h of 0.5 mg/mL and 1 mg/mL choanosome collagen, respectively).

Cell metabolic activity was assessed up to 72 h in the presence of different collagen concentrations and in their absence, the latter being considered the negative control (Figure 4). The results demonstrated that collagen isolated from ectosome did not detrimentally affect the metabolic activity of the cells, as in the presence of this collagen, the cell metabolic activity increased in a concentration- and time-dependent manner, determining that there was no cytotoxic effect. In fact, higher collagen concentrations (0.5, 1, and 2 mg/mL) induced a significant increase in cell metabolism relative to the control at 48 and 72 h.

Concerning collagen isolated from choanosome, the obtained results contrasted with the obtained with ectosome collagen. Even at the lowest concentration (0.25 mg/mL), there was an inhibitory effect on cell metabolism at 72 h relative to the control. At the highest concentration (2 mg/mL), the detrimental effect on cell metabolism at 72 h was even more evident. Although at 24 h and 48 h, no effect was detected, at the last time point, cell metabolism significantly decreased when compared with the control and with the other tested choanosome collagen concentrations tested. This result clearly highlighted the choanosome's collagen-negative effect on cell metabolism, especially at 2 mg/mL.

To further complement these results, cell viability was determined via live/dead assay (Figure 5). It was possible to observe that the green signal, related to living cells, greatly increased over time in all ectosome collagen concentrations tested, demonstrating that the cells were alive and proliferated in accordance with the MTS results (Figure 5A). There was a residual red signal detected as well, related to dead cells, but the great majority of cells were alive. At 72 h, it was observed that viable cells had essentially proliferated throughout the whole culture plate. Regarding the choanosome collagen up to a 1 mg/mL concentration, the results were almost comparable to the control (Figure 5B). The green signal increased over time while the red signal was minimal, indicating that cells were alive and proliferated, although at a slightly slower rate than in the control and ectosome collagen. However, at the highest choanosome collagen concentration tested (2 mg/mL), the green signal increase was reduced while the red signal slightly increased over time. In fact, at 72 h, it was possible to see an increment of dead cells and considerable areas with no cells. Since at each time point, it was necessary to remove the culture medium before adding the culture medium with calcein-AM and PI, it is plausible that the areas with no cells were previously occupied with dead cells, which were removed during the wash. This result clearly demonstrated that cell viability was negatively affected when in contact with choanosome collagen at 2 mg/mL, which is in accordance with MTS results. Additionally, a quantitative analysis of the live/dead results was performed using the live cells at 24 h of control as reference (Figure 5C). Although this evaluation is known to be less precise than the MTS assay due to counting errors that may be involved, the obtained results were generally in agreement with the MTS data. On one hand, the highest concentration tested of ectosome collagen presented the highest percentage of viable cells. On the other hand, the highest concentration tested of choanosome collagen had the lowest number of live

cells, a detrimental effect detected at 48 h and 72 h. The inhibitory effect of this collagen at 2 mg/mL was obvious as the number of live cells was significantly lower at 48 h and barely increased from 48 h to 72 h. This reinforces the hypothesis that choanosome collagen was harmful to the cells tested.

## 3. Discussion

Although in recent years, some biomedical, cosmetical, and drug delivery applications have been developed using collagen from *Chondrosia reniformis*, an in-depth study of collagen isolated from distinct sponge body parts is still lacking [21,22,27,29]. The present work aims to clarify this overlooked issue, understanding the differences between these collagens and their effect on their biological performance.

Understanding collagen content, distribution, and type is crucial for the efficient use of a potential collagen source as well as to establish an adequate collagen isolation procedure. *C. reniformis*'s general morphological organization has previously been reported. However, no histological study focused on the sponge collagen content and distribution [18]. The examination of *C. reniformis* anatomy and overall microarchitecture allowed us to determine that the ectosome, although representing a smaller portion of the sponge's whole body, was richer in collagen than the choanosome (Figure 1), which is in agreement with previous observations [25,26,44]. Masson's Trichrome and Picrosirius red staining revealed that along with ectosome, the zone surrounding the canals of the aquiferous system present throughout the whole sponge body was an area of heavy collagen deposition (Figure 1C–F). These results are in accordance with previous observations, which demonstrate that collagen surrounding the water canals is required to support their intricate network [18,45]. Additionally, Picrosirius red staining revealed that collagen fibers were bright yellow and thicker in the ectosome and around the water canals, while in the choanosome, they were greenish and thinner (Figure 1E,F), and it has been described that type I collagen fibrils aggregate forming thick bundles while type IV collagen forms a web rather than fibrils, thus being thinner [46]. Furthermore, the dot blot results indicated that the mesohyl of ectosome possessed collagen type I and IV while the mesohyl of choanosome was mainly constituted by collagen type IV (Figure 3B). Taking all these data into account, it is clear that distinct *C. reniformis* body regions possess different collagen types; the ectosome is constituted by collagen types I and IV, while the choanosome is almost completely comprised of collagen type IV. We hypothesize that the residual amount of collagen type I detected in the choanosome is most likely the collagen surrounding and supporting the elements of the aquiferous system since the collagen fibers in those areas are thick, similar to those encountered in the ectosome. This had never been reported earlier and is valuable information for the development of future TERM applications since different tissues are constituted by distinct collagen types, and the biomaterials developed for regenerative purposes are more promising when matching the target tissue composition [5].

A comprehensive characterization of the isolated collagens is fundamental to comprehending their properties and purity, especially when aiming to employ them in biomaterials for TERM strategies. To be used in a biomaterial, collagen must undergo a strict characterization process to ensure it matches the requirements of the desired biomedical application. FTIR was performed to confirm the chemical composition of the isolated collagens, and both samples presented a similar spectrum (Figure 2A). In fact, both FTIR spectra are in accordance with previously published *C. reniformis* collagen spectra and are very similar to other previously described marine collagens obtained from other sources, indicating an apparent chemical composition conservation [23,24,26,47–50]. Curiously, *C. reniformis* collagen has been reported to have similar spectra to vertebrate collagen and, more specifically, to fibrillar calf skin type I collagen [24,26]. In the present work, collagen type I was detected by dot blot in ectosome and residually in choanosome, thus validating this observation.

The conservation of the triple helix conformation on both isolated collagens was confirmed via CD, assuring that the collagen isolation procedure employed did not denature the protein (Figure 2B). *C. reniformis* collagen CD spectra obtained from samples

isolated using water acidified with carbon dioxide did not present positive peaks, indicating the presence of random coils, which is known to diminish the performance of biological molecules [20,28,37,38]. In this sense, the *C. reniformis* collagen isolation protocol utilized in the present work is clearly advantageous as it preserves collagen triple helix conformation. Additionally, the CD spectra obtained in this study were in agreement with collagen spectra from other marine sponges, cnidarians, and vertebrates [51–53]. The amino acid composition of the isolated collagens was mostly similar, the most significant exceptions were OHpro content and the hydroxylation degree, which were higher in the ectosome collagen (Figure 2C). Pyrrolidine amino acids (Pro and OHpro) are associated with the collagen triple helix conformation thermal stability; thus, this result indicates that, theoretically, ectosome collagen had a higher thermal stability than choanosome collagen. However, this hypothesis must be confirmed using more specific techniques, such as thermogravimetric analysis or differential scanning calorimetry. Nonetheless, when considering employing collagen for biomedical applications it is quite beneficial to have higher thermal stability as this protein is structurally fundamental to support various connective tissues and is intended to be employed at body temperature [5,9]. In this sense, ectosome collagen could be preferred over choanosome collagen. Additionally, Gly is expected to be the most abundant amino acid, accounting for roughly one-third of the amino acid residues in mammal-derived collagen triple helix, as this is characterized by sequence repetitions of the triplets Gly-X-Y, where X and Y are often proline (Pro) and hydroxyproline (OHpro), respectively [54]. However, the values obtained for both collagens were lower, in line with previous observations [20,27,28], which can be explained by glycoproteins known to be strongly associated with collagen, the existence of non-collagenous spongin-specific proteins containing halogen groups or by major non-triple-helical sections in the analyzed collagen molecules [24,27,55]. Other previously reported amino acid profiles of *C. reniformis* collagen are in agreement with the obtained results, presenting remarkable similarities in nearly all amino acid contents, as the general composition is maintained [26,56]. The only exception regarding *C. reniformis* collagen amino acid composition was found in the work of Heinemann and co-workers, which presented much lower values of Gly and OHpro, probably due to the existence of major non-triple-helical sections in the collagen molecules as a result of the collagen isolation process employed [24]. The SDS-PAGE profiles of ectosome and choanosome collagens were similar, as both samples were only detected on the stacking gel (Figure 3A). Even though the separation gel was prepared with a low acrylamide composition (7.5%) to facilitate the sample's penetration, due to their heavy molecular weight, they were not able to migrate to the separation gel, indicating that both collagens preserved their fibrillar structure even after denaturation procedure have been applied. Similar results have been previously presented, in which *C. reniformis* collagen large fibrils remained trapped in the stacking gel [20,23]. However, other *C. reniformis* collagen SDS-PAGE profiles reported in the literature contrast with these results, presenting bands around 110 and 100 kDa [23,30]. These differences are attributed to different collagen isolation methods which do not preserve collagen in its fibrillar conformation, since Pozzolini and colleagues treated isolated collagen fibrils with trypsin to obtain collagen hydrolysates [30], while Fassini and co-workers, although using a similar protocol to the one employed in this work, significantly increased the *C. reniformis* incubation time in disaggregation solution [23]. Additionally, as previously described, Coomassie blue was not able to stain the collagen samples; staining was only achieved with a glycoprotein staining kit, indicating the highly glycosylated nature of the collagen [23]. High glycosylation levels are known to demonstrate interesting bioactivities such as antioxidant and antimicrobial, further suggesting the benefits of *C. reniformis* collagen for TERM applications [57].

Despite it being reported that *C. reniformis* possesses collagen similar to type I and IV, no specific antibody detection has been performed so far. In the present work, it was demonstrated by dot blot that ectosome collagen was composed of collagen type I and IV, while choanosome collagen was mostly composed of collagen type IV, having only residual amounts of collagen type I, whereas type II collagen was not detected in either body part

(Figure 3B). The FTIR spectra similarity between *C. reniformis* collagen extracted from the whole body and bovine type I collagen proposed by Heinemann et al. was presently validated, although this collagen type was detected predominantly in the ectosome [24]. The previously reported high structural resemblance of the non-fibrillar collagen encoded in *C. reniformis* to type IV basement membrane collagen was also supported by the dot blot results [25]. The previously reported findings state that non-fibrillar collagen presented a higher expression in ectosomes than in choanosomes, seeming to be involved in the formation of the *C. reniformis* ectosome [25]. In fact, genomic studies have detected collagen type IV sequences in a homoscleromorph sponge [58]. Accordingly, in the obtained dot blot results, collagen type IV appeared to be present in a higher quantity in ectosome than in choanosome collagen, with a slight concentration difference among both sponge body parts. The collagen isolation yield was similar in both sponge body parts, although it could be expected that the yield from ectosome would be superior since it has been characterized as possessing higher amounts of both fibrillar and non-fibrillar collagen than choanosome [25,26,44]. This could be due to the distinct accessibility of collagen in the different sponge body parts, as the ectosome presents a densely packed collagen matrix that possibly does not allow effective collagen isolation, while in the choanosome, the collagen matrix is looser and easily accessible. Nonetheless, the obtained yield of around 20% was identical to other *C. reniformis* collagen isolation results reported in the literature [29]. Using a similar collagen isolation procedure, Gokalp and colleagues obtained yield values ranging from 14.5% to 35.5% when isolating collagen from *C. reniformis* aquacultured under different conditions [59], while water and carbon dioxide collagen extraction procedures using this marine sponge, although faster, reported an isolation yield merely around 10% [20,28]. Additionally, Pozzolini and co-workers compared different *C. reniformis* collagen isolation methods and obtained yields ranging from 0.02% to 35% [22]. Considering that it has been determined that 30% of the *C. reniformis* freeze-dried mass is collagen, the collagen yield values reported in the current work are promising [27]. Although not being the highest yield reported in the literature, the fact that intact and highly glycosylated collagen fibers were obtained employing this collagen isolation protocol is extremely valuable. The possibility of obtaining intact collagen fibers from this marine sponge, together with its high collagen content and sustainable mariculture, makes it an attractive collagen source. These results conclusively elucidate the location and prevalence of the collagen types present in *C. reniformis*, an important step toward the valorization of this important marine collagen source, supporting the future development of tissue-specific biomedical applications.

The biological performance evaluation of the isolated collagens is essential to determine their applicability for the development of TERM strategies. In that sense, the cytotoxicity of both isolated collagens was determined (Figures 4 and 5). All ectosome collagen concentrations tested were suitable for fibroblast culture, presenting an increase in cell metabolic activity and live cells over time. In fact, higher concentrations of this collagen had a better biological performance than the control. In these cases, it was determined that it was a suitable and highly promising biomaterial for the development of TERM applications due to its beneficial action on cell metabolism and proliferation. However, using choanosome collagen, the lower cell metabolic activity and number of live cells detected when compared with the control was not encouraging. This adverse effect was observed mostly at 72 h and aggravated with the highest collagen concentration tested, as with 2 mg/mL, the inhibitory effect on the number of live cells and on cell metabolism was pronounced. Since this negative impact on cell metabolic activity was correlated with collagen concentration it may be associated with the presence of cytotoxic compounds in the extract. In fact, marine sponges are widely recognized as a source of cytotoxic compounds with potential antitumoral interest [60]. It has been previously described as the identification of a novel cytotoxic protein present in *C. reniformis*, designated chondrosin, which has selective activity against specific tumor cell lines, including L929 [61]. The extract from which this protein was isolated was obtained from the whole sponge, where choanosome mass is predominant, which may explain the fact that the cytotoxic effect was only detected

in the choanosome collagen. Nonetheless, the presence of harmful compounds should not be considerable since the cytotoxic effect was more severely detected in the highest choanosome concentration tested. However, it can be assumed that the cytotoxic effect will be intensified at higher concentrations. Collagen isolated from the whole *C. reniformis* body using carbon dioxide and acidified water did not present any cytotoxic effect, suggesting that this isolation technique probably denatures chondrosin and other possible cytotoxic compounds, as it also destroys the triple helix conformation of the isolated collagen [20]. Marine collagen hydrolysates obtained from *C. reniformis* collagen extracts purified by HPLC have been tested in vitro for wound-healing application with fibroblasts and keratinocytes and showed no degree of toxicity, stimulating cell growth [30]. Additionally, *C. reniformis* collagen-based membranes have been developed and considered suitable for TERM purposes, as they showed compatibility with both fibroblast and keratinocyte cell cultures [22,29]. These membranes were produced using collagen isolated from the whole sponge body; however, it was necessary to partially remove some of the polysaccharidic components that were co-extracted with sponge collagen to improve the biocompatibility of the structures [22,29]. These observations are in agreement with our findings since the described carbon dioxide and acidified water collagen isolation is a harsh process likely to destroy some compounds during the procedure, the collagen hydrolysates were HPLC-purified, thus having no other possibly cytotoxic compounds present, and the collagen used to produce the membranes, although isolated from the whole sponge body, which is mainly constituted by choanosome mass, required an extra purification step to improve biocompatibility.

Altogether, our data demonstrate that there are significant differences between collagen isolated from different body regions of *C. reniformis*. The most relevant dissimilarities were ectosome-derived collagen being constituted by collagen type I and IV and presenting cytocompatibility on fibroblast culture, while choanosome-derived collagen was mainly composed of collagen type IV and presented marked cytotoxic effects at 2 mg/mL concentration. The identification of different collagen types and their location is critical for the development of specific TERM applications aimed at different tissues. For instance, the presence of collagen type I may be beneficial for bone regeneration strategies, while collagen type IV may be advantageous for skin regeneration applications.

## 4. Materials and Methods

### *4.1. Reagents*

All reagents were purchased from Sigma-Aldrich (St. Louis, MO, USA) unless otherwise stated.

### *4.2. Sample Collection and Storage*

*C. reniformis* were collected by snorkeling near the Marine Station Endoume, Marseille, France, from a depth of 4 m, fixed in 4% formaldehyde in seawater, and transported to the facilities of the University of Minho, Portugal, for further histological analysis. *C. reniformis* collected by snorkeling at Pina Reef in Kas-Kekova Special Environmental Protected Area, Turkey, from a depth of 5 and 20 m, were provided by partners of Wageningen University & Research, Wageningen, The Netherlands, frozen and transported in dry ice containers to the facilities of University of Minho, Portugal, where they were stored at −20 °C until further use for collagen isolation.

### *4.3. C. reniformis Histological Characterization*

Specimens were fixed overnight by 4% formaldehyde in seawater at 4 °C. Histological sections specimens comprising the sponge's whole body, thus including the ectosome (outer cortex) and choanosome (inner part), were embedded in paraffin wax and cut on a Leica RM2255 Fully Automated Rotary Microtome (Leica, Wetzlar, Germany) at 10 μm. Cross-transversal paraffin sections were stained with Hematoxylin-eosin (H&E) for tissues' general overview and with Masson's trichome and Picrosirius Red (Abcam, Cambridge,

UK) for specific collagen observation [62,63]. Masson's trichome stains collagen blue and cytoplasm red; Picrosirius Red stains collagen green, red, or yellow under polarized light, depending on fiber thickness and packing [62,64]. H&E and Masson's trichome-stained semi-thin sections were observed under a Leica DM750 microscope (Leica, Wetzlar, Germany), and Picrosirius red stained semi-thin sections were observed with an Axio Observer (Carl Zeiss, Jena, Germany) under polarized light.

### *4.4. Collagen Isolation*

Ectosome and choanosome collagen isolation were performed separately, using a methodology previously described [59]. Briefly, marine sponge samples were thawed, exogenous materials were removed via rinsing with $dH_2O$, and the ectosome was separated from the choanosome, cut into small pieces, and left under stirring in a disaggregating solution (50 mM Tris–HCl buffer pH 7.4, 1 M NaCl, 50 mM EDTA, and 100 mM 2-mercaptoethanol) for 5 days. The collagen solution (CS) was filtered and extensively dialyzed for 7 days with 2 dialyzing buffer changes per day (CS/dialyzing buffer ratio 1:1000) against $dH_2O$. The suspension was first centrifuged for 10 min at 1200× *g* to further remove cell debris, sand particles, and other exogenous materials and then centrifuged for 30 min at 12,100× *g* to collect the collagen from the suspension, yielding pellets containing collagen. All steps for collagen extraction were carried out at 4 °C. Isolated collagen was freeze-dried and stored at room temperature until further use.

### *4.5. C. reniformis Collagen Characterization*

#### 4.5.1. Fourier Transform Infrared in Attenuated Total Reflection Mode (FTIR-ATR)

Infrared spectra of collagens were obtained via Fourier transform infrared spectroscopy (FTIR) under attenuated total reflectance (ATR) using freeze-dried collagen. FTIR-ATR measurements were performed employing an IR-Prestige-21 spectrophotometer (Shimadzu Scientific Instruments, Columbia, MD, USA) equipped with a diamond crystal. Each infrared spectrum was an average of 32 scans collected at 2 $cm^{-1}$ resolution in the wavenumber region of 4000–500 $cm^{-1}$ at room temperature.

#### 4.5.2. Circular Dichroism

To determine the protein conformation of the isolated collagen, circular dichroism (CD) analysis was performed (J1500 CD spectrometer, Jasco, Tokyo, Japan) using a quartz cylindrical cuvette with a path length of 2 mm (Hellma Analytics, Hellma, Germany). For each measurement, the cuvette was filled with 600 µL of 0.1 mg/mL collagen dissolved in $dH_2O$. CD spectra were obtained by continuous wavelength scans from 180 to 240 nm (average of three scans) at a scan rate of 50 nm/min.

#### 4.5.3. Amino Acid Analysis

The amino acid content of collagen was determined via quantitative analysis using a Biochrome 30 amino acid analyzer (Biochrome Ltd., Cambridge, UK). Briefly, the collagen was completely hydrolyzed, and the resultant amino acids were separated by an Ion Exchange column. After derivatization by ninhydrin, the obtained samples were analyzed at two wavelengths: 440 nm and 570 nm. To determine the concentration of amino acids in the sample, a norleucine standard was used. The percentage of collagen hydroxylation was calculated according to the following equation, in which pyrrolidine amino acid content was the sum of hydroxyproline (OHpro) and proline (Pro) amino acids:

$$\text{Hydroxylation } (\%) = \frac{\text{OHpro content}}{\text{pyrrolidine amino acid content}} \times 100$$

#### 4.5.4. Sodium Dodecyl Sulfate-Polyacrylamide Gel Electrophoresis (SDS-PAGE)

To evaluate protein molecular weight and purity, SDS-PAGE was performed using reagents from the SDS-PAGE Gel Preparation Kit and cast on a Bio-Rad Mini Protean II

System (Bio-Rad, Hercules, CA, USA). Freeze-dried collagen solubilized in deionized water ($dH_2O$) at 1 mg/mL was mixed with loading buffer (1:1 $v/v$) and heated for 2 min at 100 °C to denature the proteins. The SDS gel was composed of 7.5% separation and 4% stacking gel and was loaded with 20 µg of each collagen sample as well as 4 µL of protein marker (Page Ruler Prestained protein ladder, 10 to 250 kDa—Thermo Fisher Scientific, Waltham, MA, USA). After electrophoresis at 90 V, Glycoprotein Stain (Pierce® Glycoprotein Staining Kit—Thermo Fisher Scientific, Waltham, MA, USA) was performed according to the manufacturer's instructions to stain glycosylated proteins.

#### 4.5.5. Dot Blot

To detect the presence of collagen type I, II, and IV on the isolated collagen samples, a dot blot analysis was performed. Collagen samples were dissolved at 1 mg/mL in $dH_2O$, and 1, 2, and 3 µL drops were spotted onto a nitrocellulose membrane. For a negative control, the same amounts of bovine serum albumin (BSA) were also dotted in the membrane. Non-specific sites were blocked by soaking the membranes in 5% bovine serum albumin (BSA) dissolved in Tris-buffered saline with Tween 20 (TBS-T) solution. The primary antibodies used were Anti-Collagen I antibody (ab233639, Abcam, Cambridge, UK), Anti-Collagen II (ab209865, Abcam, Cambridge, UK) and Anti-Collagen IV antibody (ab6586, Abcam, Cambridge, UK), which were conjugated with adequate secondary antibody (Anti-rabbit IgG, HRP-linked Antibody, Cell Signaling Technology, Danvers, MA, USA). Primary antibodies and secondary antibodies were diluted at a ratio of 1:1000 and 1:20,000, respectively. Chemiluminescence detection was performed using the Clarity Western ECL substrate (Bio-Rad, Hercules, CA, USA) and the Odyssey Fc Imaging System (LI-COR Biosciences, Lincoln, NE, USA).

#### 4.5.6. Isolation Yield

The isolation yield was calculated for both collagen parts (ectosome and choanosome) as the ratio of freeze-dried collagen isolated per wet weight of *C. reniformis* biomass, according to the following equation:

$$\text{Yield of collagen } (\%) = \frac{\text{weight of collagen (g)}}{\text{weight of wet } C.\ reniformis \text{ biomass (g)}} \times 100$$

#### 4.5.7. In Vitro Cytotoxicity Assessment

In vitro cellular assays were performed to assess the potential cytotoxicity of *C. reniformis* collagen isolated from ectosome and choanosome. Murine fibroblasts cells (L929 cell line; ATCC CCL-1) were maintained in Dulbecco's Modified Eagle's Medium (DMEM) low glucose supplemented with sodium bicarbonate (3.7 g/L), 10% fetal bovine serum (FBS) (Thermo Fisher Scientific, Waltham, MA, USA), 1% antibiotic–antimycotic solution (Thermo Fisher Scientific, Waltham, MA, USA) and in a humidified controlled environment (37 °C, 5% $CO_2$). Before confluence, cells were trypsinized using TrypLE Express (Thermo Fisher Scientific, Waltham, MA, USA), and $1 \times 10^4$ cells/well were seeded in 48-well plates. To avoid microbial contamination, powdered collagen extracts were sterilized using ultraviolet irradiation for 1 h, dissolved in the complete medium at different concentrations (0.25, 0.5, 1, and 2 mg/mL), and added to cells 24 h after seeding. A negative control (untreated cells) was incubated under the same conditions.

The metabolic activity of cells after incubation with collagen extracts was determined by the MTS assay (CellTiter 96 Aqueous One Solution Cell Proliferation Assay, Promega, Madison, WI, USA). After 24, 48, and 72 h of incubation, the culture medium was removed, and cells were rinsed in PBS. A mixture of culture medium (without FBS and phenol red) and MTS reagent (5:1 ratio) was added to each well and left to incubate for 3 h in a humidified atmosphere (37 °C, 5% $CO_2$). Absorbance intensity is directly proportional to the metabolic activity and was measured at 490 nm using a microplate reader (Synergy HT, Biotek, Winooski, VT, USA).

Cell viability after incubation with collagen extracts was assessed by live/dead assay. Calcein-AM (Thermo Fisher Scientific, Waltham, MA, USA) and propidium iodide (PI) staining were performed after 24, 48, and 72 h of incubation with collagen extracts. Briefly, the culture medium was removed, and calcein-AM and PI at a final concentration of 1 μg/mL and 5 μg/mL in the culture medium, respectively, were added to cells. After 10 min in the dark at 37 °C in the $CO_2$ incubator, samples were immediately examined using a Zeiss Axio Imager Z1 fluorescence microscope (Carl Zeiss, Jena, Germany). Cell viability (%) was calculated by counting the live cells on the 48-well plates with reference to the counted live cells of control at 24 h generated by LAS X Image Analysis (3D) software (version 3.0.16120) and using the following equation:

$$\text{Cell viability } (\%) = \left( \frac{\text{Live cells (green)}}{\text{Live cells(green) of control at 24 h}} \right) \times 100$$

The quantification results were presented as mean ± SD of 3 independent experiments with 2 replicates and at least 3 images per replicate.

### *4.6. Statistical Analysis*

Data were presented as the mean ± standard deviation (SD) of three independent experiments. Statistical analyses were performed using GraphPad Prism 8.0.1 software (La Jolla, CA, USA). For cytotoxicity assays, data normality was evaluated by the Shapiro–Wilk test. For the two-group comparison, a two-way ANOVA test was performed, followed by Tukey's test. Statistical significance was defined as *p*-value less than 0.05 ($p < 0.05$).

## 5. Conclusions

For the first time, an in-depth evaluation of collagen isolated from different body zones of the collagen-rich marine sponge *Chondrosia reniformis* was performed. The collagen isolation procedure presented a similar isolation yield, and both collagens displayed equivalent FTIR spectra and were isolated in their fibrillar form while preserving their triple helix conformation. However, ectosome collagen had a higher hydroxylation degree than choanosome collagen, which may confer greater thermal stability and was composed of collagen type I and IV, while choanosome collagen was composed mostly of collagen type IV. Nevertheless, the most striking distinction between both isolated collagens was regarding their biological performance. Ectosome collagen enhanced cell metabolic activity and proliferation, an effect more evident at higher concentrations, whereas choanosome collagen had the opposite impact. There was an inhibitory effect detected at all tested concentrations, but at 2 mg/mL, the cytotoxic effect on cell metabolism and proliferation was severe. These data indicate that ectosome collagen was the most suitable for the production of TERM applications due to its biocompatibility, while choanosome collagen may be advantageous for designing novel cancer therapies due to its harmful effect on tumor cell lines. This information is essential to support and encourage the development of future biomedical applications using this sustainable collagen source. Future studies should include the development of TERM applications using ectosome-derived collagen, particularly scaffolds for the tridimensional culture of cells, thus assessing its suitability for human tissue engineering, enabling the valorization of marine resources in the context of blue biotechnology.

**Author Contributions:** M.S.R. and T.H.S. designed the experimental study and methodology; A.E. collected *C. reniformis* samples and assisted in the histological analyses; M.S.R., C.F.M., A.C.C. and E.M. executed the experimental investigation work; M.S.R. wrote the original draft of the manuscript; all authors were responsible for review and editing; T.H.S. was responsible for supervision and for the project administration; R.L.R. and T.H.S. were responsible for funding acquisition. All authors have read and agreed to the published version of the manuscript.

**Funding:** The authors would like to acknowledge the Foundation of Science and Technology (FCT) for a Ph.D. fellowship (M.S.R.) under the scope of the doctoral program Do*Mar, ref. PD/BD/143091/2018,

the investigator contract of C.F.M. (CEECIND/04687/2017). Funding from the European Regional Development Fund (ERDF) via the North Portugal Regional Operational Program (NORTE2020), part of the PORTUGAL2020 Partnership Agreement, under the structured program of R&D&I ATLANTIDA—Platform for the monitoring of the North Atlantic Ocean and tools for the sustainable exploitation of the marine resources (NORTE-01-0145-FEDER-000040), and under the R&D Infrastructure TERM RES-Hub (Norte-01-0145-FEDER-022190), with co-funding from FCT (PINFRA/22190/2016), is also gratefully acknowledged. The authors would also like to thank the support from the COST Action CA16203: MARISTEM—Stem cells of marine/aquatic invertebrates: from basic research to innovative applications.

**Institutional Review Board Statement:** Not applicable.

**Data Availability Statement:** The data presented in this study are available on request from the corresponding author due to privacy reasons.

**Acknowledgments:** The authors acknowledge Mert Gokalp and Ronald Osinga (Wageningen University and Research Centre, Wageningen, The Netherlands) for providing *C. reniformis* biomass for collagen isolation, Rita Sousa (3B's Research Group, University of Minho, Guimaraes, Portugal) for helping to perform the statistical analyses and Teresa Oliveira (3B's Research Group, University of Minho, Guimaraes, Portugal) for performing histological processing.

**Conflicts of Interest:** The authors declare no conflict of interest.

## References

1. Shoulders, M.D.; Raines, R.T. Collagen Structure and Stability. *Annu. Rev. Biochem.* **2009**, *78*, 929–958. [CrossRef] [PubMed]
2. Czirók, A.; Rongish, B.J.; Little, C.D. Extracellular Matrix Dynamics during Vertebrate Axis Formation. *Dev. Biol.* **2004**, *268*, 111–122. [CrossRef] [PubMed]
3. Di Lullo, G.A.; Sweeney, S.M.; Körkkö, J.; Ala-Kokko, L.; San Antonio, J.D. Mapping the Ligand-Binding Sites and Disease-Associated Mutations on the Most Abundant Protein in the Human, Type I Collagen. *J. Biol. Chem.* **2002**, *277*, 4223–4231. [CrossRef] [PubMed]
4. Junqueira, L.C.U.; Montes, G.S. Biology of Collagen-Proteoglycan Interaction. *Arch. Histol. Jpn.* **1983**, *46*, 589–629. [CrossRef] [PubMed]
5. Rezvani Ghomi, E.; Nourbakhsh, N.; Akbari Kenari, M.; Zare, M.; Ramakrishna, S. Collagen-Based Biomaterials for Biomedical Applications. *J. Biomed. Mater. Res. Part B Appl. Biomater.* **2021**, *109*, 1986–1999. [CrossRef] [PubMed]
6. Capella, G.L. Foot and Mouth Disease in Human Beings. *Lancet* **2001**, *358*, 1374. [CrossRef] [PubMed]
7. Zhang, L.; Niu, X.; Sun, L.; She, Z.; Tan, R.; Wang, W. Immune Response of Bovine Sourced Cross-Linked Collagen Sponge for Hemostasis. *J. Biomater. Appl.* **2018**, *32*, 920–931. [CrossRef]
8. Sorushanova, A.; Delgado, L.M.; Wu, Z.; Shologu, N.; Kshirsagar, A.; Raghunath, R.; Mullen, A.M.; Bayon, Y.; Pandit, A.; Raghunath, M.; et al. The Collagen Suprafamily: From Biosynthesis to Advanced Biomaterial Development. *Adv. Mater.* **2019**, *31*, 1801639–1801651. [CrossRef]
9. Lim, Y.S.; Ok, Y.J.; Hwang, S.Y.; Kwak, J.Y.; Yoon, S. Marine Collagen as a Promising Biomaterial for Biomedical Applications. *Mar. Drugs* **2019**, *17*, 467. [CrossRef]
10. Ferrario, C.; Rusconi, F.; Pulaj, A.; Macchi, R.; Landini, P.; Paroni, M.; Colombo, G.; Martinello, T.; Melotti, L.; Gomiero, C.; et al. From Food Waste to Innovative Biomaterial: Sea Urchin-Derived Collagen for Applications in Skin Regenerative Medicine. *Mar. Drugs* **2020**, *18*, 414. [CrossRef]
11. Alves, A.L.; Fraguas, F.J.; Carvalho, A.C.; Valcárcel, J.; Pérez-Martín, R.I.; Reis, R.L.; Vázquez, J.A.; Silva, T.H. Characterization of Codfish Gelatin: A Comparative Study of Fresh and Salted Skins and Different Extraction Methods. *Food Hydrocoll.* **2022**, *124*, 107238. [CrossRef]
12. Gökalp, M.; Wijgerde, T.; Murk, A.; Osinga, R. Design for Large-Scale Maricultures of the Mediterranean Demosponge Chondrosia Reniformis Nardo, 1847 for Collagen Production. *Aquaculture* **2022**, *548*, 737702. [CrossRef]
13. Diogo, G.S.; Marques, C.F.; Sotelo, C.G.; Pérez-Martín, R.I.; Pirraco, R.P.; Reis, R.L.; Silva, T.H. Cell-Laden Biomimetically Mineralized Shark-Skin-Collagen-Based 3D Printed Hydrogels for the Engineering of Hard Tissues. *ACS Biomater. Sci. Eng.* **2020**, *6*, 3664–3672. [CrossRef]
14. Alves, A.L.; Marques, A.L.P.; Martins, E.; Silva, T.H.; Reis, R.L. Cosmetic Potential of Marine Fish Skin Collagen. *Cosmetics* **2017**, *4*, 39. [CrossRef]
15. Martins, E.; Rocha, M.S.; Silva, T.H.; Reis, R.L. Remarkable Body Architecture of Marine Sponges as Biomimetic Structure for Application in Tissue Engineering. *Springer Ser. Biomater. Sci. Eng.* **2019**, *14*, 27–50. [CrossRef]
16. Langasco, R.; Cadeddu, B.; Formato, M.; Lepedda, A.J.; Cossu, M.; Giunchedi, P.; Pronzato, R.; Rassu, G.; Manconi, R.; Gavini, E. Natural Collagenic Skeleton of Marine Sponges in Pharmaceutics: Innovative Biomaterial for Topical Drug Delivery. *Mater. Sci. Eng. C* **2017**, *70*, 710–720. [CrossRef] [PubMed]
17. Lazoski, C.; Solé-Cava, A.M.; Boury-Esnault, N.; Klautau, M.; Russo, C.A.M. Cryptic Speciation in a High Gene Flow Scenario in the Oviparous Marine Sponge Chondrosia Reniformis. *Mar. Biol.* **2001**, *139*, 421–429. [CrossRef]

18. Bonasoro, F.; Wilkie, I.C.; Bavestrello, G.; Cerrano, C.; Candia Carnevali, M.D. Dynamic Structure of the Mesohyl in the Sponge Chondrosia Reniformis (Porifera, Demospongiae). *Zoomorphology* **2001**, *121*, 109–121. [CrossRef]
19. Fassini, D.; Parma, L.; Lembo, F.; Candia Carnevali, M.D.; Wilkie, I.C.; Bonasoro, F. The Reaction of the Sponge Chondrosia Reniformis to Mechanical Stimulation Is Mediated by the Outer Epithelium and the Release of Stiffening Factor(S). *Zoology* **2014**, *117*, 282–291. [CrossRef] [PubMed]
20. Silva, J.C.; Barros, A.A.; Aroso, I.M.; Fassini, D.; Silva, T.H.; Reis, R.L.; Duarte, A.R.C. Extraction of Collagen/Gelatin from the Marine Demosponge Chondrosia Reniformis (Nardo, 1847) Using Water Acidified with Carbon Dioxide—Process Optimization. *Ind. Eng. Chem. Res.* **2016**, *55*, 6922–6930. [CrossRef]
21. Swatschek, D.; Schatton, W.; Müller, W.E.G.; Kreuter, J. Microparticles Derived from Marine Sponge Collagen (SCMPs): Preparation, Characterization and Suitability for Dermal Delivery of All-Trans Retinol. *Eur. J. Pharm. Biopharm.* **2002**, *54*, 125–133. [CrossRef]
22. Pozzolini, M.; Scarfì, S.; Gallus, L.; Castellano, M.; Vicini, S.; Cortese, K.; Gagliani, M.C.; Bertolino, M.; Costa, G.; Giovine, M. Production, Characterization and Biocompatibility Evaluation of Collagen Membranes Derived from Marine Sponge Chondrosia Reniformis Nardo, 1847. *Mar. Drugs* **2018**, *16*, 111. [CrossRef] [PubMed]
23. Fassini, D.; Duarte, A.R.C.; Reis, R.L.; Silva, T.H. Bioinspiring Chondrosia Reniformis (Nardo, 1847) Collagen-Based Hydrogel: A New Extraction Method to Obtain a Sticky and Self-Healing Collagenous Material. *Mar. Drugs* **2017**, *15*, 380. [CrossRef]
24. Heinemann, S.; Ehrlich, H.; Douglas, T.; Heinemann, C.; Worch, H.; Schatton, W.; Hanke, T. Ultrastructural Studies on the Collagen of the Marine Sponge Chondrosia Reniformis Nardo. *Biomacromolecules* **2007**, *8*, 3452–3457. [CrossRef] [PubMed]
25. Pozzolini, M.; Bruzzone, F.; Berilli, V.; Mussino, F.; Cerrano, C.; Benatti, U.; Giovine, M. Molecular Characterization of a Nonfibrillar Collagen from the Marine Sponge Chondrosia Reniformis Nardo 1847 and Positive Effects of Soluble Silicates on Its Expression. *Mar. Biotechnol.* **2012**, *14*, 281–293. [CrossRef]
26. Garrone, R.; Huc, A.; Junqua, S. Fine Structure and Physicochemical Studies on the Collagen of the Marine Sponge Chondrosia Reniformis Nardo. *J. Ultrasruct. Res.* **1975**, *52*, 261–275. [CrossRef] [PubMed]
27. Swatschek, D.; Schatton, W.; Kellermann, J.; Müller, W.E.G.; Kreuter, J. Marine Sponge Collagen: Isolation, Characterization and Effects on the Skin Parameters Surface-PH, Moisture and Sebum. *Eur. J. Pharm. Biopharm.* **2002**, *53*, 107–113. [CrossRef] [PubMed]
28. Barros, A.A.; Aroso, I.M.; Silva, T.H.; Mano, J.F.; Duarte, A.R.C.; Reis, R.L. Water and Carbon Dioxide: Green Solvents for the Extraction of Collagen/Gelatin from Marine Sponges. *ACS Sustain. Chem. Eng.* **2015**, *3*, 254–260. [CrossRef]
29. Tassara, E.; Oliveri, C.; Vezzulli, L.; Cerrano, C.; Xiao, L.; Giovine, M.; Pozzolini, M. 2D Collagen Membranes from Marine Demosponge Chondrosia Reniformis (Nardo, 1847) for Skin-Regenerative Medicine Applications: An In Vitro Evaluation. *Mar. Drugs* **2023**, *21*, 428. [CrossRef]
30. Pozzolini, M.; Millo, E.; Oliveri, C.; Mirata, S.; Salis, A.; Damonte, G.; Arkel, M.; Scarfì, S. Elicited ROS Scavenging Activity, Photoprotective, and Wound-Healing Properties of Collagen-Derived Peptides from the Marine Sponge Chondrosia Reniformis. *Mar. Drugs* **2018**, *16*, 465. [CrossRef]
31. Bavestrello, G.; Cerrano, C.; Cattaneo-Vietti, R.; Sara, M.; Calabria, F.; Cortesogno, L. Selective Incorporation of Foreign Material in Chondrosia Reniformis (Porifera, Demospongiae). *Ital. J. Zool.* **1996**, *63*, 215–220. [CrossRef]
32. López De Padilla, C.M.; Coenen, M.J.; Tovar, A.; De la Vega, R.E.; Evans, C.H.; Müller, S.A. Picrosirius Red Staining: Revisiting Its Application to the Qualitative and Quantitative Assessment of Collagen Type I and Type III in Tendon. *J. Histochem. Cytochem.* **2021**, *69*, 633–643. [CrossRef] [PubMed]
33. Cao, H.; Xu, S.Y. Purification and Characterization of Type II Collagen from Chick Sternal Cartilage. *Food Chem.* **2008**, *108*, 439–445. [CrossRef]
34. Sun, L.; Hou, H.; Li, B.; Zhang, Y. Characterization of Acid- and Pepsin-Soluble Collagen Extracted from the Skin of Nile Tilapia (Oreochromis Niloticus). *Int. J. Biol. Macromol.* **2017**, *99*, 8–14. [CrossRef] [PubMed]
35. Yang, H.; Wang, H.; Zhao, Y.; Wang, H.; Zhang, H. Effect of Heat Treatment on the Enzymatic Stability of Grass Carp Skin Collagen and Its Ability to Form Fibrils in Vitro. *J. Sci. Food Agric.* **2015**, *95*, 329–336. [CrossRef] [PubMed]
36. Engel, J.; Bächinger, H.P. Structure, Stability and Folding of the Collagen Triple Helix. *Top. Curr. Chem.* **2005**, *247*, 7–33. [CrossRef]
37. Greenfield, N.J. Using Circular Dichroism Spectra to Estimate Protein Secondary Structure. *Nat. Protoc.* **2007**, *1*, 2876–2890. [CrossRef]
38. Brodsky, B.; Ramshaw, J.A.M. The Collagen Triple-Helix Structure. *Matrix Biol.* **1997**, *15*, 545–554. [CrossRef]
39. Gorres, K.L.; Raines, R.T. Prolyl 4-Hydroxylase. *Crit. Rev. Biochem. Mol. Biol.* **2010**, *45*, 106–124. [CrossRef]
40. Leuenberger, B.H. Investigation of Viscosity and Gelation Properties of Different Mammalian and Fish Gelatins. *Top. Catal.* **1991**, *5*, 353–361. [CrossRef]
41. Sipila, K.H.; Drushinin, K.; Rappu, P.; Jokinen, J.; Salminen, T.A.; Salo, A.M.; Käpyla, J.; Myllyharju, J.; Heino, J. Proline Hydroxylation in Collagen Supports Integrin Binding by Two Distinct Mechanisms. *J. Biol. Chem.* **2018**, *293*, 7645–7658. [CrossRef] [PubMed]
42. Liu, W.; Tian, Z.; Li, C.; Li, G. Thermal Denaturation of Fish Collagen in Solution: A Calorimetric and Kinetic Analysis. *Thermochim. Acta* **2014**, *581*, 32–40. [CrossRef]
43. Gelse, K.; Pöschl, E.; Aigner, T. Collagens—Structure, Function, and Biosynthesis. *Adv. Drug Deliv. Rev.* **2003**, *55*, 1531–1546. [CrossRef]

44. Bavestrello, G.; Benatti, U.; Calcinai, B.; Cattaneo-Vietti, R.; Cerrano, C.; Favre, A.; Giovine, M.; Lanza, S.; Pronzato, R.; Sara, M. Body Polarity and Mineral Selectivity in the Demosponge Chondrosia Reniformis. *Biol. Bull.* **1998**, *195*, 120–125. [CrossRef] [PubMed]
45. Harrison, F.W. Phylogenesis of Connective Tissue. Morphological Aspects and Biosynthesis of Sponge Intercellular Matrix. Robert Garrone. *Q. Rev. Biol.* **1979**, *54*, 468–469. [CrossRef]
46. Stecco, C.; Hammer, W.; Vleeming, A.; De Caro, R. *Functional Atlas of the Human Fascial System*; Elsevier Health Sciences: Amsterdam, The Netherlands, 2015; ISBN 9780702044304.
47. Pati, F.; Adhikari, B.; Dhara, S. Isolation and Characterization of Fish Scale Collagen of Higher Thermal Stability. *Bioresour. Technol.* **2010**, *101*, 3737–3742. [CrossRef] [PubMed]
48. Hoyer, B.; Bernhardt, A.; Heinemann, S.; Stachel, I.; Meyer, M.; Gelinsky, M. Biomimetically Mineralized Salmon Collagen Scaffolds for Application in Bone Tissue Engineering. *Biomacromolecules* **2012**, *13*, 1059–1066. [CrossRef]
49. Duan, R.; Zhang, J.; Du, X.; Yao, X.; Konno, K. Properties of Collagen from Skin, Scale and Bone of Carp (Cyprinus Carpio). *Food Chem.* **2009**, *112*, 702–706. [CrossRef]
50. Araújo, T.A.T.; de Souza, A.; Santana, A.F.; Braga, A.R.C.; Custódio, M.R.; Simões, F.R.; Araújo, G.M.; Miranda, A.; Alves, F.; Granito, R.N.; et al. Comparison of Different Methods for Spongin-like Collagen Extraction from Marine Sponges (Chondrilla Caribensis and Aplysina Fulva): Physicochemical Properties and in Vitro Biological Analysis. *Membranes* **2021**, *11*, 522. [CrossRef]
51. Tziveleka, L.A.; Ioannou, E.; Tsiourvas, D.; Berillis, P.; Foufa, E.; Roussis, V. Collagen from the Marine Sponges Axinella Cannabina and Suberites Carnosus: Isolation and Morphological, Biochemical, and Biophysical Characterization. *Mar. Drugs* **2017**, *15*, 152. [CrossRef]
52. Sousa, R.O.; Alves, A.L.; Carvalho, D.N.; Martins, E.; Oliveira, C.; Silva, T.H.; Reis, R.L. Acid and Enzymatic Extraction of Collagen from Atlantic Cod (Gadus Morhua) Swim Bladders Envisaging Health-Related Applications. *J. Biomater. Sci. Polym. Ed.* **2020**, *31*, 20–37. [CrossRef] [PubMed]
53. Smith, I.P.; Domingos, M.; Richardson, S.M.; Bella, J. Characterization of the Biophysical Properties and Cell Adhesion Interactions of Marine Invertebrate Collagen from Rhizostoma Pulmo. *Mar. Drugs* **2023**, *21*, 59. [CrossRef] [PubMed]
54. Ramshaw, J.A.M.; Shah, N.K.; Brodsky, B. Gly-X-Y Tripeptide Frequencies in Collagen: A Context for Host-Guest Triple-Helical Peptides. *J. Struct. Biol.* **1998**, *122*, 86–91. [CrossRef] [PubMed]
55. Junqua, S.; Lemonnier, M.; Robert, L. Glycoconjugates from "Spongia Officinalis" (Phylum Porifera). Isolation, Fractionation by Affinity Chromatography on Lectins and Partial Characterization. *Comp. Biochem. Physiol.—Part B Biochem.* **1981**, *69*, 445–453. [CrossRef]
56. Tassara, E.; Orel, B.; Ilan, M.; Cavallo, D.; Dodero, A.; Castellano, M.; Vicini, S.; Giovine, M.; Pozzolini, M. Seasonal Molecular Difference in Fibrillar Collagen Extracts Derived from the Marine Sponge Chondrosia Reniformis (Nardo, 1847) and Their Impact on Its Derived Biomaterials. *Mar. Drugs* **2023**, *21*, 210. [CrossRef] [PubMed]
57. Hong, P.K.; Gottardi, D.; Ndagijimana, M.; Betti, M. Glycation and Transglutaminase Mediated Glycosylation of Fish Gelatin Peptides with Glucosamine Enhance Bioactivity. *Food Chem.* **2014**, *142*, 285–293. [CrossRef] [PubMed]
58. Boute, N.; Exposito, J.Y.; Boury-Esnault, N.; Vacelet, J.; Noro, N.; Miyazaki, K.; Yoshizato, K.; Garrone, R. Type IV Collagen in Sponges, the Missing Link in Basement Membrane Ubiquity. *Biol. Cell* **1996**, *88*, 37–44. [CrossRef] [PubMed]
59. Gökalp, M.; Kooistra, T.; Rocha, M.S.; Silva, T.H.; Osinga, R.; Murk, A.J.; Wijgerde, T. The Effect of Depth on the Morphology, Bacterial Clearance, and Respiration of the Mediterranean Sponge Chondrosia Reniformis (Nardo, 1847). *Mar. Drugs* **2020**, *18*, 358. [CrossRef]
60. Calcabrini, C.; Catanzaro, E.; Bishayee, A.; Turrini, E.; Fimognari, C. Marine Sponge Natural Products with Anticancer Potential: An Updated Review. *Mar. Drugs* **2017**, *15*, 310. [CrossRef]
61. Scarfì, S.; Pozzolini, M.; Oliveri, C.; Mirata, S.; Salis, A.; Damonte, G.; Fenoglio, D.; Altosole, T.; Ilan, M.; Bertolino, M.; et al. Identification, Purification and Molecular Characterization of Chondrosin, a New Protein with Anti-Tumoral Activity from the Marine Sponge Chondrosia Reniformis Nardo 1847. *Mar. Drugs* **2020**, *18*, 409. [CrossRef]
62. Foot, N.C. The Masson Trichrome Staining Methods in Routine Laboratory Use. *Biotech. Histochem.* **1933**, *8*, 101–110. [CrossRef]
63. Junqueira, L.C.U.; Bignolas, G.; Brentani, R.R. Picrosirius Staining plus Polarization Microscopy, a Specific Method for Collagen Detection in Tissue Sections. *Histochem. J.* **1979**, *11*, 447–455. [CrossRef]
64. Lattouf, R.; Younes, R.; Lutomski, D.; Naaman, N.; Godeau, G.; Senni, K.; Changotade, S. Picrosirius Red Staining: A Useful Tool to Appraise Collagen Networks in Normal and Pathological Tissues. *J. Histochem. Cytochem.* **2014**, *62*, 751–758. [CrossRef]

MDPI AG
Grosspeteranlage 5
4052 Basel
Switzerland
Tel.: +41 61 683 77 34
www.mdpi.com

*Marine Drugs* Editorial Office
E-mail: marinedrugs@mdpi.com
www.mdpi.com/journal/marinedrugs

Academic Open
Access Publishing

mdpi.com

ISBN 978-3-7258-2554-7